Methods in Molecular Biology 1271

Springer Protocols

Beata Jastrzebska *Editor*

Rhodopsin

Methods and Protocols

Humana Press

METHODS IN MOLECULAR BIOLOGY

Series Editor
John M. Walker
School of Life and Medical Sciences
University of Hertfordshire
Hatfield, Hertfordshire, AL10 9AB, UK

For further volumes:
http://www.springer.com/series/7651

Rhodopsin

Methods and Protocols

Edited by

Beata Jastrzebska

Department of Pharmacology, School of Medicine, Case Western Reserve University, Cleveland, OH, USA

Humana Press

Editor
Beata Jastrzebska
Department of Pharmacology, School of Medicine
Case Western Reserve University
Cleveland, OH, USA

ISSN 1064-3745 ISSN 1940-6029 (electronic)
Methods in Molecular Biology
ISBN 978-1-4939-2329-8 ISBN 978-1-4939-2330-4 (eBook)
DOI 10.1007/978-1-4939-2330-4

Library of Congress Control Number: 2015931509

Springer New York Heidelberg Dordrecht London

Printed on acid-free paper

Humana Press is a brand of Springer
Springer Science+Business Media LLC New York is part of Springer Science+Business Media (www.springer.com)

Preface

Rhodopsin is a prototypical G protein-coupled receptor (GPCR) that transmits a signal of light across the membrane to initiate a signaling cascade, which results in neuronal responses in the brain and the perception of our surroundings. Over the past several decades, rhodopsin has served as a valuable model system to study GPCR activation, signal transduction, modulation, and desensitization. Rhodopsin is highly expressed in rod outer segment (ROS) membranes, structures composed of stacked disc membranes surrounded by a plasma membrane where it constitutes more than 90 % of all disc membrane proteins. Dense packing of rhodopsin is needed for the photoreceptor function and ROS membrane formation. High expression and availability from natural sources, as well as development of novel biochemical and biophysical methods, have made rhodopsin research a leading contributor to understanding GPCR structure and function. In fact, rhodopsin is the first GPCR for which the crystal structure of its native form in the inactive conformation has been solved to atomic resolution.

Technological improvements in protein engineering, expression, purification, and crystallization allowed crystallization of several rhodopsin photoactive intermediates, increasing our understanding of rhodopsin activation. Crystallization efforts were also rewarded by solving the structure of a rhodopsin mutant causing congenital night blindness providing molecular insights into the mechanism of this degenerative disease. Although unquestionably important, these multiple structures of rhodopsin captured in different activation states deliver only a snap-freeze view; therefore development of other, complementary methods, looking into rhodopsin structural dynamics, is necessary to extend our knowledge of the structure-function relationship of this extremely important molecule. Moreover, rhodopsin is an integral component of biological membranes; thus its function is highly influenced by interactions with specific lipids. Therefore, the first few chapters of this volume focus on methods developed to study fundamentals of rhodopsin structure and function, starting with established and improved purification protocols of native and mutated rhodopsin, followed by methods used for rhodopsin reconstitution into lipid bilayers stabilizing rhodopsin functional properties, and finally describing recently developed methods to study structural dynamics of rhodopsin activation and its mechanistic properties.

Development of high-resolution imaging techniques such as atomic force microscopy (AFM) revealed the existence of densely packed rows of rhodopsin dimers in native disc membranes, and its propensity to self-associate was confirmed by many other biophysical and biochemical approaches challenging the simplified view of rhodopsin as a single mobile signaling molecule freely diffusing in the membrane. Although not quite yet understood, this higher order organization of rhodopsin presumably has major implications for the mechanism of signal transduction. Therefore, the next few chapters underline techniques that have been developed to visualize the rhodopsin dimer and to study its functional significance.

Every day numerous copies of new rhodopsin molecules are produced to replace the ones phagocytized by the RPE (retinal pigment epithelium) cells in daily shedding of mature photoreceptors. These newly synthesized rhodopsins must be transported from the

cell body to the base of rod outer segments where they are utilized in generating new photoreceptor discs. Rhodopsin trafficking is highly dynamic and precisely controlled by various protein chaperons. Lack of this precision can lead to rhodopsin mislocalization and ultimately to photoreceptor degenerative diseases. Significant progress has been recently made in monitoring of rhodopsin trafficking in live cells and in high-resolution imaging of cellular compartments essential for rhodopsin delivery to the rod outer segments; thus useful protocols to study these topics are presented in the next chapters.

Finally, dysfunction of rhodopsin leads to visual impairments. Thus, the last few chapters of this book present developments potentially beneficial in patient treatments. To sustain vision continuos regeneration of the visual chromophore 11-cis-retinal is critical and is achieved in so-called 'visual cycle' present in the photoreceptors and the retinal pigmented epithelium (RPE). Functional defects of any key enzyme involved in this cycle are associated with various retinal degenerative diseases. One such disease is Leber congenital amaurosis (LCA), which causes severe visual impairment due to mutations either in lecithin/retinol acyltransferase (LRAT) or epithelium-specific 65 KDa protein (RPE65). Currently LCA is incurable. However, the substantial efforts taken toward finding a cure for this disease suggest that retinoid supplementation can be a promising strategy to improve visual sensations.

Other devastating human visual disorders are retinitis pigmentosa (RP) and congenital stationary night blindness (CSNB), caused by numerous missense and nonsense mutations in the rhodopsin gene. Gene therapy utilizing replacement of the defective gene is one of the potential strategies to prevent photoreceptor death. Another possibility is an intense search for small molecule compounds with protective effects alleviating symptoms of the disease. Therefore, the final chapters are devoted to treatment strategies for retinal degenerative diseases.

I thank all the authors for their insightful contributions to this volume of Methods in Molecular Biology and their willingness to provide timely protocols useful to study structural and functional properties of rhodopsin.

Cleveland, OH, USA *Beata Jastrzebska*

Contents

Preface . . . . . *v*
Contributors . . . . . *xi*

PART I HISTORICAL OVERVIEW

1 The G Protein-Coupled Receptor Rhodopsin: A Historical Perspective 3
Lukas Hofmann and Krzysztof Palczewski

PART II RHODOPSIN EXPRESSION, REGENERATION, AND PURIFICATION FOR STRUCTURAL STUDIES

2 Rhodopsin Purification from Dark-Adapted Bovine Retina 21
Elise Blankenship and David T. Lodowski

3 Mammalian Expression, Purification, and Crystallization of Rhodopsin Variants 39
Daniel Mattle, Ankita Singhal, Georg Schmid, Roger Dawson, and Jörg Standfuss

4 Imaging of Rhodopsin Crystals with Two-Photon Microscopy 55
Grazyna Palczewska and David Salom

PART III STRUCTURE–FUNCTION CHARACTERIZATION OF RHODOPSIN

5 Functional Stability of Rhodopsin in a Bicelle System: Evaluating G Protein Activation by Rhodopsin in Bicelles 67
Ali I. Kaya, T.M. Iverson, and Heidi E. Hamm

6 The Rhodopsin-Arrestin-1 Interaction in Bicelles 77
Qiuyan Chen, Sergey A. Vishnivetskiy, Tiandi Zhuang, Min-Kyu Cho, Tarjani M. Thaker, Charles R. Sanders, Vsevolod V. Gurevich, and T.M. Iverson

7 Detection of Structural Waters and Their Role in Structural Dynamics of Rhodopsin Activation 97
Liwen Wang and Mark R. Chance

8 Probing Conformational Changes in Rhodopsin Using Hydrogen-Deuterium Exchange Coupled to Mass Spectrometry 113
Tivadar Orban and Yaroslav Tsybovsky

9 Analysis of Conformational Changes in Rhodopsin by Histidine Hydrogen–Deuterium Exchange 123
David T. Lodowski and Masaru Miyagi

10 Investigation of Rhodopsin Dynamics in Its Signaling State by Solid-State Deuterium NMR Spectroscopy 133
Andrey V. Struts, Udeep Chawla, Suchithranga M.D.C. Perera, and Michael F. Brown

11 Sequential Structural Changes in Rhodopsin Occurring upon Photoactivation 159
Naoki Kimata, Andreyah Pope, Dawood Rashid, Philip J. Reeves, and Steven O. Smith

12 Dynamic Single-Molecule Force Spectroscopy of Rhodopsin in Native Membranes 173
Paul S.-H. Park and Daniel J. Müller

Part IV Rhodopsin Supramolecular Organization and Its Complexes with Partner Proteins

13 High-Resolution Atomic Force Microscopy Imaging of Rhodopsin in Rod Outer Segment Disk Membranes 189
Patrick D. Bosshart, Andreas Engel, and Dimitrios Fotiadis

14 Detection of Rhodopsin Dimerization In Situ by PIE-FCCS, a Time-Resolved Fluorescence Spectroscopy 205
Adam W. Smith

15 Oligomeric State of Rhodopsin Within Rhodopsin–Transducin Complex Probed with Succinylated Concanavalin A 221
Beata Jastrzebska

16 Quantification of Arrestin–Rhodopsin Binding Stoichiometry 235
Ciara C.M. Lally and Martha E. Sommer

17 Rhodopsin Transient Complexes Investigated by Systems Biology Approaches 251
Daniele Dell'Orco

Part V Rhodopsin and Photoreceptors

18 Three-Dimensional Architecture of Murine Rod Cilium Revealed by Cryo-EM 267
Theodore G. Wensel and Jared C. Gilliam

19 Monitoring of Rhodopsin Trafficking and Mistrafficking in Live Photoreceptors 293
Kerrie H. Lodowski and Yoshikazu Imanishi

20 Measurements of Rhodopsin Diffusion Within Signaling Membrane Microcompartments in Live Photoreceptors 309
Mehdi Najafi and Peter D. Calvert

Part VI Treatment Strategies of Retinal Degenerative Disease

21 Kinetics of Rhodopsin's Chromophore Monitored in a Single Photoreceptor 327
Leopold Adler IV, Nicholas P. Boyer, Chunhe Chen, and Yiannis Koutalos

22 Supplementation with Vitamin A Derivatives to Rescue Vision in Animal Models of Degenerative Retinal Diseases 345
Lindsay Perusek, Akiko Maeda, and Tadao Maeda

23 Sustained Delivery of Retinoids to Prevent Photoreceptor Death 363
Peter H. Tang and Rosalie K. Crouch

24 High-Throughput Screening Assays to Identify Small Molecules Preventing Photoreceptor Degeneration Caused by the Rhodopsin P23H Mutation 369
Yuanyuan Chen and Hong Tang

25 Gene Therapy to Rescue Retinal Degeneration Caused by Mutations in Rhodopsin 391
Brian P. Rossmiller, Renee C. Ryals, and Alfred S. Lewin

Index *411*

Contributors

Leopold Adler IV • *Departments of Ophthalmology and Neurosciences, Medical University of South Carolina, Charleston, SC, USA*

Elise Blankenship • *Case Center for Proteomics and Bioinformatics, School of Medicine, Case Western Reserve University, Cleveland, OH, USA*

Patrick D. Bosshart • *Institute of Biochemistry and Molecular Medicine, University of Bern, Bern, Switzerland; Swiss National Centre of Competence in Research (NCCR) TransCure, University of Bern, Bern, Switzerland*

Nicholas P. Boyer • *Departments of Ophthalmology and Neurosciences, Medical University of South Carolina, Charleston, SC, USA*

Michael F. Brown • *Department of Chemistry and Biochemistry, University of Arizona, Tucson, AZ, USA; Department of Physics, University of Arizona, Tucson, AZ, USA*

Peter D. Calvert • *Department of Ophthalmology and the Center for Vision Research, State University of New York Upstate Medical University, Syracuse, NY, USA; Departments of Biochemistry and Molecular Biology, State University of New York Upstate Medical University, Syracuse, NY, USA; Department of Neuroscience and Physiology, State University of New York Upstate Medical University, Syracuse, NY, USA; SUNY Eye Institute, State University of New York Upstate Medical University, Syracuse, NY, USA*

Mark R. Chance • *Center for proteomics and Bioinformatics, School of Medicine, Case Western Reserve University, Cleveland, OH, USA*

Udeep Chawla • *Department of Chemistry and Biochemistry, University of Arizona, Tucson, AZ, USA*

Chunhe Chen • *Departments of Ophthalmology and Neurosciences, Medical University of South Carolina, Charleston, SC, USA*

Qiuyan Chen • *Department of Pharmacology, Vanderbilt University Medical Center, Nashville, TN, USA*

Yuanyuan Chen • *Department of Pharmacology, School of Medicine, Case Western Reserve University, Cleveland, OH, USA*

Min-Kyu Cho • *Department of Biochemistry, Vanderbilt University Medical Center, Nashville, TN, USA; Department of Chemistry, New York University, New York, NY, USA*

Rosalie K. Crouch • *Department of Ophthalmology, Storm Eye Institute, Medical University of South Carolina, Charleston, SC, USA*

Roger Dawson • *F. Hoffmann-La Roche AG, Pharma Research and Early Development (pRED), Small Molecule Research, Discovery Technologies, Basel, Switzerland*

Daniele Dell'Orco • *Department of Life Sciences and Reproduction, Section of Biological Chemistry, University of Verona, Verona, Italy*

Andreas Engel • *Department of Pharmacology, School of Medicine, Case Western Reserve University, Cleveland, OH, USA; Department of Bionanoscience, Kavli Institute of Nanoscience, Delft University of Technology, Delft, The Netherlands*

Dimitrios Fotiadis • *Institute of Biochemistry and Molecular Medicine, University of Bern, Bern, Switzerland; Swiss National Centre of Competence in Research (NCCR) TransCure, University of Bern, Bern, Switzerland*

Jared C. Gilliam • *Department of Systems Medicine and Bioengineering, Houston Methodist Research Institute, Houston, TX, USA*
Vsevolod V. Gurevich • *Department of Pharmacology, Vanderbilt University Medical Center, Nashville, TN, USA*
Heidi E. Hamm • *Department of Pharmacology, Vanderbilt University Medical Center, Nashville, TN, USA*
Lukas Hofmann • *Department of Pharmacology, School of Medicine, Case Western Reserve University, Cleveland, OH, USA; Cleveland Center for Membrane and Structural Biology, School of Medicine, Case Western Reserve University, Cleveland, OH, USA*
Yoshikazu Imanishi • *Department of Pharmacology, School of Medicine, Case Western Reserve University, Cleveland, OH, USA*
T.M. Iverson • *Department of Pharmacology, Vanderbilt University Medical Center, Nashville, TN, USA; Department of Biochemistry, Vanderbilt University Medical Center, Nashville, TN, USA*
Beata Jastrzebska • *Department of Pharmacology, School of Medicine, Case Western Reserve University, Cleveland, OH, USA*
Ali I. Kaya • *Department of Pharmacology, Vanderbilt University Medical Center, Nashville, TN, USA*
Naoki Kimata • *Department of Biochemistry and Cell Biology, Stony Brook University, Stony Brook, NY, USA*
Yiannis Koutalos • *Departments of Ophthalmology and Neurosciences, Medical University of South Carolina, Charleston, SC, USA*
Ciara C.M. Lally • *Institut für Medizinische Physik und Biophysik (CC2), Charité—Universitätsmedizin Berlin, Berlin, Germany*
Alfred S. Lewin • *Department of Molecular Genetics and Microbiology, University of Florida, Gainesville, FL, USA*
David T. Lodowski • *Case Center for Proteomics and Bioinformatics, School of Medicine, Case Western Reserve University, Cleveland, OH, USA; Department of Pharmacology, School of Medicine, Case Western Reserve University, Cleveland, OH, USA*
Kerrie H. Lodowski • *Department of Pharmacology, School of Medicine, Case Western Reserve University, Cleveland, OH, USA*
Akiko Maeda • *Department of Ophthalmology and Visual Sciences, School of Medicine, Case Western Reserve University, Cleveland, OH, USA; Department of Pharmacology, School of Medicine, Case Western Reserve University, Cleveland, OH, USA*
Tadao Maeda • *Department of Ophthalmology and Visual Sciences, School of Medicine, Case Western Reserve University, Cleveland, OH, USA; Department of Pharmacology, School of Medicine, Case Western Reserve University, Cleveland, OH, USA*
Daniel Mattle • *Laboratory of Biomolecular Research, Paul Scherrer Institute, Villigen, Switzerland; F. Hoffmann-La Roche AG, Pharma Research and Early Development (pRED), Small Molecule Research, Discovery Technologies, Basel, Switzerland*
Masaru Miyagi • *Case Center for Proteomics and Bioinformatics, School of Medicine, Case Western Reserve University, Cleveland, OH, USA*
Daniel J. Müller • *Department of Biosystems Science and Engineering, Basel, Switzerland*
Mehdi Najafi • *Department of Ophthalmology and the Center for Vision Research, State University of New York Upstate Medical University, Syracuse, NY, USA*
Tivadar Orban • *Department of Pharmacology, School of Medicine, Case Western Reserve University, Cleveland, OH, USA*
Grazyna Palczewska • *Polgenix Inc., Cleveland, OH, USA*

Krzysztof Palczewski • *Department of Pharmacology, School of Medicine, Case Western Reserve University, Cleveland, OH, USA; Cleveland Center for Membrane and Structural Biology, School of Medicine, Case Western Reserve University, Cleveland, OH, USA*
Paul S.-H. Park • *Department of Ophthalmology and Visual Sciences, Case Western Reserve University, Cleveland, OH, USA*
Suchithranga M.D.C. Perera • *Department of Chemistry and Biochemistry, University of Arizona, Tucson, AZ, USA*
Lindsay Perusek • *Department of Ophthalmology and Visual Sciences, School of Medicine, Case Western Reserve University, Cleveland, OH, USA*
Andreyah Pope • *Department of Biochemistry and Cell Biology, Stony Brook University, Stony Brook, NY, USA*
Dawood Rashid • *Department of Biochemistry and Cell Biology, Stony Brook University, Stony Brook, NY, USA*
Philip J. Reeves • *Department of Biological Sciences, University of Essex, Essex, UK*
Brian P. Rossmiller • *Department of Molecular Genetics and Microbiology, University of Florida, Gainesville, FL, USA*
Renee C. Ryals • *Department of Opthalmology, University of Florida, Gainesville, FL, USA*
David Salom • *Polgenix Inc., Cleveland, OH, USA; Department of Pharmacology, School of Medicine, Case Western Reserve University, Cleveland, OH, USA*
Charles R. Sanders • *Department of Biochemistry, Vanderbilt University Medical Center, Nashville, TN, USA*
Georg Schmid • *F. Hoffmann-La Roche AG, Pharma Research and Early Development (pRED), Small Molecule Research, Discovery Technologies, Basel, Switzerland*
Ankita Singhal • *Laboratory of Biomolecular Research, Paul Scherrer Institute, Villigen, Switzerland*
Adam W. Smith • *Department of Chemistry, University of Akron, Akron, OH, USA*
Steven O. Smith • *Department of Biochemistry and Cell Biology, Stony Brook University, Stony Brook, NY, USA*
Martha E. Sommer • *Institut für Medizinische Physik und Biophysik (CC2), Charité—Universitätsmedizin Berlin, Berlin, Germany*
Jörg Standfuss • *Laboratory of Biomolecular Research, Paul Scherrer Institute, Villigen, Switzerland*
Andrey V. Struts • *Department of Chemistry and Biochemistry, University of Arizona, Tucson, AZ, USA; Laboratory of Biomolecular NMR, St. Petersburg State University, St. Petersburg, Russia*
Hong Tang • *Drug Discovery Center, College of Medicine, University of Cincinnati, Cincinnati, OH, USA*
Peter H. Tang • *Department of Ophthalmology and Visual Neurosciences, University of Minnesota, Minneapolis, MN, USA*
Tarjani M. Thaker • *Department of Biochemistry, Vanderbilt University Medical Center, Nashville, TN, USA; Department of Cellular and Molecular Pharmacology, University of California San Francisco, San Francisco, CA, USA*
Yaroslav Tsybovsky • *Department of Pharmacology, School of Medicine, Case Western Reserve University, Cleveland, OH, USA*
Sergey A. Vishnivetskiy • *Department of Pharmacology, Vanderbilt University Medical Center, Nashville, TN, USA*
Liwen Wang • *Center for Proteomics and Bioinformatics, School of Medicine, Case Western Reserve University, Cleveland, OH, USA*

Theodore G. Wensel • *Department of Biochemistry and Molecular Biology, Baylor College of Medicine, Houston, TX, USA*
Tiandi Zhuang • *Department of Biochemistry, Vanderbilt University Medical Center, Nashville, TN, USA; Department of Molecular Physiology and Biological Physics, University of Virginia, Charlottesville, VA, USA*

Part I

Historical Overview

Chapter 1

The G Protein-Coupled Receptor Rhodopsin: A Historical Perspective

Lukas Hofmann and Krzysztof Palczewski

Abstract

Rhodopsin is a key light-sensitive protein expressed exclusively in rod photoreceptor cells of the retina. Failure to express this transmembrane protein causes a lack of rod outer segment formation and progressive retinal degeneration, including the loss of cone photoreceptor cells. Molecular studies of rhodopsin have paved the way to understanding a large family of cell-surface membrane proteins called G protein-coupled receptors (GPCRs). Work started on rhodopsin over 100 years ago still continues today with substantial progress made every year. These activities underscore the importance of rhodopsin as a prototypical GPCR and receptor required for visual perception—the fundamental process of translating light energy into a biochemical cascade of events culminating in vision.

Key words Rhodopsin, Rod cell(s), Phototransduction, G protein-coupled receptor(s), Receptor phosphorylation, Structure of membrane proteins, Signal transduction

1 Introduction

Molecular studies of rhodopsin began with the work of German physiologist Friedrich Wilhelm Kühne (1837–1900) who extracted rhodopsin from bovine retina with a precursor of modern detergent bile salts [1]. This scientist made the critical observation that rhodopsin's red color faded after exposure to light in the visible range. Denatured by organic solvents but not by salt, rhodopsin could be precipitated out of aqueous solutions with ammonium sulfate, a strategy used later for crystallization of this transmembrane protein [2, 3].

From early work it was clear that rhodopsin's red color could be restored when an illuminated retina was placed on the retinal pigmented epithelium (RPE), a monolayer of cells located in the back of the eye [1]. This regenerative process, known as the visual or retinoid cycle, is achieved by a series of enzymatic reactions that regenerate the light-sensitive chromophore [4]. The identity of the chromophore, the light-sensitive 11-*cis*-retinal ligand of rhodopsin, was not discovered until the work of George Wald [5].

Beata Jastrzebska (ed.), *Rhodopsin: Methods and Protocols*, Methods in Molecular Biology, vol. 1271,
DOI 10.1007/978-1-4939-2330-4_1,

Since ancient times it was known that absence of carotenoids in a diet lacking retinoids could lead to progressive retinal degeneration and blindness. But it was Wald who provided chemical evidence that rhodopsin is composed of two elements: an apoprotein opsin and a prosthetic, covalently linked 11-*cis*-retinal [6–8]. First, bleaching of rhodopsin caused isomerization of the chromophore to the all-*trans*-isomer that eventually was released from the binding pocket of rhodopsin [9]. Then the spent chromophore was recycled back through the retinoid cycle to regenerate the photoactive chromophore which recombined with opsin.

The color of rhodopsin is derived from the chromophore 11-*cis*-retinal, but surprisingly this chromophore absorbs light at 360 nm rather than at 500 nm like rhodopsin. This shift is caused by interaction of the chromophore with the protein and is termed the "opsin shift." Interactions of this universal chromophore of vision with other visual pigment apoproteins also lead to significantly shorter (hypsochromic) and longer wavelength (bathochromic) light absorption shifts producing the "spectral tuning" of cone pigments. The protonated Schiff base linkage of 11-*cis*-retinal with opsin [7, 10, 11] is critical for specifically tuning its spectral absorbance.

Exposure of rhodopsin to light leads to the highly unstable intermediates metarhodopsin I (Meta I) and metarhodopsin II (Meta II) that achieve an equilibrium between these two states within milliseconds [7]. Meta II is the signaling form of rhodopsin that subsequently interacts with the G protein transducin, rhodopsin kinase (GRK1), and arrestin (reviewed in ref. 12, 13).

Though rhodopsin has been studied by almost all molecular techniques, there is still more to discover. Our level of understanding increases as novel approaches are developed. With its exquisite sensitivity to detect a single photon of light in a highly reproducible way, rhodopsin provides our scotopic window to the world. As such, rhodopsin comprises the center of our interest, and hopefully this series of articles will provide inspiration for pursuing all remaining unanswered questions about this molecular complex.

2 Expression Systems

The rhodopsin transcript is among the most highly expressed in the eye and retina, accounting for 9,114 and 11,745 normalized fragments per kilobase of exon per million mapped reads (FPKM), respectively [14]. The retina is a neuronal tissue composed of several cell types but rods constitute about 80 % (or about 10^8 photoreceptor cells) of the cells in the human, mouse, and bovine retina [15, 16]. Once expressed, rhodopsin is transported to and inserted in elongated cilia called rod outer segments (ROS), which consist of stacks of 600–1,600 independent disk membranes surrounded by a

plasma membrane. Rhodopsin is the major protein in rod outer segment membranes (>90 % with a 5 mM concentration within ROS) [17]. This high abundance in membranes of a native source was initially one of the main attractions of this GPCR. The amount of material isolated from just one bovine retina was about 0.5–1 mg of protein [18]. The native protein also lacked any artifacts generated by heterologous expression systems (such as changes in post-translational modifications), making the study of native rhodopsin highly relevant to mammalian/human physiology. Expression of this protein in other model systems was also needed to probe its structure using mutagenesis, but the key to these approaches was rhodopsin's reliable expression and purification. Toward this goal the most critical work was pioneered by Oprian and colleagues [19]. A number of mutagenesis studies followed, including spin labeling of Cys residues throughout the rhodopsin structure [20] and employment of unnatural amino acids to obtain structural information by the Sakmar group [21, 22]. Today, rhodopsin can be expressed in heterologous systems ranging from transformed cells to whole organisms such as *Caenorhabditis elegans* [23]. Because in heterologous systems rhodopsin can couple to Go/I, illumination causes a sudden and transient loss of worm motility dependent on cyclic adenosine monophosphate [24].

3 Three-Dimensional Structure of Rhodopsin

The high expression level and newly developed purification methods for rhodopsin led to the first crystallization of any GPCR [25]. For the first time, a single study revealed the internal organization of rhodopsin at amino acid resolution. Much has been written about the structure of rhodopsin as an archetypical membrane-bound GPCR [12, 18, 20, 26–28], and there is no need to repeat it here. As predicted, rhodopsin is composed of seven-transmembrane α-helical segments embedded in the plasma membrane with an almost equally distributed mass between the extracellular (intradiscal) and intracellular domains. The chromophore is embedded in the hydrophobic region, about 2/3 of the way from the cytoplasmic surface (Fig. 1). Many other GPCR structures followed that of rhodopsin crystallized under different conditions or as photoactivated intermediate states [29–42] (recently reviewed in ref. 43).

4 Posttranslational Modifications of Rhodopsin

The amino acid sequence of opsin was determined by the laboratories of Ovchinnikov [44] and Hargrave [45]. It was noted that rhodopsin's predicted topology resembles that of bacteriorhodopsin [44].

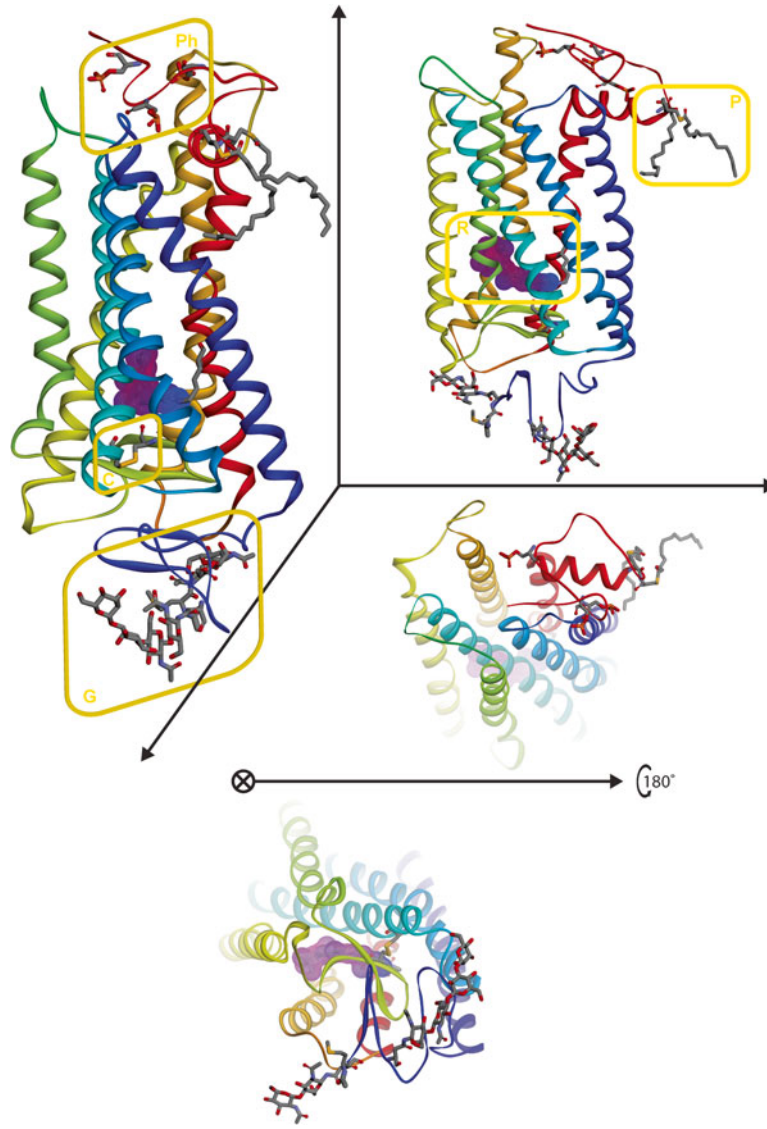

Fig. 1 Three-dimensional structure of rhodopsin. Rhodopsin is depicted in a perspective with *x*, *y*, and *z* axes with structures colored in *blue* to *red* from the N- to C-termini in a ribbon representation. Posttranslational modifications are highlighted with *yellow panels*. *P* palmitoylation, *R* 11-*cis*-N-retinylidene-Lys, *Ph* phosphorylation, *C* disulfide bond, and *G* glycosylation

Once the sequence was obtained, it became possible to assemble the seven-transmembrane helix topology and posttranslational modifications of this protein required for its function (Figs. 2, 3, 4, 5, and 6).

4.1 Disulfide Bridge

The primary sequences of GPCRs are highly diverse [46] but structurally very similar [43], with frequently conserved specific features. One of these is the extracellular disulfide bridge that connects loop

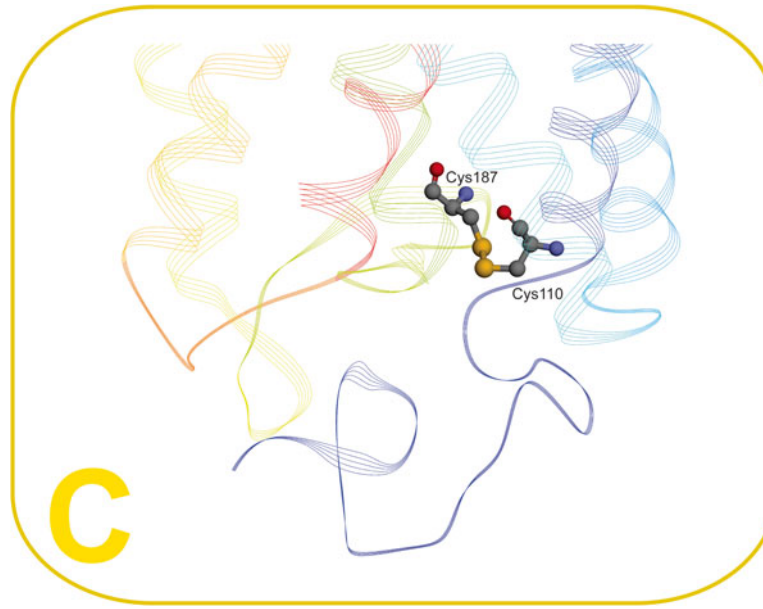

Fig. 2 Conserved disulfide bonds in rhodopsin. Conserved disulfide bonds are found in many family A GPCRs between Cys187 and Cys110. Rhodopsin is colored in *blue* to *red* from N- to the C-terminus in a wire representation. Cys residues are shown in a *scaled ball* and *stick* representation according to element color

II to helix III (Fig. 2) [47]. This bridge between Cys-110 and Cys-187 is essential for the correct tertiary structure of the protein [48, 49]. In rhodopsin, this part also forms a "plug" underneath the chromophore. When this disulfide bridge is formed remains to be determined, so it could be a co-translational rather than a posttranslational modification.

4.2 Palmitoylation and Acylation

Among class A GPCRs, most contain single- and double-Cys residues at the end of cytoplasmic helix 8 that are frequently, if not always, palmitoylated. Rhodopsin is double palmitoylated (Fig. 3) [50, 51]. The palmitoylated Cys residues are close to the NPxxY region, which suggests they are important for activation. Separate in vivo studies indicate they are also important for the structural integrity of the protein [52]. It is unclear if S-palmitoylation is an enzymatic or nonenzymatic reaction in vivo. In addition to S-acylation at these Cys residues, the N-terminus is acetylated as well (Fig. 4).

4.3 Glycosylation

Glycosylation of family A GPCRs usually occurs at the N-terminal end and extracellular side of these receptors. As in other GPCRs, rhodopsin is glycosylated at the (N-X-S/T) site or, more precisely, at the two Asn2 and Asn15 residues located within the N-terminal region [53–55] (Fig. 4). N-terminal glycosylation, especially at Asn15, is crucial for proper folding and function of rhodopsin [53].

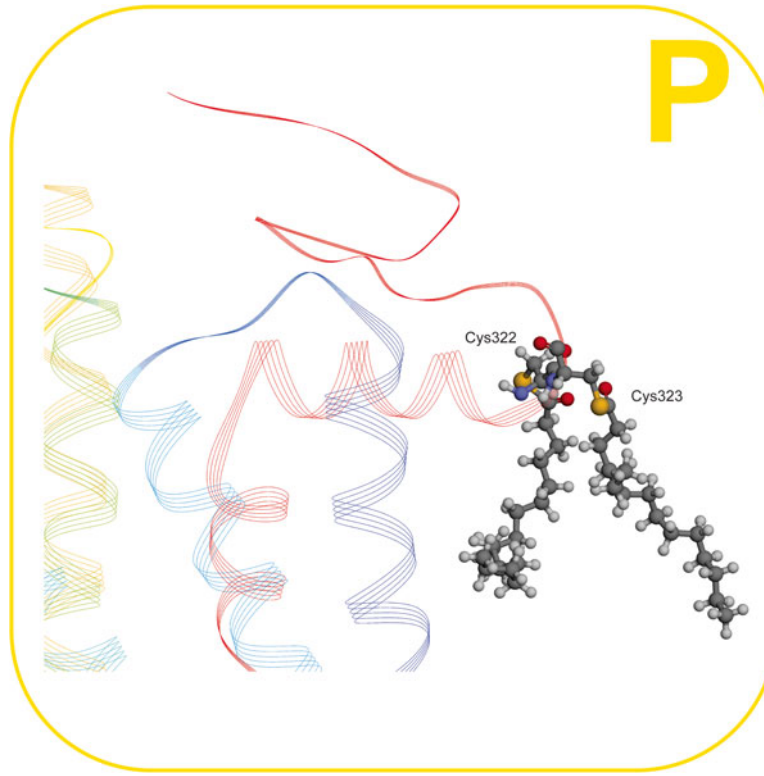

Fig. 3 Palmitoylation sites on rhodopsin. Palmitoylation of rhodopsin takes place at the C-terminus on Cys322 and Cys323 portrayed in a s*caled ball stick* representation according to element colors. Rhodopsin is colored in *blue* to *red* from N- to the C-terminus in a *wire* representation

Furthermore, it has been reported that the N15S mutation causes autosomal dominant retinitis pigmentosa in humans due to the lack of glycosylation [56]. Thus, glycosylation of rhodopsin and members of family A GPCRs in general is essential for the transportation and function of these receptors. It was believed that the core structure of $(Man)_3(GlcNAc)_2$ is fairly uniform [57], but recently more sensitive methods have revealed some heterogeneity of the glycosylation modifications at both sites [58].

5 Regeneration with *Cis*-Chromophores

Rhodopsin forms a permanent Schiff base linkage with only some *cis*-retinals. Though the native chromophore is 11-*cis*-retinal (Fig. 5), visual pigment in biochemical assays can be formed with 9-*cis*-retinal (isorhodopsin), 7-*cis*-retinal, and some of the double *cis*-retinals, but not with 13-*cis*-retinal. Many retinal analogs have been successfully used to probe rhodopsin photoactivation

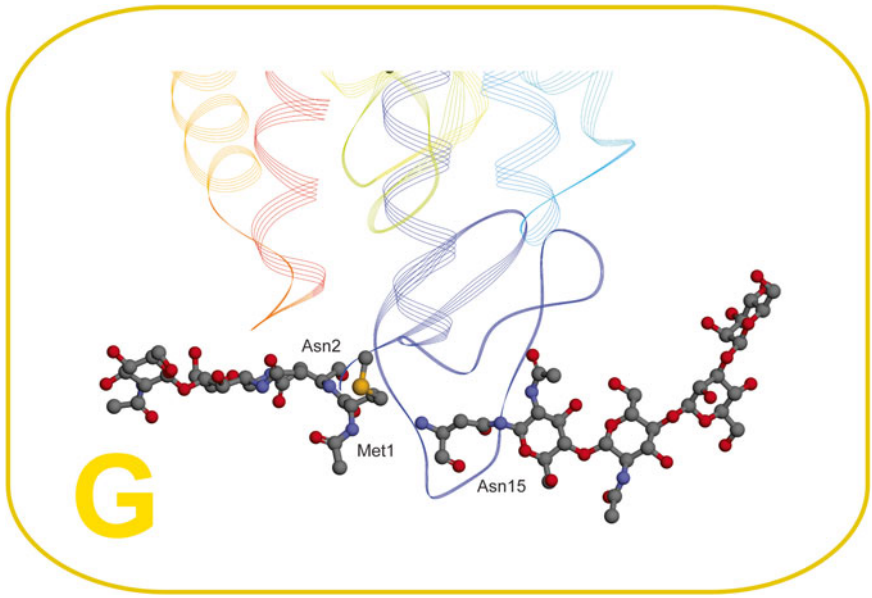

Fig. 4 Glycosylation sites on rhodopsin. Glycosylation sites on rhodopsin are located at Asn2 and Asn 15 of the N-terminus. The N-terminal Met1 is acetylated and depicted in a *scaled ball stick* representation according to element colors. Rhodopsin is colored in *blue* to *red* from the N- to C-terminus in a *wire* representation

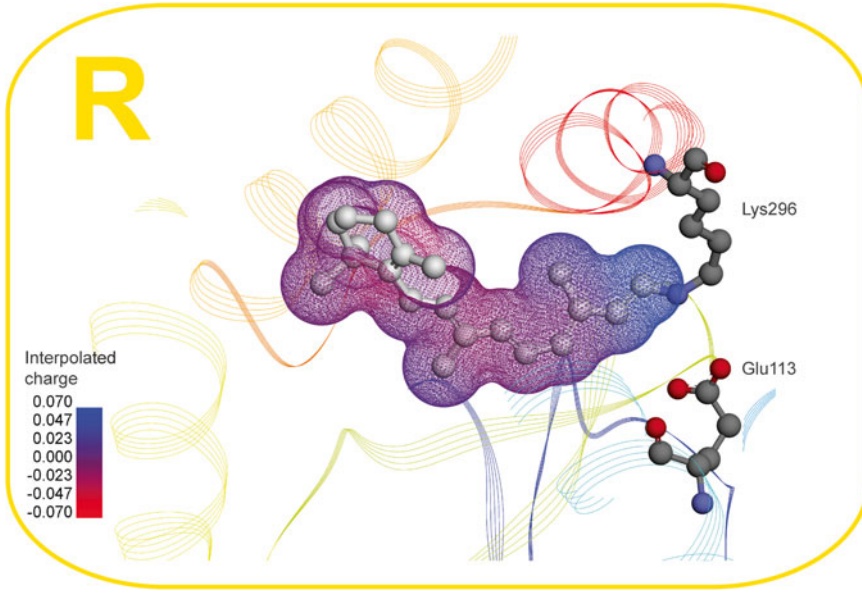

Fig. 5 The chromophore-binding site of rhodopsin. The 11-*cis*-retinal chromophore is covalently attached to rhodopsin via a Schiff base at Lys296. The counter ion, Glu113, causes protonation of the Schiff base. 11-*cis*-N-Retinylidene-Lys is depicted in a *scaled ball stick* representation; coloring is according to elements except for the chromophore, which is shown in *white*. The surface of 11-*cis*-N-retinylidene-Lys is portrayed in mesh and stained according to interpolated charges determined with Accelrys Discovery Studio software. Rhodopsin is colored in *blue* to *red* from N- to the C-terminus in a *wire* representation

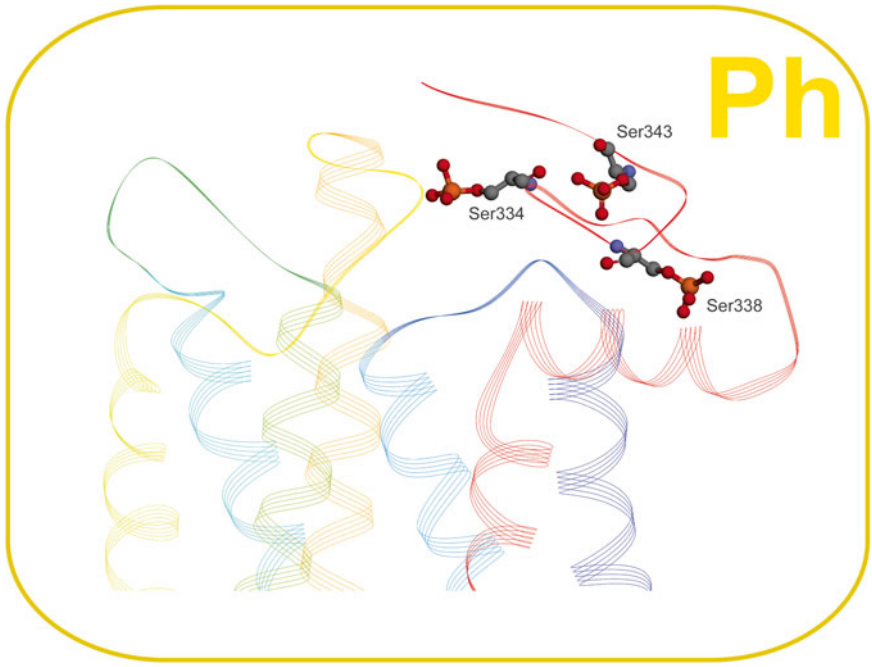

Fig. 6 Phosphorylation sites on rhodopsin. Phosphorylation sites on rhodopsin are localized at the C-terminus on the three Ser334, Ser338, and Ser343 residues shown in a *scaled ball stick* representation according to element colors. Rhodopsin is colored in *blue* to *red* from N- to the C-terminus in a *wire* representation

(e.g., the desmethyl series) [59, 60]. All-*trans*-retinal only increased the basal activity of opsin, but the mechanism is unknown [61]. Regeneration with 9-*cis*-retinal (or derivatives) could have clinical applications when the visual cycle is non-functional as in Leber congenital amaurosis (LCA) [62].

6 Phosphorylation

Rhodopsin phosphorylation was accidently discovered in 1972–1973 when rod outer membranes were incubated with radioactive γ-^{32}P-ATP (reviewed in ref. 63). Today, we know that this is one of the major desensitizing mechanisms of GPCRs. One of the first applications of mass spectrometry in vision research [64], in combination with a specific cleavage of rhodopsin at the C-terminal region by Asp endopeptidase, provided information as to the major site of phosphorylation [65]. Hurley and colleagues showed that photoactivated rhodopsin is repeatedly phosphorylated and dephosphorylated in an ordered fashion [66, 67]. All phosphorylation sites are located in the C-terminal region of rhodopsin. The phosphorylated molecules include Ser334, Ser338, and Ser343 (Fig. 6). Phosphorylation is strictly dependent on photoactivation of rhodopsin and multiple sites can be phosphorylated in photoactivated rhodopsin, contributing to subsequent recognition by arrestin.

7 Photoactivation Mechanism of Rhodopsin

Conformational changes in the opsin moiety occur after rhodopsin is activated by light and the chromophore is isomerized from 11-*cis*-retinylidene to all-*trans*-retinylidene. Generally, these changes were much smaller than anticipated from biophysical studies prior to X-ray crystallography and found mostly in the area of the cytoplasmic end of helix VI (reviewed in ref. 29). Based on solid state NMR data, Brown and colleagues proposed a multiple step activation mechanism and reported helix fluctuations in the Meta I-Meta II equilibrium on a microsecond-to-millisecond timescale [68]. This proposal would simply suggest that rhodopsin becomes more flexible during the activation process, allowing formation of new productive complexes with partner proteins. Perhaps small conformational changes, changes in protonation of the transmembrane and cytoplasmic residues, and an increase in overall dynamics is how rhodopsin achieves a conformation that can induce a specific fit with prebound transducin. Subsequent nucleotide exchange on the α-subunit of the G protein would then activate the visual cascade.

7.1 Water Molecules

Water molecules, perhaps as many as 30, are integral components of rhodopsin. Identified by various methods, these are located within the transmembrane segment of rhodopsin and some are exchangeable with bulk water. However, many are not and likely were incorporated during biogenesis and inserted into the membrane of rhodopsin [69, 70]. Internal waters are located within a cavity that extends from the chromophore to the cytoplasmic surface (Fig. 7). Water is also required for chromophore hydrolysis from all-*trans*-retinylidene [71, 72]. Water is a critical element for the activation process [73] and is involved in multiple steps, including the protonation and deprotonation of key intermolecular sites within the core and cytoplasmic surface of rhodopsin [74]. Importantly, internal water is conserved among all GPCRs, suggesting a universal role for these prosthetic-like groups in receptor activation [75].

8 Conformationally Sensitive Regions

Three regions in rhodopsin were identified that are critical for photoactivation (Fig. 8). All protein and water molecule changes are initiated by chromophore isomerization. This signal is propagated to two independent surface regions, namely, the DRY and NPxxY regions [76]. The latter are also conserved regions among GPCRs, suggesting some commonality in the activation mechanism among these receptors.

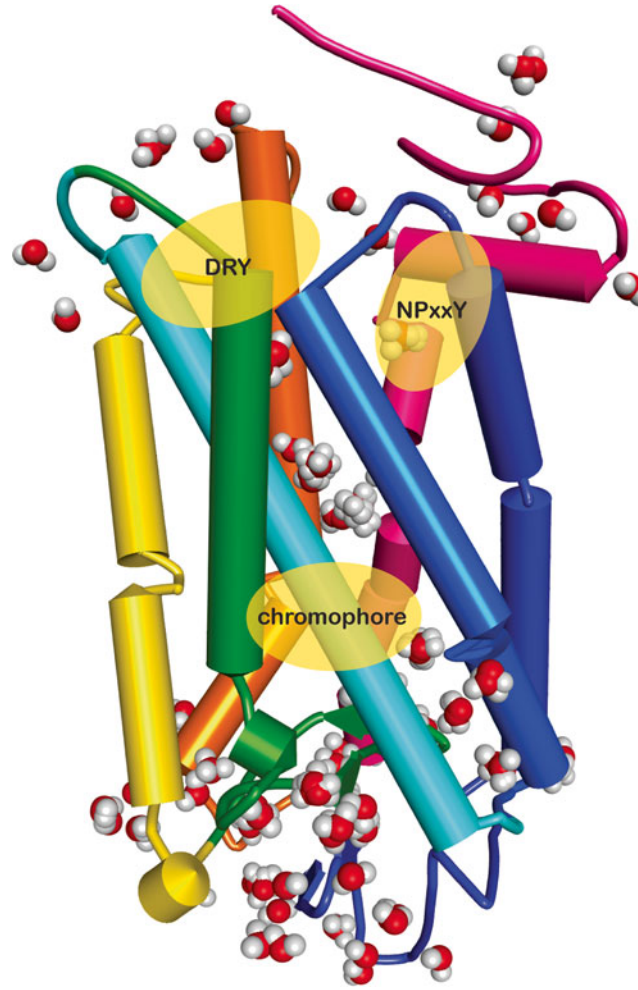

Fig. 7 Water molecules in rhodopsin. Internal water molecules are shown as *spheres* represented with element colors (H, *white*; O, *red*). Water molecules were combined and aligned according to the protein structure derived from ten published rhodopsin coordinates. This picture shows that the waters are distributed throughout rhodopsin in a channel-like alignment. Furthermore, the number of water molecules is greater at the N-terminal cytoplasmic site than at the C-terminal luminal site. The regions DRY, NPxxY, and chromophore, believed to be involved in the activation and transformation of photoactivated rhodopsin, are highlighted with *yellow ovals*. Rhodopsin is colored in *blue* to *red* from N- to the C-terminus in a schematic representation

9 Human Diseases Associated with Mutations in the Opsin Gene

Mutations in the opsin gene can cause a hereditary retinal degenerative disease called retinitis pigmentosa (RP) (RetNet, https://sph.uth.edu/RetNet/) [77]. RP is manifested by progressively decreased vision under low light and loss of peripheral visual fields [78, 79]. To date, more than 100 mutations were identified to be associated with autosomal dominant RP (30–40 % of all cases) [79].

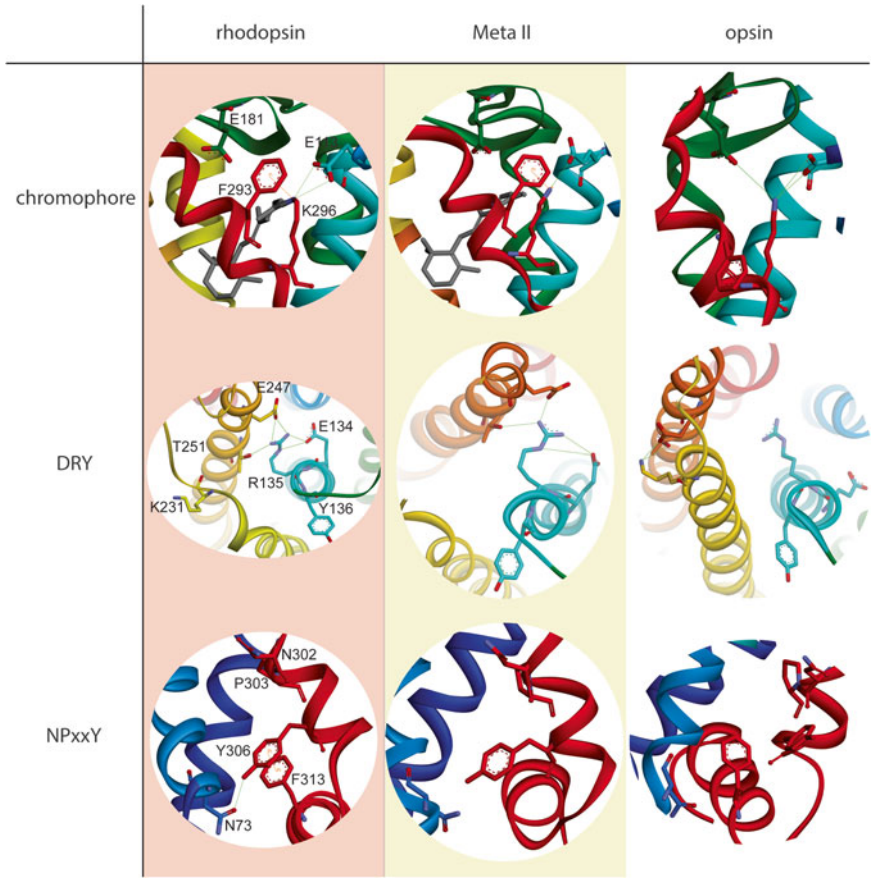

Fig. 8 Key regions within rhodopsin that undergo conformational changes upon photoactivation. The three regions, chromophore, DRY, and NPxxY, believed to be involved in activation and transformation of photoactivated rhodopsin, are shown at three horizontal levels. The different states of rhodopsin, Meta II, and opsin are distributed in the three rows. The amino acids which undergo a significant change in their conformation and/or an interaction between these states are depicted in a *stick* representation. Rhodopsin is colored *blue* to *red* from N- to the C-terminus in a ribbon representation. Changes at the chromophore site are dominated by interactions with Lys296. In the rhodopsin state, Phe293 residue coordinates Lys296 residue via π-interactions, whereas the Asp113 residue stabilizes the positive charge located at the Schiff base. These interactions undergo changes in the Meta II state that finally produce a different rotamer for the Phe293 residue and a coordination of the Lys296 residues through Asp181 and Asp113 residues. Changes found in the DRY motif are dominated by the interactions of Arg135 residues. In the rhodopsin state Arg135 residues are coordinated by Asp247, Asp134, and Thr251 residues. During photoactivation, interactions with Arg135 residues are weakened and finally abolished. Asp247 and Thr251 are found as different rotamers which interact with Lys231 through electrostatic interactions in the opsin state. Changes in the NPxxY motif are mainly found in the hydrogen bond interactions between the Tyr306 and Asp73 residues, whereas this conformation is further stabilized by the π–π interaction between the Tyr306 and Phe313 residues. These interactions are weakened during photoactivation and found abolished in the opsin state

In contrast, the c.448G>A (p.E150K) mutation and severe truncation of the opsin gene are inherited in an autosomal recessive pattern [80, 81]. These inherited diseases remain without a cure, and active research is ongoing to retain the vision and stop the progression of retinal degeneration of those affected [82, 83].

10 Future Directions

In the opinion of these authors, there are five crucial areas for research that have yet to be fully pursued. Judging from the great interest in this receptor, it is only a question of time when a fuller picture of how rhodopsin works will become available.

There is a need to understand how rhodopsin specifically interacts with the G protein transducin, rhodopsin kinase, and arrestin. Although some low resolution studies have been accomplished [84], the most informative would be X-ray structures of these complexes followed by their biophysical probing. No single structure will be fully informative for any of these complexes, as it would represent only one stable conformation trapped in extremely high concentrations of a precipitating agent. But such structures will set the boundaries for possible conformational changes of this receptor. Several of these structures would provide an even fuller picture and possibly the mechanism of activation of these partner proteins. NMR methods could also add much more information about the dynamics of these complexes.

Rhodopsin is a highly dynamic, chromophore-bound protein with intrinsic water molecules. How this receptor and these waters reorganize during activation needs to be solved. Perhaps a combination of computational [85, 86] and NMR studies [68, 87] will dominate in this area of investigation.

Like almost all other GPCRs, rhodopsin forms oligomers in native membranes [88–90]. Here, two questions remain as top priorities. One is how are these rhodopsin molecules specifically arranged in rod outer segment membranes? It is unclear which helices of rhodopsin are involved and form complexes. Perhaps recently developed methodologies [91] will provide tools to answer these questions and provide thermodynamic parameters for these interactions along with their specificities. The measured Kd between two opsin molecules was about 10^{-5} M [91]. Second, what are functional consequences of rhodopsin oligomerization? Improved tools combined with knowledge derived from previous reports [92, 93] are needed to answer this question.

Comparative studies between rhodopsin and cone visual pigments are needed to understand the spectral tuning of these pigments, which use a common chromophore. Again, the first step could involve X-ray crystallography to obtain and analyze the structure of these pigments.

And finally, pharmacological and genetic rescue of mutant rhodopsin molecules should be anticipated. Toward this goal, proper animal models must be generated, as has already been achieved recently with two informative mutations of this receptor [94–96]. Taken together, innovative approaches could bring an end to blinding diseases caused by mutations in the opsin genes.

Thus, there remain many challenges, and much needs to be accomplished!

Acknowledgments

We thank Dr. Leslie T. Webster, Jr., and the members of Palczewski's laboratory for their comments on the manuscript. The work was supported by funding from the National Eye Institute, National Institutes of Health Grants R01EY008061 (to K.P.). K.P. is the John H. Hord Professor of Pharmacology.

References

1. Kuhne W (1977) Chemical processes in the retina. Vision Res 17:1269–1316
2. Salom D, Le Trong I, Pohl E et al (2006) Improvements in G protein-coupled receptor purification yield light stable rhodopsin crystals. J Struct Biol 156:497–504
3. Salom D, Lodowski DT, Stenkamp RE et al (2006) Crystal structure of a photoactivated deprotonated intermediate of rhodopsin. Proc Natl Acad Sci U S A 103:16123–16128
4. Kiser PD, Golczak M, Palczewski K (2014) Chemistry of the retinoid (visual) cycle. Chem Rev 114:194–232
5. Wald G (1968) Molecular basis of visual excitation. Science 162:230–239
6. Wald G (1935) Carotenoids and the visual cycle. J Gen Physiol 19:351–371
7. Hubbard R, Wald G (1952) Cis-trans isomers of vitamin A and retinene in the rhodopsin system. J Gen Physiol 36:269–315
8. Wald G, Brown PK (1953) The molar extinction of rhodopsin. J Gen Physiol 37:189–200
9. Matthews RG, Hubbard R, Brown PK et al (1963) Tautomeric forms of metarhodopsin. J Gen Physiol 47:215–240
10. Zhukovsky EA, Robinson PR, Oprian DD (1992) Changing the location of the Schiff base counterion in rhodopsin. Biochemistry 31:10400–10405
11. Zvyaga TA, Min KC, Beck M et al (1993) Movement of the retinylidene Schiff base counterion in rhodopsin by one helix turn reverses the pH dependence of the metarhodopsin I to metarhodopsin II transition. J Biol Chem 268:4661–4667
12. Palczewski K (2006) G protein-coupled receptor rhodopsin. Annu Rev Biochem 75:743–767
13. Palczewski K (2012) Chemistry and biology of vision. J Biol Chem 287:1612–1619
14. Mustafi D, Maeda T, Kohno H et al (2012) Inflammatory priming predisposes mice to age-related retinal degeneration. J Clin Invest 122:2989–3001
15. Jeon CJ, Strettoi E, Masland RH (1998) The major cell populations of the mouse retina. J Neurosci 18:8936–8946
16. Curcio CA, Sloan KR Jr, Packer O et al (1987) Distribution of cones in human and monkey retina: individual variability and radial asymmetry. Science 236:579–582
17. Nickell S, Park PS, Baumeister W et al (2007) Three-dimensional architecture of murine rod outer segments determined by cryoelectron tomography. J Cell Biol 177:917–925
18. Filipek S, Stenkamp RE, Teller DC et al (2003) G protein-coupled receptor rhodopsin: a prospectus. Annu Rev Physiol 65:851–879
19. Oprian DD, Molday RS, Kaufman RJ et al (1987) Expression of a synthetic bovine rhodopsin gene in monkey kidney cells. Proc Natl Acad Sci U S A 84:8874–8878
20. Hubbell WL, Altenbach C, Hubbell CM et al (2003) Rhodopsin structure, dynamics, and activation: a perspective from crystallography, site-directed spin labeling, sulfhydryl reactivity, and disulfide cross-linking. Adv Protein Chem 63:243–290
21. Grunbeck A, Huber T, Abrol R et al (2012) Genetically encoded photo-cross-linkers map the binding site of an allosteric drug on a G protein-coupled receptor. ACS Chem Biol 7:967–972
22. Daggett KA, Sakmar TP (2011) Site-specific in vitro and in vivo incorporation of molecular probes to study G-protein-coupled receptors. Curr Opin Chem Biol 15:392–398
23. Salom D, Cao P, Sun W et al (2012) Heterologous expression of functional G-protein-coupled receptors in Caenorhabditis elegans. FASEB J 26:492–502
24. Cao P, Sun W, Kramp K et al (2012) Light-sensitive coupling of rhodopsin and melanopsin to G(i/o) and G(q) signal transduction in Caenorhabditis elegans. FASEB J 26:480–491
25. Palczewski K, Kumasaka T, Hori T et al (2000) Crystal structure of rhodopsin: a G protein-coupled receptor. Science 289:739–745

26. Teller DC, Okada T, Behnke CA et al (2001) Advances in determination of a high-resolution three-dimensional structure of rhodopsin, a model of G-protein-coupled receptors (GPCRs). Biochemistry 40:7761–7772
27. Menon ST, Han M, Sakmar TP (2001) Rhodopsin: structural basis of molecular physiology. Physiol Rev 81:1659–1688
28. Smith SO (2010) Structure and activation of the visual pigment rhodopsin. Annu Rev Biophys 39:309–328
29. Park JH, Morizumi T, Li Y et al (2013) Opsin, a structural model for olfactory receptors? Angew Chem Int Ed Engl 52:11021–11024
30. Choe HW, Kim YJ, Park JH et al (2011) Crystal structure of metarhodopsin II. Nature 471:651–655
31. Scheerer P, Park JH, Hildebrand PW et al (2008) Crystal structure of opsin in its G-protein-interacting conformation. Nature 455:497–502
32. Park JH, Scheerer P, Hofmann KP et al (2008) Crystal structure of the ligand-free G-protein-coupled receptor opsin. Nature 454:183–187
33. Park JH, Krauss N, Pulvermuller A et al (2005) Crystallization and preliminary X-ray studies of mouse centrin1. Acta Crystallogr Sect F Struct Biol Cryst Commun 61:510–513
34. Singhal A, Ostermaier MK, Vishnivetskiy SA et al (2013) Insights into congenital stationary night blindness based on the structure of G90D rhodopsin. EMBO Rep 14:520–526
35. Deupi X, Edwards P, Singhal A et al (2012) Stabilized G protein binding site in the structure of constitutively active metarhodopsin-II. Proc Natl Acad Sci U S A 109:119–124
36. Standfuss J, Xie G, Edwards PC et al (2007) Crystal structure of a thermally stable rhodopsin mutant. J Mol Biol 372:1179–1188
37. Li J, Edwards PC, Burghammer M et al (2004) Structure of bovine rhodopsin in a trigonal crystal form. J Mol Biol 343:1409–1438
38. Nakamichi H, Okada T (2007) X-ray crystallographic analysis of 9-cis-rhodopsin, a model analogue visual pigment. Photochem Photobiol 83:232–235
39. Schreiber M, Sugihara M, Okada T et al (2006) Quantum mechanical studies on the crystallographic model of bathorhodopsin. Angew Chem Int Ed Engl 45:4274–4277
40. Nakamichi H, Okada T (2006) Local peptide movement in the photoreaction intermediate of rhodopsin. Proc Natl Acad Sci U S A 103:12729–12734
41. Okada T, Sugihara M, Bondar AN et al (2004) The retinal conformation and its environment in rhodopsin in light of a new 2.2 A crystal structure. J Mol Biol 342:571–583
42. Nakamichi H, Buss V, Okada T (2007) Photoisomerization mechanism of rhodopsin and 9-cis-rhodopsin revealed by x-ray crystallography. Biophys J 92:L106–L108
43. Palczewski K, Orban T (2013) From atomic structures to neuronal functions of g protein-coupled receptors. Annu Rev Neurosci 36: 139–164
44. Ovchinnikov YA (1987) Structure of rhodopsin and bacteriorhodopsin. Photochem Photobiol 45:909–914
45. Hargrave PA (2001) Rhodopsin structure, function, and topography the Friedenwald lecture. Invest Ophthalmol Vis Sci 42:3–9
46. Mirzadegan T, Benko G, Filipek S et al (2003) Sequence analyses of G-protein-coupled receptors: similarities to rhodopsin. Biochemistry 42:2759–2767
47. Applebury ML, Hargrave PA (1986) Molecular biology of the visual pigments. Vision Res 26:1881–1895
48. Karnik SS, Sakmar TP, Chen HB et al (1988) Cysteine residues 110 and 187 are essential for the formation of correct structure in bovine rhodopsin. Proc Natl Acad Sci U S A 85: 8459–8463
49. Karnik SS, Khorana HG (1990) Assembly of functional rhodopsin requires a disulfide bond between cysteine residues 110 and 187. J Biol Chem 265:17520–17524
50. Papac DI, Thornburg KR, Bullesbach EE et al (1992) Palmitylation of a G-protein coupled receptor. Direct analysis by tandem mass spectrometry. J Biol Chem 267:16889–16894
51. Ovchinnikov YA, Abdulaev NG, Bogachuk AS (1988) Two adjacent cysteine residues in the C-terminal cytoplasmic fragment of bovine rhodopsin are palmitylated. FEBS Lett 230:1–5
52. Maeda A, Okano K, Park PS et al (2010) Palmitoylation stabilizes unliganded rod opsin. Proc Natl Acad Sci U S A 107:8428–8433
53. Kaushal S, Ridge KD, Khorana HG (1994) Structure and function in rhodopsin: the role of asparagine-linked glycosylation. Proc Natl Acad Sci U S A 91:4024–4028
54. Wheatley M, Wootten D, Conner MT et al (2012) Lifting the lid on GPCRs: the role of extracellular loops. Br J Pharmacol 165: 1688–1703
55. Wheatley M, Hawtin SR (1999) Glycosylation of G-protein-coupled receptors for hormones central to normal reproductive functioning: its occurrence and role. Hum Reprod Update 5:356–364

56. Kranich H, Bartkowski S, Denton MJ et al (1993) Autosomal dominant 'sector' retinitis pigmentosa due to a point mutation predicting an Asn-15-Ser substitution of rhodopsin. Hum Mol Genet 2:813–814
57. Fukuda MN, Papermaster DS, Hargrave PA (1979) Rhodopsin carbohydrate. Structure of small oligosaccharides attached at two sites near the NH2 terminus. J Biol Chem 254: 8201–8207
58. Salom D, Wang B, Dong Z et al (2012) Post-translational modifications of the serotonin type 4 receptor heterologously expressed in mouse rod cells. Biochemistry 51:214–224
59. Crouch RK (1986) Studies of rhodopsin and bacteriorhodopsin using modified retinals. Photochem Photobiol 44:803–807
60. Estevez ME, Kolesnikov AV, Ala-Laurila P et al (2009) The 9-methyl group of retinal is essential for rapid Meta II decay and phototransduction quenching in red cones. J Gen Physiol 134:137–150
61. Buczylko J, Saari JC, Crouch RK et al (1996) Mechanisms of opsin activation. J Biol Chem 271:20621–20630
62. Palczewski K (2010) Retinoids for treatment of retinal diseases. Trends Pharmacol Sci 31:284–295
63. Maeda T, Imanishi Y, Palczewski K (2003) Rhodopsin phosphorylation: 30 years later. Prog Retin Eye Res 22:417–434
64. Ohguro H, Palczewski K, Ericsson LH et al (1993) Sequential phosphorylation of rhodopsin at multiple sites. Biochemistry 32:5718–5724
65. Palczewski K, Buczylko J, Kaplan MW et al (1991) Mechanism of rhodopsin kinase activation. J Biol Chem 266:12949–12955
66. Kennedy MJ, Lee KA, Niemi GA et al (2001) Multiple phosphorylation of rhodopsin and the in vivo chemistry underlying rod photoreceptor dark adaptation. Neuron 31:87–101
67. Lee KA, Nawrot M, Garwin GG et al (2010) Relationships among visual cycle retinoids, rhodopsin phosphorylation, and phototransduction in mouse eyes during light and dark adaptation. Biochemistry 49:2454–2463
68. Struts AV, Salgado GF, Martinez-Mayorga K et al (2011) Retinal dynamics underlie its switch from inverse agonist to agonist during rhodopsin activation. Nat Struct Mol Biol 18:392–394
69. Renthal R (2008) Buried water molecules in helical transmembrane proteins. Protein Sci 17:293–298
70. Buss V, Sugihara M, Entel P et al (2003) Thr94 and Wat2b effect protonation of the retinal chromophore in rhodopsin. Angew Chem Int Ed Engl 42:3245–3247
71. Jastrzebska B, Palczewski K, Golczak M (2011) Role of bulk water in hydrolysis of the rhodopsin chromophore. J Biol Chem 286:18930–18937
72. Padayatti PS, Wang L, Gupta S et al (2013) A hybrid structural approach to analyze ligand binding by the serotonin type 4 receptor (5-HT4). Mol Cell Proteomics 12:1259–1271
73. Angel TE, Gupta S, Jastrzebska B et al (2009) Structural waters define a functional channel mediating activation of the GPCR, rhodopsin. Proc Natl Acad Sci U S A 106:14367–14372
74. Hofmann KP, Scheerer P, Hildebrand PW et al (2009) A G protein-coupled receptor at work: the rhodopsin model. Trends Biochem Sci 34:540–552
75. Angel TE, Chance MR, Palczewski K (2009) Conserved waters mediate structural and functional activation of family A (rhodopsin-like) G protein-coupled receptors. Proc Natl Acad Sci U S A 106:8555–8560
76. Fritze O, Filipek S, Kuksa V et al (2003) Role of the conserved NPxxY(x)5,6F motif in the rhodopsin ground state and during activation. Proc Natl Acad Sci U S A 100:2290–2295
77. Dryja TP, McGee TL, Reichel E et al (1990) A point mutation of the rhodopsin gene in one form of retinitis pigmentosa. Nature 343:364–366
78. Nathans J (1992) Rhodopsin: structure, function, and genetics. Biochemistry 31: 4923–4931
79. Malanson KM, Lem J (2009) Rhodopsin-mediated retinitis pigmentosa. Prog Mol Biol Transl Sci 88:1–31
80. Rosenfeld PJ, Cowley GS, McGee TL et al (1992) A null mutation in the rhodopsin gene causes rod photoreceptor dysfunction and autosomal recessive retinitis pigmentosa. Nat Genet 1:209–213
81. Kumaramanickavel G, Maw M, Denton MJ et al (1994) Missense rhodopsin mutation in a family with recessive RP. Nat Genet 8:10–11
82. Hamel C (2006) Retinitis pigmentosa. Orphanet J Rare Dis 1:40
83. Hartong DT, Berson EL, Dryja TP (2006) Retinitis pigmentosa. Lancet 368:1795–1809
84. Jastrzebska B, Ringler P, Lodowski DT et al (2011) Rhodopsin-transducin heteropentamer: three-dimensional structure and biochemical characterization. J Struct Biol 176:387–394
85. Sekharan S, Morokuma K (2011) QM/MM study of the structure, energy storage, and origin of the bathochromic shift in vertebrate and

invertebrate bathorhodopsins. J Am Chem Soc 133:4734–4737

86. Gonzalez-Luque R, Garavelli M, Bernardi F et al (2000) Computational evidence in favor of a two-state, two-mode model of the retinal chromophore photoisomerization. Proc Natl Acad Sci U S A 97:9379–9384
87. Mertz B, Struts AV, Feller SE et al (2012) Molecular simulations and solid-state NMR investigate dynamical structure in rhodopsin activation. Biochim Biophys Acta 1818:241–251
88. Liang Y, Fotiadis D, Maeda T et al (2004) Rhodopsin signaling and organization in heterozygote rhodopsin knockout mice. J Biol Chem 279:48189–48196
89. Fotiadis D, Liang Y, Filipek S et al (2003) Atomic-force microscopy: rhodopsin dimers in native disc membranes. Nature 421:127–128
90. Park PS, Filipek S, Wells JW et al (2004) Oligomerization of G protein-coupled receptors: past, present, and future. Biochemistry 43:15643–15656
91. Comar WD, Schubert SM, Jastrzebska B et al (2014) Time-resolved fluorescence spectroscopy measures clustering and mobility of a G protein-coupled receptor opsin in live cell membranes. J Am Chem Soc 136:8342–8349
92. Fotiadis D, Jastrzebska B, Philippsen A et al (2006) Structure of the rhodopsin dimer: a working model for G-protein-coupled receptors. Curr Opin Struct Biol 16:252–259
93. Jastrzebska B, Orban T, Golczak M et al (2013) Asymmetry of the rhodopsin dimer in complex with transducin. FASEB J 27:1572–1584
94. Sakami S, Maeda T, Bereta G et al (2011) Probing mechanisms of photoreceptor degeneration in a new mouse model of the common form of autosomal dominant retinitis pigmentosa due to P23H opsin mutations. J Biol Chem 286:10551–10567
95. Sakami S, Kolesnikov AV, Kefalov VJ et al (2013) P23H opsin knock-in mice reveal a novel step in retinal rod disc morphogenesis. Hum Mol Genet 23:1723–1741
96. Zhang N, Kolesnikov AV, Jastrzebska B et al (2013) Autosomal recessive retinitis pigmentosa E150K opsin mice exhibit photoreceptor disorganization. J Clin Invest 123:121–137

Part II

Rhodopsin Expression, Regeneration, and Purification for Structural Studies

Chapter 2

Rhodopsin Purification from Dark-Adapted Bovine Retina

Elise Blankenship and David T. Lodowski

Abstract

Structural and biophysical studies of rhodopsin have long depended upon the ready availability of bovine retina from the meat-packing industry and the relative ease of obtaining homogenous preparations of rhodopsin in the quantities and purities necessary for such study. Herein we present a modular purification methodology employing a combination of several strategies, beginning with sucrose gradient isolation of rod outer segments (ROS) from bovine retina, detergent solubilization of ROS, selective extraction of rhodopsin starting from this detergent-solubilized ROS, and further purification via size-exclusion chromatography, resulting in a preparation of high-purity rhodopsin at high concentration suitable for crystallization or other biophysical study.

Key words Rhodopsin, Purification, Zinc extraction, Size-exclusion chromatography

1 Introduction

With its initial characterization in the 1870s by Boll and Kühne [1], the retina (and extracts thereof) has formed the basis of much that is understood about G protein-coupled receptor structure and function, providing much of the raw material from which biochemical, biophysical, and structural work have initiated. Critical in these studies have been the high concentration of rhodopsin present in the rod outer segment (ROS) of retinal rod cells and the ability of mechanical disruption to shear these ROS from the residual retinal tissue. Isolation of these ROS can be achieved through the use of sucrose gradient centrifugation resulting in an ~80 % pure preparation of rhodopsin imbedded in ROS membranes [2]. Detergent extracts of these ROS membranes were later used to purify the rhodopsin utilizing concanavalin A (lectin) affinity, hydroxyapatite chromatography, size-exclusion chromatography, or ion exchange affinity chromatography [3–7]. However, it was not until the discovery that alkyl glucoside detergent extracts of these ROS preparations could be further purified by treatment with divalent cations [8], resulting in the precipitation of opsin

Beata Jastrzebska (ed.), *Rhodopsin: Methods and Protocols*, Methods in Molecular Biology, vol. 1271,
DOI 10.1007/978-1-4939-2330-4_2,

(apoprotein rhodopsin) and other membrane proteins, while the majority of ground-state rhodopsin remained in solution, that diffracting crystals of rhodopsin in its ground-state were obtained [9]. This purification was critical in obtaining the first structures of ground-state rhodopsin and still is utilized as an initial step in the purification of rhodopsin. Additional ground-state structures have employed a combination of concanavalin A (lectin) affinity chromatography followed by a secondary purification utilizing anion exchange chromatography and utilized C_8E_4 detergent rather than the alkyl glucoside detergents employed in previous ground-state studies [10]. Recognizing that these extractions still left a large amount of lipids, an undefined amount of detergent, and Zn^{2+} ions bound to the rhodopsin, additional purification with 1D4 antibody affinity chromatography was necessary to obtain diffracting crystals which were stable upon light exposure [11, 12].

Contemporary studies necessitating the isolation and reconstitution of rhodopsin complexes have routinely utilized combinations of the above methodologies [13]. Yields of 50–70 mg of >95–99 % pure rhodopsin are typical for preparations from 100 dark-adapted bovine retinas. It is unnecessary to analyze fractions via SDS-PAGE during the purification as the specific absorbance of rhodopsin at 500 nm is diagnostic of the presence of ground-state rhodopsin [14], and the ratio of this number to the total protein contained in the sample as measured by absorbance at 280 nm is indicative of purity [15, 16]. Furthermore, SDS-PAGE analysis yields little information on the fraction of active rhodopsin in the sample as it is insensitive to discerning between the apoprotein opsin (a, if not the, major contaminant in these preparations) and rhodopsin.

2 Materials

Prepare all solutions using ultrapure water (18.3 MΩ/cm at 25 °C) and analytical grade reagents. All buffers and stock solutions should be stored at 4 °C unless otherwise stated. We do not add sodium azide to the sucrose solutions, but it may be added at 0.05 % w/v if long-term storage of excess buffer is desired.

2.1 Bovine Eye Dissection

1. Scalpel and/or surgical scissors.
2. Blunt tip forceps.
3. Amber pill bottle(s) for retinal storage.
4. Aluminum foil.
5. Fresh bovine eyes: these can be procured by special request from a local slaughterhouse (*see* **Note 1**).

2.2 ROS Membrane Isolation

2.2.1 Required Supplies

1. Hydrometer(s) capable of measuring specific gravity spanning the range of 1.10–1.15 (Fisherbrand).
2. 50 ml polycarbonate capless tubes (Nalgene).
3. Tube rack for 50 ml tubes.
4. Cannula (14 G, 6 in. long, blunt point needle) (Cadence Science).
5. Disposable 10 and 30 ml syringes.
6. 250 ml glass graduated jar with Teflon seal in lid (Qorpak).
7. 250 ml graduated cylinder (three needed). We prefer polycarbonate graduated cylinders for use in the darkroom as they are less fragile than glass and easier to read than polypropylene cylinders.
8. 500 ml graduated cylinder.
9. Glass funnel large enough to sit on top of the 250 ml graduated cylinder.
10. Two $4 \times 4''$ gauze surgical sponges, unfolded to create an $8 \times 8''$ 4 ply liner for the funnel.
11. Beckman JA-17 or JA-20 rotor or equivalent rotor (*see* **Note 2**).
12. Beckman JS-13.1 rotor or equivalent rotor.
13. Beckman Avanti J26XP centrifuge or equivalent high-speed centrifuge located in a darkroom.
14. Quartz semimicro cuvette, 0.6 ml volume (Starna).
15. Electric pipette aid and disposable 10 ml pipettes for resuspension of pelleted crude ROS membranes (optional: 10 ml syringe and a cannula can be used for this task).

2.2.2 Required Buffers

The protocol presented here is suitable for large-scale purification, and buffer amounts are enough for 3–4 purifications of 100–150 retinas (*see* **Note 3**); smaller volumes of each buffer can be prepared for smaller preparations, although the time involved in making these solutions should discourage the preparation of just enough solution for a single preparation at a time.

1. Kühn's buffer: 67 mM $KH_{(x)}PO_4$, pH 7.0, 1 mM $Mg(C_2H_3O_2)_2$, 0.1 mM EDTA, and 1 mM DTT (optionally, sodium azide can be added at a concentration of 0.05 % to inhibit bacterial and fungal growth in the buffer during storage).
2. Kühn's buffer containing 45 % (w/v) sucrose.
3. Kühn's buffer containing sucrose to make the following specific densities: 1.10, 1.11, 1.13, and 1.15 (*see* **Note 4** and Table 3 for detailed instructions on how to make the sucrose gradient buffers required for this purification).

2.2.3 Determination of Rhodopsin Concentration

1. Rhodopsin determination buffer: 10 mM β-D-dodecyl maltoside (DDM) or 30 mM 3-[(3-Cholamidopropyl) dimethylammonio]-1-propanesulfonate (CHAPS) detergent, 20 mM Bis tris propane pH 7.5, and 20 mM Hydroxylamine. This buffer can be prepared in advance and 5-10 ml aliquots can be stored at -20 °C until needed (*see* **Note 5**).

2.3 Rhodopsin Purification

2.3.1 Zinc Extraction

1. 500 mM 2-(*N*-morpholino)ethanesulfonic acid (MES), pH 6.3 stock solution.
2. 50 mM MES pH 6.3 (prepared from above stock).
3. $Zn(O_2CCH_3)_2 \cdot (H_2O)_2$ or $ZnCl_2$ (*see* **Note 6**).
4. N-β-D-nonyl-glucoside (NG) (Affymetrix) powder or 500 mg/ml stock (in 50 mM MES, pH 6.3) (*see* **Note 7**).

2.3.2 Dialysis for Zinc Removal and Detergent Exchange

Due to the fact that buffers containing high concentrations of zinc spontaneously, albeit slowly, form insoluble $Zn(OH)_2$, samples should be dialyzed soon after extraction to remove the majority of zinc; the use of mildly acidic buffers for the zinc extraction and dialysis minimizes the formation of $Zn(OH)_2$ (*see* **Note 8** for comments on detergent exchange during dialysis).

1. Dialysis buffer: 20 mM MES, pH 6.3, 6.5 mM NG, 200 mM NaCl, 10 mM EDTA, and 1 mM DTT.
2. Dialyzer membrane: Slide-A-Lyzer (Pierce) or Float-A-Lyzer (Spectrum) with at least a 20 kDa molecular weight cutoff to allow for ease of movement of detergent across the membrane (*see* **Note 9**). Dialyzer membrane should be wetted with water or dialysis buffer prior to loading.

2.3.3 Size-Exclusion Chromatography

Size-exclusion chromatography should be carried out at 4 °C using an HPLC or equivalent chromatography system which has been adapted to run under dark conditions. This is best accomplished with a chromatography refrigerator placed in a darkroom. In order to adapt the HPLC to operation in the dark, all non-red LED lights on the HPLC must be covered with foil tape (Nashua) or other lighttight coverings. It is best to further protect the sample from light by wrapping all tubing as well as the column in aluminum foil. If the HPLC cannot be controlled from outside of the darkroom, the monitor can be covered with a dark red filter (Roscolux Medium Red Filter) (*see* **Note 10** for details on filter material).

1. For dealing with the large volume of concentrated rhodopsin produced in these large-scale purifications, a large preparative gel filtration column such as a GE HiLoad 16/600 Superdex 200 pg with a column volume of 120 ml is suggested.

Table 1
Recommended detergents and concentrations for gel filtration and detergent exchange

Detergent	CMC (mM)	Suggested detergent concentration (mM)
n-Heptyl-β-D-glucoside (C_7G, HG)	70	70
n-Octyl-β-D-glucoside (C_8G, OG)	20	20–40
n-Nonyl-β-D-glucoside (C_9G, NG)	6.5	6.5–13
n-Decyl-β-D-glucoside (C_{10}G, DM)	2.2	4.4
n-Nonyl-β-D-maltoside (C_9M, NM)	6.0	12
n-Dodecyl-β-D-maltoside (C_{12}M, DDM)	0.17	1
Octyl glucose neopentyl glycol (OGNG)	1.02	2.0
Lauryl maltose neopentyl glycol (LMNG)	0.01	0.1–1.0

2. For smaller-scale purifications, we suggest either a GE 10/300 Superdex 200 or a Sepax SRT-C 10/300 column. Both of these columns have similar column volumes (~25 ml); however, the silica-based media in the Sepax columns has significantly better separation efficiency, resulting in tighter, more concentrated peaks, although this comes at the expense of reduced pH range over which the protein can be exchanged (pH 2.5–8.0).
3. Size-exclusion buffer containing detergent: 10 mM MES, pH 6.3, 150 mM NaCl, 1 mM $MgCl_2$, 1 mM DTT, and 6.5 mM NG (or another suggested detergent in appropriate concentration; *see* Table 1). Filter through a 0.22 μm filter. If desired, buffer can also be degassed by sparging with argon or helium at this stage. Add dry detergent to at least the critical micelle concentration (CMC) of the detergent (*see* Table 1) and stir until fully dissolved. Ranges are presented only when multiple concentrations have been tested (*see* **Note 11**).

3 Methods

All procedures are carried out in a darkroom with only dim red light illumination. All buffers should be at 4 °C.

3.1 Procuring/ Dissecting Bovine Retina

Dissection of the retina should be performed as soon as possible after removal from the bovine carcass as the retina deteriorates over time and becomes less attached to the retinal pigmented

epithelium. Due to the time and monetary expense of bovine eye procurement and retinal dissection, when experimentally allowable, frozen dark-adapted bovine retinas are a time-saving and cost-effective source of rhodopsin (W.L. Lawson Co. or InVision BioResources). The purification of rhodopsin from these frozen tissues produces homogenously pure rhodopsin which is of sufficient quality for crystallization or other biophysical study. Gloves and adequate eye protection must be used for the retinal dissection. Ocular tissue must be discarded according to institutional rules for neurological material. A headlamp with a red filter or red LED light conveniently illuminates the workspace while keeping the undissected eyes and dissected retinas in the dark. *See* Fig. 1 for a schematic representation of the bovine eye and optimal cutting location on the eye to expose the retina (s*ee* **Note 12** for safety concerns when dealing with bovine eyes and other neurological material).

1. Arrange eyes "facing" upward in a glass or metal dish sitting in a container of ice; this ensures that the rear of the eye and retina is kept as cool as possible, slowing the detachment of the retina which complicates the dissection.
2. Before cutting into the eye, it may be necessary to pull back the fat and connective tissue which may slip forward over the eye after removal in order to reach the sclera and cornea of the eye for dissection.
3. Remove the cornea using a sharp scalpel or sharp surgical scissors (*see* **Note 13**) to puncture the sclera (white of the eye)

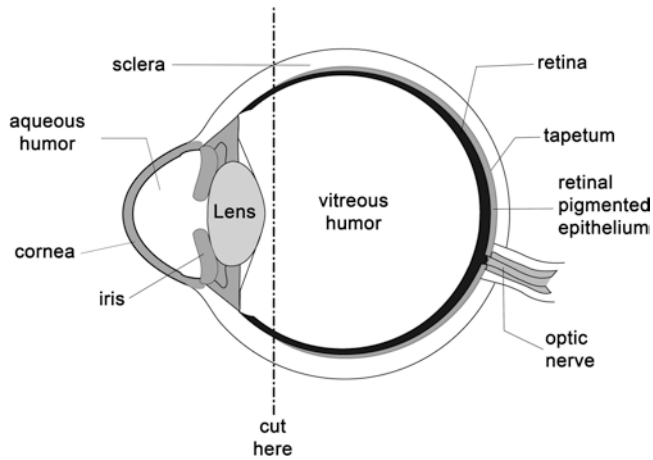

Fig. 1 Bovine eye anatomy and dissection guide. A bovine eye is shown in sagittal cross section with approximate location (*dotted line*) for the incision through the sclera to produce an eyecup for the retinal dissection. If the cut around the circumference of the eye is too close to the iris, it may be difficult to turn the eyecup inside out; conversely, simply cutting the eye in half equatorially will decrease the amount of retina harvested from each eye

close to the cornea (*see* Fig. 1), then slice around the circumference of the sclera forming an "eyecup." The eyecup should comprise the back 60–75 % of the eye.

4. Gently turn the eyecup inside out over your thumb and discard the lens and vitreous humor. If this is done too vigorously, the retina may detach and be discarded along with the vitreous and lens (*see* **Note 14**).
5. Using a pair of forceps, gently detach the retina. Starting at the periphery of the retina, gently scrape the retina off the retinal pigmented epithelium toward the optic nerve. Once the retina is gathered up around the optic nerve, grasp the retina at the optic nerve with the forceps, detach by twisting the forceps a quarter turn, and place detached retina into an amber pill bottle on ice (*see* **Note 15**).
6. Rod outer segments can be isolated immediately or the amber vials containing retinas can be wrapped in two layers of aluminum foil and stored at −80 °C until needed.

3.2 Preparation of Rod Outer Segments from the Retinal Tissue

This purification is based upon the procedures developed by the Papermaster laboratory [2] and relies upon a strategy employing flotation of ROS on high-density sucrose solutions and sedimentation under low-density sucrose solutions to selectively float or pellet crude ROS membranes, to affect their crude isolation from cellular debris. This is then followed by further purification on a discontinuous sucrose gradient to remove other membrane components. All centrifugations are performed in a darkroom at 4 °C.

1. Thaw 100 frozen bovine retinas by floating the bottles in 20 °C water (or one may begin with freshly dissected retina).
2. Transfer thawed retinas to a 250 ml graduated bottle and add an equivalent volume of ice-cold 45 % sucrose solution. There should be at least 50 ml of "empty" volume in the bottle to allow for efficient disruption of the retina in the following step.
3. Seal the graduated bottle with the lid and further seal with Parafilm to avoid leaks during the shaking step and shake vigorously (as hard as you can) by hand for 1 min to disrupt the retinal tissue, shearing off the rod outer segments at the connecting cilium.
4. Distribute the suspension to six 50 ml centrifuge tubes and centrifuge in JA-17 rotor for 5 min at 5,000 rpm (~3,400 × *g*).
5. Pour supernatant from each tube through a gauze-lined funnel into a 250 ml graduated cylinder and dilute the filtrate 1:1 with ice-cold Kühn's buffer. Mix suspension gently by wrapping the end of the graduated cylinder with Parafilm and rocking back and forth slowly by hand. Transfer this diluted supernatant to 50 ml centrifuge tubes and centrifuge in a JA-17 rotor for 10 min at 10,000 rpm (13,800 × *g*).

6. During this centrifugation step, prepare six 50 ml tubes containing a three-step sucrose gradient (1.11, 1.13, and 1.15 densities), using a cannula attached to a 20 ml syringe (*see* **Notes 2** and **16**). The preparation of the gradients should be accomplished outside of the darkroom as it is difficult to observe the formation and/or disruption of the interface between the various densities of sucrose solution under darkroom illumination (*see* **Note 16** for additional detail on preparation of sucrose gradients). Fill all tubes with 10 ml of 1.11 solution; next slowly inject 15 ml of 1.13 solution underneath the 1.11 layer, avoiding air bubbles and disturbing the interface between the two solutions. The final layer is formed by injecting an additional 10 ml of 1.15 solution underneath the 1.13 layer. Ensure that all gradients fill the tubes to the same level as the crude ROS resuspension will be layered on the top of the gradient in the dark (Fig. 2a) and it is difficult to discern between crude ROS and the foam that will form during the resuspension of the crude ROS.

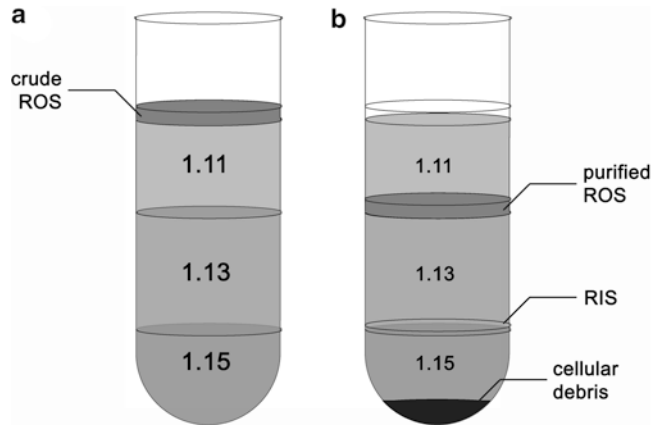

Fig. 2 Sucrose gradient construction and purification of crude ROS. (**a**) Representative diagram of the locations of each density of sucrose solution. Note that construction of the gradient is done in the reverse order, outside of the darkroom; 10 ml of 1.11 density sucrose solution is added first, followed by 15 ml of 1.13 density sucrose solution which is very slowly injected *under* the 1.11 layer; this is followed by the injection of 10 ml of 1.15 density solution *under* the 1.13 layer. These gradients are transported carefully back into the darkroom and the resuspended ROS membranes from Subheading 3.2, and **steps 5** and **7** are layered on top of the 1.11 density solution; for best results, the ROS layer should be very slowly layered on top by allowing the suspension to flow down the side of the tube. (**b**) Location of ROS layer after centrifugation. The ROS layer collects at the interface between the 1.11 and 1.13 density layers. Vesicles derived from the rod inner segment form a weak diffuse band at the 1.13 -- 1.15 interface wheras celular debris collects as a pellet under the 1.15 density solution.

7. After the centrifugation of the ROS suspension, carefully pour off the supernatant and discard. Resuspend the crude ROS membrane pellets in 4–6 ml of 1.10 density solution and 2–3 ml Kühn's buffer using a cannula attached to a 10 ml syringe. Once resuspended, rinse the interior of the centrifuge tubes where the crude ROS pellet was attached with an additional 2 ml of Kühn's buffer to remove any additional membrane pellet stuck to the interior of the tube and combine with the resuspended membranes (*see* **Note 17**).
8. Using a cannula, slowly and gently dispense an equal volume of the resuspended crude ROS pellet down the edge of the tube onto the top of each step gradient. Take care to make sure that the total volume in each tube contains the same volume, as it is difficult to observe the volume of the tubes in the darkroom; allow the layer to settle to observe the interface between the foam formed during the resuspension and the resuspended ROS.
9. Centrifuge for 30 min in a JS-13.1 swinging bucket rotor at 12,000 rpm (22,500 × *g*) with the centrifuge brake turned off (this is critical to preserve the gradient during rotor deceleration *see* **Note 18**).
10. After centrifugation, take great care to not disturb the gradients when removing the centrifuge tubes from the rotor. The ROS membranes will collect at the interface between the 1.11 and 1.13 layers (Fig. 2b). It should be noted that the ROS band is considerably more diffuse when utilizing frozen retina for the purification (*see* **Note 19**).
11. Collect the interface between the 1.11–1.13 layers by gently inserting the tip of the cannula into the ROS band at this interface and gently moving the tip of the cannula around the circumference of the tube while applying suction with the syringe. It is helpful to illuminate the gradient from behind using a flashlight with a red filter while extracting the interface as the ROS membranes appear as an opaque dark band while the gradient solution appears translucent or transparent. Efficiency of removing the ROS layer should be checked after the first tube by removing it to white light and immediately observing if any red layer still exists (indicating incomplete removal of the ROS layer); if there is a red layer still present, then more solution at the interface should be extracted from the remaining gradients.
12. Transfer the purified ROS suspension harvested from this interface to a 250 ml graduated cylinder and diluted 1:1 with ice-cold Kühn's buffer, wrap the end of the cylinder with Parafilm and mix gently by rocking back and forth slowly, and then pellet ROS by centrifugation at 12,000 rpm (22,500 × *g*) for 5 min in the JS 13.1 rotor.

13. Discard the supernatant and leave pelleted ROS. Seal these tubes with Parafilm, wrap with aluminum foil, label, and store at −80 °C until use. Ensure the tubes containing the pellets freeze upright so the ROS pellet does not flow down the side of the tube during freezing (*see* **Note 20**).

3.3 Purification of ROS Membrane Extracts by Size-Exclusion Chromatography

While the ROS preparation removes the majority of soluble proteins present from the retina, resulting in membranes that contain primarily rhodopsin, in many cases it is desirable to further purify the rhodopsin to remove residual membrane proteins. This includes a considerable amount of the apoprotein, opsin, which forms as a result of the cattle/eye harvesting being performed under lighted conditions and its incomplete regeneration back to rhodopsin. Because opsin and rhodopsin chemically differ only in the presence of the covalently bound retinal chromophore, it is difficult to chromatographically separate the two via affinity chromatography. However, when solubilized into detergent solution, opsin is less stable than rhodopsin, allowing for a selective precipitation which employs conditions just harsh enough to precipitate opsin and other membrane proteins while leaving the rhodopsin in solution. In the past, immunoaffinity or anion exchange chromatography has been utilized to further delipidate and purify the rhodopsin after detergent extraction from membranes. We have found that these additional purification steps can be substituted with a single size-exclusion chromatography step on zinc-extracted solubilized membranes. This size-exclusion step enables determination of oligomeric state, estimates of bound detergent amount, and comes with the added bonus of allowing for exchange into a chemically defined buffer and the ability to switch to an alternative detergent (*see* Table 1 and **Note 21**).

3.3.1 Zinc Extraction of Rhodopsin from Purified ROS Membranes

1. Thaw ROS membranes from 100 bovine retinas and resuspend using a 10 ml serological pipette with an electric Pipet-Aid in 4 ml of 50 mM MES, pH 6.3.
2. Quantify the resuspended rhodopsin spectrophotometrically, utilizing the change in the absorbance maximum at 500 nm upon light exposure to calculate the amount of ground-state rhodopsin present (ΔA_{500}). A 1:100 dilution of rhodopsin in the rhodopsin determination buffer is used to blank the spectrophotometer (*see* **Note 22**). After blanking with sample, the sample is removed from the darkroom and exposed to bright light for 5–10 min, and then the absorbance at 500 nm is determined spectrophotometrically (ΔA_{500}). The absolute value of this change in absorbance is proportional to the amount of ground-state rhodopsin in the original suspension, and using the molar extinction coefficient for rhodopsin (40,600 $M^{-1}cm^{-1}$), the molecular weight of rhodopsin (40,000 Da), and the dilution factor (1:100 in this case), the total concentration in mg/ml can be calculated:

$$(100 \times 40{,}000 \times \Delta A_{500} / 40{,}600 = [\text{Rho}]\text{mg/ml}).$$

Typical concentrations of rhodopsin after resuspension are 6–10 mg/ml, depending primarily on the residual buffer left over from the final ROS preparation and the volume of buffer used for resuspension of the pellet.

3. Solubilized the resuspended rhodopsin in a 50 ml polycarbonate centrifuge tube with n-β-D-nonyl-glucoside (NG) at a ratio of 2.2–2.5 mg NG/mg of rhodopsin, which can either be added as a 500 mg/ml stock (in 50 mM MES, pH 6.3) or simply by adding dry powder to the resuspended rhodopsin. Stir the suspension containing detergent and ROS membranes on a magnetic stir plate for 30–60 min at 4 °C to dissolve the detergent and fully solubilize the sample.
4. Measure the volume of sample, and then adjust the concentration of MES to 40 mM with 1 M MES, pH 6.3 stock solution, and enough solid zinc acetate or zinc chloride is added to the suspension to bring the final concentration to 100 mM. Mix the solution on a magnetic stir plate in a 50 ml polycarbonate centrifuge tube for 15–30 min at slow speed and stored on ice overnight (*see* **Note 23**). During this overnight incubation, the resuspended ROS pellet will become opaque due to precipitation of the opsin and membrane lipids.
5. Remove the magnetic stir bar and remove the precipitated opsin, other membrane proteins, and lipids (which have precipitated out of solution due to treatment with zinc) by centrifugation (JA-17 rotor at 10,000 rpm (13,750 × *g*) for 10 min).
6. Carefully decant supernatant and quantify rhodopsin. Rather than measuring the concentration via ΔA_{500} method as described above, a more accurate measure of rhodopsin purity can be obtained by taking the absorbance spectrum of the sample and calculating the ratio of absorbance at 280:500 nm (A_{280}/A_{500}). An A_{280}/A_{500} ratio of 1.56 indicates pure rhodopsin with no other significant contaminating proteins, and at this point in the purification, this ratio should be close to this number. For crystallization of ground-state rhodopsin, the A_{280}/A_{500} ratio should be <1.8.

   Concentration and yield vary based upon total volume into which the ROS membranes were resuspended, but typically from 100 commercially sourced frozen retinas, 60–70 mg of >95 % purity rhodopsin is obtained at a concentration of 5–10 mg/ml. When initiating the purification with the fresh retina, the yield and purity should be slightly higher with 70–80 mg of 98 % pure rhodopsin purified per 100 retinas.

3.3.2 Dialysis to Remove Zinc, Detergent Exchange

While the zinc extraction step is adequate to remove opsin and other membrane proteins, the presence of high concentrations of zinc after extraction may destabilize the rhodopsin in solution or

interfere with downstream assays or further purification steps. It is critical to remove zinc prior to size-exclusion chromatography or concentration in a centrifugal concentrator as zinc spontaneously forms insoluble precipitates of $Zn(OH)_2$ which can irreversibly clog a size-exclusion column or centrifugal concentrator. In some cases it is desirable to replace the high CMC detergent (NG) with a lower CMC detergent such as (DDM) or lauryl maltose neopentyl glycol (LMNG). Dialysis against LMNG, and in some cases even DDM, can result in the precipitation of some or all of the rhodopsin due to the high CMC detergent (NG), dialyzing away before the low CMC detergent can make its way into the dialyzer. To avoid this, it is recommended that dialysis be performed in the presence of 6.5 mM NG to remove excess zinc, which will avoid this result (*see also* **Note 8** for an alternative to dialysis against NG). The use of 1× the CMC of the detergent at this step minimizes the concentration of detergent along with rhodopsin, which when over-concentrated will result in an extremely viscous solution that is difficult to pipette accurately and in some cases may result in protein precipitation/sample loss.

1. Transfer 5 ml of the zinc-extracted rhodopsin to a 5 ml 20 kDa MWCO Float-A-Lyzer/Slide-A-Lyzer and dialyzed against 100 ml of dialysis buffer (6.5 mM NG, 20 mM MES, pH 6.3, 200 mM NaCl, 10 mM EDTA, 1 mM DTT) for 2–4 h at 4 °C.
2. The dialysate is discarded and the dialysis is repeated against an additional 100 ml of buffer for an additional 2–4 h or overnight.

3.3.3 Size-Exclusion Chromatography

1. If the sample is to be further purified and/or detergent exchanged by size-exclusion chromatography, transfer the dialyzed rhodopsin to an Amicon ultra 4 or ultra 15 centrifugal concentrator (MWCO 30 kDa) and concentrate to the desired loading volume for the selected size-exclusion column.
2. The loading volume for a size-exclusion column should not exceed 1–2 % of the total column volume. For example, for a large-scale purification (as described here) when exchanging the rhodopsin into LMNG, 1.25 ml of concentrated rhodopsin is loaded at 20 cm/h onto a Superdex 200 16/600 preparative size-exclusion column which has been pre-equilibrated with size-exclusion buffer (*see* **Note 24**). Figure 3 shows a representative chromatogram of rhodopsin purified in NG and dialyzed against NG containing buffer before being buffer exchanged into LMNG.
3. Following size-exclusion chromatography, measure the A_{280}/A_{500} for all peak fractions and pool fractions containing both a concentration of rhodopsin >1 mg/ml and an A_{280}/A_{500} ratio <1.8. Then concentrate these fractions in an Amicon ultra 4 centrifugal concentrator (MWCO 30 kDa) to desired volume/concentration.

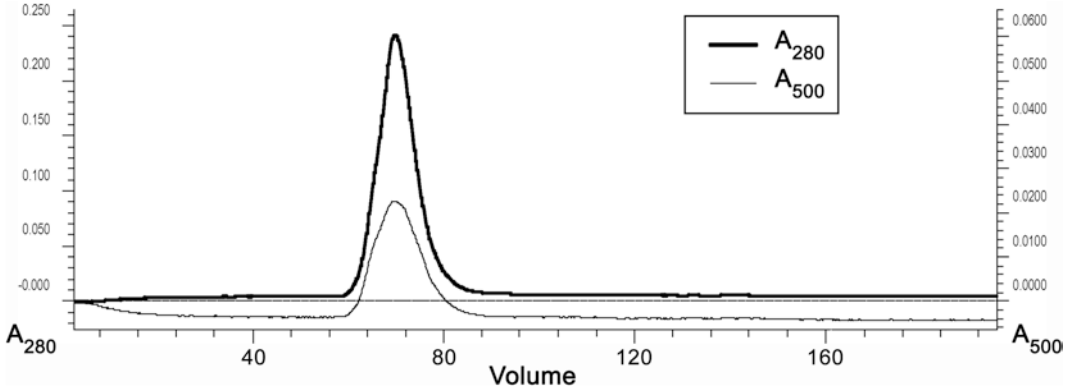

Fig. 3 Representative chromatogram showing separation of zinc-extracted rhodopsin. After dialysis against dialysis buffer consisting of 6.5 mM NG, 20 mM MES, pH 6.3, 200 mM NaCl, 1 mM DTT, and 10 mM Na(EDTA), 10 mg of rhodopsin at a concentration of 10 mg/ml and (1 ml total) of this sample was loaded onto an XK 16/1000 column containing 200 ml of Superdex 200 preparative media which was pre-equilibrated with size-exclusion buffer (20 mM MES, pH 6.3, 150 mM NaCl, 1 mM $MgCl_2$, 1 mM DTT, and 2 mM OGNG detergent). Absorbance at 280 nm is plotted as a thick line and absorbance at 500 nm is denoted as a thin line. It is not practical nor is it useful to measure the A_{500} inline when purifying ground-state rhodopsin as this will partially or fully photoactivate the rhodopsin, resulting a significant amount of contaminating opsin. Rather, aliquots of peak fractions should be diluted 1:50 in the rhodopsin determination buffer (10 mM DDM, 20 mM Bis–Tris propane, pH 7.5, and 20 mM hydroxylamine) and their absorbance spectra measured. Samples with A_{280}/A_{500} ratios less than 1.8 and concentrations of rhodopsin greater than 1 mg/ml are then pooled and centrifugally concentrated

4. At this point rhodopsin can be aliquoted into microcentrifuge tubes, wrapped in two layers of aluminum foil, snap frozen in liquid nitrogen, and stored at −80 °C until needed. Alternatively, because of its stability, for short-term storage, rhodopsin can simply be stored protected from light on ice.
5. When exchanged into LMNG or OGNG detergent, rhodopsin can be concentrated to >50 mg/ml with no appreciable increase in viscosity or precipitation. In glucoside/maltoside detergents, concentrations >20 mg/ml, while possible, are discouraged as consequent concentration of detergent micelles along with the rhodopsin during centrifugal concentration results in a viscous solution which is difficult to accurately pipette and manipulate.

4 Notes

1. Eyes are generally discarded by a slaughterhouse along with the brain and bones of the cow/steer, so the price paid to the slaughterhouse is in actuality for the additional labor in removing the eye from the skull. Consultation with the person performing the enucleation is useful as it should be stressed that the eyes should be stored in a lighttight black plastic

bag on ice as soon as they are extracted from the bovine carcass, to avoid additional photoactivation of the rhodopsin. Dissection of the retina should be performed as soon as possible after death as the retina will become less attached to the retinal pigmented epithelium, complicating its intact dissection.

2. If rhodopsin from 200 to 300 retinas is needed, the protocol can be modified to utilize a larger rotor such as a JA-14 for the initial crude isolation of ROS membranes; however, for best results, the resultant crude ROS should be split into two sucrose gradient purification steps.
3. When scaling down the size of the preparation to around 25 retina, it is possible to use a single continuous gradient of sucrose spanning the density range of 1.10–1.15. With fresh, unfrozen retina this should give an extremely tight band for the ROS. Given the time and issues with reproducibility in the preparation of six large continuous gradients, the step gradient methodology detailed here is a reasonable compromise between volume of the ROS layer, purity, and time required for purification.
4. All buffers for the ROS isolation are prepared from Kühn's buffer: preparation of 5 l of Kühn's buffer is more sufficient to prepare the sucrose solutions and perform several ROS isolations. Buffer is prepared from dry ingredients with no adjustment of final pH as indicated in Table 2.

   Prepare 45 % sucrose solution: dissolve 900 g of sucrose in Kühn's buffer to a final volume of 2 l (45 % (w/v)).

   Prepare sucrose gradient solutions: utilizing the 45 % sucrose solution and the Kühn's buffer prepared above, four additional sucrose solutions of defined density are prepared; approximate volumes of each solution required for a single purification and amounts of 45 % sucrose solution and Kühn's buffer required to prepare each solution are listed in Table 3. Pour appropriate volumes of each solution into a 500 ml graduated cylinder. Final specific gravity must be adjusted at 25 °C using a hydrometer.

Table 2
Preparation of Kühn's buffer

Component	Grams (for 5 l)
K_2HPO_4	35.70
KH_2PO_4	17.70
$Mg(C_2H_3O_2)_2 \cdot 4H_2O$	1.072
EDTA-$Na_2 \cdot 2H_2O$	0.186
Dithiothreitol (DTT)	0.771
Sodium azide (optional)	2.5

Table 3
Preparation of sucrose solutions for ROS isolation

Density	Approximate volume of 45 % sucrose (ml)	Approximate volume of Kühn's buffer (ml)	Approximate volume required for 100 retina (ml)
1.15	420	82	60
1.13	330	144	90
1.11	315	208	60
1.10	107	93	6
The following two solutions are also needed for the purification			
45 % sucrose	800 (left over from gradient solution preparation)		100
Kühn's buffer		1,000 (left over from gradient solution preparation)	300

If buffer is intended for use over the course of several weeks to months, DTT should be omitted from initial preparation and added just before use due to its instability in aqueous solutions. Addition of dry DTT to the sucrose solutions avoids changes in the density of the sucrose solution were the DTT stock solution to be added. If sodium azide is included in the solution, storage for longer than 6 months at 4 °C is possible, but solutions should be checked for signs of bacterial/fungal growth prior to use (often manifested as small cotton ball-like growths in the bottom of the bottle).

5. Addition of hydroxylamine to the buffer is only necessary for the ΔA_{500} assay to ensure complete removal of chromophore through formation of the retinal oxime after photoactivation. Hydroxylamine can be included in the dilution buffer for the A_{500} determination of purified rhodopsin with no negative consequences.
6. $ZnCl_2$ can be substituted for the acetate salt in this case. Solid zinc is preferred over zinc stock solutions to minimize generation of the insoluble $Zn(OH)_2$ precipitate.
7. Most alkyl glucoside/maltoside detergents can be used as long as enough detergent is employed to solubilize the entirety of the membranes and the rhodopsin; OG, NG, and DDM have all been used successfully for the solubilization and zinc extraction of rhodopsin. Use of a high CMC detergent such as OG or NG enables detergent removal/exchange during dialysis.
8. Detergent exchange can be accomplished during the removal of zinc, but dialysis against low CMC detergents must be preceded

by a preincubation of the sample with adequate amounts of the desired detergent, such that the concentration of new detergent is isotonic with the dialysate; if this preincubation is neglected, the solubilizing detergent dialyzes away from the rhodopsin more rapidly than the low CMC detergent can dialyze into the dialyzer, resulting in widespread precipitation of the rhodopsin.

9. Alternatively, standard dialysis tubing and clips can be used, although the cartridge type dialyzers are much easier to load/unload in the darkroom. Dialysate should be stirred during dialysis.
10. The red filter material can be obtained from a photographic or theatrical supply store. This film can be used to convert a white light to a red safelight. It is also available as tubes that fit over standard fluorescent light bulbs. This film should be replaced on a regular basis as it begins to lose its efficiency over time, resulting in a more orange transmission spectrum.
11. Low CMC detergents are considerably more cost-effective as significantly less detergent is required for purification.
12. Keep in mind that there is a possibility of exposure to prions in handling bovine eyes as they are in fact neurological material, which could result in the contraction of bovine spongiform encephalopathy ("mad cow disease"). Proper protective equipment should be worn during all steps of the procedure; this should include at minimum: gloves, goggles, and a lab coat. Institutional rules for disposal of neurological material must be followed for the disposal of eye tissue.
13. Some people prefer to use a fresh single-edged razor blade to make the initial incision in the eye and then use surgical scissors to complete the incision.
14. Premature detachment of the retina at this step can also be caused by failing to store the intact eyes on ice immediately after death.
15. The retina is quite delicate and has the structural integrity of wet tissue paper. Great care should be taken to only gently tease the retina off from the RPE layer; avoid overzealous scraping of the eyecup as significant amounts of RPE and other tissue will contaminate the retina, resulting in a poorer-quality final preparation of ROS/rhodopsin.
16. When preparing sucrose step gradients with the sucrose stock solutions, it is advantageous to have adequate lighting (i.e., do not attempt to prepare in the darkroom) and the tubes at eye level in a tube rack that securely holds the tubes, thus ensuring that one can observe the higher-density solution filling the space under the lower-density solution. For best results, flow of the higher-density solution must be slow enough that no mixing with the adjacent layer occurs.

17. It is advantageous to use new centrifuge tubes for this step as scratches and discolorations found on used tubes can be mistaken for residual ROS membranes. Under the dim red light illumination of a darkroom, it is difficult to determine if all the ROS pellet has been resuspended; after removal of the resuspended ROS, the tube can be inspected using a flashlight with red film over the bulb.
18. Modern centrifuges have considerably less internal friction than the older J-2/J-20 centrifuges with which these procedures were developed. Turning the brakes off with a new centrifuge may result in a deceleration that takes more than 2 h! In newer centrifuges there are gentle braking options which can be employed to slow the rotor without disturbing the gradients in a reasonable (~10 min) time frame.
19. When harvesting the ROS layer, it is sometimes necessary to take the entire 1.11 and the majority of the 1.13 layer. This is not a major issue, but may require a second "pelleting" run to harvest the ROS from the solution. Nevertheless, the total amount of gradient harvested should be minimized, as while the A_{280}/A_{500} ratio may not appreciably change when additional gradient solution is harvested, additional nonprotein components such as additional lipids sediment into the 1.11 and 1.13 layers leading to their co-purification.
20. Optionally, the pelleted ROS membranes from the above step after centrifugation can be resuspended in ~30 ml of Kühn's buffer and pelleted in a single tube for storage purposes.
21. The amount of detergent required for solubilization of ROS membranes is considerably higher than would be desired for a crystallization experiment, and the actual free concentration of detergent is unknown due to the inability to control for the amount of lipid that forms mixed micelles during solubilization, the amount of detergent that binds the rhodopsin, and the consequent loss of detergent during the zinc extraction process.
22. Spectrophotometer should be located in the darkroom for ease of measurement if possible. Otherwise, all dilutions for rhodopsin concentration and purity assay must be prepared in the darkroom, wrapped in foil, and read immediately on the spectrophotometer. A dark cloth can be used to assist in the protection of the sample from light.
23. Alternatively, a 2–4-h room-temperature zinc extraction can be performed; if this is extended further, some of the rhodopsin will also precipitate. When performing this extraction, after centrifugation the pellet will be pale pink; a red pellet indicates the precipitation of rhodopsin along with opsin, other membrane proteins, and lipids.
24. In the case of expensive detergents, the column can be equilibrated 60% prior to beginning chromatographic separation, as

the column will be fully equilibrated before the rhodopsin peak elutes from the column. While the column can be completely equilibrated prior to the start, this minimizes the amount of detergent required.

Acknowledgments

Funding was provided by the NIH EY019718 (DTL), the Mt. Sinai Health Care Foundation (DTL), Ohio First (EB), and the Cleveland Foundation (DTL). We thank Dr. David Salom for editorial assistance and critical reading of the manuscript.

References

1. Kühne W (1877) Zur Photochemie der Netzhaut. Carl Winter's Universitätsbuchhandlung, Heidelberg
2. Papermaster DS (1982) Preparation of retinal rod outer segments. Methods Enzymol 81:48–52
3. Litman BJ (1982) Purification of rhodopsin by concanavalin A affinity chromatography. Methods Enzymol 81:150–153
4. De Grip WJ (1982) Purification of bovine rhodopsin over concanavalin A: sepharose. Methods Enzymol 81:197–207
5. Matthews RG, Hubbard R, Brown PK et al (1963) Tautomeric forms of metarhodopsin. J Gen Physiol 47:215–240
6. Irreverre F, Stone AL, Shichi H et al (1969) Biochemistry of visual pigments. I. Purification and properties of bovine rhodopsin. J Biol Chem 244:529–536
7. Heller J (1968) Structure of visual pigments. I. Purification molecular weight and composition of bovine visual pigment500. Biochemistry 7:2906–2913
8. Okada T, Takeda K, Kouyama T (1998) Highly selective separation of rhodopsin from bovine rod outer segment membranes using combination of bivalent cation and alkyl(thio)glucoside. Photochem Photobiol 67:495–499
9. Palczewski K, Okada T, Stenkamp RE et al (2001) Crystal structure of rhodopsin: a G-protein coupled receptor. FASEB J 15:A29
10. Mielke T, Villa C, Edwards PC et al (2002) X-ray diffraction of heavy-atom labelled two-dimensional crystals of rhodopsin identifies the position of cysteine 140 in helix 3 and cysteine 316 in helix 8. J Mol Biol 316:693–709
11. Salom D, Lodowski DT, Stenkamp RE et al (2006) Crystal structure of a photoactivated deprotonated intermediate of rhodopsin. Proc Natl Acad Sci U S A 103:16123–16128
12. Salom D, Le Trong I, Pohl E et al (2006) Improvements in G protein-coupled receptor purification yield light stable rhodopsin crystals. J Struct Biol 156:497–504
13. Jastrzebska B, Ringler P, Lodowski DT et al (2011) Rhodopsin-transducin heteropentamer: three-dimensional structure and biochemical characterization. J Struct Biol 176:387–394
14. Wald G, Brown PK (1953) The molar extinction of rhodopsin. J Gen Physiol 37:189–200
15. Hubbard R (1954) The molecular weight of rhodopsin and the nature of the rhodopsin-digitonin complex. J Gen Physiol 37:381–399
16. McConnell DG, Dangler CA, Eadie DM et al (1981) The effect of detergent selection on retinal outer segment A280/A500 ratios. J Biol Chem 256:4913–4918

Chapter 3

Mammalian Expression, Purification, and Crystallization of Rhodopsin Variants

Daniel Mattle, Ankita Singhal, Georg Schmid, Roger Dawson, and Jörg Standfuss

Abstract

After 25 years of intensive research, the understanding of how photoreceptors in the eye perceive light and convert it into nerve signals has largely advanced. Central to this is the structural and mechanistic exploration of the G protein-coupled receptor rhodopsin acting as a dim-light sensing pigment in the retina. Investigation of rhodopsin by X-ray crystallographic, electron microscopic, and biochemical means depends on the ability to produce and isolate pure rhodopsin protein. Robust and well-defined protocols permit the production and crystallization of rhodopsin variants to investigate the inactive ground, the fully activated metarhodopsin II state, or disease-causing rhodopsin mutations. This chapter details how we express and purify biologically active variants of rhodopsin from HEK293S GnTI$^-$ cells in a quality and quantity suitable for biochemical assays, crystallization, and structure determination.

Key words Photoreceptor, Retinitis pigmentosa, Retinal, Rhodopsin, Membrane protein crystallography, Membrane protein expression, Membrane protein purification, GPCR, HEK293 cells

1 Introduction

Highly abundant in the outer segments of rod cells, rhodopsin senses the light-induced isomerization of its covalently bound chromophore retinal. Upon absorption of light 11-*cis*-retinal (inverse agonist) is converted into all-*trans*-retinal (full agonist) followed by a switch in conformation of rhodopsin from an inactive to a fully activated conformation (metarhodopsin II) [1].

The first crystal structure of the inverse agonist-bound bovine rhodopsin provided insight into the molecular details of receptor activation [2]. In the following years, further structures of bovine rhodopsin isolated from native source were published reporting different crystallographic space groups and conformational states including the fully activated all-*trans*-retinal-bound state [3–8].

Crystallization and therefore the mechanistic characterization were in part so successful because rhodopsin is highly abundant in

Beata Jastrzebska (ed.), *Rhodopsin: Methods and Protocols*, Methods in Molecular Biology, vol. 1271,
DOI 10.1007/978-1-4939-2330-4_3,

rod outer segments and can be extracted in a few relatively simple steps [9, 10]. The starting point to study the structure of rhodopsin mutations was set by the development of a ligand-free opsin that is highly stable in detergent-solubilized environments [11]. The use of this engineered opsin led to the structure determination of a stabilized rhodopsin ground state [12]. Later, it advanced into the crystallization of constitutively active mutations to understand the rhodopsin activation mechanism [13, 14] and to the first structural model of a disease-causing rhodopsin mutation [15].

Here, we describe the mammalian expression and purification strategy used to study these rhodopsin variants. We produce homogenous glycosylated opsin in HEK293S GnTI$^-$ stable cell lines using a tetracycline-induced expression system to achieve high and consistent protein expression yields [16, 17]. We reach good reproducibility by growing our stable cell line cultures under controlled conditions in fermenters or bioreactors, followed by a standardized opsin purification protocol with the 1D4 antibody affinity chromatography and size-exclusion chromatography [18]. The described methodology can be used for biochemical and structural characterization of further rhodopsin variants, to study transient complexes [19] and enable drug discovery projects on disease-causing mutations [20]. It is furthermore straightforward to adapt the described methods for the expression and purification of other pharmacologically interesting GPCRs and membrane proteins.

2 Materials

2.1 Cloning

1. pCMV-tetO vector kindly provided by P.J. Reeves and H.G. Khorana [17].
2. *Escherichia coli* Mach 1 cells (Life Technologies) or any other engineered *E. coli* strain to produce high amount of plasmids.
3. Ampicillin (100 mg/ml) dissolved in 50 % (v/v) ethanol.
4. Gene Elute™ HP Plasmid Midiprep Kit (Sigma-Aldrich) or any supplier of your convenience.
5. NanoDrop ND-1000 Spectrophotometer (Thermo Scientific) or other UV-visible spectrophotometer.

2.2 Stable Cell Lines

1. HEK293S GnTI$^-$ cells (mutant cell line for restricted and homogenous glycosylation [16]) kindly provided by P.J. Reeves and H.G. Khorana.
2. DMEM high glucose with L-glutamine (AmiMed).
3. Trypsin 0.05 % in PBS, with EDTA (AmiMed).
4. Cell and tissue culture plates with treated surface (six-well plate, Jet BioFil).

5. Cell and tissue culture dishes with treated surface (100 and 150 mm, BioFil).
6. Gibco standard fetal bovine serum (FBS) (Life Technologies).
7. Penicillin/streptomycin (AmiMed).
8. 100 mg/ml Geneticin (G418) in water and sterile filtered (Merck Millipore).
9. 10 mg/ml Blasticidin (InvivoGen).
10. Mr. Frosty™ freezing container (Thermo Scientific).
11. Dimethyl sulfoxide ACS reagent, ≥99.9 % (Sigma-Aldrich).
12. 1× phosphate buffered saline (PBS), pH 7.4, autoclaved.
13. 1 mg/ml polyethylenimine (PEI) in water, sterile filtered (25 kDa linear) (Sigma-Aldrich).
14. Nunc™ biobanking and cell culture cryogenic tubes (Thermo Scientific).

2.3 Expression Small Scale

1. 2 mg/ml tetracycline hydrochloride in 100 % ethanol (suitable for cell culture, Sigma-Aldrich).
2. 500 mM sodium butyrate dissolved in water and sterile filtered (Sigma-Aldrich).
3. 10 mM 9-*cis*-retinal dissolved in 100 % ethanol under dim-light conditions (Sigma-Aldrich).
4. 12.5 % (w/v) n-decyl-β-D-maltopyranoside dissolved in water (Sol-Grade, Anatrace).
5. Complete, EDTA-free, protease inhibitor cocktail tablets (Roche). 10× PBS buffer, pH 7.4.
6. 1 M 4-(2-hydroxyethyl)-1-piperazine-1-ethanesulfonic acid (HEPES), pH 7.0 stock solution.
7. PureCube Rho1D4 affinity resin (Cube Biotech).
8. 800 μM Rho1D4 peptide (TETSQVAPA) dissolved in water (Cube Biotech) or any other supplier of your convenience.
9. 100 μl Ultra-Micro Quartz Cuvette with 10 mm light path (Hellma Analytics) and a UV-visible spectrophotometer of your choice (e.g., Cary UV50, Agilent Technologies).
10. Imagelite Lite Mite series with >495 nm long-pass filter.

2.4 Fermentation

1. Protein Expression Medium (PEM) (Life Technologies).
2. L-Glutamine (Sigma-Aldrich).
3. FBS (Sigma-Aldrich).
4. Feeding solution (Roche proprietary composition).
5. 2 M sodium butyrate stock solution.
6. Tetracycline hydrochloride (Serva) or similar.

7. Geneticin (G418) sulfate (Life Technologies).
8. 10 mg/ml Blasticidin stock solution (Life Technologies).
9. Vi-CELL cell counter (Beckman Coulter) or similar cell counting device.
10. Bioprofile analyzer 100 plus (Nova Biomedical) for metabolite analyses.
11. Fully instrumented 10 l WAVE or 20 l stirred-tank bioreactors with temperature, pH, and dissolved oxygen control (Sartorius, Göttingen, Germany) or equivalent.
12. Avanti J-HC centrifuge (Beckman Coulter) for biomass harvesting.

2.5 Purification

1. Complete, EDTA-free, protease inhibitor cocktail tablets (Roche).
2. 10× PBS buffer, pH 7.4.
3. 12.5 % (w/v) n-decyl-β-D-maltopyranoside (DM) dissolved in water (Sol-Grade, Anatrace).
4. Wash buffer 1: 1× PBS, pH 7.4, and 0.125 % (w/v) DM.
5. Wash buffer 2: 10 mM HEPES, pH 7.0, and 0.125 % (w/v) DM.
6. 1 M HEPES, pH 7.0 stock solution.
7. 800 μM Rho1D4 peptide (TETSQVAPA) dissolved in water.
8. Elution buffer: 80 μM Rho1D4 peptide (TETSQVAPA), 10 mM HEPES-NaOH, pH 7.0, and 0.125 % (w/v) DM.
9. 1 M sodium acetate, pH 5.0 stock solution.
10. 10 % (w/v) *n*-octyl-β-D-glucopyranoside (OG), dissolved in water (Anagrade, Anatrace).
11. 5 M NaCl stock solution.
12. Novex 12 % Tris-Glycine Midi Protein Gels, 12 + 2 well (Life Technologies) and Novex Tris-Glycine SDS Running Buffer (10×).
13. Hand homogenizer (e.g., ULTRA-TURRAX, IKA).
14. Econo-Column chromatography columns, 2.5 × 10 cm (Bio-Rad).
15. 15 and 6 ml 30 kDa cutoff concentrators (Vivaspin).
16. Ti45 tubes, Ti45 rotor and ultracentrifuge (Beckmann Coulter).
17. Superdex 200 10/300 GL column (GE Healthcare) and an HPLC system of your choice (e.g., AKTA prime or purifier, GE Healthcare).
18. Gel filtration buffer: 10 mM sodium acetate, pH 5.0, 100 mM NaCl, and 1 % (w/v) OG.

2.6 Activation Assay and Crystallization

1. 100 µl Ultra-Micro Quartz Cuvette and a UV-visible spectrophotometer of your choice (e.g., Cary UV50).
2. 2× Assay buffer: 20 mM HEPES pH 7.4, 400 NaCl, and 0.25 % (w/v) DM.
3. 11-*cis*-retinal (a kind gift from Rosalie Crouch).
4. 4 M ammonium sulfate.
5. 1 M sodium acetate, pH 4.5, 5.0, 5.5, 6.0.
6. Brain polar lipid extract (porcine) (Avanti Lipids).
7. VDX Plate with sealant (Hampton Research) and plain glass cover slides (Hampton Research).
8. 50 % (w/v) D-(+)-trehalose dehydrate (Sigma-Aldrich).

3 Methods

3.1 Construct Design, Cloning, and Plasmid for HEK293S GnTI⁻ Expression

1. Construct your rhodopsin gene of interest (RGOI) with a KpnI enzyme restriction site on the 5′ end of your leading DNA strand, followed by the Kozak consensus sequence (5′-gccacc-3′), your RGOI including the ATG start codon, and an NotI enzyme restriction site on the 3′ (*see* **Note 1**).
2. Clone your RGOI into the tetracycline-inducible mammalian cell expression pCMV-tetO vector [17, 21] between the KpnI and NotI enzyme restriction site using a standard polymerase chain reaction method (Fig. 1).
3. Add 1 µl 100 ng/µl plasmid to 30 µl *Escherichia coli* Mach1 cells, and amplify your plasmid DNA by a standard heat-shock transformation.
4. Plate your cells on an LB agar plate with ampicillin (final concentration, 100 µg/ml), and incubate at 37 °C overnight.
5. Pick a colony and follow the amplification and purification procedure of the protocol of Gene Elute™ HP Plasmid Midiprep Kit.
6. Measure the plasmid concentration using the NanoDrop ND-1000 spectrophotometer. Typically, we obtain 100 ng/µl plasmid in a total volume of 2 ml autoclaved ddH_2O from 100 ml Mach1 cells overnight culture.
7. Sterile filter the plasmids with a 0.22 µm filter before use.
8. Sequence your plasmid to confirm your RGOI sequence.

3.2 Generation of Stable Cell Lines

Generally, HEK293S GnTI⁻ cells are kept as adhesion cultures in DMEM high glucose with L-glutamine medium supplemented with a final concentration of 10 % FBS, a 1:100 dilution of penicillin/streptomycin, and 5 µg/ml Blasticidin. Geneticin (G418) (200 µg/ml) is supplemented for selection and maintenance of the generated cell lines. Cell cultures are kept at 37 °C, 5 % CO_2.

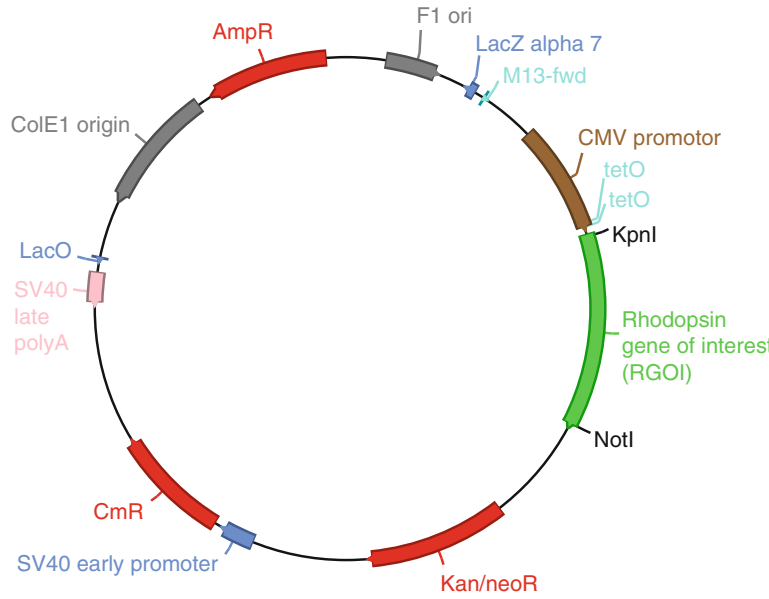

Fig. 1 Vector map of tetracycline-inducible pCMV-tetO [17] with the rhodopsin gene of interest. A CMV promoter with two tetO sequences is followed by your rhodopsin gene of interest between a KpnI and NotI restriction site. An ampicillin resistance (AmpR) in the plasmid is used for selection in prokaryotic cells. Geneticin, an analog of neomycin sulfate and kanamycin, is used to select in mammalian expression in the presence of the dominant-acting resistance gene (neoR)

All media that are applied to cell culture are heated to 37 °C in a water bath, and handling of mammalian cells is done under sterile conditions in a flow-bench.

Day 0

1. Plate about 5×10^6 HEK293S GnTI$^-$ cells from a frozen stock supplemented with 10 % DMSO onto a 100 mm (78 cm^2) cell culture tissue plate supplied with 8 ml DMEM high glucose with L-glutamine, 10 % (v/v) FBS. Incubate the cells at 37 °C in 5 % CO_2.
2. Aspirate the medium after most of the cells are adherent to the plate (ca. 4 h) with 8 ml DMEM high glucose with L-glutamine, 10 % (v/v) FBS, and 5 µg/µl Blasticidin, and incubate overnight at 37 °C and 5 % CO_2.

Day 1

3. Wash HEK293S GnTI$^-$ cells with 6 ml 1× PBS, and aspirate the 1× PBS.
4. Trypsinize the cells with 1.5 ml 0.05 % trypsin in 1× PBS, with EDTA, aspirate the medium until 200 µl of the solution is left, and incubate for about 5 min at room temperature. Loosen the cells through knocking at the plate.

5. Add 4 ml DMEM high glucose with L-glutamine, 10 % (v/v) FBS, to the trypsinized cells, and mix the cells with a 5 ml pipette and a Pipet-Aid to have an even distribution in the medium.
6. Distribute approximately 200 µl into a six-well tissue culture plate that already has 2.5 ml DMEM high glucose with L-glutamine, 10 % (v/v) FBS (*see* **Note 2**).
7. Incubate the cells at 37 °C and 5 % CO_2 for 24 h.

Day 2

8. Prepare a DNA complex with your RGOI of interest (*see* **Note 3**).
   (a) Add 15 µg plasmid DNA with your RGOI to 7.5 ml DMEM high glucose with L-glutamine medium.
   (b) Add 62.5 µl 1 mg/ml PEI (25 kDa linear), vortex, and incubate for 15 min at room temperature.
   (c) Supplement the DNA-PEI complex with 6 ml DMEM high glucose with L-glutamine and 1.5 ml DMEM high glucose with L-glutamine, 10 % (v/v) FBS.
9. Aspirate the cell culture medium from the six-well culture tissue plate.
10. Add 3 ml of the DNA complex from **step 5** to the six-well tissue culture plate with the adherent HEK293S GnTI$^-$ cell culture.
11. Incubate the DNA-PEI complex for 1–4 h, wash the cells with 2 ml PBS, and incubate the cells for 24 h with 3 ml DMEM high glucose with L-glutamine.

Day 3

12. Wash the cells with 1.5 ml PBS and replace the medium with full medium (DMEM high glucose with L-glutamine, 10 % (v/v) FBS, 5 µg/ml Blasticidin, 1 mg/ml Geneticin (G418)).
13. Repeat this procedure every second to third day until the cells without plasmid DNA (negative control, *see* **Note 3**) have completely disappeared (*see* **Note 4**).

Day 17 or latest Day 21

14. Expand the generated stable cell lines to a 150 mm cell culture dishes, and let them grow to 70–80 % confluency using DMEM high glucose with L-glutamine, 10 % (v/v) FBS, 5 µg/µl Blasticidin, 200 µg/ml Geneticin (G418).
15. Trypsinize the HEK293S GnTI$^-$ with your RGOI using 3 ml trypsin 0.05 % in PBS, with EDTA, and aspirate until 500 µl medium is left.
16. Resuspend the cells in 10 ml DMEM high glucose with L-glutamine, 10 % (v/v) FBS, and take 1 ml for a new passing round on a 150 mm cell culture dish for a small-scale expression test (*see* Subheading 3.3).

17. Harvest the cells for 5 min at 100 × *g* at room temperature.
18. Aspirate the medium and resuspend the cells in 10 ml preservation medium (DMEM high glucose with L-glutamine, 20 % (v/v) FBS, 10 % (v/v) DMSO) (*see* **Note 5**).
19. Distribute 1 ml of the resuspended cells to cryogenic tubes, and place them into the Mr. Frosty™ freezing container and store at –80 °C overnight.
20. Transfer the stable cell lines into a liquid nitrogen tank until further use and for long-term storage.

3.3 Small-Scale Expression and Purification for Functional Test

Day 1

1. Split 70–90 % confluent HEK293S GnTI$^-$ cells containing RGOI 1:1 from a 150 mm cell culture dish into two 150 mm cell culture dishes to bring them into exponential phase.

Day 2

2. Induce the two plates with a final concentration of 2 μg/ml tetracycline and 5 mM sodium butyrate in DMEM high glucose with L-glutamine medium.
3. Incubate the cells for >48 h at 37 °C and 5 % CO_2.

Day 5

4. Aspirate the medium from the plates, and add 3 ml 0.05 % trypsin in PBS, with EDTA; reduce the volume to 500 μl and incubate for 5 min.
5. Add 7 ml to each culture dish plate, and centrifuge the cells for 10 min at 3,000 × *g* at 4 °C.
6. Wash the cells with 1 ml 1× PBS containing a cOmplete protease inhibitor cocktail tablet (1 tablet for 25 ml PBS).
7. Aspirate the 1× PBS and weigh the cell pellet. Usually, 250 mg of cell pellet can be obtained from two 150 mm cell culture dishes.
8. Resuspend the cells into 2× the cell volume (e.g., 500 μl for 250 mg cells) with 1× PBS containing a cOmplete protease inhibitor tablet.

   All further steps in this Section are carried out under dimred light and on ice, if not stated differently (*see* **Note 6**).
9. Add 9-*cis*-retinal to a final concentration of 50 μM, and incubate for 45 min at 4 °C (*see* **Note 7**).
10. Add DM to a final concentration of 1.25 % (w/v) to solubilize the rhodopsin variant.
11. Transfer the sample to a 1.5 ml microfuge tube (Beckman Coulter), and centrifuge the solubilized cells for 45 min at 200,000 × *g* at 4 °C in a tabletop ultracentrifuge (e.g., Beckman Coulter).

12. Apply the supernatant to 0.1 ml PureCube Rho1D4 affinity resin, and incubate for >2 h at 4 °C under rotation (*see* **Note 8**).
13. Centrifuge for 5 min, 1,000 × *g* at 4 °C, and discard the supernatant.
14. Apply 1 ml ice-cold wash buffer 1, invert the tube, and centrifuge for 5 min, 1,000 × *g* at 4 °C.
15. Discard the supernatant and repeat **step 14** one more time.
16. Apply 1 ml of ice-cold wash buffer 1, invert the tube, and centrifuge for 5 min, 1,000 × *g* at 4 °C.
17. Incubate the resin with 0.3 ml elution buffer for 45 min.
18. Collect the supernatant by centrifugation for 5 min at 1,000 × *g* at 4 °C (Fig. 2a).
19. Load 100 µl of the elution into an Ultra-Micro Quartz Cuvette (100 µl, 10 mm light path), and record a UV-visible spectrum (Fig. 2b).
20. Illuminate the sample for 10–15 min with an Imagelite source and >495 nm long-pass filter, and record a UV-visible spectrum again (Fig. 2b).

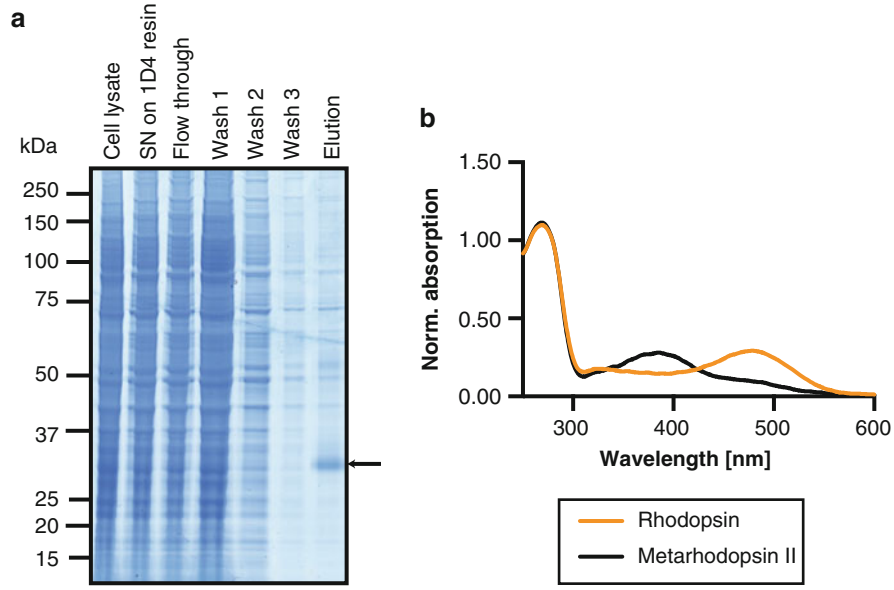

Fig. 2 Small-scale expression test. (**a**) The rhodopsin gene of interest can be purified in a small-scale setup in the presence of 9- or 11-*cis*-retinal. The *arrow* indicates the rhodopsin gene of interest between the 37 and 25 kDa marker bands. (**b**) Activity of your rhodopsin gene of interest can be measured by a UV-visible spectrometer. In addition to the protein peak at 280 nm, the spectrum should show the 485 nm absorption peak of 9-*cis* or 500 nm of 11-*cis*-retinal. Illumination with a >495 nm long-pass filter for 5–15 min leads to formation of metarhodopsin II and a peak maximum of around 380 nm due to deprotonation of the retinal Schiff base

3.4 Inoculum Cultures/Fermentation

1. Collect confluent cells from T175 flasks, and seed them into 200 ml Protein Expression Media (PEM) supplemented with 3 % FBS, 5 mM glutamine, 200 μg/ml Geneticin (G418), and 5 μg/ml Blasticidin in a 1 l shake flask (Corning). The cell density should be $>0.3 \times 10^6$ cells/ml.
2. Shake the cell culture on an orbital shaker with 120 rpm at 37 °C in a 5 % CO_2 incubator.
3. Split the cells every 3–4 days to 0.3×10^6 cell/ml, and expand to 3 l Fernbach flasks (Corning) within about a week (*see* **Note 9**).
4. Inoculate the 2 l of cells as soon as they reached about $4–5 \times 10^6$ viable cells/ml (usually within 5 days) into 18 l of PEM supplemented with 3 % FBS 5 mM glutamine, 200 μg/ml G418, and 5 μg/ml Blasticidin.
5. Grow the cells under controlled conditions (120 rpm, pH 7.2, pO_2 30 % air saturation) in a fully instrumented 10 l WAVE or 20 l stirred-tank bioreactor (*see* **Note 10**).
6. Induce the cells by the addition of 500 ml PEM supplemented with tetracycline to reach a final concentration of 2 μg/ml in the bioreactor. Cells should be induced at a density of $2.5–3.5 \times 10^6$ viable cells/ml and within 3 days after inoculating the bioreactor.
7. Add 800 ml concentrated feeding solution (Roche, proprietary composition) to avoid nutrient limitations (optional).
8. Add sodium butyrate to a final concentration of 3 mM 48 h after post-induction, and supplement with an additional 400 ml feeding solution.
9. Harvest the cells 72 h post-induction by centrifugation in 1 l bottles (Beckman) at $3{,}000 \times g$ for 10 min at 4 °C.
10. Wash the cell pellets once with PBS, and centrifuge at $900 \times g$ in 500 ml conical tubes for 10 min at 4 °C.
11. Store the cell pellets at –80 °C in appropriate portions to carry out the purification later (*see* **Note 11**).

3.5 Large-Scale Purification of Rhodopsin Mutants

1. Typically, we thaw about 50 g of HEK293S GnTI$^-$ cells for each crystallization experiment (*see* **Note 12**).
2. Add two cOmplete protease inhibitor cocktail tablets as soon as the cells are thawed.
3. Dilute the cells into ice-cold 1× PBS, pH 7.4, to a final volume of 225 ml including the cells.
4. Homogenize the cells with a hand homogenizer with five on/off pulses of 30 s.
5. Add slowly 25 ml of 12.5 % (w/v) DM to reach a final concentration of 1.25 % (w/v) DM.

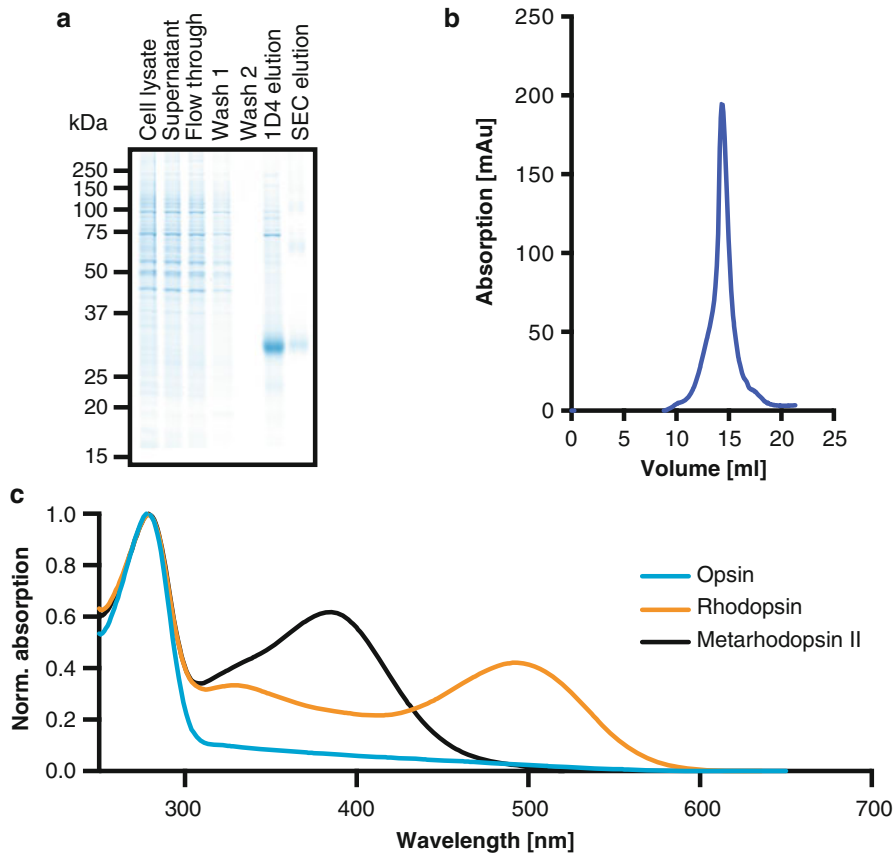

Fig. 3 A typical crystallization scale purification of an opsin variant. (**a**) 12 % SDS-PAGE gel is used to check for the purity of the rhodopsin gene of interest. Opsin runs between 37 and 25 kDa; a tryptic digest and a MALDI-TOF can be used to confirm your rhodopsin gene of interest. (**b**) The size-exclusion chromatography on a Superdex 200 10/300 GL column shows a monodisperse peak of opsin with a retention volume of 14 ml. (**c**) Purified opsin absorbs at 280 nm. The equimolar titration of 11-*cis*-retinal to opsin yields an additional absorption maximum at around 500 nm. Light activation with a 495 long-pass filter shifts the second peak maximum to 380 nm. This indicates deprotonation of the retinal Schiff base and formation of the active metarhodopsin II species

6. Fill the cell suspension into four Ti45 tubes, and rotate the tubes for no more than 1 h in the cold room to solubilize the cells. Take out 10 µl for a subsequent SDS-PAGE analysis, and call the sample cell lysate (Fig. 3a).
7. Centrifuge the solubilized cells (120,000×*g*, 1 h, 4 °C, Ti45 rotor).
8. Combine the supernatants and take another 10 µl sample for a subsequent SDS-PAGE analysis (Fig. 3a).
9. Add the combined supernatant to 4 ml of a 50 % suspension of 1D4 resin, and incubate the resin for 2–4 h under rotation at 4 °C (*see* **Note 13**).
10. Apply the supernatant to the 2.5×10 cm gravity Econo-Column (Bio-Rad).

11. Wash the 1D4 resin with 100 ml wash buffer 1 and 200 ml wash buffer 2 (*see* **Note 14**).
12. Take a 20 µl sample of the first wash step (wash 1) and of the second wash step (wash 2) for an SDS-PAGE analysis (Fig. 3a).
13. Add 12.5 ml of elution buffer to 1D4 resin, and incubate for 45 min prior to collection by gravity. Repeat this step until most rhodopsin is eluted (*see* **Note 15**).
14. Concentrate the elution to <0.5 ml with a 15 ml 30 kDa cut-off concentrator to an approximate concentration of 5 mg/ml (*see* **Note 16**). Take 2 µl for an SDS-PAGE analysis (Fig. 3a).
15. Freeze a small aliquot of the purified opsin for activation assay tests (*see* Subheading 3.6).
16. Inject the concentrated (rhod)opsin construct into Superdex 200 10/300 GL column (GE Healthcare) that is pre-equilibrated with gel filtration buffer on a high-performance liquid-chromatography (HPLC) system.
17. Elute the sample slowly with a flow rate of 0.1 ml/min, and collect the elution (Fig. 3b).
18. Concentrate the peak of the elution with a 6 ml 30 kDa cutoff concentrator to approximate 10–15 mg/ml. Take 1 µl for SDS-PAGE analysis (Fig. 3a).
19. Run a 12 % SDS-PAGE gel of the collected samples during the purification procedure to analyze the purity of the purified rhodopsin variant.

3.6 Retinal Binding Test

1. Add 50 µl 2× assay and 46 µl of H_2O and 4 µl of 5 mg/ml opsin to an Ultra-Micro Quartz Cuvette (100 µl, 10 mm light path), and gently mix with a pipette.
2. Take a UV-visible spectrum; *see* Fig. 3c.
3. Estimate the protein concentration by analyzing the 280 nm peak and the ProtParam extinction coefficient.
4. Add equimolar amounts of 11-*cis*-retinal with a pipette. Mix gently and incubate for at least 10 min under red light conditions to avoid prior activation. Work under red light conditions until the end of your activity test.
5. Take another UV-visible spectrum to obtain the rhodopsin spectrum with a second peak at around 500 nm.
6. Estimate the 280–500 nm ratio of the peak. This ratio should be between 1.6 and 2 (*see* **Note 17**).
7. Illuminate the sample through 495 nm long-pass filter using an Imagelite source for 30 min.
8. Take another UV-visible spectrum to observe the metarhodopsin II spectrum with a peak shift from 500 to 380 nm.

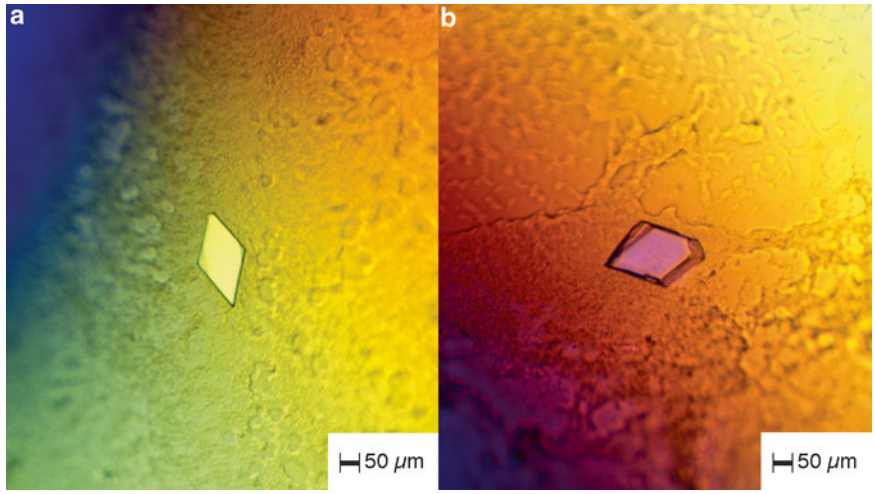

Fig. 4 Three-dimensional crystals of opsin. Single opsin crystals can be obtained in high ammonium sulfate (3.4–3.6 M) in the absence (**a**) or presence of 5 % (w/v) trehalose (**b**). Crystals grow to their full size between 50 and 100 μm within 2 weeks. Crystals are visualized with a polarization filter to enhance their visibility

3.7 Crystallization Setups

1. Add your protein to a reaction tube with dry lipids from brain extract (Avanti) in a 0.5–1 (w/w) ratio. We typically set up several crystallization plates with protein concentrations of 5–10 mg/ml (*see* **Note 18**).
2. Resuspend the lipids by mixing the opsin solution.
3. Set up a 24-well VDX Plate with sealant (hanging-drop vapor diffusion crystallization) after 30 min using a condition around 3.4 M ammonium sulfate and 100 mM sodium acetate, pH 4.5. Use a protein to precipitant drop ratio of 1:1 (*see* **Note 19**).
4. Crystals should appear within 2 days and reach their full size within 2 weeks (Fig. 4).
5. Add a final concentration of 10 % (w/v) D-(+)-trehalose in reservoir solution to the crystallization drop through exchange of the liquid prior to flash-freezing of the crystals in liquid nitrogen (*see* **Note 20**).

4 Notes

1. We observed that the introduction of a disulfide bond between amino acid 2 and 282 is beneficial for crystallization and biochemical assays in detergent-solubilized environments. This engineered rhodopsin variant behaves in its biological activity like wild-type rhodopsin [11, 12, 22].
2. Further cell dilution series can be made to compensate for growth.
3. Typically, we have a DNA to PEI ratio between 1–2 and 1–4 and have up to five constructs on one six-well cell culture plate

or several dilution series. The last well should be used as a blank, where you add no DNA. This provides a negative control for the selection procedure.

4. Single colonies appear within 2–3 weeks. These can be picked for monoclonal selection. The testing of monoclonal selection can yield a higher amount of protein per cell [23].
5. Higher cell densities in the preservation medium allow a faster start of initial cultures. We recommend to freeze at a cell density of around 0.5×10^6 to 10^7 HEK293S GnTI$^-$ cells.
6. If some of your instruments are under normal light conditions, use aluminum foil to make sure that rhodopsin is in the dark and no inadvertent activation occurs.
7. 9-*cis*-retinal is commercially available and acts also as an inverse agonist, similarly to 11-*cis*-retinal.
8. Rho1D4 affinity resin can also be made by mixing 1D4 antibody from the University of British Columbia (http://www.rho1d4.com/) and CNBr-activated Sepharose 4B (GE Healthcare). The manufacturer provides a detailed protocol for the ligand coupling.
9. The culture volume in a 3 l Fernbach flask should not exceed 1 l during the process.
10. As an alternative, you can use a 10 l WAVE bioreactor (GE Healthcare, 20 l bag). However, we noted that the amount of biomass reached in a fermenter is about double (20–25 g/l PEM) compared to a WAVE bag (10–12.5 g/l PEM).
11. Due to convenience we shock-freeze the biomass in 25 g portions in a 50 ml falcon tube on dry ice.
12. We place the falcon tubes with the frozen cell pellets into room temperature water and exchange the water every 10 min. This allows us to start with the purification procedure after 30 min.
13. We found that 1 ml of 1D4 resin is able to bind up to 2 mg of rhodopsin.
14. You can incubate rhodopsin bound on 1D4 resin with a final concentration of 50 μM 9- or 11-*cis*-retinal in 10 ml PBS/0.125 % (w/v) DM prior to washing with wash buffer 2. This step is necessary for the crystallization of ground-state or light-activated rhodopsin (compare **Note 18**).
15. We find that most (rhod)opsins are eluted after 3–4 elutions.
16. While concentrating mix the sample approximately every 5 min with a 1 ml pipette. If your rhodopsin construct starts to precipitate at lower concentration than 5 mg/ml, try to add 50–200 mM NaCl. Furthermore, check the flow through of the concentrator by a UV-visible spectrophotometer. We found that sometimes the membrane of the concentrator can break and no concentrated rhodopsin can be obtained.

17. Higher ratios even after addition of excess 11-*cis*-retinal indicate contaminations with non-retinal-binding opsin or other proteins.
18. For the crystallization of light-activated rhodopsin variants, opsin must have been reconstituted with 9- or 11-*cis*-retinal (*see* **Note 14**). For light activation, we are using a 5 min exposure with a >515 nm long-pass filter to prevent isomerization of unprotonated and free retinal.
19. It is also possible to set up the crystallization trials in a sitting drop experiment with either 24 or 96 conditions.
20. This procedure allows you to cryoprotect your crystals and increases the diffraction power of the crystals and therefore the final resolution you will obtain from your atomic model.

Acknowledgments

We thank Marcello Foggetta, Martin Siegrist, and Agnese Baronina for technical assistances and valuable discussions. We are grateful for the financial support from the Roche Postdoctoral Research Fellowship RPF298 (to D.M.) and from the Swiss National Science Foundation (SNSF) grant 31003A_141235 (to J.S.).

References

1. Palczewski K (2012) Chemistry and biology of vision. J Biol Chem 287:1612–1619
2. Palczewski K, Kumasaka T, Hori T et al (2000) Crystal structure of rhodopsin: a G protein-coupled receptor. Science 289:739–745
3. Li J, Edwards PC, Burghammer M et al (2004) Structure of bovine rhodopsin in a trigonal crystal form. J Mol Biol 343:1409–1438
4. Nakamichi H, Okada T (2006) Local peptide movement in the photoreaction intermediate of rhodopsin. Proc Natl Acad Sci U S A 103: 12729–12734
5. Nakamichi H, Okada T (2006) Crystallographic analysis of primary visual photochemistry. Angew Chem Int Ed Engl 45:4270–4273
6. Salom D, Lodowski DT, Stenkamp RE et al (2006) Crystal structure of a photoactivated deprotonated intermediate of rhodopsin. Proc Natl Acad Sci U S A 103:16123–16128
7. Choe HW, Kim YJ, Park JH et al (2011) Crystal structure of metarhodopsin II. Nature 471:651–655
8. Park JH, Scheerer P, Hofmann KP et al (2008) Crystal structure of the ligand-free G-protein-coupled receptor opsin. Nature 454: 183–187
9. Edwards PC, Li J, Burghammer M et al (2004) Crystals of native and modified bovine rhodopsins and their heavy atom derivatives. J Mol Biol 343:1439–1450
10. Okada T, Le Trong I, Fox BA et al (2000) X-Ray diffraction analysis of three-dimensional crystals of bovine rhodopsin obtained from mixed micelles. J Struct Biol 130:73–80
11. Xie G, Gross AK, Oprian DD (2003) An opsin mutant with increased thermal stability. Biochemistry 42:1995–2001
12. Standfuss J, Xie G, Edwards PC et al (2007) Crystal structure of a thermally stable rhodopsin mutant. J Mol Biol 372:1179–1188
13. Deupi X, Edwards P, Singhal A et al (2012) Stabilized G protein binding site in the structure of constitutively active metarhodopsin-II. Proc Natl Acad Sci U S A 109:119–124
14. Standfuss J, Edwards PC, D'Antona A et al (2011) The structural basis of agonist-induced activation in constitutively active rhodopsin. Nature 471:656–660
15. Singhal A, Ostermaier MK, Vishnivetskiy SA et al (2013) Insights into congenital stationary night blindness based on the structure of G90D rhodopsin. EMBO Rep 14:520–526

16. Reeves PJ, Callewaert N, Contreras R et al (2002) Structure and function in rhodopsin: high-level expression of rhodopsin with restricted and homogeneous N-glycosylation by a tetracycline-inducible N-acetylglucosaminyltransferase I-negative HEK293S stable mammalian cell line. Proc Natl Acad Sci U S A 99:13419–13424
17. Reeves PJ, Kim JM, Khorana HG (2002) Structure and function in rhodopsin: a tetracycline-inducible system in stable mammalian cell lines for high-level expression of opsin mutants. Proc Natl Acad Sci U S A 99: 13413–13418
18. Molday RS, MacKenzie D (1983) Monoclonal antibodies to rhodopsin: characterization, cross-reactivity, and application as structural probes. Biochemistry 22:653–660
19. Maeda S, Sun D, Singhal A et al (2014) Crystallization scale preparation of a stable GPCR signaling complex between constitutively active rhodopsin and G-protein. PloS One 9:e98714
20. Krebs MP, Holden DC, Joshi P et al (2010) Molecular mechanisms of rhodopsin retinitis pigmentosa and the efficacy of pharmacological rescue. J Mol Biol 395:1063–1078
21. Chaudhary S, Pak JE, Pedersen BP et al (2011) Efficient expression screening of human membrane proteins in transiently transfected human embryonic kidney 293S cells. Methods 55: 273–280
22. Standfuss J, Zaitseva E, Mahalingam M et al (2008) Structural impact of the E113Q counterion mutation on the activation and deactivation pathways of the G protein-coupled receptor rhodopsin. J Mol Biol 380:145–157
23. Chaudhary S, Pak JE, Gruswitz F et al (2012) Overexpressing human membrane proteins in stably transfected and clonal human embryonic kidney 293S cells. Nat Protoc 7:453–466

Chapter 4

Imaging of Rhodopsin Crystals with Two-Photon Microscopy

Grazyna Palczewska and David Salom

Abstract

Two-photon microscopy has been shown to be an invaluable tool for detecting and monitoring protein crystallization trials and characterizing membrane protein crystals. This imaging method has proven especially useful for rhodopsin, because of the dependence of rhodopsin's fluorescence spectra on the isomerization state of its intrinsic chromophore (retinylidene) and, as such, it can provide additional information about the identity and functional state of rhodopsin in crystals. Here, we describe the acquisition of images and two-photon excitation and emission spectra using a commercial two-photon microscope, along with detailed instructions for the handling of rhodopsin crystals and specific examples of rhodopsin data.

Key words Nonlinear microscopy, Protein crystals, Rhodopsin, Two-photon microscopy

1 Introduction

Nonlinear optical (NLO) imaging, based on two-photon microscopy (TPM) of protein crystals, has emerged as a powerful method to monitor protein crystal growth, differentiate salt crystals from protein crystals, and identify protein microcrystals against opaque or nonuniform media [1, 2]. One of the advantages of NLO imaging of protein crystals is the possibility of using an incident beam in the deep red or infrared (IR) range, with the concomitant low scattering by crystallization plates and media, and little background noise, which results in an excellent contrast of the crystal images.

Second harmonic generation (SHG) and two-photon excited fluorescence (TPEF) are two different second-order NLO processes that contribute to signals during the imaging of crystals. In SHG, two photons interact with a nonlinear optical material nearly simultaneously to form a new photon with energy equal to the sum of energy of the initial photons and thus twice the incident frequency [2, 3]. Theoretical calculations estimate that SHG microscopy should be able to detect ~84 % of all protein crystals in the protein database (PDB) [4], although, practically, this percentage

Beata Jastrzebska (ed.), *Rhodopsin: Methods and Protocols*, Methods in Molecular Biology, vol. 1271,
DOI 10.1007/978-1-4939-2330-4_4,

may be lower due to a poor signal-to-noise ratio [2]. A further complication is that some inorganic and organic crystals of non-protein origin also can give rise to an SHG signal [2, 5].

In the case of TPEF, two photons are absorbed by a fluorophore nearly simultaneously and thus elevate the molecule to an excited energy state. The energy difference between the two states is approximately equal to the sum of energies of the two impinging photons. The fluorophore molecule then discharges a photon along the traditional (one-photon) fluorescence emission pathway. The majority of proteins have tryptophan residues that absorb at ~280 nm and fluoresce at 320–350 nm, allowing their imaging by TPEF with ~560-nm incident light [6]. TPEF imaging with infrared incident light is possible for proteins with fluorescent cofactors absorbing in the visible range, such as green fluorescent protein [7] or rhodopsin [2]. Additionally, a strategy for imaging crystals of non-fluorescent proteins involves the trace labeling of such proteins with fluorescent probes [8, 9], but this requires protein modifications that may interfere with crystal growth. Interestingly, we recently found that most proteins can be imaged by TPEF, thanks to the two-photon absorption of 700–850-nm light by oxidized tryptophan residues [2]. The intensity of this intrinsic indole-derived TPEF signal increases with the age of a particular crystal being imaged [2]. Finally, the addition of fluorescent dyes to preformed crystals can also be used to image protein crystals by TPEF [2].

In the case of rhodopsin crystals, imaging with TPM is possible as a result of the combined contribution to TPEF by the retinylidene moiety and oxidized tryptophan residues [2]. In addition, a small contribution of SHG to the NLO signal has not been totally ruled out. TPM microscopy of crystals is especially useful for rhodopsin, because of the dependence of fluorescence spectra on the isomerization state of the chromophore. An additional advantage of this technique is minimizing the possibility of photoactivation of ground-state rhodopsin by imaging the crystals with laser light at ~850 nm. In this chapter, we show images and spectra from trigonal rhodopsin crystals that were grown in the ground state but were able to withstand photoactivation without losing their physical integrity [10–12].

2 Materials

1. Kodak darkroom lamp with Kodak Safelight Filter GBX-2 (5.5 in. diameter).
2. Rosco Roscolux Medium Red, 20×24 in. Color Effects Lighting Filter.
3. Glass-bottomed 35-mm dish (MatTek Corp.).
4. Paraffin oil.

5. Magnetic wand and 0.05–0.2-mm mounted nylon cryoloops.
6. Glass microscope slides, 3 × 1 in.
7. Microscope coverslips, 1 × 1 in.
8. Die-cut double stick spacer (3 M 9500PC double stick tape, 0.140 mm thick) (*see* **Note 1**).
9. Laser power meter, FieldMax-TO with PM10 sensor (Coherent).
10. Dissecting microscope.

3 Methods

All procedures related to the handling of ground-state rhodopsin crystals, including their placement on the microscope stage, should be done in darkness or with only dim red light illumination. Trigonal crystals of ground-state bovine rhodopsin were grown as previously detailed [10, 12]. Small ground-state rhodopsin crystals grown on microbridges by vapor diffusion can be obtained in 1 week, whereas larger crystals (>0.1 mm) need 3–4 weeks to grow.

3.1 Microscope Setup

A typical two-photon microscope (TPM) can be used to image rhodopsin crystals with the setup described here. Either inverted or upright microscope stands can be used. The system in an upright configuration is shown in Fig. 1. The average power of pulsed fs laser light is attenuated with the use of an electro-optic modulator (EOM). After the EOM, the laser beam is directed to scanners that trace the raster pattern on the crystal. Then the beam is routed through a set of lenses (not shown) that magnify its diameter to match the back aperture of the objective. In addition to the scanning mirrors, the scanner unit houses a spectral detector. Excitation light is focused on the sample by an objective with a numerical aperture (NA) of 0.4, 0.7, or 0.9 NA. Imaging with 0.4 NA is sufficient for obtaining good-quality images of rhodopsin crystals. Light emanating from the crystal is collected by the same lens and, after reflecting off a dichroic mirror, is directed to Detector 1 (EPI configuration). Alternatively, in transmission configuration, light is collected by the lens located behind the sample and, after passing through a bandpass filter (BF), is directed to Detector 2. The EPI configuration is preferable for NLO imaging based on TPEF. To maximize detection efficiency, highly sensitive detectors such as a Hamamatsu R6357 photomultiplier tube (PMT) (Shizuoka, Japan) or a hybrid GaAsP detection system recently introduced by Leica can be used.

3.2 Transferring Rhodopsin Crystals for TPM Imaging

1. Open a single well from a 24-well plate containing trigonal rhodopsin crystals sitting on a microbridge [10, 12] (*see* **Note 2**). Although the crystals are grown at 4 °C, procedures can be carried at room temperature.

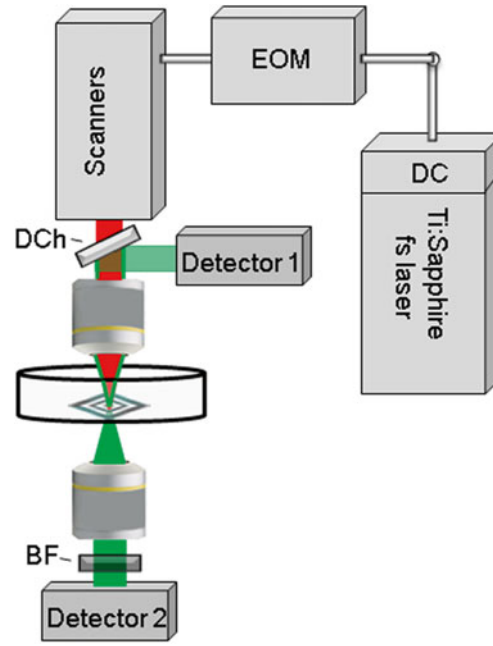

Fig. 1 Microscope setup. Laser light delivered by the Ti:Sapphire Coherent Vision-S is modulated with dispersion precompensation (DC) and an electro-optic modulator (EOM). Scanners trace the raster pattern over the sample. An objective with 0.4 numerical aperture (NA) focuses laser light on the sample. Fluorescence or second harmonic signals are collected in a non-descanned manner. In the EPI configuration, light emanating from the sample is collected by the same lens, and after reflecting off a dichroic mirror (DCh) is directed to Detector 1. In the transmission configuration, the signal emanating from the sample is collected by the lens located behind the sample and directed to Detector 2 after passing through the bandpass filter (BF). Spectral data are obtained with the detector in the descanned configuration located inside the scanner's enclosure

2. Add ~10 μl of reservoir solution (typically 3.0–3.3 M ammonium sulfate in 10 mM MES, pH 6.4) to slow evaporation and concomitant formation of ammonium sulfate crystals.
3. Under a dissecting microscope, transfer a single crystal with the help of a nylon cryoloop to a 1-2-μl drop of paraffin oil placed in a glass-bottomed 35-mm dish (Fig. 2a). Remove most of the aqueous mother liquor surrounding the crystal in the loop by smearing the loop or touching the loop to the dish prior to depositing the crystal in the paraffin oil drop. A second cryoloop, held in the other hand, might be helpful to free the crystal from the first cryoloop into the paraffin drop.
4. Cover the glass dish with its lid and draw a circle on the bottom of the dish with a black marker to indicate the location of the crystal to facilitate finding the crystal under the microscope. Crystals transferred in this manner are stable in the paraffin oil drop for months.

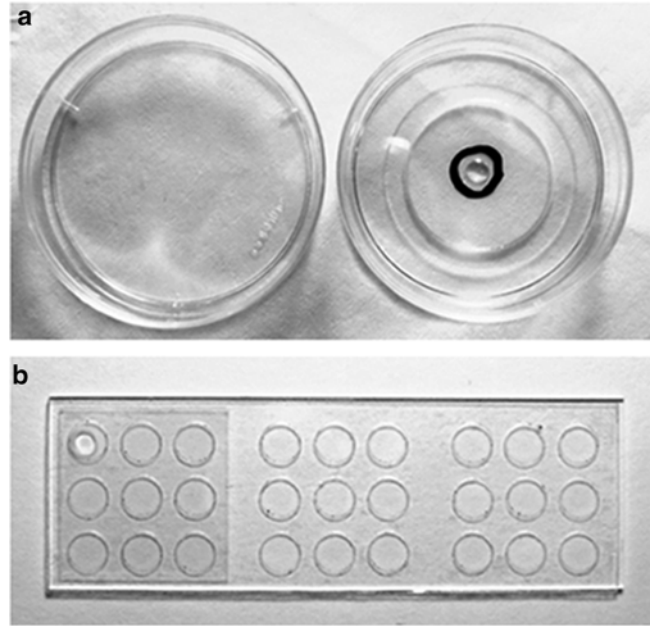

Fig. 2 Two formats for preparing rhodopsin crystals for TPM imaging. (**a**) A 35-mm dish containing a 1-μl drop of paraffin oil on the (glass) *bottom*; lid is on the *left*. (**b**) Glass sandwich plate, with a 1-μl drop in the *top-left* well. The *left* side of the microscope slide is sealed by a coverslip

3.3 Placement of the Rhodopsin Crystal on the Microscope

1. Place the dish with rhodopsin crystal(s) on the two-photon microscope stage (upside down if using an upright microscope).
2. Locate the crystal in the focus of the objective using X, Y, Z stage and dim bright-field illumination (if available) with a Roscolux red filter placed between the crystal and the white light source. Alternatively, to locate crystals and place them in focus, one can use 850-nm laser light at 5–15 mW and feedback from the non-descanned detector. Another option for centering the crystal under the objective is simply to use an external dim red light for illumination.

3.4 Crystal Imaging

1. Images are obtained using the detector in the non-descanned configuration to minimize the laser power needed for imaging. Begin by setting the imaging conditions to minimal zoom, 75 % detector gain, and a low laser power in the range of 2–10 mW.
2. Adjust objective clearance above the crystal until maximal signal from the crystal is obtained.
3. Set IR wavelength of the incident light in the range from 730 to 1,000 nm. To minimize bleaching of ground-state rhodopsin during the imaging, use 850-nm laser light.

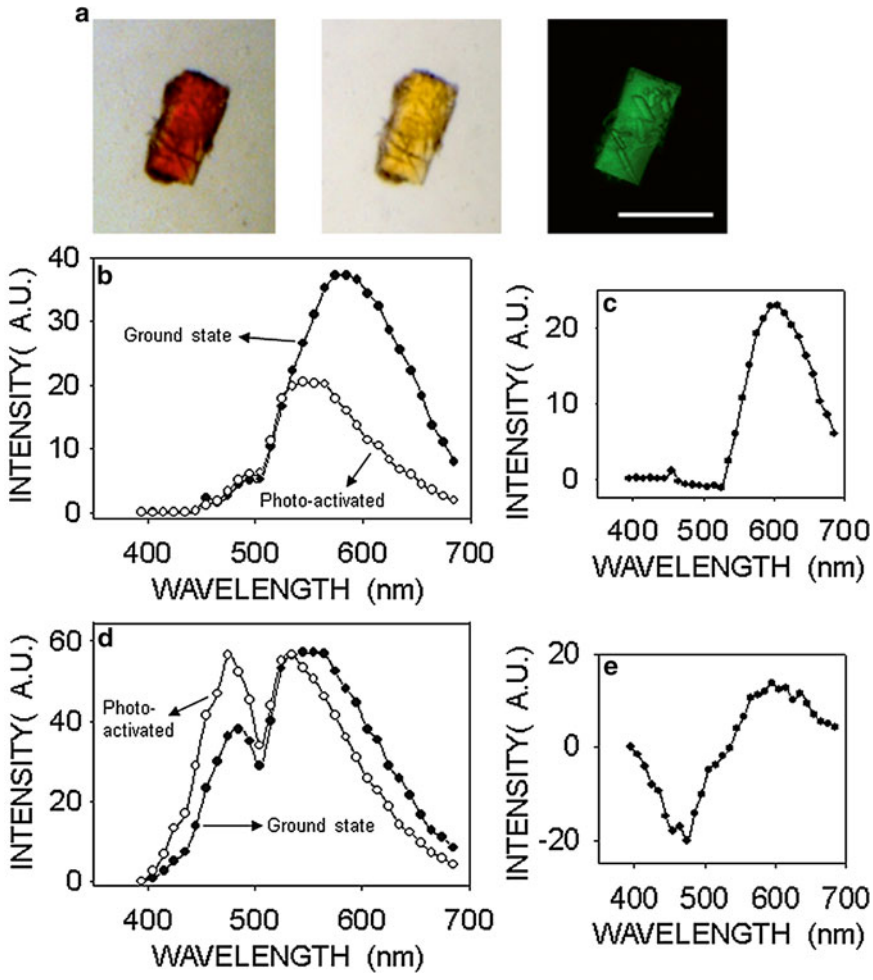

Fig. 3 TPM imaging and emission spectra of rhodopsin crystals. (**a**) Trigonal rhodopsin crystals were imaged with a bright-field microscope before (*left*) and after photoactivation (*center*). In the TPM image (730-nm excitation wavelength), smaller rhodopsin crystals are visible over a larger crystal (*right*). Scale bar represents 150 μm. (**b**, **d**) Emission spectra from rhodopsin crystals in the ground state (*closed circles*) and after photoactivation (*open circles*), with 910 nm (**b**) or 730 nm (**d**) used as excitation wavelengths. (**c**, **e**) Difference emission spectra of rhodopsin crystals (ground state minus photoactivated state) with an excitation wavelength of 910 nm (**c**) or 730 nm (**e**). Figure adapted with permission from Padayatti P., Palczewska G., Sun W., Palczewski K., and Salom D. "Imaging of protein crystals with two-photon microscopy" *Biochemistry*. 51(8):1625–1637 (2012). Copyright 2012 American Chemical Society

4. To obtain low-noise images, reduce the detector gain to about 50 % and average two or more frames together. A two-photon microscope image of rhodopsin crystal is shown in Fig. 3a (right).

3.5 TPEF Spectrum of Ground-State Rhodopsin Crystals

The TPEF spectrum of a single crystal is obtained using detectors in the descanned configuration. In this setup, light emitted from the sample is collected by the detector after passing through a prism which splits the light into a spectrum ranging from 400 to

750 nm. The emission spectrum will contain light emitted by the 11-*cis*-retinylidene moiety and oxidized tryptophan residues of rhodopsin. SHG signal, if any, is negligible as compared to TPEF in the EPI configuration (Fig. 3b, d). The emission spectrum will be dependent on the excitation wavelength [2, 13].

3.6 TPEF Spectrum of Photoactivated Rhodopsin Crystals

1. Without moving the crystal (if possible), photoactivate the crystal with ~500 nm or white light. The change in crystal color from red to yellow will be very apparent, (Fig. 3a) [10, 11]. Continue illumination until the yellow color is stable. This will take ~1–2 min, depending on the light intensity (*see* **Note 3**).
2. Image and collect the spectra of the photoactivated crystal under the same conditions as used for the ground-state crystal (Fig. 3b, d). The difference spectrum between ground state and photoactivated state reveals the contribution of the 11-*cis*-retinylidene chromophore to the TPEF spectrum (Fig. 3c, e).

3.7 Excitation Spectra of Ground-State and Photoactivated Rhodopsin Crystals

1. Excitation spectra need to be collected with the same laser power at each wavelength because TPEF is proportional to the square of the excitation power [14]. Before measuring the excitation spectra, place a laser power meter in the sample plane (*see* **Note 4**).
2. At each excitation wavelength, adjust the dispersion compensation and record the EOM settings that will produce the same average power.
3. Remove the laser power meter and place the rhodopsin crystal in focus as described in Subheading 3.3. Collect crystal images at each excitation wavelength using the EOM settings just obtained.
4. Plot the mean pixel value over the area of the crystal as a function of the excitation wavelength.

3.8 Placement of Rhodopsin Crystals in a Sandwich Format

An alternative method to placing the rhodopsin crystals in an arrangement compatible with TPM imaging is adapted from the sandwich format used for crystallization in a lipidic cubic phase (LCP) [15] (*see* **Note 5**). In this case, a closed space of a volume 1–2 μl is created between a glass microscope slide and a coverslip separated by die-cut double stick tape (Fig. 2b). This format is especially useful to analyze crystals that are difficult to harvest into a cryoloop due to their small size (<40 μm in the longest dimension) (Fig. 4). Crystals transferred to the sandwich setups in mother liquor are stable for weeks at room temperature.

The double stick tape can be perforated manually, or it can be obtained with die-cut holes from a die-cutting company (e.g., Saunders Corporation). Specifications for this example are 5–7-mm-diameter holes, 27 holes total, 7 mm spacing between holes, and overall size 1 × 3 in. Each coverslip covers 9 wells, and the microscope slide contains 27 wells in total [15].

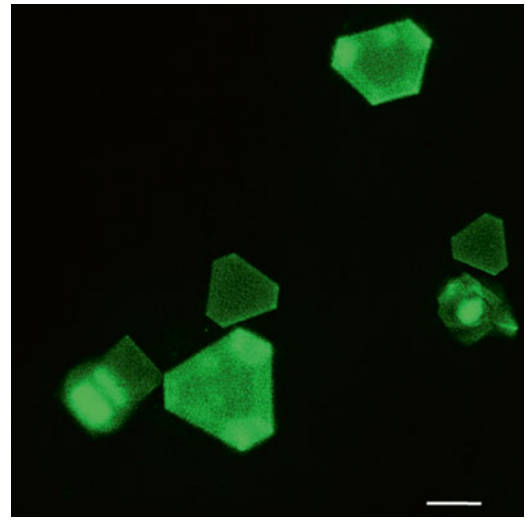

Fig. 4 TPM imaging of photoactivated trigonal rhodopsin crystals in a sandwich format. Images were obtained in an EPI configuration with 730-nm laser light. Scale bar represents 40 μm

1. Cut the perforated tape into a 1 × 1 in. piece leaving nine wells. Remove the protective paper from one side of the perforated double stick tape, and adhere it to a glass microscope slide.
2. Remove the second protective paper from the spacer tape.
3. With a micropipette with a 10-μl tip, transfer 1 μl of mother liquor containing rhodopsin crystals from a microbridge (in a vapor diffusion plate) to each well in the slide. If the sample is precious, fill just 2–3 wells per microscope slide, to enable the independent handling, imaging, and photoexposure of each sample.
4. Cover the filled wells with a siliconized coverslip.
5. Place the plate under the objective and then image with settings similar to those used for crystals in glass-bottomed dishes. Place the side with the thinner glass (coverslip) facing the objective.

4 Notes

1. Alternatively, a 96-well LCP glass sandwich plate from Hampton Research can be used (HR3-151).
2. It is also possible to image or obtain the TPEF spectra of ground-state, photoactivated, or apo-rhodopsin (opsin) crystals grown in space groups other than trigonal $P3_112$. A number of rhodopsin crystals in different crystallographic space groups have been reported since the initial crystal structure of

rhodopsin was determined in 2000. The first ground-state rhodopsin crystal structures solved were obtained from crystals grown in $P4_1$ and $P6_4$ symmetries [16–18], and at least nine crystal structures with all-*trans*-retinal-bound rhodopsin or opsin have since been described (in space groups R3 and R32). However, crystals in $P4_1$ and $P6_4$ symmetries are not stable after photoactivation. The advantage of trigonal $P3_112$ crystals [10, 11] is the possibility of scanning the same crystal before and after photoactivation and, therefore, obtaining a difference spectrum that will reflect only the contribution of the retinylidene moiety to the spectrum (after subtracting the contribution of SHG and TPEF from oxidized tryptophan residues) (Fig. 3c). In addition, we also have described a method to grow R32 crystals of ground-state rhodopsin that are stable after photoactivation [10] and therefore are also amenable to imaging by TPM before and after photoactivation. Opsin crystals could also be imaged by TPM, thanks to the contribution of their oxidized tryptophans [2]. Finally, a major advantage of this technique would be to monitor crystallization trials of rhodopsin, especially in LCP format, as non-rhodopsin crystals would not evidence a contribution of the retinylidene moiety to the TPEF signal.

3. Alternatively, a ground-state crystal can be bleached in the mother liquor solution before being transferred to the paraffin oil, but this precludes the ability to measure the TPEF contribution due to the chromophore.
4. Because laser power can fluctuate, one should make the laser power and EOM settings measurements immediately before obtaining excitation spectra but at least 1 h after EOM is switched on and the microscope is equilibrated with laser light. After collecting excitation spectra, verify EOM settings with the laser power meter.
5. Crystals grown in the LCP sandwich format can be imaged in situ (e.g., *see* bacteriorhodopsin and photosynthetic reaction center in Fig. A2 and B2 of ref. 2). Therefore, sandwich plates would also be the preferred format for the crystallization of rhodopsin in LCP because of the ease of monitoring the trials by TPM.

Acknowledgments

We thank David T. Lodowski for his critical review and Krzysztof Palczewski for stimulating discussions. Research described herein was funded in part by the grants from the National Eye Institute of the National Institutes of Health RO1EY008061 and RO1EY009339.

References

1. Haupert LM, Simpson GJ (2011) Screening of protein crystallization trials by second order nonlinear optical imaging of chiral crystals (SONICC). Methods 55:379–386
2. Padayatti P, Palczewska G, Sun W et al (2012) Imaging of protein crystals with two-photon microscopy. Biochemistry 51:1625–1637
3. Mohler W, Millard AC, Campagnola PJ (2003) Second harmonic generation imaging of endogenous structural proteins. Methods 29:97–109
4. Haupert LM, DeWalt EL, Simpson GJ (2012) Modeling the SHG activities of diverse protein crystals. Acta Crystallogr D Biol Crystallogr 68:1513–1521
5. Closser RG, Gualtieri EJ, Newman JA et al (2013) Characterization of salt interferences in second-harmonic generation detection of protein crystals. J Appl Crystallogr 46:1903–1906
6. Madden JT, DeWalt EL, Simpson GJ (2011) Two-photon excited UV fluorescence for protein crystal detection. Acta Crystallogr D Biol Crystallogr 67:839–846
7. Wampler RD, Kissick DJ, Dehen CJ et al (2008) Selective detection of protein crystals by second harmonic microscopy. J Am Chem Soc 130:14076–14077
8. Forsythe E, Achari A, Pusey ML (2006) Trace fluorescent labeling for high-throughput crystallography. Acta Crystallogr D Biol Crystallogr 62:339–346
9. Kissick DJ, Gualtieri EJ, Simpson GJ et al (2010) Nonlinear optical imaging of integral membrane protein crystals in lipidic mesophases. Anal Chem 82:491–497
10. Salom D, Le Trong I, Pohl E et al (2006) Improvements in G protein-coupled receptor purification yield light stable rhodopsin crystals. J Struct Biol 156:497–504
11. Salom D, Lodowski DT, Stenkamp RE et al (2006) Crystal structure of a photoactivated deprotonated intermediate of rhodopsin. Proc Natl Acad Sci U S A 103:16123–16128
12. Salom D, Padayatti PS, Palczewski K (2013) Crystallization of G protein-coupled receptors. Methods Cell Biol 117:451–468
13. Kochendoerfer GG, Mathies RA (1996) Spontaneous emission study of the femtosecond isomerization dynamics of rhodopsin. J Phys Chem 100:14526–14532
14. Denk W, Strickler JH, Webb WW (1990) Two-photon laser scanning fluorescence microscopy. Science 248:73–76
15. Caffrey M, Cherezov V (2009) Crystallizing membrane proteins using lipidic mesophases. Nat Protoc 4:706–731
16. Li J, Edwards PC, Burghammer M et al (2004) Structure of bovine rhodopsin in a trigonal crystal form. J Mol Biol 343:1409–1438
17. Palczewski K, Kumasaka T, Hori T et al (2000) Crystal structure of rhodopsin: a G protein-coupled receptor. Science 289:739–745
18. Stenkamp RE (2008) Alternative models for two crystal structures of bovine rhodopsin. Acta Crystallogr D Biol Crystallogr D64:902–904

Part III

Structure–Function Characterization of Rhodopsin

Chapter 5

Functional Stability of Rhodopsin in a Bicelle System: Evaluating G Protein Activation by Rhodopsin in Bicelles

Ali I. Kaya, T.M. Iverson, and Heidi E. Hamm

Abstract

Rhodopsin is a prototypical member of the G protein-coupled receptors (GPCRs). This photoreceptor is responsible for initiating the visual signaling transduction cascade upon interaction with its heterotrimeric G protein, transducin (Gt), after light activation. Like all transmembrane proteins, rhodopsin is embedded within a phospholipid bilayer. Many studies have proposed that the membrane composition of this bilayer is an important factor for receptor function during the activation process. Here we describe the methods and assays used to evaluate the function of purified and reconstituted rhodopsin in bicelles.

Key words Rhodopsin reconstitution, Transducin, Bicelles, Receptor–G protein interaction, Receptor stability

1 Introduction

G protein-coupled receptors (GPCRs) are the largest family of cell surface proteins and use a conserved signaling mechanism to transmit information across biological membranes. In the vision, rhodopsin (in rod photoreceptors) and cone opsins (in cone photoreceptors) are responsible for the signal transduction cascade that mediates night and color vision, respectively [1]. Like all integral membrane proteins, rhodopsin is surrounded by a phospholipid bilayer and the composition of the lipid bilayer influences receptor function [2]. Several groups have been studying different GPCRs reconstitution systems and the effects the membrane composition has on receptor activity. These studies show that detergent-solubilized rhodopsin does not retain the functionality as seen in the native environment [3–9]. As a result, biophysical and structural studies of rhodopsin using techniques that require purified protein, such as NMR spectroscopy, EPR spectroscopy, and X-ray crystallography, have been particularly challenging and the studies performed in detergents may not represent a fully functional state of the protein.

Beata Jastrzebska (ed.), *Rhodopsin: Methods and Protocols*, Methods in Molecular Biology, vol. 1271,
DOI 10.1007/978-1-4939-2330-4_5,

One well-established reconstitution medium that allows the evaluation of lipids on function is bicelles [10, 11]. Bicelles are mixture of long- and short-chain phospholipids that self-assemble into long-chain bilayers capped by short-chain lipids or detergents. The structure and stability of bicelles are highly dependent on both temperature and pH. Likewise, their biochemical properties can be influenced by phospholipid-specific differences in composition [11–14]. To better mimic the native membranes, bicelle composition can be modified by incorporating phospholipids with different polar head groups and acyl chain lengths [14–17].

In the rhodopsin–G protein system, negatively charged phospholipids, such as phosphatidylglycerol, phosphatidylserine, phosphatidylethanolamine, and phosphatidic acid, improve the efficiency of rhodopsin activation and G protein interaction [5, 9, 18, 19]. Depending on the negatively charged phospholipid composition and concentration, bicelles can stabilize the receptor–G protein complex to the same extent as the native membrane [9].

In the following sections, we describe the methods used in our laboratory to reconstitute rhodopsin into bicelles and the methods we used to test the effects of different phospholipid compositions on the rhodopsin–G protein interaction.

2 Materials

2.1 Solubilization of Rhodopsin from Urea-Washed ROS Membranes

1. *N*-dodecyl β-D-maltoside (DDM) powder or concentrated stock solution.
2. Lauryl Maltose Neopentyl Glycol (MNG3) powder or concentrated stock solution.
3. Concanavalin A (Con A) Binding Buffer (*see* below, Subheading 2.2).

2.2 Purification of Rhodopsin from ROS Membranes by Concanavalin A Sepharose

1. 1 ml HiTrap Con A 4B Column.
2. Con A Binding Buffer: 20 mM Tris–HCl, pH 7.4, 500 mM NaCl, 1 mM $CaCl_2$, 1 mM $MnCl_2$, 0.5 mM DDM or MNG3.
3. Wash Buffer: Con A Binding Buffer. Change detergent or its concentration, if necessary.
4. Elution Buffer: 20 mM Tris–HCl, pH 7.4, 500 mM NaCl, 200–500 mM methyl-α-D-glucopyranoside (methyl-α-D-glucoside) or methyl-α-D-mannopyranoside (methyl-α-D-mannoside), DDM or MNG3 (vary detergent concentration).

2.3 Determining the Concentration of Rhodopsin

1. 20 mM Hexadecyl-cetyltrimethylammonium chloride (HTAC) Buffer.

2.4 Bicelle Preparation

1. Long-chain lipids:
   1,2-Dimyristoyl-sn-glycero-3-phospho-L-serine (DMPS).
   1,2-Dihexanoyl-sn-glycero-3-phosphocholine (DMPC).
   1,2-Dimyristoyl-sn-glycero-3-phosphate (DMPA).
   1,2-Dimyristoyl-sn-glycero-3-phospho-(1′-rac-glycerol) (DMPG).
2. Short-chain lipids or detergents:
   1,2-Dihexanoyl-sn-glycero-3-phosphocholine (DHPC).
   3-[(3-Cholamidopropyl)dimethylammonio]-1-propanesulfonate (CHAPS).
   3-[(3-Cholamidopropyl)dimethylammonio]-2-hydroxy-1-propanesulfonate (CHAPSO).

2.5 Metarhodopsin-II (Meta-II) Assay

1. Meta-II Assay Buffer: 20 mM 4-(2-hydroxyethyl)-1-piperazine-1-ethanesulfonic acid (HEPES), pH 7.2, 100 mM NaCl, 1 mM $MgCl_2$, 1 mM DTT.
2. Purified rhodopsin in bicelles.

2.6 Intrinsic Tryptophan Fluorescence Assays

1. Nucleotide Exchange Assay Buffer: 20 mM HEPES pH 7.2, 100 mM NaCl, 1 mM $MgCl_2$, 1 mM DTT.
2. 10 μM GTPγS.

3 Methods

Urea-washed ROS membrane preparation, G protein expression, and purification methods are well described in previous studies [5, 8, 20–23].

3.1 Solubilization of Rhodopsin from Urea-Washed ROS Membrane

1. All steps should be performed under dim red light and on ice or at 4 °C. Thaw 200 μl (~10 mg) urea-washed dark-adapted ROS membranes on ice.
2. Centrifuge the membranes for 20 min at 4 °C at 16,000 × *g* in a benchtop centrifuge.
3. Discard the supernatant and resuspend the pellet with 200 μl of Con A Binding Buffer containing detergent (*see* **Note 1**). Incubate the resuspended pellet on ice for 25 min. Mix the sample by pipetting every 15 min during the incubation.
4. Centrifuge the sample for 20 min at 4 °C at 16,000 × *g* in a benchtop centrifuge.
5. Collect the supernatant and discard the pellet.

3.2 Purification of Detergent-Extracted Rhodopsin by Concanavalin A Affinity Chromatography

1. Equilibrate the Concanavalin A (Con A) column with Con A Binding Buffer at a flow rate of 0.5 ml/min overnight (*see* **Note 2**).
2. Load detergent-solubilized rhodopsin at a flow rate of 0.1–0.25 ml/min (*see* **Note 3**). Rhodopsin should be loaded into the column in the dark and at 4 °C.
3. Wash the column with Wash Buffer (use 10× the column volume) at a flow rate of 0.25 ml/min.
4. Elute rhodopsin with elution buffer (use 5× the column volume) at a flow rate of 0.25 ml/min.
5. Concentrate the elution fractions in a 50 kDa molecular weight cutoff concentrator in the dark. Centrifuge the concentrator in a benchtop centrifuge at 4 °C at 2,000 × *g* in 10 min intervals (*see* **Note 4**).

3.3 Measuring the Concentration of Rhodopsin

The concentration of solubilized rhodopsin is determined by measuring its absorbance at λ_{500} and λ_{650} nm before and after photobleaching in the presence of 20 mM of the fluorescence-enhancing reagent, HTAC.

1. To measure the baseline, record an absorption spectrum from $\lambda_{350–650}$ nm of 20 mM HTAC Buffer (*see* **Note 5**).
2. Dilute the rhodopsin sample with HTAC Buffer and record the absorption spectrum from $\lambda_{350\text{-}650}$ nm for the dark-adapted sample.
3. Photobleach the rhodopsin-containing sample by using a camera flash. Mix the sample by pipetting up and down within the cuvette and pulse the sample with light a second time to ensure complete light activation. Mix the sample again and record a third spectrum from $\lambda_{350\text{-}650}$ nm for the light-adapted sample.
4. Absorbance can be calculated by using the equation below:

$$\begin{aligned}\mathrm{Abs}(\text{dark-light}) = {} & \mathrm{Abs}(\lambda_{500} - \lambda_{650})(\text{in the dark-adapted spectrum}) \\ & - \mathrm{Abs}(\lambda_{500} - \lambda_{650})(\text{in the light-adapted spectrum})\end{aligned}$$

5. The concentration of the rhodopsin sample can then be calculated using the following equations from Beer's Law:

$$\mathrm{Abs}(\text{dark-light}) = \varepsilon b C$$

where Abs is the absorbance value, ε corresponds to the molar extinction coefficient for rhodopsin, b corresponds to the path length (in cm), and C is the concentration (in units of molarity (mol/l)). The molar extinction coefficient (ε) is 42,000/M/cm for rhodopsin in ROS membranes and 40,600/M/cm for detergent-extracted rhodopsin.

3.4 Bicelle Preparation and Rhodopsin Incorporation

Bicelles can be prepared from a number of long- and short-lipid (or detergents) combinations and at different stock concentrations. The final bicelle concentration can be chosen to range between 10 and 40 % (*see* **Note 6**).

3.4.1 Bicelle Preparation

1. Weigh out long and short lipids (or detergents) and add deionized water to the final volume and vortex (*see* **Note 6**). The molar ratio (q value) of long/short-chain lipids should be between 2.6 and 3.5 (*see* **Note 7**).
2. To obtain complete hydration and homogenous solution, the mixture requires heating and cooling cycles. Heat the mixture to 40–50 °C for 5 min then place on ice for 2 min to cool down and briefly vortex the sample (*see* **Note 8**).
3. The mixture should be a viscous liquid on ice but gel upon raising the temperature to 30 °C after complete hydration, which reflects phase change of lipids.
4. Charged bicelles (DMPA, DMPG, or DMPS) can be prepared by substituting a percentage of the total molar lipid content of the neutral bicelles (*see* **Note 9**).
5. For long-term storage, the bicelle mixture should be stored at −80 °C.

3.4.2 Incorporation of Rhodopsin into Bicelles

1. Thaw the bicelles at room temperature until the phase changes the samples into a clear gel (*see* **Note 10**).
2. Place the bicelle mixture on ice and vortex briefly to reestablish a homogenous phase and place the sample back on ice. While chilled on ice, it will remain in the liquid phase making it capable to pipette.
3. Add the bicelle solution to the purified detergent-solubilized and Con A-purified rhodopsin in the dark (*see* **Note 11**).
4. Gently pipette the bicelle–protein mixture until the solution becomes clear and homogenous (*see* **Note 12**).
5. Incubate the mixture on ice for at least 30 min to allow for complete reconstitution of the proteins into bicelles (*see* **Note 13**).

3.5 Metarhodopsin-II (Meta-II) Assay

Metarhodopsin-II is the active state of rhodopsin that binds and catalyzes release of GDP from the G protein. The Meta-II assay can be used to detect receptor–G protein interactions and monitor the high-affinity state of rhodopsin in the presence of heterotrimeric G proteins.

1. Mix dark-adapted rhodopsin with Meta-II Assay Buffer (*see* **Note 14**) for a final concentration of 2 μM of rhodopsin.
2. Incubate the sample on ice for 30 min in the dark or under dim red light. Pipette the incubated sample into a spectrophotometer cuvette and collect an absorption spectrum from $\lambda_{350\text{-}650}$ nm for the dark-adapted sample.

3. Light-activate the sample by pulsing with a camera flash. Wait 1 min to allow the sample to be completely activated, mix thoroughly by pipetting, and collect a second absorption spectrum from $\lambda_{350\text{-}650}$ nm for the light-adapted sample (*see* **Note 15**).
4. To determine the signal contributed by Meta-II, calculate the difference in the absorbance between λ_{380} and λ_{440} nm for both the dark-adapted and light-adapted readings using equation below:

$$\text{Meta-II single (Abs(light-dark))} = [\text{Abs at } \lambda_{380} - \lambda_{440} \text{ (in light-adapted spectrum)}] - [\text{Abs at } \lambda_{380} - \lambda_{440} \text{ (in dark-adapted spectrum)}]$$

5. To calculate the extra Meta-II signal, which is Meta-II pulled out of the Meta-I–Meta-II equilibrium by interaction with the heterotrimeric G protein, mix the 2 μM dark-adapted rhodopsin solution with 10 μM of purified Gt in Meta-II Assay Buffer (*see* **Notes 16** and **17**). Incubate the sample on ice for 30 min under dim red light and measure the Meta-II signal as described above. The extra Meta-II signal can be calculated by subtracting the signal with and without G protein present (Fig. 1a). To determine the extra Meta-II decay, light spectrum can be recorded every 10–20 min for several hours (Fig. 1b). The decay of the samples can be calculated by fitting the extra Meta-I signal for each time point by using an exponential decay equation.

3.6 Receptor-Catalyzed GTPγS Exchange Assay

The rate of receptor-mediated nucleotide exchange can be measured by monitoring the increase in intrinsic tryptophan fluorescence in the alpha subunit of the G protein in the presence of light-activated rhodopsin.

1. Mix 500 nM of the heterotrimeric G protein in a quartz cuvette containing Nucleotide Exchange Assay Buffer (*see* **Note 18**).
2. Set the excitation wavelength to 280 nm and emission wavelength to 340 nm.
3. Add 50 nM purified rhodopsin in the dark. Mix thoroughly by pipetting.
4. For the baseline, collect the emission spectrum at 340 nm for 5 min.
5. Add 10 μM GTPγS and activate the rhodopsin by pulsing with a light flash and collect the emission spectrum for another 45 min (*see* **Note 19**).
6. To determine the receptor-catalyzed nucleotide exchange rate, fit the data to an exponential association equation:

$$I_0 = I_{\max}\left(1 - \exp\right)^{-kt}$$

where I_0 is the emission intensity at time 0, $I_{\max}$ is the maximum intensity, k is the rate constant, and t is the time (Fig. 2).

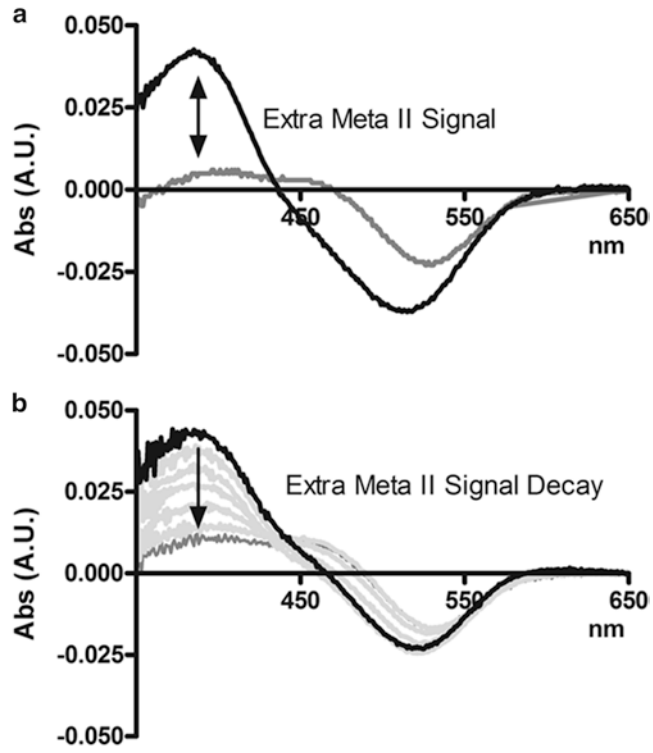

Fig. 1 Differences in light and dark absorption spectra of rhodopsin. (**a**) UV-visible absorption spectrum of 2 μM rhodopsin (*black*) and 2 μM rhodopsin +10 μM heterotrimeric G protein (*grey*). The difference between spectra was obtained by subtracting the light spectrum from the dark spectrum. An *arrow* indicates the extra Meta-II signal. (**b**) Decay of the extra Meta-II signal. UV-visible absorption spectrum of 2 μM rhodopsin +10 μM heterotrimeric G protein (*grey*). *Light grey* spectrums shows signal decay for each relative time point (Color figure online)

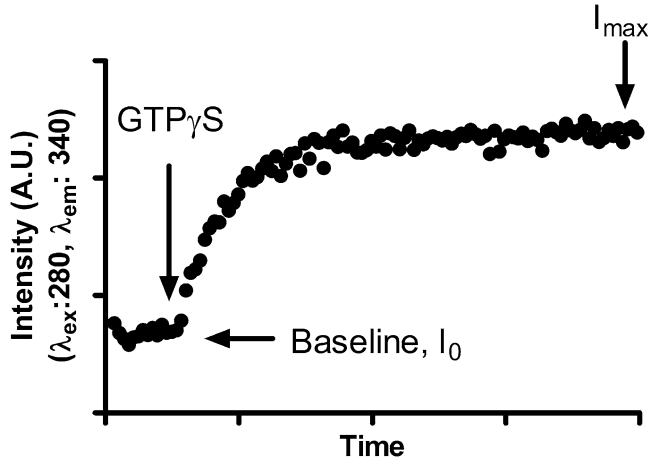

Fig. 2 Rhodopsin-mediated nucleotide exchange of G protein. Nucleotide exchange was monitored by measuring intrinsic tryptophan fluorescence over time. *Arrows* indicate the time of GTPγS addition, initial intensity, and maximum intensity

4 Notes

1. Final detergent concentration should be ~2 and ~1 mM for DDM and MNG3, respectively.
2. To avoid protein aggregation, it is important to pre-equilibrate the Con A column overnight (at least) with constant flow in a buffer containing the relevant detergent.
3. To increase the binding efficiency of rhodopsin to the Con A column, the loading flow should be decreased as much as possible or a continuous loop should be used.
4. Buffers may be exchanged for assay buffer (Meta-II or Nucleotide Exchange Assay Buffer) using the same concentrator. If it is necessary, detergent concentration may be decreased during buffer exchange.
5. Baseline buffer should also contain the same final concentration of detergent as the sample fraction.
6. Preparation of a high bicelle concentration might be challenging due to problems with dissolving phospholipids at such a high viscosity. However, a concentrated bicelle solution can be needed when the protein concentration is low. In our laboratory, we prepare a 35 % bicelle stock solution, and we use a final 8 % concentration in the assays.
7. The q value is the ratio of long-chain to short-chain lipids, which controls the physical diameter of the bicelles. It is important to maintain protein function upon reconstitution into bicelles. Like the q value, temperature affects the bicelle shape. At low temperatures and low q values, the system exists as a fluid; it can form characteristic bicelles with the long-chain lipids residing in the planar bilayer regions and the short-chain lipid, or detergent, in the highly curved regions at the cap of the disk. Higher temperatures, in the range of the fluid-to-gel transition temperature, transform the system into flexible worm-like, quasi-cylindrical, elongated micelles. These structures have high concentrations of the short-chain lipids along the lengths of the micelles. As the temperature increases further, the system transitions into the perforated lamellar phase, which consists of multi-lamellar vesicles with pore-like defects in the lamellar sheets. The edges of the pores are lined with the short-chain lipids. The lamellar phase is gel-like and is also referred to as the Swiss cheese form. Bicelle dimensions and purity can be monitored with dynamic light scattering [24–27].
8. Depending on the q value and lipid composition, this step may take more than one cycle. Do not use ultrasound devices. When the mixture is homogeneous and fully hydrated, this stock can be used multiple times for many protein samples.

9. Different negatively charged phospholipids can be used in the same bicelle preparation. In addition to charged phospholipids, bicelles can also be prepared with longer chain sizes, like palmitoyl phosphatidylcholine (DPPC) or dilauroyl phosphatidylcholine (DLPC). Bilayer thickness may also affect membrane protein stability and functionality.
10. Multiple freeze-thaws do not affect bicelle behavior.
11. The final desired protein concentration will depend on the assay type. For instance, protein concentration increases up to 20 mg/ml in the crystallization setup. However, the final bicelle concentration should be kept between 4 and 8 %.
12. A quick and gentle spin with a benchtop centrifuge may help to remove bubbles that may appear during mixing.
13. Rhodopsin is stable in the presence of phospholipids and in the dark for several hours. Keep the rhodopsin-bicelle mixture on ice until ready to perform assays.
14. To avoid possible phospholipid scattering, the rhodopsin concentration should be kept as low as possible based on the instrument's detection limits.
15. Rhodopsin's activation efficiency depends on the light source wavelength and intensity. This may require protocol optimization for full activation. To avoid excess heat from the light source, heat filters should be used.
16. To detect the binding curve between rhodopsin and the heterotrimeric G protein, G protein concentrations can be titrated.
17. Assay results may vary due to different temperatures and pH levels. pH directly affects rhodopsin activation.
18. This assay can be performed with either transducin ($G t\alpha\beta\gamma$) or with $G\alpha i$ and the $G\beta 1\gamma 1$ subunit. If recombinant $G\alpha$ subunit is being used, incubate the α and $\beta\gamma$ subunits together for at least 10 min in a small volume to allow subunit association before adding into full volume within the cuvette.
19. Nucleotide exchange rates can be altered by temperature. If the exchange rate is slow, the assay time may need to be extended.

References

1. Palczewski K (2006) G protein-coupled receptor rhodopsin. Annu Rev Biochem 75:743–767
2. Ostermeier C, Iwata S, Ludwig B et al (1995) Fv fragment-mediated crystallization of the membrane protein bacterial cytochrome c oxidase. Nat Struct Biol 2:842–846
3. Fung JJ, Deupi X, Pardo L et al (2009) Ligand-regulated oligomerization of beta(2)-adrenoceptors in a model lipid bilayer. EMBO J 28:3315–3328
4. Litman BJ, Niu SL, Polozova A et al (2001) The role of docosahexaenoic acid containing phospholipids in modulating G protein-coupled signaling pathways: visual transduction. J Mol Neurosci 16:237–242, discussion 279–284
5. Jastrzebska B, Goc A, Golczak M et al (2009) Phospholipids are needed for the proper formation, stability, and function of the photoactivated rhodopsin-transducin complex. Biochemistry 48:5159–5170

6. Bayburt TH, Leitz AJ, Xie G et al (2007) Transducin activation by nanoscale lipid bilayers containing one and two rhodopsins. J Biol Chem 282:14875–14881
7. Luecke H, Schobert B, Stagno J et al (2008) Crystallographic structure of xanthorhodopsin, the light-driven proton pump with a dual chromophore. Proc Natl Acad Sci U S A 105:16561–16565
8. Jastrzebska B, Golczak M, Fotiadis D et al (2009) Isolation and functional characterization of a stable complex between photoactivated rhodopsin and the G protein, transducin. FASEB J 23:371–381
9. Kaya AI, Thaker TM, Preininger AM et al (2011) Coupling efficiency of rhodopsin and transducin in bicelles. Biochemistry 50: 3193–3203
10. Sanders CR, Schwonek JP (1992) Characterization of magnetically orientable bilayers in mixtures of dihexanoylphosphatidylcholine and dimyristoylphosphatidylcholine by solid-state NMR. Biochemistry 31:8898–8905
11. Sanders CR, Prosser RS (1998) Bicelles: a model membrane system for all seasons? Structure 6:1227–1234
12. Wu H, Su K, Guan X et al (2010) Assessing the size, stability, and utility of isotropically tumbling bicelle systems for structural biology. Biochim Biophys Acta 1798:482–488
13. Glover KJ, Whiles JA, Wu G et al (2001) Structural evaluation of phospholipid bicelles for solution-state studies of membrane-associated biomolecules. Biophys J 81:2163–2171
14. Struppe J, Whiles JA, Vold RR (2000) Acidic phospholipid bicelles: a versatile model membrane system. Biophys J 78:281–289
15. Struppe J, Komives EA, Taylor SS et al (1998) 2H NMR studies of a myristoylated peptide in neutral and acidic phospholipid bicelles. Biochemistry 37:15523–15527
16. Crowell KJ, Macdonald PM (1999) Surface charge response of the phosphatidylcholine head group in bilayered micelles from phosphorus and deuterium nuclear magnetic resonance. Biochim Biophys Acta 1416:21–30
17. Marcotte I, Dufourc EJ, Ouellet M et al (2003) Interaction of the neuropeptide met-enkephalin with zwitterionic and negatively charged bicelles as viewed by 31P and 2H solid-state NMR. Biophys J 85:328–339
18. Gibson NJ, Brown MF (1991) Role of phosphatidylserine in the MI-MII equilibrium of rhodopsin. Biochem Biophys Res Commun 176:915–921
19. Gibson NJ, Brown MF (1993) Lipid headgroup and acyl chain composition modulate the MI-MII equilibrium of rhodopsin in recombinant membranes. Biochemistry 32: 2438–2454
20. Thaker TM, Kaya AI, Preininger AM et al (2012) Allosteric mechanisms of G protein-coupled receptor signaling: a structural perspective. Methods Mol Biol 796:133–174
21. Aris L, Gilchrist A, Rens-Domiano S et al (2001) Structural requirements for the stabilization of metarhodopsin II by the C terminus of the a subunit of transducin. J Biol Chem 276:2333–2339
22. Oldham WM, Van Eps N, Preininger AM et al (2006) Mechanism of the receptor-catalyzed activation of heterotrimeric G proteins. Nat Struct Mol Biol 13:772–777
23. Mazzoni MR, Malinksi JA, Hamm HE (1991) Structural analysis of rod GTP-binding protein Gt. Limited proteolytic digestion pattern of Gt with four proteases defines monoclonal antibody epitope. J Biol Chem 266: 14072–14081
24. van Dam L, Karlsson G, Edwards K (2004) Direct observation and characterization of DMPC/DHPC aggregates under conditions relevant for biological solution NMR. Biochim Biophys Acta 1664:241–256
25. van Dam L, Karlsson G, Edwards K (2006) Morphology of magnetically aligning DMPC/DHPC aggregates-perforated sheets, not disks. Langmuir 22:3280–3285
26. Faham S, Boulting GL, Massey EA et al (2005) Crystallization of bacteriorhodopsin from bicelle formulations at room temperature. Protein Sci 14:836–840
27. Prosser RS, Hwang JS, Vold RR (1998) Magnetically aligned phospholipid bilayers with positive ordering: a new model membrane system. Biophys J 74:2405–2418

Chapter 6

The Rhodopsin-Arrestin-1 Interaction in Bicelles

Qiuyan Chen, Sergey A. Vishnivetskiy, Tiandi Zhuang, Min-Kyu Cho, Tarjani M. Thaker, Charles R. Sanders, Vsevolod V. Gurevich, and T.M. Iverson

Abstract

G-protein-coupled receptors (GPCRs) are essential mediators of information transfer in eukaryotic cells. Interactions between GPCRs and their binding partners modulate the signaling process. For example, the interaction between GPCR and cognate G protein initiates the signal, while the interaction with cognate arrestin terminates G-protein-mediated signaling. In visual signal transduction, arrestin-1 selectively binds to the phosphorylated light-activated GPCR rhodopsin to terminate rhodopsin signaling. Under physiological conditions, the rhodopsin-arrestin-1 interaction occurs in highly specialized disk membrane in which rhodopsin resides. This membrane is replaced with mimetics when working with purified proteins. While detergents are commonly used as membrane mimetics, most detergents denature arrestin-1, preventing biochemical studies of this interaction. In contrast, bicelles provide a suitable alternative medium. An advantage of bicelles is that they contain lipids, which have been shown to be necessary for normal rhodopsin-arrestin-1 interaction. Here we describe how to reconstitute rhodopsin into bicelles, and how bicelle properties affect the rhodopsin-arrestin-1 interaction.

Key words Arrestin, Bicelles, Lipid, Model membrane, Receptor, Rhodopsin

1 Introduction

The light receptor rhodopsin is located in the disk membranes of rod outer segments in the retina. When rhodopsin absorbs a photon of light, it initiates an electrical signal that allows dim light vision. Rhodopsin belongs to the largest membrane protein family: G-protein-coupled receptors (GPCRs). Rhodopsin signals through its cognate G protein transducin, and this signaling is quenched by visual arrestin-1. Light activation and subsequent phosphorylation by G-protein-receptor kinase-1 (GRK1, a.k.a. rhodopsin kinase) collectively promote arrestin-1 binding, which precludes any further coupling of activated rhodopsin to transducin (Fig. 1) [1, 2].

Structure-function studies of both rhodopsin and arrestin-1 have advanced our understanding of the molecular mechanisms of vision.

Beata Jastrzebska (ed.), *Rhodopsin: Methods and Protocols*, Methods in Molecular Biology, vol. 1271,
DOI 10.1007/978-1-4939-2330-4_6,

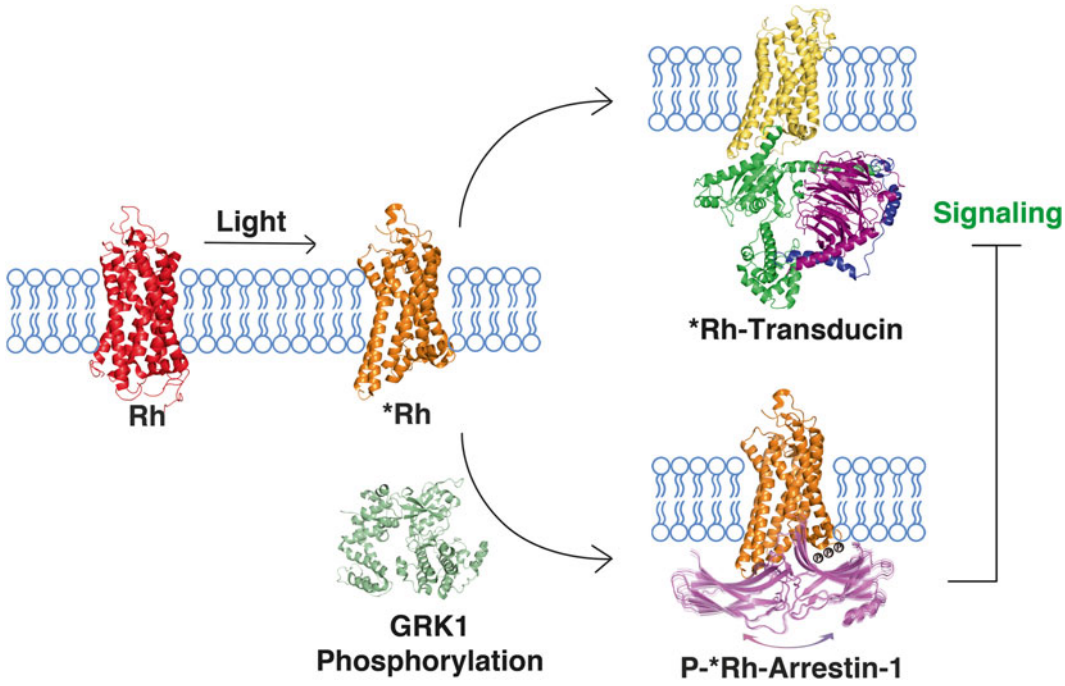

Fig. 1 Role of arrestin-1 in rhodopsin signaling. Rhodopsin is located in the disk membranes of the outer segments of rod photoreceptor cells. Upon light activation, dark rhodopsin (Rh PDB: 1F88) [52] undergoes conformational change to the active state (*Rh PDB: 3PQR) [53]. Its cognate G protein, transducin, binds to the active rhodopsin and initiates the downstream signaling (structure from molecular simulation) [54]. Active rhodopsin also recruits and activates GRK1 (PDB: 3C50) [55]. *Rh is phosphorylated at multiple sites by GRK1. Arrestin-1 binds to active phosphorylated rhodopsin (p-*Rh), blocking further transducin activation by steric exclusion. The displayed p-*Rh-arrestin-1 complex is the assembly of *Rh (PDB: 3PQR) [53] and pre-activated arrestin-1 (PDB: 4J2Q) [14] in Pymol. Arrestin-1 gains conformational flexibility in the receptor bound state

However, caution should be taken when applying these in vitro findings to the interpretation of the physiological process of vision. A major concern comes from the fact that most studies begin by extracting the receptor or the receptor complex from the lipid bilayer into detergent micelles, and thus the influence of the membrane is not accounted for. However, the lipid composition of the highly specialized disk membranes dramatically affects rhodopsin signaling (reviewed in [3, 4]). For this reason, several alternative membrane model systems have been explored that may be more native-like than micelles. Here we focus on the reconstitution of rhodopsin into bicelles and its consequences for rhodopsin signaling, particularly arrestin-1-mediated signal termination.

1.1 Introduction to the Role of Arrestin-1 in Rhodopsin Signaling

Arrestin-1 (a.k.a. S antigen, 48 kDa protein, rod or visual arrestin) mediates rhodopsin signal termination, which involves two steps. In the first step, light-activated rhodopsin (*Rh) is phosphorylated at multiple sites by GRK1. Arrestin-1 requires a minimum of three rhodopsin-attached phosphates for high-affinity binding [5, 6].

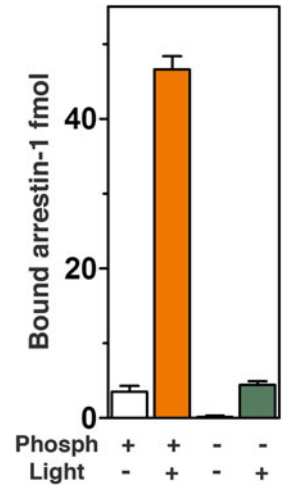

Fig. 2 Arrestin-1 has very high selectivity for phosphorylated active rhodopsin. Its binding to phosphorylated active rhodopsin is about 10- to 20-fold higher than to only-activated or only-phosphorylated rhodopsin, while its binding to dark rhodopsin is barely detectable

In the second step, arrestin-1 binds to active phosphorylated rhodopsin (p-*Rh) and blocks further transducin coupling by steric exclusion (Fig. 1) [2]. The high selectivity of arrestin-1 for p-*Rh (Fig. 2) ensures that signaling is terminated only when rhodopsin is in the activated and phosphorylated state [7–10].

The molecular mechanism underlying arrestin-1 selectivity has been extensively explored (reviewed in [11]). Arrestin-1 has two distinctly folded domains, termed the N- and C-domains (Fig. 3) [12–14]. In the basal, non-receptor-binding state, the distal C-terminal segment binds to the N-domain through two major interaction interfaces. One is the polar core comprising five charged residues in the N-domain (D30, R175), the C-domain (D296, D303), and the distal C-terminus (R382) (Fig. 3). The other is the hydrophobic three-element interaction between β-strand I (V11, I12, F13) and α-helix I (L103, L107, L111) in the N-domain and F375, V376, F377 in the C-terminus (Fig. 3) [12]. Receptor binding is proposed to disrupt the polar core and destabilize the three-element interaction [9, 15–17], which results in the release of the distal C-terminus [15, 18, 19]. Complementary studies employing site-directed spin labeling and electron paramagnetic resonance (EPR), functional mapping of arrestin-1 at single amino acid resolution, and X-ray crystallography of pre-activated arrestin-1 have also suggested that several arrestin-1 loops are involved in receptor binding [19–23]. In addition to these discrete conformational changes, recent evidence strongly suggests that arrestin-1 gains significant conformational flexibility upon binding to p-*Rh [15].

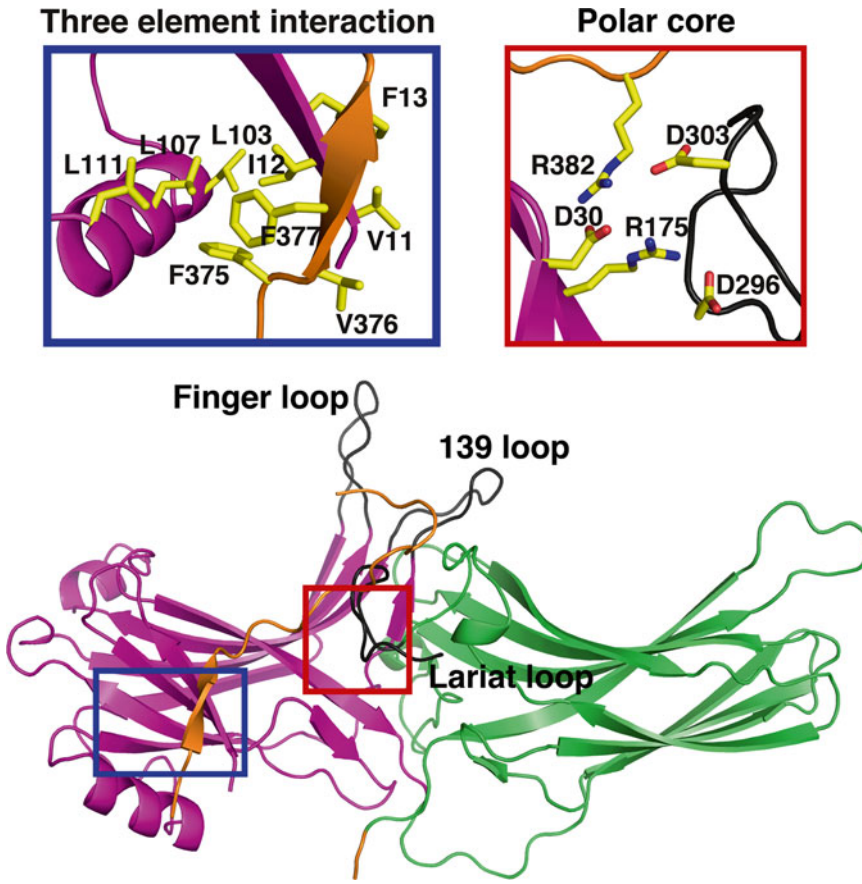

Fig. 3 The crystal structure of arrestin-1 (PDB: 1CF1) [12]. The N-domain is colored *magenta*, the C-domain is colored *green*, and the C-terminus is colored *orange*. Three loops have been reported to be involved in receptor binding: the finger loop, the 139 loop (referred to as the middle loop for nonvisual arrestins), and the lariat loop are shown in *dark gray*. Two major interactions that stabilize arrestin-1 in the basal state are displayed in details. The polar core comprises five charged residues distributed between the N-domain (D30, R175), the C-domain (D296, D303), and the C-terminus (R382). The hydrophobic three-element interaction is between β-strand I (V11, I12, F13) and α-helix I (L103, L107, L111) in the N-domain and F375, V376, F377 in the C-terminus

1.2 Introduction to Bicelles

Bicelles, first introduced by the Prestegard lab [24–27], have a central planar bilayer formed by long-chain lipids and edges shielded by either short-chain lipids or detergents (Fig. 4). The planar surface of bicelles and bilayered interior mimics the biological membrane much better than detergent micelles, while due to their small size and monodispersity, the attractive features of conventional micelles are retained. Indeed, bicelles have been successfully used to crystallize several membrane proteins (reviewed in [26]), particularly the GPCR β2 adrenergic receptor [28], after decades of efforts using traditional detergent crystallization failed.

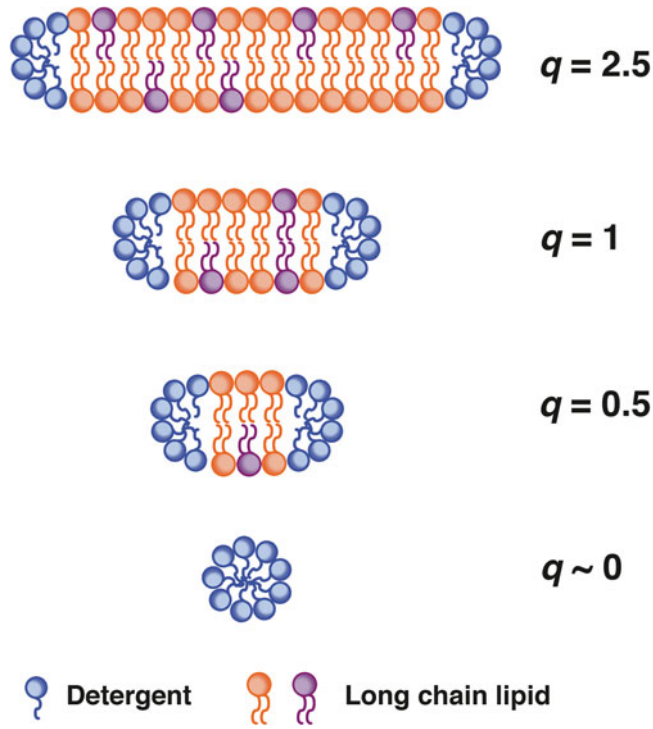

Fig. 4 Bicelles**.** Bicelles have a central planar bilayer formed by long-chain lipids (*orange*) with the edges stabilized by either short-chain lipids or detergents (*blue*). Phospholipids with different head groups (*purple*) can be used to tailor the charge characteristics of the surface and provide lipid composition versatility. The bicelles with a higher q value (e.g., $q=2.5$) have more extended lipid bilayers than ones with a lower q value (e.g., $q=0.5$). In this sense, detergent micelles can be viewed as bicelles with the q value equal to 0

The long-chain lipid determines the thickness of the lipid bilayer, while phospholipids with different head groups can tailor the charge characteristics of the surface and provide lipid composition versatility. Both the total phospholipid concentration (c) and ratio (q) of long-chain/short-chain phospholipid (or long-chain phospholipid/detergent) play an important role in shaping bicelles. Intuitively, a high q value indicates an extended bilayer, while bicelles with a low q value (e.g., $q<1$) more closely resemble round isotropic spheres (Fig. 4). It is a matter of some debate as to whether bicelles with $q\leq 0.5$ retain any of the characteristics of ideal bicelles or whether they should be regarded as classical mixed micelles (*see*, e.g., [29, 30]). Interestingly, it has been reported that mixtures of n-Dodecyl β-D-maltoside (DDM) and cholesteryl hemisuccinate (CHS) have an architecture more reminiscent of bicelles than micelles. The modulation of micelle morphology was shown to contribute significantly to stabilizing GPCRs, such as opioid-like receptor ORL-1 [31]. In fact, it is now common practice to include 10 % CHS in detergent micelle solutions for the purification and structural characterization of GPCRs [32].

1.3 Introduction to Reconstitution of Rhodopsin into Bicelles

The idea of including phospholipids in detergent micelles was applied to the study of rhodopsin as early as 1995, although at that time, what are termed bicelles were simply called a "phospholipid-detergent mixture" [33]. In that study, the influence of lipids on the stability of opsin, the apoprotein of rhodopsin, was assessed. Opsin denatures rapidly in detergent solution, losing its ability to bind 11-*cis*-retinal and regenerate to rhodopsin [34]. However, the presence of asolectin, a mixture of phospholipids, significantly improved the stability of opsin such that the protein was functional following detergent extraction and subsequent purification [33]. Shortly thereafter, the Khorana group replaced asolectin with a single phospholipid, dimyristoylphosphatidylcholine (DMPC), while keeping the 3-[(3-cholamidopropyl) dimethylammonio]-1-propanesulfonate (CHAPS) as the detergent component [35]. The DMPC/CHAPS bicelles successfully extracted opsin from membranes, and opsin reconstituted into these bicelles retained its retinal binding activity [35]. The effects of DMPC/CHAPS and DMPC/dihexanoylphosphatidylcholine (DHPC) bicelles on rhodopsin and opsin were more extensively characterized in 2007 [36]. The authors showed that rhodopsin and opsin had significantly increased stability in both types of bicelles as compared to their stability in detergent micelles. The q value modulated the opsin stability, which suggests that the bicelle size impacts opsin stability. Interestingly, the authors also showed that inclusion of CHAPS rather than DHPC in the DMPC/CHAPS bicelles further stabilized opsin [36]. This indicates that the detergent component of bicelles can affect protein stability either by directly interacting with the protein or by altering the bilayer properties. Due to high working lipid/protein ratios, bicelles usually contain monomeric GPCRs [15]. While this could create problems for constitutively dimeric class C GPCRs [37, 38], monomeric rhodopsin was shown to be sufficient for effective coupling to transducin [39, 40], efficient phosphorylation by GRK1 [6], and also arrestin-1 binding with physiologically relevant nanomolar affinity [6], which leads to the same conformational rearrangements in bound arrestin-1 as its interaction with p-*Rh in native disk membranes [20]. Mutations that select for monomeric-only protomers of rhodopsin were also shown to be phosphorylated by GRK1 and bind arrestin-1 effectively [41, 42].

Bicelles not only serve as an excellent model membrane system for rhodopsin but also greatly facilitate structural and dynamics studies of the rhodopsin-arrestin-1 interaction. Indeed, prior to the application of bicelles to the rhodopsin-arrestin-1 interaction, studies of this complex in a defined, purified system were dramatically hindered since arrestin-1 binding to rhodopsin is severely diminished when the receptor is solubilized with commonly used detergents ([43] and unpublished results). Near-UV circular dichroism spectra indicate that detergents cause significant changes

of arrestin-1 tertiary structure [15]. One possibility is that detergent penetration can potentially disrupt one of the two key interactions that hold arrestin-1 in the basal state (Fig. 3) and result in the "melting" of the arrestin-1 global structure. Interestingly, acidic phospholipids can restore the binding of arrestin-1 to rhodopsin purified in DDM. Moreover, arrestin-1 retains its selective binding to rhodopsin reconstituted in bicelles [43]. In addition to the fact that bicelles provide a milder environment than detergents, they also have several other clear advantages over detergent micelles in case of rhodopsin-arrestin interactions. First, the central planar bilayer of bicelles creates an extended native membrane-like surface, while detergent micelles might cover some receptor elements involved in arrestin-1 binding. Second, bicelles contain phospholipids that can regulate the rhodopsin-arrestin-1 interaction either via electrostatics or by directly binding to either rhodopsin or arrestin-1. It was found that acidic phospholipids significantly prolong the half-life of the rhodopsin-arrestin-1 complex and that 20–50 % lipids with negatively charged head group are essential to promote maximum binding [6, 43].

2 Materials

2.1 Preparation of Bicelles

1. Buffer A: 25 mM Bis–Tris, pH 6.5, 100 mM NaCl, 0.1 mM EDTA.
2. 1,2-Dimyristoyl-*sn*-glycero-3-phosphoglycerol (DMPG).
3. 1,2-Dimyristoyl-*sn*-glycero-3-phosphocholine (DMPC).
4. 1,2-Dihexanoyl-*sn*-glycero-3-phosphocholine (DHPC).

2.2 Reconstitution of Rhodopsin with Bicelles

1. Rod outer segment (ROS) membranes.
2. Buffer A: 25 mM Bis–Tris, pH 6.5, 100 mM NaCl, 0.1 mM EDTA.

2.3 Assessment of Structural Integrity of Arrestin by Near-UV Circular Dichroism (CD)

1. Buffer A: 25 mM Bis–Tris, pH 6.5, 100 mM NaCl, 0.1 mM EDTA.
2. Denaturing Buffer: 8 M urea in Buffer A.

2.4 Preparation of Radiolabeled Arrestin-1

1. Transcription mix [44]: 120 mM 4-(2-hydroxyethyl)-1-piperazine-1-ethanesulfonic acid (HEPES), pH 7.5, 2 mM spermidine, 16 mM $MgCl_2$, 40 mM dithiothreitol (DTT), 3 mM each of adenosine triphosphate (ATP), guanosine triphosphate (GTP), cytidine triphosphate (CTP), and uridine triphosphates (UTP), 2.5 U/ml inorganic pyrophosphatase, 200 U/ml RNasin, and 1,500 U/ml SP6 RNA polymerase.

2. 7.5 M LiCl.
3. 2.5 M LiCl.
4. 70 % (v/v) ethanol.
5. 3 M sodium acetate, pH 5.2.
6. 100 % ethanol.
7. Translation mix [7, 45]: 70 % rabbit reticulocyte lysate, 120 mM potassium acetate, 30 mM creatine phosphate, 200 μg/ml creatine kinase, 200 U/ml RNasin or Prime RNase inhibitor, 0.1 μg/ml pepstatin, 0.1 μg/ml leupeptin, 0.1 mg/ml soybean trypsin inhibitor, 5 mM cAMP, 50 μM 19 unlabeled amino acids and 40–50 μM [^{14}C]-leucine (14,000–35,000 dpm/ml). When [^{3}H]-leucine is used, 800,000–1,000,000 dpm/ml is added along with [^{14}C]-leucine to a final concentration of 30–50 μM.
8. 40 mM ATP.
9. 40 mM GTP.
10. 10 % (w/v) trichloroacetic acid (TCA).
11. 5 % (w/v) trichloroacetic acid (TCA).
12. Scintillation fluid.
13. Buffer B: 50 mM Tris–HCl pH 7.5, 50 mM potassium acetate and 2 mM EDTA.
14. Buffer C: 10 mM Tris–HCl, pH 7.5, 100 mM NaCl.

2.5 Direct Binding Assay in Bicelles with Radiolabeled Arrestin-1

1. Binding Buffer: 50 mM Tris–HCl, pH 7.5, 0.5 mM $MgCl_2$, 1.5 mM DTT, 100 mM potassium acetate.
2. Buffer C: 10 mM Tris–HCl, pH 7.5, 100 mM NaCl.
3. Scintillation fluid.

2.6 Expression of Isotopically Labeled Arrestin-1

1. BL21(DE3) cells.
2. LB agar plate with 100 mg/l ampicillin.
3. LB with 100 mg/l ampicillin (LB/A).
4. 1 l M9 minimal media prepared in D_2O supplement with 1 g/l of $^{15}NH_4Cl$: dissolve 6 g Na_2HPO_4, 3 g KH_2PO_4, 0.5 g NaCl, 4 g glucose, 1 mM $MgSO_4$, 0.1 mM $CaCl_2$ and 1 g of $^{15}NH_4Cl$ in D_2O.
5. 100 mM isopropyl-β-D-thiogalactopyranoside (IPTG).
6. ^{15}N, ^{2}H-Bioexpress.
7. 1 l LB prepared in D_2O with 100 mg/l ampicillin: dissolve 10 g tryptone, 5 g yeast extract and 10 g NaCl in 950 ml D_2O.
8. Glucose-D6, α-ketovaleric acid salt (3-methyl-^{13}C,3,4,4,4-D4), α-ketobutyric acid salt (methyl-^{13}C,3,3-D2).

2.7 NMR Study of Arrestin-1 Binding to Rhodopsin in Different States

1. Buffer D: 25 mM Bis–Tris, pH 6.5, 100 mM NaCl, 0.1 mM EDTA.
2. 1 M dithiothreitol (DTT).
3. D_2O.

3 Methods

3.1 Preparation of Bicelles

Two different methods of bicelle preparation are used, depending on both the stock solution concentration and the q value. For relatively low stock concentrations (<20 % w/v) or low q values ($q < 1$), we varied the temperature to induce phase transitions, as described in Subheading 3.1.1. The gel-to-liquid crystalline phase transition temperature for DMPG-DMPC mixtures is roughly 24 °C. For relatively high stock concentrations (>20 % w/v) or high q values ($q > 1$), we use a custom extrusion apparatus to mix bicelles in addition to varying the temperature change to induce phase transition, as described in Subheading 3.1.2.

3.1.1 Preparation of Bicelles at Low Stock Concentration or Low q Value

1. Calculate the amount of each component needed. For 1 ml 12.5 % w/v stock solution with $q = 0.33$ (molar ratio), this means 1 mol lipid (DMPC + DMPG) per 3 mol DHPC at a ratio of 1 mol DMPG per 4 mol DMPC: 32 mg of DMPC, 8 mg of DMPG, and 85 mg of DHPC (*see* **Note 1**).
2. Dissolve 85 mg of DHPC in 500 µl of Buffer A in one tube and mix 8 mg of DMPG and 32 mg of DMPC in 500 µl of Buffer A in another tube by vortexing. DHPC solution will become clear, while the DMPG and DMPC mixture remains cloudy.
3. Combine the solutions in these two tubes and mix them well by vortexing.
4. Cycle by incubating the mixture at 42 °C for 2 min and then at 0 °C (on ice) for 2 min. Repeat this cycle until the solution is completely clear (*see* **Note 2**).
5. Spin at 13,000 × *g* in a tabletop centrifuge for 10 min to remove of any insoluble material. The supernatant is the bicelle solution, now ready to use.

3.1.2 Preparation of Bicelles at a High Stock Concentration or a High q Value

1. Calculate the amount of each component needed. For 1 ml of 35 % w/v stock solution with $q = 3$ (molar ratio), that is 3 mol of lipid (DMPC + DMPG) per 1 mol of DHPC at a ratio of 1 mol of DMPG per 4 mol DMPC: 224 mg of DMPC, 57 mg of DMPG, and 66 mg of DHPC.
2. Dissolve 66 mg of DHPC in 1 ml of Buffer A.
3. Weigh 224 mg of DMPC and 57 mg of DMPG in one tube, add 500 µl of DHPC solution, mix by vortexing, and add it to one syringe (Fig. 5).

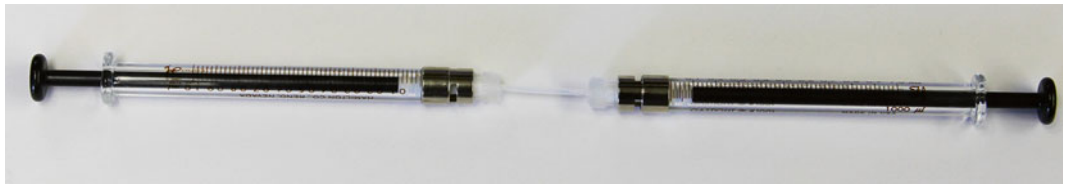

Fig. 5 Apparatus to make bicelles. Two Hampton syringes are connected by a plastic coupler for extrusion. For example, to make 1,000 μl 35 % (w/v) bicelle stock, add 500 μl of DHPC solution to one syringe and 500 μl of DHPC solution homogenized with 224 mg of DMPC and 57 mg of DMPG to another syringe. The bicelles are homogenized by passing the contents back and forth between syringes multiple times. For this process, the entire apparatus is incubated at 4 and 55 °C and homogenized after equilibration at each temperature

4. Add the remaining 500 μl DHPC solution to another syringe, which is then attached nose to nose with the other (lipid solution containing) syringe. Mix by extruding the solution back and forth between the syringes, effectively extruding the mixture through the narrow connecting tube.
5. Cycle the bicelle mixture through its phase transition temperature (24 °C) four times by incubating the entire apparatus at 4 and 55 °C; homogenize between cycles.
6. Dispense the bicelle mixture to a tube on ice and centrifuge at 13,000 × *g* for 10 min to remove bubbles and insoluble material. The supernatant is the bicelle solution, now ready for use.

3.2 Reconstitution of Rhodopsin into Bicelles

1. All steps are performed in the dark under dim red light at 4 °C.
2. Measure the rhodopsin 500 nm absorption in the dark (extinction coefficient: 40,600 M^{-1} cm^{-1}) to determine the rhodopsin concentration.
3. Pellet ROS membranes by centrifugation at 13,000 × *g* for 30 min, discard supernatant, and wash the pellet twice with Buffer A.
4. Pellet ROS membranes after washing and estimate the volume of the membrane pellet by weighing in a pre-weighted 1.5 ml eppendorf tube (*see* **Note 3**). Add equal volume of 11.25 % stock of bicelles to the membranes, pipette up and down to dissolve the membranes, and incubate on a shaker in dark cold room for 30 min (*see* **Note 4**).
5. Centrifuge as above to remove insoluble material and save the supernatant.
6. Determine the concentration of rhodopsin in the supernatant (using absorption at 500 nm) and calculate the bicelle concentration using $\frac{11.25\% \times V1}{V2}$ (V1 is the added bicelle volume and V2 is the final volume) (*see* **Note 5**).

7. Typically, 70 μl of 11.25 % bicelle stock are added to ROS membranes containing 1 mg of rhodopsin, which yields a final rhodopsin concentration around 8 mg/ml and bicelle concentration around 8 %. The lipid from ROS membrane is also dissolved in bicelles and the concentration is around 8 mg/ml.

3.3 Assessment of the Structural Integrity of Arrestin-1 by Near-UV Circular Dichroism (CD) Spectroscopy

1. Prepare 500 μl arrestin-1 protein samples at the concentration of 50 μM in Buffer A, Denaturing Buffer, and the model membrane conditions of choice: for example, 0.2 % DDM micelles or 4 % bicelle mixtures prepared as described in Subheading 3.1. Incubate arrestin-1 in these conditions at room temperature overnight, ~12 h (*see* **Note 6**).
2. Transfer the samples to a masked cell (1 cm pathlength) with a minimum volume of 500 μl, and collect the near-UV CD spectra over the wavelength range of 250–320 nm using the CD spectropolarimeter with the bandwidth of 1 nm. Average five scans for each sample to achieve reasonable signal to noise. For each protein sample, collect the near-UV CD spectrum of the same buffer without protein, which yields the blank signal that should be subtracted from the spectrum of protein sample to reveal the signal from protein only.
3. The raw data from Jasco J-810 is given in ellipticity (measured in millidegrees). Apply the following equation: $[\theta] = \frac{100 \times (\text{signal})}{c \times n \times l}$ (c is the protein concentration in mM, n is the total number of amino acid residues, and l is the cell pathlength in cm) to convert the output to units of mean residue ellipticity (degrees squared centimeters per decimole) (Fig. 6).

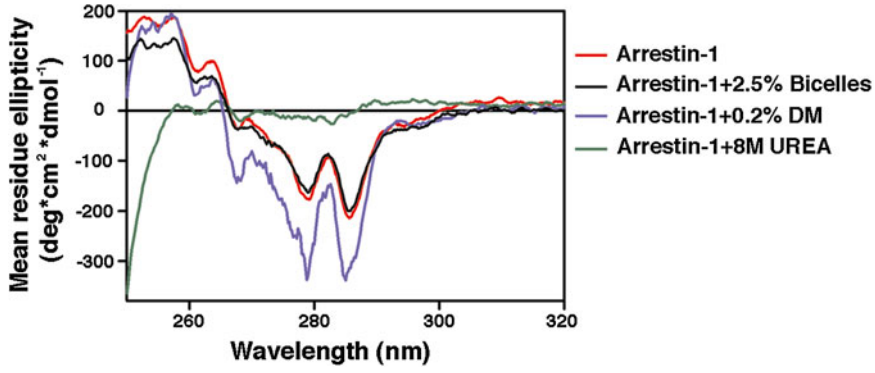

Fig. 6 Near-UV CD spectra of arrestin-1 in the presence of model membranes. Arrestin-1 (50 μM) samples were prepared in detergent micelles composed of DM (*blue*) and DMPC/DHPC bicelles (*black*). The reference spectrum for native conformation of arrestin-1 in Buffer A is shown in *red*. The spectrum of fully denatured arrestin-1 in 8 M urea is shown in *green*

3.4 Preparation of Radiolabeled Arrestin-1

1. Purify and linearize plasmid DNA where arrestin-1 coding sequence is under control of a SP6 promoter [44, 46].
2. Incubate 10 μg of linearized DNA in 300 μl of the transcription mix at 38 °C for 90 min.
3. Add 150 μl of 7.5 M LiCl, incubate on ice for 10 min, and centrifuge for 10 min at 16,100 × *g* and 4 °C to pellet mRNA.
4. Wash the pellet with 1 ml of 2.5 M LiCl at 4 °C.
5. Wash the pellet with 1 ml of 70 % (v/v) ethanol at room temperature.
6. Let the pellet dry for 5–7 min or until it is completely dry and then dissolve it in 300 μl of ultrapure distilled water (we use a volume equal to that of the transcription reaction). Remove an aliquot to measure the amount of mRNA via absorption at 260 nm.
7. Add 30 μl of 3 M sodium acetate, pH 5.2, and 960 μl of ethanol. Then vortex and incubate on ice for 10 min (*see* **Note 7**).
8. Before translation, pellet the necessary amount (~24 μg for 0.2 ml translation) of mRNA from this suspension, wash with 70 % ethanol, dry for 5–7 min, and dissolve in 16 μl of ultrapure distilled water.
9. Incubate mRNA with 184 μl translation mix [7, 45] for 2 h at 22.5 °C.
10. Add 4 μl of 40 mM ATP and 4 μl of 40 mM GTP (1 mM final concentrations) and incubate at 37 °C for 7 min (ribosome runoff).
11. Cool the samples on ice and centrifuge at 600,000 × *g* for 60 min at 4 °C (in TLA 120.1 rotor, Beckman TLA tabletop ultracentrifuge) to pellet ribosomes and aggregated proteins. The supernatant contains [^{14}C]- and [^{3}H]-labeled arrestin-1 and free [^{14}C]- and [^{3}H]-leucine.
12. Take a 2 μl aliquot, add it to 18 μl water (tenfold dilution), and spot 5 μl of diluted sample onto Whatman 3MM paper (1 cm × 1 cm square); incubate the paper in ice-cold 10 % (w/v) TCA for >10 min (to wash away free radiolabeled leucine) and then in boiling 5 % TCA for exactly 10 min (hydrolyzes aminoacyl-tRNA and removes radiolabeled leucine attached to tRNA). Then, let the paper dry and add each square to a separate scintillation vial, let the protein dissolve in 0.5 ml of Buffer B, then add 5 ml of scintillation fluid, briefly shake, and quantify protein-incorporated radioactivity using scintillation counter capable of quantifying ^{3}H and ^{14}C separately.
13. Measure the radioactivity of the control sample (translation mix without mRNA).

14. Calculate protein yield based on specific activity of the radiolabeled leucine used. Dividing the total protein-incorporated radioactivity (dpm per microliter of translation mix with the value from the control sample subtracted) by the specific activity (dpm/fmol) of the arrestin-1 gives the yield in fmol/μl (*see* [44] for details).
15. To separate the free [^{14}C]- and [^{3}H]-leucine from [^{14}C]- and [^{3}H]-labeled arrestin-1, load the supernatant onto a 2 ml Sephadex G-75 column equilibrated with Buffer C. Add 100 μl of Buffer C and collect the eluted 100 μl buffer. Repeat this for 15 times. For the last elution, add 500 μl of Buffer C and collect the eluted 500 μl buffer.
16. Take 2 μl of each elution and add it to 18 μl H_2O, add 5 ml of scintillation fluid, and determine the radioactivity in each elution fraction to get the elution profile and pool the fractions containing arrestin-1 together. This is translated arrestin-1 ready to use.

3.5 Direct Binding Assay in Bicelles with Radiolabeled Arrestin-1

1. Incubate 100 fmol of radiolabeled arrestin-1 with the 7.5 pmol of p-*Rh in bicelles in a final volume of 50 μl of Binding Buffer at 30 °C under ambient light.
2. Cool the samples on ice and load them on 2 ml Sephadex G-75 columns equilibrated with Buffer C (*see* **Note 8**).
3. Wash the column with 100 μl and then 500 μl Buffer C.
4. Elute with 600 μl Buffer C into scintillation vials, add 5 ml of scintillation fluid, and count the radioactivity from bound arrestin-1 as total binding.
5. Determine the nonspecific binding in the presence of equal amount of empty bicelles.
6. Subtract the nonspecific binding from total binding to obtain the specific binding. Dividing specific binding (dpm) by arrestin-1-specific activity (dpm/fmol) gives the fmol of arrestin bound to the p-*Rh (*see* Fig. 7).

3.6 Expression of NMR Isotopically Labeled Arrestin-1

3.6.1 Preparation of ^{2}H, ^{15}N-Labeled Arrestin-1

1. Transform a pTrc-based plasmid encoding arrestin-1 [44] to BL21(DE3) cells and plate on LB agar with 100 mg/l ampicillin.
2. Start a 10 ml small culture from a single colony in LB with 100 mg/l ampicillin (LB/A) at 30 °C overnight.
3. Centrifuge the 10 ml small culture for 3–5 min at 2,000 rpm (800 × *g*). Resuspend the cell pellet in 1 l M9 minimal media prepared in D_2O supplemented with 1 g/l of $^{15}NH_4Cl$.
4. Incubate the culture at 30 °C with vigorous shaking at 250 rpm until OD reaches 0.8.
5. Add 250 μl of 100 mM IPTG to 1 l culture. The final IPTG concentration is 25 μM. Continue shaking for another 18 h (*see* **Note 9**).

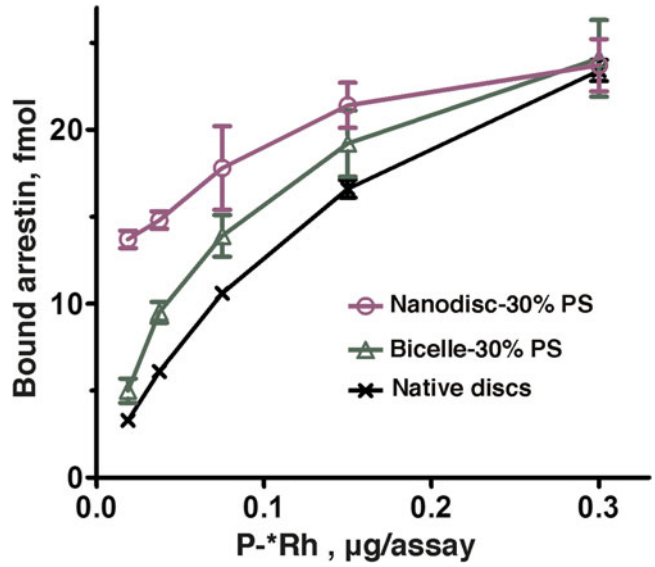

Fig. 7 Arrestin-1 binding to P-*Rh. P-Rh from the same batch (0.3 μg) in native disk membranes (*black crosses*), or solubilized and reconstituted in DMPC bicelles with 30 % DMPS (*green triangles*), or solubilized and reconstituted in POPC nanodisks with 30 % POPS (*purple circles*) was incubated with radiolabeled arrestin-1 (100 fmol) in 50 μl at 30 °C for 5 min. The samples were light activated and cooled on ice, and bound and free arrestin-1 was separated by gel filtration on Sephadex G-75 (bicelles and nanodisks) or Sepharose 2B (native disk membranes). Means ± SD from three experiments performed in duplicate are shown

3.6.2 Preparation of ^{13}C, ^{1}H-Methyl-Labeled Perdeuterated Arrestin-1

1. Transform a pTrc-based plasmid encoding arrestin-1 to BL21 (*DE3*) cells and plate on LB agar with 100 mg/l ampicillin.
2. Start a 5 ml small culture from a single colony in a LB prepared in D_2O with 100 mg/l ampicillin at 30 °C overnight.
3. Transfer 50 μl of overnight cultures prepared in **step 2** into 5 ml M9 minimal medium prepared in D_2O and contains 4 g/l glucose-D6.
4. Inoculate 5 ml of cultures in **step 3** to 500 ml of M9 minimal medium that is prepared in D_2O and contains 4 g/l glucose-D6, 37.5 mg/l 3-methyl-^{13}C, 3,4,4,4-D_4-α-ketovaleric acid salt, and 22.5 mg/l methyl-^{13}C, 3,3-D_2-α-ketobutyric acid salt.
5. Shake the cultures at 30 °C until OD600 reaches 0.6. Add additional 3-methyl-^{13}C, 3,4,4,4-D_4-α-ketovaleric acid salt and methyl-^{13}C, 3,3-D_2-α-ketobutyric acid salt to the culture to make the final concentration 75 and 45 mg/l, respectively.
6. Continue shaking for 30 more min.
7. Add 250 μl of 100 mM IPTG to 1 l culture. The final IPTG concentration is 25 μM.

8. Harvest the cells by centrifugation after induction for 18 h.
9. Purify the proteins as described in [44].

3.7 NMR Study of Arrestin-1 Binding to Rhodopsin in Different States

3.7.1 Sample Preparation

1. Buffer exchange arrestin-1 to Buffer D using the Amicon Ultra centrifugal filters with 30 kDa molecular-weight cutoff.
2. Concentrate arrestin-1 sample to the desired concentration. Ideally the concentration should be at least double the concentration in final working solution (*see* **Note 10**).
3. Mix arrestin-1 and rhodopsin reconstituted into bicelles at the molar ratios of 1:1, 1:3, and 1: 5 in dark. The final volume is 200 μl. Add 1 μl of 1 M DTT and 10 μl of D_2O. Adjust the final bicelle concentration to 4 % with the bicelle stock. The solution should contain 30 μM arrestin-1; 30, 90, or 150 μM rhodopsin; 5 mM DTT; 5 % D_2O; and 4 % bicelle.
4. To investigate arrestin-1 binding to activated rhodopsin or phosphorylated rhodopsin, light activate the sample on ice for 30 min or until the A500 nm absorption decreases to the baseline. The preparation of phosphorylated rhodopsin is described in [5].
5. To investigate arrestin-1 binding to rhodopsin or phosphorylated rhodopsin in an inactive state, everything should be kept in the dark during sample preparation, sample transfer, and data collection.
6. Add 200 μl sample to a 5 mm Shigemi NMR or to a 3 mm conventional tube. It is ready for NMR experiments.

3.7.2 NMR Titration Experiments

1. All NMR data are obtained in Bruker Avance spectrometers with ^{1}H resonance frequency of either 800 MHz or 600 MHz at 308 K. Collect the two-dimensional ^{1}H–^{15}N correlated spectra using sensitivity-enhanced, phase-sensitive transverse relaxation optimized spectroscopy (TROSY) pulse sequence. It is important to use a version of this sequence that filters out all extraneous signal (from protons not directly attached to an ^{15}N) using pulsed field gradients rather than via phase cycling [47] (*see* **Note 11**). Key NMR parameters include the ^{1}H and ^{15}N 90° pulse widths and the relaxation recovery delay between scans, which are kept the same during the same series of titration points.
2. Two-dimensional methyl-TROSY spectra were obtained using heteronuclear multiple-quantum correlated spectroscopy (^{1}H, ^{13}C-HMQC) pulse sequence (reviewed in [48]). Set the ^{1}H and ^{13}C spectra widths at 14 and 22 ppm, respectively, with the ^{13}C carrier frequency corresponding to 20 ppm (*see* **Note 12**).
3. Collect one-dimensional TROSY spectra before and after each titration point to monitor the decaying of rhodopsin in different states. Process ^{1}H,^{15}N-TROSY data using a program such as

nmrPipe [49] with zero filling, Gaussian apodization, and linear prediction in indirect dimension (^{15}N) before Fourier transformation. For ^{1}H,^{13}C-methyl-TROSY spectra, process the data with one-time zero filling and squared sine-bell function. Visualize and analyze the spectra using programs such as nmrDraw, NMRview, and Sparky [50, 51].

4. Plot the titration curve as arrestin NMR peak chemical shift against the concentration of rhodopsin. The calculation of K_d from the concentration dependence of NMR resonance chemical shift changes has been described previously in [15].

4 Notes

1. We include DMPG in the DMPC/DHPC bicelles because DMPG contains the negatively charged head group, which is essential for the maximum binding of arrestin-1 to rhodopsin. Whether or not DMPG is added, the ratio of DMPG to DMPC can be adjusted for each individual study.
2. Typically, it takes about 3–4 iterations to get the solution clear. Homogenizing the DMPG and DMPC mixture greatly assists this process.
3. We estimate the volume of membrane by weight, assuming 1 mg is approximately 1 μl.
4. The solution should become clear after the bicelles are added and the sample is mixed. If the solution is cloudy, more bicelles should be added.
5. Measure the final volume with a pipette.
6. The incubation time and temperature is case dependent.
7. mRNAs in this suspension can be stored at −80 °C for several years.
8. Different columns are used to separate rhodopsin-bound or free arrestin-1. For rhodopsin in native disk membranes, we use Sepharose 2B, while for rhodopsin reconstituted in bicelles or nanodisks, we use Sephadex G-75.
9. Optional: 5–10 ml of ^{15}N, ^{2}H-Bioexpress can be added to the M9 minimal media. This can significantly shorten the cell growth time in **step 4** from 3 days to 1 day.
10. The arrestin-1F85/197A mutant used in the NMR study can be concentrated up to 640 μM without visible precipitation.
11. Typical TROSY spectra for NMR titration experiments are obtained using 1,024 × 128 complex points with 200 scans per increment, which requires total acquisition time of 20 h for one spectrum.

12. A typical HMQC spectrum contains 1,024 × 256 complex points with 128 scans per increment, which requires total acquisition time of 20 h for one spectrum.

References

1. Wilden U, Hall SW, Kühn H (1986) Phosphodiesterase activation by photoexcited rhodopsin is quenched when rhodopsin is phosphorylated and binds the intrinsic 48-kDa protein of rod outer segments. Proc Natl Acad Sci U S A 83:1174–1178
2. Krupnick JG, Gurevich VV, Benovic JL (1997) Mechanism of quenching of phototransduction. Binding competition between arrestin and transducin for phosphorhodopsin. J Biol Chem 272:18125–18131
3. Jastrzebska B, Debinski A, Filipek S et al (2011) Role of membrane integrity on G protein-coupled receptors: rhodopsin stability and function. Prog Lipid Res 50:267–277
4. Brown MF (1994) Modulation of rhodopsin function by properties of the membrane bilayer. Chem Phys Lipids 73:159–180
5. Vishnivetskiy SA, Raman D, Wei J et al (2007) Regulation of arrestin binding by rhodopsin phosphorylation level. J Biol Chem 282: 32075–32083
6. Bayburt TH, Vishnivetskiy SA, McLean MA et al (2011) Monomeric rhodopsin is sufficient for normal rhodopsin kinase (GRK1) phosphorylation and arrestin-1 binding. J Biol Chem 286:1420–1428
7. Gurevich VV, Benovic JL (1993) Visual arrestin interaction with rhodopsin. Sequential multisite binding ensures strict selectivity toward light-activated phosphorylated rhodopsin. J Biol Chem 268:11628–11638
8. Gurevich VV (1998) The selectivity of visual arrestin for light-activated phosphorhodopsin is controlled by multiple nonredundant mechanisms. J Biol Chem 273:15501–15506
9. Gurevich VV, Benovic JL (1995) Visual arrestin binding to rhodopsin: diverse functional roles of positively charged residues within the phosphorylation-recognition region of arrestin. J Biol Chem 270:6010–6016
10. Gurevich VV, Benovic JL (1997) Mechanism of phosphorylation-recognition by visual arrestin and the transition of arrestin into a high affinity binding state. Mol Pharmacol 51:161–169
11. Gurevich VV, Gurevich EV (2004) The molecular acrobatics of arrestin activation. Trends Pharmacol Sci 25:105–111
12. Hirsch JA, Schubert C, Gurevich VV et al (1999) The 2.8 angstrom crystal structure of visual arrestin: a model for arrestin's regulation. Cell 97:257–269
13. Granzin J, Cousin A, Weirauch M et al (2012) Crystal structure of p44, a constitutively active splice variant of visual arrestin. J Mol Biol 416: 611–618
14. Kim YJ, Hofmann KP, Ernst OP et al (2013) Crystal structure of pre-activated arrestin p44. Nature 497:142–146
15. Zhuang TD, Chen QY, Cho MK et al (2013) Involvement of distinct arrestin-1 elements in binding to different functional forms of rhodopsin. Proc Natl Acad Sci U S A 110:942–947
16. Vishnivetskiy SA, Schubert C, Climaco GC et al (2000) An additional phosphate-binding element in arrestin molecule: implications for the mechanism of arrestin activation. J Biol Chem 275:41049–41057
17. Vishnivetskiy SA, Paz CL, Schubert C et al (1999) How does arrestin respond to the phosphorylated state of rhodopsin? J Biol Chem 274:11451–11454
18. Vishnivetskiy SA, Francis DJ, Van Eps N et al (2010) The role of arrestin alpha-helix I in receptor binding. J Mol Biol 395:42–54
19. Hanson SM, Francis DJ, Vishnivetskiy SA et al (2006) Differential interaction of spin-labeled arrestin with inactive and active phosphorhodopsin. Proc Natl Acad Sci U S A 103: 4900–4905
20. Kim M, Vishnivetskiy SA, Van Eps N et al (2012) Conformation of receptor-bound visual arrestin. Proc Natl Acad Sci U S A 109: 18407–18412
21. Ostermaier MK, Peterhans C, Jaussi R et al (2014) Functional map of arrestin-1 at single amino acid resolution. Proc Natl Acad Sci U S A 111:1825–1830
22. Vishnivetskiy SA, Baameur F, Findley KR et al (2013) Critical role of the central 139-loop in stability and binding selectivity of arrestin-1. J Biol Chem 288:11741–11750
23. Vishnivetskiy SA, Chen Q, Palazzo MC et al (2013) Engineering visual arrestin-1 with special functional characteristics. J Biol Chem 288:11741–11750

24. Sanders CR, Hare BJ, Howard KP et al (1994) Magnetically-oriented phospholipid micelles as a tool for the study of membrane-associated molecules. Prog Nucl Magn Reson Spectrosc 26:421–444
25. Sanders CR, Prosser RS (1998) Bicelles: a model membrane system for all seasons? Struct Folding Des 6:1227–1234
26. Ujwal R, Bowie JU (2011) Crystallizing membrane proteins using lipidic bicelles. Methods 55:337–341
27. Durr UHN, Gildenberg M, Ramamoorthy A (2012) The magic of bicelles lights up membrane protein structure. Chem Rev 112:6054–6074
28. Rasmussen SG, Choi HJ, Rosenbaum DM et al (2007) Crystal structure of the human beta2 adrenergic G-protein-coupled receptor. Nature 450:383–387
29. Ye WH, Lind J, Eriksson J et al (2014) Characterization of the morphology of fast-tumbling bicelles with varying composition. Langmuir 30:5488–5496
30. Beaugrand M, Arnold AA, Henin J et al (2014) Lipid concentration and molar ratio boundaries for the use of isotropic bicelles. Langmuir 30:6162–6170
31. Thompson AA, Liu JJ, Chun E et al (2011) GPCR stabilization using the bicelle-like architecture of mixed sterol-detergent micelles. Methods 55:310–317
32. Zocher M, Zhang C, Rasmussen SG et al (2012) Cholesterol increases kinetic, energetic, and mechanical stability of the human beta2-adrenergic receptor. Proc Natl Acad Sci U S A 109:E3463–E3472
33. Rim J, Oprian DD (1995) Constitutive activation of opsin – interaction of mutants with rhodopsin kinase and arrestin. Biochemistry 34:11938–11945
34. Degrip WJ (1982) Thermal-stability of rhodopsin and opsin in some novel detergents. Methods Enzymol 81:256–265
35. Reeves PJ, Hwa J, Khorana HG (1999) Structure and function in rhodopsin: kinetic studies of retinal binding to purified opsin mutants in defined phospholipid-detergent mixtures serve as probes of the retinal binding pocket. Proc Natl Acad Sci U S A 96: 1927–1931
36. McKibbin C, Farmer NA, Jeans C et al (2007) Opsin stability and folding: modulation by phospholipid bicelles. J Mol Biol 374: 1319–1332
37. Gurevich VV, Gurevich EV (2008) GPCR monomers and oligomers: it takes all kinds. Trends Neurosci 31:74–81
38. Gurevich VV, Gurevich EV (2008) How and why do GPCRs dimerize? Trends Pharmacol Sci 29:234–240
39. Bayburt TH, Leitz AJ, Xie G et al (2007) Transducin activation by nanoscale lipid bilayers containing one and two rhodopsins. J Biol Chem 282:14875–14881
40. Whorton MR, Jastrzebska B, Park PSH et al (2008) Efficient coupling of transducin to monomeric rhodopsin in a phospholipid bilayer. J Biol Chem 283:4387–4394
41. Vishnivetskiy SA, Ostermaierm MK, Singhal A et al (2013) Constitutively active rhodopsin mutants causing night blindness are effectively phosphorylated by GRKs but differ in arrestin-1 binding. Cell Signal 25:2155–2162
42. Singhal A, Ostermaier MK, Vishnivetskiy SA et al (2013) Insights into congenital night blindness based on the structure of G90D rhodopsin. EMBO Rep 14:520–526
43. Sommer ME, Smith WC, Farrens DL (2006) Dynamics of arrestin-rhodopsin interactions: acidic phospholipids enable binding of arrestin to purified rhodopsin in detergent. J Biol Chem 281:9407–9417
44. Gurevich VV, Benovic JL (2000) Arrestin: mutagenesis, expression, purification, and functional characterization. Methods Enzymol 315:422–437
45. Gurevich VV, Benovic JL (1992) Cell-free expression of visual arrestin. Truncation mutagenesis identifies multiple domains involved in rhodopsin interaction. J Biol Chem 267: 21919–21923
46. Gurevich VV (1996) Use of bacteriophage RNA polymerase in RNA synthesis. In: Kuo LC, Olsen DB, Carroll SS (eds) Methods in enzymology, 275: 382–397
47. Weigelt J (1998) Single scan, sensitivity- and gradient-enhanced TROSY for multidimensional NMR experiments. J Am Chem 120: 10778–10779
48. Tugarinov V, Kay LE (2005) Methyl groups as probes of structure and dynamics in NMR studies of high-molecular-weight proteins. Chembiochem 6:1567–1577
49. Delaglio F, Grzesiek S, Vuister GW et al (1995) NMRPipe: a multidimensional spectral processing system based on UNIX pipes. J Biomol NMR 6:277–293
50. Johnson BA (2004) Using NMRView to visualize and analyze the NMR spectra of macromolecules. Methods Mol Biol 278: 313–352
51. Goddard TD, Kneller DG (2008) SPARKY 3. University of California, San Francisco

52. Palczewski K, Kumasaka T, Hori T et al (2000) Crystal structure of rhodopsin: A G protein-coupled receptor. Science 289:739-745
53. Choe HW, Kim YJ, Park JH et al (2011) Crystal structure of metarhodopsin II. Nature 471:651–655
54. Alexander NS, Preininger AM, Kaya AI et al (2014) Energetic analysis of the rhodopsin-G-protein complex links the α5 helix to GDP release. Nat Struct Mol Biol 21:56–63
55. Singh P, Wang B, Maeda T et al (2008) Structures of rhodopsin kinase in different ligand states reveal key elements involved in G protein-coupled receptor kinase activation. J Biol Chem 283:14053–14062

Chapter 7

Detection of Structural Waters and Their Role in Structural Dynamics of Rhodopsin Activation

Liwen Wang and Mark R. Chance

Abstract

Conserved structural waters trapped within GPCRs may form water networks indispensable for GPCR's signaling functions. Radiolysis-based hydroxyl radical footprinting (HRF) strategies coupled to mass spectrometry have been used to explore the structural waters within rhodopsin in multiple signaling states. These approaches, combined with ^{18}O labeling, can be used to identify the locations of structural waters in the transmembrane region and measure rates of water exchange with bulk solvent. Reorganizations of structural waters upon activation of signaling can be explicitly observed with this approach, and this provides a unique look at the structural modules driving the signaling process.

Key words Hydroxyl radical labeling, Mass spectrometry, Protein footprinting, Structural waters

1 Introduction

Covalent labeling of proteins coupled to mass spectrometry, often called protein footprinting, is a valuable technique to define structure, assembly, and conformational changes of macromolecules in solution. These approaches have been extensively reviewed [1–3]. One of the most popular (irreversible) labeling reagents is the hydroxyl radical, which has a van der Waals surface similar to water, and thus due to its small size, it can easily access and label protein surface providing very high-resolution structural information. In synchrotron-based HRF experiments, hydroxyl radicals are generated isotropically in solution by synchrotron X-ray radiolysis of water; these OH radicals react with protein side chains, generating well-understood chemical products via a multiplicity of oxidation reactions [4]. Subsequent to labeling, proteins are digested with specific proteases and the digests are subjected to LC/MS (liquid chromatography coupled with mass spectrometry) analysis. Radiolytic protein footprinting was used to investigate the conformational dynamics of the rhodopsin ground state (Rho), photoactivated state (Meta II or Rho*), inactive ligand-free receptor

Beata Jastrzebska (ed.), *Rhodopsin: Methods and Protocols*, Methods in Molecular Biology, vol. 1271,
DOI 10.1007/978-1-4939-2330-4_7,

(opsin), and photoactivated state complexed with rod G protein (Rho^*-G_t) in detergent and membrane preparations [5–7]. Based on prior studies, residues in contact with the bulk solvent were expected to be labeled, but an unexpected number of residues located in the Rho's transmembrane domains (TM) [8] were labeled as well. Using rapid mixing of Rho with H_2O^{18}-containing buffer revealed that the TM labeling was not derived from bulk water [5, 7], but rather from internal water molecules. Thus the source of this labeling was of considerable interest. Concurrent examination of emerging GPCR crystal structures indicated that multiple ordered water molecules located in TM domains were within hydrogen bonding distance of functionally conserved residues [9], suggesting a role in the regulation of Rho activation. For example, structural waters embedded in the TM domains of Rho were suggested to be involved in proton transfer process that follows photoactivation [10]. HRF experiments on Rho and the 5-HT_4 receptor [11] have confirmed that TM labeling events are mediated by structural waters. Therefore, measurement of the dynamic interactions between structural waters and conserved residues by footprinting can be used to precisely define water-mediated communication channels in GPCR signaling [12].

2 Materials

Prepare all buffers with nanopure water. Use analytical grade reagents. Purified proteins are typically utilized in protein footprinting analysis. All protein solutions need to be stored at −20 °C (−80 °C for long storage). The choice of buffer for protein preparation is critical for radiolysis because many buffers quench the hydroxyl radicals in solution (*see* **Note 1**), yet such buffers may have been chosen in order to stabilize the protein sample.

2.1 Sample Preparation

2.1.1 1D4-Immunoafinity Chromatography

1. 5 mM sodium cacodylate, pH 7.2 or other pH if desired.
2. Solubilization Buffer: 10 mM cacodylate buffer, pH 7.2, 100 mM NaCl, 20 mM n-dodecyl-β-D-maltoside (DDM).
3. 1D4-coupled CNBr-activated Sepharose 4B column (binding capacity 0.5 mg protein/ml resin).
4. Equilibration Buffer: 10 mM sodium cacodylate, pH 7.2, 100 mM sodium chloride, and 1 mM DDM.
5. Wash Buffer: 10 mM sodium cacodylate buffer, pH 7.2, and 0.4 mM DDM.
6. Elution Buffer: Wash Buffer containing 100 μM TETSQVAPA, a 1D4 nonapeptide from the rhodopsin C-terminal sequence.

2.1.2 Succinylated Concanavalin A (sConA) Affinity Chromatography

1. Succinylated Concanavalin A (sConA): sConA-coupled CNBr-activated Sepharose 4B column (8 mg of sConA bound to 1 ml of CNBr-activated Sepharose according to standard protocol).

2. Equilibration Buffer: 20 mM BTP, pH 6.9, 100 mM NaCl, 0.4 mM $MgCl_2$, 0.4 mM $MnCl_2$, 0.4 mM $CaCl_2$, 0.5 mM DTT, 0.5 mM DDM.
3. Elution Buffer: 20 mM BTP, pH 6.9, 100 mM NaCl, 1 mM $MgCl_2$, 0.4 mM $MnCl_2$, 0.4 mM $CaCl_2$, 0.4 mM DTT, 0.5 mM DDM, 200 mM α-methyl-D-mannoside.

2.1.3 Determination of Sample Concentration

1. UV-Buffer: 10 mM BTP, pH 7.5, 100 mM NaCl, 2 mM DDM, 1 mM hydroxylamine.
2. Bradford ULTRA (Novexin).
3. 1 mg/ml BSA standard.
4. Spectrophotometer Cary 50 (Varian).

2.2 Protein Radiolytic Labeling

1. Isotopic Labeling Buffer: 97 % H_2O^{18} water (Cambridge Isotopes Laboratories).
2. X28C [13] beamline of the National Synchrotron Light Source.

   X-ray beam parameter optimization reagent—10 μM Alexa Fluor 488 dye: Add 0.32 μg Alexa Fluor 488 dye (Mw: 643 g/mol, Invitrogen) to 50 ml of 10 mM sodium cacodylate, pH 7.0. Spike 10 μM Alexa Fluor 488 dye solution to each protein sample at 1:10 (v:v) to make 1.0 μM of Alexa Fluor 488 dye in sample solution.
3. Sample delivery equipment: KinTek stopped-flow apparatus for exposure (KinTex corporation).
4. Quench Buffer: 0.5 M methionine amide (Met-NH_2): Add 7.4 g Met-NH_2 to 100 ml water and adjust pH to 7.0. Add 0.5 M methionine amide (Met-NH_2) to the X-ray-exposed sample at ratio of 1:50 (v:v) to make 10 mM Met-NH_2 in sample solution.

2.3 Protein Proteolysis

1. Proteolytic enzymes: Freshly prepared 1 μg/μl porcine pepsin (Worthington).
2. Neat formic acid (98 %, Thermo Scientific).
3. 0.1 % formic acid (pH 2.0).
4. 500 mM dithiothreitol (DTT, reducing reagents): Add 77 mg DTT to 1 ml water. Prepare 50 μl aliquots of DTT solution and store them at −80 °C before further use.
5. 500 mM iodoacetamide (IA, alkylation reagent): Add 15.2 mg IA to 164 μl water. Make it freshly and store at 4 °C in the dark. Use within 1 h.
6. Sample Cleanup Buffer: Ice-cold acetone (kept on ice or at 4 °C).

2.4 LC/MS Analysis

1. LC mobile phase: 0.05 % TFA in water (phase A), acetonitrile (phase B).
2. LC column: a reverse-phase C18 PepMap trapping column, a reverse-phase C18 Acclaim PepMap 100 column of 0.075 × 150 mm (Dionex Inc.).
3. LC: Ultimate 3,000 parallel LC system (Dionex, Inc.).
4. MS: Orbitrap-LTQ linear ion trap MS (Thermo-Finnigan) equipped with a nanospray source operated in a positive mode.

3 Methods

3.1 Sample Preparation

3.1.1 Rhodopsin Purification by 1D4-Immunoafinity Chromatography

1. Prepare bovine rod outer segment (ROS) membranes from fresh retinas under dim red light [14].
2. Wash ROS with 5 mM sodium cacodylate, pH 7.2, five times to remove soluble and membrane-associated proteins. Extract Rho from ROS by membrane solubilization with Solubilization Buffer or using $ZnCl_2$-opsin precipitation method [15].
3. Pellet insoluble material at 25,000 × *g* for 30 min. Collect supernatant and use for further purification steps, and discard pellet.
4. Equilibrate 1D4-coupled immunoaffinity column with the Equilibration Buffer consisting.
5. Load extracted Rho onto the column and wash it with ten column volumes of the Equilibration Buffer followed by the Wash Buffer.
6. Elute Rho with the Elution Buffer containing 100 μM synthetic 1D4 peptide (TETSQVAPA) (*see* **Note 1**).
7. Quantify Rho concentration (*see* below Subheading 3.1.3).

In case of photoactivated rhodopsin (Rho* or Meta II) experiment, illuminate the purified Rho just before footprinting with a 150 Watt fiber light through the 480–520 nm band pass filter (Chroma Technology) for 5 min from the distance of 10 cm to avoid heat accumulation.

3.1.2 Purification by sConA Affinity Chromatography

This method is applicable to Rho purification and Rho*-G_t complex purification. Rho*-G_t complex is purified according to the protocol described in [16].

1. Equilibrate affinity sConA-coupled CNBr-activated Sepharose 4B column with the Equilibration Buffer.
2. Load $ZnCl_2$-extracted Rho and wash out excess of Rho with the same Equilibration Buffer. For Rho purification, pursue protein elution with the Elution Buffer.
3. For Rho*-G_t complex purification illuminate bound to the resin Rho with a 150 Watt fiber light through the 480–520 nm

band pass filter for 5 min and immediately saturate with bovine G protein purified as described in [17].

4. Wash excess of G_t with the Equilibration Buffer.
5. Then elute Rho*-G_t complex with the Elution Buffer.
6. Pool fractions containing Rho*-G_t complex and concentrate.
7. Measure protein concentration.

3.1.3 Determination of Sample Concentration

1. To quantify Rho concentration, dilute Rho sample in the UV-Buffer. Determine Rho concentration by measuring its UV-visible absorbance at 498 nm, along with appropriate dilution and molar extinction coefficient $\varepsilon_{498\ nm} = 40.600/M/cm$.
2. Measure concentration of the Rho*-G_t complex by the Bradford assay using Bradford ULTRA and 1 mg/ml BSA as a standard (*see* **Note 2**).

3.2 Radiolytic Labeling

1. Exchange of the protein buffer with H_2O^{18} water: Dry affinity-purified Rho, Rho*, and Rho*-G_t samples with a speed vacuum. Reconstitute protein sample with an equal volume of H_2O^{18} water before X-ray radiolysis (*see* **Note 3**).
2. Optimization of X-ray beamline with sample solution: Spike a fluorescent dye (Alexa 488) into the sample to measure the overall radiolysis dose, e.g., function as a dosimeter. Measure the intensity of Alexa 488 at each radiolysis doses ranging from 1 to 10 ms (*see* **Note 4**).
3. X-ray exposure: Generate the high X-ray flux density by focusing the beam with a mirror (mirror angle to 5.5 mrad and the bender value to 8.0 mm). Deliver protein sample solution continuously with KinTek apparatus to beamline for exposure. Expose three replicas of each protein sample (Rho, Rho*, and Rho*-G_t in the buffer containing H_2O^{16} or in the buffer containing H_2O^{18}) at time intervals of 0, 1, 2.5, and 5 ms. Collect 100 μl of each sample at working concentration of 1–10 μM. Add methionine amide to the exposed protein samples to 10 mM to quench radiolysis (*see* **Note 5**).
4. Time-resolved $^{18}O/^{16}O$ exchange: Mix protein samples with H_2O^{18} at 1:1 (H_2O^{16} buffer:H_2O^{18} buffer) rapidly with 2–3 ms instrument dead time before X-ray exposure. Expose mixed sample for synchrotron doses of 6 or 40 ms time intervals by delays of 50, 100, 500, 5,000, and 30,000 ms after mixing to measure dynamic exchange rate of H_2O^{16} buffer versus H_2O^{18} buffer. Add methionine amide to the exposed protein samples to 10 mM to quench radiolysis (*see* **Note 6**).

All experiments are conducted at 4 °C. Freeze samples in dry ice and stored at −80 °C before protein proteolysis and LC/MS analysis.

3.3 Protein Proteolysis

1. Protein sample cleanup: Add 5 mM DTT to reduce exposed protein samples for 45 min at room temperature. Add 10 mM IA to alkylate free cysteines of the protein for 1 h in the dark. Precipitate all protein samples with ice-cold acetone (sample/acetone =1:4, e.g., 100 µl sample/400 µl acetone) at −80 °C overnight. Then wash samples three times with acetone to remove detergent and small molecules (*see* **Note 7**).
2. Protein digestion: Resuspend protein pellets with 5 µl of 98 % formic acid. Add 95 µl HPLC water to the protein samples. Incubate sample with pepsin at ratio of 1:25 overnight at room temperature. Dry sample with spin vacuum to stop reaction (*see* **Note 8**).

3.4 LC/MS Analysis

3.4.1 Data Collection

1. Each sample of the protein digests is reconstituted by 10 µl water (HPLC grade) for LC/MS analysis. Inject protein digests to LC trap column. Separate peptides by LC C18 column by using a 60 min gradient of acetonitrile running from 5 to 60 % in 0.1 % formic acid at a flow rate of 300 nl/min.
2. Acquire MS spectra of these peptides in a data-dependent manner consisting of a full scan followed by several MS/MS scans of the five most abundant precursor ions at the normalized collision energy of 30 % (*see* **Note 9**).

3.4.2 Data Analysis

1. Peptide identification: Convert MS raw data to *.mgf or *.mzXML files by MM file conversion tool [18]. Search the data by bioinformatics software such as MassMatrix [18] or Mascot, against the database consisting of Rho and its reverse sequence as a decoy sequence. Many frequently used modifications such as phosphorylation (+80 Da), acetylation (+42 Da), methylation (+14 Da), methionine oxidation (+16 Da), and deamidation (+1 Da), just to name a few, are built in the standard package. Add special modifications manually by typing in their composition change on particular sites. Manually add the specific oxidations known in synchrotron radiolysis due to their unique qualities (Table 1) [1]. Set mass accuracy of 10 ppm and 0.8 Da for the precursor ion and the product ion search, respectively. Limit maximum modifications in each peptide to three. Evaluate peptide identification by the statistical score given from the software (*see* **Note 10**).
2. Protein footprinting quantitative analysis: Integrate the selected ion chromatogram [19] of the unmodified and modified peptides and extract the SIC (Selected Ion Chromatograms) peak area in 10 ppm around the mass value of interest, which corresponds to the relative amounts of the unmodified and modified peptide species in radiolysis at different time. Plot the dose-response curve for each oxidized peptide by calculating

Table 1
Composition change and mass shift of most common radiolytic oxidation products for various amino acid side chains

Amino acid residues	Composition change	Mass shift (Da)
W, M, Y, F, H, L, I, R, V, T, P, K	+ O	+15.9949
L, I, R, V, P, K	+O, −2H	+13.9793
M, W, Y, F, C	+2O	+31.9898
M	+O, −S, −C, −4H	−31.9898
C	+O, −S	−15.9772
C	+3O	+47.9847
H	+O, −2C, −N, −H	−23.0160
H	+2O, −2C, −2N, −2H	−22.0320
H	+2O, −C, −2N, −2H	−10.0320
R	+O, −3N, −C, −5H	−43.0534
D, E	−C, −2H, −O	−30.0106

the fraction of unmodified peptide versus exposure time, where the unmodified intensity is divided by the sum of intensities of all modified species plus the unmodified, e.g., the total (Fig. 1). Fit the dose-response curve to a first-order kinetic equation:

$$y(t) = e^{-kt}$$

where y is the fraction of unmodified peptide, t is the exposure time in seconds, and k is the oxidation rate constant, and determine the rate of radiolytic modification [1].

3. Organize the peptide rate constants into a table with the peptide identifications for comparison of the protein rate constants in different Rho activation states. Use ProtMapMS [20], to quantify the dose-response curve, and calculate the oxidation rate constant automatically (*see* **Notes 11–13**).
4. Structural water analysis: Map the oxidized residues in 2D model of Rho (Fig. 2) [5, 7]. Locate the oxidized residues in 3D crystal structure containing structural waters (Fig. 3). Compare the oxidation sites and rate of protein samples in H_2O^{16}, in H_2O^{18}:H_2O^{16} (1:1) buffer, and in H_2O^{18} buffer (dehydration and rehydration with H_2O^{18}). Plot the ratio of peak intensity of O^{18} versus O^{16} isotopologue against delay times to reveal the exchange rate of internal water interaction with specific side chains [21] (*see* **Note 14**).

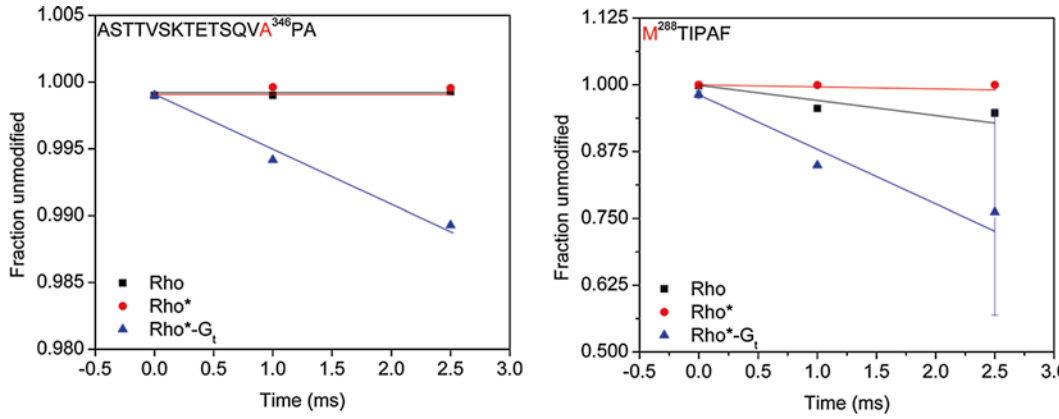

Fig. 1 Dose-response curve plot showing fraction unmodified as a function of exposure time (ms). (*Left*) shows example Rho peptic peptide ASTTVSKTETSQVAPA with oxidation at Ala 346. (*Right*) shows peptide MTIPAF with oxidation at Met 288. Data of peptides from Rho are indicated by *black squares*, Rho* by *red spheres*, and Rho*-G_t by *blue triangles*. Figure adapted with permission from Orban, T., Jastrzebska, B., Gupta, S., et al. (2012) "Conformational dynamics of activation for the pentameric complex of dimeric G protein-coupled receptor and heterotrimeric G protein," *Structure* 20, 826–840. Copyright holder (2012) Elsevier

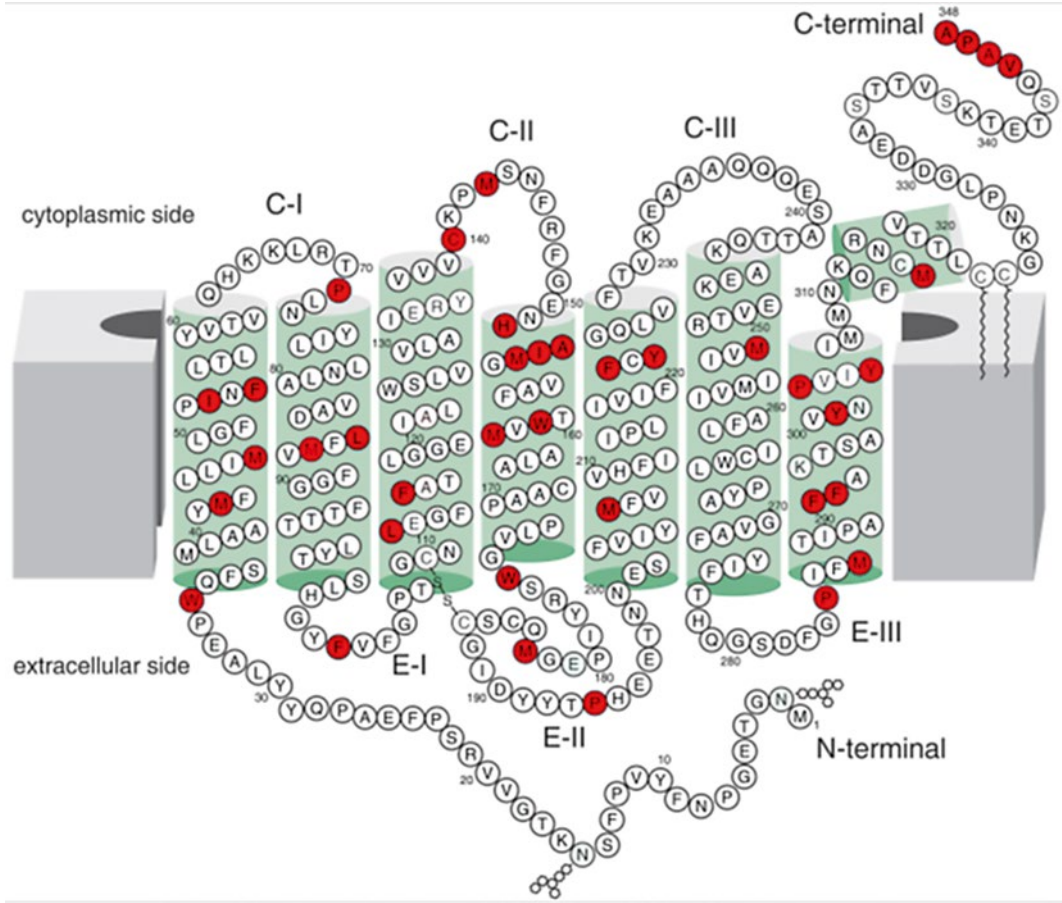

Fig. 2 Protein footprinting data mapped on a 2D model of Rho. Oxidized residues are colored in *red*. Total of 24 residues located in the TM domains of Rho were identified as being modified following X-ray exposure

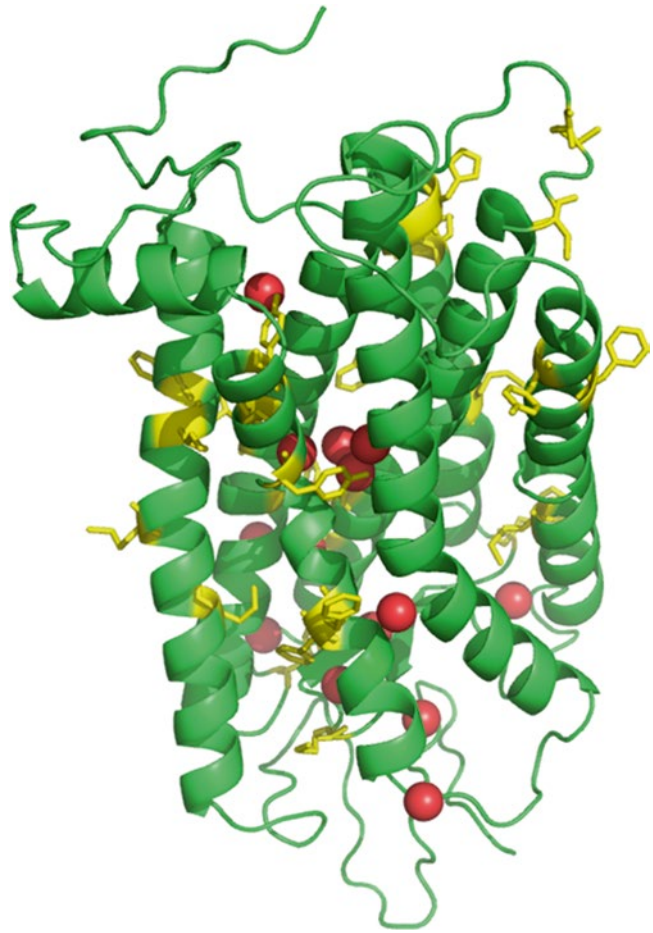

Fig. 3 Protein footprinting mapped on 3D crystal structural of Rho (PDB entry 1u19) [27]. *Yellow sticks* represent labeled side-chain residues of Rho, and *red balls* represent location of "best occupied" structural water molecules in TM domains

4 Notes

1. All protein purification steps are performed in the dark or under dim red light. Wash sample thoroughly with buffer containing 10 mM sodium cacodylate to ensure removal of reagents that will interfere with radiolysis. Tris, HEPES, MOPS, CAPS, citrate, and CAPSO buffers reduce the Alexa dose response. Sodium cacodylate or phosphate buffers at neutral pH are ideal for radiolysis experiments as the Alexa dose responses in these buffers follow apparent first-order kinetics with minimal scavenging.

2. Novexin's Bradford ULTRA is an improvement of classical Bradford formulation that cannot tolerate detergent in the protein sample. With Bradford ULTRA, concentration of membrane proteins purified in detergent-containing solutions can be quantified. This reagent tolerates up to 1 % detergent.
3. Dry protein in a lyophilizer completely and store in −20 °C. Add H_2O^{18} of the same volume as original sample before X-ray radiolysis to measure any possibility of bulk water exchange with structure water in the protein helix bundle. Irradiated samples were completely evaporated to dryness under vacuum at 60 °C to remove any water from the samples. Reconstitute sample with buffer right before enzyme digestion.
4. The intensity of Alexa fluorescence decreases with the radiolysis dose with first-order kinetics. The degradation rate of Alexa fluorophore in the samples collected under different conditions can be used to determine the dose needed for the Rho samples and also for data normalization. It is highly recommended to perform radiolytic footprinting of all the different Rho states at same time with similar sample concentrations. But if the experiments are performed at different time or sample concentrations differ, the peptides oxidation rate can be normalized by dividing the degradation rate of Alexa fluorophore.
5. Focusing the beam with a mirror permits a sufficient dose to be delivered in a few milliseconds, reducing chemical noise, and enhances LC/MS data acquisition. KinTek apparatus is required to deliver samples when very short exposure (< = 5 ms) is applied to sample. At least four time points, including the control sample (0 ms) without X-ray exposure, are suitable for analysis of dose-response curves to calculate the oxidation rate for each peptide. The control sample (0 ms) is used to normalize the dataset to reduce bias caused by possible oxidation from factors other than radiolysis. Additionally, duplicates or triplicates are advisable to assess reproducibility of samples and to permit statistical analysis of the results. Working concentration of protein samples is usually within 10 μM to ensure efficient radiolysis. Hydrogen peroxide and other secondary oxidizing species are generated in radiolysis due to bimolecular recombination of radical species. These species can oxidize methionine (Met) and cysteine (Cys) through secondary oxidation reactions [22]. Secondary oxidation interferes with an accurate determination of oxidation rate. Addition of millimolar concentrations of Met-NH_2 (or Met-OH) buffer immediately after irradiation is necessary to suppress secondary oxidation shortly (1–2 min) after radiolysis.
6. Mixing the two buffers thoroughly is important for this procedure. These experiments are carried out in a modified KinTek quench flow mixer using a two-step (push-pause-push) flow

method. In the first step, the protein sample was mixed with equal amount of H_2O^{18} (1:1 mixing) by a T-mixer. In the second step after millisecond to second delay time (50 ms–30 s), the mixed sample was passed through an irradiation cell. The flow speed was adjusted to achieve irradiation times from 6 ms to 40 ms. The overall dead time was the sum of the travel time of the mixed solution right up to the irradiation cell and the sample irradiation time.

7. Detergents required for membrane protein stabilization will interfere with MS signal and contaminate the HPLC system. Removal of detergent by acetone precipitation is necessary for membrane protein cleanup before LC/MS analysis. DTT is used to reduce disulfide bond of the protein. IA is used to alkylate free cysteines released by DTT reduction. These two steps also ensure that detergent bound or buried in the protein will be released by breaking disulfide bonds and be cleaned by acetone wash. Other strategies can be used such as a pierce detergent removal column (Thermal Scientific), SDS-Out SDS precipitation reagent (Thermal Scientific), or FASP procedure using protein spin filters [23] (Millipore). But detergent such as CHAPS which is frequently used for membrane protein purification should be avoided because it is very hard to remove by any of the above procedures. Different detergent might require a different protocol. A pilot experiment testing the efficiency of detergent removal from the sample by using MALDI-MS before LC/MS/MS is strongly recommended.
8. Proteolysis of membrane proteins requires additional procedures due to their insolubility in water. Firstly, do not dry sample completely after last wash with acetone. Secondly, denaturation of protein at high temperature (70 °C) in addition to denaturation with acetonitrile or urea and/or reduction with DTT/TCEP is often used before proteolysis to facilitate protein solubility and thus increase digestion efficiency. In this protocol, 98 % formic acid is used to dissolve and denature the Rho samples. In order to digest Rho with pepsin, adjust pH to 1.0–2.0 with formic acid (~5 % final concentration). Pepsin is the most suitable enzyme to cleave proteins with high content of hydrophobic amino acid residues.
9. Nano-LC is an ideal choice for separating and analyzing radiolytic samples when only small sample amounts (~μg) are available. Desalting of protein samples is required before LC/MS analysis because salt is known to generate high background noise and signal suppression. The use of high mass accuracy in the LC/MS analysis is highly recommended to decrease complexity of data analysis and reduce false-positives.
10. Table 1 [1] lists the composition change and mass shift corresponding to the currently known modifications for the reactive residues. An unambiguous localization of the modification site

is very important for structural analysis but also challenging due to the complexity of radiolytic oxidation. An MS analyzer cannot separate isobaric peptides with the same type of modification on different sites, and this is very common for radiolytic-modified peptides with multiple available reactive residues. Therefore, manual verification of modified peptides, especially localizing product ions that are cleaved before and after the modified residues, is critical in the early phase of the analysis. Two to three modifications are suggested per search. This is done mainly because setting too many modifications in the same peptide may result in many unwanted false-positive hits.

11. The longer time points are removed if they systematically deviate from the fit and the rate constant is then reexamined using the shorter time data. The final oxidation rates result from replicates of a series dataset containing 3–4 time points (Fig. 1) with 2–3 replicates of the overall experiment. Conformational dynamics of the different protein states can be checked by use of the dose-response curves as shown in Fig. 1. The slope of the curve represents the oxidation rates of each peptide during radiolysis. Change of oxidation rate of each peptide suggested conformational change between different states. For example, two peptides (ASTTVSKTETSQVAPA and MTIPAF) represented faster oxidation rate of Rho*-G_t than those of Rho and Rho*, which indicates more accessibility of these protein regions in Rho*-G_t than in other two states of Rho. Figure 4 shows fold of difference in the oxidation rate between Rho and Rho* as well as between Rho* and Rho*-G_t on each modified residue using different colors.
12. *Origin* can be used to monitor the first-order curve based on the datasets of the three replicates. Oxidation rate and statistical deviation can be calculated at the same time.
13. Hydrophobicity of an oxidized peptide is generally different than its unmodified parent species. Modified peptides with addition of simple alcohol or ketone are usually eluted earlier in LC than unmodified peptides [24]. For example, oxidized methionine-containing peptides elute few minutes earlier and oxidized phenylalanine-, tyrosine-, and tryptophan-containing peptides elute one or half minute prior to their unmodified counterpart [2, 25, 26]. Thus it is possible that the same precursor ion of oxidized species show several separated chromatographic peaks. In this case, peptides of isobaric mass or isotopic peaks need to be examined very carefully to reduce bias.
14. Residues in TM domains within hydrogen bonding distance to the structural waters in the crystal structure are prone to be oxidized during radiolysis. Locating radiolytic labeled residues that can make contact to structural waters can help reveal dynamics between internal water and functional residues in TM domains (Fig. 4). Mixing of O^{18}/O^{16} helps to detect the

a

Peptide	Rho S^{-1}	Rho* S^{-1}	Rho*-G_t S^{-1}	Fold of Change	
				Rho*/Rho	Rho*-G_t/Rho*
FM[86]VFGGF	15.3	25.4	90.9	1.66	3.58
TWVM[163]A	90.0	87.3	142.8	0.97	1.64
M[288]TIPAF	0.2	28.6	117.6	143	4.11
FAKTSAVYNP[303]VIF	3.5	11.1	14.0	3.17	1.26
SATTQKAEKEVTRM[253]	<0.01	<0.01	22.2	~1	2220
ASTTVSKTETSQVA[346]PA	0.2	0.08	1.1	0.40	13.75

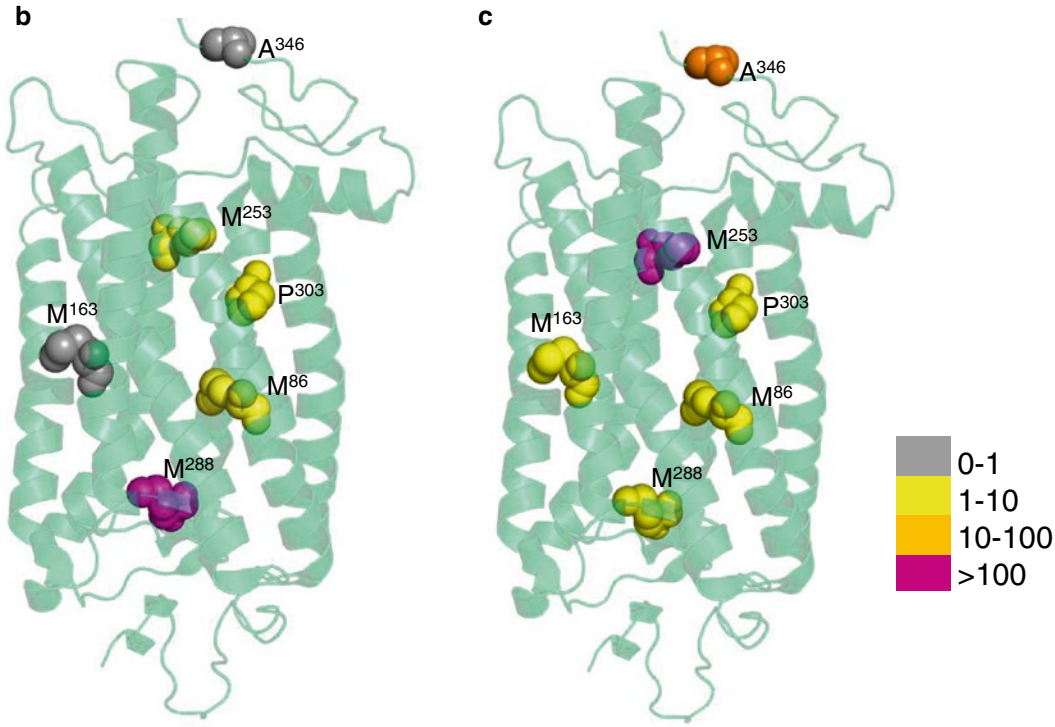

Fig. 4 Differences in oxidation rate change between different states of Rho. (**a**) Indicates several peptic peptides identified in three states of Rho: dark Rho, Rho*, and Rho*-G_t. Modified amino acid residues are colored in *red* and their modification rates are shown. Differences in oxidation rates between Rho and Rho* (**b**) and between Rho* and Rho*-G_t (**c**) are mapped on 3D crystal structure of Rho (PDB entry 1u19) [27]. These differences in oxidation rates are presented as fold of change and demonstrated in different colors

possibility of exchange of bulk water with internal water. No residue in Rho TM domains is labeled by O^{18}, indicating negligible exchange of internal water with bulk water. Thus, specific residues within TM helices are oxidized by hydroxyl radicals generated from internal structural water molecules.

References

1. Wang L, Chance MR (2011) Structural mass spectrometry of proteins using hydroxyl radical based protein footprinting. Anal Chem 83: 7234–7241
2. Kiselar JG, Chance MR (2010) Future directions of structural mass spectrometry using hydroxyl radical footprinting. J Mass Spectrom 45:1373–1382
3. Konermann L, Stocks BB, Pan Y et al (2010) Mass spectrometry combined with oxidative labeling for exploring protein structure and folding. Mass Spectrom Rev 29:651–667
4. Xu G, Chance MR (2007) Hydroxyl radical-mediated modification of proteins as probes for structural proteomics. Chem Rev 107: 3514–3543
5. Orban T, Jastrzebska B, Gupta S et al (2012) Conformational dynamics of activation for the pentameric complex of dimeric G protein-coupled receptor and heterotrimeric G protein. Structure 20:826–840
6. Angel TE, Chance MR, Palczewski K (2009) Conserved waters mediate structural and functional activation of family A (rhodopsin-like) G protein-coupled receptors. Proc Natl Acad Sci U S A 106:8555–8560
7. Angel TE, Gupta S, Jastrzebska B et al (2009) Structural waters define a functional channel mediating activation of the GPCR, rhodopsin. Proc Natl Acad Sci U S A 106:14367–14372
8. Hoskison TK, Wortmann RL (2006) Advances in the management of gout and hyperuricemia. Scand J Rheumatol 35:251–260
9. Okada T, Fujiyoshi Y, Silow M et al (2002) Functional role of internal water molecules in rhodopsin revealed by X-ray crystallography. Proc Natl Acad Sci U S A 99:5982–5987
10. Hofmann KP, Scheerer P, Hildebrand PW et al (2009) A G protein-coupled receptor at work: the rhodopsin model. Trends Biochem Sci 34:540–552
11. Padayatti PS, Wang L, Gupta S et al (2013) A hybrid structural approach to analyze ligand binding by the serotonin type 4 receptor (5-HT4). Mol Cell Proteomics 12: 1259–1271
12. Orban T, Gupta S, Palczewski K et al (2010) Visualizing water molecules in transmembrane proteins using radiolytic labeling methods. Biochemistry 49:827–834
13. Gupta S, Sullivan M, Toomey J et al (2007) The beamline X28C of the center for synchrotron biosciences: a national resource for biomolecular structure and dynamics experiments using synchrotron footprinting. J Synchrotron Radiat 14:233–243
14. Papermaster DS (1982) Preparation of antibodies to rhodopsin and the large protein of rod outer segments. Methods Enzymol 81:240–246
15. Okada T, Tsujinimoto R, Muraoka M et al (2005) Methods and results in X ray crystallography of bovine rhodopsin, in G protein-couples receptors. In: Haga T (ed) Structure, function, and ligand screening. CRC Press LLC, Boca Raton, FL, pp 245–261
16. Jastrzebska B, Ringler P, Lodowski DT et al (2011) Rhodopsin-transducin heteropentamer: three-dimensional structure and biochemical characterization. J Struct Biol 176: 387–394
17. Goc A, Angel TE, Jastrzebska B et al (2008) Different properties of the native and reconstituted heterotrimeric G protein transducin. Biochemistry 47:12409–12419
18. Xu H, Freitas MA (2010) A dynamic noise level algorithm for spectral screening of peptide MS/MS spectra. BMC Bioinformatics 11:436
19. Sun ZY, Oh KJ, Kim M et al (2008) HIV-1 broadly neutralizing antibody extracts its epitope from a kinked gp41 ectodomain region on the viral membrane. Immunity 28:52–63
20. Kaur P, Kiselar JG, Chance MR (2009) Integrated algorithms for high-throughput examination of covalently labeled biomolecules by structural mass spectrometry. Anal Chem 81:8141–8149
21. Gupta S, D'Mello R, Chance MR (2012) Structure and dynamics of protein waters revealed by radiolysis and mass spectrometry. Proc Natl Acad Sci U S A 109:14882–14887
22. Xu G, Kiselar J, He Q et al (2005) Secondary reactions and strategies to improve quantitative protein footprinting. Anal Chem 77: 3029–3037
23. Wisniewski JR, Zougman A, Nagaraj N et al (2009) Universal sample preparation method for proteome analysis. Nat Methods 6:359–362
24. Takamoto K, Chance MR (2006) Radiolytic protein footprinting with mass spectrometry to probe the structure of macromolecular complexes. Annu Rev Biophys Biomol Struct 35:251–276
25. Maleknia SD, Chance MR, Downard KM (1999) Electrospray-assisted modification of

proteins: a radical probe of protein structure. Rapid Commun Mass Spectrom 13: 2352–2358

26. Kiselar JG, Mahaffy R, Pollard TD et al (2007) Visualizing Arp2/3 complex activation mediated by binding of ATP and WASp using structural mass spectrometry. Proc Natl Acad Sci U S A 104:1552–1557
27. Okada T, Sugihara M, Bondar AN et al (2004) The retinal conformation and its environment in rhodopsin in light of a new 2.2 A crystal structure. J Mol Biol 342:571–583

Chapter 8

Probing Conformational Changes in Rhodopsin Using Hydrogen-Deuterium Exchange Coupled to Mass Spectrometry

Tivadar Orban and Yaroslav Tsybovsky

Abstract

Hydrogen-deuterium exchange coupled to mass spectrometry is a powerful tool to evaluate changes in protein conformation between two or more states. Here, we describe a complete methodology that can be used to assess conformational changes in rhodopsin accompanying its transition from the inactive to activated state upon light exposure. This approach may be employed to investigate the structure and conformational changes of various membrane proteins.

Key words Hydrogen-deuterium exchange, Mass spectrometry, Rhodopsin, Rod outer segments, Protein conformational changes

1 Introduction

Elucidation of protein structure and discrete conformational states represents a fundamental problem in structural biology. Although many membrane proteins are attractive drug targets, their characterization is often very challenging, with only a handful of structures determined so far using the conventional methods such as X-ray crystallography and NMR. Hydrogen-deuterium exchange (H/DX) monitored with mass spectrometry represents an alternative approach to probing the structure and conformational dynamics of membrane proteins.

Hydrogen atoms in the protein are constantly exchanged with protons of the surrounding milieu. Therefore, if a protein solution is diluted with D_2O, such an exchange will occur between hydrogen and deuterium atoms. For most hydrogen atoms within the protein, this exchange and consequent back-exchange occur on a microsecond to millisecond time scale. Such rapid exchanges cannot be evaluated with the method we describe herein. However, the amide hydrogen atom in the peptide bond exchanges with

Beata Jastrzebska (ed.), *Rhodopsin: Methods and Protocols*, Methods in Molecular Biology, vol. 1271,
DOI 10.1007/978-1-4939-2330-4_8,

deuterium from the bulk solvent on a minutes to hours time scale, allowing quantification of the exchanged amounts using mass spectrometry based on the difference in mass between hydrogen and deuterium atoms. The rate of exchange of the amide hydrogen is affected by pH, percent dilution with D_2O, temperature, ionic strength, and, most importantly, the immediate environment. Thus, the number of deuterium atoms absorbed by a given peptide within the protein of interest and the corresponding exchange rates depend on the local protein environment, its conformational flexibility, and accessibility of the peptide to the solvent. Therefore, mapping of exchange amounts and rates can provide valuable insights into the protein conformation and its transformations in response to relevant biological signals and environmental changes [1].

The simplified flowchart (Fig. 1a) illustrates the exchange of hydrogen atoms with deuterium atoms. Specific setups are intended to minimize the back-exchange by careful temperature, pH, and dilution control, to increase the efficiency of protein proteolysis, and to minimize the negative effect of detergent that must be present to keep the membrane protein in solution. After proteolysis, the deuterium-enriched peptides are separated using reverse-phase liquid chromatography and analyzed using mass spectrometry. The amount of amide H/DX is then evaluated and correlated with the changes taking place in the intimate protein environment. The following protocols describe H/DX of rhodopsin after its extraction from rod outer segment (ROS) membranes. This procedure will evaluate the conformational changes that accompany rhodopsin's activation upon light exposure.

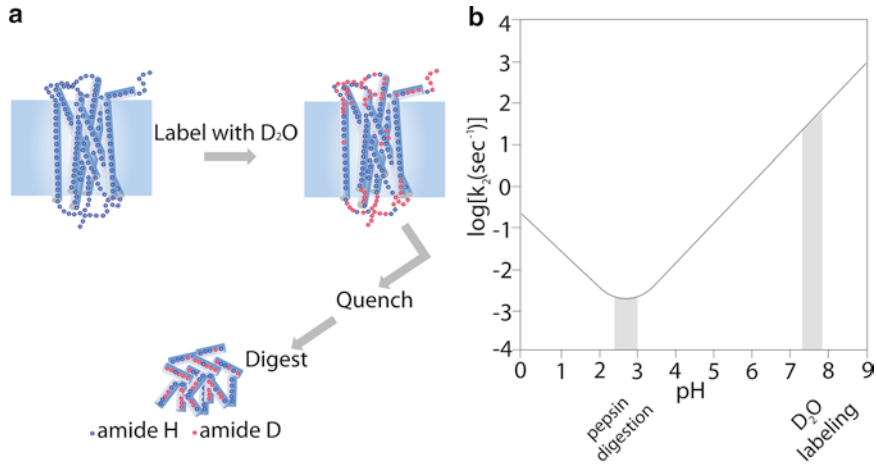

Fig. 1 Schematic of a hydrogen-deuterium exchange experiment. (**a**) A simplified illustration of the D_2O labeling procedure together with the short peptide generation schematic. Amide hydrogen atoms (*blue spheres*) are exchanged to deuterium atoms (*red spheres*) in residues accessible to bulk solvent. The exchange rate is decreased when hydrogen atoms participate in hydrogen bonding. (**b**) The dependence of the rate of exchange between hydrogen and deuterium atoms (k) on pH. D_2O labeling is performed at the physiologically relevant pH 7.4. The exchange is quenched by lowering the pH from 7.4 to 2.5. Pepsin digestion is performed at pH 2.5 as well

2 Materials

1. ROS membranes purified from fresh or frozen bovine retinas as described previously [2].
2. 1 μg/μl pepsin protease (Worthington) for rhodopsin proteolysis at low pH. Prepare the pepsin solution by dissolving pepsin powder in ultrapure water (Mili-Q H_2O) followed by incubation on ice for at least 15 min before use (*see* **Note 1**).
3. Quench Solution: 0.2 mM DDM in Mili-Q H_2O or D_2O, pH 2.5 (adjusted using formic acid).
4. Standard synthetic peptide derived from rhodopsin amino acid sequence: F^{293}AKTSAVYNPVIY^{305}.
5. Hewlett-Packard 1100 high-performance liquid chromatography system equipped with two pumps.
6. Solvent A: Mili-Q H_2O with 0.1 % formic acid (Sigma-Aldrich).
7. Solvent B: acetonitrile with 0.1 % formic acid.
8. Thermo Finnigan mass spectrometer equipped with an electrospray ionization source operated at 300 °C. The mass spectrometer is tuned using direct injection of the standard peptide (F^{293}AKTSAVYNPVIY^{305}).

3 Methods

3.1 Rhodopsin Sample

1. Solubilize rhodopsin from ROS membranes in n-dodecyl-β-D-maltoside (DDM) using the $ZnCl_2$-opsin extraction procedure [3].
2. Remove $ZnCl_2$ by dialysis against 0.2 mM DDM [3].
3. Evaluate the purity of rhodopsin preparation using a spectrophotometer based on the absorption ratio between 280 nm (protein peak) and 500 nm (chromophore peak) (*see* **Note 2**).
4. Calculate rhodopsin concentration using the extinction coefficient ε =40,600/M/cm at 500 nm.

3.2 Hydrogen-Deuterium Exchange

H/DX is initiated by the addition of D_2O to the sample. During the hydrogen-deuterium exchange reaction, special attention should be paid to the following parameters: (1) The temperature should be kept constant. Thus, perform all operations on ice. (2) The dilution by D_2O should be kept constant for all samples. (3) The pH of the samples needs to be controlled.

All manipulations are performed in the dark under dim red light. The tubes containing rhodopsin samples should be wrapped in one layer of aluminum foil:

1. Prepare D_2O with the same concentration of the detergent as in the rhodopsin sample. This step is necessary to keep the detergent concentration constant throughout the exchange process. It is also important to keep the dilution of samples with D_2O identical for all samples since this is a parameter that affects the exchange rate (*see* **Note 3**).
2. Take 10 μl of the 1 μg/μl rhodopsin solution, and add 70 μl of D_2O/0.2 mM DDM solution kept for 10 min on ice.
3. In the case of activated rhodopsin, first bleach the sample on ice for 30 s using a 150 W bulb covered with a band-pass filter (480–520 nm) (Chroma Technology Corp.) from the distance of 10 cm. Maintain this distance constant throughout all experiments. Immediately after bleaching add D_2O/0.2 mM DDM solution.
4. Set the time scale for the exchange. Typical incubation times are 10, 20, 300, and 600 s.
5. Start the timer when the solution is mixed and let the exchange go on for the set amount of time. Keep the samples on ice to minimize back-exchange.
6. At the end of the set exchange time, add 10 μl of the Quench Solution to stop the exchange process. Quench Solution is added to lower the pH so that the deuterium exchange and back-exchange are minimized. This step is critical since the pH of the final exchange medium heavily influences the rates of exchange and back-exchange. Figure 1b shows the dependence of the rate of exchange (k) on pH. The pH of the solution after quenching should be 2.5.
7. Immediately after addition of Quench Solution, add 10 μl of the 1 μg/μl pepsin solution to start the digestion process.
8. Digest the sample for 5 min on ice (*see* **Note 4**).

3.3 HPLC

3.3.1 Pre-Run Preparations

1. Keep the HPLC column (Luna 20×2.00 mm C18 column (Phenomenex)) on ice and start the run with a wash program (i.e., mock injection of 10 μl solvent A). This run is important to make sure that the carry-over from the previous run is either undetectable or negligible.
2. Perform the wash run. Several washes may be required between runs to achieve the desired run-to-run performance.
3. Establish the coefficient of variation from run to run (described in Subheading 3.5, quality control). A run-to-run variation of base peak relative intensity of 0–4 % was found to be acceptable (*see* **Note 5**).

Table 1
HPLC peptide elution program

Time (min)	Solvent A (%)	Solvent B (%)
0–4	98	2
4–12	2	98
12–20	98	2

3.3.2 Production Run

1. After 5 min of digestion of the rhodopsin sample with pepsin, load 100 µl of the reaction sample to a chromatography column. Set the solvent temperature to 4 °C using a temperature-controlled Peltier heating/cooling system (Hewlett-Packard).
2. Elute peptides at a flow rate of 0.2 ml/min using the gradient program as shown in Table 1.

3.4 Mass Spectrometry

1. Tune the mass spectrometer equipped with an electrospray ionization source using the synthetic standard rhodopsin peptide mentioned above. The tuning is performed following the manufacturer's user manual provided with the LXQ Thermo Finnigan mass spectrometer (Thermo Fisher). Choose the automatic tune mode and set the mass to 1,473.72 (i.e., the singly charged positive ion of the FAKTSAVYNPVIY standard peptide).
2. Set general mass spectrometric conditions such as temperature to 300 °C and the normalized collision energy to 35 % for MS^2 acquisitions.
3. Set the ion selection threshold to 500 counts for MS^2.

3.5 Analysis

3.5.1 Identification of the Peptic Fragments from Non-deuterated Samples

1. Replace D_2O with Mili-Q H_2O and perform the digestion of rhodopsin as described in Subheading 3.2**.**
2. Peptic fragments generated are identified using an automatic search of the generated MS^2 against the theoretical *y* and *b* ions obtained during collision-induced differentiation (Fig. 2; *see* **Note 6**).
3. Use MassMatrix, a freely available software package, to identify peptic peptide fragments [4–8] (www.massmatrix.net). Create a database file that contains the primary sequence of bovine rhodopsin using the FASTA format (*see* **Note 7**).
4. Specify settings to identify peptic peptides analyzed using LXQ Thermo Finnigan mass spectrometer (*see* **Note 8**):
   - Set the precursor ion tolerance to 0.8 Da.
   - Set the maximum number of variable modifications to 2.
   - Set the minimum peptide length to 4.

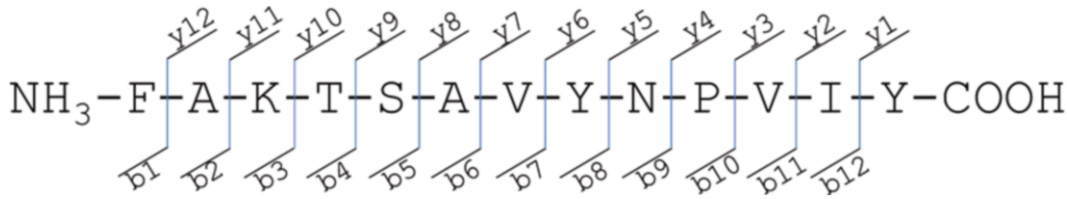

Fig. 2 MS^2 fragmentation pattern used to identify peptides resulting from the pepsin digest. In the soft ionization mode, as described in Subheading 3.4, the mass spectrometer will generate specific fragmentation ions denoted as *y* and *b* ions. A typical fragmentation pattern showing the *y* and *b* ions is presented for the standard peptide with the amino acid sequence FAKTSAVYNPVIY. Identification of peptic peptides is based on the identification of the theoretical *y* and *b* ions in the MS^2 spectrum

- Set the minimum pp score to 5.
- Set the pp_{tag} score to 1.3.
- Set the product ion tolerance to 0.8 Da and the mass type to "average."
- Include search for the disulfide bond between Cys^{110} and Cys^{187}.
- Include modification with palmitoyl of residues Cys^{322} and Cys^{323} (molecular formula $C_{16}H_{31}O_1$, an average mass addition of 239.23 Da).

5. Peptic peptide fragments are identified from the list of automatic hits.
6. Manually verify the list of automatic hits to ensure that the most intense peaks from the MS^2 list are correctly assigned to the theoretical *y* and *b* ions.

3.5.2 Evaluation of Deuterium Uptake from Deuterated Samples

1. Deuterium uptake analysis is initiated by constructing a spreadsheet with the following columns: [1] peptide sequence, [2] theoretical mass (Da), [3] recorded mass, [4] *m/z* (i.e., charge state (*see* **Note 9**)), [5] mass of the deuterated peptide (Da), and [6] standard error (SE) derived from a minimum of three independent measurements.
2. Use the determined specific retention time of the peptide to export the raw data in the form of relative signal intensity (%) as a function of *m/z*. Use Xcalibur 2.1.0 Qual Browser supplied with the LXQ mass spectrometer to load the raw data and export the signal as a function of *m/z* (*see* **Note 10**).
3. Next, use HDExpress software [9] to perform a semiautomatic peak detection and deconvolution.
4. Deuterium uptake for each peptide fragment is evaluated from the raw data (*m/z* as a function of signal intensity). If the sequence contains a proline residue, the number of exchangeable sites is decreased by one.

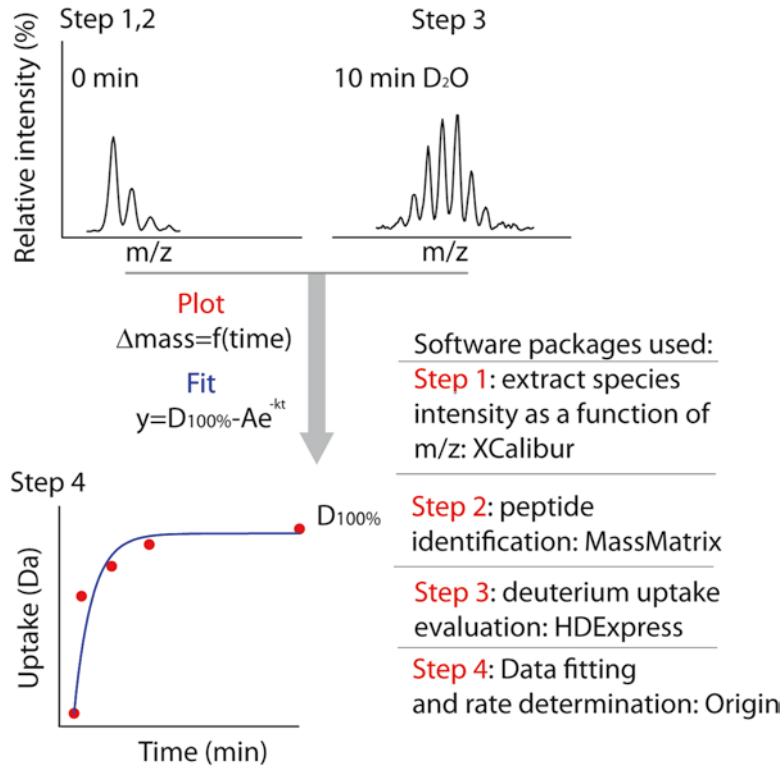

Fig. 3 Semiautomatic processing of raw signals. The relative ion intensity (%) is represented as a function of *m/z*. The isotopic distribution of a non-deuterated peptide is shown at time 0. Following 10 min of incubation in D_2O, the signal shows a different isotopic distribution profile. The semiautomatic procedure is used to evaluate the median value of *m/z* and the mass change (Da). Next, the change in mass (Da) is plotted as a function of incubation time, and the graph is fit using the equation described in Subheading 3.5.2, **step 6**

5. Next, the experimentally evaluated deuterium uptake is normalized to the percent dilution used (*see* **Note 11**).
6. Origin™ software is used to fit the data points (Fig. 3) using the equation:

$$y = D_{100\%} - Ae^{-kt}$$

where $D_{100\%}$ represents the maximum deuteration level for each specific peptide, A represents the normalized deuterium uptake, k is the rate of deuterium uptake, and t is time.

3.5.3 Data Representation

1. H/DX used to study protein conformational changes does have a few inherent drawbacks. Specifically, the fragments can be of different lengths, pepsin digestion may not generate consistently the same peptides, the extent of back-exchange may differ depending on the time spent on the HPLC column, and

the exchanged deuterium cannot be localized to a specific amino acid. With these shortcomings in mind, comparisons of uptakes between peptides with different lengths and amino acid compositions are not recommended. The only reliable information is the change in the amount or rate of exchange within the same peptide in response to protein conformational transitions (e.g., initiated with light exposure).

4 Notes

1. High-purity water (Mili-Q H_2O) has maximum resistivity of 18.2 MΩ · cm determined at 25 °C. Use high-purity water for all preparations.
2. This approach can be used to evaluate the presence of opsin and other contaminating proteins. Purity close to 100 % has been achieved if the ratio between the absorption at 280–500 nm is smaller than 1.6. In our preparations we typically achieved a ratio of 1.8 [1].
3. It is important to choose the concentration of pepsin so that the sample volume P_{volume} (μl) is constant for all experiments.
4. We found that it is best to prepare pepsin fresh and use it within 8 h.
5. The intensity of the peak is not a measured parameter in the evaluation of total mass uptake. The necessary and sufficient criterion is to have intensities always above a preestablished minimum baseline.
6. Identification of all peptides will be performed using non-deuterated samples. During the electrospray ionization, the deuterium atom is shuffled among all amino acid residues; hence, the exact position of the deuterium atom will remain unidentified. Identification of the deuterated species is done by correlating m/z of the deuterated peptides with m/z of non-deuterated peptides sharing the same retention time.
7. The FASTA format is a text-based representation of the amino acid sequence of a protein using single-letter codes for each amino acid.
8. Different MS will require different settings depending on the sensitivity.
9. The charge state of a peptide is determined based on the difference between two consecutive isotopic peaks (Δi). For example, $\Delta i = 1$ corresponds to singly charged species, $\Delta i = 0.5$ corresponds to a doubly charged species, $\Delta i = 0.33$[3] corresponds to triply charged species, etc.

10. It is useful to save the "layout" in a separate file. This will ensure that identical retention time and averaging procedures will be used for all time points and replicas when a specific *m/z* will be evaluated as linked to a specific retention time.
11. It is important to correct for the actual dilution of the sample in D_2O. In our example, the maximum dilution is 80 % (80 μl of D_2O in 100 μl of total reaction volume).

Acknowledgements

We would like to thank Dr. Malligarjunan Rajavel and Ms. Alicia Quick for their helpful comments and critical reading of the manuscript.

References

1. Orban T, Jastrzebska B, Gupta S et al (2012) Conformational dynamics of activation for the pentameric complex of dimeric G protein-coupled receptor and heterotrimeric G protein. Structure 20:826–840
2. Papermaster DS (1982) Preparation of retinal rod outer segments. Methods Enzymol 81: 48–52
3. Okada T, Le Trong I, Fox BA et al (2000) X-Ray diffraction analysis of three-dimensional crystals of bovine rhodopsin obtained from mixed micelles. J Struct Biol 130:73–80
4. Su X, Lucas DM, Zhang L et al (2009) Validation of an LC-MS based approach for profiling histones in chronic lymphocytic leukemia. Proteomics 9:1197–1206
5. Xu H, Freitas MA (2007) A mass accuracy sensitive probability based scoring algorithm for database searching of tandem mass spectrometry data. BMC Bioinformatics 8:133
6. Xu H, Freitas MA (2008) Monte carlo simulation-based algorithms for analysis of shotgun proteomic data. J Proteome Res 7:2605–2615
7. Xu H, Freitas MA (2009) MassMatrix: a database search program for rapid characterization of proteins and peptides from tandem mass spectrometry data. Proteomics 9:1548–1555
8. Xu H, Zhang L, Freitas MA (2008) Identification and characterization of disulfide bonds in proteins and peptides from tandem MS data by use of the MassMatrix MS/MS search engine. J Proteome Res 7:138–144
9. Weis DD, Engen JR, Kass IJ (2006) Semi-automated data processing of hydrogen exchange mass spectra using HX-Express. J Am Soc Mass Spectrom 17:1700–1703

Chapter 9

Analysis of Conformational Changes in Rhodopsin by Histidine Hydrogen–Deuterium Exchange

David T. Lodowski and Masaru Miyagi

Abstract

Hydrogen–deuterium exchange (HDX) is a technique that measures the exchange of protein hydrogens for deuteriums in a D_2O-containing buffer, providing readout of the structural dynamics. Histidine hydrogen–deuterium exchange mass spectrometry (His-HDX-MS) is a variation of this technique that measures the slow HDX of imidazole C_2 hydrogens of histidines. This measurement, when accompanied by pH titration, provides both pK_as and half-lives ($t_{1/2}$) of the HDX reaction for individual histidine residues in proteins. The pK_a and $t_{1/2}$ values indicate the electrostatic environment and the degree of side-chain solvent accessibility of the histidine residues, respectively. Herein we describe an experimental protocol to characterize rhodopsin by His-HDX-MS. This technique can be used to monitor different states of rhodopsin and might be useful for monitoring longtime scale events in other GPCRs.

Key words Histidine, Hydrogen–deuterium exchange, Mass spectrometry, pK_a, Solvent accessibility

1 Introduction

Hydrogen atoms in a protein that are covalently bonded to oxygen, nitrogen, or sulfur atoms are exchanged quickly with deuterium atoms (<1 s at physiological pH and 37 °C) in deuterium oxide (D_2O) solvent, if they are exposed to the bulk solvent [1]. In addition to these hydrogens, the imidazole C_2 hydrogen of histidine also exchanges with a deuterium at significantly slower rate (Fig. 1); the half-life ($t_{1/2}$) of the reaction for a fully exposed imidazole side chain in proteins is 1–2 days [2–4]. Histidine hydrogen–deuterium exchange mass spectrometry (His-HDX-MS) measures this slow HDX of histidine imidazole groups in proteins using mass spectrometry [5] and has been used to determine the pK_a and solvent accessibility of individual histidine residues in proteins [6–9] and more recently to identify the metal-bound histidine residues in metalloproteins [10].

Beata Jastrzebska (ed.), *Rhodopsin: Methods and Protocols*, Methods in Molecular Biology, vol. 1271,
DOI 10.1007/978-1-4939-2330-4_9,

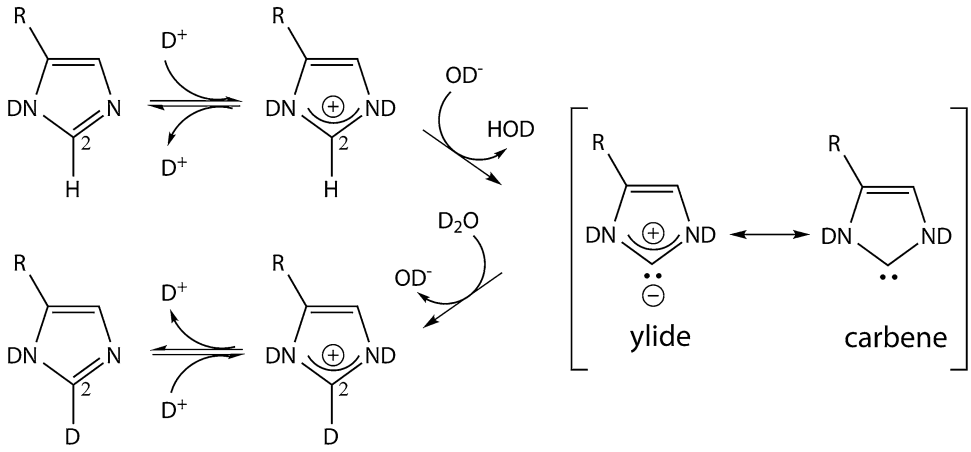

Fig. 1 Mechanism of the HDX reaction at the imidazole C_2 hydrogen of histidine. The HDX reaction follows pseudo first-order kinetics, involving abstraction of the C_2 proton from the cationic imidazolium by OD^- to form an ylide or a carbene intermediate as the rate-determining step. Figure adapted with permission from Mullangi, V., Zhou, X., Ball, D. W., et al. (2012) "Quantitative Measurement of Solvent Accessibility of Histidine Imidazole Groups in Proteins," *Biochemistry* 51, 7202–7208. Copyright (2012) American Chemical Society

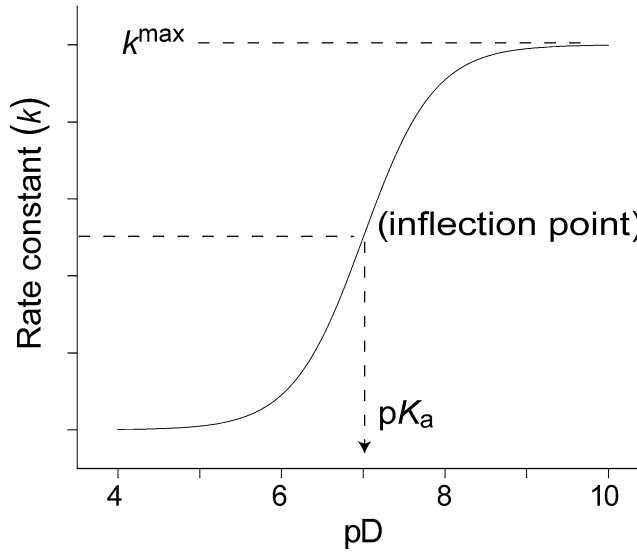

Fig. 2 Rate profile of the HDX reaction of the imidazole C_2 hydrogen. The pK_a of the imidazole group can be obtained from the inflection point of the sigmoidal curve and the maximum pseudo first-order rate constant, k^{max}, from the upper plateau of the sigmoidal curve

The rate of the HDX reaction as a function of pD yields a sigmoidal curve, which exhibits a progression from the acidic side that accelerates and approaches the plateau on the alkaline side of the curve (Fig. 2) [5]. The rate profile provides two useful parameters that indicate the local environment of the given imidazole

group in a protein. The first is the pK_a of the imidazole N–H group, which coincides with the inflection point of the sigmoidal curve, because the rate of the reaction depends on both the concentrations of the conjugate acid of imidazole and OD^- [2]. The second is the maximum rate constant, k^{max}, which corresponds to the upper plateau of the sigmoidal curve and indicates the solvent accessibility of the imidazole group [6]. We have found these two parameters to be useful to probe the structural changes of proteins [7–9].

Since the back-exchange rate of C_2 hydrogen from deuteron to proton is slow, His-HDX-MS does not require a special analytical setup like required for amide-HDX. The slow back-exchange of C_2 hydrogen allows the use of proteases that work at neutral pH and have strict substrate specificities (e.g., trypsin) rather than the requirement of pepsin for amide-HDX experiments. Such proteases are more suitable to analyze complex protein mixtures and provide higher peptide discrimination power. Below we present a detailed experimental protocol to carry out His-HDX-MS on rhodopsin.

2 Materials

2.1 Preparation of Rhodopsin and Opsin Samples

1. Rod outer segments (ROS) membranes from bovine retinas (*see* **Note 1**).
2. Rhodopsin solubilized in *n*-dodecyl-β-D-maltopyranoside (DDM).
3. 50 mM desired buffer (*see* **Note 2**).
4. 50 mM desired buffer containing 20 mM hydroxylamine.
5. 1 ml dounce homogenizer.
6. Lamp with 150 W bulb.

2.2 Titration Buffers Made with D_2O

1. Deuterium oxide (D_2O, >99 % atom % D).
2. Deuterium chloride (DCl, 35 wt% in D_2O).
3. Sodium deuteroxide (NaOD, 30 wt% in D_2O).
4. 50 mM sodium acetate, pH* 4.0–5.0 (*see* **Note 3**).
5. 50 mM 2-(*N*-morpholino)ethanesulfonic acid (MES), pH* 4.0–5.0.
6. 4-(2-Hydroxyethyl)-1-piperazine-1-ethanesulfonic acid (HEPES), pH* 7.5–9.0.
7. *N*-Cyclohexyl-2-aminoethanesulfonic acid (CHES), pH* 9.0–10.0.
8. 50 mM sodium acetate, 0.2 mM DDM, pH* 3.5–5.0.
9. 50 mM MES, 0.2 mM DDM, pH* 5.0–7.5.
10. 50 mM HEPES, 0.2 mM DDM, pH* 7.5–9.0.
11. 50 mM CHES, 0.2 mM DDM, pH* 9.0–10.0.

2.3 Sample Preparation for Mass Spectrometry Analysis

1. Water (HPLC grade).
2. Neat formic acid.
3. Cold acetone kept at −20 °C.
4. 90 % acetone (v/v).
5. Hydrogen peroxide (30 wt% in H_2O).
6. 1 % SDS (w/v), 1 % formic acid (v/v).
7. Formic acid–methanol (5:1, v/v).
8. Performic acid (*see* **Note 4** for preparation instructions).
9. Immobilized pepsin (Princeton Separations, Inc.).

2.4 LC–MS/MS Analysis

1. Water (HPLC grade).
2. 0.1 % trifluoroacetic acid (TFA) (v/v).
3. 0.1 % formic acid (v/v).
4. 98 % acetonitrile (v/v) containing 0.1 % formic acid (v/v).
5. Reverse-phase C18 PepMap trapping column (0.3 × 5 mm, Dionex).
6. Reverse-phase C18 Acclaim PepMap 100 column (0.075 × 150 mm, Dionex).
7. The LC–MS/MS system consisting of a Finnigan LTQ-Orbitrap XL mass spectrometer (Thermo Finnigan) and an UltiMate 3000 LC system (Dionex) (*see* **Note 5**).
8. Software, Xcalibur (Thermo Finnigan), is used to operate the system, including data acquisition and analysis.

3 Methods

3.1 Preparation of Rhodopsin and Opsin Samples

3.1.1 Preparation of Detergent Solubilized Rhodopsin

1. Resuspend ROS membranes in a desired buffer (*see* **Note 2**) containing 5 mg of DDM detergent per mg of rhodopsin present.
2. Solubilize the above mixture by stirring for 30 min at 4 °C in a darkroom.
3. Pellet unsolubilized material by centrifugation at 16,000 × *g* for 30 min at 4 °C.
4. Collect the supernatant containing solubilized rhodopsin and discard the pellet.

3.1.2 Preparation of Opsin from ROS Membranes

1. Resuspend 0.5 ml of ROS membranes in 0.5 ml of a desired buffer (*see* **Note 2**) containing 20 mM hydroxylamine using 1 ml dounce homogenizer and place in a 1.5 ml microcentrifuge tube.
2. Place this tube on its side on a bed of ice and expose to bright light (lamp with 150 W bulb) for 15 min. Membranes should become white.

3. Harvest membranes containing opsin by a 5 min, 16,000 × *g* centrifugation, and discard the supernatant.
4. To remove residual hydroxylamine, resuspend membranes in 1 m of desired buffer (which does not contain hydroxylamine) and again harvest by centrifugation.
5. Following the second centrifugation, membranes can be resuspended in the D_2O containing titration buffer to initiate HDX.

3.2 pH* Titration

Carry out all procedures under dim red light illumination.

3.2.1 pH* Titration of Rhodopsin/Opsin in ROS Membrane

1. Aliquot ROS membrane preparations into 10–15 Eppendorf tubes, each containing about 0.1 mg of rhodopsin/opsin (*see* **Note 6**). Save one tube as a reference sample. The reference sample is not incubated in D_2O buffer; therefore, skip **steps 2–4** and proceed to **step 5**.
2. Centrifuge at 16,000 × *g* for 5 min, and remove the supernatant.
3. Add 100 µl of D_2O, centrifuge at 16,000 × *g* for 5 min, and remove the supernatant. Repeat three times (*see* **Note 7**).
4. Add 100 µl of D_2O buffer with different pHs* (pH* 4–10) into the tubes, and incubate at 37 °C for 72 h (*see* **Note 8**).
5. After the incubation, centrifuge at 16,000 × *g* for 5 min, and remove the supernatant.
6. Add 100 µl of 1 % SDS (w/v), 1 % formic acid (v/v) to extract proteins from the ROS membrane and stop the HDX reaction (*see* **Note 9**).
7. Centrifuge at 16,000 × *g* for 5 min, and collect the supernatant (*see* **Note 10**).

3.2.2 pH* Titration of Detergent Solubilized Rhodopsin

1. Aliquot the detergent solubilized rhodopsin into 10–15 Eppendorf tubes, so each tube contains about 0.01 mg of rhodopsin/opsin. Save one tube as a reference sample. The reference sample will not be incubated in D_2O buffer.
2. Add ten times the sample volume of D_2O buffer containing 0.2 mM DDM with different pHs* (pH* 4–10) into the tubes, and incubate at 37 °C for 72 h (*see* **Note 11**).
3. After the incubation, add formic acid to a final concentration of 1 % to stop the reaction (*see* **Note 12**).

3.3 Preparation of Rhodopsin/Opsin Digest for LC–MS/MS

1. To the solution containing the deuterated protein from the previous step, add four times the sample volume of cold acetone (−20 °C), and leave for 1 h at −20 °C (*see* **Note 13**).
2. Centrifuge at 3,000 × *g* for 1 min, and collect the pellet.
3. Add 100 µl of 90 % acetone, gently shake the solution, centrifuge at 3,000 × *g* for 1 min, and remove the supernatant. Repeat three times (*see* **Note 14**).

4. Dissolve the protein pellet in 100 µl of formic acid–methanol (5:1, v/v).
5. Add 5 µl of performic acid and incubate at room temperature for 1 h (*see* **Note 4**).
6. Dry the protein sample in a Speed Vac.
7. Dissolve the dried protein sample in 10 µl of neat formic acid and then add 90 µl H_2O.
8. Add 5 µl of immobilized pepsin and incubate for 1 h (*see* **Note 15**).
9. Centrifuge at 3,000 × *g* for 1 min, and collect the supernatant for LC–MS/MS.

3.4 LC–MS/MS of Rhodopsin/Opsin Digest

1. Install a reverse-phase C18 PepMap trapping column (0.3 × 5 mm) and a reverse-phase C18 Acclaim PepMap 100 analytical column (0.075 × 150 mm).
2. Equilibrate the trapping column with 0.1 % TFA (*see* **Note 16**).
3. Equilibrate the analytical column with 0.1 % formic acid.
4. Inject the ~20 pmol of protein digest into the trapping column, and wash the trapping column with 0.1 % TFA for 5 min at a flow rate of 25 µl/min.
5. After washing, place the trapping column in-line with the analytical column.
6. Separate the peptides with a linear gradient of 0–50 % acetonitrile in 0.1 % formic acid over a period of 60 min at 300 nl/min flow rate, and directly introduce the eluate into the mass spectrometer.
7. Acquire the data by a data-dependent MS to MS/MS switching mode, with the ten most intense ions in each MS scan subjected to MS/MS analysis (*see* **Note 17**).

3.5 Data Analysis

1. Identify histidine-containing peptides with the acquired LC–MS/MS data using a database search engine (*see* **Note 18**).
2. Open the raw LC–MS/MS data in Xcalibur software, and extract the precursor ion of each histidine-containing peptide from the MS data. Figure 3 shows hypothetical mass spectra of a histidine-containing peptide from the reference sample and a deuterated sample.
3. Calculate the HDX rate constant (k) from the spectra using the following equation:

$$k = -ln\left\{1 - \left[\frac{\left(R(t) - R(0)\right)}{\left(1 + R(t) - R(0)\right)}\right] \times \frac{1}{P}\right\} / t$$

where $R(0) = I_{M+1}(0)/I_M(0)$, $R(t) = I_{M+1}(t)/I_M(t)$, P is the fractional D_2O content in the solvent ($P = 1$ when D_2O content is 100 %), and t is the incubation time (h) (*see* **Note 19**).

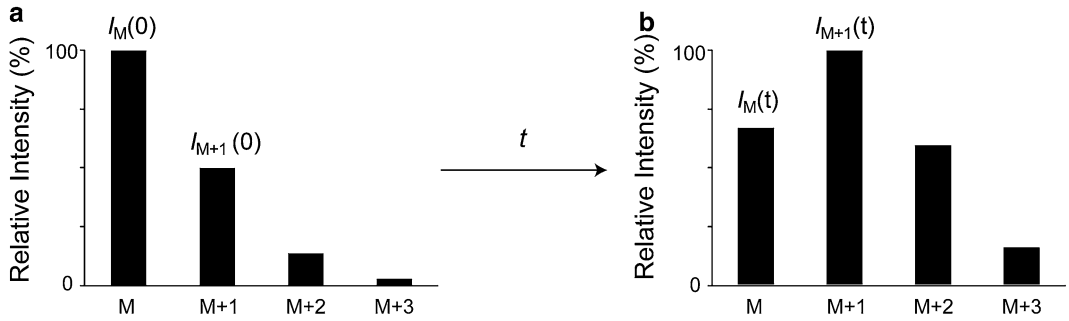

Fig. 3 Hypothetical mass spectra of a histidine-containing peptide from a reference and a deuterated sample. (**a**) Mass spectrum of a peptide from a reference sample. The peptide gives multiple isotopic peaks (M, M + 1, M + 2, M + 3) reflecting the natural abundances of heavy isotopes such as ^{13}C (1.1 %) and ^{15}N (0.4 %). (**b**) The same peptide from a deuterated sample. Incubation of the peptide in D_2O solvent results in partial deuterium incorporation at the imidazole C_2-position of the histidine residue and the relative abundance of isotopic peaks changes as shown. Only peaks M and M + 1 are used for the calculation of rate constant (*k*). The intensities of the M and M + 1 peaks from the reference sample are represented as $I_M(0)$ and $I_{M+1}(0)$, respectively, and the intensities of the same peaks from the deuterated sample are represented as $I_M(t)$ and $I_{M+1}(t)$. Figure adapted with permission from Miyagi, M., and Nakazawa, T. (2008) "Determination of pKa values of individual histidine residues in proteins using mass spectrometry", *Anal Chem* 80, 6481–6487. Copyright (2008) American Chemical Society

4. Plot k as a function of pH*. A sigmoidal curve like shown in Fig. 2 is typically obtained by fitting the data to the following equation:

$$y = A_2 + \frac{A_1 - A_2}{1 + e^{(x - x_0)/\delta_x}}$$

where A_1 is the minimum rate constant at the lowest pH*, A_2 is the maximum rate constant at the highest pH*, x_0 is the point of inflection, and δ_x is the change in x corresponding to the most significant change in y values. From the plot of k vs pH*, the pK_a and k^{max} values can be obtained (*see* legend of Fig. 2 and **Note 20**).

5. Calculate the half-life ($t_{1/2}$, in days) of the exchange reaction from the k^{max} value using the following equation:

$$t_{1/2} = \left(\frac{ln2}{k^{max}}\right) / 24$$

4 Notes

1. *See* Chapter 2 in this volume for an in-depth procedure for the isolation/purification of rod outer segment (ROS) membranes from either fresh bovine eyes or frozen dark-adapted bovine retinas.
2. Various buffers can be used. Most commonly used are phosphate buffer, bis-tris-propane (BTP), MES, HEPES, and Tris–HCl. pH can vary between 6.5 and 8.

3. pH* values represent direct pH meter readings of the D_2O buffer solutions calibrated with standard buffer solutions made with H_2O and are uncorrected for the isotope effect at the glass electrode. Adjust pH* with either DCl or NaOD.
4. Mix 950 μl of formic acid and 50 μl of 30 % hydrogen peroxide, and leave for 2–3 h at room temperature. This will produce performic acid and the amount will reach its maximum level in 2–3 h [11]. This treatment converts cysteine/cystine to cysteic acid, methionine to methionine sulfone, and tryptophan to formylkynurenine. We employed performic acid treatment to convert cystines to the unreactive residues in our published work [9], because deuteron to proton back-exchange does not occur under the acidic reaction condition. However, more commonly used cysteine alkylation methods such as carbamidomethylation could also be used. If cysteine alkylation methods that proceed at alkaline pH are employed, we recommend only short (<1 h) exposure of protein samples to minimize deuterium back-exchange.
5. Other types of LC–MS/MS instruments can be used such as a quadrupole time-of-flight (TOF) instruments; however, low-resolution instruments whose resolution is lower than 5,000 (FWHM) are not recommended, because the calculation of HDX rates using mass spectra of histidine-containing peptide ions requires base peak separations between isotopic peaks for accurate calculation.
6. Typically, at least ten different pH* points (spanning pH* 4–10) are needed to obtain reliable pK_a values of histidine residues. The amount required differs depending on the detection sensitivity of the subsequent LC–MS/MS analysis.
7. This step is to minimize the amount of H_2O present in samples before starting the deuteration. It also significantly reduces the amount of contaminating soluble proteins leading to better (cleaner) MS spectra.
8. Incubation time can be extended as long as the protein is stable. The temperature during the incubation can be lower; however, it will require a longer incubation time, because the HDX reaction slows down ~4-fold for every 10 °C lower in temperature [6].
9. The HDX reaction is negligible at pH below 4; therefore, the reaction cannot proceed in this acidic solution. By adding this solution, all the rapidly exchanging deuterons are back-exchanged for protons, leaving only the slowly exchanging C_2-position of histidine residues as the only deuterated sites.
10. Rhodopsin/opsin will be extracted from the membranes by the SDS present in the buffer into the supernatant. The protein sample can be stored at −20 °C at this step.

11. This makes the final concentration of D_2O in the solvent 90 %. Since higher D_2O content in the titration buffers leads to faster exchange, making it easier to monitor the HDX reaction, we recommend maintaining at least 80 % D_2O content in the exchange buffer.
12. The protein sample in this solution can be stored at –20 °C.
13. Protein precipitate should be visible after 1 h with the protein amount used in this protocol. If not, leave for a longer time at –20 °C.
14. Washing the pellet will remove the residual detergent (SDS for ROS membrane samples, DDM for detergent solubilized samples) from the protein sample. Since these detergents are not compatible with the subsequent LC–MS/MS analysis, it is important to fully remove the detergents before proceeding with the subsequent steps.
15. We used pepsin for rhodopsin digestion because the protease was predicted to produce appropriate sizes (500–3,000 Da) of histidine-containing peptides for tandem mass spectrometry using collision-induced dissociation. If other proteases that require neutral to alkaline pH are employed, digest should be limited to no more than 1 h; otherwise, significant deuteron to proton back-exchange will occur.
16. TFA is an ion-pair reagent. Adding TFA in the mobile phase allows hydrophilic peptides to be retained in the reverse-phase trapping column. We recommend using 0.1 % TFA as a mobile phase for the trapping column to help ensure that hydrophilic histidine-containing peptides are retained.
17. We typically acquire the data by a data-dependent MS to MS/MS switching mode, with the ten most intense ions in each MS scan subjected to MS/MS analysis. The identities of all the histidine-containing peptides should be verified by MS/MS.
18. We use the Mascot database search engine (Matrix Science) for this purpose. We create a database containing only the rhodopsin sequence and search against the rhodopsin sequence to identify histidine-containing peptides. It is possible to identify histidine-containing peptides manually without using search engines; however we recommend the use of search engines, because it does not require expertise and is more efficient.
19. Only a single histidine residue is allowed in the peptide to determine the k at the peptide level. When a peptide contains more than one histidine residue, it is required to have a tandem mass spectrum of the peptide and use a fragment ion that contains a single histidine residue of interest for calculating the k for the histidine residue [7].
20. We use Origin 8 (OriginLab) to fit the data to the equation.

Acknowledgments

The work was supported by funding from the Cleveland Foundation and National Eye Institute EY019718.

References

1. Dempsey CE (2001) Hydrogen exchange in peptides and proteins using NMR-spectroscopy. Prog Nucl Magn Reson Spectrosc 39:135–170
2. Harris TM, Randall JC (1965) Deuterium exchange reactions at the C2-position of imidazoles. Chem Ind 41:1728–1729
3. Amyes TL, Diver ST, Richard JP et al (2004) Formation and stability of N-heterocyclic carbenes in water: the carbon acid pKa of imidazolium cations in aqueous solution. J Am Chem Soc 126:4366–4374
4. Vaughan JD, Mughrabi ZE, Wu C (1970) The kinetics of deuteration of imidazole. J Org Chem 35:1141–1145
5. Miyagi M, Nakazawa T (2008) Determination of pKa values of individual histidine residues in proteins using mass spectrometry. Anal Chem 80:6481–6487
6. Mullangi V, Zhou X, Ball DW et al (2012) Quantitative measurement of solvent accessibility of histidine imidazole groups in proteins. Biochemistry 51:7202–7208
7. Miyagi M, Wan Q, Ahmad MF et al (2011) Histidine hydrogen-deuterium exchange mass spectrometry for probing the microenvironment of histidine residues in dihydrofolate reductase. PLoS One 6:e17055
8. Wimalasena DS, Janowiak BE, Lovell S et al (2010) Evidence that histidine protonation of receptor-bound anthrax protective antigen is a trigger for pore formation. Biochemistry 49:6973–6983
9. Lodowski DT, Palczewski K, Miyagi M (2010) Conformational changes in the G protein-coupled receptor rhodopsin revealed by histidine hydrogen-deuterium exchange. Biochemistry 49:9425–9427
10. Dong J, Callahan KL, Borotto NB et al (2014) Identifying Zn-bound histidine residues in metalloproteins using hydrogen-deuterium exchange mass spectrometry. Anal Chem 86: 766–773
11. Hirs CHW (1967) Performic acid oxidation. Methods Enzymol 11:197–199

Chapter 10

Investigation of Rhodopsin Dynamics in Its Signaling State by Solid-State Deuterium NMR Spectroscopy

Andrey V. Struts, Udeep Chawla, Suchithranga M.D.C. Perera, and Michael F. Brown

Abstract

Site-directed deuterium NMR spectroscopy is a valuable tool to study the structural dynamics of biomolecules in cases where solution NMR is inapplicable. Solid-state ^{2}H NMR spectral studies of aligned membrane samples of rhodopsin with selectively labeled retinal provide information on structural changes of the chromophore in different protein states. Moreover ^{2}H NMR relaxation time measurements allow one to study the dynamics of the ligand during the transition from the inactive to the active state. Here we describe the methodological aspects of solid-state ^{2}H NMR spectroscopy for functional studies of rhodopsin, with an emphasis on the dynamics of the retinal cofactor. We provide complete protocols for the preparation of NMR samples of rhodopsin with 11-*cis*-retinal selectively deuterated at the methyl groups in aligned membranes. In addition we review optimized conditions for trapping the rhodopsin photointermediates; and we address the challenging problem of trapping the signaling state of rhodopsin in aligned membrane films.

Key words G protein-coupled receptor, Lipids, Membrane, Nuclear magnetic resonance, Protein dynamics, Relaxation, Rhodopsin, Vision

1 Introduction

Rhodopsin is responsible for dim-light vision in vertebrates and is a representative of a large family of G protein-coupled receptors (GPCRs) that regulate many important signaling functions in humans [1]. Despite progress in recent years in crystallizing GPCRs for X-ray studies [2–4], the available structures of rhodopsin in the signaling state [5–7] do not provide a complete picture of the protein activation. Alternatively, methods such as NMR spectroscopy can yield additional structural information. Yet the most innovative and valuable aspect is the ability to produce experimental knowledge about the molecular dynamics as a complement

Beata Jastrzebska (ed.), *Rhodopsin: Methods and Protocols*, Methods in Molecular Biology, vol. 1271,
DOI 10.1007/978-1-4939-2330-4_10,

to X-ray crystallography [8, 9]. In particular, site-directed ^{2}H NMR spectroscopy gives orientational constraints for functional molecular groups, and relaxation times characterize their thermal fluctuations. The results can be further analyzed using a generalized model-free approach [9–11] to obtain novel information about the molecular dynamics. Structural and dynamical modeling allows one to determine both the local conformation and correlation times of the molecular motions at an atomistically resolved level [10, 11]. In this article, we outline the methodology for solid-state ^{2}H NMR studies of the retinal cofactor bound to rhodopsin. Trapping of rhodopsin photointermediates in aligned membrane films is described, as well as data reduction and analysis at an introductory level appropriate for nonspecialists.

2 Materials

Protocols for the preparation and characterization of aligned phospholipid bilayers containing rhodopsin for solid-state ^{2}H NMR studies are presented. Native rod outer segment (ROS) disk membranes (also referred to as RDM, retinal disk membranes) are prepared from bovine retinas following standard procedures [12]. Recombinant membranes with a defined lipid composition are prepared by purifying detergent-solubilized rhodopsin on a hydroxyapatite column, followed by recombination with solubilized phospholipids, and subsequent detergent dialysis. Proteolipid membrane bilayers with rhodopsin then are harvested by ultracentrifugation:

1. Retinas: Frozen bovine retinas are purchased from W. L. Lawson, Co. (Omaha, NE, USA), and delivered in 30 % (w/w) sucrose solution containing 10 mM Tris-acetate buffer, pH 7.4, 1 mM dithiothreitol (DTT), and 0.001 % (v/v) aprotinin (A6279, Sigma-Aldrich), on dry ice. Retinas are stored in lightproof glass containers under nitrogen or argon at −80 °C until use.
2. Homogenizing solution: 30 % sucrose (w/w), 5 mM Tris-acetate, pH 7.4, 65 mM NaCl, 2 mM $MgCl_2$, and 2 mM ethylenediaminetetraacetic acid (EDTA).
3. Dilution buffer: 10 mM Tris-acetate, pH 7.4.
4. Stock detergent buffer: 3 % (v/v) Ammonyx LO containing 100 mM NH_2OH (hydroxylamine) and 10 mM sodium phosphate buffer, pH 6.8.
5. Opsin buffer: 10 mM 2-[4-(2-hydroxyethyl)piperazin-1-yl] ethanesulfonic acid (HEPES) buffer containing 50 mM

NH_2OH and 10 mM $MgCl_2$ at pH 6.8. Adjust pH using 1 M NaOH (approximately 7 drops).

6. Regeneration buffer: 10 mM HEPES, pH 6.8.
7. Dialysis buffer: 5 mM HEPES, 1 mM EDTA, and 1 mM DTT (add fresh).
8. DTAB chromatography detergent buffer: 100 mM dodecyltrimethylammonium bromide (DTAB), 15 mM sodium phosphate, pH 6.8, containing 0.02 % (w/w) NaN_3 (sodium azide) and 1 mM DTT (optional, for regenerating the column if desired).
9. Storage buffer: 15 or 67 mM sodium phosphate buffer, pH 7.0.
10. Retinal stock solution: 0.02 mM 11-*cis*-retinal in 99.5 % ethanol.
11. Deuterium-depleted buffer: 5 mM 2-(*N*-morpholino)ethanesulfonic acid (MES) buffer prepared with deuterium-depleted water containing 5 mM NaCl, pH 7.0 (at room temperature for the dark or Meta I state) or pH 5.5 (at 4 °C and pH 5.0 at room temperature for the Meta II state).
12. Detergents: 29–30 % Ammonyx LO (main component is lauryldimethylamine oxide) (Stepan Co.) stock solution, DTAB (Sigma-Aldrich) powder (*see* **Note 1**).
13. Column packing materials: hydroxyapatite (Bio-Gel HTP Gel; Bio-Rad Laboratories).
14. Phospholipids: 1-palmitoyl-2-oleoyl-*sn*-glycero-3-phosphocholine (POPC) and 1,2-dioleoyl-*sn*-glycero-3-phosphoethanolamine (DOPE) (Avanti Polar Lipids).
15. Density gradient solutions: 1.10 g/ml, 1.11 g/ml, 1.13 g/ml, and 1.15 g/ml sucrose gradient solutions prepared in 100-ml volumetric flasks by mixing 62.4 g, 68.4 g, 81.4 g, or 93.0 g of a 42 % (w/w) sucrose solution, respectively, with 0.1 ml of 1 M Tris-acetate buffer, pH 7.4, containing 0.1 ml of 0.1 M $MgCl_2$, and adding double-distilled water to make the total volume of each solution 100 ml.
16. Isomerically pure 11-*cis*-retinal (US National Eye Institute).
17. Selectively deuterated 11-*cis*-retinals having ^2H isotope labels at the C5-, C9-, or C13-methyl groups, denoted as 11-Z-[5-C^2H_3]-, 11-Z-[9-C^2H_3]-, and 11-Z-[13-C^2H_3]-retinal, synthesized in the laboratory of Prof. K. Nakanishi (Department of Chemistry, Columbia University, New York) as described [13].
18. High-affinity transducin-derived GαCT2 peptide with the amino acid sequence ILENLKDVGLF, also denoted as $G\alpha_t$340–350 (K341L, C347V) (Biomatik).

3 Methods

3.1 Sample Preparation

3.1.1 Purification of Retinal Disk Membranes Containing Rhodopsin

1. Preparation of ROS disk membranes: All procedures are performed on ice or at 4 °C under dim red light (11-W Bright Lab™ Universal Red Safelight bulb, CPM Delta1, Inc.; or an 11-W incandescent white bulb with red filter, Kodak Safelight red filter 1, Eastman Kodak Co.).
2. Begin the preparation by thawing the frozen bovine retinas overnight at 4 °C. Transfer the thawed bovine retinas to a loose-fitting Teflon homogenizer (chamber clearance is 0.3–0.45 mm). Add 30 ml of homogenizing solution per 50 retinas under a gentle stream of argon gas (*see* **Note 2**).
3. Homogenize the retinas by applying about ten strokes of the pestle slowly under a gentle argon gas stream. Centrifuge at 2,600 × *g* (Sorvall GSA rotor) for 20 min at 4 °C. The centrifuge speed is expressed as maximum relative centrifugal force (× *g*) throughout the text. Collect the supernatant with a spring-loaded syringe (18-gauge cutoff needle), and transfer the pellet to a tight-fitting Teflon homogenizer (chamber clearance is 0.1–0.15 mm). Add an equal volume of homogenizing solution, and apply about 6–8 strokes of the pestle under a gentle argon gas stream for the release of additional ROS disk membranes. Centrifuge at 2,600 × *g* for 20 min at 4 °C, and collect the supernatant.
4. Combine the supernatants from the two centrifugation steps, and add 2 volumes of dilution buffer (10 mM Tris-acetate, pH 7.4) (*see* **Note 2**). Centrifuge at 8,000 × *g* (Sorvall GSA rotor) for 50 min at 4 °C. Resuspend the pellet in a small volume of 1.10 g/ml sucrose density gradient solution (to yield 25 ml or less of total volume). Prepare sucrose step gradients on ice or in the cold room in polyallomer 38.5-ml centrifuge tubes. The volumes of the layers are 8 ml, 10 ml, and 10 ml for the 1.15 g/ml, 1.13 g/ml, and 1.11 g/ml gradient solutions, respectively. Four tubes are required for 50 retinas or six tubes for 100 retinas.
5. Pull up the resuspended pellet using a syringe with an 18-gauge cutoff needle, then switch to a 20-gauge needle, and expel it to fragment the crude rod outer segments. Place an equal amount of the ROS solution on the top of the 1.11 g/ml density gradient solution of each of the centrifuge tubes, and use additional 1.10 g/ml sucrose density gradient solution to balance the tubes. Centrifuge at 113,000 × *g* in a swinging bucket rotor (Beckman SW 28 rotor) for 1 h at 4 °C. Collect the carpet (band) at the 1.11/1.13 g/ml interface with a spring-loaded syringe, having a cutoff 18-gauge needle tip.

6. Removing the sucrose: Combine the collected bands, and dilute with 2 volumes of double-distilled deionized water. Add argon gas to the centrifuge bottles, and centrifuge at 48,000 × *g* (Sorvall SS-34 rotor) for 30 min at 4 °C.
7. After centrifugation, take the pellet, resuspend it in water, and centrifuge for 30 min at 48,000 × *g* at 4 °C. Repeat 1–2 times to ensure the removal of sucrose. Note that hypotonic water "washing" produces membrane fragments due to the osmotic shock. Resuspend the ROS disk membranes in either 15 or 67 mM (for longer storage) sodium phosphate buffer. Transfer to low-temperature freezer storage vials, e.g., Eppendorf safe-lock tubes or polypropylene leakproof screw cap centrifuge tubes (e.g., Nunc™ 15-ml graduated centrifuge tubes, Thermo Fisher Scientific). Overlay with argon gas, wrap in aluminum foil, and store at −80 °C until use.

3.1.2 Characterization of Rhodopsin by UV-Visible Spectroscopy

1. The procedure is carried out under red dim light. The UV-visible absorption spectra are acquired using a Cary 4000 dual-beam scanning spectrophotometer (Varian, Inc.) from 700 to 250 nm with 10-mm path length quartz cuvettes at room temperature. Alternatively, a single beam Cary 50 spectrophotometer (Varian, Inc.) with xenon flash lamp technology is used.
2. First record the baseline using a blank solution containing 980 μl of stock detergent buffer and 20 μl of 15 mM storage buffer.
3. Dissolve and mix thoroughly 20 μl of a suspension of disk membranes with rhodopsin in 980 μl of stock detergent buffer. Acquire the spectrum of this test sample.
4. Photobleach the test sample completely using about six flashes from a handheld flash lamp (Sunpak auto 555 or equivalent) equipped with a 515-nm long-wavelength pass filter (OG515, Schott), and record the spectrum of the bleached sample.
5. Measure the absorbance at 500 nm of the dark spectrum versus the bleached spectrum (A_{500}) and at 280 nm for the dark spectrum (A_{280}). Generally rhodopsin in purified disk membranes has a A_{280}/A_{500} ratio of 2.4. For comparison, a representative spectrum is provided in Fig. 1a (*see* **Note 3**).
6. Calculate the molar concentration of rhodopsin using the molar absorption coefficient of $\varepsilon = 40{,}600\ M^{-1}\ cm^{-1}$ at 500 nm. Alternatively, optical density units (OD) can be used. 1 OD unit is defined as 1 ml of a solution with absorbance of $A_{500} = 1$ in a 10-mm path length cuvette, and affords a convenient measure of the equivalents of retinal. 1 OD corresponds to 24.6 nmol or 0.958 mg rhodopsin, assuming its relative molecular mass is $M_r = 39{,}000$ Da.

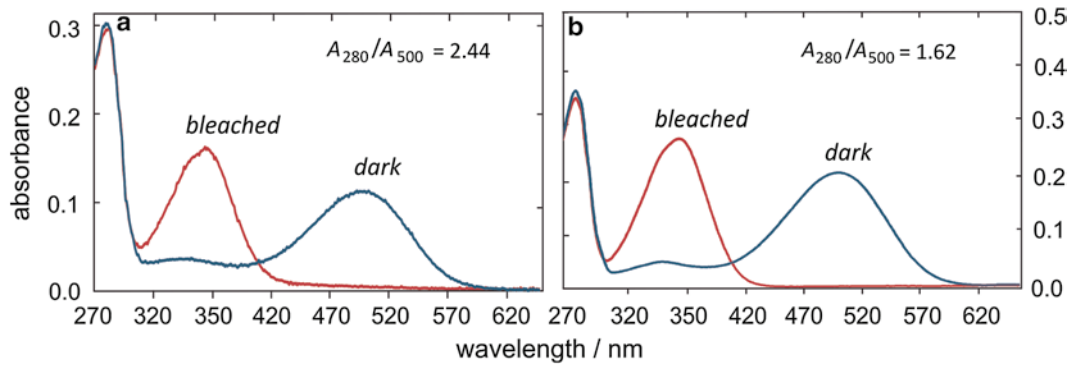

Fig. 1 Representative UV-visible absorption spectra of rhodopsin (**a**) in ROS disk membranes solubilized in 3 % Ammonyx LO, pH 6.8 (Subheading 3.1.2), and (**b**) after column purification in 100 mM DTAB detergent buffer, pH 6.8, in the presence of 10 mM hydroxylamine. The 11-*cis*-retinal absorption in the dark-state rhodopsin is shifted to 500 nm due to the protonated Schiff base covalently bound to the protein, and by its interaction with surrounding amino acids in the binding pocket. After bleaching in the presence of hydroxylamine, the absorption with maximum around 360 nm is due to free hydrolyzed retinal oxime. The A_{280}/A_{500} absorption ratio characterizes the spectral purity of rhodopsin (*see* **Note 3**)

3.1.3 Regeneration Assay for Testing Rhodopsin Photochemical Functionality

A regeneration assay is carried out to determine the amount of bleached rhodopsin present in the disk membranes, their regenerability, and the post-regeneration A_{280}/A_{500} ratio:

1. Prepare 11-*cis*-retinal solution in 99.5 % ethanol with a concentration of about 20 mM (*see* **Note 4**).
2. UV-visible characterization of 11-*cis*-retinal: Record the absorption spectrum using 1 μl of the retinal solution in ethanol as follows. Prepare two cuvettes with 1 ml of ethanol (≥99.5 % w/w). Add 1 μl of 11-*cis*-retinal solution into the sample cuvette; the other cuvette is the blank (reference sample). Record the absorption spectrum from 600 to 200 nm. At 380 nm the absorbance should be in the range 0.3–0.8, and the ratio A_{380}/A_{250} should be in the range of 1.2–1.5. As the 11-c*is*-retinal isomerizes, this ratio increases considerably up to a value of 8 [14].
3. Place 200 μl of ROS disk membranes in each of three 1.5-ml Eppendorf tubes. Label them as "control" (C), "bleached + regenerated" (B), and "regenerated" (R). Photobleach the "bleached + regenerated" sample using the flash lamp with the 515-nm long-wavelength pass filter, as described in the previous section.
4. Add the same amount of ODs at 380 nm of 11-*cis*-retinal as the amount of rhodopsin ODs in disk membranes to the tubes labeled "bleached + regenerated" and "regenerated," but not to the "control." Taking into account that the molar absorption coefficient for retinal in ethanol at 376.5 nm is

$\varepsilon \approx 25{,}000\ M^{-1}\ cm^{-1}$ [15] and for rhodopsin $\varepsilon = 40{,}600\ M^{-1}\ cm^{-1}$ at 500 nm, the molar retinal–rhodopsin ratio is about 1.6:1.

5. Incubate all the three tubes at 37 °C in the water bath for about 1.5 h. Take the UV-visible absorption spectra after adding 800 μl of stock detergent buffer, pH 6.8, as described earlier.
6. The percent of regenerability is calculated by the ratio of A_{500} of sample (B) to A_{500} of sample (R) multiplied by 100. For calculating the percentage of rhodopsin in the membrane sample that is bleached, take the ratio of A_{500} of sample (C) to A_{500} of sample (R) and multiply by 100. Subtract this number from 100 to obtain the percentage of rhodopsin bleached. The post-regenerated A_{280}/A_{500} ratio is calculated by dividing the A_{280} absorption of sample (C) by the A_{500} absorption of sample (R) and multiplying by 100.
7. Typical results are 93 % regenerability, 3–5 % bleached, and 2.1 post-regeneration A_{280}/A_{500} ratio. For further details *see* Ref. 16.

3.1.4 Regeneration of Disk Membranes with Deuterium-Labeled Retinals

All regeneration procedures are carried out in the dark (except opsin handling before regeneration) on ice, or in the cold room (at 4 °C). Always work with and store the disk membrane suspensions under a gentle stream or blanket of argon gas:

1. Retinal preparation: Synthetic deuterated 11-*cis*-retinals are stored in benzene at −80 °C. Typically each vial contains about 0.5 mg of deuterated 11-*cis*-retinal. Take the vial from the freezer, and evaporate the benzene under a gentle stream of argon or nitrogen gas. Add 300 μl of ethanol (≥99.5 % w/w) to the retinal bottle, dissolve the retinal, and measure the UV-visible absorption spectrum as described above (Subheading 3.1.3, **step 2**). Calculate the amount of 11-c*is*-retinal in OD units at 380 nm.
2. Calculate the amount of rhodopsin required for regeneration using a 1:1 retinal–rhodopsin ratio in OD units. Because the retinal molar absorption coefficient in ethanol is $\varepsilon \approx 25{,}000\ M^{-1}\ cm^{-1}$ at 380 nm [15] and for rhodopsin $\varepsilon = 40{,}600\ M^{-1}\ cm^{-1}$ at 500 nm, the molar retinal–rhodopsin ratio is about 1.6:1 (*see* **Note 5**).
3. Check the purity and concentration of rhodopsin in disk membranes as described above (Subheading 3.1.2). The purity of the protein is very important: With an A_{280}/A_{500} ratio of about 2.6, the regeneration gives approximately 75 % yield.
4. Opsin preparation: Centrifuge the exact amount of the disk membranes previously calculated (according to the exact amount of deuterated retinal) for 30 min at 48,000 × *g* (Sorvall SS-34 rotor). Resuspend the pellet in ca. 50 ml of opsin buffer containing hydroxylamine. Suspension is a crucial point; first mix everything using a Pasteur pipette, and then use a syringe

with an 18-gauge needle (the syringe is used to disperse material visible to the naked eye in the protein suspension; try to pass the protein through the syringe only once) to obtain a homogeneous suspension. Bleach the ROS membranes at 4 °C using a 150-W tungsten halogen light source (Schott-Fostec ACE light source; Fostec) fitted with yellow filter ($\lambda > 500$ nm) for 30 min. Check that all the protein is in suspension. Take a UV-visible spectrum of the opsin using a 20-μl aliquot of this solution. The color of the suspension changes visibly from pink to slightly pink, then slightly yellow, and finally white. Centrifuge again for 30 min at 48,000 × *g* at 4 °C. Discard the supernatant; the pellet should be very tight. Then resuspend the pellet in 60 ml of regeneration buffer very gently to avoid denaturation. This time do *not* use a syringe when you are manipulating the opsin, use only a Pasteur pipette, and centrifuge again for 30 min at 48,000 × *g* at 4 °C. Repeat this step 4 times to completely remove the hydroxylamine.

5. Opsin regeneration: After the last centrifugation, take out the supernatant, and resuspend the pellet completely in ca. 30 ml of regeneration buffer. Again do *not* use a syringe. Add all the ethanol solution of the deuterated 11-*cis*-retinal to the opsin. More ethanol can be used to rinse the residual 11-*cis*-retinal from the vial; however, do not exceed 1 % for the ethanol concentration in the total volume of the sample (for instance, use less than 350 μl for a $V_{tot} = 35$ ml). Put the tube in the water bath at 37 °C for 1.5 h in the dark. At the end of the regeneration, check the UV-visible spectra using about 20 μl of the solution. Calculate the amount of regenerated rhodopsin as described above (Subheading 3.1.2). Centrifuge for 30 min at 48,000 × *g* at 4 °C. After centrifugation, follow the purification protocol (Subheading 3.1.5) starting with solubilizing the rhodopsin and lipids in the DTAB chromatography detergent buffer (**step 1**), or resuspend the pellet in 10 ml of storage buffer, and store in the −80 °C freezer.

3.1.5 Rhodopsin Purification by Hydroxyapatite Column Chromatography

All procedures are carried out at 4 °C under dim red light conditions:

1. Take the suspension of the ROS disk membranes kept in storage buffer from the −80 °C freezer and thaw. Centrifuge the disk membranes at 48,000 × *g* for 30 min at 4 °C. After centrifugation, remove the supernatant, and solubilize the rhodopsin and lipids by resuspending the pellet in 10–15 ml of the DTAB chromatography detergent buffer. The concentration of rhodopsin should be about 3–5 mg/ml. Incubate for 1 h, and then centrifuge at 163,000 × *g* (Sorvall T-865.1 rotor) for 20 min at 4 °C. The solubilized rhodopsin and lipids should not have any insoluble precipitate. Any pellet observed at this point is discarded (*see* **Note 6**).

2. Prepare a 2.5-cm (diameter) column by weighing 18 g of hydroxyapatite (DNA grade, Bio-Rad), which is enough to purify about 50 mg of rhodopsin. The length of the column with this amount of hydroxyapatite is about 8 cm. For more rhodopsin than this amount, the column needs to be proportionately longer.
3. Equilibrate the column using 120 ml (about three times the column volume) of DTAB chromatography detergent buffer. Load the detergent-solubilized rhodopsin onto the hydroxyapatite column. Elute the rhodopsin using a gradient mixer with a linear gradient of 0–0.5 M salt (NaCl) in DTAB chromatography detergent buffer.
4. Elute the fractions with a flow rate of 1.2 ml/min, and collect using a fraction collector. Check the absorption spectrum of the fractions to monitor the fractions containing rhodopsin. Normally after about 3 h, the protein starts eluting. The pure rhodopsin has purity (A_{280}/A_{500} ratio) of 1.60–1.75; *see* Fig. 1b.
5. Combine the rhodopsin-containing fractions together, to determine the overall yield and the purity of rhodopsin. Generally 70–75 % of rhodopsin is recovered. For specifics *see* Refs. 17, 18.

3.1.6 Preparation of Rhodopsin–Lipid Recombinant Membranes

All the procedures are performed in the dark or under dim red light conditions at 4 °C. Always work with and store the disk membrane suspension under a stream or blanket of argon gas. Rhodopsin is recombined with POPC at a 1:50 rhodopsin–lipid molar ratio for the dark and the Meta I states. For the Meta II sample, a mixture of POPC with DOPE (3:1 POPC–DOPE ratio) is used, and the rhodopsin–lipid molar ratio is decreased to 1:75:

1. After combining the eluted rhodopsin fractions from hydroxyapatite column chromatography (typically ≈50 ml) as mentioned above, adjust the DTAB concentration to 300 mM.
2. Calculate the amount of lipids corresponding to the amount of purified rhodopsin. Dissolve the phospholipids in 3–4 ml of DTAB chromatography detergent buffer having higher DTAB concentration (300 mM DTAB instead of 100 mM).
3. Mix the rhodopsin solution with the solubilized phospholipids in the desired molar ratio, cover the sample, and vortex. Gently overlay the sample with argon gas, cap the sample tightly with parafilm, cover in aluminum foil, and incubate for 1–2 h at 4 °C.
4. In the meantime, prepare the dialysis tubing (molecular weight cutoff 12–14 kDa; 1.6 cm diameter; approximately 2 ml solution per centimeter of dialysis tubing) (Spectrum Laboratories, Inc.) by immersing the dialysis bag in hot boiling water for a few seconds, then transfer from the hot water to the colder

(4 °C) water (repeat three times), and leave it in the refrigerator (4 °C) for 30 min, after which it is ready to be used.

5. Transfer the sample (rhodopsin solution incubated with the lipids) into the dialysis tubing as prepared already. Securely clamp both ends, and place the tubing with the sample in the dialysis buffer (5 mM HEPES and 1 mM EDTA, pH 6.8), with a continuous gentle purging of N_2 gas through the buffer using a gas dispersion tube. Dialyze with one exchange of the dialysis buffer every 6–8 h, giving a total of eight or more exchanges. The total volume of buffer used for the whole dialysis procedure is about 900 ml of buffer per 1 ml of DTAB solution in the dialysis bag.
6. Take out the dialysis bag, and record the UV-visible absorption spectrum of the recombinant sample to check the yield and the A_{280}/A_{500} ratio.
7. Centrifuge the contents of the dialysis bag at 48,000 × *g* for 1 h at 4 °C. Resuspend the pellet in 67 mM sodium phosphate buffer, pH 7.0, or 100 mM HEPES buffer, pH 7.0, containing 1 mM EDTA. Overlay with argon and freeze it at −80 °C. The recombinant membrane samples can be stored for several years at −80 °C. For further details, *see* Refs. 17–19.

3.2 Solid-State Deuterium NMR Spectroscopy for Nonaligned Samples of Rhodopsin

Site-directed deuterium NMR spectroscopy allows one to study the local dynamics and structure of biological systems by specifically ^{2}H-labeling the molecular groups of interest. The deuteron has a spin $I = 1$, and like other nuclei with spin larger than ½, it has a lower symmetry of the nuclear charge distribution than spin-½ nuclei. The measure of the charge asymmetry is called the quadrupole moment, which can interact with the electric field gradient of the carbon–deuterium bond present in the molecule [20]. This interaction leads to two transitions present in the solid-state ^{2}H NMR spectrum [21]. Examples are provided in Fig. 2 and are further discussed below. Unlike a solution ^{2}H NMR spectrum, where the angular-dependent interactions are averaged to zero giving a single peak, in the solid-state NMR spectrum, more information is available. The quadrupolar splittings carry information regarding the spatial orientation of the carbon–deuterium bonds, including their average orientation and the amplitude of their angular fluctuations. Below we include the protocols for the preparation of aligned samples of lipid bilayers containing rhodopsin, and provide a description of structural and relaxation ^{2}H NMR methods for the bound retinal chromophore.

In the so-called powder-type samples, the membranes are randomly oriented (hence the analogy to a random powder). Orientational constraints for the labeled group are not available, because the ^{2}H NMR spectral line shape is the same for any orientation (e.g., a methyl group) with respect to the protein. Figure 2 presents examples of solid-state ^{2}H NMR spectra

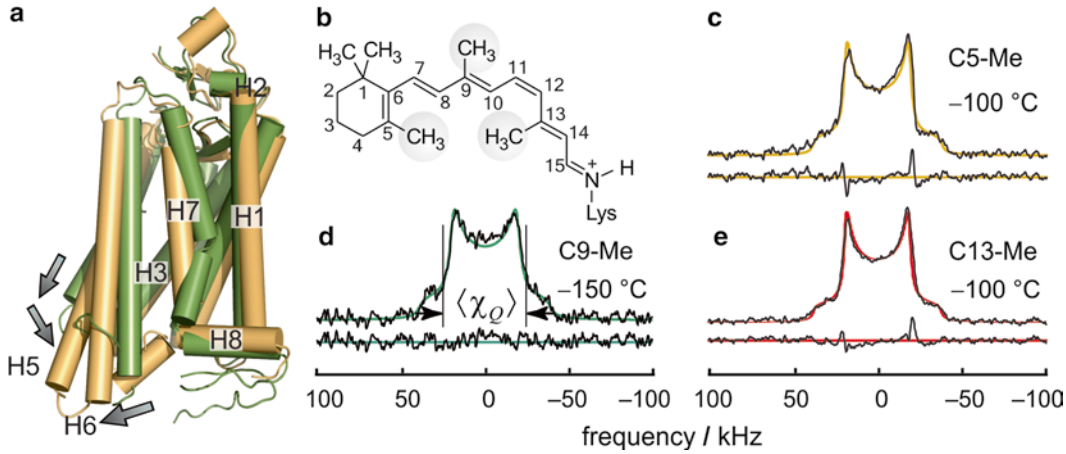

Fig. 2 Solid-state deuterium NMR spectroscopy of selectively ^{2}H-labeled retinal bound to rhodopsin in randomly oriented membranes. (**a**) Structure of the Meta II state of rhodopsin (*yellow orange*) (protein data bank accession code 4A4M) compared to dark-state rhodopsin (*green*) (code 1U19) showing activating movement of helices. (**b**) Numbering scheme of retinal ligand indicating methyl groups studied. (**c**–**e**) Solid-state ^{2}H NMR spectra of deuterated retinal specifically labeled at C5-, C9-, or C13-Me positions bound to rhodopsin in unoriented membranes [10]. The spectra are calculated by the convolution of the frequency distribution for the randomly oriented quadrupolar coupling tensor and intrinsic line broadening $\Delta\nu$. The spectral fitting indicates that the average quadrupolar coupling constant $\langle\chi_Q\rangle$ is reduced by a factor of 3 due to rapid methyl group spinning, and by another 10 % due to off-axial fluctuations with respect to the average orientation (*see* text). The line broadening $\Delta\nu$ is in the range of 3.2–5.0 kHz. Figure adapted from Struts, A.V., Salgado, G.F.J., and Brown, M.F. (2011) "Solid-state ^{2}H NMR relaxation illuminates functional dynamics of retinal cofactor in membrane activation of rhodopsin," *Proc Natl Acad Sci U S A* **108**, 8263–8268

obtained for randomly oriented samples of rhodopsin with specifically ^{2}H-labeled methyl groups of retinal at the C5, C9, or C13 carbon positions. An important aspect is that experimental information about the molecular dynamics is uniquely available from such solid-state ^{2}H NMR studies [11]. Moreover, certain information on the orientational distribution of the labeled molecular groups (distribution versus the average orientation) can be derived from the spectral line shape, as described below:

1. In the solid-state ^{2}H NMR spectrum, the weak shoulders are due to the C^2H_3 groups oriented parallel (lower relative probability) to the external magnetic field. The two stronger peaks are due to the C^2H_3 groups oriented perpendicular (higher relative probability) to the external magnetic field.
2. For rapidly rotating methyl groups, the static quadrupolar coupling constant χ_Q (=170 kHz) is reduced by the spinning. The effective quadrupolar coupling is $\chi_Q^{\text{eff}} = \chi_Q P_2(\cos\theta_t) = -(1/3)\chi_Q$, where $\theta_t = 109.47°$ is the tetrahedral angle defining the geometry of the methyl group and $P_2(\cos\theta)$ is the second-order Legendre polynomial, defined as $P_2(\cos\theta) = (1/2)(3\cos^2\theta - 1)$. The effective quadrupolar coupling constant is calculated by using

the ideal tetrahedral angle for a rapidly spinning methyl group ($\chi_Q^{eff} = 56.67$kHz).

3. The effective quadrupolar interaction (χ_Q^{eff}) of the deuterium nuclei is further reduced by the fluctuations of the methyl group symmetry axis (aligned with C–C^2H_3 bond) about its mean orientation. The average quadrupolar coupling constant $\langle\chi_Q\rangle$ is given by the relation $\langle\chi_Q\rangle = \chi_Q^{eff}\langle P_2 \cos\theta\rangle = \chi_Q^{eff} S_{C3}$, where θ is the angle between the instantaneous and averaged orientations of the methyl group, and S_{C3} is the order parameter characterizing the amplitude of the off-axial fluctuations of the threefold axis of the methyl group. Here the brackets $\langle\ldots\rangle$ indicate the angular average. The value of the order parameter (S_{C3}) for the methyl threefold axis is calculated by assuming that the value of $\langle\chi_Q\rangle$ (*see* Fig. 2d) is 51 kHz ($S_{C3} = 0.9$). Note that for all three labeled methyl groups at carbon positions C5, C9, or C13, the order parameter is found to be practically the same (≈ 0.9), despite the different environment in the rhodopsin binding pocket and the very different rotational dynamics (see below).
4. The order parameter (S_{C3}) is related to the angular amplitude (range) of the fluctuations by

$$S_{C3} = \int_0^{\Delta\theta} (1/2)(3\cos^2\theta - 1)\sin\theta\, d\theta \,/\, \int_0^{\Delta\theta} \sin\theta\, d\theta$$
$$= (1/2)\cos\Delta\theta(1 + \cos\Delta\theta).$$

It is assumed for simplicity that the probability of the methyl angle is constant over the angular range $\Delta\theta$ and is zero otherwise (rectangular probability distribution). To establish a physical picture of the fluctuations, calculate the value of $\Delta\theta$ for the methyl group fluctuations from the order parameter (S_{C3}) obtained directly from the solid-state ^{2}H NMR spectrum. (Answer: $\Delta\theta = 21°$.)

3.3 Preparation of Aligned Membranes Containing Rhodopsin in the Dark State

All procedures are performed in the dark or under dim red light conditions at 4 °C unless mentioned otherwise. Always work with and store the rhodopsin samples under a gentle steam or blanket of argon gas. The best alignment of proteolipid membranes containing rhodopsin can be achieved by isopotential spin-dry ultracentrifugation [22, 23] (*see* **Note 7**):

1. Prepare a suspension of POPC membranes with rhodopsin (rhodopsin–lipid ratio 1:50) using 5 ml of deuterium-depleted 5 mM MES buffer containing 5 mM NaCl, pH 7, at 4 °C. Place an ultrathin glass slide ($16 \times 6 \times 0.07$ mm, Marienfeld Laboratory Glassware) on the isopotential surface of the stainless steel plate (*see* **Note 7**). Assemble the insert, and place it into the centrifuge tube. Transfer about 150 μl of a membrane suspension containing ca. 1 mg of rhodopsin (1:50 rhodopsin–POPC molar ratio) into the sample compartment.

2. Centrifuge the membranes at 141,000 × *g* (Beckman SW 28 rotor) for ca. 2 h at 4 °C.
3. After slow evaporation, rehydrate the membrane film by isopiestic transfer in a closed container (desiccator), using saturated K_2CO_3 in ^{2}H-depleted water with a relative humidity ≈43 % at 4 °C. Stack the individual glass plates (Fig. 3a), each with a membrane film, insert them into an 8 × 22-mm cutoff NMR tube, and tightly seal with a machined Teflon plug.
4. Check the alignment by ^{31}P NMR spectroscopy at room temperature. Well-aligned samples with the director axis (the average membrane normal) parallel to the magnetic field of the NMR spectrometer ($\theta = 0°$) give a single peak, with a chemical shift of about 30–35 ppm depending on the lipid (Fig. 3b). Unoriented lipid bilayers produce a powder-type spectrum with a maximum around −15 to −20 ppm, corresponding to $\theta = 90°$ (most probable orientation) (Fig. 3c, dashed line). The fraction of aligned bilayers can be readily estimated by the area of a single peak with respect to the total area of the spectrum (Fig. 3c). Knowing the amounts of aligned and unoriented membranes, one can simulate and subtract the contribution from unoriented membranes to the ^{2}H NMR spectrum (*see* **Note 8**) and use incompletely aligned samples in structural studies. Examples of solid-state ^{2}H NMR spectra of selectively deuterated retinal bound to dark-state rhodopsin in aligned membranes are shown in Fig. 3d.

3.4 Experimental Protocol for Trapping of Metarhodopsin I in Aligned Membranes

The complete procedure is performed under dim red light conditions at 4 °C unless stated otherwise. Always overlay the rhodopsin samples with a blanket of argon gas:

1. Prepare a suspension of POPC membranes with rhodopsin (rhodopsin–lipid ratio 1:50) using 5 ml of deuterium-depleted 5 mM MES buffer containing 5 mM NaCl, pH 7, at 4 °C. Align the proteolipid membranes on glass slides by isopotential ultracentrifugation, as described above for the dark state (*see* Subheading 3.3).
2. Rehydrate the aligned membrane films by isopiestic transfer using a saturated solution of KCO3 in 2H-depleted water with a relative humidity ≈43% at 2 °C.
3. Irradiate each glass slide with the aligned membranes containing rhodopsin for approximately 30 s at 2 °C using a 150-W Fostec light source (*see* Subheading 3.1.4) fitted with a green band-pass filter (A08071, with a maximum transmittance at $\lambda = 530$ nm).
4. Record the UV-visible absorption spectrum between 700 and 250 nm (the baseline may be recorded with an empty glass slide). The photolyzed sample gives a band with $\lambda_{max} \approx 479$ nm indicative of the Meta I state (Fig. 4a). Freeze the glass slide

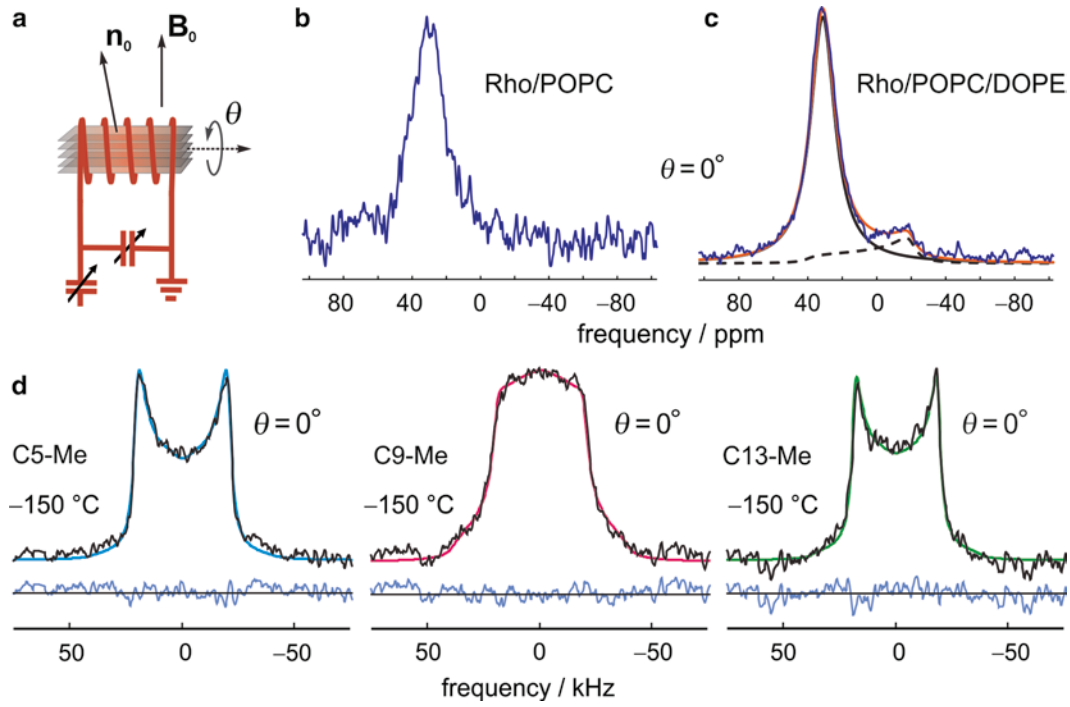

Fig. 3 Examples of phosphorus-31 and deuterium NMR spectra of aligned membranes containing rhodopsin with ^{2}H-labeled retinal. (**a**) Glass slides with aligned membrane films in the radio-frequency coil of the NMR probe. (**b**) Solid-state ^{31}P NMR spectrum of rhodopsin–POPC (1:50 protein–lipid ratio) recombinant membranes with a largely complete alignment and (**c**) solid-state ^{31}P NMR spectrum of recombinant membranes (3:1 POPC–DOPE molar ratio) with rhodopsin (1:75 protein–lipid ratio) in 5 mM ^{2}H-depleted MES buffer (pH 5.5 at 4 °C). One can see a noticeable peak at about −20 ppm in the right-hand spectrum, corresponding to the $\theta = 90°$ contribution of unoriented bilayers. The experimental spectrum (*blue*) in Fig. 3c is fitted to the theoretical spectrum (*red solid line*), approximated as a superposition of a Lorentzian (corresponding to aligned fraction, indicated by *black solid line*) and a powder-type spectrum (*dashed line*). The fitting parameters are the chemical shift anisotropy ($\Delta\sigma$), line broadening ($\Delta\nu$), and intensities of the aligned and powder-type spectra. The calculated unoriented fraction is 14 %. The ^{31}P NMR spectra are measured with a Bruker AMX-500 spectrometer (magnetic field 11.7 T) at room temperature using a locally constructed ("home-built") ^{31}P probe with a transverse solenoid coil (8-mm diameter, 10-mm length). Spectral resolution is high enough to resolve a contribution to the spectrum from unoriented bilayers even without proton decoupling. (**d**) Experimental and simulated ^{2}H NMR spectra of 11-*cis*-retinal with selectively ^{2}H-labeled C5-, C9-, or C13-Me groups bound to rhodopsin in aligned membranes. The rhodopsin–POPC molar ratio is 1:50. Experimental ^{2}H NMR spectra are measured on a Bruker AMX-500 spectrometer (*see* **Note 12**) at −150 °C with the average bilayer normal inclined at $\theta = 0°$ to the magnetic field

with the membrane film at −30 °C or below (e.g., by placing it immediately on dry ice).

5. Collect ca. 25 glass slides with the membrane film containing rhodopsin in the Meta I state, and stack them in an 8-mm NMR tube in a thermally insulated Styrofoam glove box at −30 °C (*see* **Notes 9–11**). Store the sample at −80 °C, and always keep and handle the sample below −30 °C to prevent transformation of the Meta I state into the Meta II state.

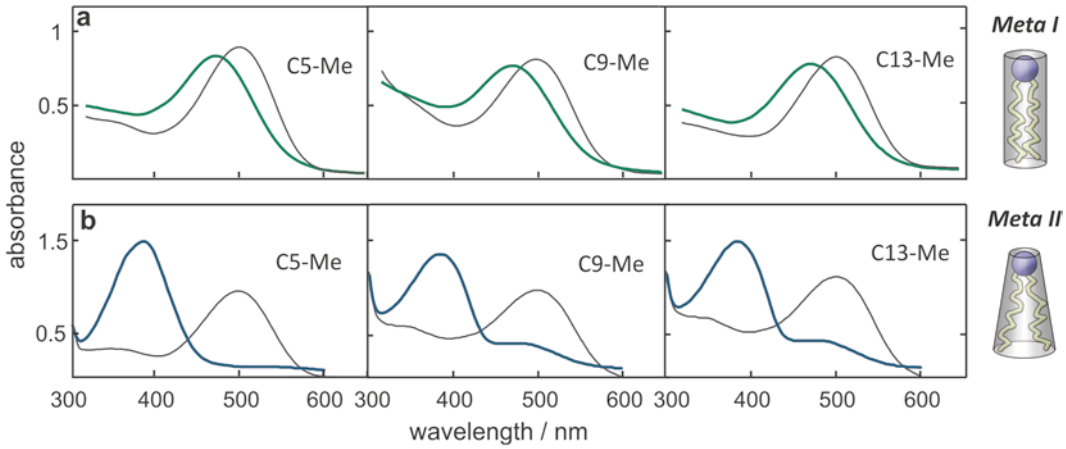

Fig. 4 UV-visible absorption spectra of aligned membrane films containing rhodopsin (on glass slides) in the dark (*thin black lines*) and trapped Meta I (**a**) and Meta II (**b**) states (*green and blue lines*, *respectively*). The Meta I state was obtained by illuminating rhodopsin–POPC recombinant membranes (1:50 protein–lipid ratio) with actinic light at 2 °C, pH 7, and 43 % relative humidity. The Meta II state was trapped by bleaching recombinant membranes (3:1 POPC–DOPE molar ratio) with rhodopsin (1:75 protein–lipid ratio) in 5 mM ^{2}H-depleted MES buffer at room temperature, pH 5.0, and 100 % relative humidity. The average shape of the DOPE lipid molecule, shown on the *right* (*bottom*), corresponds to a negative spontaneous (intrinsic) monolayer curvature, which favors the Meta II state. By contrast POPC, shown on the *right* (*top*), favors flat bilayers, thus shifting the metarhodopsin equilibrium back to Meta I in accord with a flexible surface model [35]

3.5 Experimental Protocol for Trapping of Metarhodopsin II in Aligned Membranes

All the procedures are performed under dim red light conditions in a cold room at 4 °C unless mentioned otherwise. Keep the rhodopsin samples under argon gas at all times:

1. Centrifuge the proteolipid membranes (3:1 POPC–DOPE ratio) containing rhodopsin (1:75 rhodopsin–lipid ratio) kept in the storage buffer (15 or 67 mM sodium phosphate, pH 7) at 48,000 × *g* (Sorvall T-865.1 rotor), discard the supernatant, and resuspend the pellet in 5 ml of 5 mM MES buffer prepared with deuterium-depleted water containing 5 mM NaCl, pH 5.5 (at 4 °C). Centrifuge again at the same speed, and resuspend the pellet in the same buffer to make sure the pH is adjusted to 5.5 (very important to trap the Meta II state), and that the water is replaced with deuterium-depleted water.
2. Calculate the amount of GαCT2 peptide (*see* Subheading 2) required to stabilize the Meta II state based on a 1:5 protein–peptide ratio.
3. Dissolve the calculated amount of GαCT2 peptide in 300 μl of 5 mM MES buffer prepared with deuterium-depleted water containing 5 mM NaCl, pH 5.5. Add the solution of the GαCT2 peptide to rhodopsin suspension.
4. Align the proteolipid membranes on glass slides by isopotential ultracentrifugation as described above for the dark state (*see* Subheading 3.3).

5. Rehydrate the aligned membrane films at 100 % relative humidity by isopiestic transfer using ^{2}H-depleted water at room temperature for about 1 h. Note that the alignment can decrease at this point due to the hydration; however, it can be restored later by dehydrating the sample (*see* **Note 9**). At the same time, the pH at room temperature decreases to 5.0.
6. Bleach the aligned membranes with rhodopsin on a glass slide for about 30 s at room temperature using the 150-W Fostec light source fitted with a green band-pass filter (*see* Subheading 3.4).
7. Record the UV-visible absorption spectrum between 700 and 250 nm (with the baseline measured for an empty glass slide). If the 500-nm peak in the Meta II sample does not disappear completely (incomplete conversion into Meta II), most likely it is because of insufficient hydration (Fig. 4b). The spectrophotometer cuvette must be sealed (e.g., with parafilm) to prevent dehydration of the sample during the measurement.
8. Dehydrate and cool the membrane film on a glass slide under a stream of nitrogen or argon gas at 4 °C for 20–30 s (*see* **Note 9**). This step can be avoided for the preparation of samples that are used only for the relaxation studies (*see* **Note 10**).
9. Freeze the sample at –60 °C or below (e.g., by placing it in the Styrofoam box with dry ice or liquid nitrogen; *see* **Note 11**). Because the membrane film on the glass slide is thin, it freezes rapidly to trap the Meta II state.
10. After collecting 20–30 slides with membranes containing rhodopsin in the Meta II state, stack them in an 8-mm cutoff NMR tube at –60 °C (*see* **Note 11**). Store the sample at –80 °C, and from this point on, it is recommended to always handle the sample below –60 °C to prevent decay of the Meta II state (*see* **Notes 9** and **11**).

3.6 Experimental Protocol for Structural Studies of Rhodopsin in Aligned Bilayers Using Solid-State Deuterium NMR Spectroscopy

The structural studies are performed under dim red light conditions as described above. All manipulations of the samples in the Meta I state are carried out at temperatures below –30 °C. For the Meta II state, all manipulations are done below –60 °C, except for measurements of the ^{2}H NMR spectra and relaxation times at –30 °C:

1. Acquire solid-state ^{2}H NMR spectra of the rhodopsin in aligned lipid bilayers (Fig. 3d) by applying a quadrupolar-echo pulse sequence (*see* **Note 12**). The ^{2}H NMR spectra are recorded with a Bruker AMX-500 spectrometer using a deuterium probe with a transverse radio-frequency coil (*see* **Note 12**). The sample with aligned membranes can be rotated in the NMR coil (*see* Fig. 3a), which allows one to study the angular dependence of the ^{2}H NMR spectra and increase the accuracy of the method. The presence of unoriented bilayers can be determined from

solid-state ^{31}P NMR spectroscopy (typically 10 %) and is taken into account by spectral subtraction (*see* **Note 8**). If necessary, the ^{2}H NMR signals from the natural ^{2}H abundance of the lipids are also subtracted (*see* **Note 13**).

2. Determine the orientation of the methyl groups in rhodopsin (θ_B) to the local membrane normal (**n**) by fitting the experimental spectra for aligned samples to theoretical ones (Fig. 3d). The latter are calculated using a Monte Carlo method (*see* **Note 14**) by assuming a static uniaxial distribution of the methyl group orientations about the local membrane normal **n** [24]. The distribution is static because the experimental temperatures are set below −30 °C (lipid gel phase), to prevent rotational diffusion of the proteins in the membrane. In addition, the alignment disorder, namely, the distribution of the local membrane normal **n** with respect to the average normal $\mathbf{n}_0$ (mosaic spread), is taken into account. It is assumed to be uniform in the plane of the glass slide (the directions perpendicular to $\mathbf{n}_0$) and Gaussian (with a standard deviation of σ) for the angle θ' between the **n** and $\mathbf{n}_0$ axes. Apart from the orientation of the ^{2}H-labeled methyl groups (θ_B), the mosaic spread (σ) is also determined from the ^{2}H NMR spectral data fitting procedures. Excellent fits of the simulated (color lines) and experimental (black lines) spectra (Fig. 3d) and the sharp minima in the error surfaces (not shown; *see* Ref. 9) indicate high accuracy and sensitivity of this method for determining orientational constraints (for selectively deuterated methyl groups in this case).
3. The calculated orientations of the methyl groups can be used for direct comparison with X-ray crystallography data (if available), which is quite valuable considering that NMR is a completely different and independent technique. The ^{2}H NMR results can also be used as orientational constraints in computer simulations of rhodopsin (e.g., in Ref. 25 they are used to evaluate the retinal counterion switch mechanism), or in retinal structure modeling in Ref. 9 (*see* **Note 15**).

3.7 Experimental Protocol for Solid-State Deuterium NMR Relaxation Studies of Rhodopsin Dynamics

Manipulations of the samples for the relaxation experiments are carried out under dim red light at temperatures below 4 °C for the dark state. For the Meta I state, temperatures are kept below −30 °C and generally below −60 °C for the Meta II state. To obtain information on the dynamics of the retinal cofactor, the relaxation measurements are performed using either freely suspended (unoriented, so-called powder-type) or aligned membrane samples. However, for the structural studies, only aligned samples can provide the orientational constraints. Aligned samples of rhodopsin also have the advantage of a small membrane film thickness as compared to the unoriented membrane specimens,

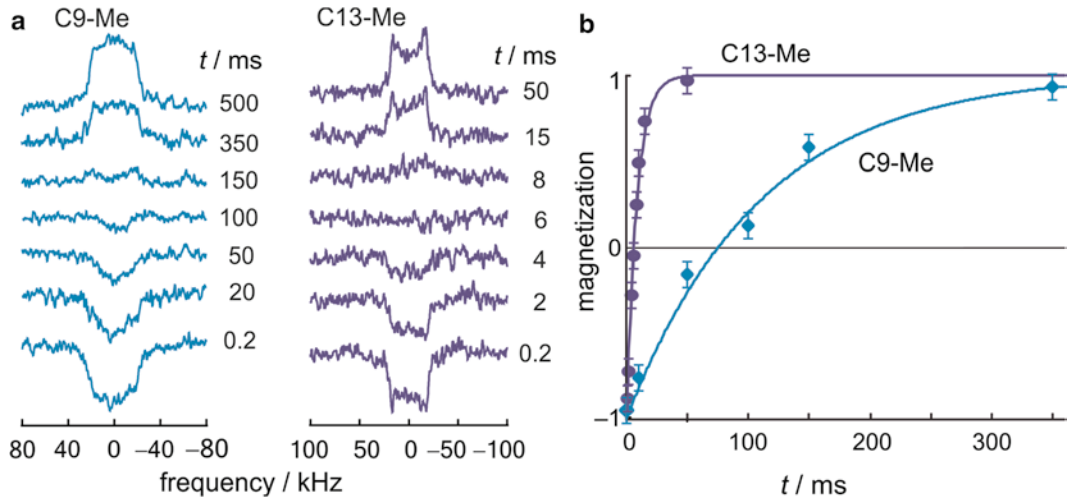

Fig. 5 Inversion-recovery solid-state ^{2}H NMR spectra (**a**) for methyl groups of 11-*cis*-retinal ^{2}H-labeled at the C9- or C13-Me positions bound to rhodopsin (in the dark state) and magnetization-recovery plots (**b**) used to determine the spin–lattice (T_{1Z}) relaxation time ($T = -150$ °C). One can observe much faster relaxation for the C13-Me than for C9-Me group, indicating the different environments for the retinylidene methyl groups in the rhodopsin binding pocket [8]. Figure adapted from Struts, A.V., Salgado, G.F.J., Martínez-Mayorga, K., et al. (2011) "Retinal dynamics underlie its switch from inverse agonist to agonist during rhodopsin activation," *Nat Struct Mol Biol* **18**, 392–394

which makes them easier to bleach with the actinic light. In general, for both relaxation and structural studies, it is most desirable to use aligned samples (*see* **Note 10**):

1. Measure inversion-recovery relaxation spectra (Fig. 5a) in the available temperature range (usually from −30 to −150 °C) using the quadrupolar-echo inversion-recovery pulse sequence (*see* **Note 12**). The repetition time t_1 for the pulse sequence is adjusted in the course of experiment according to the longitudinal (T_{1Z}) relaxation time ($t_1 \sim 3$–$5\ T_{1Z}$). Integrate the spectra and plot their relative intensities with respect to the equilibrium spectrum (proportional to the magnetization of the ^{2}H nuclei in the sample) versus the time t between the 180 and 90° pulses (*see* **Note 12**) (Fig. 5b).
2. Fit the time dependencies for Zeeman relaxation (Fig. 5b) using a single-exponential function for the recovery of nuclear magnetization: $M / M_0 = 1 - b\exp(-t / T_{1Z})$ with three fitting parameters—viz., the equilibrium magnetization, M_0; longitudinal relaxation time, T_{1Z}; and the inversion parameter b (≤ 2, characterizing incomplete spectral inversion). Determine the T_{1Z} relaxation times from fitting the inversion-recovery plots (Fig. 5b). Examples of the T_{1Z} values plotted against temperature are provided in Fig. 6.

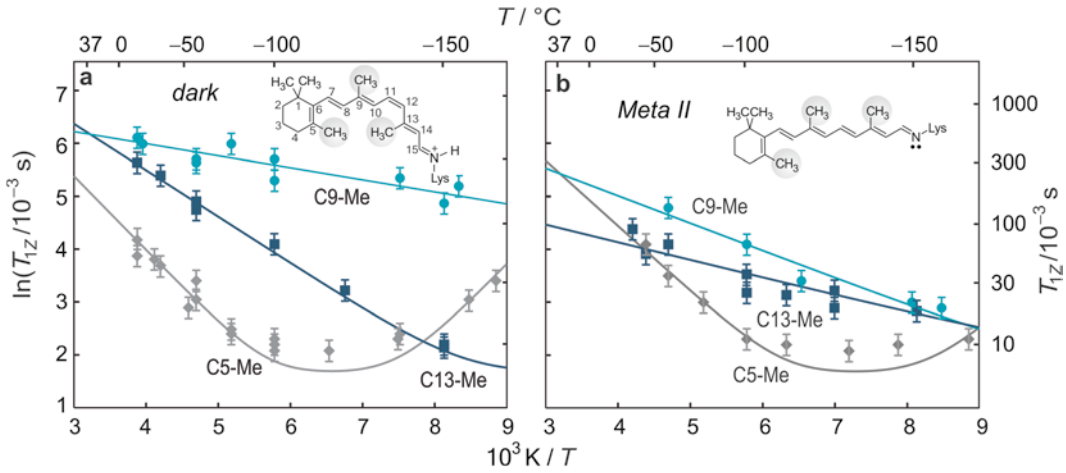

Fig. 6 Temperature dependences of the Zeeman (T_{1Z}) relaxation times characterize the molecular dynamics of retinal ligand [8, 10] in the dark (**a**) and Meta II states (**b**). The slope of the plots directly provides the activation energy for methyl group spinning. The pre-exponential factors for motional parameters k, $D_{\|}$, and $D_{\perp}$ (see text) can be determined by fitting the T_{1Z} temperature dependences. The analysis of the relaxation data indicates relatively fast rotation of the C9-Me group, intermediate for the C13-Me group, and slow for the C5-Me group at low temperatures. The rotational rates correlate with the corresponding activation energies E_a for these groups and are mainly related to intraretinal potential barriers [10]. It is also shown that both threefold hops and rotational diffusion models give good agreement with the experimental T_{1Z} relaxation times [8, 10]. Figure adapted from Struts, A.V., Salgado, G.F.J., Martínez-Mayorga, K., et al. (2011) "Retinal dynamics underlie its switch from inverse agonist to agonist during rhodopsin activation," *Nat Struct Mol Biol* **18**, 392–394

3. According to NMR relaxation theory [26–29], the ^{2}H NMR longitudinal relaxation rates R_{1Z} (or relaxation times T_{1Z}) correspond to the spectral densities $J_m(\omega)$ (or power spectra) of the thermal fluctuations of the ^{2}H-labeled group (i.e., the quadrupolar coupling tensor) near the resonance frequency (ω_0) by $R_{1Z} = 1/T_{1Z} = (3/4)\pi^2\chi_Q^2\left[J_1(\omega_0) + 4J_2(2\omega_0)\right]$. The spectral densities depend on the orientation of the methyl group in the sample with respect to the magnetic field, together with the mean-square amplitudes and rates of the motions. The analysis of the NMR relaxation times in terms of molecular motions can be performed using our generalized model-free approach [11], which provides the spectral densities $J_m(\omega)$ for time-dependent rotational transformations connecting components of the quadrupolar tensor in the molecular and laboratory frames. As an alternative, specific motional models can be introduced [10]. For methyl groups, two motional models can be considered: threefold hops about the methyl axis with a rate constant k or continuous diffusion within a potential of mean torque, with axial ($D_{\|}$) and off-axial ($D_{\perp}$) rotational diffusion coefficients. For detailed relationships between spectral densities $J_m(\omega)$ and parameters of the molecular motion (k, $D_{\|}$, and $D_{\perp}$), *see* Refs. 11, 27, 28.

4. Simulate and fit the T_{1Z} temperature dependences (Fig. 6), for the ^{2}H-labeled methyl groups, e.g., using threefold hops or continuous diffusion in a potential of mean torque model [11, 27, 28]. The Arrhenius equation $A = A_0 \exp(-E_a/RT)$ is introduced for motional parameters k, $D_\parallel$, and $D_\perp$ (Fig 6). Simulation is performed using locally written MATLAB scripts (*see* **Note 14**), where the spectral densities $J_m(\omega)$ are calculated according to Refs. 11, 27, 28 with activation energies (E_a) and motional parameters (k, $D_\parallel$, and $D_\perp$) as fitting parameters. Determine the pre-exponential factors for reorientational jump rates (k_0), or rotational diffusion coefficients (D_0), and corresponding activation energies E_a; calculate the spectral densities and correlation times at different temperatures.
5. Information on local molecular dynamics obtained from relaxation data is very important, as the protein functioning is believed to be directly related to mobility. Moreover, this information can be used to study inter- and intramolecular interactions, because the activation energies E_a for molecular motions are determined by the potential barriers. On the other hand, the analysis of the dynamical data with regard to molecular interactions requires structural information. Once the structure is available, one might qualitatively analyze the dynamical parameters with respect to steric hindrances [10, 30] or apply molecular mechanics or quantum mechanical simulations to calculate potential barriers. The results can be compared with experimentally obtained activation energies [31] and used to improve the force field or refine the protein structure.

4 Notes

1. Rhodopsin can also be solubilized in other detergents, including digitonin, *n*-dodecyl-*β*-D-maltopyranoside (DDM), DTAB, [(Cholamidopropyl)dimethylammonio]-propanesulfonate (CHAPS), Emulphogene, lauryldimethylamine oxide (LDAO), octaethylene glycol *n*-dodecyl monoether ($C_{12}E_8$), *n*-octyl-*β*-D-glucopyranoside (OG), sodium cholate, *n*-nonyl-*β*-D-glucopyranoside (NG), *n*-heptyl-*β*-D-thioglucoside (HTG), or Tween 80. However, Ammonyx LO (lauryldimethylamine oxide) is an inexpensive detergent and gives reliable results.
2. The yield of rhodopsin in the retinal disk membranes can be increased by dissecting and storing the retinas in 10 mM Tris-acetate buffer, pH 7.4, containing 30 % sucrose, 1 mM dithiothreitol (DTT), and 0.001 % (v/v) aprotinin (instead of only buffer) as obtained from the supplier (W. L. Lawson, Co., Omaha, NE, USA). The volume of the homogenizing

buffer added in the second homogenization step is generally about 25 ml. The amount of dilution buffer (10 mM Tris-acetate buffer, pH 7.4) should be added meticulously (Subheading 3.1.1, **step 4**). The excess of the buffer will result in higher yield but lower purity, whereas a lower amount will lead to good purity but lower yields. Generally, the optimum value is 2–3 volumes of the dilution buffer. This ratio should be optimized for each shipment of retinas depending on the purpose. For disk membrane studies, the highest purity is required, while for the purification of rhodopsin, the yield is more important.

3. The band at 500 nm in the UV-visible rhodopsin spectrum (Fig. 1) is related to the retinal absorption, and consequently, it is proportional to the rhodopsin concentration. The maximum at 280 nm is due to the absorption of aromatic amino acids, and it can be used to estimate the overall protein concentration (not just rhodopsin). Hence the A_{280}/A_{500} spectral ratio is a reliable indicator of the rhodopsin purity.
4. The 11-*cis*-retinal is best stored as dry crystals in a lightproof container at –80 °C. Before opening the jar containing retinal, keep it at room temperature for 1–2 h to make sure the retinal is warmed. Cold crystals may condense water from the air and isomerize if they are wet. Dry crystals can be handled in visible light (not recommended). Take one or two small crystals, about the size of fine table salt crystals, and under red light, dissolve them in approximately 200 μl of 99.5 % ethanol.
5. One can use a smaller molar retinal–rhodopsin ratio (down to 1:1) at the expense of extra rhodopsin to obtain more rhodopsin regenerated with ^{2}H-labeled retinal. (Note that deuterated retinal is much more valuable than rhodopsin.) In that case, the absolute yield of regenerated rhodopsin would be higher; but the percentage yield would be lower.
6. During solubilization of rhodopsin in DTAB (Subheading 3.1.5, **step 1**), rhodopsin should be solubilized completely before loading onto the column. The total volume should not exceed 15 ml for the column length specified (8 cm) (Subheading 3.1.5). More than this volume will lead to rhodopsin elution in a broader band or even in two bands with worse quality. Note that DTAB is a denaturing detergent, and thermally bleaches the rhodopsin at temperatures above 4 °C. It is essential that all the procedures with rhodopsin in DTAB should be conducted in the cold room at 4 °C.
7. Isopotential spin-dry ultracentrifugation [22, 23] is carried out using custom-designed inserts for polycarbonate centrifuge tubes. The insert consists of two main parts: a black delrin body with the sample compartment and a stainless steel plate

with the isopotential surface (the surface is curved according to the radius of rotation of the steel plate, providing the same relative centrifugal force on the whole surface during centrifugation). A glass slide serves as a substrate for membrane alignment, and it is placed on the isopotential surface. The bottom of the polycarbonate centrifuge tube is filled with epoxy resin and polymerized to make a flat surface supporting the insert.

8. Alignment of recombinant membranes with rhodopsin on supporting glass slides is difficult. Evidently the difficulty is related to the fact that substantial portions of the protein are protruding from both sides of the lipid bilayers. In our hands, near-perfect alignment as in Fig. 3b is rarely achieved. That is why estimating the fraction of unoriented bilayers and subtracting the powder-type contribution from the experimental ^{2}H NMR spectrum is very important. However, this subtraction leads to a reduction of the signal–noise ratio in the experimental spectrum, and therefore can be used only for relatively small fractions of unoriented bilayers. We would not recommend using samples with an unoriented fraction larger than 20 %. The reason is that apart from unoriented bilayers, there is also additional alignment disorder due to the deviation of the local membrane normal from the average membrane normal in the sample (mosaic spread, σ). In lipid bilayers containing rhodopsin, the mosaic spread may be in the range of $\sigma = 10–20°$. It changes the line shape of the ^{2}H NMR spectra, making it more powder type and additionally reducing the accuracy of the method, because the greater the mosaic spread, the smaller the effect of alignment on the line shape. At the limit of very large mosaic spread, the orientational distribution becomes random.
9. Trapping of the Meta II state in aligned lipid bilayers is challenging. The reason is that alignment is favored by the sample dehydration, yet Meta II formation requires fully hydrated membranes. These opposite requirements can be overcome by initially preparing the aligned bilayers with rhodopsin in the dark state by isopotential spin-dry ultracentrifugation [22, 23], followed by rehydration at 100 % relative humidity, and then bleaching with the actinic light. Subsequent dehydration of the thin membrane film under an intensive stream of cold (4 °C) N_2 gas allows one to quickly (within 20–30 s) dehydrate the membranes, while rhodopsin still remains in the Meta II state. Stabilization of the Meta II state at low temperature and in dehydrated membranes (both conditions favoring Meta I state) is achieved by low pH 5 and GαCT2 peptide binding. Another option is to skip the last dehydration step (**step 8** in Subheading 3.5) and to work with a poorly aligned sample by subtracting the powder-type contribution to the ^{2}H NMR spectrum. However, a large fraction of unoriented bilayers

(which may increase up to 50 % in a fully hydrated sample) will essentially reduce the accuracy of the method. The temperature conditions for storage and handling the samples with rhodopsin in the Meta II state after trapping are stricter than for the Meta I state, because the Meta I state is stabilized by the low hydration of the membranes. The Meta II state is mostly stabilized by low pH and the peptide binding. Additional measures must be taken to freeze the sample, including bound water (in the vicinity of the protein and the lipid bilayer, which may be in a liquid phase down to −30 °C [13]), to prevent dissociation of the peptide. That is why the recommended temperatures for the storage and manipulation of the Meta I and the Meta II samples are below −30 °C and −60 °C, respectively.

10. For relaxation measurements, the alignment is less essential (unless one wants to study the angular dependence of relaxation). Hence there may be no need to dehydrate the membrane film with rhodopsin at all (**step 8** in Subheading 3.5). However, it is still logical to prepare the sample on glass slides for more complete bleaching and fast cooling upon trapping the Meta I and Meta II states. The isopotential ultracentrifugation method (**step 4** in Subheading 3.5) may be avoided in this case. Instead, one may just spread the suspension of disk membranes over the glass slides, and let them dry partially under a stream of N_2 gas to reduce the volume of the sample. That allows one to put more rhodopsin into the NMR tube (up to 40 mg in an 8×22-mm tube). To be certain that the sample is fully hydrated, it can be rehydrated at 100 % relative humidity.
11. The Meta I and Meta II states are unstable, and therefore it is recommended to freeze the Meta I and Meta II samples immediately after preparation, and handle them afterward at temperatures below −30 °C and −60 °C, respectively. Stacking the glass slides with membranes containing rhodopsin in the Meta I and Meta II states at these temperatures is carried out in a custom-designed, thermally insulated Styrofoam glove box (with window and thermometer), which is cooled by placing dry ice on the sides and liquid nitrogen at the bottom. A similar Styrofoam box is used to place the sample into the NMR probe and to precool the NMR probe before the experiment. The transfer line which carries the cold N_2 gas to the NMR probe to stabilize the temperature should also be precooled by turning on the liquid N_2 evaporator 5–10 min before the experiment.
12. Typically, the ^{2}H NMR spectra are acquired using a Bruker AMX-500 spectrometer with a narrow-bore magnet (magnetic field $\mathbf{B}_0$ is 11.7 T, corresponding to a deuterium frequency of 76.77 MHz). The ^{2}H NMR probe is locally constructed ("home built") and has an 8-mm-diameter and 12-mm-long

transverse solenoid as the radio-frequency coil, with high-voltage capacitors (Polyflon Company, Norwalk, CT, USA; or Jennings Technology, Vandalia, OH, USA). The membrane tilt angle to the magnetic field is adjusted manually using a protractor by rotating the sample in the radio-frequency coil (Fig. 3a). The transmitter pulses are amplified with a 2-kW Henry Radio amplifier (Henry Radio, Inc., Los Angeles, CA, USA) or equivalent, providing a 4.2-μs 90° pulse. Acoustical ringing of the radio-frequency coil can be minimized by increasing the delay τ (see pulse sequences below) up to 70 μs if necessary. The repetition time for the pulse sequence is in the range of 0.1–1.5 s depending on the longitudinal (T_{1Z}) relaxation time. The spectra are processed with locally written data processing software (MATLAB, The MathWorks, Inc., Natick, MA, USA). Echo signals are multiplied by a decaying exponential, representing a line broadening of 500 Hz in the frequency domain. The number of scans depends on the temperature and the delay τ and is in the range of $\approx 0.2\text{–}1 \times 10^6$ (typically 1 d signal acquisition). The solid-state ^{2}H NMR spectra are recorded using a composite-pulse, quadrupolar-echo sequence $\left(135°_{-x}90°_{x}45°_{-x} - \tau - 135°_{y}90°_{-y}45°_{y} - \tau - \text{acquisition}\right)$. Experimental longitudinal (spin–lattice) ^{2}H NMR relaxation rates (T_{1Z}) (Figs. 5 and 6) for selectively ^{2}H-labeled methyl groups are measured by an inversion-recovery $180° - t - (90°)_{\phi} - \tau - (90°)_{\phi \pm 90°} - \tau -$ acquire pulse sequence. The ^{31}P NMR spectra are acquired with a Hahn echo $(90°)_{\phi} - \tau - (180°)_{\phi} - \tau -$ acquire pulse sequence. Appropriate phase (ϕ) cycling is applied in each case [9, 10].

13. The most straightforward way to subtract the spectrum, which accounts for the natural abundance of deuterium in phospholipids, is to prepare a sample with the same amount of lipids (it can be with natural, unlabeled rhodopsin, or without rhodopsin) and measure the ^{2}H NMR spectrum below the gel to liquid-crystalline phase transition temperature. The spectrum amplitude may be adjusted before subtraction according to the number of scans acquired. The ^{2}H NMR spectrum of water is usually not observed, because the signal is too weak for deuterium-depleted water and because it is very broad. However, if necessary, the subtraction may be performed for the water signal as well.

14. Monte Carlo simulation is performed using a locally written program (MATLAB; The MathWorks, Inc., Natick, MA, USA) as follows. For rapidly rotating ^{2}H-labeled methyl groups (assuming an axially symmetric quadrupolar coupling tensor), the ^{2}H NMR spectrum represents a symmetric doublet. The two quadrupolar frequencies are determined by the angle $\tilde{\theta}$ between the methyl group symmetry axis (parallel to C–C^{2}H$_3$

bond) and the external magnetic field $\mathbf{B}_0$ and are given by $\nu_Q^{\pm} = \pm(3/8)\,\chi_Q^{eff}\,(3\cos^2\tilde{\theta} - 1)$, where $\chi_Q{}^{eff}$ is the effective quadrupolar coupling constant (*see* Subheading 3.2). The angle $\tilde{\theta}$ depends on the orientation of the methyl group in rhodopsin θ_B, the deviation of the local membrane normal $\mathbf{n}$ from the average membrane normal $\mathbf{n}_0$, and the orientation of the sample θ (tilt angle) with respect to the magnetic field $\mathbf{B}_0$; *see* Fig. 3a. The ^{2}H NMR spectra are simulated by randomly generating the orientations of methyl group according to their distribution functions (*see* Subheading 3.6) and calculating the quadrupolar frequencies. The distribution of the quadrupolar frequencies is then convoluted with the intrinsic line broadening. Finally, the theoretical and experimental spectra can be fitted using the methyl bond angle θ_B and mosaic spread σ as fitting parameters.

15. Apart from the ^{2}H-labeled C5-, C9-, or C13-methyl groups, and the electronic transition dipole moment of retinal [9], the two C1-methyl groups can also be explored for structural studies. However, the number of orientational constraints is still limited for detailed conformational analysis. The same is valid for any protein segment. That is why the method of solid-state ^{2}H NMR spectroscopy of selectively ^{2}H-labeled aligned samples is greatly enhanced by complementary ^{13}C NMR rotational resonance distance measurements [32, 33]. The distance restraints allow one to eliminate the ambiguity in structural models, based on orientational restraints due to the symmetry of NMR interactions [9, 13, 34], and provide additional structural parameters that allow one to refine the molecular structure.

References

1. Lagerström MC, Schiöth HB (2008) Structural diversity of G protein-coupled receptors and significance for drug discovery. Nat Rev Drug Discov 7:339–357
2. Teller DC, Okada T, Behnke CA et al (2001) Advances in determination of a high-resolution three-dimensional structure of rhodopsin, a model of G-protein-coupled receptors (GPCRs). Biochemistry 40:7761–7772
3. Okada T, Sugihara M, Bondar A-N et al (2004) The retinal conformation and its environment in rhodopsin in light of a new 2.2 Å crystal structure. J Mol Biol 342:571–583
4. Li J, Edwards PC, Burghammer M et al (2004) Structure of bovine rhodopsin in a trigonal crystal form. J Mol Biol 343:1409–1438
5. Choe H-W, Kim YJ, Park JH et al (2011) Crystal structure of metarhodopsin II. Nature 471:651–655
6. Standfuss J, Edwards PC, D'Antona A et al (2011) The structural basis of agonist-induced activation in constitutively active rhodopsin. Nature 471:656–660
7. Deupi X, Edwards P, Singhal A et al (2012) Stabilized G protein binding site in the structure of constitutively active metarhodopsin-II. Proc Natl Acad Sci U S A 109:119–124
8. Struts AV, Salgado GFJ, Martínez-Mayorga K et al (2011) Retinal dynamics underlie its switch from inverse agonist to agonist during rhodopsin activation. Nat Struct Mol Biol 18:392–394
9. Struts AV, Salgado GFJ, Tanaka K et al (2007) Structural analysis and dynamics of retinal chromophore in dark and Meta I states of rhodopsin from ^{2}H NMR of aligned membranes. J Mol Biol 372:50–66
10. Struts AV, Salgado GFJ, Brown MF (2011) Solid-state ^{2}H NMR relaxation illuminates

functional dynamics of retinal cofactor in membrane activation of rhodopsin. Proc Natl Acad Sci U S A 108:8263–8268

11. Xu, X., Struts, A.V., and Brown, M.F. (2014) Generalized model-free analysis of nuclear spin relaxation experiments. eMagRes 3:275–286
12. Papermaster DS, Dreyer WJ (1974) Rhodopsin content in the outer segment membranes of bovine and frog retinal rods. Biochemistry 13: 2438–2444
13. Tanaka K, Struts AV, Krane S et al (2007) Synthesis of CD_3-labeled 11-*cis*-retinals and application to solid-state deuterium NMR spectroscopy of rhodopsin. Bull Chem Soc Jpn 80:2177–2184
14. Sperling W, Rafferty CN (1969) Relationship between absorption spectrum and molecular conformations of 11-*cis*-retinal. Nature 224: 591–594
15. Garwin GG, Saari JC (2000) High-performance liquid chromatography analysis of visual cycle retinoids. Methods Enzymol 316:313–324
16. Raubach RA, Franklin LK, Dratz EA (1974) A rapid method for the purification of rod outer segment disk membranes. Vision Res 14:335–337
17. Hong K, Knudsen PJ, Hubbell WL (1982) Purification of rhodopsin on hydroxyapatite columns, detergent exchange, and recombination with phospholipids. Methods Enzymol 81:144–150
18. Botelho AV, Gibson NJ, Thurmond RL et al (2002) Conformational energetics of rhodopsin modulated by nonlamellar forming lipids. Biochemistry 41:6354–6368
19. Brown MF (1997) Influence of non-lamellar forming lipids on rhodopsin. Curr Top Membr 44:285–356
20. Brown MF, Chan SI (1996) Bilayer membranes: deuterium and carbon-13 NMR. In: Grant DM, Harris RK (eds) Encyclopedia of nuclear magnetic resonance. Wiley, New York, NY, pp 871–885
21. Brown MF (1996) Membrane structure and dynamics studied with NMR spectroscopy. In: Merz K Jr, Roux B (eds) Biological membranes. A molecular perspective from computation and experiment. Birkhäuser, Basel, pp 175–252
22. Gröbner G, Taylor A, Williamson PTF et al (1997) Macroscopic orientation of natural and model membranes for structural studies. Anal Biochem 254:132–138
23. Clark NA, Rothschild KJ, Luippold DA et al (1980) Surface-induced lamellar orientation of multilayer membrane arrays. Biophys J 31: 65–96
24. Nevzorov AA, Moltke S, Heyn MP et al (1999) Solid-state NMR line shapes of uniaxially oriented immobile systems. J Am Chem Soc 121: 7636–7643
25. Martínez-Mayorga K, Pitman MC, Grossfield A et al (2006) Retinal counterion switch mechanism in vision evaluated by molecular simulations. J Am Chem Soc 128:16502–16503
26. Brown MF (1982) Theory of spin-lattice relaxation in lipid bilayers and biological membranes. ^2H and ^{14}N quadrupolar relaxation. J Chem Phys 77:1576–1599
27. Trouard TP, Alam TM, Brown MF (1994) Angular dependence of deuterium spin-lattice relaxation rates of macroscopically oriented dilaurylphosphatidylcholine in the liquid-crystalline state. J Chem Phys 101:5229–5261
28. Nevzorov AA, Brown MF (1997) Dynamics of lipid bilayers from comparative analysis of ^2H and ^{13}C nuclear magnetic resonance relaxation data as a function of frequency and temperature. J Chem Phys 107:10288–10310
29. Nevzorov AA, Trouard TP, Brown MF (1998) Lipid bilayer dynamics from simultaneous analysis of orientation and frequency dependence of deuterium spin-lattice and quadrupolar order relaxation. Phys Rev E 58:2259–2281
30. Brown MF, Salgado GFJ, Struts AV (2010) Retinal dynamics during light activation of rhodopsin revealed by solid-state NMR spectroscopy. Biochim Biophys Acta 1798:177–193
31. Mertz B, Struts AV, Feller SE et al (2012) Molecular simulations and solid-state NMR investigate dynamical structure in rhodopsin activation. Biochim Biophys Acta 1818: 241–251
32. Spooner PJR, Sharples JM, Verhoeven MA et al (2002) Relative orientation between the β-ionone ring and the polyene chain for the chromophore of rhodopsin in native membranes. Biochemistry 41:7549–7555
33. Verdegem PJE, Bovee-Geurts PHM, de Grip WJ et al (1999) Retinylidene ligand structure in bovine rhodopsin, metarhodopsin-I, and 10-methylrhodopsin from internuclear distance measurements using ^{13}C-labeling and 1-D rotational resonance MAS NMR. Biochemistry 38:11316–11324
34. Salgado GFJ, Struts AV, Tanaka K et al (2006) Solid-state ^2H NMR structure of retinal in metarhodopsin I. J Am Chem Soc 128: 11067–11071
35. Brown MF (2012) Curvature forces in membrane lipid-protein interactions. Biochemistry 51:9782–9795

Chapter 11

Sequential Structural Changes in Rhodopsin Occurring upon Photoactivation

Naoki Kimata, Andreyah Pope, Dawood Rashid, Philip J. Reeves, and Steven O. Smith

Abstract

We describe the use of solid-state magic angle spinning NMR spectroscopy for characterizing the structure and dynamics of dark, inactive rhodopsin and the active metarhodopsin II intermediate. Solid-state NMR spectroscopy is well suited for structural measurements in both detergent micelles and membrane bilayer environments. We first outline the methods for large-scale production of stable, functional rhodopsin containing ^{13}C- and ^{15}N-labeled amino acids. The expression methods make use of eukaryotic HEK293S cell lines that produce correctly folded, fully functional receptors. We subsequently describe the basic methods used for solid-state magic angle spinning NMR measurements of chemical shifts and dipolar couplings, which provide information on rhodopsin structure and dynamics, and describe the use of low-temperature methods to trap the active metarhodopsin II intermediate.

Key words Solid-state NMR, Magic angle spinning, Rhodopsin, Metarhodopsin II, HEK293 cells

1 Introduction

Solid-state magic angle spinning (MAS) NMR spectroscopy provides an approach for probing specific structural elements of native G protein-coupled receptors (GPCRs) in membrane environments. Solid-state NMR measurements of internuclear distances, protonation changes, and conformational changes complement structural studies by protein crystallography, infrared spectroscopy, and deuterium NMR spectroscopy described in other articles in this volume. Here, we provide a brief description of how isotope-enriched, functional rhodopsin can be obtained for structural studies using solid-state NMR spectroscopy and then describe the basic methods for setting up solid-state NMR experiments and obtaining one- and two-dimensional spectra of rhodopsin and its intermediates at low temperature. There are many outstanding reviews of magic angle spinning NMR and advanced methods for obtaining information on both structure and dynamics [1, 2].

Beata Jastrzebska (ed.), *Rhodopsin: Methods and Protocols*, Methods in Molecular Biology, vol. 1271,
DOI 10.1007/978-1-4939-2330-4_11,

Our aim here is to provide a detailed step-by-step description for the nonexpert to understand how rhodopsin is isotopically labeled for NMR measurements and how the basic NMR experiments are conducted. These protocols underlie our reported structure-function studies on rhodopsin [3–7].

Solid-state NMR is characterized by the absence of rapid isotropic motion. In solution NMR spectroscopy, rapid motion averages the chemical shift interaction to its isotropic value and the dipolar interaction to zero. In the solid-state, these interactions lead to broadening of the NMR resonances. There are several different strategies for narrowing the NMR line widths in the solid-state in order to observe individual, narrow resonances. A common strategy is the use of magic angle spinning (MAS) [8–11]. Both the chemical shift and the dipolar interactions have a $3\cos^2\theta - 1$ dependence on orientation with respect to the external magnetic field. Rapid mechanical rotation of the sample at the magic angle ($\theta = 54.7°$ is the angle between the Z direction of the external Bo field and the spinning axis) averages the chemical shift interaction to its isotropic value and the dipolar interaction to zero. The dipolar interaction yields information on internuclear distances (which are used for structural constraints) in the solid-state. Consequently, while MAS has the advantage of producing narrow NMR resonances, it has the disadvantage of averaging the dipolar couplings between spins. However, the averaging of the dipolar interaction by MAS is not by random motion as in solution NMR but by a well-defined rotation of the sample. As a result, many methods have been used to reintroduce the dipolar interaction in the MAS experiment, allowing one to measure dipolar couplings and hence internuclear distances.

2 Materials

The experimental protocols described below will require access to equipment typically found in a laboratory equipped for molecular biology, mammalian cell culture, and protein purification. For NMR structural studies, solid-state NMR instrumentation is required. The basic instrumentation requires a magic angle spinning NMR probe with low-temperature capability and high-power amplifiers. For our experiments, we typically use a double-resonance probe that can be tuned to ^{1}H and either ^{13}C or ^{15}N or a triple-resonance probe that can be tuned to all three nuclei (^{1}H, ^{13}C, and ^{15}N). We also typically pack our sample in NMR rotors that have an outer diameter of 4 mm. These rotors have a working volume of ~30–80 μl (depending on whether the sample is restricted to the center of the rotor) and reach MAS frequencies of ~15 kHz.

2.1 Constructs

1. pCDNA6-TR plasmid.
2. pACMV-tetO plasmid with rhodopsin gene.

2.2 Expression and Isotope Labeling of Rhodopsin in HEK293S Cells

1. Human embryonic kidney (HEK) 293S cells. These cells have been adapted for suspension growth.
2. Dulbecco's Modified Eagle's medium (DMEM) supplemented with heat-inactivated fetal bovine serum (FBS) 10 % (v/v) as well as penicillin and streptomycin both at 100 I.U./ml final concentration. For large-scale suspension growth of cell lines, low-calcium DMEM formulations are required.
3. 50 mg/ml geneticin sulfate (G418) solution.
4. Phosphate buffer saline (PBS): 137 mM NaCl, 2.7 mM KCl, 1.5 mM KH_2PO_4, 8 mM Na_2HPO_4, pH 7.2.
5. Commercial trypsin-EDTA solution (Corning Cellgro): 0.05 % trypsin and 0.53 mM EDTA.
6. Tetracycline and sodium butyrate.
7. Bioreactor system (*see* **Note 1**).

2.3 Cells Harvesting and Protein Purification

1. PBS supplemented with protease inhibitors: 400 μM PMSF, 50 μg/m benzamidine.
2. Unlabeled and ^{13}C-labeled 11-*cis*-retinal.
3. PBS with 1 % (w/v) *n*-dodecyl-β-D-maltoside (DDM).
4. PBS containing 0.02 % (w/v) DDM.
5. 2 mM sodium phosphate buffer, pH 6.0.
6. Rho-1D4 antibody coupled to Sepharose (by CNBr activation) at a binding capacity of 1 mg rhodopsin/1 ml of beads.
7. 2 mM sodium phosphate buffer with 0.02 % DDM supplemented with 100 μM of 9-mer peptide corresponding to C-terminal sequence of rhodopsin (TETSQVAPA).

2.4 Solid-State Magic Angle Spinning NMR Spectroscopy

1. Solid-state NMR spectrometer with MAS probes and sample rotors.
2. Standard samples (KBr, adamantane, and glycine).
3. Low-temperature apparatus, liquid nitrogen, and nitrogen gas.

3 Methods

Eukaryotic membrane proteins are often not expressed in a correctly folded, functional form in bacteria. For structural studies on rhodopsin, protein expression is carried out in mammalian HEK293S cells. The cells are grown in media containing specifically labeled amino acids. Selective incorporation can be achieved for

all of the amino acids except glutamine, glutamate, asparagine, aspartate, proline, and alanine. The protein is immuno-purified and concentrated for NMR measurements.

3.1 Making Stable Cell Lines

1. In order to procure stable HEK293S cell lines that contain the inducible rhodopsin gene, transfect sequentially two plasmids into HEK293S cells. First, transfect the pCDNA6-TR plasmid, which encodes a selectable marker (blasticidin) and the tet operon repressor protein (TetR). After transfection of pCDNA6-TR, isolate the cells that are resistant to blasticidin [12, 13].
2. Transfect the pACMV-tetO plasmid into the pool of cells isolated above. This plasmid contains the rhodopsin gene, which has been subcloned [13]. The specific use of this construct allows rhodopsin expression to be governed by the CMV promoter sequence. However, in this case, the CMV promoter sequence contains two (tetO) binding sites for the tet repressor protein, which in turn inhibits gene expression of rhodopsin in HEK293S cells producing TetR. This interaction between the tetO sequences in the CMV promoter sequence and the tetR repressor protein is, however, disrupted by the addition of tetracycline, which thus induces expression of rhodopsin.

3.2 Bioreactor Growth of HEK293S Cells

1. Grow the cell monolayers on 10-cm cell culture dishes with 10 ml of DMEM whose composition is described in Table 1 and that has been supplemented with 10 % (v/v) heat-inactivated FBS, penicillin (100 units/ml), and streptomycin (100 μg/ml) [14, 15]. To maintain the cells having two plasmids, add 2 g/l of G418 (Geneticin) and 5 mg/l blasticidin to cell culture medium.
2. When the cells reach about 70 % confluence (typically 2 days after starting the cultures), feed the cells by changing the spent DMEM with new DMEM containing G418 and blasticidin at the same concentration.
3. Once the cells reach ~90 % confluence (about 10^7 cells per plate [16]), remove spent medium, wash the monolayer with PBS, and detach the cells from the plate by using 1 ml of trypsin-EDTA solution. Cells are dispersed in 9 ml of complete DMEM and then distributed between two 15-cm dishes each containing 24 ml of complete DMEM containing G418 and blasticidin as before.
4. Upon reaching near confluence (3 days), cells from the two 15-cm plates are trypsinized and distributed between twenty 15-cm plates following the method described above in **step 3**.
5. The cells should be at about 80 % confluent and cover most of the dish at ~48 h following **step 4**. At this point, the cells are fed by changing the spent DMEM culture with fresh DMEM, which has a reduced calcium concentration (680 μM [16])

Table 1
Composition of DMEM for plate and suspension growth

Component	Concentration (mg/l)
Salts	
$CaCl_2 \cdot 2H_2O$	50 in suspension; 250 on plates
$Fe(NO_3)_3 \cdot 9H_2O$	0.1
$MgSO_4$ (anhydrous)	97.67
KCl	400
NaCl	6,400
NaH_2PO_4	109
$NaHCO_3$	3,700
Amino acids	
L-Arginine*HCl	84
L-Cysteine*HCl	63
L-Glutamine	350; original 584
Glycine	30
L-Histidine*HCl $\cdot H_2O$	42
L-Isoleucine	105
L-Leucine	105
L-Lysine*HCl	146
L-Methionine	30
L-Phenylalanine	66
L-Serine	42
L-Threonine	95
L-Tryptophan	16
L-Tyrosine*2Na	97
L-Valine	94
Vitamins	
D-Ca pantothenate	4
Choline chloride	4
Folic acid	4
i-Inositol	7.2
Niacinamide	4
Pyridoxine*HCl	4
Riboflavin	0.4
Thiamine*HCl	4
Others	
D-Glucose	4,500; add more during suspension growth
Phenol red*Na	15
Pluronic acid	1,000, only for suspension growth
Dextran sulfate	300, only for suspension growth

and without G418 and blasticidin. The reduced calcium facilitates cell growth in suspension in a bioreactor.

6. Prepare the bioreactor for suspension growth of the cells that have been growing in the 20 plates. Autoclave the bioreactor, and calibrate the pH, dissolved O_2, and temperature electrodes. Introduce fresh DMEM (3 l) to the bioreactor

vessel. This DMEM can contain specific ^{13}C- or ^{15}N-labeled amino acids (*see* **Note 1**).

7. Inoculate the media in the bioreactor with the cells from the 20 culture plates (~5×10^8 cells) [16].
8. Feed cells with a cocktail containing amino acids (the same amount as in the initial DMEM, *see* Table 1) and glucose (2.4 mg/l) on day 4. The following day, induce rhodopsin expression by adding tetracycline (2 mg/l, final concentration) and sodium butyrate (5 mM, final concentration). These solutions should be dissolved in ultrapure water, sterile filtered, and fed slowly into the vessel.
9. Harvest cells on day 7 [13].

3.3 Regeneration and Purification of Rhodopsin

1. Collect the cell suspension from the bioreactor vessel into an ice-cold container, and separate the cells from spent growth medium by centrifugation at 4,000 × *g* for 20 min at 4 °C.
2. Wash the cell pellet twice by suspending it in ice-cold PBS supplemented with protease inhibitors (400 μM PMSF, 50 μg/ml benzamidine) and harvesting via centrifugation at 4,000 × *g* for 30 min at 4 °C. All subsequent steps are carried out under dim red light.
3. Suspend cells in PBS with protease inhibitors, and add 125 nmol per gram of cell pellet of 11-*cis*-retinal from a 10-mM stock in ethanol. Then incubate the cell suspension in the dark at 4 °C with nutation. After 2 h, add an additional 125 nmol of 11-c*is*-retinal, and continue nutation for another 2 h. After 4 h of nutation, harvest the cell pellet by centrifugation at 4,000 × *g* for 30 min at 4 °C.
4. To extract rhodopsin from the cell membrane, suspend the cell pellet in ice-cold PBS with 1 % (w/v) DDM (5 ml of buffer per gram of wet pellet) and nutate for 30 min. Then centrifuge it for 60 min at 25,000 × *g* and 4 °C to separate solubilized membrane fraction from the remaining cell debris. Determine the amount of rhodopsin expressed by UV-visible absorbance spectroscopy on the basis of the intensity of the 500-nm absorption peak.
5. To purify rhodopsin, apply the detergent-solubilized lysate to a rho-1D4-Sepharose column via gravity flow. Then wash the column with 50 column volumes of PBS containing 0.02 % (w/v) DDM.
6. To equilibrate the column for elution, wash the column with 2 mM sodium phosphate buffer, pH 6.0 with 0.02 % DDM. After that, elute purified rhodopsin by adding the 2 mM sodium phosphate buffer with 0.02 % DDM supplemented with 100 μM of 9-mer peptide corresponding to the C-terminus of rhodopsin (TETSQVAPA).

7. For solid-state NMR experiments, we often regenerate the purified rhodopsin in DDM micelles with ^{13}C-labeled 11-*cis*-retinal. First, equilibrate the rhodopsin sample with a 2:1 molar ratio of the labeled 11-*cis*-retinal (dissolved in a small, known quantity of ethanol) in the dark room. Then illuminate the rhodopsin sample with a 400-W lamp with a >495-nm cutoff filter for ~45–60 s at room temperature. It is important that the ethanol concentration must not exceed 1.0 % of the total volume in DDM or other detergents. The sample is then nutated for 1 h at room temperature in the dark to allow efficient regeneration of rhodopsin with the labeled retinal. Calculate regeneration efficiency by the recovery of the 500-nm peak in the visible absorption spectrum.
8. Concentrate the rhodopsin sample solubilized in DDM for NMR measurements or reconstitute into membrane bilayers (*see* **Note 2**).

3.4 Standard Samples for Calibrating Magic Angle Spinning (MAS) NMR Spectroscopy

1. The standard samples used to set up an NMR spectrometer for double-resonance ^{1}H-^{13}C solid-state magic angle spinning experiments are KBr, adamantane, and glycine. None of these samples need be isotopically enriched.
2. Set the magic angle with KBr. Quadrupolar nuclei such as ^{79}Br are advantageous in that their signal is very sensitive to angle misalignment. Also, it is useful to use ^{79}Br because its resonance frequency is similar to that of ^{13}C. When setting the magic angle, a large set of rotational echoes is observed in the free induction decay (FID) that will result in a number of peaks (spinning side bands) in the ^{79}Br spectrum. The width and intensity of the side bands are sensitive to the magic angle setting. Therefore, optimize the magic angle by increasing the number of rotational echoes in the time domain and/or by decreasing the line widths for the side bands in the frequency domain (Fig. 1a, b). The widths of the side bands should be the same as the width of the center band.
3. Adjust the room temperature shims to improve the homogeneity of the external Bo magnetic field with adamantane. Typically the Z, X, Y, and Z^2 shims are the most sensitive. Adamantane has two ^{13}C resonances, and the shims are adjusted iteratively until the line widths are less than 5 Hz. We typically shim down to a 2-Hz line width.
4. Determine the ^{1}H and ^{13}C 90° pulse length with adamantane. A 90° pulse yields the maximum signal. To obtain the 90° pulse length, first determine the length of a 360° pulse, which yields no signal, and divide it by a factor of 4.
5. Set the Hartmann-Hahn (HH) match for cross polarization, and optimize the ^{1}H decoupling pulse with glycine. Figure 1c–e show spectra of glycine at different MAS frequencies with

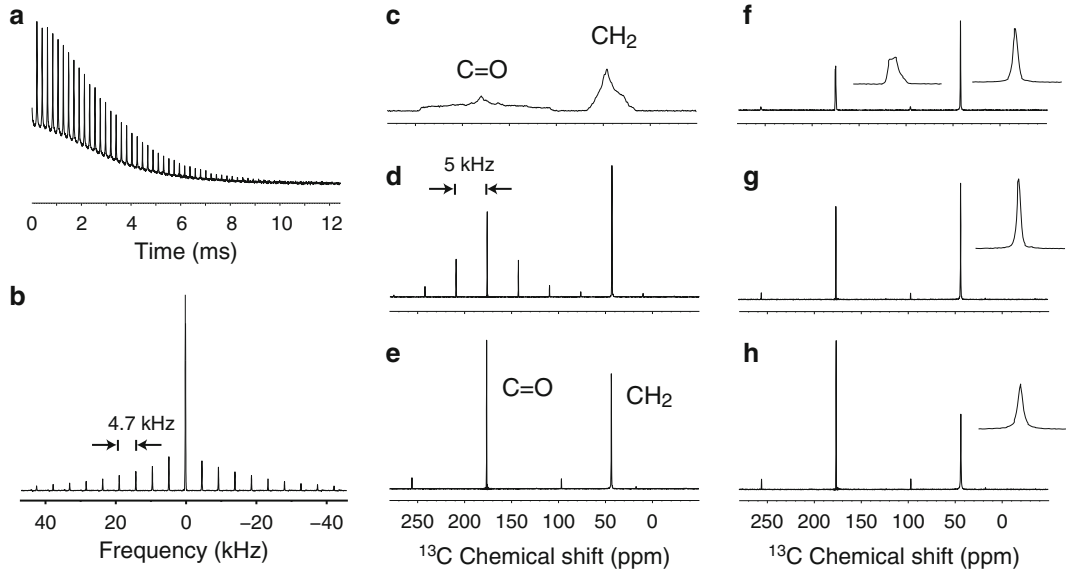

Fig. 1 Optimizing experimental parameters for solid-state NMR of rhodopsin. (**a**) Time-domain signal of ^{79}Br in KBr. The free induction decay of ^{79}Br exhibits a string of rotational echoes that decay in intensity as a function of the time. The magic angle is set by maximizing the number of rotational echoes. (**b**) Frequency domain spectrum of ^{79}Br. The ^{79}Br spectrum has a single center band that is flanked by a series of rotational side bands separated by a frequency equal to the MAS frequency, which here is 4.7 kHz. (**c**) The ^{13}C-CPMAS spectrum of glycine consists of a ^{13}C=O and $^{13}CH_2$ resonance. In the absence of MAS, one observes very broad line widths. With MAS, the line widths narrow dramatically, and the center bands for the ^{13}C=O and $^{13}CH_2$ resonances are flanked by rotational side bands spaced at the spinning frequency. The spectrum in (**d**) was obtained at 5 kHz. Increasing the MAS frequency to 12 kHz in (**e**) decreases the number of spinning side bands. The spectra in (**f**–**g**) were obtained of glycine with a MAS frequency of 12 kHz, but where the magic angle (**f**), HH match (**g**), and decoupling frequency (**h**) have not been optimized. In (**f**) and (**g**), the influence of the magic angle and HH is seen most clearly on the C=O resonance, which has a larger chemical shift anisotropy than the CH_2 resonance. In (**h**), the decoupling frequency has the most influence on the CH_2 resonance, due to the directly attached protons

optimized conditions. To optimize the HH match, change the power level of the ^{13}C pulse, and maximize the intensity of the C=O resonance. The amplitude of the ^{1}H cross polarization pulse is ramped to improve polarization transfer at high MAS speeds and to compensate for B1 inhomogeneity. A phase-modulated decoupling scheme (SPINAL64) is used to effectively suppress ^{1}H-^{13}C dipolar interactions. Optimize the ^{1}H decoupling pulse length by monitoring the intensity of the CH_2 signal from glycine (Fig. 1e–g).

3.5 One-Dimensional (1D) CP MAS NMR

1. Set up the apparatus for running rhodopsin and meta II at low temperature. Low temperature is used to stabilize thermally labile intermediates of rhodopsin. For example, meta II is stable for weeks below ~250 K but will decay to opsin within hours at room temperature. Low temperature also reduces

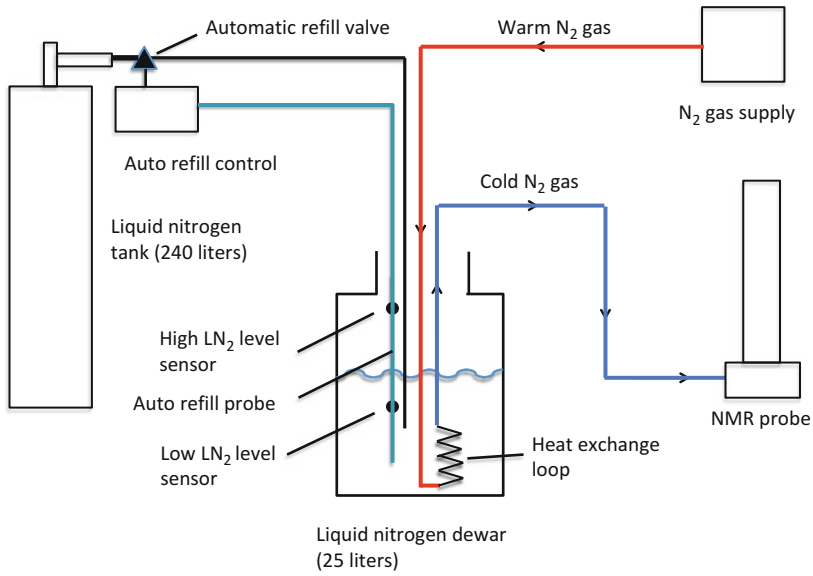

Fig. 2 Low-temperature set up for MAS NMR experiments. Nitrogen is used for the spinning gas and for temperature control. The N_2 gas is taken from the boil-off of a bulk nitrogen dewar and run through a heat exchanger to cool it to low temperature. The heat exchanger is immersed in a small dewar (25 l) of liquid nitrogen. This dewar is refilled using a 240-l storage dewar that itself can be refilled during a long-term experiment. The refill of the small dewar is done using an automatic refill system (Model 460) and custom sensor probe (Gordinier Electronics, Inc.)

rotational diffusion of membrane proteins, which would otherwise interfere with the mechanical averaging ability of MAS. The low-temperature apparatus is shown in Fig. 2 (*see* **Note 3**).

2. Precool the NMR probe to 285 K, and insert the sample (*see* **Note 4**).
3. Increase the spinning speed of the rotor slowly to ~3 kHz, and then decrease the temperature to 200 K. The tuning curve can be used to determine when the sample is frozen. It will shift to the position of solid glycine when the sample freezes. Slow spinning minimizes the loss of water out of the rotor and prevents the end cap from popping off. After the sample freezes, increase the MAS speed to the desired frequency.
4. Load in the pulse program for CP using the parameters that were optimized on adamantane and glycine.
5. Retune the probe and acquire the 1D spectrum (*see* **Note 5**).

3.6 Two-Dimensional MAS NMR

1. There are a number of 2D MAS NMR experiments that are designed to yield information on protein structure. Typical experiments yield cross peaks between residues that are coupled through the dipolar interaction. First, select a spinning speed to avoid overlap between side bands and cross peaks (*see* **Note 6**).

2. Optimize any parameters that are specific for the 2D experiment. For example, we typically use dipolar-assisted rotational resonance (DARR) to recouple resonances [17, 18]. In this case, set the power level of the proton recoupling pulse such that the RF field strength (in kHz) matches the MAS frequency.
3. Collect the 2D spectrum. We present the 1D (Fig. 3a) and 2D spectra (Fig. 3b) of U-^{13}C threonine to illustrate the DARR NMR method for measuring dipolar couplings.

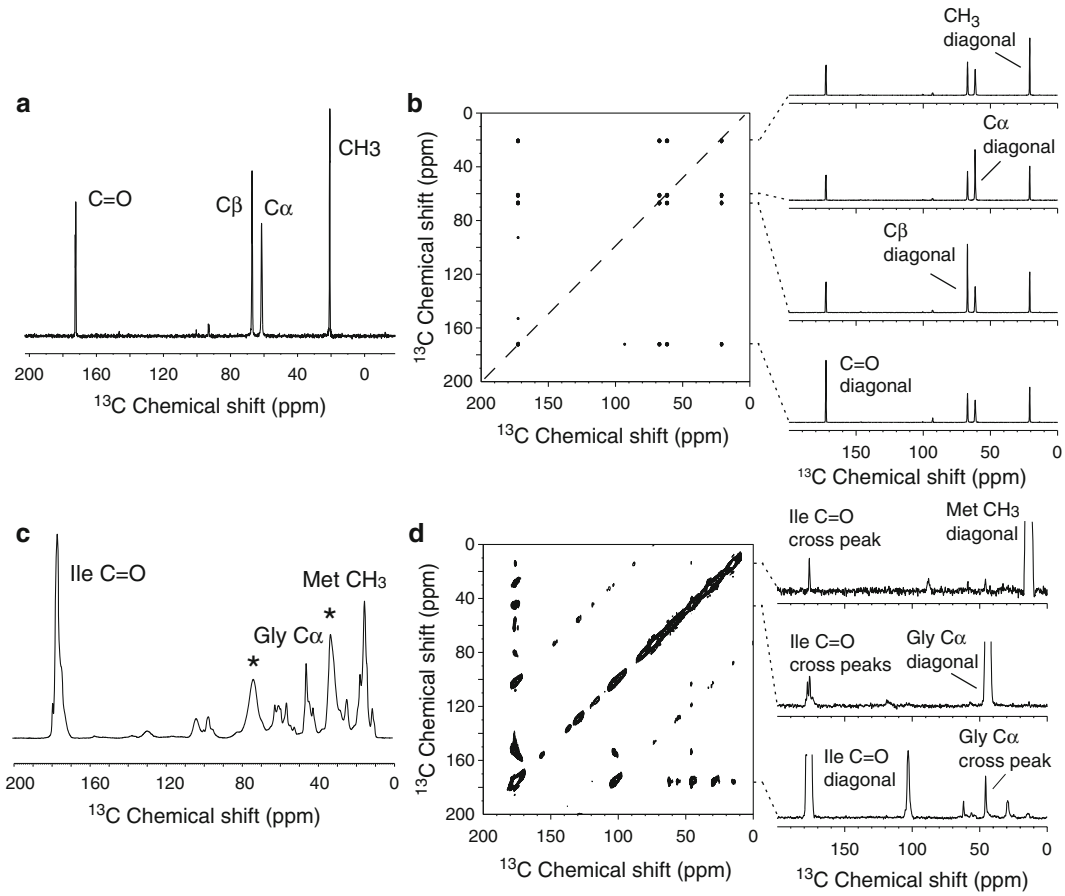

Fig. 3 One- and two-dimensional MAS NMR of threonine and rhodopsin using dipolar-assisted rotational resonance. (**a**) The 1D spectrum of uniformly ^{13}C-labeled threonine contains four NMR resonances. In the 2D spectrum (**b**), these resonances are observed as contours along the diagonal. Cross peaks (off diagonal peaks) occur between ^{13}C nuclei that coupled through the dipolar interaction. In threonine, all of the NMR sites are dipole coupled to one another. 1D slices (or rows) through the intense diagonal resonances more clearly reveal the cross peaks. (**c**) The 1D spectrum of rhodopsin contains both the labeled ^{13}C resonances and ^{13}C resonances from the detergent and protein that can be observed at natural abundance levels. (**d**) The 2D spectrum of rhodopsin reveals cross peaks between the 5-^{13}C methionine resonance (diagonal at 20 ppm) and 2-^{13}C glycine at 40 ppm, between the 2-^{13}C glycine resonance (diagonal) and 1-^{13}C isoleucine at 175 ppm, and between the 1-^{13}C isoleucine resonance (diagonal) and 5-^{13}C methionine. For rhodopsin, we typically use ~6–8 mg of protein, and require 2 days to acquire a 2D data set

These spectra are compared with the 1D (Fig. 3c) and 2D spectra (Fig. 3d) of rhodopsin that has been expressed using media enriched in 1-^{13}C isoleucine, 2-^{13}C glycine, and 5-^{13}C methionine.

3.7 Conversion of Rhodopsin to Metarhodopsin II

1. With the Bruker sample ejection stack, rhodopsin can be converted to meta II outside of the NMR probe. After obtaining the spectrum of rhodopsin, eject the sample and let it warm to room temperature in the dark. Illuminate with a 400-W lamp equipped with a >495-nm-long pass filter for 60 s (*see* **Note 7**).
2. Place the rotor into an Eppendorf Tube and centrifuge for 30 s in order to ensure even packing of the sample.
3. Insert the rotor into the precooled NMR probe, and proceed rapidly through the steps described in Subheading 3.5, **step 3**. The time from start of illumination to the sample freezing is typically about 3–4 min.
4. Collect the 1D and 2D spectra of meta II. We present the 1D spectra of rhodopsin and meta II in Fig. 4a. The difference spectrum between them reveals those ^{13}C resonances changing frequency upon activation. The 2D spectrum of meta II (Fig. 4b) is obtained in a manner similar as that of rhodopsin. Extracting rows through the individual diagonal resonances (Fig. 4c) allows one to compare how the cross peak intensities change between rhodopsin and meta II.

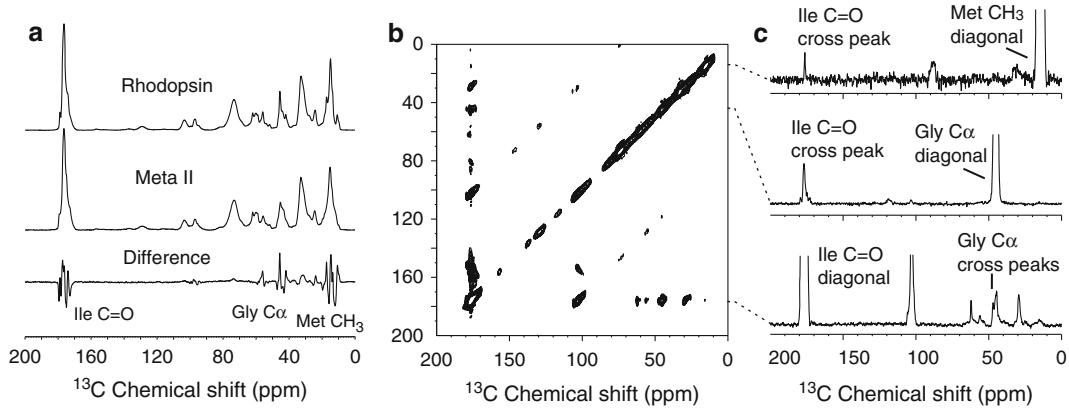

Fig. 4 NMR spectra of metarhodopsin II. (**a**) Difference spectroscopy reveals only those NMR resonances that change frequency between rhodopsin and meta II. In this example, we present the difference spectrum between rhodopsin and meta II containing 1-^{13}C isoleucine, 2-^{13}C glycine, and 5-^{13}C methionine. (**b**) 2D spectrum of meta II obtained by illumination and low-temperature trapping of the same sample used to obtain Fig. 3d. Comparison with the rhodopsin spectrum reveals resonances that change intensity upon activation. An increase in the intensity of the cross peak indicates that the ^{13}C sites have a shorter internuclear distance (i.e., stronger dipolar coupling). A decrease in intensity corresponds to a longer internuclear distance. (**c**) 1D rows extracted out of the 2D spectrum more clearly show the frequency and intensity changes in the cross peaks

4 Notes

1. We make use of a New Brunswick Scientific bioreactor (5-l maximum capacity) for cell growth. Alternatively, the cells can be grown in spinner flasks in a CO_2 incubator. Growth in the bioreactor is more reproducible, as it allows tight control over temperature, pH, and dissolved gases (O_2, CO_2, and N_2).
2. The purification protocol yields DDM-solubilized rhodopsin. For structural studies, detergent solubilization is advantageous, as the protein can be easily concentrated to greater than 1 mM, which is a benefit for NMR studies, given its inherently low sensitivity, and there is no loss of protein with an additional reconstitution step. Nevertheless, rhodopsin can easily be reconstituted into a variety of membranes having different lipid compositions.
3. The low-temperature setup used here is based on cooling N_2 gas with liquid nitrogen. Alternatively, there are low-temperature configurations that make use of air with a low dew point (i.e., water vapor is removed with the use of air dryers) and low-temperature cooling systems that do not require liquid nitrogen. Parker-Balston manufactures commercial air dryers for NMR spectrometers, and FTS Systems manufactures cooling systems. However, in our hands the residual water that remains still leads to clogging of air lines and microarcing within the probe coil during long-term (>3–4 days) experiments.
4. We use a Bruker NMR spectrometer that has a sample ejection stack that allows the NMR rotor to be inserted into the probe without removing the probe from the magnet. This configuration allows us to illuminate the sample outside of the magnet to convert to meta II. An alternative arrangement is to insert the sample into the probe at room temperature outside of the magnet, and then cool to the desired temperature. The conversion to meta II in this arrangement is carried out by irradiating the sample with an optic fiber built into the MAS stator.
5. The probe tuning is best monitored with an oscilloscope on the basis of reflected power.
6. The number of spinning side bands depends on the MAS frequency, the chemical shift anisotropy (CSA), and the size of magnetic field. The intensity of side bands is reduced at high MAS, small CSA, and small Bo fields.
7. One can change the temperature or the lipid or detergent composition in order to trap additional intermediates [7, 19].

Acknowledgments

This work was supported by NIH-NSF instrumentation grants (S10 RR13889 and DBI-9977553), a grant from the NIH to S. O. S (GM-41412). We gratefully acknowledge the W.M. Keck Foundation for support of the NMR facilities in the Center of Structural Biology at Stony Brook.

References

1. Baldus M (2002) Correlation experiments for assignment and structure elucidation of immobilized polypeptides under magic angle spinning. Prog Nucl Magn Reson Spec 41:1–47
2. Hong M, Zhang Y, Hu F (2012) Membrane protein structure and dynamics from NMR spectroscopy. Annu Rev Phys Chem 63:1–24
3. Ahuja S, Hornak V, Yan ECY et al (2009) Helix movement is coupled to displacement of the second extracellular loop in rhodopsin activation. Nat Struct Mol Biol 16:168–175
4. Ahuja S, Crocker E, Eilers M et al (2009) Location of the retinal chromophore in the activated state of rhodopsin. J Biol Chem 284:10190–10201
5. Ahuja S, Eilers M, Hirshfeld A et al (2009) 6-s-cis conformation and polar binding pocket of the retinal chromophore in the photoactivated state of rhodopsin. J Am Chem Soc 131:15160–15169
6. Goncalves JA, South K, Ahuja S et al (2010) Highly conserved tyrosine stabilizes the active state of rhodopsin. Proc Natl Acad Sci U S A 107:19861–19866
7. Eilers M, Goncalves JA, Ahuja S et al (2012) Structural transitions of transmembrane helix 6 in the formation of metarhodopsin I. J Phys Chem B 116:10477–10489
8. Lowe IJ (1959) Free induction decays of rotating solids. Phys Rev Lett 2:285–287
9. Andrew ER, Bradbury A, Eades RG (1958) Nuclear magnetic resonance spectra from a crystal rotated at high speed. Nature 182:1659
10. Schaefer J, Stejskal EO (1976) Carbon-13 nuclear magnetic resonance of polymers spinning at the magic angle. J Am Chem Soc 98:1031–1032
11. Maricq MM, Waugh JS (1979) NMR in rotating solids. J Chem Phys 70:3300–3316
12. Reeves PJ, Thurmond RL, Khorana HG (1996) Structure and function in rhodopsin: high level expression of a synthetic bovine opsin gene and its mutants in stable mammalian cell lines. Proc Natl Acad Sci U S A 93:11487–11492
13. Reeves PJ, Kim JM, Khorana HG (2002) Structure and function in rhodopsin: a tetracycline-inducible system in stable mammalian cell lines for high-level expression of opsin mutants. Proc Natl Acad Sci U S A 99: 13413–13418
14. Dulbecco R, Freeman G (1959) Plaque production by the polyoma virus. Virology 8:396–397
15. Smith JD, Freeman G, Vogt M et al (1960) The nucleic acid of polyoma virus. Virology 12:185–196
16. Eilers M, Reeves PJ, Ying WW et al (1999) Magic angle spinning NMR of the protonated retinylidene Schiff base nitrogen in rhodopsin: expression of ^{15}N-lysine and ^{13}C-glycine labeled opsin in a stable cell line. Proc Natl Acad Sci U S A 96:487–492
17. Takegoshi K, Nakamura S, Terao T (2003) ^{13}C-^{1}H dipolar-driven ^{13}C-^{13}C recoupling without ^{13}C rf irradiation in nuclear magnetic resonance of rotating solids. J Chem Phys 118:2325–2341
18. Takegoshi K, Nakamura S, Terao T (2001) ^{13}C-^{1}H dipolar-assisted rotational resonance in magic-angle spinning NMR. Chem Phys Lett 344:631–637
19. Smith SO, Courtin J, de Groot H et al (1991) ^{13}C magic-angle spinning NMR studies of bathorhodopsin, the primary photoproduct of rhodopsin. Biochemistry 30:7409–7415

Chapter 12

Dynamic Single-Molecule Force Spectroscopy of Rhodopsin in Native Membranes

Paul S.-H. Park and Daniel J. Müller

Abstract

Membrane proteins are an important class of proteins in biology and therapeutics. Understanding the dynamic nature of the molecular interactions that stabilize membrane protein structure is critical to dissect the mechanism of action and dysfunction of these proteins. Single-molecule force spectroscopy (SMFS) and dynamic SMFS (DFS) are emerging nanotechniques that allow the study of membrane proteins under the physiologically relevant conditions of a lipid bilayer and buffer conditions. These techniques directly probe the molecular interactions underlying protein structure and reveal unique insights about their properties. Outlined in this report will be procedures on how to conduct SMFS and DFS on rhodopsin in native retinal membranes. Rhodopsin is a membrane protein belonging to the G protein-coupled receptor family of proteins, one of the largest families of proteins in nature.

Key words Atomic force microscopy, Biological membranes, Energy landscape, Membrane proteins, Intramolecular interactions, Protein stability, Protein unfolding

1 Introduction

The atomic force microscope (AFM) has become a multifaceted instrument providing novel insights about the dynamic structure of membrane proteins [1, 2]. Molecular interactions formed by membrane proteins underlie their function, fold, and stability. AFM-based single-molecule force spectroscopy (SMFS) is a powerful tool that has allowed the direct probing and detection of molecular interactions in membrane proteins at the single-molecule level [3]. In contrast to more traditional structural methods, SMFS allows for the study of membrane proteins within the physiological context of a lipid bilayer and physiological buffer conditions. Thus, the dynamic molecular interactions underlying protein structure can be investigated under near-native conditions.

SMFS has been successfully applied to rhodopsin to investigate the influence of various factors on the molecular interactions that stabilize this membrane protein. Rhodopsin is a prototypical G

Beata Jastrzebska (ed.), *Rhodopsin: Methods and Protocols*, Methods in Molecular Biology, vol. 1271,
DOI 10.1007/978-1-4939-2330-4_12,

protein-coupled receptor (GPCR) found in the rod outer segment (ROS) disc membranes of photoreceptor cells in the retina. Rhodopsin is highly expressed in ROS disc membranes representing about 90 % of all proteins in that compartment [4]. Thus, isolation of ROS disc membranes essentially provides a purified preparation of rhodopsin embedded in a native lipid bilayer at high concentrations, an ideal preparation for SMFS. The availability of different animal models has provided a method to obtain native preparations of genetically modified forms of rhodopsin.

Initial SMFS studies carried out on rhodopsin from native retinal tissue revealed that the structure of rhodopsin is organized into distinct regions that exhibit intrinsic stability and require mechanical force to unfold [5], which are referred to as stable structural segments [3]. SMFS allowed for the determination of the relative stability of each stable structural segment in rhodopsin. The ability to determine the relative stability of different regions of rhodopsin allowed for the determination of the effect of zinc ions and post-translational modification on the structure of rhodopsin. Zinc ions appear to bind specifically to rhodopsin and exert a stabilizing effect since most stable structural segments exhibited a dose-dependent increase in relative stability [6]. The absence of normal palmitoylation of rhodopsin in its C-terminal region has been shown by SMFS to destabilize this region while leaving the rest of the rhodopsin structure unperturbed [7]. The functional effect of this destabilization appears to impact the efficiency of signaling to transducin.

Dynamic SMFS (DFS) is a related method whereby SMFS is conducted at different pulling velocities [8]. DFS allows the determination of parameters that describe the underlying energy landscape of protein unfolding, thereby providing information about the kinetic, energetic, and mechanical properties of stable structural segments of rhodopsin [9]. DFS has been applied to rhodopsin to determine the effect of amino acid substitutions and the binding of the chromophore 11-*cis* retinal on the molecular interactions formed in stable structural segments. Investigation of bovine and murine rhodopsin, where there are 23 amino acid residue differences between the receptor homologues, revealed that the kinetic, energetic, and mechanical properties of stable structural segments are largely conserved despite differences in amino acid sequence [10]. Thus, although there are over 100 point mutations in rhodopsin that cause retinal disease [11], the structure of rhodopsin can accommodate a certain level of amino acid residue substitutions without displaying significant perturbations in structure.

DFS was able to uncover the perturbations resulting from an amino acid substitution observed in patients with retinal disease, a G90D mutation that causes constitutive activity in rhodopsin and leads to congenital night blindness [12]. DFS revealed that the G90D mutant exhibited lower conformational variability, increased

unfolding rates, decreased activation energy, and increased mechanical rigidity in most stable structural segments compared to wild-type rhodopsin [13]. These changes may underlie the disease-causing constitutive activity promoted by the mutation and may be characteristic of constitutive activity in general since similar changes were also detected by DFS on the apoprotein opsin [14], which exhibits a low level of constitutive activity. Moreover, DFS studies on the apoprotein opsin revealed that the impact of bound 11-*cis* retinal on stable structural segments in rhodopsin shares some similarities with the impact of bound ligands on stable structural segments of the β_2 adrenergic receptor [15], another member of the GPCR family. Thus, DFS studies support the notion that some mechanistic and structural features of GPCRs are conserved.

The SMFS and DFS studies on rhodopsin highlighted here point to the incredible promise the methodology holds to reveal pertinent molecular information required to understand the mechanism underlying the function, folding, and stability of rhodopsin and other GPCRs. Reported in the following sections are detailed procedures for conducting SMFS and DFS on rhodopsin embedded in native ROS disc membranes. The reader is also directed to several excellent reports detailing general methods for the study of membrane proteins by an AFM and for conducting SMFS [16–18].

2 Materials

1. ROS disc membranes. ROS disc membranes prepared from fresh bovine and murine retina have been used previously in SMFS/DFS applications [5, 7].
2. Mica supports for sample adsorption. Detailed methods for preparing mica supports have been reported previously [16–18].
3. Scotch tape.
4. AFM. We have used the Multimode AFM (Bruker Corporation) and the NanoWizard AFM (JPK Instruments) in our studies. Both AFMs give similar results. Other commercial AFMs should be suitable as well. AFMs equipped with red or infrared lasers will not bleach rhodopsin and are therefore suitable. A 16-bit data acquisition card (NI PCI-6221, National Instruments) is required to collect data at high pulling speeds (>1,500 nm/s).
5. Si_3N_4 AFM probes (NPS, Bruker Corporation) with nominal spring constants of 0.06–0.08 N/m. Spring constants for AFM probes should be experimentally determined in the buffer that will be used for experiments. Spring constants can be determined using a thermal noise method [19].

6. Ringer's buffer: 10 mM 4-(2-hydroxyethyl)-1-piperazine-1-ethanesulfonic acid (HEPES), 130 mM NaCl, 3.6 mM KCl, 2.4 mM $MgCl_2$, 1.2 mM $CaCl_2$, 0.02 mM EDTA, pH 7.4.
7. IGOR Pro (WaveMetrics, Inc., Lake Oswego, OR) graphing and data analysis software.

3 Methods

All procedures involving rhodopsin should be carried out in the dark under dim red light conditions. All light sources should be covered with red filters.

3.1 Preparation of Samples for SMFS

1. Dilute the ROS disc membrane sample (0.5–1 mg/ml) in Ringer's buffer. A 100-fold dilution is usually suitable but may be modified as required (*see* **Note 1**).
2. Cleave mica with tape. The adhesive of the tape will remove a layer of the mica to expose an atomically flat surface on which the sample will adsorb.
3. Add 30 μl of the diluted ROS disc membrane sample (5–10 μg/ml) onto a freshly cleaved mica support. Incubate for 10–20 min to allow ROS disc membranes to adsorb onto the mica.
4. Remove the liquid from the mica surface. Wash the mica surface at least five times with 30 μl of Ringer's buffer to remove unadsorbed debris.
5. After the last wash, add 30 μl of Ringer's buffer to the mica support (*see* **Note 2**). Mount the mica support onto the AFM. Using an appropriate fluid cell, conduct experiments at ambient temperatures in buffer solution.

3.2 Collecting Force-Distance (F–D) Curves in SMFS (See Note 3)

1. Set the AFM for contact mode imaging.
2. Engage the AFM with the scan area set to 0 μm in order to avoid contamination of the AFM probe.
3. Once the AFM is engaged, retract the AFM probe from the mica surface, and set the scan area to the maximum.
4. Slowly extend the AFM probe to the mica surface until contact is made. Adjust settings so that sufficient force is applied by the probe to maintain contact with the sample surface but minimized so that the sample is not deformed or disrupted. Typically, about 100 pN or less is sufficient. Scan rates and gains should also be optimized. Scan rates of 4–6 Hz usually are satisfactory.
5. Zoom in on a very small area of exposed mica that does not have any adsorbed material. Obtain a *F–D* curve to check cleanliness of the AFM probe, and determine the deflection

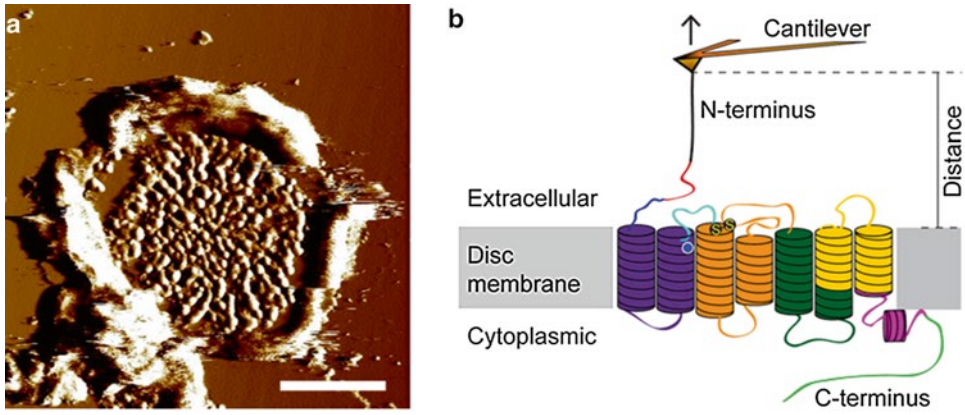

Fig. 1 (**a**) An AFM deflection image of a ROS disc membrane adsorbed on mica. Scale bar, 500 nm. (**b**) Illustration of a SMFS experiment. The AFM probe attached to a flexible cantilever is nonspecifically bound to the N-terminal end of rhodopsin embedded in ROS disc membranes. As the AFM probe is retracted from the sample surface, rhodopsin is mechanically unfolded in a stepwise manner. The stable structural segments of rhodopsin are highlighted in different colors. This figure was originally published in the Journal of Biological Chemistry, Kawamura, S., Colozo, A.T., Ge, L., et al. "Structural, energetic, and mechanical perturbations in rhodopsin mutant that causes congenital stationary night blindness," 2012, *J Biol Chem* 287, 21826–35. Copyright holder, the American Society for Biochemistry and Molecular Biology

sensitivity of the cantilever. The AFM probe must be clean to obtain good quality *F–D* curves.

6. Zoom out to the maximum scan area, and survey the adsorbed membranes on the surface of the mica.
7. Zoom in to the central region of an adsorbed ROS disc membrane (Fig. 1a) (*see* **Note 4**). An area of the ROS disc membrane filling a frame size of 40–60 nm is suitable for manual *F–D* curve collection.
8. Collect *F–D* curves from the zoomed in area. *F–D* curve collection begins by extending the AFM probe so that it pushes into the membrane with a force of 0.5–1 nN for about 1 s. This contact allows the probe to form nonspecific interactions with rhodopsin that is sufficiently strong to allow for protein unfolding. Retract the AFM probe at a constant pulling velocity to unfold a rhodopsin molecule (Fig. 1b). *F–D* curves record unfolding events that occur during this retraction (Fig. 2a, b) (*see* **Notes 5**–**7**).
9. For DFS analysis, *F–D* curves must be collected at different pulling velocities. Pulling velocities in the range of 100–6,000 nm/s have been previously used.

3.3 Analysis of SMFS Data

1. Collected *F–D* curves must be exported and analyzed in appropriate graphing software. Analysis procedures outlined here are based on those conducted in IGOR Pro (*see* **Notes 8** and **9**).

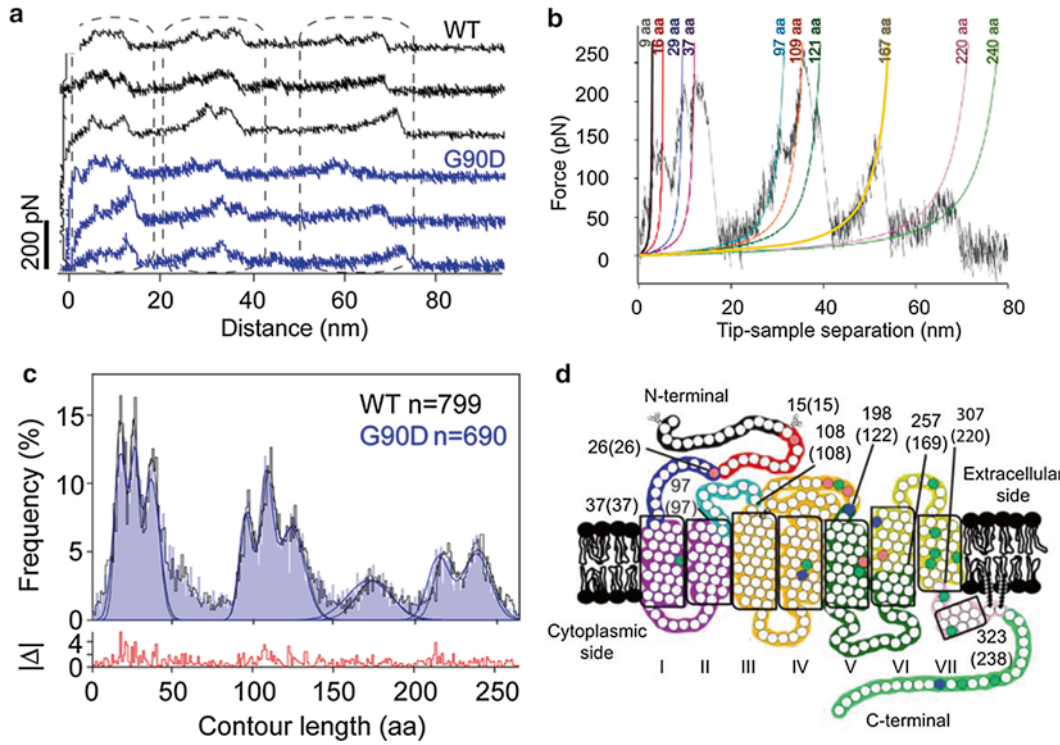

Fig. 2 (**a**) A set of *F–D* curves obtained from ROS disc membranes from mice expressing wild-type (*black*) or G90D mutant rhodopsin (*blue*). Each *F–D* curve records the unfolding events of a single rhodopsin molecule. (**b**) A single *F–D* curve analyzed by the WLC model. Each peak in the *F–D* curve has been fit with the WLC model (*colored curves*). Contour lengths obtained from the fit are denoted. (**c**) A histogram of contour lengths obtained from WLC model analyses of *F–D* curves obtained from ROS disc membranes containing wild-type (*black*) or G90D mutant (*blue*) rhodopsin. The histogram shows the fitting of peaks to a Gaussian function to determine the mean contour length of major force peaks occurring with high frequency. (**d**) Stable structural segments are highlighted on the secondary structure of rhodopsin by different colors. The boundary amino acid residues are denoted with the corresponding contour length determined from contour length histogram analysis in *parentheses*. Panels **b** and **d** were originally published in Biochemistry, Kawamura, S., Colozo, A.T., Müller, D.J., et al. "Conservation of molecular interactions stabilizing bovine and mouse rhodopsin," 2010, *Biochemistry* 49, 10412–20. Copyright holder, the American Chemical Society. Panels **a** and **c** were originally published in the Journal of Biological Chemistry, Kawamura, S., Colozo, A.T., Ge, L., et al. "Structural, energetic, and mechanical perturbations in rhodopsin mutant that causes congenital stationary night blindness," 2012, *J Biol Chem* 287, 21826–35. Copyright holder, the American Society for Biochemistry and Molecular Biology

2. Select *F–D* curves that correspond to the unfolding of a single rhodopsin molecule from the N-terminal end (Fig. 2a, b) (*see* **Notes 10** and **11**).
3. Overlay *F–D* curves. Exclude *F–D* curves that do not exhibit similar patterns of force peaks. *F–D* curves that correspond to the unfolding of rhodopsin will exhibit similar patterns of force peaks. Curves are aligned using frequently observed peaks as a reference (*see* **Note 12**).

4. Once *F–D* curves are aligned, individual curves are analyzed using the worm-like-chain (WLC) model [20]. Each force peak is fit with the WLC model to determine the contour length (L) (Fig. 2b) (*see* **Note 13**).
5. A histogram of contour lengths is generated from fits of each force peak in all *F–D* curves analyzed for a single condition (Fig. 2c). The histogram is fit by a Gaussian function to determine the most frequently observed populations of contour lengths (*see* **Note 14**). Force peaks are classified according to these populations of contour lengths determined from histograms.
6. Using the contour length information, map the location of stable structural segments on the secondary structure of rhodopsin (Fig. 2d) (*see* **Note 15**).
7. For each class of force peaks, determine the rupture forces for the corresponding stable structural segment (*see* **Note 16**). Generate a histogram of rupture forces, and fit the histogram with a Gaussian function to determine the most probable rupture force for a given stable structural segment. Separate histograms should be generated for each data set obtained from different pulling velocities.

3.4 Analysis of DFS Data

1. For each class of force peaks, determine the loading rate. The loading rate is the product of the pulling velocity and the effective spring constant. The effective spring constant can be determined by taking the slope of the force peak prior to rupture. Generate a histogram of loading rates, and fit the histogram with a Gaussian function to determine the most probable loading rate for a given class of force peaks. Separate histograms should be generated for each data set obtained from different pulling velocities.
2. For each class of force peaks, generate a DFS plot by plotting the most probable rupture force versus the logarithm of the most probable loading rate (Fig. 3).
3. Fit data in the DFS plot with the Bell-Evans model to compute parameters that describe the underlying energy landscape of unfolding a stable structural segment (Fig. 4) [21]. Energy landscape parameters computed from this fitting include x_u, the distance from the free-energy minimum to the transition-state barrier, and k_u, the rate of unfolding in the absence of applied force (*see* **Notes 17** and **18**). These parameters provide insights about the conformational variability (x_u) and kinetic stability (k_u) of a stable structural segment.
4. Parameters determined from fits of the DFS data to Eq. 2 are used to determine the height of the energy barrier, ΔG, and mechanical spring constant, κ (*see* **Notes 19** and **20**). These parameters provide insights about the activation energy (ΔG) and mechanical rigidity (κ) of a stable structural segment.

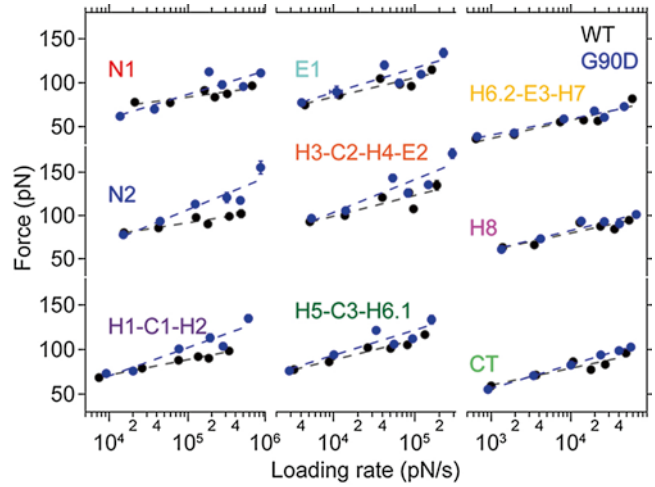

Fig. 3 DFS plots for wild-type (*black*) and G90D mutant (*blue*) rhodopsin. DFS plots for each stable structural segment of rhodopsin are shown. Data were fit using the Bell-Evans model (Eq. 2). This figure was originally published in the Journal of Biological Chemistry, Kawamura, S., Colozo, A.T., Ge, L., et al. "Structural, energetic, and mechanical perturbations in rhodopsin mutant that causes congenital stationary night blindness", 2012, *J Biol Chem* 287, 21826–35. Copyright holder, the American Society for Biochemistry and Molecular Biology

4 Notes

1. Procedures outlined here are based on ROS disc membrane preparations obtained from the eyes of 15 mice. Both frozen and freshly prepared membranes have been investigated and shown to give similar results.
2. Buffer composition can have a significant effect on SMFS results. Thus, only results from data obtained in the same buffer should be compared.
3. For general considerations pertaining to AFM imaging and SMFS of membrane proteins, the reader can refer to detailed reports published previously [16–18].
4. ROS disc membranes have a distinct morphology and are easily recognizable (Fig. 1a). About 90 % of all proteins in the ROS disc membrane are rhodopsin [4]. Rhodopsin is found throughout the ROS disc membrane except in the rim region, where there is a high concentration of structural proteins [22]. Thus, SFMS studies are conducted in the central region of disc membranes.
5. When *F–D* curves are collected manually, the AFM probe is set to continuously undergo extension/retraction cycles. The drift of the piezoelectric scanner allows for sampling of different regions in the membrane. Only 1–10 % of the extension/retraction cycles will result in an interaction between the AFM

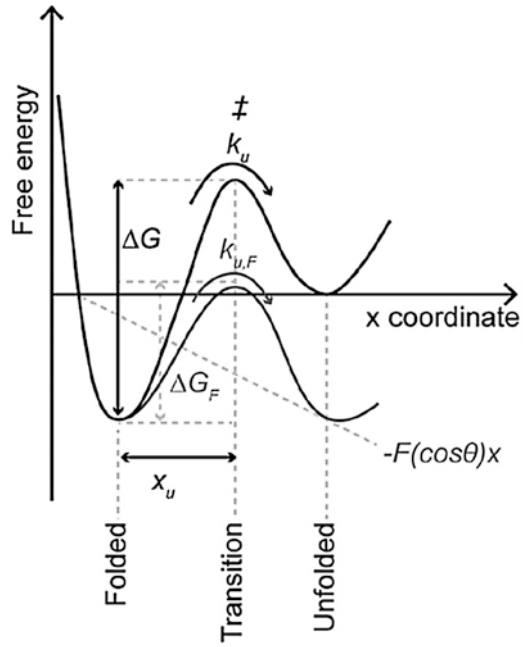

Fig. 4 An unfolding energy landscape for a stable structural segment. The folded state of a stable structure segment is separated from the unfolded state by a free-energy barrier. In the absence of an externally applied force (i.e., at equilibrium), the folded structure unfolds with a certain rate (k_u) by overcoming the transition state (*double dagger*). The distance from the folded state to the transition state is characterized by x_u, and the height of the unfolding free-energy barrier is characterized by ΔG. According to the Bell-Evans model, an externally applied force (F) tilts the energy landscape due to the mechanical energy ($-F(\cos\theta)x$), thereby lowering the free-energy barrier (ΔG_F) that separates the folded state from the unfolded state and increasing the rate of unfolding (k_{uF}). Lowering of the free-energy barrier is dependent on the pulling direction (x) and the angle (θ) of the externally applied force (F). This figure was originally published in the Journal of Biological Chemistry, Kawamura, S., Colozo, A.T., Ge, L., et al. "Structural, energetic, and mechanical perturbations in rhodopsin mutant that causes congenital stationary night blindness", 2012, *J Biol Chem* 287, 21826–35. Copyright holder, the American Society for Biochemistry and Molecular Biology

probe and polypeptide chain of rhodopsin sufficiently strong for protein unfolding [16]. The *z*-position of the piezoelectric scanner must be monitored and adjusted to maintain the appropriate force with which the AFM probe pushes into the membrane. Automation of *F–D* curve collection is possible with AFMs that have an *x*-*y*-*z* closed-loop piezoelectric scanner (e.g., [23]).

6. When the rate of *F–D* curve collection begins to decrease, a different region of the same ROS disc membrane or a different ROS disc membrane should be selected. Adsorbed ROS disc membranes are typically investigated by SMFS for 30–60 min.
7. The sidedness of ROS disc membranes adsorbed on mica was previously determined utilizing a strategy that involved the digestion of membranes with endoproteinase Glu-C [5]. The majority of ROS disc membranes adsorb onto mica exposing

the extracellular surface of rhodopsin. Thus, *F–D* curves obtained from disc membranes represent unfolding of rhodopsin from the N-terminus.

8. Homemade macros can be created in IGOR Pro to help speed up the manual analysis process. Automated algorithms for analysis of *F–D* curves have been attempted (e.g., [23–25]), however, at the moment these procedures are not suitable for analysis of rhodopsin data.
9. *F–D* curves should plot the retraction curve with the tip-sample distance on the *x*-axis and force on the *y*-axis (Fig. 2a, b). Accurate values for tip-sample distance and force require proper determination of the deflection sensitivity and spring constant of the AFM probe.
10. *F–D* curves that represent pulling of a shorter length of polypeptide chain are ambiguous, as they can arise from multiple sources. Since attachment of the AFM probe to rhodopsin occurs in a nonspecific manner, the probe can make contact at any point of the polypeptide chain of rhodopsin that is exposed to the probe. Pulling from these regions will result in shorter *F–D* curves. Shorter curves can also arise from a loss of contact between the AFM probe and N-terminal region of rhodopsin prior to the unfolding of the entire polypeptide chain.
11. Rhodopsin contains a conserved disulfide bond between Cys110 and Cys187. As a result, two major populations of curves are observed [5]. One corresponding to the unfolding of the receptor where the disulfide bond remains intact (curve length about 65 nm, Fig. 2a, b) and another population corresponding to the unfolding of the receptor in the absence of this disulfide bond (curve length about 95 nm). Since the native receptor contains a disulfide bond, the shorter length curves have been the focus of most of the studies to date.
12. Unfolding of rhodopsin results in a sequence of force peaks in *F–D* curves (Fig. 2a, b). Each force peak represents the sequential unfolding of a stable structural segment of the membrane protein [3]. The last force peak in rhodopsin *F–D* curves is presumed to arise from palmitate groups that anchor two cysteine residues in the C-terminal region [7].
13. The WLC model describes the stretching of a polymer such as the polypeptide chain of proteins. The WLC model expression used in analyses is

$$F = \frac{k_B T}{p}\left(\frac{1}{4\left(1-\frac{x}{L}\right)^2} - \frac{1}{4} + \frac{x}{L}\right) \quad (1)$$

A persistence length (p) of 0.4 nm and a monomer length (x) of 0.36 nm are used [26]. F denotes force, k_B the Boltzmann constant, and T the temperature. Each force peak in a F–D curve is fit by Eq. 1 to determine the contour length (L) (Fig. 2b). The contour length is converted to units of amino acid residues using a value of 0.36 nm for the length of a single amino acid residue.

14. Frequently observed populations of contour lengths were originally determined by manually grouping force peaks into classes (e.g., [5–7]). To more accurately determine frequently observed populations of contour lengths, contour length histograms were utilized in subsequent studies. Individual peaks in histograms were initially fit manually by a Gaussian function to reveal the mean contour length of major force peaks occurring with high frequency (e.g., [10, 13]) (Fig. 2c). More recently, peaks in histograms were fit simultaneously using a single Gaussian mixture model [14]. This most recent method avoids bias present in previous methods and was able to resolve an additional population of frequently observed contour lengths. To improve the resolution of the histograms, data collected at all pulling velocities can be combined. The frequently observed populations of contour lengths appear to be independent of the pulling velocity [10].
15. The contour length provides an estimate for the number of amino acid residues stretched above the sample surface (Fig. 1b). This information, along with the location of secondary structural elements and thickness of the lipid bilayer (≈4 nm), is used to determine the location of unfolding barriers in rhodopsin and to map the location of stable structural segments in rhodopsin [27] (Fig. 2d).
16. The height of force peaks in F–D curves represents the rupture force for a stable structural segment. The most probable rupture force for a class of force peaks is an indicator of the relative stability of the corresponding stable structural segment.
17. A linear relationship observed in DFS plots indicates that a single energy barrier separates the folded and unfolded states of a stable structural segment (Figs. 3 and 4).
18. The Bell-Evans model can be expressed as a function of the most probable rupture force, F_P:

$$F_p = \frac{k_B T}{x_u} \ln\left(\frac{x_u r_f}{k_B T k_u}\right) \tag{2}$$

In Eq. 2, x_u is the distance from the free-energy minimum to the transition-state barrier, k_u is the rate of unfolding in the absence of applied force, and r_f is the loading rate. Data in

DFS plots are fit by Eq. 2 using a nonlinear least squares algorithm to determine x_u and k_u (Fig. 3).

19. The height of the free-energy barrier (ΔG) can be determined using the Arrhenius equation:

$$\Delta G = -k_B T \ln\left(\tau_A k_u\right) \tag{3}$$

In Eq. 3, $1/\tau_A$ is the Arrhenius frequency factor describing the diffusive relaxation time [28]. A value of 10^{-9} s for τ_A is typically used [29].

20. The mechanical spring constant (κ) can be determined using Eq. 4 [9, 30]:

$$\kappa = \frac{2\Delta G}{x_u^{\,2}} \tag{4}$$

Acknowledgments

This work was funded by the European Community's Seventh Framework Programme [*FP7/2007–2013*] under *grant agreement* n° [211800], Swiss National Science Foundation, National Institutes of Health (R01EY021731), and Research to Prevent Blindness (Career Development Award).

References

1. Müller DJ (2008) AFM: a nanotool in membrane biology. Biochemistry 47:7986–7998
2. Whited AM, Park PS (2014) Atomic force microscopy: a multifaceted tool to study membrane proteins and their interactions with ligands. Biochim Biophys Acta 1838:56–68
3. Kedrov A, Janovjak H, Sapra KT et al (2007) Deciphering molecular interactions of native membrane proteins by single-molecule force spectroscopy. Annu Rev Biophys Biomol Struct 36:233–260
4. Papermaster DS, Dreyer WJ (1974) Rhodopsin content in the outer segment membranes of bovine and frog retinal rods. Biochemistry 13:2438–2444
5. Sapra KT, Park PS, Filipek S et al (2006) Detecting molecular interactions that stabilize native bovine rhodopsin. J Mol Biol 358:255–269
6. Park PS, Sapra KT, Kolinski M et al (2007) Stabilizing effect of Zn^{2+} in native bovine rhodopsin. J Biol Chem 282:11377–11385
7. Park PS, Sapra KT, Jastrzebska B et al (2009) Modulation of molecular interactions and function by rhodopsin palmitylation. Biochemistry 48:4294–4304
8. Evans E (2001) Probing the relation between force–lifetime–and chemistry in single molecular bonds. Annu Rev Biophys Biomol Struct 30:105–128
9. Sapra KT, Park PS, Palczewski K et al (2008) Mechanical properties of bovine rhodopsin and bacteriorhodopsin: possible roles in folding and function. Langmuir 24:1330–1337
10. Kawamura S, Colozo AT, Müller DJ et al (2010) Conservation of molecular interactions stabilizing bovine and mouse rhodopsin. Biochemistry 49:10412–10420
11. Mendes HF, van der Spuy J, Chapple JP et al (2005) Mechanisms of cell death in rhodopsin retinitis pigmentosa: implications for therapy. Trends Mol Med 11:177–185
12. Sieving PA, Richards JE, Naarendorp F et al (1995) Dark-light: model for nightblindness from the human rhodopsin Gly-90–>Asp mutation. Proc Natl Acad Sci U S A 92:880–884
13. Kawamura S, Colozo AT, Ge L et al (2012) Structural, energetic, and mechanical perturbations in rhodopsin mutant that causes congenital stationary night blindness. J Biol Chem 287:21826–21835

14. Kawamura S, Gerstung M, Colozo AT et al (2013) Kinetic, energetic, and mechanical differences between dark-state rhodopsin and opsin. Structure 21:426–437
15. Zocher M, Fung JJ, Kobilka BK et al (2012) Ligand-specific interactions modulate kinetic, energetic, and mechanical properties of the human beta2 adrenergic receptor. Structure 20:1391–1402
16. Müller DJ, Engel A (2007) Atomic force microscopy and spectroscopy of native membrane proteins. Nat Protoc 2:2191–2197
17. Fotiadis D, Müller DJ (2013) High-resolution imaging of 2D outer membrane protein F crystals by atomic force microscopy. Methods Mol Biol 955:461–474
18. Sapra KT (2013) Atomic force microscopy and spectroscopy to probe single membrane proteins in lipid bilayers. Methods Mol Biol 974:73–110
19. Butt H-J, Jaschke M (1995) Calculation of thermal noise in atomic force microscopy. Nanotechnology 6:1–7
20. Bustamante C, Marko JF, Siggia ED et al (1994) Entropic elasticity of lambda-phage DNA. Science 265:1599–1600
21. Evans E (1999) Looking inside molecular bonds at biological interfaces with dynamic force spectroscopy. Biophys Chem 82:83–97
22. Molday RS, Hicks D, Molday L (1987) Peripherin. A rim-specific membrane protein of rod outer segment discs. Invest Ophthalmol Vis Sci 28:50–61
23. Bosshart PD, Casagrande F, Frederix PL et al (2008) High-throughput single-molecule force spectroscopy for membrane proteins. Nanotechnology 19:384014
24. Bosshart PD, Frederix PL, Engel A (2012) Reference-free alignment and sorting of single-molecule force spectroscopy data. Biophys J 102:2202–2211
25. Struckmeier J, Wahl R, Leuschner M et al (2008) Fully automated single-molecule force spectroscopy for screening applications. Nanotechnology 19:384020
26. Rief M, Gautel M, Oesterhelt F et al (1997) Reversible unfolding of individual titin immunoglobulin domains by AFM. Science 276:1109–1112
27. Müller DJ, Kessler M, Oesterhelt F et al (2002) Stability of bacteriorhodopsin alpha-helices and loops analyzed by single-molecule force spectroscopy. Biophys J 83:3578–3588
28. Dietz H, Rief M (2004) Exploring the energy landscape of GFP by single-molecule mechanical experiments. Proc Natl Acad Sci U S A 101:16192–16197
29. Bieri O, Wirz J, Hellrung B et al (1999) The speed limit for protein folding measured by triplet-triplet energy transfer. Proc Natl Acad Sci U S A 96:9597–9601
30. Howard J (2001) Mechanics of motor proteins and the cytoskeleton. Sinauer Associates, Inc., Sunderland, MA

Part IV

Rhodopsin Supramolecular Organization and Its Complexes with Partner Proteins

Chapter 13

High-Resolution Atomic Force Microscopy Imaging of Rhodopsin in Rod Outer Segment Disk Membranes

Patrick D. Bosshart, Andreas Engel, and Dimitrios Fotiadis

Abstract

Atomic force microscopy (AFM) is a powerful imaging technique that allows recording topographical information of membrane proteins under near-physiological conditions. Remarkable results have been obtained on membrane proteins that were reconstituted into lipid bilayers. High-resolution AFM imaging of native disk membranes from vertebrate rod outer segments has unveiled the higher-order oligomeric state of the G protein-coupled receptor rhodopsin, which is highly expressed in disk membranes. Based on AFM imaging, it has been demonstrated that rhodopsin assembles in rows of dimers and paracrystals and that the rhodopsin dimer is the fundamental building block of higher-order structures.

Key words Atomic force microscopy, Disk membrane, G protein-coupled receptor, High-resolution imaging, Rhodopsin, Rod outer segment

1 Introduction

During the last three decades, atomic force microscopy (AFM) has developed into a versatile and extremely useful tool in biophysical research to study membrane proteins in their native environment, i.e., in the lipid bilayer and under near-physiological conditions (reviewed in [1]). In contact-mode AFM, a sharp probe located at the end of a flexible cantilever is moved over a surface using a piezoelectric scanner. Simultaneously, the cantilever deflection that is caused by the probe–sample interaction is measured by an optical system. In order to keep the cantilever deflection at a constant value, i.e., at a constant force, the deflection signal drives a feedback system, which positions the sample vertically. The surface topography is computed from the vertical movement of the piezoelectric scanner. The lateral resolution is influenced by the probe geometry that raster-scans the surface, and it can reach values of up to 5 Å, whereas the vertical resolution can be even better, e.g., 1 Å [2]. The advantage of AFM is that it does not require any staining that might perturb the

Beata Jastrzebska (ed.), *Rhodopsin: Methods and Protocols*, Methods in Molecular Biology, vol. 1271,
DOI 10.1007/978-1-4939-2330-4_13,

ultrastructure of the specimen. Furthermore, the instrument can be operated in an aqueous environment, which allows the biological sample to remain completely hydrated, at normal pressure, and at physiological and near-physiological temperatures.

Particularly, the laboratories of Paul Hansma, Andreas Engel, and Daniel J. Müller advanced the application of AFM in biology. In membrane protein research, AFM was applied to investigate topography (reviewed in [1]), conformational dynamics [3–8], dynamic diffusion [9, 10], assembly processes [11], and oligomeric states [12–21] of reconstituted membrane proteins. Furthermore, AFM in combination with elaborated membrane isolation procedures even allowed studying the supramolecular organization of membrane proteins in their native membranes [22–24]. A remarkable breakthrough was achieved when Fotiadis et al. [22] were able to unveil by infrared-laser AFM the packing of the G protein-coupled receptor (GPCR) rhodopsin in disk membranes of native vertebrate retina rod outer segments (ROS). With the help of AFM imaging, rhodopsin has been shown to assemble in rows of dimers and paracrystals, which was in stark contrast to the old dogma of monomeric rhodopsin.

This chapter introduces sample preparation methods and AFM measuring procedures that are crucial for acquiring high-resolution topography images of rhodopsin in ROS disk membranes. The presented protocols can also be applied with minor modifications to any other membrane protein when it is incorporated into a lipid bilayer at a sufficiently high surface density.

2 Materials

2.1 Preparation of Mica Supports for Sample Adsorption (See Note 1)

1. Flat stainless magnetic steel disks with a diameter of 12 mm (Ted Pella, Inc.).
2. 0.25 mm-thick single-side etched Teflon sheets (Maag Technic AG).
3. 0.3–0.6 mm-thick mica sheets (Mica House).
4. “Punch & Die” Set (Precision Brand Products, Inc.).
5. Ethanol (puriss. p.a., ≥99.8 %).
6. Hydrochloric acid (fuming, 37 %).
7. Cyanoacrylate-based instant adhesive (e.g., Loctite 406 Superglue, Henkel Corp.).
8. Two-part epoxy adhesive (e.g., Araldite Rapid, Huntsman International LLC).
9. Adhesive tape (Scotch Magic Tape, 3M).

2.2 Disk Membranes and Buffers

1. The isolation of ROS disk membranes containing rhodopsin was described in [24]. Samples must be stored at 4 °C and have to be protected from exposure to light.
2. Adsorption buffer: 2 mM Tris–HCl, pH 7.4.
3. Imaging buffer: 150 mM KCl, 25 mM $MgCl_2$, 20 mM Tris–HCl, pH 7.8.
4. 0.2 μm-pore size syringe filters (e.g., Minisart syringe filters, Sartorius AG).
5. Sterile syringes.

2.3 Atomic Force Microscope and Accessories

1. Commercial atomic force microscope (AFM) from the multimode series equipped with a 120-μm scanner (J scanner) and a liquid cell that holds the cantilever chip (Bruker Biosciences Corporation). The AFM has to be equipped with an infrared laser to prevent rhodopsin from bleaching.
2. Image processing software (e.g., NanoScope Control software, SEMPER image processing system [25]).
3. Active vibration isolation platform (Halcyonics GmbH) (*see* **Note 2**).
4. Light and sound protection cabinet (custom-built) (*see* **Note 2**).
5. Oxide-sharpened triangular silicon nitride cantilevers of 100-μm length and a nominal spring constant of $k = 0.08$ N/m (OMCL TR400PSA, Olympus Optical Co., Ltd.). These cantilevers are equipped with probes with a radius of <10 nm (*see* **Note 3**).
6. Red light-transmitting filter foil (Rosco Supergel 027 "Medium Red", Rosco) (*see* **Note 2**).

3 Methods

3.1 Preparation of Mica Supports for Sample Adsorption (See Note 1)

1. Incubate the steel disks in fuming hydrochloric acid overnight. The steel disks have to be rinsed extensively with ultrapure water to remove hydrochloric acid after overnight incubation.
2. Prepare mica disks with a diameter of 6 mm as well as Teflon disks of 13 mm diameter using the "Punch & Die" Set.
3. Thoroughly clean the stainless steel disks and the Teflon disks with ethanol and ultrapure water. Dry them using a lint-free paper wipe.
4. Glue the etched side of the Teflon sheet on the steel disk using instant adhesive.
5. Glue the mica disk on the Teflon disk using the two-part epoxy adhesive.
6. The prepared supports should be cured for at least 24 h.

3.2 Adsorption of Isolated Disk Membranes on Mica and Sample Mounting

1. Prepare adsorption and imaging buffer. Remove any potential sub-μm particles from the solutions by filtering the freshly prepared buffers through a 0.22 μm-pore size syringe filter (*see* **Note 4**).
2. Rinse the support with ethanol and ultrapure water (18 MΩ cm). Subsequently, dry the support with nitrogen gas.
3. Rinse the AFM fluid cell with ultrapure water, and clean it using a dishwashing detergent. Rinse the fluid cell extensively with ethanol and ultrapure water to remove the detergent completely. Dry the cell with nitrogen gas.
4. Remove upper layers of the mica disk using adhesive tape until an intact layer was removed (*see* **Notes 1** and **4**). This exposes a clean and atomically flat surface. Do not expose the fresh surface too long to ambient conditions because this might lead to contamination. Therefore, immediately proceed with the next step.
5. Apply 30 μl of adsorption buffer to the freshly cleaved mica disk, add 3 μl of isolated disk membranes, and mix it carefully using a pipet.
6. Incubate 15–60 min depending on the concentration of the disk membranes stock.
7. During sample adsorption, mount the cantilever firmly in the fluid cell, and fix the cell in the AFM head. Fill the fluid channels with 60 μl of imaging buffer each.
8. After incubation, remove disk membranes that have not adsorbed to the mica surface by removing 20 μl of the buffer-sample mixture and re-adding 20 μl of imaging buffer. Repeat the washing procedure at least five times.
9. Transfer the support onto the piezoelectric scanner without disturbing the buffer droplet.
10. Mount the AFM head on the microscope.

3.3 Operation of the AFM

1. Decrease the distance between the fluid cell and the support until the cantilever is completely immersed in the buffer droplet.
2. Make sure that there are no air bubbles in the buffer because this leads to severe cantilever drift.
3. Align the laser on the cantilever such that the detection sensitivity of the system is high (i.e., low deflection sensitivity value). Furthermore, optimize the optical system (i.e., position of the mirror) such that the photodiode signal is maximal.
4. Let the AFM equilibrate until the drift of the cantilever deflection level is minimal.
5. Approach the AFM cantilever to the surface. For that purpose the deflection set point, which is used to determine the contact between the AFM stylus tip and the surface, should not be chosen too high to avoid tip damage. The scan size has to be

set to 0 μm to avoid that the approaching AFM stylus becomes contaminated by the biological specimen or even damaged due to high lateral forces when touching the surface. Before scanning the sample surface, the operating cantilever deflection set point is set to forces <0.5 nN. Overview images at low magnification (frame size >1 μm) are acquired at forces <0.5 nN. However, for high-resolution imaging, the applied force has to be reduced to values <0.1 nN (frame size <1 μm). The forces must be adjusted manually to compensate for thermal drift arising from cantilever bending that is induced by different thermal expansion coefficients of the cantilever material and its metal coating.

6. Record two frames of 512 by 512 pixels either showing height or deflection signal in trace and/or retrace scanning direction.
7. Set the scan rate to ~4–6 Hz (i.e., ~4–6 lines per second).
8. The (integral and proportional) gains of the feedback loop must be optimized by increasing them stepwise until the AFM cantilever oscillates. This can be detected acoustically and observed as fringes in the cantilever deflection image. At this point reduce the gains until cantilever oscillations are not detectable any more. It is important that cantilevers do not oscillate at low forces since this would impede the acquisition of high-resolution images and might lead to irreversible sample damage.
9. At low magnification (scan area size >1 μm), record height and deflection signals as shown in Fig. 1 (*see* **Note 5**).
10. From low-magnification images, determine the adsorption density, sample homogeneity, and purity (*see* **Note 4**). Furthermore, such images serve to measure the dimensions (e.g., size, height) of adsorbed disk membranes (*see* Subheading 3.4 for procedure).
11. When approaching higher magnification (scan area size <1 μm), exclusively acquire height signals in trace and retrace scanning directions. Compare the two scan directions with each other to judge whether the cantilever deforms the sample in either one direction. Minimize possible deformations by decreasing the applied force and by adapting the scanning rate. If deformations still persist after optimization of imaging conditions, adapt the imaging buffer (*see* **Note 6**).
12. At high magnification, reduce the vertical range of the piezoelectric scanner to enhance the vertical resolution by the digitalization of the signal (AD conversion). The imaging force, the gains, and the scanning rate must be continuously checked and optimized to obtain optimal results and to avoid sample damage. Particularly, the deflection set point, which reflects the applied force, must be adjusted due to cantilever drift [26]. For expected results, *see* **Note 7**.

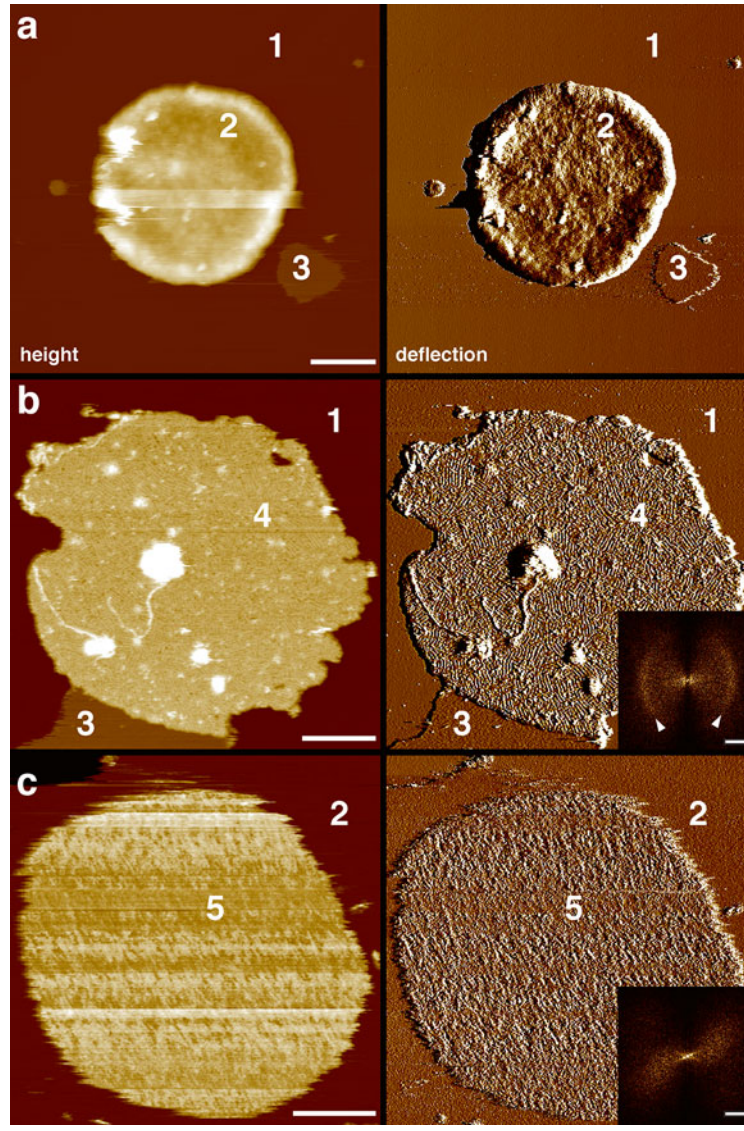

Fig. 1 Morphology of intact ROS disks and topography of osmotically burst disks. Shown are flattened height images (*left panels*) and cantilever deflection images (*right panels*) (*see* Subheading 3.4). (**a**) Image of an intact disk with a typical height of 16–17 nm from the mica surface. Three different surface types can be distinguished (type *1–3*): atomically flat mica surface (*see* **Note 4**) (type *1*), intact double-layered disk (type *2*), and lipid bilayer (type *3*). (**b**) Single-layered spread-flattened disk membrane showing three different surface types: atomically flat mica (type *1*), membrane surface with paracrystalline arrays of rhodopsin (type *4*), and lipid bilayer (type *3*). The *inset* in the *right panel* shows a power spectrum (*see* **Note 8**) with a discernible ring (*arrowheads*) at $(8.4\ \text{nm})^{-1}$, which is characteristic for regularly packed rows of rhodopsin dimers. (**c**) Single-layered disk membrane, which does not exhibit paracrystalline rows of rhodopsin (type *5*) as can be seen from the power spectrum in the *right panel*. Scale bars represent 250 nm (**a**), 200 nm (**b**), $(15\ \text{nm})^{-1}$ (**b**, *inset*), 150 nm (**c**), and $(15\ \text{nm})^{-1}$ (**c**, *inset*)

3.4 Image Processing and Analysis

1. Before further analysis, AFM raw images must be processed, e.g., with the NanoScope Control software, to compensate for sample tilt. For this purpose use the *Flatten* tool of the NanoScope Control software, which fits a user-defined polynomial to each data line and subtracts it from the image data. Exclude regions where membranes or other high objects (e.g., contaminants) are located from the flattening process. Adjust the color range of the height or deflection image to make objects of interest clearly discernible.
2. Determine the height of the disk membranes (*see* **Note 5**) or the height of the proteins' mass protruding above the membrane using the *Section analysis* tool of the NanoScope Control software.
3. Extract lattice parameters of (para)crystalline areas (*see* **Note 8**). This can be computed using the *Spectrum 2D* tool of the NanoScope Control software or image processing programs (e.g., SEMPER image processing system [25]).

4 Notes

1. Preparation of sample supports
   Pickling (incubation) of the stainless steel disks in fuming hydrochloric acid removes surface impurities (e.g., heavy metals, stains, inorganic contaminants, rust). Work in a fume hood and wear appropriate eye and skin protection. Be aware that hydrochloric acid fume will also corrode other metal surfaces in the laboratory.

   Care must be taken when punching mica disks that they are not too thick because in such cases the mica layers might not be firmly attached to each other particularly at the edges. This leads to uncontrolled cantilever vibrations during approach and imaging, which make the acquisition of high-resolution images impossible. Using a Teflon sheet on top of the stainless steel disk provides a combination of a hydrophilic (mica) and a hydrophobic (Teflon) surface that prevents spreading of the buffer droplet, thus avoiding a shortcut in the piezoelectric scanner. It is important that no air bubbles are produced while mixing the two-part epoxy adhesive, since this leads to support vibrations during imaging. Furthermore, the glue must be distributed uniformly on the mica sheet, and it should be completely cured in order to counteract small support drift movements. The instant adhesive cannot be used to glue the mica on the Teflon sheet. Before cleaving off the upper layers of mica using the adhesive tape, the supports must be cleaned with ethanol and water to remove any contamination that could potentially contaminate the sample and cause

vibrations and drift. According to experimental experience, it is recommended to use exclusively the Scotch Magic Tape (3M). The prepared sample supports can be used until no layers can be cleaved off the mica disks any more.

2. Damping, and sound and light protection
   A setup that protects the microscope from acoustic and vibrational disturbance is a prerequisite for the acquisition of high-resolution AFM images. In the best case the microscope is set up in the basement of the building, whereas this is not absolutely necessary. Furthermore, it is recommended to protect the instrument from any sources that might generate electronic or mechanic noise (e.g., fridge, freezer) or temperature variations (e.g., radiator). Acoustic and vibrational noise can be easily assessed by freeware tools (e.g., applications on smart phones) or by imaging a mica surface at low force and analyzing the cantilever deflection image that is particularly susceptible to acoustic and vibrational noise. Therefore, it is recommended to install the microscope on an active or home-built damping table. For sound protection, the microscope can be covered with a glass bell or the damping table can be put into an acoustic enclosure. When working with light-sensitive samples (e.g., rhodopsin), the room in which the microscope is set up has to be protected from any light contamination: windows must be completely darkened, and computer screens and lamps must be covered with a foil that exclusively transmits light of a wavelength that does not induce any photochemical reactions (e.g., isomerization of 11-*cis*-retinal in rhodopsin).
3. Suitable AFM cantilevers and equipment
   Various AFM cantilevers have been developed, whereas only a limited number of models have physical properties making them useful for contact-mode high-resolution AFM imaging of membrane proteins. The vertical cantilever deflection detection is mainly limited by thermal fluctuations of the cantilever. Therefore, the force applied on the tip by thermal motion is the limiting factor for the minimally detectable force. The amplitude of thermal fluctuations, and thus the lower limit of force detection, can be estimated by treating the cantilever as a damped, simple harmonic oscillator [27, 28]. According to this assumption, cantilevers should be soft (i.e., low spring constant $\leq$0.1 N/m) and should have (high) resonance frequencies in buffer solution such that they can precisely contour surface features at the used scanning speed [29]. Since the recorded topography features always reflect the convolution of the tip geometry with the real surface features, the radius of the AFM cantilever tips must be small and the tip must not contain any defects. Experimentally, oxide-sharpened silicon nitride cantilevers have very good physical and chemical properties

allowing high-resolution imaging of membrane proteins without disturbing the integrity of the sample. The suitability of new types of cantilevers for high-resolution imaging should always be assessed by imaging a well-known test sample such as 2D crystals of bacteriorhodopsin. This sample allows sub-nanometer resolution images to be acquired under optimal conditions [2].

Technological advancement, such as the development of new cantilevers with a sharp stylus and a small tip radius, deflection sensors (e.g., interferometers [30]), high-speed scanning technologies [31–37], and highly sensitive and quantitative imaging modes [38], opens new possibilities to acquire data more effectively or investigate biological processes at various timescales. More sensitive imaging modes improve the control of the tip–sample interaction allowing images to be recorded with small forces (~50 pN [38]) at pN precision, thus reducing tip-induced sample deformation. Although a very high resolution can be achieved with this microscopy technique even under near-physiological conditions, it should not be forgotten that a properly prepared sample is the prerequisite for best results.

4. Suitable AFM supports and sample adsorption
Various ultraflat and chemically inert materials served as adsorption supports for high-resolution AFM imaging of membrane proteins (e.g., mica [39, 40], highly-ordered pyrolytic graphite (HOPG) [4, 39], template-stripped gold or platinum [39], molybdenum disulfide [39]). The small surface corrugation of these materials allows subtle height changes to be measured. HOPG has been used for the adsorption of two-dimensional crystals of bacterial porins [4, 40], which contain a very low amount of lipids. However, for many other samples, it could not be used due to its hydrophobic character. Due to the conducting properties of template-stripped metal surfaces, they have been mainly used for combined topographical and electrochemical recordings [39]. Freshly cleaved mica has proven to be very suitable for the adsorption of most biological membranes due to its atomic flatness and its net negative charge (−0.0025 C/m^2 at neutral pH), which can be manipulated by adjusting pH, electrolyte type, and concentration [40]. For new experiments, adsorption conditions have to be optimized. In the case of mica, the support surface has a negative surface charge density, which might counteract the adsorption of a membrane, which also carries a net negative charge density. The resulting repulsive forces acting between the mica and membrane surfaces can be balanced by raising the electrolyte concentration to build up a counter ion layer on both surfaces. At a certain point, the attractive van der Waals force between the surfaces overcomes the repulsive electrostatic

force, and there is a net attractive force allowing successful adsorption. The theoretical and practical principles of the adsorption of biological molecules to a solid support surface have been extensively investigated [40].

If no membranes are adsorbed onto the mica surface, the amount of adsorbed membranes might have been too low or the composition of the adsorption buffer (i.e., electrolyte type, concentration, or pH) has to be optimized. The observation of a support surface that is contaminated with a "carpet" of small objects (<200 nm) is an indication for either contaminated buffers or impurities in the membrane sample. In the case of contaminated buffers, they must be prepared freshly and filtered. Impurities in the sample might be removed by gentle centrifugation–resuspension cycles or by an improved purification protocol. Insufficiently cleaned equipment (e.g., cantilever holder, forceps) can also contaminate the sample.

5. AFM imaging of ROS disk membranes at low magnification
AFM of isolated disk membranes adsorbed to freshly cleaved mica shows different surface types: the ultraflat background corresponds to the mica surface (Fig. 1a, 1), whereas circular objects with a diameter of 0.9–1.5 μm are intact native disks (Fig. 1a, 2) exposing the cytoplasmic side of the disk membrane to the AFM tip. Completely untextured surfaces correspond to empty lipid bilayers (Fig. 1a, 3), which have a height of 3.7 ± 0.2 nm ($n = 86$) and can be observed as co-purified impurities or at the borders of disk membranes. Furthermore, osmotically burst single-layered disk membranes (Fig. 1b) with an average height of 7.8 ± 0.2 nm ($n = 55$) are found. Bursting occurs during isolation and sample adsorption where the disks are exposed to low ionic strength buffers. At low magnification, the cantilever deflection image provides important information about the surface of membranes such as the markedly textured surface topography of single-layered, paracrystalline membranes consisting of densely packed lines (Fig. 1b, right panel). In addition to the paracrystalline surface (Fig. 1b), another membrane type was also detected but less frequently (Fig. 1c). This membrane type is characterized by a corrugated, irregular, and flexible surface, which impedes AFM imaging at high resolution.

6. Optimizing imaging conditions
Imaging buffer conditions (i.e., type of electrolyte, electrolyte concentration, and pH) must be optimized such that tip–sample interactions do not perturb the sample [41]. The force, which is defined by the deflection set point and is applied to the cantilever tip, should be distributed over a large surface area. The tip apex should barely touch the protein surface. If the ionic strength of the buffer solution is low, electrostatic

forces acting between the tip and the sample decay over more than 100 nm. This can be observed in force–distance curves recorded on a sample where the cantilever deflection increases long before the cantilever is in physical contact with the surface. In contrast to long-range electrostatic interactions, attractive van der Waals forces are short-range and decay over ~1 nm. These forces are independent of pH or ionic strength. By adjusting the buffer solution, the electrostatic force that counteracts the van der Waals attraction can be optimized such that there is no tip-induced sample deformation. It has been shown experimentally that high-resolution topography images can be obtained if there is a very small net repulsive force between the cantilever tip and the sample. Therefore, different electrolyte concentrations have to be screened. If severe sample distortions are observed, the AFM operator should consider changing the imaging buffer but also checking the alignment of the laser on the cantilever. Misalignment can lead to bad deflection sensitivity and thus to extremely high imaging forces. Müller et al. have carefully addressed all crucial steps that are necessary for optimizing the imaging buffer [41].

7. AFM imaging of ROS disk membranes at high magnification
   At high magnification, the membrane shown in Fig. 1b exhibits a highly textured topography consisting of densely packed double rows of protrusions assembling into paracrystals (Fig. 2a). These protrusions correspond to the protein mass of rhodopsin protruding out of the lipid bilayer. In some cases individual dimers break off the regular rows of protrusions indicating that the rhodopsin dimer is the fundamental building block of the paracrystals (Fig. 2b, broken ellipse). Occasionally, single rhodopsin monomers can be observed (Fig. 2b, arrowhead). The packing density of rhodopsin in disk membranes can easily be determined by counting protrusions on AFM topographs (typically between 30,000 and 55,000 per μm^2, average $48{,}300 \pm 8{,}300$ per μm^2 [22]). Well-ordered paracrystals of opsin, which is the 11-*cis*-retinal less form of rhodopsin, are also observed in disk membranes isolated from Rpe65−/− mice (Fig. 2c) [24]. The AFM experiments on opsin (i.e., disk membranes isolated from Rpe65−/− mice) have clearly revealed that the morphology of opsin-containing disk membranes and the supramolecular arrangement were not markedly affected by the absence of the chromophore 11-*cis*-retinal.

8. Evaluation of lattice parameters
   AFM images are suited to measure dimensions of particles, to determine distances between objects, or to evaluate lattice parameters. This can be done by direct measurement in real space or by evaluating a power spectrum, which is proportional to the square of the modulus of the Fourier transform, of a

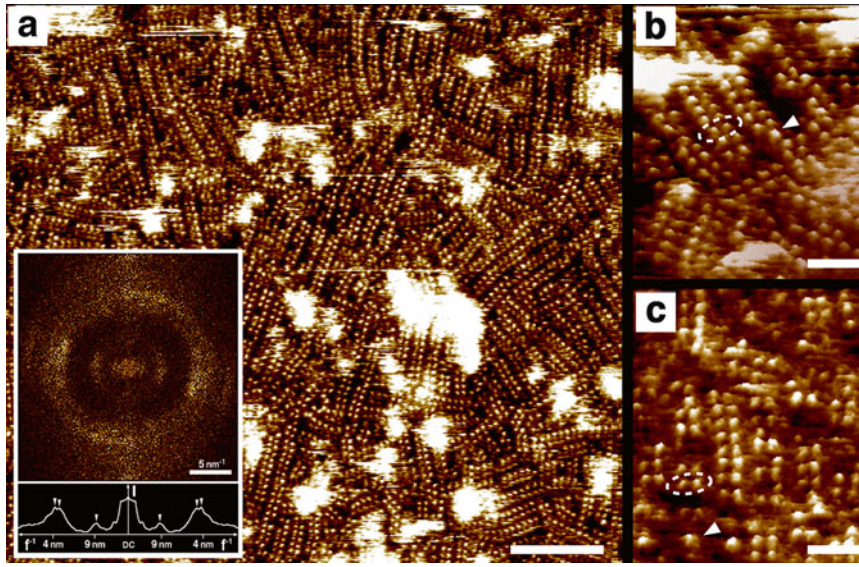

Fig. 2 High-resolution AFM imaging of ROS disk membranes. (**a**) AFM topograph of a densely packed disk membrane containing paracrystalline rows of rhodopsin dimers. The *inset* shows a calculated power spectrum and the angularly averaged power spectrum revealing peaks at $(8.4\ \text{nm})^{-1}$, $(4.2\ \text{nm})^{-1}$ and $(3.8\ \text{nm})^{-1}$ (indicated by *arrowheads*) (*see* **Note 8**). (**b**) Magnification of a region in (**a**) showing rows of rhodopsin dimers and a monomer of rhodopsin (*arrowhead*), which are rarely found. (**c**) Region showing the paracrystalline arrangement of opsin dimers in disk membranes isolated from Rpe65−/− mice. Representative (rhod)opsin dimers and monomers in (**b**) and (**c**) are highlighted by *broken ellipses* and *arrowheads*, respectively. Scale bars represent 50 nm (**a**) and 15 nm (**b** and **c**)

(para)crystalline area. Generally, power spectra can be computed and evaluated using the NanoScope Control software or using an image processing software such as the SEMPER image processing system [25]. Distances between single rhodopsin molecules in paracrystals can be extracted from angularly averaged powder-diffraction patterns computed from topography images of rhodopsin paracrystals (Fig. 2a, *inset*). If a power spectrum is calculated from a biological membrane containing randomly oriented microcrystalline protein domains as observed for disk membranes, spots reflecting the lattice parameters are not detectable. In contrast, discontinuous rings result from the randomly oriented microcrystalline domains. Continuous rings would result if the orientations of the domains covered all possible angular orientations. The precise position of these rings (i.e., frequencies) can be extracted from an angularly averaged power spectrum and provides the lattice distances of microcrystalline domains of rhodopsin molecules in the paracrystals (Fig. 2a, *inset*). The innermost arc peak at $(8.4\ \text{nm})^{-1}$ results from regularly packed rows of rhodopsin dimers, and the ring at $(4.2\ \text{nm})^{-1}$ reflects the second order of the double-row repeat. The axial repeat of paired rhodopsins

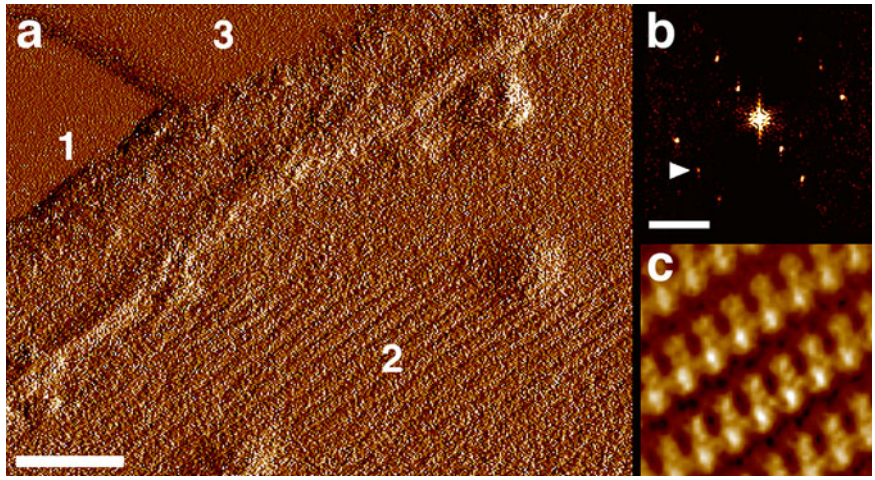

Fig. 3 AFM imaging of ROS disk membranes isolated from Rpe65−/− mice. (**a**) Deflection image of a disk membrane containing rows of opsin dimers. Three different surface types are visible: atomically flat mica (type *1*), opsin paracrystal (type *2*), and empty lipid bilayer (type *3*). (**b**) Power spectrum computed from the paracrystalline region in (**a**). The *arrowhead* highlights the first-order diffraction spot at $(3.8\ \text{nm})^{-1}$. (**c**) Cross-correlation average [42] calculated from 229 motifs extracted from the opsin paracrystal (surface type *2*). The average was generated using the SEMPER image processing system [25] and highlights clearly visible rows of dimers. Scale bars represent 50 nm (**a**) and $(5\ \text{nm})^{-1}$ (**b**). The frame size in panel (**c**) corresponds to 25 nm

that form these rows yields a third ring at $(3.8\ \text{nm})^{-1}$. Because of the remarkably high signal-to-noise ratio in AFM images, distances between single rhodopsin molecules can easily be measured in real space, e.g., the distance between protrusions within rhodopsin dimers: 3.8 ± 0.2 nm ($n = 40$) [22]. In contrast to powder-diffraction patterns, angles between lattice vectors can be measured in real space, e.g., $85 \pm 2°$ ($n = 8$) for (rhod)opsin paracrystals [22]. Ideally, large well-ordered paracrystals can be recorded by AFM, and the lattice parameters can then be directly extracted from calculated power spectra. This is illustrated in Fig. 3, which shows a well-ordered opsin paracrystal imaged on a disk membrane isolated from Rpe65−/− mice. Unit cell parameters in paracrystals in disk membranes isolated from wild-type and Rpe65−/− mice are similar [24]. Finally, determined cell parameters make possible the estimation of the highest possible packing density of (rhod)opsin, i.e., 62,900 monomers per μm^2 [22].

Acknowledgements

Financial support from the University of Bern, the Bern University Research Foundation, the Swiss National Science Foundation, and the National Centres of Competence in Research (NCCR) TransCure and Molecular Systems Engineering is gratefully acknowledged.

References

1. Bippes CA, Müller DJ (2011) High-resolution atomic force microscopy and spectroscopy of native membrane proteins. Rep Prog Phys 74: 086601
2. Stahlberg H, Fotiadis D, Scheuring S et al (2001) Two-dimensional crystals: a powerful approach to assess structure, function and dynamics of membrane proteins. FEBS Lett 504:166–172
3. Müller DJ, Büldt G, Engel A (1995) Force-induced conformational change of bacteriorhodopsin. J Mol Biol 249:239–243
4. Müller DJ, Engel A (1999) Voltage and pH-induced channel closure of porin OmpF visualized by atomic force microscopy. J Mol Biol 285:1347–1351
5. Müller DJ, Sass HJ, Müller SA et al (1999) Surface structures of native bacteriorhodopsin depend on the molecular packing arrangement in the membrane. J Mol Biol 285:1903–1909
6. Yu J, Bippes CA, Hand GM et al (2007) Aminosulfonate modulated pH-induced conformational changes in Connexin26 hemichannels. J Biol Chem 282:8895–8904
7. Mari SA, Köster S, Bippes CA et al (2010) pH-induced conformational change of the β-barrel-forming protein OmpG reconstituted into native *E. coli* lipids. J Mol Biol 396:610–616
8. Mari SA, Pessoa J, Altieri S et al (2011) Gating of the MlotiK1 potassium channel involves large rearrangements of the cyclic nucleotide-binding domains. Proc Natl Acad Sci USA 108:20802–20807
9. Müller DJ, Engel A, Matthey U et al (2003) Observing membrane protein diffusion at subnanometer resolution. J Mol Biol 327: 925–930
10. Yamashita H, Voïtchovsky K, Uchihashi T et al (2009) Dynamics of bacteriorhodopsin 2D crystal observed by high-speed atomic force microscopy. J Struct Biol 167:153–158
11. Muller DJ, Engel A (2008) Strategies to prepare and characterize native membrane proteins and protein membranes by AFM. Curr Opin Colloid Interface Sci 13:338–350
12. Seelert H, Poetsch A, Dencher NA et al (2000) Structural biology: proton-powered turbine of a plant motor. Nature 405:418–419
13. Stahlberg H, Müller DJ, Suda K et al (2001) Bacterial Na^+-ATP synthase has an undecameric rotor. EMBO Rep 2:229–233
14. Cisneros DA, Oesterhelt D, Müller DJ (2005) Probing origins of molecular interactions stabilizing the membrane proteins halorhodopsin and bacteriorhodopsin. Structure 13:235–242
15. Meier T, Yu J, Raschle T et al (2005) Structural evidence for a constant c_{11} ring stoichiometry in the sodium F-ATP synthase. FEBS J 272: 5474–5483
16. Pogoryelov D, Yu J, Meier T et al (2005) The c_{15} ring of the *Spirulina platensis* F-ATP synthase: F1/F0 symmetry mismatch is not obligatory. EMBO Rep 6:1040–1044
17. Pogoryelov D, Reichen C, Klyszejko AL et al (2007) The oligomeric state of c rings from cyanobacterial F-ATP synthases varies from 13 to 15. J Bacteriol 189:5895–5902
18. Fritz M, Klyszejko AL, Morgner N et al (2008) An intermediate step in the evolution of ATPases—a hybrid F_0–V_0 rotor in a bacterial $Na^+F_1F_0$ ATP synthase. FEBS J 275:1999–2007
19. Klyszejko AL, Shastri S, Mari SA et al (2008) Folding and assembly of proteorhodopsin. J Mol Biol 376:34–41
20. Matthies D, Preiss L, Klyszejko AL et al (2009) The c_{13} ring from a thermoalkaliphilic ATP synthase reveals an extended diameter due to a special structural region. J Mol Biol 388:611–618
21. Preiss L, Klyszejko AL, Hicks DB et al (2013) The c-ring stoichiometry of ATP synthase is adapted to cell physiological requirements of alkaliphilic *Bacillus pseudofirmus* OF4. Proc Natl Acad Sci USA 110:7874–7879
22. Fotiadis D, Liang Y, Filipek S et al (2003) Atomic-force microscopy: rhodopsin dimers in native disc membranes. Nature 421:127–128
23. Hoogenboom B, Suda K, Engel A et al (2007) The supramolecular assemblies of voltage-dependent anion channels in the native membrane. J Mol Biol 370:246–255
24. Liang Y, Fotiadis D, Filipek S et al (2003) Organization of the G protein-coupled receptors rhodopsin and opsin in native membranes. J Biol Chem 278:21655–21662
25. Saxton WO (1996) Semper: distortion compensation, selective averaging, 3-D reconstruction, and transfer function correction in a highly programmable system. J Struct Biol 116: 230–236
26. Mueller DJ, Engel A (2007) Atomic force microscopy and spectroscopy of native membrane proteins. Nat Protoc 2:2191–2197
27. Sader JE (1998) Frequency response of cantilever beams immersed in viscous fluids with applications to the atomic force microscope. J Appl Phys 84:64–76
28. Yasumura KY, Stowe TD, Chow EM et al (2000) Quality factors in micron- and submicron-thick cantilevers. J Microelectromech Syst 9:117–125

29. Frederix PTLM, Bosshart PD, Engel A (2009) Atomic force microscopy of biological membranes. Biophys J 96:329–338
30. Hoogenboom BW, Frederix PLTM, Yang JL et al (2005) A Fabry-Perot interferometer for micrometer-sized cantilevers. Appl Phys Lett 86:074101
31. Ando T, Kodera N, Takai E et al (2001) A high-speed atomic force microscope for studying biological macromolecules. Proc Natl Acad Sci USA 98:12468–12472
32. Fantner GE, Schitter G, Kindt JH et al (2006) Components for high speed atomic force microscopy. Ultramicroscopy 106:881–887
33. Picco ML, Bozec L, Ulcinas A et al (2007) Breaking the speed limit with atomic force microscopy. Nanotechnology 18:044030
34. Yamamoto D, Uchihashi T, Kodera N et al (2010) Chapter twenty—High-speed atomic force microscopy techniques for observing dynamic biomolecular processes. In: Walter NG (ed) Biomembranes Part A. Academic, New York, pp 541–564
35. Shibata M, Yamashita H, Uchihashi T et al (2010) High-speed atomic force microscopy shows dynamic molecular processes in photoactivated bacteriorhodopsin. Nat Nanotechnol 5:208–212
36. Uchihashi T, Ando T (2011) High-speed atomic force microscopy and biomolecular processes. Methods Mol Biol 736:285–300
37. Shibata M, Uchihashi T, Yamashita H et al (2011) Structural changes in bacteriorhodopsin in response to alternate illumination observed by high-speed atomic force microscopy. Angew Chem Int Ed 50:4410–4413
38. Medalsy I, Hensen U, Muller DJ (2011) Imaging and quantifying chemical and physical properties of native proteins at molecular resolution by force-volume AFM. Angew Chem Int Ed 50:1–7
39. Frederix PLTM, Bosshart PD, Akiyama T et al (2008) Conductive supports for combined AFM-SECM on biological membranes. Nanotechnology 19:384004
40. Müller DJ, Amrein M, Engel A (1997) Adsorption of biological molecules to a solid support for scanning probe microscopy. J Struct Biol 119:172–188
41. Müller DJ, Fotiadis D, Scheuring S et al (1999) Electrostatically balanced subnanometer imaging of biological specimens by atomic force microscopy. Biophys J 76:1101–1111
42. Saxton WO, Baumeister W (1982) The correlation averaging of a regularly arranged bacterial cell envelope protein. J Microsc 127:127–138

Chapter 14

Detection of Rhodopsin Dimerization In Situ by PIE-FCCS, a Time-Resolved Fluorescence Spectroscopy

Adam W. Smith

Abstract

Rhodopsin self-associates in the plasma membrane. At low concentrations, the interactions are consistent with a monomer-dimer equilibrium (Comar et al., J Am Chem Soc 136(23):8342–8349, 2014). At high concentrations in native tissue, higher-order clusters have been observed (Fotiadis et al., Nature 421: 127–128, 2003). The physiological role of rhodopsin dimerization is still being investigated, but it is clear that a quantitative assessment is essential to determining the function of rhodopsin clusters in vision. To quantify rhodopsin interactions, I will outline the theory and methodology of a specialized time-resolved fluorescence spectroscopy for measuring membrane protein-protein interactions called pulsed-interleaved excitation fluorescence cross-correlation spectroscopy (PIE-FCCS). The strength of this technique is its ability to quantify rhodopsin interactions in situ (i.e., a live cell plasma membrane). There are two reasons for restricting the scope to live cell membranes. First, the compositional heterogeneity of the plasma membrane creates a complex milieu with thousands of lipid, protein, and carbohydrate species. This makes it difficult to infer quaternary interactions from detergent solubilized samples or construct a model phospholipid bilayer that recapitulates all of the interactions present in native membranes. Second, organizational structure and dynamics is a key feature of the plasma membrane, and fixation techniques like formaldehyde cross-linking and vitrification will modulate the interactions.

PIE-FCCS is based on two-color fluorescence imaging with time-correlated single-photon counting (TCSPC) (Becker et al., Rev Sci Instrum 70:1835–1841, 1999). By time-tagging every detected photon, the data can be analyzed as a fluorescence intensity distribution, fluorescence lifetime histogram, or fluorescence (cross-)correlation spectra (FCS/FCCS) (Becker, Advanced time-correlated single-photon counting techniques, Springer, Berlin, 2005). These analysis tools can then be used to quantify protein concentration, mobility, clustering, and Förster resonance energy transfer (FRET). In this paper I will focus on PIE-FCCS, which interleaves two wavelength excitation events in time so that the effects of spectral cross-talk and FRET can be isolated. In this way it is possible to characterize monomer-dimer-oligomer equilibria with high accuracy (Müller et al., Biophys J 89:3508–3522, 2005). Currently, PIE-FCCS requires a customized equipment configuration that will be described below. There is an excellent protocol that outlines traditional FCCS on a commercially available instrument (Bacia and Schwille, Nat Protoc 2:2842–2856, 2007). The PIE-FCCS approach is a relatively recent advance in FCCS that has been used in live cell assays to quantify lipid-anchored protein clustering (Triffo et al., J Am Chem Soc 134:10833–10842, 2012), epidermal growth factor receptor dimerization (Endres et al., Cell 152:543–556, 2013), and recently the dimerization of opsin (Comar et al., J Am Chem Soc 136(23):8342–8349, 2014). This paper will outline the theory and instrumentation requirements for PIE-FCCS, as well as the data collection and analysis process.

Key words Rhodopsin dimerization, Membrane protein dynamics, Fluorescence correlation spectroscopy, Time-correlated single-photon counting, Pulsed-interleaved excitation

Beata Jastrzebska (ed.), *Rhodopsin: Methods and Protocols*, Methods in Molecular Biology, vol. 1271,
DOI 10.1007/978-1-4939-2330-4_14,

1 Introduction

Fluorescence microscopy is widely used in bio-imaging because of its high contrast, molecular specificity, and live cell/animal compatibility. Image contrast is generated by the Stokes shift, which splits the energy required to excite a fluorophore from the energy emitted as a photon when the fluorophore relaxes to the ground state. Using dichroic mirrors these energies are spatially separated so that the background light reaching the detectors is very low. In this way the signal-to-noise ratio can be quite high even for low numbers of molecules by using high-sensitivity cameras and point detectors now readily available. Molecular specificity can be achieved through several methods, but to simplify the discussion I will focus on fluorescent fusion proteins that are co-expressed with the protein of interest [9].

In fluorescence correlation spectroscopy and related methods, time-dependent fluctuations in fluorescence intensity are analyzed to extract microscopic parameters from the system [10]. A central requirement for these methods is that the amplitude of the fluctuations be significant compared to the average fluorescence intensity. This is achieved by observing relatively low fluorophore concentrations in small volumes. Experimentally, concentration is controlled by the expression level of the fluorescent fusion protein in the cell, and volume is limited via confocal detection.

In a confocal detection geometry, the fluorescence intensity at a specific detector is denoted $F(t)$. For this time-dependent variable, a temporal autocorrelation function can be calculated:

$$C(\tau) = \frac{1}{T}\int_0^T F(t)\cdot F(t+\tau)\,\mathrm{d}t = \langle F(t)\cdot F(t+\tau)\rangle$$

At $\tau = 0$, the correlation function is equal to the mean square value of the fluorescence intensity:

$$C(\tau = 0) = \langle F(t)\cdot F(t+0)\rangle$$

$$C(0) = \langle F(t)^2\rangle$$

At long times, the correlation function is equal to the square of the mean value:

$$\lim_{\tau\to\infty} C(\tau) = \langle F(t)\rangle\langle F(t)\rangle = \langle F(t)\rangle^2$$

The difference between these two values is the variance of the fluorescence intensity:

$$\sigma^2 = \langle F(t)^2\rangle - \langle F(t)\rangle^2$$

Thus, the correlation function reflects the magnitude of the variance and how the microscopic variables that cause fluorescence fluctuations are averaged out over time.

In practice, the correlation function is defined using the fluctuation of fluorescence in channel i around the average value.

$$\delta F_i(t) = F_i(t) - \langle F_i(t) \rangle$$

The autocorrelation function or fluorescence correlation spectrum is defined as

$$G_i(\tau) = \frac{\langle \delta F_i(t) \cdot \delta F_i(t+\tau) \rangle}{\langle F_i(t) \rangle^2}$$

In this formulation, $G_i(0)$ is directly proportional to the variance of the fluorescence intensity fluctuations. Over a large range of time scales, fluorescence fluctuations are dominated by movement of molecules in and out of the confocal volume. This means that low numbers of molecules will exhibit large fluctuations (high variance), whereas large numbers of molecules will exhibit smaller fluctuations (low variance). The decay of the correlation function is the timescale over which these fluctuations are averaged out and is directly related to the diffusion coefficient of the molecules.

For a single species diffusing in three dimensions, the autocorrelation function can be fit to the following model function:

$$G_i(\tau) = \frac{1}{N_i} \cdot \frac{1}{1+\frac{\tau}{\tau_{D,i}}} \cdot \frac{1}{\sqrt{1+\frac{\omega_0^2 \cdot \tau}{z_0^2 \cdot \tau_{D,i}}}}$$

Here, N_i is the average number of molecules in the confocal volume, τ_D is the average dwell time of the molecules in the confocal volume, ω_0 is the lateral radius, and z_0 is the axial radius of the confocal volume. In this form the effective confocal volume is

$$V_{eff} = \omega_0^2 \cdot z_0 \cdot \pi^{3/2}$$

For the experiments described in Subheading 3, two corrections to the model function are necessary. First, membrane protein diffusion is restricted to two dimensions, so the third term in the model function is dropped. Second, fluorescent proteins display complex photophysics that can be fit with an expression for triplet relaxation, where T is the fraction of molecules in the triplet state and τ_T is the relaxation time for the triplet state:

$$G_i(\tau) = \frac{1}{N_i} \cdot \frac{1-T+Te^{-\tau/\tau_{Ti}}}{1-T} \cdot \frac{1}{1+\tau/\tau_{D,i}}$$

Autocorrelation curves of membrane proteins can therefore be used to determine the local concentration, or surface density of the protein and the mobility, or effective diffusion constant of the proteins.

In the experiments described below, rhodopsin proteins are expressed as two populations—one fused to the green fluorescent protein, eGFP, and the other with a red fluorescent protein,

mCherry. The fluorophores are excited by pulsed 488 and 561 nm laser light and fluorescence from each population is split by a dichroic mirror onto two detector channels. Channel A is filtered for "red" detection ($\lambda \approx 615$ nm) and channel B is filtered for "green" detection ($\lambda \approx 520$ nm). In a traditional fluorescence cross-correlation study, all of the photons recorded by the detector are used to calculate the fluorescence intensity function, $F_R(t)$ or $F_G(t)$ [6]. And the cross-correlation spectrum will be calculated according to

$$G_{RG}(\tau) = \frac{\langle \delta F_R(t) \cdot \delta F_G(t+\tau) \rangle}{\langle F_R(t) \rangle \cdot \langle F_G(t) \rangle}$$

In PIE-FCCS, each of the photons is sorted into two time gates according to their arrival time relative to a synchronization pulse that clocks the arrival time of the 488 and 561 nm laser pulses, which are delayed ~50 ns with respect to each other (Fig. 1) [5]. This makes it possible to define two time gates, 0 and 1, that divide photons emitted after a 488 nm laser pulse from those emitted after a 561 nm laser pulse. This interleaved pulse scheme allows for the separation of several complicating events that arise from the broad excitation/emission spectra of fluorescent proteins. As seen in the schematic below, a 488 nm laser pulse will ideally excite GFP, which will emit in a photon detected in channel B. However, there is some probability that GFP will emit a photon that is detected by channel A and that a 488 pulse will directly excite mCherry. In addition, it is possible for a GFP in the excited state to resonantly transfer its energy to an mCherry protein, which will then emit a photon detected by Channel A. These processes can lead to excess photons in the red channel that complicate the number analysis and lead to false-positive cross-correlation (Fig. 2).

In PIE-FCCS, these processes can be separated using time gates around the laser pulse arrival times [3–5]. Only photons arriving in channel A during time gate 1 and channel B during time gate 0 are used to calculate the auto- and cross-correlation functions:

$$G_{A1}(\tau) = \frac{\langle \delta F_{A1}(t) \cdot \delta F_{A1}(t+\tau) \rangle}{\langle F_{A1}(t) \rangle^2}$$

$$G_{B0}(\tau) = \frac{\langle \delta F_{B0}(t) \cdot \delta F_{B0}(t+\tau) \rangle}{\langle F_{B0}(t) \rangle^2}$$

$$G_{AB}(\tau) = \frac{\langle \delta F_{A1}(t) \cdot \delta F_{B0}(t+\tau) \rangle}{\langle F_{A1}(t) \rangle \cdot \langle F_{B0}(t) \rangle}$$

Each of these is fit with the model function described earlier, except for $G_{AB}(\tau)$, for which the triplet relaxation term is omitted.

The three correlation curves produce a large set of well-defined parameters related to the microscopic state of the system. These parameters are described in Table 1.

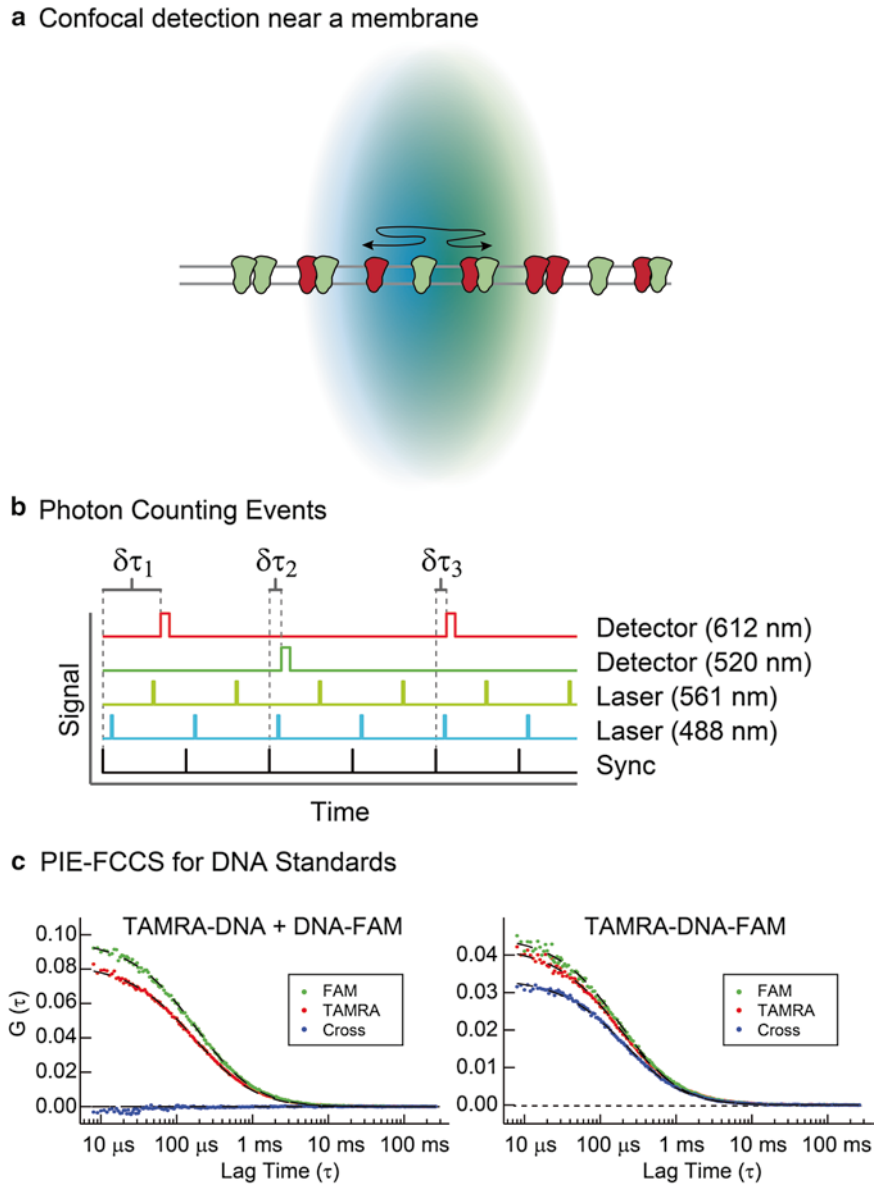

Fig. 1 Schematic of PIE-FCCS experiments. (**a**) Confocal detection near a membrane. Drawing of rhodopsin diffusion in a membrane and the confocal detection volume. (**b**) Photon counting events. In PIE-FCCS each detected photon is time-stamped with its absolute arrival time and the delay time, $\delta\tau$, of its arrival with respect to the synchronization pulse. In this way the data is filtered to ignore photons resulting from spectral cross-talk and FRET in the PIE-FCCS analysis. (**c**) PIE-FCCS for DNA standards. Example data for two DNA standards. On the *left* is data for a mixture of noninteracting single-strand DNA molecules labeled with TAMRA or FAM. On the *right* is data for a dual-labeled single strand of DNA, which serves as a positive control for cross-correlation. Panels **a** and **b** are adapted with permission from Comar, W.D., Schubert, S.M., Jastrzebska, B., et al., "Time-resolved fluorescence spectroscopy measures clustering and mobility of a G protein-coupled receptor opsin in live cell membranes," *J Am Chem Soc.* Copyright (2014) American Chemical Society

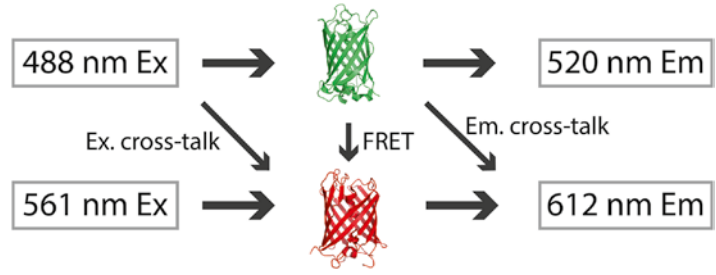

Fig. 2 Schematic of complications in a two-color fluorescence experiment

Table 1
Parameters obtained from the raw and fitted PIE-FCCS data

Parameter	Description
N_R	This is equal to $1/G_{A1}(0)$. For a monomeric population, N_R is equal to the average number of red (mCherry)-labeled molecules. If dimers or larger oligomers are present, N_R is equal to the number of *diffusing species* that contain a red-labeled molecule
N_G	This is equal to $1/G_{B0}(0)$. Similar to N_R, N_G is equal to the average number of green (eGFP)-labeled molecules for a monomeric population. If dimers or larger oligomers are present, N_G is equal to the number of diffusing species that contain a green-labeled molecule
N_{AB}	This is simply equal to $1/G_{AB}(0)$ and is not to be confused with the total number of double-labeled species, which is calculated in Table 2
$\tau_{D,i}$	Average time spent in the detection volume. This is a direct measure of the average mobility of the green-labeled $(i = G)$, red-labeled $(i = R)$, or double-labeled species $(i = AB)$
cps_i	cps_i or counts per second, is the photon detection rate and is obtained by dividing the total number of photons collected in channel i by the total collection time

2 Materials

2.1 Microscope Instrumentation

1. Microscope: In the methods below we use a Nikon Eclipse Ti microscope system, but any research-grade inverted microscope is sufficient. Rather than purchase a commercial confocal system from Nikon or another supplier, we use custom-built laser excitation and confocal fluorescence detection systems that will be described later. Some useful microscope options include:
   (a) Focus drift correction system: This is especially important for membrane measurements, which are sensitive to drifts in the focal plane.
   (b) Motorized stage.
   (c) At least two 100 % output ports.
   (d) Two dichroic filter block turrets. In the Nikon Eclipse the upper turret can be used as the input port for laser excitation.

Table 2
Observables that can be calculated from the parameters in Table 1

Equation	Description
$N_X = \frac{G_{AB}(0)}{G_{A1}(0) \cdot G_{B0}(0)}$	N_X is the number of diffusing species that have at least one eGFP and one mCherry probe
$f_c = \frac{N_X}{N_{R\,or\,G}}$	f_c is the fraction correlated. It reports on the how many of the red-labeled species co-diffuse with a green-labeled molecule. It varies from 0 to 1
$\eta_i = \frac{N_i}{\mathrm{cps}_i}$	η_i is called the molecular brightness and has units of counts per molecule per second (cpms). For a monomeric population it can reveal the number of photons each fluorophore emits per unit time. For an oligomeric population, it will be proportional to the oligomer size
$D_{\mathrm{eff},i} = \frac{\omega_{0,i}^2}{4 \cdot \tau_{D,i}}$	The effective diffusion coefficient, $D_{\mathrm{eff},i}$, is calculated by using the fit mobility, $\tau_{D,i}$, and the calibrated radius of the detection volume, $\omega_{0,i}$. For model systems, this is equal to the true diffusion coefficient, but for live cell membranes, the mobility is not purely Brownian and is thus referred to as the effective diffusion coefficient
$C_X = \frac{N_X}{\pi \cdot \omega_{0,G}^2}$	C_X is the area concentration of dual-labeled complexes
$C_i = \frac{N_i - N_X}{\pi \cdot \omega_{0,i}^2}$	C_i is the area concentration of single-labeled species $(i = \mathrm{R\,or\,G})$

2. Laser source: For PIE-FCCS, two pulsed light sources are required. This can be achieved with electro-optic gating of continuous wave lasers [5] or with short pulse diode or mode-locked lasers [1, 7, 8, 11]. The latter will provide a simultaneous measure of fluorescent lifetime and are used in the instrument below. In our experience the supercontinuum source based on a mode-locked fiber laser is the best current choice because of the short pulse duration and wide spectral flexibility [1]. Below are several features to consider in a supercontinuum source:
   (a) Several companies now sell suitable laser systems including NKT photonics, Fianium Inc., and Toptica.
   (b) Base repetition rates for the laser sources is ~80 MHz, so an internal pulse picker is required to achieve a repetition rate of 10 MHz, which is ideal for the PIE-FCCS experiments.
   (c) Spectral selection can be achieved with an acousto-optic tunable filter often available as an integrated add-on to the system.
   (d) Spectral selection can also be achieved with a series of dichroic beamsplitters and filters. In either case, cleanup filters are needed to eliminate any spectral leakage away from the desired excitation bands. In the instrument described below, we use the following two filters: a 488 nm

filter with a 1.9 nm full width half max (FWHM) bandwidth (LL01-488-12.5, Semrock) and a 561 nm filter with a 2.1 FWHM bandwidth (LL02-561-12.5, Semrock).

3. Pulse-delay generator: If one is using a supercontinuum source for both excitation beams, the pulses arrive coincident in time and a pulse-delay generator is needed. To achieve this we direct the 488 nm beam through a 3 m single mode fiber and the 561 nm pulse through an 18 m fiber (QPMJ-3AF3U-488-3.5/125-3AS-18-1-SP and QPMJ-3AF3U-488-3.5/125-3AS-3-1-SP, OZ Optics).
4. Beam combiner: To spatially overlap the beams, we use a 503 nm cut-off dichroic beamsplitter (LM01-503-25, Semrock).
5. Laser power adjustment: variable neutral density filters are available from several optomechanics supplies companies.
6. Microscope dichroic block: Two-color dichroic mirror and laser blocking filter (zt488/561rpc and zet488/561m, Chroma Technology).
7. Objective: 100× TIRF objective, NA 1.49, (Nikon).
8. Incubator stage: To maintain cells at 37 °C use a stage-top incubator (Chamlide IC, Quorum Technologies).
9. Confocal pinhole: 50 μm confocal pinhole (Thorlabs).
10. Detection dichroic beamsplitter and filters:
    (a) 560 nm longpass dichroic filter (FF560-FDi01-25x36, Semrock).
    (b) 612/69 nm filter (FF01-621/69-25, Semrock).
    (c) 520/44 nm filter (FF01-520/44-25, Semrock).
11. Avalanche photodiodes: single-photon avalanche diode (SPAD) with a 50 μm active area, 30 ps timing resolution, and 25 dark counts per second (Micro Photon Devices).
12. Four-channel-routed time-correlated single-photon counting (TCSPC) device: PicoHarp 300 (PicoQuant).
13. Camera for cell identification and localization: Evolve 512 EMCCD (Photometrics).
14. Laser power meter with μW sensitivity.

2.2 Data Processing

1. Computer should have a modern processor and 16–32 GB memory for data analysis.
2. MatLab scripts (available upon request from the author):
    (a) Convert *.pt3 file (PicoQuant) to MatLab data format file (*.mat).
    (b) Implement time gate and sort *.mat single-photon data to intensity file.
    (c) Calculate red and green autocorrelation spectra and the cross-correlation spectrum for each data set.

3. Additional files for averaging and displaying data.

2.3 Control Samples

Several organic dyes and dye-labeled systems are useful for instrument alignment and as a control to verify proper alignment. These include:

1. A free dye of known diffusion coefficient. These are used to calibrate the confocal detection volume and should be chosen to match the absorbance/emission of the dyes of interest. Two examples are fluorescein and Alexa Fluor 568.
2. Positive control for dimerization. It is valuable to have a molecular system that is labeled with a red and a green dye to serve as a positive control for cross-correlation. The most common example of this is a single strand of DNA labeled with a red dye on the 5′ end and green dye on the 3′ end. The requirements for this are that the DNA strand should contain enough bases to minimized FRET and not form any secondary structure. A commercial version of this is available (e.g., Cat. #5-0000-604, IBA GmbH). We have also used the following custom synthesized sequence, which showed superior cross-correlation compared to the IBA standards in our hands: 5′-/56-TAMN/ CCC TAG AGT GAG TCG TAT GAT AGT GAC AGC TGG ATC GTT AC/36-FAM/-3′.
3. *In cellulo* controls: In recent live cell work, it has been shown that live cell controls are necessary because of the complications arising from the photophysics of fluorescent proteins and the statistics of dimerization [8]. Plasmids for these constructs are available upon request from the author.
4. For the alignment procedure below, prepare the following solutions:
   (a) Mixture of 2 μM fluorescein and 2 μM Alexa Fluor 568.
   (b) 100 nM solution of the dual-labeled DNA sample.

2.4 Cell Culture Requirements

1. Cell line: COS-7 (kidney fibroblast), African green monkey (*Cercopithecus aethiops*), available from ATCC (CRL-1651).
2. Media: 1× Dulbecco's Modified Eagle's Medium (DMEM) + GlutaMAX (Life Technologies) supplemented with 10 % fetal bovine serum (FBS) (Life Technologies) and 1 % penicillin/ streptomycin (BioReagent, Sigma-Aldrich). Opti-MEM I media without phenol red (Life Technologies).
3. Plasmids: pEGFP-N3 and pmCherry-N1 original vectors (Clontech) and constructs encoding mouse opsin gene (AAH31766) as a fusion with eGFP or mCherry, respectively.
4. Lipofectamine 2000 transfection reagent (Life Technologies).
5. Plastic ware: 35 × 10 mm uncoated glass bottom dishes with #1 coverslips (MatTek).

3 Methods

3.1 Instrument Setup

1. Configure supercontinuum source to emit light with center wavelengths 488 and 561 nm for eGFP and mCherry excitation. Position bandpass filters listed in Subheading 2 to clean up the excitation spectra.
2. Set laser repetition rate to around 10 MHz with internal pulse picker.
3. Spatially separate beams with dichroic beamsplitter.
4. Align the 488 nm beam to the 3 m fiber and the 561 nm beam to the 18 m fiber using commercial fiber aligners.
5. Decouple the fibers with commercial fiber aligners near the microscope using a high-quality apochromatic lens.
6. After exiting the fibers, overlap both beams using mirrors and a laser mixing filter (*see* Subheading 2).
7. Align overlapped beam to the excitation pathway. For the Nikon Eclipse Ti, this is done by directing the beams into the rear of the microscope to the top dichroic filter turret, which houses the two-line laser dichroic filter block described in Subheading 2. The lasers are aligned to the optical axis using the two preceding pointing mirrors.
8. Position the confocal pinhole at the image plane of one of the side ports of the microscope.
9. Position a lens after the pinhole to collimate the light.
10. Split off the green light with a longpass dichroic mirror.
11. Position bandpass filters for green and red beams.
12. Position lenses to focus light onto each of the SPAD detectors. In our current setup, we include one adjustable mirror between the lens and the detector to align the beam to the active area of the detector. In other setups, the detector itself is on a movable stage, eliminating the need for an additional mirror.

3.2 Instrument Alignment

1. Set laser powers to ~10 μW by measuring with laser power meter before light enters the microscope path.
2. Position fluorescein/Alexa Fluor 568 sample on the stage and set the focal plane ~5 μM above the glass slide.
3. Configure the microscope settings so that the laser is illuminating the sample and the light path is directed to the camera.
4. Confirm that the lasers are illuminating the sample within the camera field of view.
5. Adjust laser trajectory so that the illumination spot is a symmetric Gaussian shape.

6. Confirm that the 488 and 561 lasers are spatially overlapped to within the resolution of the camera. Adjust relative positions using mirrors not common to both beams.
7. Minimize the size of each laser illumination region in the camera using the fiber output couplers.
8. Note the pixel position of laser illumination. If this is a repeated alignment, confirm that the spot is near an earlier position. Some drift is tolerable, but a large displacement will make realignment of the SPAD positions difficult.
9. Direct microscope light path to the confocal detection port.
10. Turn on TCSPC instrument and SPAD detectors.
11. With confocal pinhole removed, align the SPADs in axial and lateral dimensions to maximize photon counts. (If no signal is visible, *see* **Note 1**.)
12. Replace pinhole and adjust axial and lateral positions of pinhole to maximize the signal on the SPADs.
13. Remove free dye solution from the sample stage and place 100 nM DNA sample. Set focus to ~5 μm above the glass-water interface.
14. Collect TCSPC data with PicoQuant software in full time-tagged mode (*pt3 files). For the dilute solutions of the FCCs control, the ideal data collection time is 30–60 s repeated five to ten times. With proper alignment, this typically gives PIE-FCCS data with low noise.

3.3 Cell Culture and Preparation

1. Cells are cultured in 100 × 20 mm petri dishes with 1× DMEM + GlutaMAX supplemented with 10 % FBS and 1 % penicillin/streptomycin. Cells are routinely split upon reaching 80–90 % confluency.
2. Three days prior to imaging, split cells and seed into 35 × 10 mm glass bottom dishes.
3. One day prior to imaging, co-transfect cells with control plasmids or plasmids encoding fusion opsin-mCherry and opsin-EGFP. Since low concentrations are ideal for FCCS, we find that the best DNA transfection volume is about ten times lower than for typical transfection protocols.
4. At least 30 min prior to imaging, exchange media to one without phenol red.

3.4 Cell PIE-FCCS Data Collection

1. Make sure TCSPC instrument and SPAD detectors are on and aligned according to Subheading 3.2.
2. If using stage-top incubator, position it and an objective warmer and allow them to temperature stabilize for about 30 min.

3. Set laser powers to between 0.4 and 2.0 μW. Note power and keep consistent throughout experiments. The specific power depends on fluorophore, protein mobility and clustering, and instrumentation. Choose powers that are high enough for good signal to noise and low enough to avoid significant photobleaching over the ~2 min illumination of the cell.
4. Load cultured transfected cells in phenol-red-free media into the stage-top incubator.
5. Set focal plane at glass-water interface.
6. Using wide-field fluorescence imaging with camera, raster scan the stage until a cell is found with relatively low level of brightness (*see* **Note 2** and Fig. 3a).

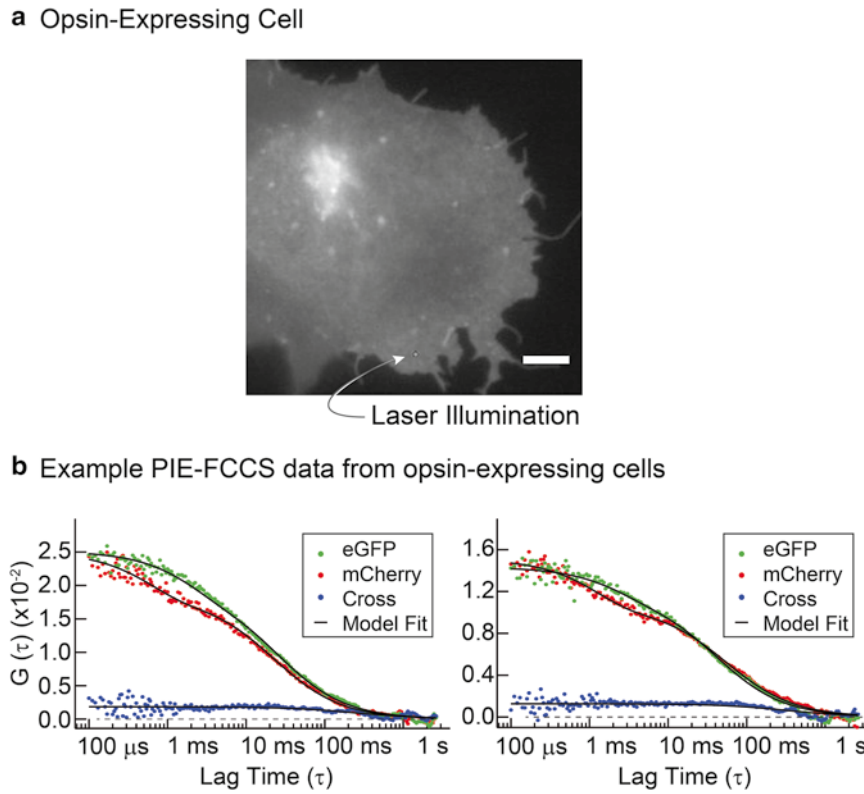

Fig. 3 Example data for live cells expressing opsin. (**a**) An epi-fluorescence image of an opsin-eGFP-expressing Cos-7 cell is merged with an image of fluorescence excited by the laser used for PIE-FCCS (scale bar = 5 μm). The *arrow* points to the laser illumination area shown in *green*, which has a radius of ~220 nm. (**b**) Representative PIE-FCCS data for two live cells expressing opsin-eGFP and opsin-mCherry. In each plot, *colored dots* are the measured data points, whereas the *solid black lines* indicate the fitted functions. *Red dots* are the FCS data for the mCherry fusion protein, $G_{A1}(\tau)$; *green dots* are the FCS data for the eGFP fusion, $G_{B0}(\tau)$; and *blues dots* are the FCCS data, $G_{AB}(\tau)$. In each plot, a *horizontal dashed line* marks the zero value for comparison with the cross-correlation amplitude, $G_{AB}(\tau)$. Figure and caption is adapted with permission from Comar, W.D., Schubert, S.M., Jastrzebska, B., et al., "Time-resolved fluorescence spectroscopy measures clustering and mobility of a G protein-coupled receptor opsin in live cell membranes," *J Am Chem Soc*. Copyright (2014) American Chemical Society

7. Using the stage controller, position cell over the pixel area where the laser illumination has been aligned (*see* Subheading 3.2, **step 8**, and **Note 3**).
8. Change microscope setting to the multi-line laser dichroic and illuminate cell with both lasers. View laser-induced fluorescence on camera and fine-tune the focus to minimize the spot size (*see* Fig. 3a, laser illumination spot).
9. Change microscope light path to the confocal detection box.
10. With lasers on, collect several 10–20 s TCSPC data sets. We find that ~5 repeats are sufficient for robust fitting and data analysis. If using the PicoHarp TCSPC system, collect data as *.pt3 files using the correlator option. This allows you to monitor the FCS data in real time but saves the raw photon data for PIE correction later.
11. After collecting TCSPC data, record and save fluorescence images of both eGFP and mCherry. This can be done before and after FCS data collection to ensure that no significant photobleaching or photodamage has occurred within the cell. If there is damage, adjust the laser power.

3.5 Data Analysis

1. After collecting TCSPC data, it needs to be parsed before calculating the FCS and FCCS curves. This can be done via custom MatLab routines available from the author.
2. Choose the time delays that define the 0 and 1 time gates. For the analysis shown below, two intensity traces are constructed. The first includes photons arriving in the red channel during time gate 1 (~1 ns before and ~40 ns after the arrival of the 561 nm laser pulse). The second includes photons arriving during time gate 0 (~1 ns before and ~40 ns after the arrival time of the 488 nm laser pulse).
3. Once the intensity traces are constructed, calculate the auto- and cross-correlation functions as defined in the introduction (Fig. 3b).
4. The resulting curves are then fit using a nonlinear least squares minimization routine to the functions described in the Introduction. In practice, several FCS curves from the same position in the same cell can be averaged together for a better fit (*see* **Note 4**, and Fig. 3b).
5. The fit parameters can then be used to calculate observables like those shown in Table 2.

4 Notes

1. If no light is detected by SPADs during early alignment, follow this procedure:
   (a) Turn off and unplug SPADs to avoid irreversible photodamage.
   (b) Replace sample with a silver mirror or aluminum-coated glass coverslip.
   (c) Oil between the objective and mirror is necessary, so re-use of the same mirror is suggested.
   (d) Remove laser blocking filter (not dichroic mirror) from the two-line laser dichroic block.
   (e) Direct reflected laser light to confocal detection box.
   (f) Remove pinhole.
   (g) Adjust focus so that the reflected laser beam comes to a focus at the confocal pinhole position.
   (h) Follow beam and adjust mirrors to direct it to the active area of the SPADs.
   (i) Replace pinhole and adjust until some light passes through.
   (j) Replace laser blocking filter in the dichroic block and remove the mirror from the sample stage.
   (k) Align sample as above, Subheading 3.2, **steps 2–12**.
2. To gauge the appropriate level of fluorescence, take FCS data as described in Subheading 3.4, **step 10**, checking to see if the autocorrelation amplitude is between 0.005 and 0.5. Assuming constant imaging conditions, the camera intensity will be directly proportional to fluorophore population and can be used to choose the cells within the appropriate range of expression.
3. When positioning the cell relative to the laser focus, be sure to avoid bright features indicative of internal organelles. Also avoid being too close to the edge of the cell. The best position is one where the plasma membrane shows even intensity around the periphery of the cell.
4. During the averaging process, some FCS curves will display large amplitudes, long decay times, or periodic oscillations. These normally result from bright features like internal organelles or the edge of the cell crossing the confocal detection volume. These do not reflect 2D membrane diffusion and should be excluded from analysis.

References

1. Comar WD, Schubert SM, Jastrzebska B et al (2014) Time-resolved fluorescence spectroscopy measures clustering and mobility of a G protein-coupled receptor opsin in live cell membranes. J Am Chem Soc 136(23): 8342–8349
2. Fotiadis D, Liang Y, Filipek S et al (2003) Atomic-force microscopy: rhodopsin dimers in native disc membranes. Nature 421: 127–128
3. Becker W, Hickl H, Zander C et al (1999) Time-resolved detection and identification of single analyte molecules in microcapillaries by time-correlated single-photon counting (TCSPC). Rev Sci Instrum 70:1835–1841
4. Becker W (ed) (2005) Advanced time-correlated single photon counting techniques, vol 81. Springer, Berlin
5. Müller BK, Zaychikov E, Bräuchle C et al (2005) Pulsed interleaved excitation. Biophys J 89:3508–3522
6. Bacia K, Schwille P (2007) Practical guidelines for dual-color fluorescence cross-correlation spectroscopy. Nat Protoc 2:2842–2856
7. Triffo SB, Huang HH, Smith AW et al (2012) Monitoring lipid anchor organization in cell membranes by PIE-FCCS. J Am Chem Soc 134:10833–10842
8. Endres NF, Das R, Smith AW et al (2013) Conformational coupling across the plasma membrane in activation of the EGF receptor. Cell 152:543–556
9. Giepmans BNG, Adams SR, Ellisman MH et al (2006) The fluorescent toolbox for assessing protein location and function. Science 312:217–224
10. Digman MA, Gratton E (2011) Lessons in fluctuation correlation spectroscopy. Annu Rev Phys Chem 62:645–668
11. Olofsson L, Margeat E (2013) Pulsed interleaved excitation fluorescence spectroscopy with a supercontinuum source. Opt Express 21:3370–3378

Chapter 15

Oligomeric State of Rhodopsin Within Rhodopsin–Transducin Complex Probed with Succinylated Concanavalin A

Beata Jastrzebska

Abstract

Rhodopsin—a prototypical G protein-coupled receptor (GPCR)—is abundantly expressed in the eye and stabilized by its covalently bound chromophore 11-*cis*-retinal. The signal of light is amplified and transmitted through the binding of heterotrimeric G protein transducin (G_t) to photoactivated rhodopsin following downstream pathways activation leading to light sensing in the brain. As demonstrated by atomic force microscopy (AFM), rhodopsin exists in the native membrane of the rod outer segment disks as dimers highly organized in tightly packed oligomers. However, functional importance of this organization is still debated. To clarify the role of the rhodopsin dimer in signaling activation and thus the binding of transducin, the complex between rhodopsin and transducin can be formed, purified, and probed with succinylated concanavalin A. This method can be potentially applied to other GPCRs to verify their oligomeric state.

Key words Rhodopsin, Photoreceptor, Heterotrimeric G protein, Transducin, Succinylated concanavalin A, Membrane proteins, Purification, Transmission electron microscopy

1 Introduction

The GPCRs are the largest and diverse group of integral membrane proteins that in response to various stimuli via activation of specific G proteins help to control variety of biological processes. Undeniably they are key targets for pharmacological manipulations; thus complete understanding of their function, structure, and oligomeric organization is crucial for development of new, more specific medications and therapies. Despite this large diversity, GPCRs share a common architecture of seven transmembrane helices and several conserved motives critical for their function. Many GPCRs form dimers and higher-ordered oligomers in the membrane bilayers, and their importance has been recognized not only in allosteric modulation of ligand binding but also in signaling activation [1–3]. For example, the binding of a dimer to a single heterotrimeric G protein with formation of pentameric complexes

Beata Jastrzebska (ed.), *Rhodopsin: Methods and Protocols*, Methods in Molecular Biology, vol. 1271,
DOI 10.1007/978-1-4939-2330-4_15,

is supported by reconstitution experiments involving the leukotriene B4 receptor BLT1, serotonin 5-HT(4) receptor, and dopamine D2 receptor, each with their respective G proteins [4–6]. But the most compelling evidence for the functional importance of a GPCR dimer comes from in vivo studies on the luteinizing hormone receptor (LHR), which revealed intermolecular cooperation between a ligand-binding deficient GPCR and G protein activation defective mutants [7] resulting in rescue of receptor function. Predominate organization of opsin into dimeric clusters was recently observed in single cells by time-resolved pulsed-interleaved excitation fluorescence cross-correlation spectroscopy (PIE-FCCS) [8]. Dimeric organization of GPCR in "membrane-like" orientation has been detected also in the crystal structures of several family A GPCRs, including rhodopsin in several different activation forms, CXCR4, μ-opioid, and κ-opioid receptors [9–12]. Moreover, the presence of two distinct interfaces found on opposite sides of the μ-opioid receptor raises the possibility for formation of higher-ordered oligomers in a fashion similar to the packing observed by AFM for rhodopsin oligomers in native disk membranes [13]. Because structures of GPCRs, G proteins, and other GPCR-interacting proteins are highly homologous, general activation mechanisms are most likely shared among all GPCRs. Thus, if oligomers serve as functional units for some class A GPCRs [7], they likely do the same for most if not all GPCRs [14].

Here we demonstrate the method useful for the probing of the binding stoichiometry between rhodopsin and its cognate G protein transducin (G_t) within the rhodopsin–G_t complex stabilized by cross-linking and purified in conditions preventing disruption of the native rhodopsin dimer. Rhodopsin contains two sugar groups that modify the opsin structure through an asparagine linkage: mannose $(Man)_3$ attached to Asp^{15} and *N*-acetyl glucosamine $(GlcNAc)_3$ attached to Asp^2 [15]; thus the oligomeric state of rhodopsin in the rhodopsin–G_t complex can be probed by sugar-binding protein that binds only one kind of sugar. One of the possibilities is a dimeric form of concanavalin A (succinylated ConA) that binds only mannose [16] and provides two sugar-binding sites. Negatively stained particles of the triple complex formed between rhodopsin–G_t and succinylated ConA analyzed by transmission electron microscopy (TEM) unequivocally prove oligomeric state of rhodopsin [17]. This method can be potentially useful for studding binding stoichiometry of other GPCR–G protein complexes.

2 Materials

2.1 Extraction and Purification of Transducin (G_t)

1. ROS membranes isolated from 200 retinas according to [18] (*see* **Notes 1** and **2**).
2. Pentyl–agarose beads.

3. Superdex S200 size exclusion column (two connected in tandem) (GE Healthcare Life Sciences).
4. Amicon Centricon 30,000 MWCO (Millipore).
5. Beckman J-20 rotor.
6. High-speed 50 ml (Nalgene) centrifuge tubes.
7. Isotonic extraction buffer: 20 mM 4-(2-hydroxyethyl)-1-piperazine-1-ethanesulfonic acid (HEPES), pH 7.5, 100 mM NaCl, 5 mM $MgCl_2$, 1 mM DTT (*see* **Note 3**).
8. Hypotonic extraction buffer: 5 mM HEPES, pH 7.5, 0.1 mM EDTA, 1 mM DTT.
9. 1 M $MgCl_2$ stock solution.
10. 1 M HEPES, pH 7.5 stock solution.
11. Equilibration buffer: 10 mM HEPES, pH 7.5, 2 mM $MgCl_2$, 1 mM DTT.
12. Washing buffer: 10 mM HEPES, pH 7.5, 75 mM NaCl, 2 mM $MgCl_2$, 1 mM DTT.
13. Elution buffer: 10 mM HEPES, pH 7.5, 400 mM NaCl, 2 mM $MgCl_2$, 1 mM DTT.
14. Cleaning buffer: 10 mM HEPES, pH 7.5, 2 M NaCl, 2 mM $MgCl_2$, 1 mM DTT, 0.01 % sodium azide.
15. Gel filtration buffer: 10 mM HEPES, pH 7.5, 100 mM NaCl, 2 mM $MgCl_2$, 1 mM DTT.

2.2 Extraction of Bovine Rhodopsin from Dark-Adapted Rod Outer Segments (ROS)

1. ROS membranes isolated from 200 retinas (*see* **Notes 1** and **2**).
2. Glass–glass homogenizer.
3. Beckman J-20 rotor.
4. High-speed 50 ml (Nalgene) centrifuge tubes.
5. Membrane washing buffer: 5 mM Bis–Tris-propane (BTP), pH 7.5.
6. 0.5 M 2-(*N*-morpholino)ethanesulfonic acid (MES), pH 6.3.
7. 1 M $ZnCl_2$ stock solution.
8. 1 M DTT stock solution.
9. 10 % NaN_3 stock solution.
10. 1 M hydroxylamine pH 7.5 stock solution (*see* **Note 4**).
11. Resuspension buffer: 50 mM BTP pH 7.5 and 100 mM NaCl.
12. Solubilization buffer: 10 mM BTP pH 7.5, 100 mM NaCl, 20 mM DDM.
13. UV buffer: 10 mM BTP pH 7.5, 100 mM NaCl, 2 mM DDM, 1 mM hydroxylamine.
14. Dialysis buffer: 10 mM (BTP), pH 7.5, 100 mM NaCl, 0.02 mM DDM.

2.3 Preparation of Rhodopsin–Transducin Complex

1. Succinylated concanavalin A (sConA) (Vector Laboratories).
2. CNBr-activated agarose (Santa Cruz Biotechnology Inc.).
3. SRT™ SEC-300 size exclusion column (SEPAX-Technologies Inc.).
4. 150 W fiber light (Dolan-Jenner Industries Inc.).
5. 480–520 band-pass filter (Chroma Technology).
6. Amicon Centricon 30,000 MWCO (Millipore).
7. Bradford ULTRA (Novexin).
8. Disuccinimidyl glutarate (DSG) cross-linker.
9. Equilibration buffer A: 20 mM BTP, pH 6.9, 120 mM NaCl, 1 mM $MgCl_2$, 1 mM $MnCl_2$, 1 mM $CaCl_2$, 1 mM DTT, 0.5 mM dodecyl-β-D-maltoside (DDM).
10. Elution buffer: 20 mM BTP, pH 6.9, 120 mM NaCl, 1 mM $MgCl_2$, 1 mM $MnCl_2$, 1 mM $CaCl_2$, 1 mM DTT, 0.5 mM DDM, 200 mM α-methyl-D-mannoside.
11. Regeneration buffer: 10 mM BTP, pH 6.9, 500 mM NaCl, 2 mM EDTA, 2 mM EGTA, 1 % Triton, 1 mM DTT.
12. Storage buffer: 10 mM BTP, pH 6.9, 500 mM NaCl, 1 mM $MgCl_2$, 1 mM $MnCl_2$, 1 mM $CaCl_2$.
13. Gel filtration buffer A: 20 mM BTP, pH 6.9, 120 mM NaCl, 1 mM $MgCl_2$, 1 mM $MnCl_2$, 1 mM DTT, 1 mM DDM.
14. 10 mM lauryl maltose neopentyl glycol (LMNG) stock solution.
15. Gel filtration buffer B: 20 mM BTP, pH 6.9, 120 mM NaCl, 1 mM $MgCl_2$, 1 mM $MnCl_2$, 1 mM DTT, 0.05 mM LMNG.

2.4 Visualization of Rhodopsin–G_t and sConA–Rhodopsin–G_t Complexes by Transmission Electron Microscope (TEM)

1. 400 mesh, carbon-coated grids (Quantifoil Micro Tools GmBH).
2. 0.22 μm syringe filter (Millipore).
3. FEI TF20 microscope.
4. Tobacco mosaic virus (TMV) (*see* **Note 5**).
5. Dilution buffer: 20 mM BTP, pH 6.9, 120 mM NaCl, 1 mM $MgCl_2$, 1 mM $MnCl_2$, 1 mM DTT, and specified detergent (0.05 mM LMNG or 1 mM DDM) (*see* **Note 6**).

3 Methods

3.1 Extraction and Purification of Transducin

1. All steps must be performed under dim red light and on ice.
2. If using frozen ROS membranes, thaw them on ice. Resuspend them in 40 ml of the isotonic extraction buffer, transfer to the centrifuge 50 ml Beckman tubes, and centrifuge at 18,000 × *g* in Beckman J-20 rotor at 4 °C for 15 min.
3. Discard supernatant 1 and resuspend pellet in 40 ml of the hypotonic extraction buffer.

4. Extract membrane-associated proteins by homogenizing them 4–5 times in glass–glass homogenizer and then pellet homogenized membranes by centrifugation at 25,000 × *g* in Beckman J-20 rotor at 4 °C for 30 min.
5. Collect supernatant 2 and keep it on ice. Repeat extraction step. Collect supernatant 3 and combine it with supernatant 2 (*see* **Note 7**).
6. Spin combined supernatants at 25,000 × *g* in Beckman J-20 rotor at 4 °C for 45 min to pellet residual membrane contaminants.
7. To the resulted supernatant, add HEPES, pH 7.5 to a final concentration 10 mM and $MgCl_2$ to a final concentration of 2 mM, each from 1 M stock solution, and centrifuge the sample again using the above conditions (Fig. 1a).
8. The resulting supernatant applies at a flow rate of 15 ml/h to the 10 × 100 mm column containing 5 ml of pentyl-agarose pre-equilibrated with the equilibration buffer.
9. Wash the column with 10 column volumes of the same equilibration buffer following 30–50 ml of the washing buffer.

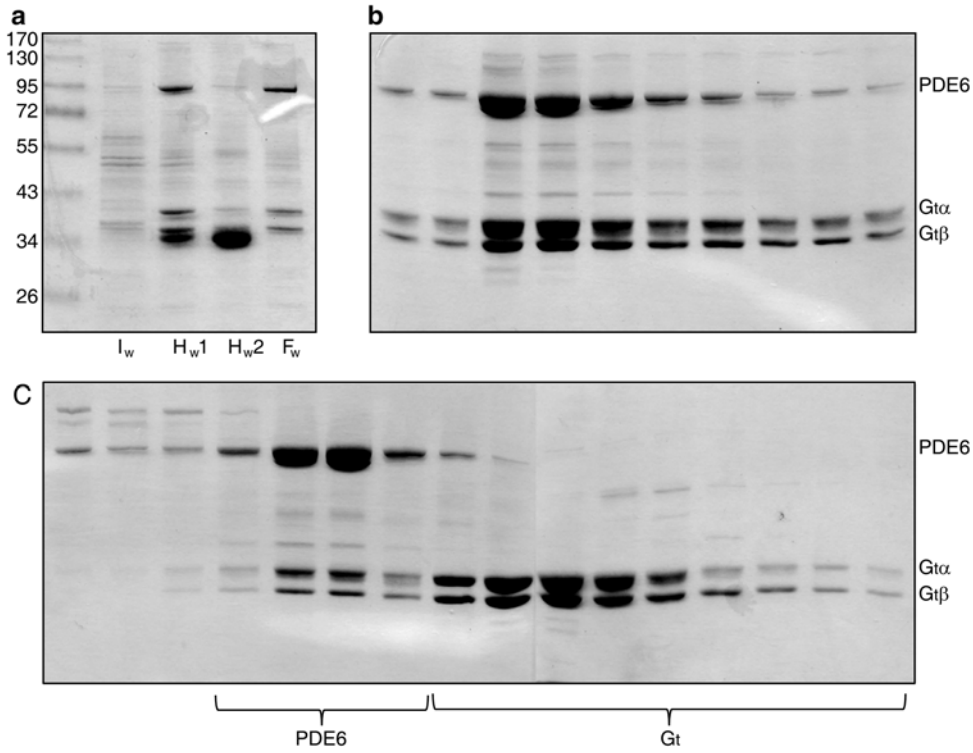

Fig. 1 Extraction and purification of G protein from rod outer segments. (**a**) SDS-PAGE gel electrophoresis demonstrating protein composition in subsequent washes of ROS membranes. I_w isotonic wash, H_w1 hypotonic wash 1, H_w2 hypotonic wash 2, F_w final wash used for purification of G_t. (**b**) SDS-PAGE gel electrophoresis demonstrating protein composition in the fractions eluted from pentyl–agarose column. (**c**) SDS-PAGE gel electrophoresis of protein fractions eluted from gel filtration column

10. Elute bound proteins with ~50 ml of the elution buffer, collecting 1 ml fractions.
11. Check the content of every other fraction by SDS-PAGE gel electrophoresis (*see* **Note 8**) (Fig. 1b).
12. Pool all fractions containing G_t and concentrate with 30,000 NMWL Centricon device to ~400 μl (*see* **Notes 9** and **10**).
13. Clean pentyl–agarose resin with 5–10 column volumes of the cleaning buffer (*see* **Note 11**).
14. To purify G_t to homogeneity, apply 200 μl (half) of the sample prepared in **step 12** on tandem S200 gel filtration column equilibrated with the gel filtration buffer at a flow rate of 0.4 ml/min and collect 0.5 ml fractions.
15. Purify second half of G_t.
16. Check the content of every other fraction by SDS-PAGE gel (Fig. 1c).
17. Pool all fractions containing G_t and concentrate with 30,000 NMWL Centricon device to ~10 mg protein/ml.
18. Determine protein concentration by the Bradford assay [19].

3.2 Extraction of Bovine Rhodopsin from Dark-Adapted Rod Outer Segments (ROS)

1. Use G_t-extracted ROS membranes (*see* **Note 7**). Thaw them on ice, resuspend in 50 ml of membrane washing buffer, and gently homogenize 4–5 times by using glass–glass homogenizer.
2. Transfer homogenized membranes to the centrifuge 50 ml Beckman tubes and pellet them by centrifugation at 25,000 × *g* in Beckman J-20 rotor at 4 °C for 30 min.
3. Repeat membrane wash in membrane washing buffer 2–3 times (*see* **Note 12**).
4. Then spin wash ROS in the resuspension buffer. Resuspend final ROS pellet in small volume (3–4 ml) of the above buffer and measure rhodopsin concentration.
5. To measure rhodopsin concentration, transfer an aliquot (10–20 μl) of ROS to the 1 ml of solubilization buffer and incubate 10–15 min at room temperature mixing on the rotating platform followed by sample centrifugation at 16,000 × *g* for 5 min at 4 °C in the Eppendorf top bench centrifuge. Measure UV-visible absorption spectrum between 260 and 650 nm in the resulted supernatant. Use the absorbance at 498 nm, along with appropriate dilution and molar extinction coefficient $\varepsilon_{498\text{nm}} = 40.600/\text{M/cm}$ to estimate initial rhodopsin concentration.
6. To extract rhodopsin pipette ROS membranes containing about 1 mg of rhodopsin to 2 ml Eppendorf tube and pellet by centrifugation at 16,000 × *g* for 15 min at 4 °C in the Eppendorf top bench centrifuge.

7. Descant residual liquid and to the ROS pellet, add 1 M stock solutions of the following components to reach final concentrations of 55 mM MES, pH 6.3, 100 mM $ZnCl_2$, 1 mM DTT, 0.02 % sodium aside and DDM powder in 4–5 w/w of rhodopsin.
8. Incubate overnight at room temperature mixing on the rotating platform.
9. Remove precipitated proteins by ultracentrifugation at 100,000 × *g* in Beckman TLA-55 rotor at 4 °C for 30 min (*see* **Notes 13** and **14**).
10. Collect supernatant containing solubilized rhodopsin and reduce concentration of $ZnCl_2$ by dialysis against the dialysis buffer for at least 24 h at 4 °C and in the dark (*see* **Note 15**).
11. Measure rhodopsin concentration. Typically it should reach between 8 and 13 mg/ml. The A_{280nm}/A_{498nm} ratio should be about 1.6–1.8 indicating rhodopsin purity about 90 % (Fig. 2).
12. Aliquot rhodopsin sample, wrap in aluminum foil, and freeze to −20 °C for storage.

3.3 Preparation of Rhodopsin–Transducin Complex (Fig. 3)

Rhodopsin–G_t complex should be prepared freshly from $ZnCl_2$-extracted rhodopsin and freshly purified G_t. It is important to control temperature (keep it 4 °C) during complex purification since room temperature promotes complex dissociation.

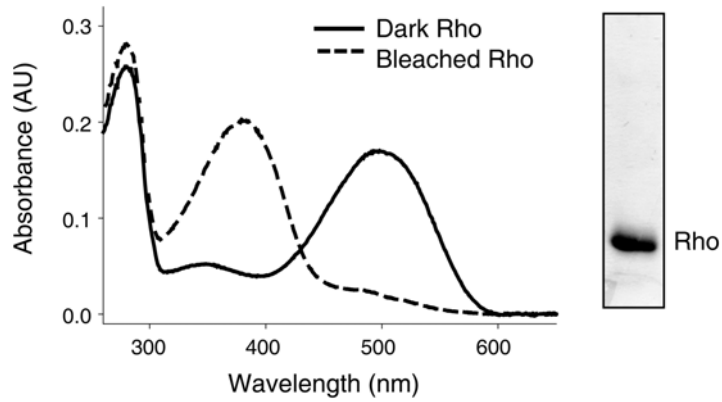

Fig. 2 Absorption spectrum of Zn^{2+}-extracted rhodopsin. *Solid line*, spectrum of dark rhodopsin; *broken line*, spectrum of rhodopsin sample bleached for 5 min through band pass 480–520 nm. SDS-PAGE gel indicates more than 95 % purity of rhodopsin sample

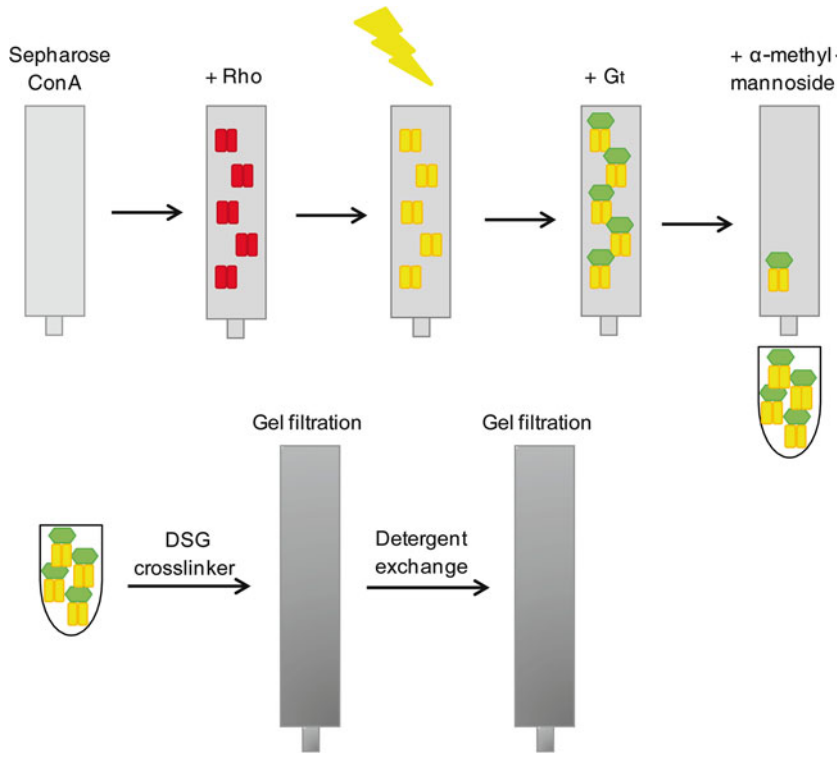

Fig. 3 Purification scheme of sConA-rhodopsin-G_t (sConA-Rho*–G_t) complex. Zn^{2+}-extracted rhodopsin was bound to succinylated concanavalin A (sConA) affinity resin in the dark. After wash rhodopsin bound to the resin was illuminated for 7 min and G_t was immediately loaded on the column. After wash Rho*–G_t complex was eluted with elution buffer containing competing sugar α-methyl-mannopyranoside. Rho*–G_t complex was immediately cross-linked with DSG cross-linker and purified by size exclusion chromatography. To exchange detergent Rho*–G_t complex was passed through the same gel filtration column the second time. To prepare triple sConA–Rho*–G_t complex, cross-linked Rho*–G_t was incubated with sConA and then separated by gel filtration

3.3.1 Formation and Purification of Rhodopsin–Transducin Complex by sConA Affinity Chromatography

1. First prepare sConA affinity resin by coupling of sConA to CNBr-activated agarose at a density of 8 mg sConA/ml of resin according to standard protocol.
2. Pack ~6–7 ml of sConA affinity resin to 5 × 200 mm long, thin column and equilibrate the resin with the equilibration buffer.
3. Dilute solubilized rhodopsin with the same equilibration buffer to the final concentration ~0.2 mg/ml and load it at a flow rate of 0.5 ml/min onto the sConA column (*see* **Note 16**).
4. Wash the column with 5 column volumes of the same ice-cold buffer.
5. Then illuminate the column for 10 min with a 150 W fiber light covered with 480–520 nm band-pass filter.
6. Immediately after light exposure load purified and diluted in the equilibration buffer A to ~0.2 mg/ml native G_t at a flow rate of 0.5 ml/min.
7. Wash the column with 10 column volumes of the above buffer.

8. Elute the complex with the elution buffer containing 200 mM α-methyl-D-mannoside at a flow rate of 0.2 ml/min (*see* **Note 17**). Collect 1 ml fractions.
9. Take 20 µl aliquot and check the content of each fraction by SDS-PAGE gel.
10. Perform chemical cross-linking in all fractions containing rhodopsin–G_t complex.

3.3.2 Chemical Cross-Linking of Rhodopsin–Transducin Complex

1. To each fraction eluted from the sConA resin and containing rhodopsin–G_t complex, add 100 mM DSG to the final concentration of 1 mM and incubate the samples 2 h on ice.
2. Stop cross-linking reaction by adding 1 M Tris, pH 8.0 to the final concentration of 50 mM and incubate for 15 min on ice.
3. Take 20 µl aliquot and run SDS-PAGE gel to check efficiency of the cross-linking reaction (Fig. 4a).

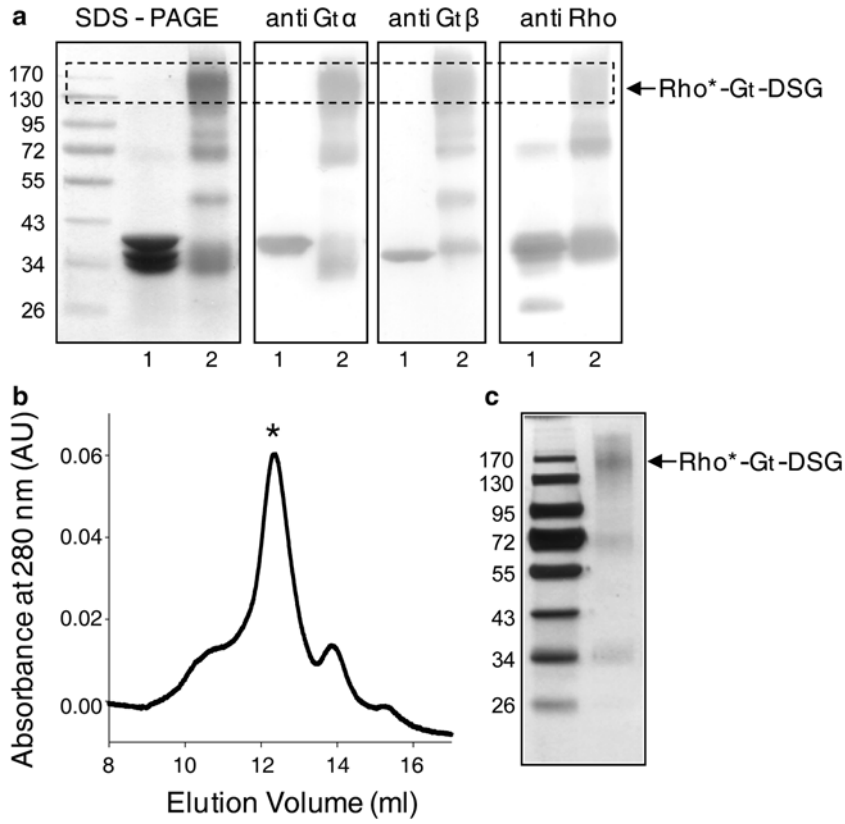

Fig. 4 Preparation and purification of rhodopsin-G_t (Rho*-G_t) complex. (**a**) DSG cross-linking of the Rho*–G_t complex purified by sConA affinity chromatography. SDS-PAGE gel, stained with Coomassie blue and immunoblot analyses with antibody against $G_t\alpha$, $G_t\beta$, and rhodopsin, indicated formation of intact Rho*–G_t complex after treatment with DSG (lanes 1, non-cross-linked complex and lanes 2, DSG-cross-linked complex). (**b**) Gel filtration elution profile of DSG-cross-linked Rho*–G_t complex. (**c**) Silver-stained SDS-PAGE gel analysis of the peak fraction indicated with a *star*

4. Pool all fractions containing cross-linked rhodopsin–G_t complex and concentrate to 200 µl with 30,000 NMWL Centricon device. Use this sample for size exclusion chromatography.
5. Regenerate sConA affinity resin by washing with 5–10 column volumes of the regeneration buffer at a slow rate of 0.2 ml/min.
6. Then wash the column with 5 column volumes of the storage buffer and store it at 4 °C (*see* **Note 18**).

3.3.3 Isolation of Cross-Linked Rhodopsin–Transducin Complex by Gel Filtration

1. Load 200 µl of cross-linked rhodopsin–G_t complex onto a SRT™ SEC-300 gel filtration column equilibrated with the gel filtration buffer A at a flow rate of 0.4 ml/min. Fractions containing cross-linked complex will separate from free rhodopsin and free G_t (*see* **Note 19**) (Fig. 4b, c).
2. Pool fractions containing cross-linked rhodopsin–G_t complex, concentrate to 200 µl, and process on the same gel filtration to increase sample homogeneity.
3. If the exchange of the detergent (from DDM to LMNG) is desired, pool fractions containing rhodopsin–G_t complex and concentrate to 100 µl. Then add 100 µl of 10 mM LMNG stock solution dissolved in the gel filtration buffer lucking detergent and incubate for 1 h on ice.
4. Gel filtrate this sample using the same column (SRT™ SEC-300) equilibrated with the gel filtration buffer B.
5. Determine protein concentration in the peak fractions by the Bradford assay.
6. Use peak fractions containing rhodopsin–G_t complex for negative staining and analysis by transmission electron microscopy (TEM).

3.3.4 Labeling of Rhodopsin–Transducin Complex with sConA

1. Concentrate fractions containing rhodopsin–G_t–LMNG complex to 100 µl and incubate at 4 °C with the excess of sConA in the gel filtration buffer B at least 1 h (*see* **Notes 20** and **21**).
2. Purify triple sConA–rhodopsin–G_t complex by the same gel filtration column (SRT™ SEC-300) equilibrated with the gel filtration buffer B (Fig. 5a).
3. Determine protein concentration in the peak fractions by the Bradford assay.
4. Use peak fractions containing rhodopsin–G_t complex for negative staining and analysis by TEM.

3.4 Visualization of Rhodopsin–G_t and sConA–Rhodopsin–G_t Complexes by TEM

1. Dilute all purified complexes to ~20 µg/ml with the dilution buffer (*see* **Note 5**).
2. Glow discharge carbon-coated 400 mesh grids for 1 min just before adsorption of protein complexes.

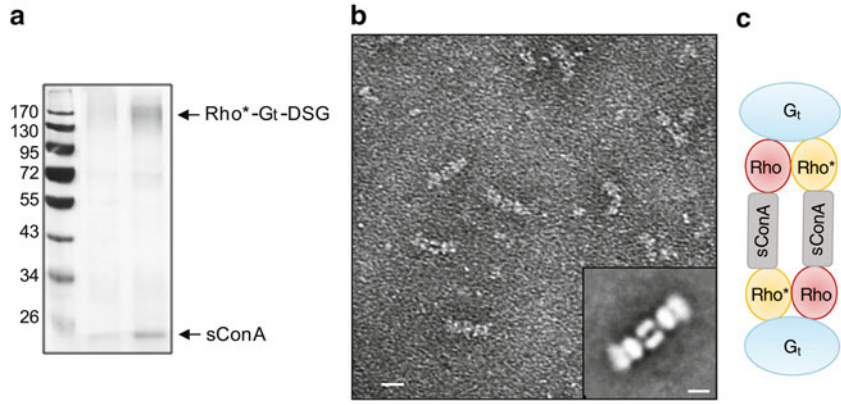

Fig. 5 Purification and EM analysis of sConA-decorated Rho*–G_t complex. (**a**) Silver-stained SDS-PAGE gel analysis of protein fractions eluted from gel filtration column, containing triple sConA–Rho*–G_t complex. (**b**) TEM image of negatively stained sConA–Rho*–G_t complex. Scale bar 20 nm. *Inset*, 2-dimensional average of multiple sConA–Rho*–G_t particles. (**c**) Scheme of sConA–Rho*–G_t composition indicating stoichiometry of the Rho*–G_t complex

3. Load 4 μl of protein on the grid and incubate for 1 min.
4. Adsorb the excess of protein solution with the filter paper, and immediately wash grids with four drops of distilled H_2O (*see* **Note 22**).
5. Negatively stain protein complexes with 2 % (w/v) uranyl acetate (*see* **Note 23**).
6. Image the sample with available TEM (Fig. 5b, c).

4 Notes

1. Fresh bovine retinas can be isolated from fresh bovine eyes obtained from local slaughter house. Frozen retinas can be purchased from W L Lawson Company LLC.
2. Bovine rod outer segment (ROS) membranes can be isolated by step sucrose gradient centrifugations described in detailed previously in ref. 18 and in Chapter 2 of this book.
3. All buffers that contain DTT should be prepared freshly. Stock solution of 1 M DTT can be prepared in advance and stored at −20 °C.
4. Hydroxylamine solution is unstable; therefore, it should be prepared freshly or kept −20 °C in small aliquots.
5. Tobacco mosaic virus (TMV) can be added to the protein sample before imaging by TEM as an internal standard in the concentration of ~10 μg/ml. It forms larger elongated structures and can be helpful in recognizing good area on the grid covered with the appropriate thickness of stain (2 % uranyl acetate).

6. Prepare 10 mM stock solution of LMNG in the buffer of interest. Solubilization of this detergent may take a few (1–3) hours.
7. Membrane pellet stripped off G_t can be stored at −80 °C and used for rhodopsin extraction.
8. Typically 12 or 10 % SDS-PAGE gels should be used for G_t separation.
9. After pentyl–agarose column, the sample contains mixture of G_t and PDE6. Thanks to the large enough difference in molecular masses (G_t, 86 kDa and PDE6, 218 kDa), these proteins can be further separated by size exclusion chromatography.
10. At this step purification can be stopped. Keep the sample on ice until the next day.
11. Store pentyl–agarose column in the cleaning buffer at 4 °C.
12. In the hypotonic buffer, ROS membranes are very loose; thus carefully descant the supernatant with 5 ml pipette.
13. To spin the sample in the bench top ultracentrifuge in TLA-55 rotor, transfer the sample to the Eppendorf Beckman tubes for ultracentrifuge.
14. Up to 50 % of rhodopsin can be lost during this step.
15. Change dialysis buffer at least twice.
16. The entire preparation of the rhodopsin–G_t complex is performed in the dark room, except of rhodopsin light activation step.
17. To elute the rhodopsin–G_t complex from the sConA affinity resin, first apply ~3–4 ml of the elution buffer at a flow rate of 0.5 ml/min, then close the column, and incubate at 4 °C for at least 30 min.
18. sConA affinity resin can be used several times but after each use it loses its binding capacity.
19. The rhodopsin–G_t complex is light sensitive. Perform gel filtration experiment under dim red light.
20. sConA is purchased as a powder. Reconstitute this protein at least 1 h before the binding with rhodopsin–G_t complex in the buffer composed of 10 mM BTP, pH 6.9, 100 mM NaCl, 1 mM $MgCl_2$, 1 mM $MnCl_2$, 1 mM $CaCl_2$.
21. Binding of sConA to the rhodopsin–G_t complex can be performed overnight if needed.
22. In the standard protocol of negative staining, two drops of distilled H_2O are used [20]. However for membrane proteins, we recommend to use more wash to wash out the excess of detergent.
23. To prepare uranyl acetate dissolves 1 g stain in 50 ml of distilled water in 50 ml conical tube wrapped in aluminum foil. Place on the rotating platform and mix for 1 h. Filtrate this solution through the 0.22 μm syringe filter. This solution can be stored at room temperature or aliquot and kept in −20 °C.

References

1. Smith NJ, Milligan G (2010) Allostery at G protein-coupled receptor homo- and heteromers: uncharted pharmacological landscapes. Pharmacol Rev 62:701–725
2. Maurice P, Kamal M, Jockers R (2011) Asymmetry of GPCR oligomers supports their functional relevance. Trends Pharmacol Sci 32:514–520
3. Ferre S, Casado V, Devi LA et al (2014) G protein-coupled receptor oligomerization revisited: functional and pharmacological perspectives. Pharmacol Rev 66:413–434
4. Baneres JL, Parello J (2003) Structure-based analysis of GPCR function: evidence for a novel pentameric assembly between the dimeric leukotriene B4 receptor BLT1 and the G-protein. J Mol Biol 329:815–829
5. Han Y, Moreira IS, Urizar E et al (2009) Allosteric communication between protomers of dopamine class A GPCR dimers modulates activation. Nat Chem Biol 5:688–695
6. Pellissier LP, Barthet G, Gaven F et al (2011) G protein activation by serotonin type 4 receptor dimers: evidence that turning on two protomers is more efficient. J Biol Chem 286:9985–9997
7. Rivero-Muller A, Chou YY, Ji I et al (2010) Rescue of defective G protein-coupled receptor function in vivo by intermolecular cooperation. Proc Natl Acad Sci U S A 107:2319–2324
8. Comar WD, Schubert SM, Jastrzebska B et al (2014) Time-resolved fluorescence spectroscopy measures clustering and mobility of a G protein-coupled receptor opsin in live cell membranes. J Am Chem Soc 136:8342–8349
9. Wu B, Chien EY, Mol CD et al (2010) Structures of the CXCR4 chemokine GPCR with small-molecule and cyclic peptide antagonists. Science 330:1066–1071
10. Wu H, Wacker D, Mileni M et al (2012) Structure of the human kappa-opioid receptor in complex with JDTic. Nature 485:327–332
11. Manglik A, Kruse AC, Kobilka TS et al (2012) Crystal structure of the micro-opioid receptor bound to a morphinan antagonist. Nature 485:321–326
12. Salom D, Lodowski DT, Stenkamp RE et al (2006) Crystal structure of a photoactivated deprotonated intermediate of rhodopsin. Proc Natl Acad Sci U S A 103:16123–16128
13. Fotiadis D, Liang Y, Filipek S et al (2003) Atomic-force microscopy: rhodopsin dimers in native disc membranes. Nature 421:127–128
14. Jastrzebska B (2013) GPCR: G protein complexes—the fundamental signaling assembly. Amino Acids 45:1303–1314
15. Fukuda MN, Papermaster DS, Hargrave PA (1982) Structural analysis of carbohydrate moiety of bovine rhodopsin. Methods Enzymol 81:214–223
16. Lis H, Sharon N (1973) The biochemistry of plant lectins (phytohemagglutinins). Annu Rev Biochem 42:541–574
17. Jastrzebska B, Ringler P, Palczewski K et al (2013) The rhodopsin-transducin complex houses two distinct rhodopsin molecules. J Struct Biol 182:164–172
18. Papermaster DS (1982) Preparation of retinal rod outer segments. Methods Enzymol 81:48–52
19. Bradford MM (1976) A rapid and sensitive method for the quantitation of microgram quantities of protein utilizing the principle of protein-dye binding. Anal Biochem 72:248–254
20. Ohi M, Li Y, Cheng Y et al (2004) Negative staining and image classification: powerful tools in modern electron microscopy. Biol Proced Online 6:23–34

Chapter 16

Quantification of Arrestin–Rhodopsin Binding Stoichiometry

Ciara C.M. Lally and Martha E. Sommer

Abstract

We have developed several methods to quantify arrestin-1 binding to rhodopsin in the native rod disk membrane. These methods can be applied to study arrestin interactions with all functional forms of rhodopsin, including dark-state rhodopsin, light-activated metarhodopsin II (Meta II), and the products of Meta II decay, opsin and all-*trans*-retinal. When used in parallel, these methods report both the actual amount of arrestin bound to the membrane surface and the functional aspects of arrestin binding, such as which arrestin loops are engaged and whether Meta II is stabilized. Most of these methods can also be applied to recombinant receptor reconstituted into liposomes, bicelles, and nanodisks.

Key words Arrestin, Rhodopsin, Retinal, Stoichiometry, Absorbance spectroscopy, Fluorescence spectroscopy, Site-directed labeling

1 Introduction

The classical role of arrestin-1 in the rod photoreceptor cell is that of signal quencher. Light-activated Meta II is phosphorylated by rhodopsin kinase, and arrestin binds phosphorylated Meta II (Meta II-P) with nanomolar affinity [1] to block further transducin activation [2]. After hydrolysis and release of all-*trans*-retinal (ATR) from Meta II-P, arrestin remains bound to the phosphorylated aporeceptor opsin (OpsP) with micromolar affinity [3, 4]. Arrestin can induce all-*trans*-retinal uptake by OpsP, thereby reforming Meta II-P [3]. Based on this observation, we recently proposed that arrestin-1 serves an additional role as protector of the rod cell in bright light conditions [5]. Arrestin dissociation from the receptor is dependent upon the removal of ATR and receptor dephosphorylation [6].

The arrestin–rhodopsin binding stoichiometry was debated for many years, with different groups claiming exclusive 1:1 or 1:2 binding ratio (*see* [7] and [8]). In order to resolve this controversy, we developed a set of complementary methods for quantifying the

Beata Jastrzebska (ed.), *Rhodopsin: Methods and Protocols*, Methods in Molecular Biology, vol. 1271,
DOI 10.1007/978-1-4939-2330-4_16,

amount of arrestin and ATR bound to rhodopsin in the native rod disk membrane. These methods are supplemented by the well-established extra Meta II assay. When combined with titration analyses, all of these methods yield reliable values for stoichiometry and affinity (K_D).

- *Extra Meta II assay* quantifies Meta II stabilization by arrestin. In short, rhodopsin is light-activated under conditions that favor the formation of Meta I, the precursor of Meta II. Arrestin binding shifts the Meta I ↔ Meta II equilibrium toward Meta II. This method can additionally be used to quantify the percentage of receptors that are sufficiently phosphorylated to bind arrestin as light-induced Meta II. This method is applicable to rhodopsin in membranes, bicelles, or nanodisks. However, this assay cannot be used for rhodopsin solubilized in detergent, since Meta I is not formed under these conditions.
- *Centrifugal pull-down assay* employing arrestin mutants labeled with a fluorophore. The absorbance of the fluorophore is used to quantify the amount of arrestin actually bound to the membrane surface. In terms of accuracy and simplicity, this assay represents a huge improvement over previous pull-down methods that utilized radioactivity, Coomassie staining, or Western blot to quantify arrestin binding. This assay can be used with native rod outer segment (ROS) disk membranes or large vesicles that are efficiently pelleted by centrifugation.
- *Fluorescence spectroscopy* of site-specific-labeled arrestin mutants. We have developed a toolbox of different arrestin mutants, which allow monitoring of specific conformational changes involved in receptor binding. Importantly, this method discriminates between the different ways (i.e., binding modes) in which arrestin binds different functional forms of the receptor. This method can be applied to rhodopsin in membranes or membrane mimetics, including soluble micelles containing detergent.
- *Quantification of retinal Schiff base* by acid denaturation. This method quantifies arrestin-induced ATR uptake by OpsP, which occurs in native ROS membranes.

2 Materials

1. 11-*cis*-retinal generated by illumination from commercially available all-*trans*-retinal and purified using HPLC [9]. Eluted fractions are dried, resolved in ethanol, and stored at −80 °C.
2. Hydroxylamine (HA) and *o-tert*-butyl hydroxylamine (*t*-bHA) dissolved in water to yield 1 M or 500 mM stocks solutions with the pH adjusted to 7 with NaOH. Stock solutions are aliquoted

and stored at −40 °C. After thawing for use in experiments, aliquots are discarded after 1 day.

3. High-affinity peptide analogue derived from the α-subunit of transducin (Gt-HAA), VLEDLKSCGLF, commercially synthesized and dissolved at a concentration of 10 mM in water plus 50 mM DTT, and pH adjusted to 7 using NaOH. Aliquots are stored at −80 °C.
4. Standard arrestin–rhodopsin binding buffer: 50 mM 4-(2-hydroxyethyl)-1-piperazine-1-ethanesulfonic acid (HEPES) buffer at pH 7. The level of salt (NaCl and $MgCl_2$) is varied depending on the experiment. All buffers are filtered before use.

3 Methods

Since this chapter focuses on arrestin and ATR binding assays, we will give only a brief description of how to prepare the necessary protein reagents in Subheadings 3.1 and 3.2**.** Please refer to the references for more details. Note that all rhodopsin preparations must be handled under dim red light. Since the determination of binding stoichiometry is completely dependent upon knowing accurate concentrations of protein samples, we have provided relevant extinction coefficients (ε) for determining concentration by absorbance spectroscopy.

3.1 Phosphorylated Rhodopsin

1. Isolate rod outer segments (ROS) from frozen bovine retina (W L Lawson Company, USA) using a multistep centrifugation procedure employing different sucrose solutions. *See* ref. 3 for a detailed description of this procedure.
2. Phosphorylate rhodopsin in the ROS by the associated rhodopsin kinase by applying light and ATP [3].
3. Terminate phosphorylation by the addition of 20 mM HA, which converts all rhodopsin photoproducts to OpsP and retinal oxime.
4. Wash the phosphorylated membranes to remove the HA and associated ROS proteins [3]. Since publishing the protocol in Sommer et al. 2012, we generally wash the membranes 2–3 extra times.
5. Make aliquots of OpsP, snap freeze them in liquid N_2, and store at −80 °C. In these conditions, OpsP can be stored for several months.
6. Regenerate rhodopsin from OpsP by the addition of a threefold molar excess of 11-*cis*-retinal, followed by incubation at room temperature for at least 1 h under dark conditions [3].

7. After regeneration, add 20 mM HA, and wash membranes three times to remove the HA. Alternatively, 20 mM *t*-bHA can be added, in which case no washing steps are necessary, since *t*-bHA cannot hydrolyze the retinal Schiff base of light-activated rhodopsin [10]. For ATR uptake experiments, HA or *t*-bHA must be removed by washing.
8. Determine rhodopsin concentration by the absorbance difference spectrum. First, the absorbance spectrophotometer is base-lined with a 1:20 dilution of the membranes in 100 mM HA. The sample is then illuminated for 10 s with a 150-W fiber optic light source (>495 nm), and the loss of 500 nm absorbance can be converted to rhodopsin concentration using an extinction coefficient (ε) of $0.0408/\mu M^{-1}/cm^{-1}$.

   The photoactivation density (percentage of activated receptors on the membrane surface) can be modulated by varying the regeneration efficiency. Partially regenerated membranes are prepared by partial bleaching of fully regenerated membranes in the presence of HA (pH 6, 35 °C) [7].

3.2 Recombinant Arrestin and Labeled Arrestin Mutants

Our standard arrestin construct is derived from bovine arrestin-1 and lacks all native cysteine and tryptophan residues (C63A, C128S, C143A, W194F). Single residues within this construct are mutated to cysteine using standard molecular biology techniques.

1. Express arrestin constructs in *Escherichia coli* and purify arrestin by two-step ion exchange chromatography [11, 12].
2. Label purified arrestin mutants with the fluorophore monobromobimane (mBBr) or *N,N′*-dimethyl-*N*-(iodoacetyl)-*N′*-(7-nitrobenz-2-oxa-1,3-diazol-4-yl)ethylenediamine (IANBD) following published protocols [7, 11]. For maximal labeling efficiency, it is important to treat arrestin mutants with a reducing agent (e.g., 5 mM TCEP). The reducing agent should then be removed by buffer exchange just prior to labeling (*see* **Note 1**).
3. Determine the concentration and labeling efficiency by absorbance using $\varepsilon_{278nm} = 0.02076/\mu M^{-1}/cm^{-1}$ for arrestin W194F, $\varepsilon_{390nm} = 0.005/\mu M^{-1}/cm^{-1}$ for mBBr, and $\varepsilon_{500nm} = 0.025/\mu M^{-1}/cm^{-1}$ for IANBD. In the case of mBBr, the absorbance value at 390 nm should be first subtracted from the 278-nm absorbance value before calculating the arrestin concentration, to correct for the absorbance of mBBr at 278 nm [13].

3.3 Titration Setup

In order to determine binding stoichiometry and affinity, titration analyses are carried out, and arrestin binding is quantified by one of the methods described below. Either arrestin or receptor can be titrated against a fixed concentration of the binding partner. In the following example, we describe how we generally prepare samples

Table 1
Preparation of titration samples

Final arrestin concentration (μM)	*0*	*0.5*	*1*	*1.5*	*2*	*3*	*4*	*8*
Binding buffer (μl)	50	48	46	44	42	38	34	18
Arrestin (25 μM) (μl)	0	2	4	6	8	12	16	32
Receptor (8 μM) (μl)	50	50	50	50	50	50	50	50
Total volume (μl)	*100*	*100*	*100*	*100*	*100*	*100*	*100*	*100*

for an experiment in which arrestin is titrated against a 4 μM receptor. We find that this method of preparing samples minimizes pipetting error and is highly reproducible.

1. Prepare a stock of 8 μM receptor in the desired binding buffer (450 ml total volume) (*see* **Note 2**).
2. Prepare a stock of 25 μM arrestin in the desired binding buffer (100 μl volume).
3. Prepare samples as described in Table 1 (*see* **Note 3**).

3.4 Extra Meta II Assay

We perform this assay on a modified Shimadzu UV3000 dual wavelength spectrophotometer, which has previously been described in detail [14, 15]. In principle, any absorbance spectrophotometer can be used. The excitation slits of the spectrophotometer should be minimized (e.g., 2-nm opening) in order to avoid light-activation of the sample during measurement. A flash apparatus must be fitted for light-activation of the sample. The flash must be of sufficiently short duration (<1 ms) so that isorhodopsin is not formed from the irradiation of Meta I. A commercial photoflash fitted with a filter (e.g., 500 ± 20-nm band-pass) or green laser diode can be used. If light-activation of the sample occurs during measurement, the photomultiplier tube of the spectrophotometer should be protected with a blue-green glass filter. The use of a flexible fiber optic can aid in delivering the activating light to the sample, and care should be taken that the apparatus is rigidly mounted so that consistent flash intensities are obtained from experiment to experiment. The flash should activate 10–20 % of rhodopsin in the sample, and the flash intensity can be modulated with neutral density filters.

1. Turn on the spectrophotometer and allow at least 1 h for the lamp(s) to warm up.
2. Cool the cuvette holder to 0–2 °C using a Peltier cooler and/or circulating water bath. Dry air should be pumped into the sample chamber to avoid condensation on the cuvette (*see* **Note 4**).
3. Base-line the spectrophotometer with the sample cuvette (quartz) containing buffer alone.

4. Samples normally consist of 10 μM phosphorylated ROS membranes (ROS-P) in 100 mM HEPES, pH 8. For experiments employing arrestin, salt concentration should be minimized (<20 mM NaCl) (*see* **Note 5**).
5. After placing ROS membranes in the sample chamber, wait at least 3 min before measurement to allow temperature equilibration. Care should be taken to avoid sedimentation of membranes during measurement (*see* **Note 6**).
6. Take at least one spectrum of the dark-state sample before light-activation.
7. Photoactivate the sample with the flash apparatus. For time-resolved binding data, take absorbance spectra (700 nm–300 nm) at specific time intervals following light-activation. Depending on the phosphorylation level of the rhodopsin preparation and the concentration of arrestin, binding is typically complete within 1–5 min.
8. Manually correct the spectra for baseline drift (the 700-nm value of each spectrum should be zero). Then, for each spectrum, subtract the 417-nm value from the 380-nm value (=ΔABS) (*see* **Note 7**). The resulting ΔABS values correspond to "extra Meta II" and can be plotted as a function of time to yield the rate of arrestin binding.
9. As a control, the same experiment should always be performed in the absence of arrestin. In this case, no change in absorbance should be seen following light-activation.
10. The percentage of receptors that are photoactivated with each flash (*activation efficiency*) can be determined using Gt-HAA peptide. Mix 10 μM ROS (or ROS-P) with 300 μM Gt-HAA. Take a dark-state spectrum, then photoactivate the sample with a flash, and take a spectrum 1 min after the flash. Without removing the sample cuvette, flash the sample again and take a spectrum after 1 min. Repeat 12–15 times.
11. Process the spectra as described above. Plot the ΔABS values against the flash number, and fit this data to the curve $y = a \times (1-b)^x$, where a is a scalar and b is the activation efficiency (Fig. 1a).
12. Since the Gt-HAA peptide stabilizes all photoactivated rhodopsin as Meta II, the ΔABS values obtained in the presence of Gt-HAA can be used to convert ΔABS to the concentration of Meta II (*see* **Note 8**). In practical terms, the data from the multiflash experiment described in **step 11** are sequentially summed and plotted against the concentration of photoactivated rhodopsin, which can be calculated once the activation efficiency of the flash is known (the concentration of photoactivated rhodopsin after x flashes is equal to $R-(R \times (1-b)^x)$,

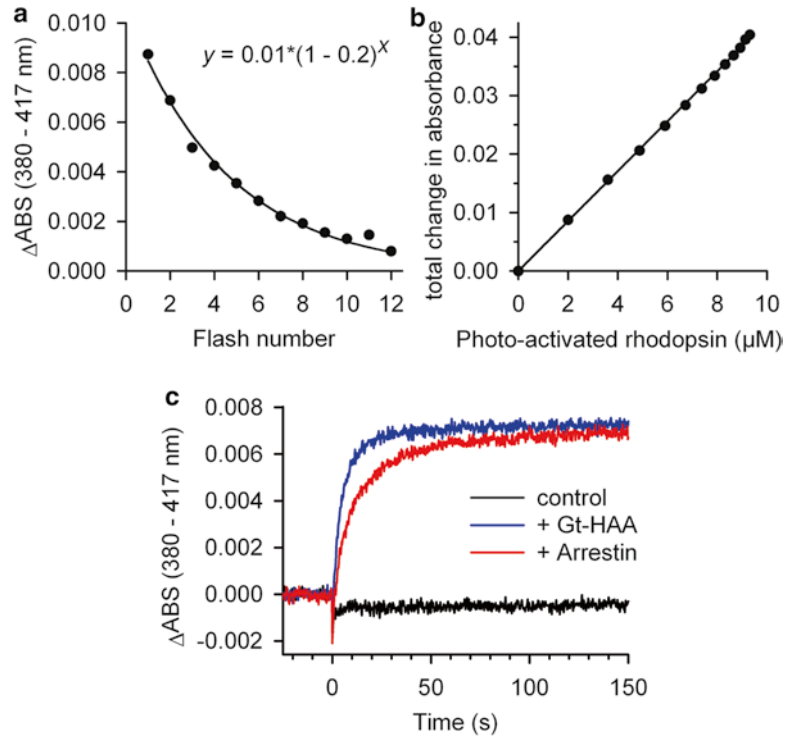

Fig. 1 Examples of extra Meta II data. (**a**) A plot of the maximal amplitude of ΔABS obtained from ROS (10 μM rhodopsin) in the presence of an excess of Gt-HAA peptide (300 μM) resulting from a series of activating flashes. The *fitted curve* indicates a flash efficiency of 20 %. (**b**) The amplitudes derived from the experiment in (**a**) are summed and plotted as a function of the concentration of photoactivated rhodopsin. The slope of the line (0.004) allows conversion of ΔABS values to concentration of Meta II. (**c**) ROS membranes containing 10 μM rhodopsin were photoactivated with a flash at $t=0$ in the presence of Gt-HAA peptide (300 μM) or arrestin (20 μM) (pH 8, 2 °C). The control trace was obtained in the absence of any binding partner

where R is the concentration of rhodopsin and b is the flash efficiency). The slope of the line yields the correction value needed to convert ΔABS values to Meta II concentration units (μM) (Fig. 1b).

13. In order to quantify the amount of rhodopsin that is sufficiently phosphorylated to bind arrestin, the ΔABS amplitude in the presence of an excess of arrestin (20 μM) is compared to that in the presence of Gt-HAA peptide (300 μM) (Fig. 1c) (*see* **Note 9**). When the ΔABS amplitude in the presence of arrestin is equal to that with Gt-HAA, then 100 % of receptors are sufficiently phosphorylated [3].

3.5 Centrifugal Pull-Down Assay

The centrifugal pull-down assay has been used to study arrestin for decades. The "pull-down" portion of this method is straightforward, since native rhodopsin resides in large membranous disks that can easily be pelleted by centrifugation. However, the quantification of bound arrestin is not so straightforward. Previously, most researchers processed the pellets and supernatants by SDS PAGE and then quantified the arrestin bands by Coomassie stain or Western blot. We have improved the quantification strategy by using arrestin mutants labeled with a fluorescent probe (IANBD), which has red-shifted absorbance ($\lambda_{max} = 500$ nm). Hence, the concentration of arrestin remaining in the supernatant after pull-down can be quickly and accurately determined by absorbance spectroscopy. For our wild-type control, we employ IANBD-labeled arrestin A366C (A366NBD), in which the fluorophore is located on the "backside" of arrestin not involved in receptor binding. If experiments employ rhodopsin, all steps should be performed under dim red light. An absorbance spectrometer with microcuvette (~100 μl volume) is required for this assay.

1. Prepare samples of IANBD-labeled arrestin and ROS membranes at the desired concentrations (120 μl volume) (*see* **Note 10**) in transparent 1.5 ml microcentrifuge tubes (with cap).
2. If binding to Meta II is to be measured, light-activate samples with a 150-W fiber optic light source with heat filter and >495-nm long-pass filter (*see* **Note 11**).
3. Immediately following light-activation, transfer the tubes to the room-temperature centrifuge rotor. Centrifuge the samples at 16,000 × *g* for 10 min (*see* **Note 12**).
4. Base-line the absorbance spectrometer with buffer.
5. Take an absorbance spectrum of each supernatant (*see* **Note 13**) (Fig. 2).
6. The concentration of labeled arrestin present in the supernatant can be determined by dividing the absorbance at 500 nm (ABS_{500nm}) by the extinction coefficient of IANBD ($0.025/\mu M^{-1}/cm^{-1}$). If samples are under-labeled (i.e., less than 100 %), then the extinction coefficient should be multiplied by the fraction of labeled arrestin.
7. If scattering is present in the absorbance spectrum, the ABS_{500nm} value can be corrected by subtracting $2 \times ABS_{550nm}$. This correction value is approximate and introduces error into the measurement. It is best to minimize scattering elements in the samples. Absorbance values from severely scattering samples should be disregarded.

3.6 Fluorescence Spectroscopy

Solvent-sensitive fluorophores like bimane and IANBD, when placed at particular sites within the arrestin-receptor binding interface, show significant changes in their steady-state emission spectra

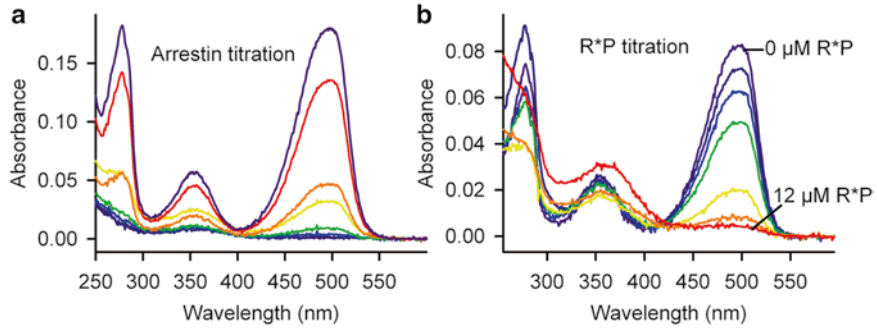

Fig. 2 Absorbance spectra from centrifugal pull-down assays. The maximal absorbance at 500 nm indicates the amount of labeled arrestin mutant remaining in the supernatant following centrifugation. (**a**) Arrestin A366NBD titration (0, 0.5, 1, 2, 4, 6, 10, 12 μM) against 4 μM light-activated, phosphorylated rhodopsin (R*P). (**b**) R*P titration (0, 0.5, 1, 2, 4, 6, 12 μM) against 4 μM arrestin A366NBD. Although higher concentrations of R*P lead to more scatter at bluer wavelengths (*red trace*), this scattering has minimal effect on the red-shifted absorbance of IANBD

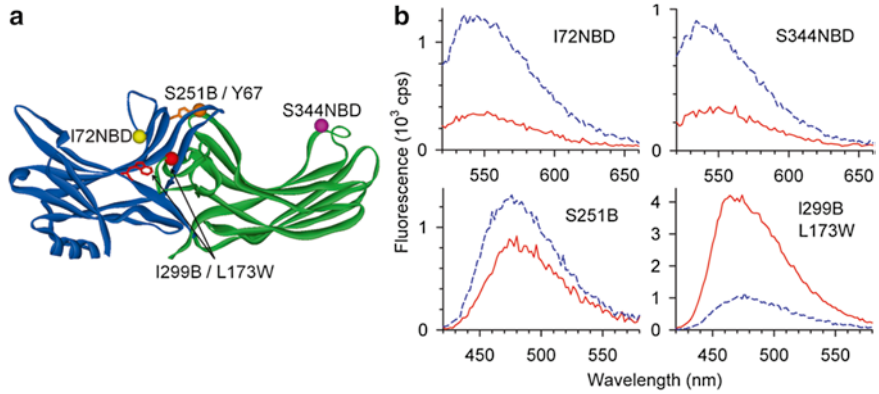

Fig. 3 Monitoring conformational changes in arrestin by site-directed fluorescence. (**a**) Model of arrestin-1 (Protein Data Bank code 1CF1, molecule D) showing locations of probe attachment (*spheres*) and quenching aromatic side chains (*sticks*). The *N*-domain of arrestin is *blue*, the *C*-domain is *green*, and the *C*-tail is omitted for clarity. Site 72 is *yellow*, site 344 is *pink*, site 251 and Y67 side chain are *orange*, and site 299 and the tryptophan side chain at site 173 are *red*. *See* text for details regarding these mutants. (**b**) For example, steady-state fluorescence spectra of the fluorescently labeled arrestin mutants in the presence of an excess of phosphorylated rhodopsin, before (*red spectra*) and after light-activation (*blue spectra*)

when arrestin binds the receptor. These changes are measured using a fluorescence spectrometer. Our most well-defined, fluorescently labeled arrestin mutants are illustrated in Fig. 3. 172B and I72NBD on the finger loop of the *N*-domain [3, 7] are sensitive to the activation state of the receptor and show increases in fluorescence only when arrestin binds Meta II-P (*see* **Note 14**). S344NBD in the *C*-domain shows increases in fluorescence when arrestin binds OpsP or Meta II-P [3, 7]. The "loop-344" engages active or

inactive phosphorylated receptor, or possibly the adjacent membrane surface [3]. S251B is sensitive to changes in the interface between the *N*- and *C*-domains and shows increase in fluorescence when arrestin binds OpsP or Meta II-P [13, 16]. This fluorescence change is due to changes in the distance between the bimane at site 251 and nearby quenching tyrosine residue in the *N*-domain (Y67) [13]. I299B/L173W reports conformational changes within the gate loop, which only occur when arrestin binds the active Meta II-P [16]. Gate loop movement places the bimane at site 299 closer to the quenching tryptophan at site 173, resulting in a decrease in fluorescence.

1. Prepare the fluorescence spectrometer. Excitation slits should be narrowed to minimize light-activation of rhodopsin samples (<0.2-nm band-pass). Emission slits should be opened wide (4-nm band-pass) (*see* **Note 15**).
2. Prepare samples of fluorescently labeled arrestin mutant and receptor at desired concentrations (*see* **Note 16**).
3. Place sample in a quartz cuvette for fluorescence measurement. A sample temperature of 20 °C is normally used.
4. Acquire emission spectra in 2-nm steps with 0.5-s integration per point (*see* **Note 17**). For experiments measuring arrestin binding to Meta II, a spectrum should be taken from the dark-state sample and then after light-activation (*see* **Notes 18** and **19**). Wait at least 2 min between light-activation and acquiring the light-activated spectrum.
5. Subtract appropriate background spectra (e.g., spectrum of rhodopsin alone) from the spectra of fluorescently labeled arrestin.
6. The intensity of fluorescence is best quantified by integrating the area under each background-subtracted fluorescence curve. This integrated fluorescence intensity is the binding signal that is used for the titration plot (*see* **Note 20**).

3.7 Quantification of Retinal Schiff Base

This assay is based upon the classical "acid trapping" method, in which acidification denatures the opsin protein and traps the retinal Schiff base in a protonated form. Protonated Schiff base has a characteristic absorbance at 440 nm and can thus be quantified. A key improvement we have made to the classical assay is the use of *t*-bHA to cleave nonspecific retinal Schiff bases formed with solvent-exposed lysines and phospholipid headgroups. In this way, peripheral retinal Schiff bases can be disregarded, and only retinal Schiff bases within the binding pocket are quantified.

1. Prepare samples (100 μl) of ROS membranes, arrestin, and ATR (if using). If arrestin-dependent retinal uptake by opsin is being measured, allow samples to equilibrate at least 30 min before proceeding.

2. To remove peripheral retinal Schiff bases, add 4 μl of 500 mM *t*-bHA (~20 mM final concentration) to each sample and quickly mix by vortexing.
3. Exactly 2 min after the addition of *t*-bHA, add 5 μl of 4 N HCl to each sample and vortex (*see* **Note 21**).
4. Add 10 μl of 10 % *n*-dodecyl-β-D-maltoside (DDM) to each sample and vortex. Incubate at room temperature for 30 min, and then centrifuge at 16,000 × *g* for 10 min.
5. After base-lining the absorbance spectrometer with buffer, take an absorbance spectrum of each sample (600–300 nm).
6. When measuring samples of opsin in the presence of a large excess of ATR, it is important to compare samples with arrestin to identical samples that lack arrestin. Even with the use of *t-bHA*, large concentrations of ATR have considerable absorbance at 440 nm (Fig. 4).

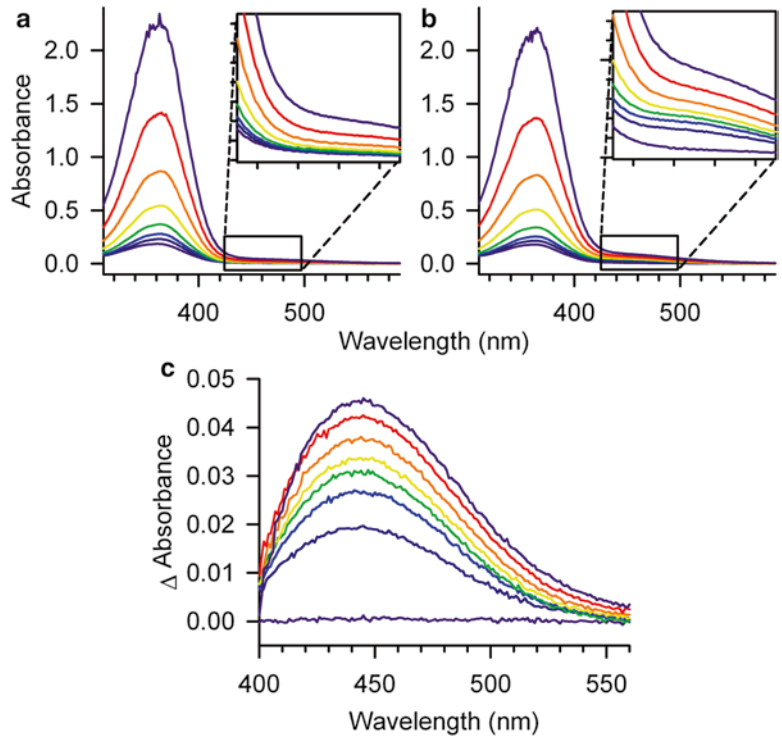

Fig. 4 Acid trapping of retinal Schiff base. (**a**) ATR titration against 4 μM phosphorylated opsin (OpsP). Samples were treated with *t*-bHA, HCl, and DDM as described in the text. (**b**) Identical ATR titration as in panel (**a**), in the presence of 4 μM arrestin. Samples were treated with *t*-bHA, HCl, and DDM as described in the text. (**c**) Spectra in panel (**a**) were subtracted from the corresponding spectra in panel (**b**) to yield difference spectra showing arrestin-dependent retinal Schiff base formation. The maximal absorbance around 440 nm is due to protonated Schiff base

7. When measuring Meta II decay, a "background spectrum" can be obtained by light-activating a sample of dark-state rhodopsin (of the same concentration as used in the experiment) in the presence of 20 mM HA. After a 10-min incubation, this sample can be treated with acid and DDM in parallel with other samples.
8. The ABS_{440nm} can be converted to retinal Schiff base concentration using the extinction coefficient $0.0361/\mu M^{-1}/cm^{-1}$ [3].

3.8 Analysis of Titration Data

The arrestin–receptor binding stoichiometry and affinity are best determined by titrating one component (the titrator) against a fixed concentration of the other (the titrand) and then quantifying the binding by one of the methods described above. The amplitude of the binding signal (y) is plotted as a function of titrator concentration (x), and these data are fit to an equation (Eq. 1) that is derived from the definition of K_D. The reader is referred to Sommer et al. 2011 for a description of how this expression is derived [7].

$$y = \frac{j + \left[s \times \left\{ \left(K_D + C + x \right) - \sqrt{\left[\left(K_D + C + x \right)^2 - 4\left(C \times x \right) \right]} \right\} \right]}{2} \quad (1)$$

K_D is the dissociation constant, C is the concentration at which saturation is reached, and the factors j and s allow the expression to be appropriately scaled to the experimental data (Fig. 5a). The stoichiometry is determined by comparing the value for C and the actual concentration of the titrand. For example, if an arrestin titration yields a C value of 2 μM and 4 μM of the titrand rhodopsin was actually present, then the stoichiometry is 1 arrestin:2 rhodopsin (Fig. 5b).

1. Fit experimental data to the equation described above using a nonlinear regression algorithm within a standard mathematical program.
2. For extra Meta II data, the fit yields apparent K_D, which must be corrected for the Meta I ↔ Meta II equilibrium. In practice, this means multiplying the apparent K_D value by the inverse of the Meta II/Meta I ratio, which is determined by the equation described by Parkes and Liebman [17]. At the conditions we normally use, 2 °C and pH 8, the Meta II/Meta I ratio is ~0.1.
3. When an arrestin titration is performed using centrifugal pull-down analysis (where concentration of bound arrestin is directly measured), the quadratic expression should be fit with no scaling factors. In this case, the final amplitude of the fit should equal the concentration at which the curve saturates.

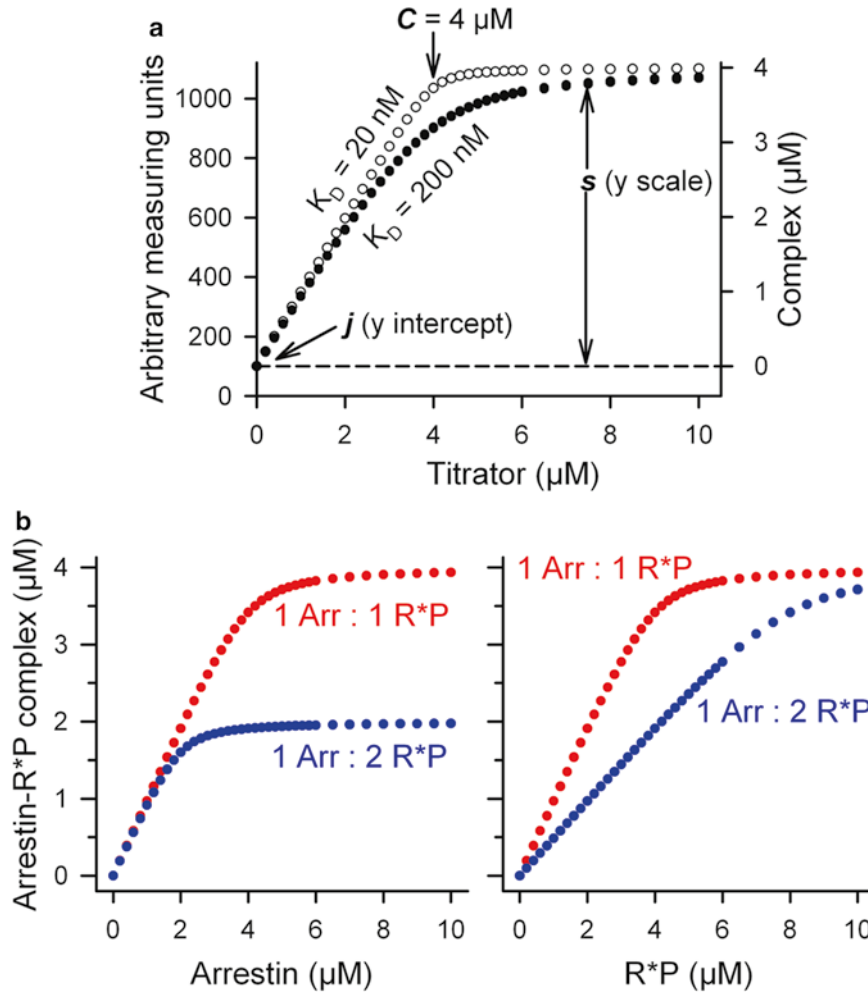

Fig. 5 Mathematical analysis of binding data. (**a**) One-to-one binding curve, calculated using Eq. 1, showing the difference in curve shape with a K_D of 20 nM (*open circles*) and a K_D of 200 nM (*filled circles*). The factors *j* and *s* scale experimental values (*left-hand axis*) to the actual concentration of the arrestin–rhodopsin complex (*right-hand axis*). In this example, the binding curve saturates at a *C* value of 4 μM. (**b**) Arrestin titration (*left*) and R*P titration (*right*) were calculated assuming a titrand concentration of 4 μM, a K_D of 100 nM, and a binding stoichiometry of one to one (*red points*) or one to two (*blue points*)

4. Centrifugal pull-down, fluorescence, and acid trapping assays yield *apparent* K_D values. These assays are generally performed at 20 °C, where the rate of Meta II decay is fast enough that a significant fraction of Meta II decays before arrestin binding is complete. This effect causes an underestimation of arrestin binding, particularly around the saturation point of the binding curve (i.e., when the ratio of arrestin and receptor is stoichiometric), which results in a rounding of the binding curve and hence higher K_D value (Fig. 5a) (*see* **Note 22**).

4 Notes

1. To prevent aggregation of arrestin during labeling, 100–150 mM NaCl should be present in the labeling buffer. Labeling reactions should be wrapped in foil and protected from light as much as possible. Some arrestin mutants label better overnight at 4 °C rather than the standard 2–3 h incubation at room temperature. If samples are "rocked" during labeling, avoid introducing too much air into the solution, as this causes precipitation of the arrestin. Generally, we label in 1.5-ml capped centrifuge tubes that are filled nearly to maximum.
2. Different assays require different buffer conditions. We often modulate the salt content of the buffer to control arrestin binding to different functional forms of rhodopsin. For example, arrestin binding to phosphorylated opsin and dark-state phosphorylated rhodopsin is enhanced in salt-free buffer.
3. Excessive pipetting of purified arrestin denatures the protein and should be avoided.
4. Control the actual temperature in the cuvette using an electronic thermometer with a small, flexible probe placed directly in the water-filled sample cuvette.
5. Although pure arrestin often aggregates in the absence of salt, we find that the presence of phosphorylated rhodopsin prevents this aggregation.
6. We find that large, intact ROS membranes are buoyant and do not settle during hour-long measurements. A cuvette fitted with a mini stir bar can be used to avoid sedimentation.
7. 417 nm is the isosbestic point of the Meta I↔Meta II equilibrium, and this subtraction corrects for scattering changes due to arrestin binding.
8. In our hands, a ΔABS value of ~0.02 corresponds to 1 μM Meta II (with a cuvette of 1 cm path length).
9. Arrestin binding is generally slower than peptide binding, so sufficient time should be allowed before measuring the arrestin-containing sample.
10. Concentrations will depend on the type of titration being done.
11. Place the end of the fiber optic on the tabletop and arrange the tubes, lying on their sides, in a semicircle around the light source. Place a sheet of aluminum foil over the end of the fiber optic and tubes, and turn on the light source for 20 s.
12. In order to allow sufficient time for arrestin binding, we typically start the centrifugation 2 min after light-activation.

13. Extreme care should be taken not to disturb the pellet. We generally only take 80 µl of the total supernatant and avoid bringing the pipette tip too close to the pellet.
14. Note that "I72B" stands for mBBr-labeled arrestin I72C, and "I72NBD" stands for IANBD-labeled arrestin I72C.
15. Calibrate the excitation slits such that a sample of 1 µM fluorescently labeled arrestin yields 200–1,000 counts per seconds (cps) at the wavelength of maximal emission (λ_{max}). The bleaching effect of the excitation light can be tested by measuring the absorbance of a sample of rhodopsin diluted in 50 mM HA, before and after exposure to the excitation beam of the fluorescence spectrometer.
16. To avoid inner filter effects, samples should have an OD (optical density) less than 0.1 at the wavelengths of excitation and emission used for the experiment.
17. Bimane λ_{ex}, 390 nm; λ_{em}, 410–600 nm; NBD λ_{ex}, 360 or 500 nm; λ_{em}, 500–550 nm. NBD is about 5 times less absorptive at 360 nm than at 500 nm.
18. We fully photoactivate rhodopsin-containing samples with a 10-s bleach from a 150-W fiber optic light source. The end of the fiber optic is mounted directly over the cuvette such that the sample chamber must not be opened in order to light-activate the sample.
19. The emission detector must be protected from activating light. Many fluorescence spectrometers are designed so that a shutter closes in front of the emission detector when the sample chamber is opened. However, if no shutter is engaged when the activating light is applied, then care should be taken to block the emission detector from the activating light.
20. The chromophore of rhodopsin can complicate fluorescence experiments. In particular, 11-*cis*-retinal of dark-state rhodopsin quenches the fluorescence of bimane and NBD by nonfluorescent energy transfer. Fluorescence changes should always be scrutinized for potential artifacts.
21. H_2SO_4 can also be used. Addition of acid should result in a pH <2.
22. There will be a larger difference between the apparent K_D and the true K_D under conditions that slow arrestin binding, such as high salt concentration or receptor preparations of lower phosphorylation content.

Acknowledgment

This work was supported by a grant from the Deutsche Forschungsgemeinschaft (SO 1037/1-2).

References

1. Schleicher A, Kühn H, Hofmann KP (1989) Kinetics, binding constant, and activation energy of the 48-kDa protein-rhodopsin complex by extra-metarhodopsin II. Biochemistry 28:1770–1775
2. Wilden U, Hall SW, Kuhn H (1986) Phosphodiesterase activation by photoexcited rhodopsin is quenched when rhodopsin is phosphorylated and binds the intrinsic 48-kDa protein of rod outer segments. Proc Natl Acad Sci U S A 83:1174–1178
3. Sommer ME, Hofmann KP, Heck M (2012) Distinct loops in arrestin differentially regulate ligand binding within the GPCR opsin. Nat Commun 3:995
4. Zhuang T, Chen Q, Cho MK et al (2013) Involvement of distinct arrestin-1 elements in binding to different functional forms of rhodopsin. Proc Natl Acad Sci U S A 110: 942–947
5. Sommer ME, Hofmann KP, Heck M (2014) Not just signal shutoff: the protective role of arrestin-1 in rod cells. Handb Exp Pharmacol 219:101–116
6. Lee KA, Nawrot M, Garwin GG et al (2010) Relationships among visual cycle retinoids, rhodopsin phosphorylation, and phototransduction in mouse eyes during light and dark adaptation. Biochemistry 49:2454–2463
7. Sommer ME, Hofmann KP, Heck M (2011) Arrestin-rhodopsin binding stoichiometry in isolated rod outer segment membranes depends on the percentage of activated receptors. J Biol Chem 286:7359–7369
8. Gurevich VV, Hanson SM, Song X et al (2011) The functional cycle of visual arrestins in photoreceptor cells. Prog Retin Eye Res 30:405–430
9. Garwin GG, Saari JC (2000) High-performance liquid chromatography analysis of visual cycle retinoids. Methods Enzymol 316:313–324
10. Piechnick R, Heck M, Sommer ME (2011) Alkylated hydroxylamine derivatives eliminate peripheral retinylidene Schiff bases but cannot enter the retinal binding pocket of light-activated rhodopsin. Biochemistry 50: 7168–7176
11. Sommer ME, Smith WC, Farrens DL (2006) Dynamics of arrestin-rhodopsin interactions: acidic phospholipids enable binding of arrestin to purified rhodopsin in detergent. J Biol Chem 281:9407–9417
12. Gurevich VV, Benovic JL (2000) Arrestin: mutagenesis, expression, purification, and functional characterization. Methods Enzymol 315:422–437
13. Sommer ME, Smith WC, Farrens DL (2005) Dynamics of arrestin-rhodopsin interactions: arrestin and retinal release are directly linked events. J Biol Chem 280:6861–6871
14. Kohl B, Hofmann KP (1987) Temperature dependence of G-protein activation in photoreceptor membranes. Transient extra metarhodopsin II on bovine disk membranes. Biophys J 52:271–277
15. Ernst OP, Bieri C, Vogel H et al (2000) Intrinsic biophysical monitors of transducin activation: fluorescence, UV-visible spectroscopy, light scattering, and evanescent field techniques. Methods Enzymol 315:471–489
16. Kim YJ, Hofmann KP, Ernst OP et al (2013) Crystal structure of pre-activated arrestin p44. Nature 497:142–146
17. Parkes JH, Liebman PA (1984) Temperature and pH dependence of the metarhodopsin I-metarhodopsin II kinetics and equilibria in bovine rod disk membrane suspensions. Biochemistry 23:5054–5061

Chapter 17

Rhodopsin Transient Complexes Investigated by Systems Biology Approaches

Daniele Dell'Orco

Abstract

The fast kinetics characterizing the phototransduction cascade in virtually any species require that rhodopsin (Rh) form transient molecular complexes with a multitude of other proteins. Isolating such transient interactions in vitro and in vivo is a challenging task, although understanding their dynamics is essential to fully understand Rh function. Here, an established bottom-up systems biology approach is summarized, which links individual biomolecular processes to the whole-cell response, namely, the light-dependent suppression of the photoreceptor dark current. The known biochemical interactions occurring in the phototransduction cascade are integrated into a comprehensive computational model that can be numerically simulated, making it possible to: (a) virtually follow the time course of transient complexes formed by Rh with other molecules, including the cognate G protein transducin (G_t), rhodopsin kinase (RK), and arrestin (Arr), and (b) focus on specific receptor states, including multiple phosphorylations and activity of the chromophore-free receptor (opsin, Ops). Successful predictions of retinal disease-associated states, such as those related to vitamin A deficiency and Leber congenital amaurosis, have been obtained with the methodology presented herein.

Key words Systems biology, Computational modeling, Phototransduction, Dynamic modeling, Parameter estimation, Kinetic modeling, GPCR

1 Introduction

Rhodopsin (Rh) is the visual pigment responsible for triggering and activating the phototransduction cascade. The peculiar nature of the light stimulus, its extreme physical variability, and the consequent adaptation requirements make the kinetics of this signaling pathway one of the fastest known to date. It is not surprising thus that Rh has to very quickly associate to other molecules, initially to its cognate G protein transducin (G_t) to catalyze the GTP-to-GDP exchange, and quickly lead to complex dissociation in order to activate other G_t molecules and yield the typically high signal amplification. Recovery of the phototransduction cascade also involves transient molecular complexes, namely, those between Rh and its kinase (RK), which by multiple phosphorylation steps

Beata Jastrzebska (ed.), *Rhodopsin: Methods and Protocols*, Methods in Molecular Biology, vol. 1271,
DOI 10.1007/978-1-4939-2330-4_17,

reduces the affinity of Rh for G_t while increasing that for the protein arrestin (Arr), which eventually deactivates Rh bringing to the termination of the light response [1].

The crucial interactions between Rh and other components of the signaling cascade have been thoroughly studied experimentally, and in several studies, the goal was to assess kinetic information on the association and dissociation rates rather than focusing on the equilibrium state, which in vivo may exist only under certain steady illumination/dark conditions. Among the other techniques, the development of on-chip strategies has demonstrated to be particularly promising. In recent applications, both native and recombinant Rh have been immobilized on the surface of a sensor chip, and the binding partner (i.e., G_t or RK) was allowed to flow and reconstitute the complex in different conditions, yielding kinetic rate constants that allow for quantitative comparisons of different Rh states [2–6].

In parallel with experimental studies, it became increasingly clear that, in order to link biomolecular processes to the whole-cell responses typically measured in electrophysiological experiments performed with wild-type or mutated animals, the typical reductionist approach that focuses just on a couple of molecules would not be suitable. Emerging properties arise at a system level, when the complexity of the network of biomolecular interactions is properly considered together with the rigorous biochemical description of each individual interaction [7–11], thus calling for a more comprehensive, "bottom-up" holistic approach. Predictions of cell responses, namely, photocurrents, generated as a direct output from the novel system-level paradigm reproduce extremely well those observed in a variety of different species, including mice (Fig. 1; *see* Ref. 12), which represent the animal model most widely studied to date. Simulations have successfully predicted the effects of complex genetic manipulations of the biochemical components of the cascade, including: (a) overexpression and downregulation of selected genes [12–14] and (b) point mutations and other manipulations associated to several retinal disease including Leber congenital amaurosis and vitamin A deficiency [7, 13], Nougaret Congenital Night Blindness [15], and cone/cone-rod dystrophy [16].

We herein provide the methodological basis for such modeling approach, highlighting how it can be applied in practice to virtually monitor any transient complex formed by any modeled state of Rh.

2 Materials

Experimental data on the kinetics of interaction between Rh and other molecules, useful to be integrated in comprehensive kinetic models, may be obtained by several techniques. Here we consider

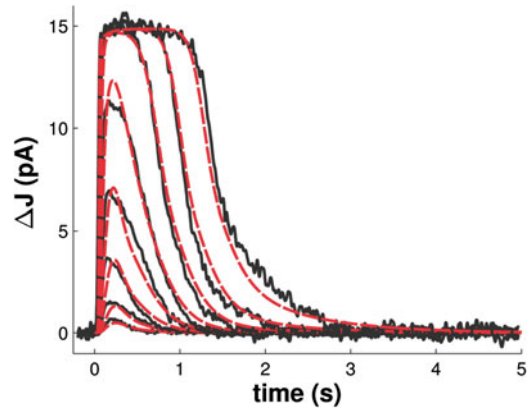

Fig. 1 Example of simulations (*red*, *dashed traces*) of flash responses in a mouse rod obtained by applying the systems biology methodology presented here. Experimental data (*black traces*) represent photocurrent measurements obtained in a 3-month-old mouse after delivering 20 ms flash stimuli at time t = 0 s, with intensities of 1.4, 4.8, 15.2, 39.4, 125, 444, 1,406, and 4,630 photons μm^{-2}. Reproduced from Ref. [12] 2014 with permission from The Royal Society of Chemistry

the extensive use of a surface plasmon resonance methodology based on the modification of a commercially available system (Biacore©). Specific applications and methodology to study interactions involving dark-adapted or photoactivated Rh and/or other GPCRs have been thoroughly described in previous work [2–6].

The modeling methodology presented here is based on the numerical simulation of a system of kinetic biochemical equations in a deterministic framework (*see* **Note 1**), with each reaction being described by an ordinary differential equation (ODE). The essential software used for model implementation, numerical simulation, and analysis is listed in this paragraph.

2.1 MATLAB Computing Environment

The methodology is based on the numerical computing environment MATLAB, developed by MathWorks (www.mathworks.com), which is widely used in academic and research institutions. At the moment of this writing, the most updated version is R2014A; however, the results described here and in the relative literature will also be obtained by running any earlier version of MATLAB, starting from R2007A, provided that there is proven compatibility with the other listed packages.

2.2 SBTOOLBOX2 Package

The Systems Biology Toolbox 2 for MATLAB (SBTOOLBOX2) [17] used for model implementation and simulation can be freely obtained for academic use from the website www.sbtoolbox2.org. The toolbox has been recently integrated in the SBPOP

extension package (SBPOP), which adds functionality related to pharmacometrics and systems pharmacology applications.

SBTOOLBOX2 is a MATLAB customizable environment that allows the user to: (a) individually implement each biochemical reaction making up the network, by specifying stoichiometry, concentrations of the molecular species, and mathematical expressions for the rate of each reaction, thus ensuring a virtually unlimited modularity; (b) separate the computational model from the different experimental data, thus making a clear distinction between the model structure, which remains unaltered, and the simulation of specific conditions (in silico experiments) for a direct comparison with experimental data; (c) perform all the necessary analyses within the same environment; and (d) export the final model also in the widely used SBML language to facilitate model sharing (*see* **Note 2**).

Moreover, by making use of typical MATLAB scripts, the user may customize the toolbox according to case-specific requirements, as well as simulate complex experimental scenarios.

2.3 SBPD Package

The SBPD extension package (SBPD) for the SBTOOLBOX2 adds high-speed simulations, combination of models, experiments, and measurement data in so-called projects. SBPD projects allow the user to group models, experiment descriptions and associated measurements data in a single object, and to run parameter estimation (PE) (*see* **Note 3**) and sensitivity analyses (SA) directly on those objects (*see* **Note 4**). The complete model-building process is supported by specific functions (modeling, simulation, identifiability analysis, model reduction, PE (multiple experiments and multiple measurement fittings), validation, etc.). Graphical user interfaces support the workflow.

SBPD has also been integrated in the SBPOP package, and it is freely available for academic use at www.sbtoolbox2.org.

3 Methods

In order to implement a mathematical model of the phototransduction cascade and monitor specific complexes (or states) involving Rh, it is essential that the required software be properly installed. Instructions providing details can be found at www.sbtoolbox2.org.

3.1 Build the Static Network Structure

Latest biological knowledge as to the biochemical reactions involving molecular species, which are relevant to the specific time and space scales of interest, is used to build up a static network structure, like the one shown in Fig. 2. The static network structure globally describes the interactions (edges) of each molecule (node) in the network with one another, that is, network connectivity,

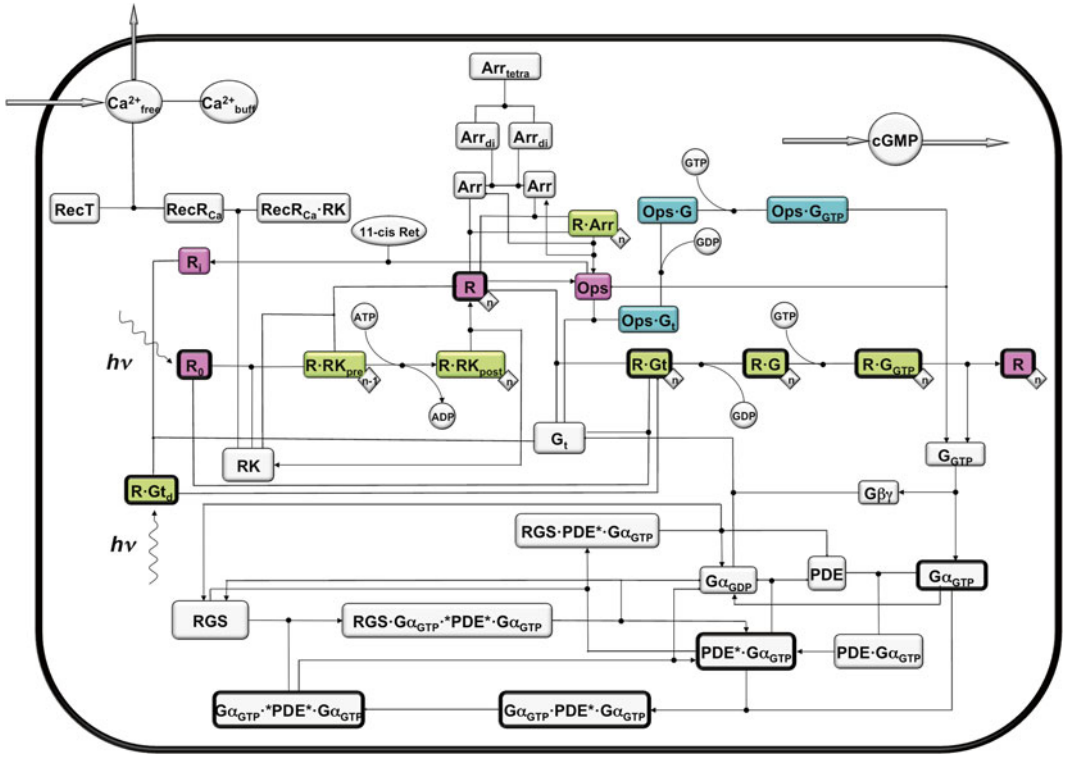

Fig. 2 Static network structure of an up-to-date comprehensive model of vertebrate phototransduction. Irreversible reactions are marked with an *arrow* indicating the direction of the reaction. *Boxes* represent the molecular species involved in the phototransduction cascade. Various forms of Rh and its molecular complexes have been colored to be distinguished from other molecular components of the cascade, in particular, inactive, dark adapted (R_i); photoactivated without any phosphate bound (R_0) or with n-phosphate groups bound following phosphorylation by RK (R_n) and chromophore-free, opsin form (Ops) are colored *magenta*. Complexes between photoactivated Rh and RK, G_t and Arr are colored *light green*, and complexes involving Ops are colored *light cyan*. *Bold borders* mark the activated molecular species involved in the amplification, while *diamonds* positioned at the *bottom right* of some of the species indicate the number of phosphate groups that can be bound upon phosphorylation, from 0 to 6. For details *see* Ref. [13]

highlighting what molecules shall be considered reactants or products in each reaction, and the direction of each reaction (reversible/irreversible). In the most recent implementation concerning a mouse rod cell, 96 reactions deterministically track the time evolution of 76 molecular species using 62 parameters [12]. The current version is the evolution of a model initially developed for amphibian rods [9, 10, 13], in which several mechanisms have been iteratively inserted to make the model more realistic [2, 14, 18], followed by a thorough adaptation to the faster dynamics observed in mouse rods [12]. The model can be conveniently implemented in MATLAB by following the syntax of the SBedit function of the SBTOOLBOX2, which also supports a graphical user interface (*see* **Note 5**).

3.2 From Static to Dynamic Models: Reaction Kinetics

Except where the characteristics of the biochemical reaction impose otherwise (*see* **Note 6**), the law of mass action is used to describe the reaction kinetics, and the amount or concentration of molecules of each species is monitored in its time evolution. The rate of change of a molecular species with time (time derivative) is calculated by summing all reaction rates that produce the species and subtracting all reaction rates that consume the species.

The model simulates the reactions taking place in a well-stirred volume; therefore, the spatial structure of the photoreceptor outer segment is not taken into account. The network of interactions built in Subheading 3.1 with the addition of appropriate kinetic and stoichiometric information can be used to obtain a dynamic model, whose time evolution can be explicitly modeled by numerically solving a system of ODE according to the relationship:

$$\dot{x}(t) = N \times v(x)$$

where the time derivative of the vector containing the concentration (or the number of molecules) of each molecular species $\dot{x}(t)$ (a 76×1 matrix in the latest implementation) is obtained by multiplying the stoichiometric matrix N (indicating which species in which reactions are involved as reactants and products; 76×96 matrix in the latest implementation) by the reaction rate vector v (96×1) containing mathematical expressions describing the kinetics of each reaction rate.

3.3 Determine/ Estimate Missing Parameters

Numerical values for each kinetic parameter appearing in the reaction rates vector should be retrieved or approximated from the literature when possible. Obtaining consistent or comparable parameters from the literature is not trivial, especially because kinetic parameters are often affected by systematic errors related to the experimental technique used for their determination. It is therefore convenient to achieve relative rather than absolute kinetic parameters by using the same experimental technique in a comparative fashion and use the inferred quantitative relationships between the parameters in the process of mathematical modeling. In this respect, the surface plasmon resonance-based technique has proven to be ideal to compare the kinetics of the interaction of Rh with different molecules, in several conditions [2–6] (*see* **Note 7**).

In cases where the true parameter values are unknown and no relative relationship can be determined, parameters should be either manually tuned (*see* **Note 8**) to meet experimental expectation or be estimated through parameter optimization (PE) techniques. Optimization should be performed against experimental electrophysiological data (or other time series reporting a measurable quantity described in the model) by performing multiple fitting procedures that attempt to simultaneously optimize a limited number of parameters over several heterogeneous dynamic behaviors of the system, which are characterized by very different

initial conditions (*see* **Note 9**). By making use of the SBPD graphical user interface (SBPDgui), several PE protocols can be run within the framework of an SBPD project, hence allowing customized and full control of: (a) the model to be optimized; (b) the experiments to be chosen for PE; (c) the boundaries for each parameter/initial condition, in terms of variations with respect to the initial nominal values; and (d) the PE algorithms and relative tolerance to be employed in each protocol step.

Any optimization method that is available in MATLAB can be used, ideally alternating between local and global optimization algorithms, to achieve acceptable values for the cost function (*see* **Note 10**).

Once the missing parameters have been estimated, their values must be kept fixed in all subsequent simulation experiments. Testing the optimized model on a variety of dynamic behaviors (test set) different from those used for parameter estimation (training set) is a fundamental step in model validation.

3.4 Numerical Simulations and Analysis of Rh Transient Complexes

Deterministic simulations are run by using the SBPDsimulate function, which creates and uses MEX functions to speed up the simulation (*see* **Note 11**). Several options may be used with the SBPDsimulate function in order to specify: (a) simulation time; (b) vector of initial conditions, if different from what is present in the model file; (c) name and values of the parameters to be changed in each simulation; and (d) options, a MATLAB© structure object for setting tolerance and integration step size.

If no output argument is given, the results of the simulations are plotted in an **SBplot** window, a self-explanatory graphical user interface that allows to visualize the time course of each molecular species present in the model, as well as the time course of each reaction/interaction rate. For further analysis, it is convenient to address the simulation output to a structure object, which will contain: (a) a vector with time instants of the results (*output.time*); (b) a cell array with state names (*output.states*); (c) a matrix with state values, each row corresponding to one time instant (*output.statevalues*); (d) a cell array with reaction names and reaction rate values (*output.reactions* and *output.reactionvalues*, respectively). By taking advantage of the typical MATLAB scripting procedures, one can generate plots of the time course of desired molecular species and perform quantitative analyses of specific functional features (i.e., analysis of time-to-peak, saturation times for photocurrents following saturating stimuli, and so on). As an example, Fig. 3 reports on the simulation of the time evolution of four different Rh transient complexes under different light stimuli, from dim light to saturating flashes. The analysis allows one to simultaneously assess various dynamic features of Rh transient complexes, such as the significantly different kinetics and the maximum number of complexes that may form under the same stimuli conditions, which

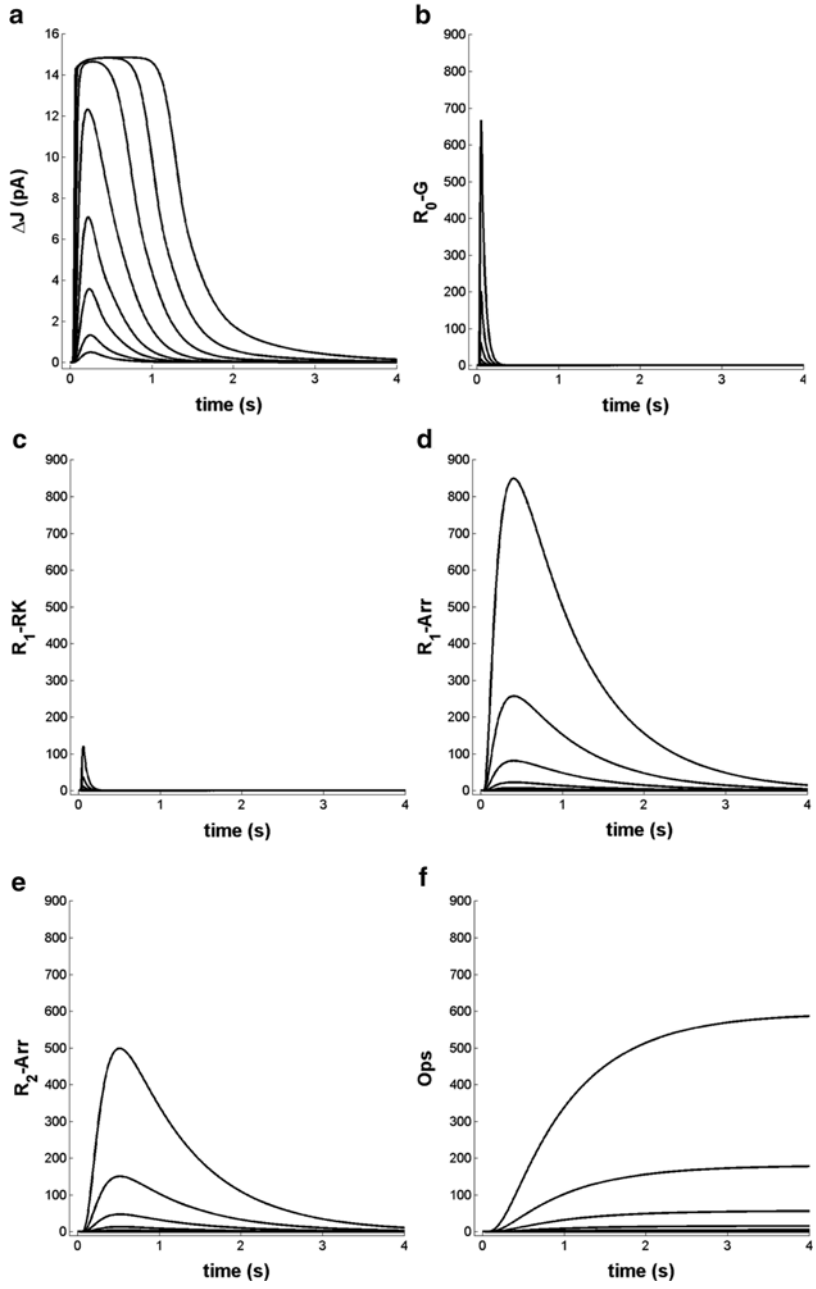

Fig. 3 Examples of transient complexes formed by Rh (**b**–**e**) and transient Ops state (**f**) resulting from the stimulation of a mouse rod cell by 20 ms flashes of increasing intensity (1.7, 4.8, 15.2, 39.4, 125, 444, 1,406 and 4,630 photons μm^{-2}) delivered at time $t=0$. (**a**) Time evolution of the photocurrent (ΔJ) at each light intensity; (**b**) time evolution of the number of unphosphorylated photoactivated Rh in complex with G_t at each corresponding light intensity; (**c**) time evolution of the complex between the RK and photoactivated Rh, phosporylated at one site only; (**d**) time evolution of the complex between Arr an Rh, undergone single (**d**) and double (**e**) phosphorylations; (**f**) time evolution of the chromophore-free form of Rh (Ops) under the same illumination conditions. Simulations are obtained by making use of the recently developed mouse model presented in Ref. [12]

significantly varies from case to case. For example, simulations clearly highlight the slow kinetics of reconstitution of the pigment from the bleached Ops, which does not occur in the simulated time frame (Fig. 3f).

3.5 Evaluate Model Robustness

Sensitivity analysis algorithms are useful to evaluate model robustness, especially global analysis algorithms (GSA), in which the parameter space is deeply explored. A number of methods are available for GSA which, in general, are computationally intensive and differ in their mathematical approach and foundation [19] (*see* **Note 12**).

The SBTOOLBOX2 offers the possibility to use several such algorithms, both for local and global analyses (*see* www.sbtoolbox2.org), which require in any case the use of standard MATLAB scripts. If the model is available in the SBML format, the SBML-SAT [20] analysis tool can also be conveniently used.

In order to run a GSA protocol, first an objective function shall be created to assess the effects of parameter perturbation on a specific quantity. For example, in previous work [13], the analysis focused on the time (T_{sat}) needed to decrease the rod photocurrent from saturation to 90 % of the maximum value, that is, the cell saturation time following bright stimuli. A selection of the parameters to be included in the analysis must be done a priori, the boundaries of parameter variations shall be selected (typical values can be a ~0.3 to 3 factor around the nominal parameter value), and the total number of simulations (at least 100,000) shall also be fixed. Parameter sensitivity rankings are returned as an output, allowing to assess the influence of each particular parameter on the chosen quantity.

4 Notes

1. Once the static network structure has been built as described in Subheading 3.1 and the set of ODE describing the kinetics for each reaction has been explicitly written, the system can be also simulated stochastically. This is often desirable, especially when simulating responses to dim light, e.g., single-photon response. The **SBstochsim** function available within the SBTOOLBOX2 (www.sbtoolbox2.org) may be used; in this case each reaction in the system must be irreversible (if necessary, a reversible reaction can always be splitted in two separate subreactions, namely, forward and reverse), and instead of molecular concentration, the number of molecules (integer) shall be used. According to the general framework of the chemical master equation (CME), the system is still represented by the same set of differential equations, which will now describe the variation over time of the probabilities that the system occupies each of the different states.

2. The Systems Biology Markup Language (SBML; www.sbml.org) is the XML-based free and open standard format for representing computational models in systems biology.
3. PE is necessary to estimate a value with specific boundaries for the parameters that have not been experimentally measured or deduced. It is a complex multi-fitting procedure that attempts the simultaneous numerical optimization of a limited number of parameters over several heterogeneous dynamic behaviors of the system characterized by very different initial conditions.
4. SA is widely used in systems theory to examine how sensitive a model response is to parameter variations and to provide insights into the relationship between the parameters and specific features of the output, as well as to unveil correlations between the parameters. For large and nonlinear biological networks, such as the phototransduction cascade, large uncertainties might be associated to the parameters; therefore, it is of particular interest to perform a global parameter sensitivity analysis (GSA) to deeply explore the parameter space.
5. The model can be implemented within the SBTOOLBOX2 either by:
   (a) Using the **SBedit** function, which implies specifying the ODE describing the rates of production and consumption of each molecular species. In the following example, the protein G is involved in only two reactions: reaction 2, which consumes G, and reaction 8 which creates G. Reaction rates have been identified by R2 and R8. The syntax would then be the following:

$$d/dt(G) = -R2 + R8$$

   The relative rates must also be specified, for example:

$$R2 = k2 * Ract * G \text{ and } R8 = k8 * Gr$$

   where Ract and Gr are other proteins interacting with G.

   (b) Using the **SBeditBC** function, which allows a more biochemically oriented and intuitive implementation that specifies reactant and products and direction of each reaction, for the same example as above:

$$G + Ract => RactG : R2$$

$$vf = k2 * Ract * G$$

   and

$$Gr => G : R8$$
$$vf = k8 * Gr$$

6. There are cases, in which reaction rates are better described by empirical relationships because the time or space/time scales of the reaction as compared to those of the system do not allow finer descriptions. For example, fast steps are conveniently lumped into fewer, slower steps, and the whole rate is considered. This is the case for processes in which small second messengers such as Ca^{2+} ions are bound/dissociate to/from a calcium sensor to regulate the activity of a target protein. The protein-ion interaction is fast compared to the time scale considered in phototransduction, but the resulting protein conformational change is the process that matters for regulating the kinetics of the reaction in the context of the whole network, and it is what shall be explicitly considered in the modeling. For example, in order to model the Ca^{2+}-mediated feedback on RK by the neuronal calcium sensor recoverin, the transition from apo to Ca^{2+}-bound forms of recoverin has been recently implemented in the phototransduction model [14], based on kinetic data on the relative conformational change rates assessed by surface plasmon resonance [21].
7. A recent example of the implementation of relative, quantitative relationships between kinetic parameters rather than absolute rate constants has been reported, to distinguish between the association/dissociation of G_t to/from Rh in dark conditions and those that follow light stimulation [2]. Experimental evidence obtained by surface plasmon resonance spectroscopy highlighted faster kinetics for G_t interaction with dark rather than photoactivated Rh ($k^{on}_{dark} \approx 1.6 \times k^{on}_{light}$ and $k^{off}_{dark} \geq 315 \times k^{off}_{light}$), and such kinetic constraints have been used in the modeling procedure, thus minimizing unavoidable discrepancies between in vitro and in vivo conditions.
8. Parameter manual tuning should be performed carefully. The effect of each tuning should be thoroughly probed on several dynamic simulations of the system and the output quantitatively compared to experimental data, when these are available.

   The **SBPDmanualtuning** function in the SBTOOLBOX2 can be conveniently used for achieving the goal. A graphical user interface allows to compare simulated experiments data to real measurements and perform manual parameter tuning around nominal parameter values chosen by the user. It is additionally possible to run simulations of selected experiments directly from the SBPDmanualtuning window, allowing for a deeper analysis of what happens in the system at each parameter change.
9. For modeling of phototransduction processes, PE is ideally performed considering simultaneously four to six different dynamic behaviors (fast flashes of different intensity, steps of light of different duration/intensity, genetic manipulations in which a key component has been knocked out, etc.), to ensure that the optimized parameters would suit a variety of stimulus

paradigms rather than being appropriate just for a limited set of light regimes (i.e., very dim or very bright light, dark-adapted conditions, etc.). If the model is implemented in a modular fashion or new mechanisms are iteratively considered at later steps, like it has been the case in the present modeling [2, 12–14], it is important to perform PE of the updated models on a similar set of dynamic behaviors and check the values for the optimization cost at each step.

10. In order to be independent of the Optimization Toolbox for MATLAB, several local and global optimization methods are available in the SBTOOLBOX2. The modeling presented here made use of a combination of the Nelder-Mead nonlinear simplex method for local optimization and a particle swarm method for global optimization, until an optimal cost ~10^{-3} was reached.
11. MEX functions are compiled C-code versions of SBmodels linked together with the CVODES integrator from SUNDIALS [22] and a MATLAB interface. A simulation performance typical of a stand-alone software application is thus obtained, while still keeping MATLAB flexibility in handling the returned simulation data and the models.
12. A GSA based on the variance-based Sobol's method [23] was employed in the first application to the phototransduction cascade study [13], focusing on the dynamic response to saturating light flashes.

Acknowledgements

The methodology presented in this work is the result of a joint effort between several colleagues. I wish to acknowledge the fundamental contributions of Henning Schmidt, Brandon M. Invergo, Simona Mariani, Francesca Fanelli, and Karl-W. Koch. This work was supported by funds from the Italian Ministry of Research and Education, via departmental grants.

References

1. Pugh EN Jr, Lamb TD (2000) Phototransduction in vertebrate rods and cones: molecular mechanisms of amplification, recovery and light adaptation. Elsevier Science B.V, New York
2. Dell'Orco D, Koch KW (2011) A dynamic scaffolding mechanism for rhodopsin and transducin interaction in vertebrate vision. Biochem J 440:263–271
3. Komolov KE, Aguila M, Toledo D et al (2010) On-chip photoactivation of heterologously expressed rhodopsin allows kinetic analysis of G-protein signaling by surface plasmon resonance spectroscopy. Anal Bioanal Chem 397:2967–2976
4. Komolov KE, Koch KW (2010) Application of surface plasmon resonance spectroscopy to

study G-protein coupled receptor signalling. Methods Mol Biol 627:249–260

5. Komolov KE, Senin II, Kovaleva NA et al (2009) Mechanism of rhodopsin kinase regulation by recoverin. J Neurochem 110:72–79
6. Komolov KE, Senin II, Philippov PP et al (2006) Surface plasmon resonance study of g protein/receptor coupling in a lipid bilayer-free system. Anal Chem 78:1228–1234
7. Dell'Orco D, Koch KW (2010) Systems biochemistry approaches to vertebrate phototransduction: towards a molecular understanding of disease. Biochem Soc Trans 38:1275–1280
8. Hamer RD (2000) Computational analysis of vertebrate phototransduction: combined quantitative and qualitative modeling of dark- and light-adapted responses in amphibian rods. Vis Neurosci 17:679–699
9. Hamer RD, Nicholas SC, Tranchina D et al (2003) Multiple steps of phosphorylation of activated rhodopsin can account for the reproducibility of vertebrate rod single-photon responses. J Gen Physiol 122:419–444
10. Hamer RD, Nicholas SC, Tranchina D et al (2005) Toward a unified model of vertebrate rod phototransduction. Vis Neurosci 22:417–436
11. Kiel C, Vogt A, Campagna A et al (2011) Structural and functional protein network analyses predict novel signaling functions for rhodopsin. Mol Syst Biol 7:551
12. Invergo BM, Dell'Orco D, Montanucci L et al (2014) A comprehensive model of the phototransduction cascade in mouse rod cells. Mol Biosyst 10:1481–1489
13. Dell'Orco D, Schmidt H, Mariani S et al (2009) Network-level analysis of light adaptation in rod cells under normal and altered conditions. Mol Biosyst 5:1232–1246
14. Invergo BM, Montanucci L, Koch KW et al (2013) Exploring the rate-limiting steps in visual phototransduction recovery by bottom-up kinetic modeling. Cell Commun Signal 11:36
15. Mariani S, Dell'Orco D, Felline A et al (2013) Network and atomistic simulations unveil the structural determinants of mutations linked to retinal diseases. PLoS Comput Biol 9:e1003207
16. Dell'Orco D, Sulmann S, Zagel P et al (2014) Impact of cone dystrophy-related mutations in GCAP1 on a kinetic model of phototransduction. Cell Mol Life Sci 71(19):3829–3840
17. Schmidt H, Jirstrand M (2006) Systems Biology Toolbox for MATLAB: a computational platform for research in systems biology. Bioinformatics 22:514–515
18. Koch KW, Dell'Orco D (2013) A calcium-relay mechanism in vertebrate phototransduction. ACS Chem Neurosci 4:909–917
19. Zhang Y, Rundell A (2006) Comparative study of parameter sensitivity analyses of the TCR-activated Erk-MAPK signalling pathway. Syst Biol (Stevenage) 153:201–211
20. Zi Z, Zheng Y, Rundell AE et al (2008) SBML-SAT: a systems biology markup language (SBML) based sensitivity analysis tool. BMC Bioinformatics 9:342
21. Dell'Orco D, Muller M, Koch KW (2010) Quantitative detection of conformational transitions in a calcium sensor protein by surface plasmon resonance. Chem Commun (Camb) 46:7316–7318
22. Hindmarsh A, Brown P, Grant K (2005) SUNDIALS: suite of nonlinear and differential/algebraic equation solvers. ACM Trans Math Softw 31:363–396
23. Sobol IM (2001) Global sensitivity indices for nonlinear mathematical models and their Monte Carlo estimates. Math Comput Simulat 55:271–280

Part V

Rhodopsin and Photoreceptors

Chapter 18

Three-Dimensional Architecture of Murine Rod Cilium Revealed by Cryo-EM

Theodore G. Wensel and Jared C. Gilliam

Abstract

The connecting cilium of the rod photoreceptor is a tubular structure that bridges two adjacent cellular compartments, the inner segment, the major site of biosynthesis and energy metabolism, and the outer segment, a highly specialized ciliary structure responsible for phototransduction. The connecting cilium allows for active processes of protein sorting and transport to occur between them. Mutations affecting the cargo, their transporters, and the structural components of the primary cilium and basal body lead to aberrant trafficking and photoreceptor cell death. Understanding the overall design of the cilium, its architectural organization, and the function of varied protein complexes within the structural hierarchy of the cilium requires techniques for visualizing their native three-dimensional structures at high magnification. Here we describe methods for isolating retinas from mice, purifying fragments of rod cells that include much of the inner segment and the rod photoreceptor cilia, vitrifying the cell fragments, and determining their structures by cryo-electron tomography.

Key words Cryo-electron tomography, Intraflagellar transport, Primary cilia, Rod outer segment

1 Introduction

The biosynthetic machinery of the rod photoreceptor neuron is sequestered in the inner segment compartment of the cell. Following synthesis and posttranslational modification of key phototransduction proteins in the inner segment, vesicles consisting of these proteins and specific membrane lipids are constructed and transported to the rod outer segment, a modified primary cilium [1, 2]. The rod outer segment contains a highly organized system of membrane disks, each of which contains a high density of rhodopsin, ~25,000 molecules per μm^2 [3]. The daily cycle of disk membrane turnover and renewal replaces ~10 % of the outer segment each day [2], which suggests that a minimum of 2,000 rhodopsin molecules per minute [4] are trafficked to the outer segment through the connecting cilium in a process called intraflagellar transport [5, 6]. The transport of different complexes through the

Beata Jastrzebska (ed.), *Rhodopsin: Methods and Protocols*, Methods in Molecular Biology, vol. 1271,
DOI 10.1007/978-1-4939-2330-4_18,

connecting cilium, which corresponds roughly to the transition zone of other primary cilia, is a coordinated series of steps that, at minimum, include cargo sorting, cargo docking, active trafficking, and cargo release. Although many proteins such as rhodopsin remain sequestered in the outer segment compartment of the cell, other proteins such as transducin are reportedly able to be reversibly redistributed between the inner and outer segments, via the primary cilium [7]. These complex processes are contained within a structure that is approximately 300 nm in diameter and a little more than 1,000 nm in length [8], dimensions which challenge the limits of most conventional imaging techniques.

Cryo-electron tomography (cryo-ET) is an imaging technique capable of capturing biological structures in their native, hydrated form while preserving their three-dimensional arrangements [9]. Specimens are applied to a copper EM grid, excess liquid is blotted away, and the grid is plunged into liquid ethane (melting temperature at −183 °C) so that it is frozen at a rate exceeding 10^4 °C/s [10]. This allows specimens up to 10 μm thick (typical specimen thickness ranges from 200 to 500 nm) to be preserved in noncrystalline (vitreous) ice, which prevents disruption of cellular membranes and redistribution of cellular contents, artifacts known to result from crystalline ice formation. Electron tomography, the process of acquiring micrograph images of vitrified biological specimen at incremental angular steps (called a tilt series), is then carried out on an electron microscope with a computer-controlled [11, 12] stage while maintaining the sample at −196 °C (specimen must always be kept below −140 °C, which is the devitrification temperature of water where ice crystals form). Using computational methods, two-dimensional tilt series micrograph projections are aligned and merged to build a three-dimensional density map (tomogram) capable of revealing the original specimen at high resolution (5–50 nm range) [13–15]. The final resolution of the tomogram is directly dependent upon the cumulative electron dose (typically 100 Å/μm^2 or less to prevent radiation damage to biological samples) and the incremental angle size between each successive projection micrograph. Physical limitations, caused by increased electron scattering at higher tilt angles due to increasing electron path length through the sample, degrade high angle image quality and practically limit tilt series to ±70° [16]. The limited angular range in electron tomography creates a data void in Fourier space during computational tomogram reconstruction known as the "missing wedge" artifact [13, 17, 18]. The missing wedge of data causes a "stretching" of structural data along the *z*-axis of the reconstructed tomogram and confounds interpretation of biological structures.

Because of its dimensions and the intricacies of its membrane and microtubule-based structures, the mammalian rod cilium is an excellent subject for cryo-ET [8, 19]. It allows a detailed

three-dimensional view of the arrangement of its molecular components under minimally perturbing conditions. We describe here methods for isolating retinas from mice, purifying fragments of the rod containing the outer segments, connecting cilia and adjacent region of the inner segments by isoosmotic density gradient ultracentrifugation, and vitrifying the cell fragments for cryo-ET by plunge freezing in liquid ethane. We also describe image collection and processing procedures for cryo-ET.

2 Materials

2.1 Mouse Retinas

Cell fragments containing rod outer segments (ROS) with attached connecting cilia and portions of inner segment (here referred to as "ROS") are isolated from maturely developed retinas of 21-day-old mice or older (Fig. 1). Widely available inbred animal strains can be obtained from commercial vendors if they are not housed directly in an institutional vivarium. We recommend preparing ROS from 10 to 12 retinas for easier visualization of purified ROS bands using the current protocol. Animals younger than 21 days or animals containing genetic mutations suspected to alter retinal development or to be subject to retinal degeneration may decrease the yield of ROS in the preparation. It may be necessary to scale the preparation to optimize yield for EM grid preparation.

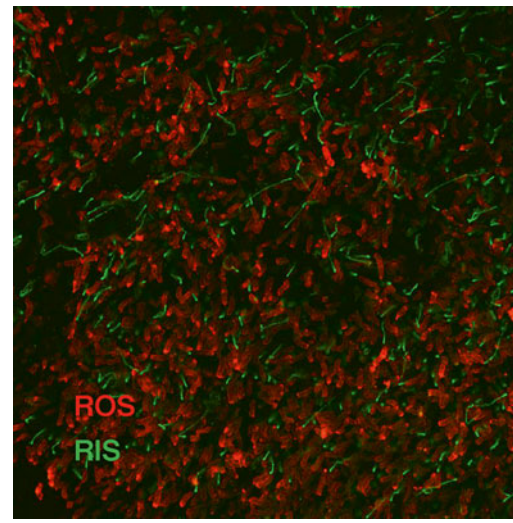

Fig. 1 Immunofluorescence of a whole-mount retina. Whole-mount retina was stained with antibodies against rhodopsin (*red*) and rootletin (*green*). Rhodopsin staining corresponds to the photoreceptor outer segment, while rootletin staining corresponds to the inner segment

2.2 Buffers and Assay Reagents

1. Ringer's Buffer (5×): 50 mM 4-(2-hydroxyethyl)piperazine-1-ethanesulfonic acid (HEPES), pH 7.4, 650 mM NaCl, 18 mM KCl, 60 mM $MgCl_2$, 6 mM $CaCl_2$, 0.1 mM ethylenediaminetetraacetic acid (EDTA). Filter through a 0.2 μm pore nitrocellulose filter and store at 4 °C. Preparing a 100 ml volume is sufficient for at least ten ROS preparations.
2. Ringer's Buffer (1×): 10 mM HEPES, pH 7.4, 130 mM NaCl, 3.6 mM KCl, 12 mM $MgCl_2$, 1.2 mM $CaCl_2$, 0.02 mM EDTA. Prepare 50 ml by diluting 1:5 from the stock of 5× Ringer's Buffer.
3. OptiPrep (Axis-Shield), 60 % (w/v) iodixanol solution, 5,5′-[(2-hydroxy-1-3propanediyl)-bis(acetylamino)]bis[*N,N*′-bis(2,3-dihydroxypropyl-2,4,6-triiodo-1,3-benzenecarboxamide)] as supplied.
4. Acetone, EM grade.
5. BSA-coated gold fiducial markers, 15 nm diameter (Electron Microscopy Sciences). Colloidal gold markers are used to aid in alignment of the micrographs during the tomographic reconstruction (*see* **Note 1**).

2.3 Density Gradient Centrifugation Media

1. 40 % OptiPrep (15 ml): 40 % OptiPrep, 1× Ringer's Buffer. Add 10 ml of 60 % OptiPrep to a 15 ml conical tube or other sealable container. Add 3 ml of 5× Ringer's Buffer and bring the final volume to 15 ml with water. Mix thoroughly by pipetting or inversion and store at 4 °C on ice.
2. 30 % OptiPrep (4 ml): Add 3 ml of 40 % OptiPrep to 1 ml of 1× Ringer's Buffer.
3. 25 % OptiPrep (4 ml): Add 2.5 ml of 40 % OptiPrep to 1.5 ml of 1× Ringer's Buffer.
4. 20 % OptiPrep (4 ml): Add 2 ml of 40 % OptiPrep to 2 ml of 1× Ringer's Buffer.
5. 15 % OptiPrep (4 ml): Add 1.5 ml of 40 % OptiPrep to 2.5 ml of 1× Ringer's Buffer.
6. 10 % OptiPrep (4 ml): Add 1 ml of 40 % OptiPrep to 3 ml of 1× Ringer's Buffer.
7. 8 % OptiPrep (4 ml): Add 0.8 ml of 40 % OptiPrep to 3.2 ml of 1× Ringer's Buffer.

2.4 Dissection Tools and Apparatus

1. Stereoscopic dissection microscope with an appropriate light source (*see* **Note 2**).
2. Variable-speed benchtop vortexer (e.g., Vortex-Genie 2).
3. Wide-bore micropipette tips: for 20, 200, and 1,000 μl volumes (*see* **Note 3**).
4. Dumont #5-style forceps (Fine Science Tools) or equivalent: two pairs required for tissue manipulation.

5. Standard scissors (Fine Science Tools) or equivalent.
6. Spring-loaded, Vannas-style microscissors (Fine Science Tools) or equivalent, required for precision cutting of the mouse eye (*see* **Note 4**).
7. Beveled, hypodermic needles, 18 G and 27 G.
8. Syringes, 1.0 ml, for gradient formation and ROS collection.
9. Microcentrifuge tubes, 1.5 ml siliconized, for tissue collection and purification.
10. Polypropylene tissue culture dish, 60 mm or 100 mm diameter, for use as a reservoir during retina dissection.
11. Ice pack for maintaining temperature during the dissection procedure.
12. Parafilm.

2.5 Infrared Visualization

Infrared visualization is not required for preparing ROS fragments for cryo-ET, as sample can be easily prepared under room light or dim red light. However, some physiological differences should be expected from photoreceptor cells conditioned to different intensities of light. We provide the additional materials for this optional condition should they be necessary for a more exacting experimental design:

1. Dark room that has been treated to limit light bleed through (*see* **Note 5**).
2. Infrared LED panel for light-free illumination of the work surface (*see* **Note 6**).
3. Night vision goggles. Binocular, head-mounted goggles allow for unobstructed, hands-free experimentation.
4. Aluminum foil.
5. Black permanent marker (*see* **Note 7**).

2.6 Ultracentrifuge, Rotor, and Tubes

1. Beckman TL-100 tabletop ultracentrifuge or equivalent.
2. TLA-100.3 fixed-angle ultracentrifuge rotor or equivalent.
3. TLS-55 swinging bucket ultracentrifuge rotor or equivalent.
4. Microcentrifuge-style 1.5 ml polyallomer tubes (Beckman) with adapters for TLA-100.3.
5. Thinwall 2.2 ml polyallomer tubes (Beckman) for TLS-55.
6. Analytical scale for balancing ultracentrifuge samples.

2.7 Cryo-supplies and EM Grids

1. EM grids: Quantifoil® Holey Carbon Films, 200 mesh, R2/2 (*see* **Note 8**).
2. Empty grid storage boxes (e.g., Electron Microscopy Sciences).
3. Vacuum dessicator for grid storage.

4. Insulated forceps for grid manipulation (e.g., Electron Microscopy Sciences).
5. Glass Petri dishes with lids, 100 mm diameter.
6. Whatman #1 round filter paper, 90 mm outer diameter.
7. Whatman #1 filter papers for Vitrobot 60 mm or precut blotting paper (Ted Pella).
8. Liquid nitrogen.
9. Ethane gas, flow regulator, and fitted Tygon® tubing.
10. Dewar transfer flask with lid (Cole-Parmer).
11. Large cryosample storage freezer (e.g., Taylor-Wharton).
12. Cryo-grid storage box (blue 4-grid "button" holder) and Teflon® handling wand (Ted Pella).
13. Glass beakers, 100 ml volume.
14. Glass microscope slides.
15. Hair dryer.
16. Large, long-handle tweezers for handling items submerged in liquid nitrogen.

2.8 Cryo-apparatus

1. Glow discharge grid cleaning system (Ted Pella).
2. Vitrobot Mark III or equivalent (FEI).
3. Vitrobot tweezers assembly (Ted Pella).
4. Vitrobot cryogen container for plunge freezing.
5. Cryo-EM microscope setup for tomography with goniometer, and computer control.
6. Gatan 655 dry pumping station.
7. Gatan 626 70° cryo-transfer holder or equivalent.
8. Gatan workstation and cover for 70° cryo-transfer holder.
9. Fitted plug to seal the support cylinder extension of the workstation.
10. Clip ring tool for 70° cryo-transfer holder.
11. Fine tweezers.
12. Small plastic funnel.

2.9 Software

1. Gatan DigitalMicrograph.
2. SerialEM.
3. IMOD [14] (http://bio3d.colorado.edu/imod/) or equivalent for micrograph alignment and reconstruction.
4. Amira 3D analysis (FEI).

3 Methods

3.1 Pre-cleaning the EM Grids

All efforts should be taken to minimize particulate contamination of the grids. Process the grids in a dust-free area, and prevent the grids from being exposed to the environment for extended times throughout the process. To limit lipid transfer to the grids, wear clean gloves and only manipulate grids with clean forceps:

1. Place a 90 mm filter paper inside each of two 100 mm glass Petri dishes, and fill a single dish with 25 ml of acetone. Leave the second dish empty and cover the dish with its lid.
2. Using forceps, transfer 10–20 new Quantifoil® EM grids to the acetone wash. Lay the grids, carbon side up (*see* **Note 9**), on the filter paper. Ensure the grids are completely covered in acetone. Cover the Petri dish and incubate undisturbed for 15 min.
3. Gently lift a single grid using forceps and remove it from the acetone wash. Without releasing the grid, sequentially immerse the grid in two clean glass beakers, each filled with deionized water to dilute excess acetone.
4. Place the clean grid, carbon side up, onto the clean 90 mm filter paper inside the second glass Petri dish. Repeat this wash process for each EM grid used. Partially cover the dish with its lid and allow the grids to dry completely for 15–30 min (*see* **Note 10**).
5. Place clean, dry EM grids in a dedicated grid box and store in a dessicator under vacuum.

3.2 Retina Dissection

1. For dissection of high-quality retinas, carefully immobilize the head of the euthanized animal with one hand against the work surface. Using the thumb and forefinger, stretch the eyelids open while also applying gentle downward pressure against the skull to cause the eye to protrude for easier manipulation (*see* **Note 11**).
2. With the free hand, use dissecting scissors to sever the extraocular muscles and optic nerve (*see* **Note 12**).
3. Collect the eye in a plastic tissue culture dish filled with chilled Ringer's Buffer. Place the dish on an ice pack under the dissection microscope.
4. Repeat **steps 1–3** to excise the second eye and store it in chilled Ringer's Buffer.
5. Using the dissecting microscope, immobilize the eyes with forceps, and use a 27 G needle to puncture the cornea (*see* **Note 13**).

6. Beginning with the corneal puncture site, use spring-loaded scissors to cut a straight line along the cornea to its edge at the ora serrata. Continue cutting around the cornea by following the ora serrata hemisphere. Completely remove the cornea and the lens from the eyecup (*see* **Note 14**).
7. Using two sets of forceps, carefully tease the neural retina away from the pigmented epithelium. Complete this process around the entire circumference of the eyecup until the retina remains attached to the eyecup by only the optic nerve. Cut the optic nerve to completely release the retina from the eyecup.
8. Transfer retinas to a 1.5 ml siliconized tube filled with 300 μl 8 % OptiPrep in Ringer's Buffer and store on ice.
9. Repeat the dissection until the necessary number of retinas, generally 10–12, has been collected.

3.3 Crude Rod Outer Segment Preparation

1. Vortex the retinas for 1 min on the lowest vortexing setting to dissociate rod outer segments from the retina (*see* **Note 15**).
2. Centrifuge the mixture at 200 × *g* for 1 min to separate the intact retinas from the detached rod outer segments.
3. Using a wide-bore 1,000 μl pipette tip, transfer 250 μl of supernatant to a fresh 1.5 ml siliconized tube.
4. Add 250 μl of 8 % OptiPrep buffer to the retinas.
5. Repeat the isolation procedure (**steps 1–4**) four times to collect ~1,250 μl of rod outer segments. All supernatant aliquots should be collected in a single 1.5 ml siliconized tube and stored on ice.
6. Prepare the 10–30 % OptiPrep gradient.

3.4 10–30 % OptiPrep Discontinuous Gradient Preparation

The following procedure is for preparing two balanced 1,500 μl discontinuous OptiPrep gradients. While the gradient solutions should be prepared before the procedure begins, the gradient should be made immediately before the centrifugation step to prevent unwanted mixing of the discrete gradient layers:

1. Mix the pre-prepared OptiPrep gradient solutions to ensure homogeneity.
2. Add 300 μl of 30 % OptiPrep to each of two 2.2 ml (11 × 35 mm) polyallomer tubes.
3. Overlay the preceding layer with 300 μl of 25 % OptiPrep using a syringe fitted with an 18 G needle.
4. Overlay each new layer with 300 μl of the next linear dilution of OptiPrep to create five layers (300 μl per layer) from 10 to 30 % of total OptiPrep concentration.
5. The layer interfaces should be clearly visible with no mixing of the layers.

6. Mark the outside of the 2.2 ml polyallomer tubes with black permanent marker to indicate the layer interface locations and to aid future assessment of ROS band quality.
7. Weigh the tubes on an analytical scale to ensure the gradients are balanced prior to addition of rod outer segments.

3.5 ROS Ultracentrifugation

1. Gently mix the crudely isolated ROS by inversion.
2. Use a 1.0 ml syringe capped with an 18 G needle to slowly collect 625 µl of crude ROS preparation. To reduce pressure-induced shearing of the ROS during collection, we recommend an approximate flow rate of 600 µl/min (*see* **Note 16**).
3. Slowly overlay the 625 µl of ROS on top of the 10 % OptiPrep gradient layer with an approximate flow rate of 600 µl/min.
4. Repeat **steps 1–3** to generate the second gradient.
5. Weigh the tubes to ensure proper weight balance prior to ultracentrifugation. Any balance offset should be corrected with cold 8 % OptiPrep solution to maintain identical centers of gravity between the two tubes.
6. To obtain a higher separation resolution of the ROS, it is recommended to create a continuous gradient to reduce the density barrier effect that occurs at layer interfaces. Cover the 2.2 ml polyallomer tube openings with Parafilm. Apply finger pressure to firmly seal the openings, and quickly invert the tubes 45° to disturb the gradient layer interfaces.
7. Centrifuge the ROS gradients for 60 min at 24,700 × *g* at 4 °C using a TLS-55 swinging bucket rotor. A slow acceleration should be used, and no brake should be applied to the rotor during deceleration (i.e., for the Optima ultracentrifuge: acceleration = 9, deceleration = 9).
8. Unbleached, intact ROS is visible as a single, bright red band that equilibrates between the 10 and 15 % OptiPrep concentration layers (*see* **Note 17**). Black, pigmented epithelial cells and granules will pellet at the bottom of the gradient. Using a 1 ml syringe fitted with an 18 G needle, puncture the sidewall of the 2.2 ml polyallomer just below the meniscus of the ROS band and angle the bevel upward. Collect the ROS band from below the meniscus while being careful to not disrupt the band (*see* **Note 18**).
9. Deposit the ROS into 1.5 ml polyallomer tubes, and dilute the concentration of OptiPrep by adding 1× Ringer's Buffer up to 1.5 ml. Mix the tubes by inversion, and pellet the ROS by centrifugation for 30 min at 26,500 × *g* at 4 °C using a TLA 100.3 rotor. Remove all supernatant, as excess OptiPrep can adversely affect the imaging quality of vitrified specimens, and place ROS pellets on ice (*see* **Note 19**).

3.6 Vitrification of Purified ROS

The following procedures involve diluting the purified ROS to an appropriate concentration, adding an appropriate concentration of electron-dense gold markers (both variables are determined empirically) (*see* **Note 20**), and preparing vitrified samples that meet a number of criteria for optimal tomographic imaging. As a general caution, vitrified EM grids are exceptionally sensitive to ice crystallization resulting from condensation of atmospheric water throughout the stages of sample preparation, storage, and imaging. As such, it is recommended to invest time to optimize the freezing conditions by screening individual vitrified grids on the microscope prior to batch freezing of grids from a single ROS prep. A key parameter in successful imaging is ice thickness. Ice becomes opaque to the electron beam as the ice thickness approaches 1,000 nm. However, if the ice layer is not at least as thick as the specimen (300 nm in the case of cilia), the sample will tend to flatten, distorting some features of the structure [20]. The thickness is best assessed using the microscope:

1. Resuspend a single ROS pellet in 20 μl of 1× Ringer's Buffer with gentle finger tapping to aid in disrupting the solid pellet (*see* **Note 21**).
2. Add 8 μl of 15 nm BSA-gold fiducial marker to the resuspended ROS (*see* **Note 22**).
3. Glow discharging the pre-cleaned, carbon-coated Quantifoil® grids renders them hydrophilic and aids in uniform distribution of the ROS across the grid surface. Prepare 4–8 precleaned grids by placing them on an uncoated glass microscope slide, carbon side up (*see* **Note 23**). Glow discharge the grids under vacuum for 10 s.
4. Condensation of the secondary cryogen using the Vitrobot cryogen holder. Cool the cryogen holder and its inner brass cup using liquid nitrogen. As the temperature of the holder equilibrates, the rate of nitrogen evaporation will decrease. Fill the holder's outer annulus with liquid nitrogen, leaving the inner ring and brass cup free of nitrogen. Condense the ethane by slowly filling the inner brass cup with a 1,000 μl pipette tip attached to the tubing. After a small quantity of ethane condenses, it will be possible to hear the ethane gently bubbling. Keep the pipette tip submerged under the surface of the liquid ethane to prevent the tip from clogging.
5. Carefully select a single grid using a dedicated pair of Vitrobot forceps, and engage the sliding tweezers lock to secure the grid. Place the forceps on the Vitrobot shaft, ensuring the carbon-coated side of the grid is facing the sample-loading port of the Vitrobot.
6. Move the grid-tweezer assembly into the enclosed blotting chamber. Allow the relative humidity of the chamber to reach

100 % to maintain sample hydration. Place the cryogen reservoir in the fitted Vitrobot holder, and ensure the surface of the ethane has not frozen (*see* **Note 24**).

7. Gently tap the ROS sample to mix and apply 2.5 μl of sample to the grid. The ROS sample should spread evenly across the surface of a properly glow-discharged grid. After adding the sample, wait 10 s and immediately blot the grid 1× for 2 s and plunge the grid into liquid ethane (*see* **Note 25**).
8. Allow the white, evaporated gas to clear from the work area. Refill the outer annulus with nitrogen, ensuring the grid holder is covered in liquid nitrogen.
9. Remove the tweezers from the Vitrobot shaft, being careful to not lift the grid from the ethane bath or to bend the grid against the wall of the brass cup (*see* **Note 26**).
10. Quickly transfer the grid from the liquid ethane into the nitrogen contained in the outer annulus. Transfer the grid into the blue 4-grid "button" holder and release the grid from the tweezers (*see* **Note 27**).
11. Warm tweezers using a hair dryer and remove condensation with an absorbent laboratory wipe.
12. Repeat **steps 5–11** until the grid holder is filled or the desired number of grids has been prepared.
13. Secure the 4-grid holder with the Teflon® rod, and transfer the samples to a transfer dewar.
14. Once the optimal freezing conditions have been verified on the cryo-electron microscope, batch-frozen grids can be stored long term in a large cryosample storage freezer under liquid nitrogen.

3.7 Cryo-specimen Holder Preparation and Sample Grid Loading

Before a sample can be loaded into the cryo-electron microscope for imaging, it is necessary to precool the microscope by filling the refrigeration tank with nitrogen. The microscope should be initialized to bring it up to the proper acceleration voltage (typically 200 or 300 kV) and beam operating current. Since this process is specific to each microscope model, follow the manufacturer's specifications to ensure the microscope is functioning properly before proceeding. The procedures below apply to a JEM2100 (JEOL) microscope with a Gatan cryo-stage:

1. Seal the workstation ports by inserting the fitted plug into the support cylinder that extends from the workstation.
2. Precool the workstation by filling its dewar with liquid nitrogen, and cover the station with the clear cover. Several iterations of this are necessary until the workstation temperature equilibrates and nitrogen bubbles stably rather than evaporates. Fill the workstation with sufficient nitrogen to fill the small reservoir.

3. Using precooled large tweezers, transfer the combined Teflon® rod and blue cryo-grid holder from a nitrogen dewar to the workstation. Insert the Teflon® rod through the loading port of the clear workstation cover and submerge in liquid nitrogen. Place the blue cryo-grid holder in the notched reservoir of the workstation, and carefully detach the Teflon® rod without disturbing the grids held in the blue holder. Submerge the Teflon® rod back into liquid nitrogen and set aside. Ensure the blue grid holder is covered with nitrogen.
4. Carefully remove the plug from the workstation, and insert the cryo-transfer holder into the workstation through the support cylinder (*see* **Note 28**).
5. Fill the specimen holder dewar with liquid nitrogen (*see* **Note 29**). If using a digital thermometer, fit the plug into the port on the side of the transfer holder dewar. Refill the dewar as needed until the temperature equilibrates (*see* **Note 30**).
6. Precool the special clip ring tool (specific to 70° holder) in the workstation reservoir (*see* **Note 31**).
7. Open the specimen holder shutter and place the tool over the clip ring (located on the tip of the transfer holder) and turn the knob to engage the clip ring and lock it to the tool. Lift the tool to remove the clip ring from the holder. Keep the tool submerged in nitrogen within the workstation reservoir.
8. Using precooled fine tweezers, transfer a prepared grid from the blue grid holder to the transfer holder. Ensure the grid is centered in the beveled slot to prevent bending the grid with the clip ring.
9. Place the clip ring tool over the grid, and press the clip ring firmly to snap it into the transfer holder. Turn the tool knob to release the clip ring and lock the grid in place. Close the specimen holder shutter to shield the grid.
10. Prepare the microscope for specimen transfer by initiating any vacuum sequences in the airlock. Remove the room temperature specimen holder from the goniometer.
11. Remove the cryo-specimen holder from the workstation, and carefully insert the tip into the goniometer airlock (*see* **Note 32**). Wait for the vacuum sequences to finish before inserting the holder fully into the microscope vacuum column (*see* **Note 33**).
12. Rotate the holder to the upright position as it is fully inserted into the goniometer, and fill the dewar to the top with liquid nitrogen (*see* **Note 34**).

3.8 Digital Image Acquisition of Vitrified Rod Outer Segments

After inserting the cryo-specimen holder into the microscope, it is necessary to carry out standard procedures to turn on the beam filament and find the electron beam. Gun alignment should be

conducted by inserting and centering the condenser lens aperture, correcting for gun tilt, correcting for condenser lens astigmatism, and aligning the condenser lens system. Following these steps, the objective lens aperture is then centered and corrected for astigmatism. The microscope should be set up in transmission electron microscopy (TEM) mode with Spot size = 1 and Alpha = 3 for a low magnification power of 4,000× and a high magnification range between 12,000× and 30,000× (*see* **Notes 35** and **36**). Carry out these procedures as specified by the manufacturer's instructions. SerialEM, the software used to collect micrographs and track incremental tilt shifts during tomography, is a user-friendly package, but it is suggested that users familiarize themselves with the program (http://bio3d.colorado.edu/SerialEM/) [21]:

1. Initialize DigitalMicrograph for acquiring and analyzing single micrographs in TEM mode.
2. After the sample is inserted into the microscope, it is useful to take 4,000× low-magnification images of the grid to map the ice thickness gradient across the grid and to identify unique features for correlating the location of images taken at higher magnification. Begin by taking an image of the center of the grid followed by images along the *x*- and *y*-axes of the grid, moving outward toward the edge of the grid (*see* **Note 37**).
3. Using the low-magnification map images, identify grid squares of interest where the carbon mesh remains intact and has acceptable sample contrast (*see* **Note 38**).
4. Set up the low-dose search mode to screen the grid while preventing excess electron damage to the cells on the grid (*see* **Note 39**).
5. In low-magnification, low-dose search mode, screen regions of the grid for closer inspection. Often, intact outer segment regions, with the cilium still attached, can be seen under low magnification as individual, oval, or cylindrical dark spots within a grid square (Fig. 2). These cells are more visually distinctive than a generally blurry and diffuse region, which is often correlated with disrupted cellular membranes and broken cilia.
6. When a sample has been identified for tilt series acquisition, initialize SerialEM. Remove the sample from the field of view by moving to an adjacent grid square to prevent specimen damage during software setup (*see* **Note 40**).
7. Using SerialEM, take a trial micrograph image to examine the contrast and brightness of the empty grid square. Set the desired magnification and brightness under which the sample micrographs will be acquired.
8. Collect a gain reference measurement consistent with the imaging parameters (magnification and spot size) of the current microscope settings (*see* **Note 41**).

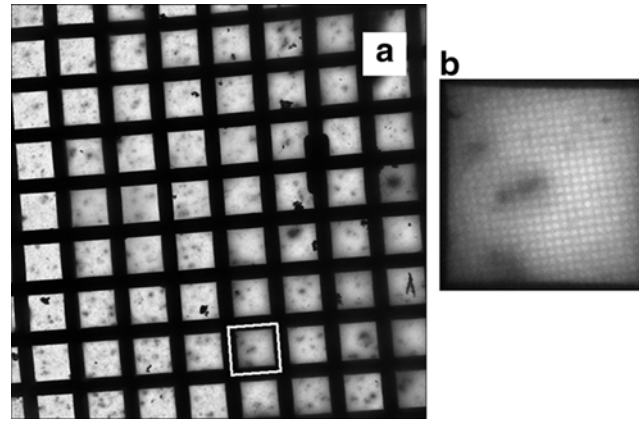

Fig. 2 Vitrified ROS specimens. (**a**) Vitrified ROS specimens on holey carbon EM grid at 50× magnification. (**b**) Magnification of single EM grid square (*white box* in **a**) at 250× magnification. Dark, elongated shapes are individual ROS

9. Begin "eucentric – rough" from the task menu.
10. Re-center the region of interest (ROI) to be imaged. Run "eucentric – fine" from the task menu.
11. Test the maximum tilt range for tomography under "Low Dose" mode using the "walkup and anchor" feature under the task menu (*see* **Note 42**).
12. Set the electron beam intensity to give a cumulative dose of 50–100 electrons per Å^2 using the "Set Intensity" command in the "Tasks" menu (*see* **Note 43**).
13. Take a final trial image and center the ROI on the desired cellular features.
14. Verify that the exposure settings for the focus, trial, and record camera modes provide images without drift.
15. Under the "Tilt Series" menu, select "Startup/Setup Tilt Series" to bring up the "Tilt Series Control Setup" window for setting the tomography parameters. Specify the tilt angle range based upon the "walkup" test. Set a basic increment of 2° per micrograph (*see* **Note 44**). Set the defocus target within a range from 7 to 12 μm (*see* **Note 45**).
16. Begin automated tilt series by selecting "Go" on the "Tilt Series Control Setup" graphical user interface (*see* **Note 46**). Figure 3a shows single micrograph corresponding to 0° tilt angle of a ROS taken during a tilt series.
17. Once the tilt series is complete, end the program from the "Tilt Series" menu and close the file.

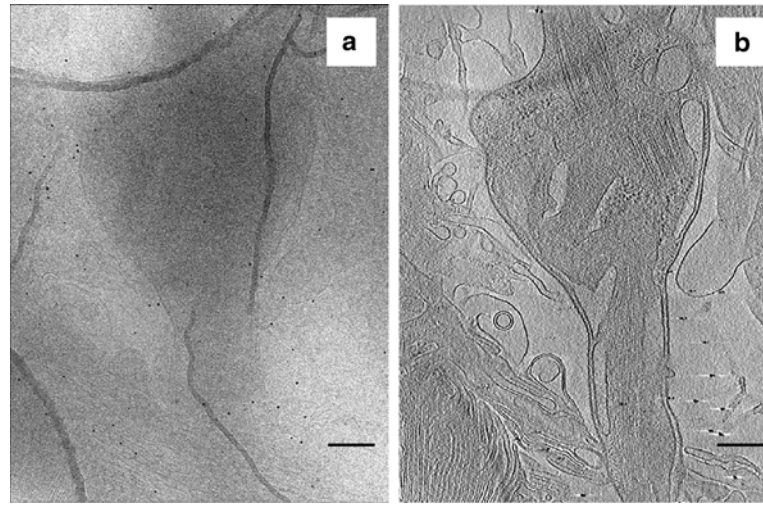

Fig. 3 Single micrograph of a ROS taken during a tilt series. (**a**) Image corresponds to the 0° tilt angle. (**b**) Projection (6 nm thick) from a tomogram (same cell as in **a**) of the inner segment, containing the base of the connecting cilium and attached structures. This projection reveals the contrast gained from tomographic reconstruction of the tilt series micrographs. Scale bars = 300 nm

3.9 Alignment, Reconstruction, and Segmentation of Rod Photoreceptor Tomograms

The process of generating three-dimensional tomograms from tilted specimens requires two closely related steps. The first step, called alignment, is required to compensate for small specimen movements that occurred within the field of view due to goniometer inaccuracies and limited accuracy of the tracking procedure. The alignment process is used to assign all projections to a common coordinate system, assign an angle of the tilt axis to all projections, and account for small variations or specimen rotations that may have occurred during imaging. The second step, called reconstruction, results in an x–y–z coordinate system to which volume elements (voxels) are mapped [22]. Tomograms can be generated with the IMOD suite (http://bio3d.colorado.edu/imod/), and it is advisable for the user to view the IMOD Tomography Guide (http://bio3d.colorado.edu/imod/doc/tomoguide.html#TOP) and the ETomo Tutorial for IMOD (http://bio3d.colorado.edu/imod/doc/etomoTutorial.html#TOP) to learn more about the functions and operation of these tools [14, 15].

Following tomogram reconstruction, manual segmentation can be carried out using commercial software packages, such as Amira, to aid in visualization of biological structures. The surface contours of structural features can be seen in the grayscale tomograms and are traced by hand through the tomogram in slice-by-slice fashion to create iso-dense surfaces within the tomogram. These surfaces can be assigned different colors to highlight the structures, which allow their surfaces to be easily visualized in context within the tomogram. Manual, hand-drawn segmentation is a

subjective, time-consuming process that is prone to interpretation errors by the investigator. For this reason, it is essential to compare the artistic renderings alongside the original grayscale tomogram images to which they correspond and to provide an opportunity for objective comparison to the scientific community in the published literature:

1. Initialize ETomo to begin the tilt series alignment. Select "Build Tomogram" to begin a new dataset.
2. Select the dataset to be used for single-axis tomograms. Select "Scan Header" to retrieve pixel size and image rotation information from the dataset (*see* **Note 47**). Manually enter the fiducial diameter (15 nm unless a different size is used). Press "Create Coms Scripts" to begin processing the images.
3. Press the "Course Alignment" button to create a coarsely pre-aligned stack from the tilt micrographs.
4. To begin creating a fiducial marker-based alignment, select "Make seed and track" where fiducial markers can be chosen manually by the user or automatically through the software. Between 15 and 25, fiducial markers should be selected to align the micrographs (*see* **Note 48**). Follow the interface prompts to generate a seed model and automatically select fiducial markers.
5. After the software has finished its routine, the preselected markers are indicated by green and magenta indicator points. At this point it is essential to manually verify that the majority of the preselected fiducials are correctly tracked throughout the entire tilt series. Any fiducials that were incompletely tracked at high tilt angles should be manually selected to fill in the gaps the software was unable to complete.
6. Once the fiducial reference map has been created by the software, press the "Compute Alignment" button under the "Fine Alignment" section of the graphical user interface to create a high-quality alignment of the data.
7. Before the final reconstruction process can occur, it is necessary to limit the dimensions of the aligned stack to focus on the specimen volume and exclude extracellular, non-specimen volume (*see* **Note 49**). Follow the on-screen prompts to create the boundary models which will limit the reconstruction to the true sample thickness.
8. To complete the tomogram reconstruction, press the "Create Final Alignment" button followed by "Generate Tomogram." Figure 3b shows projection from a tomogram of the inner segment.

4 Notes

1. Electron-dense gold particles provide high-contrast markers for aligning the micrographs acquired at various tilt angles during the reconstruction of tomograms. Gold particles coated with bovine serum albumin (BSA) are more uniformly distributed than non-coated particles. We find that a particle diameter of 15 nm is suitable at magnifications of 10,000× to 20,000×, while a diameter of 10 nm is suitable from 30,000× to 40,000× magnification. This interdependence on gold particle size and magnification power results from the computational limitations of tomogram reconstruction where larger fiducials cover a greater number of pixels, which creates difficulty in accurately determining the center of the fiducial for tracking purposes, potentially introducing alignment errors. Tomograms constructed from higher-magnification micrographs will require adjustment of the BSA-fiducial concentration, because increasing the magnification reduces the field of view and restricts the number of fiducial gold particles that can be used in the tomogram reconstruction process.
2. For this type of procedure, a fiber-optic episcopic illumination source provides a maneuverable overhead light source with the greatest control of illumination direction throughout the dissection.
3. Wide-bore pipette tips can be purchased or created by cutting the tips using scissors or a razor blade. Any solutions containing rod outer segments should be transferred using wide-bore tips to reduce cellular shearing.
4. The angled cutting edge of the spring-loaded scissors minimizes the need to adjust hand position during dissection and can improve user efficiency and comfort during the procedure.
5. The dark room can be treated for light leak by using black fabric hangings to cover the entrance. By sitting in the dark room with the lights off for 20–30 min to allow for eyes to adjust to the dark, it becomes possible to detect sources of light from cracks or seams around the door frame. These openings can be sealed using black photographic masking tape. All electrical equipment in the room should be treated to cover indicator lights or LED displays that emit light.
6. If absolute darkness is not necessary for rod outer segment preparation, low light conditions can be used instead for dark adaptation of mouse retinas. Dim light conditions can be created with low-intensity red lighting via overhead bulbs in the

dark room. Additionally, standard light bulbs can be covered with red gel filters to reduce light activation of rhodopsin protein. Night vision goggles are not essential under dim light conditions but can still enhance the user's ability to visualize the work surface and improve sample preparation.

7. Black permanent marker is visible under infrared illumination, while other colors are invisible or difficult to see.
8. EM grids with 200 mesh (compared with 400 mesh) provide grids that are large enough such that the grid partition bars are less likely to interfere with the tilt series by obstructing the field of view. Our choice to use the R2/2 spaced grids is based upon the relative balance between the ratio of carbon to hole area and the overall size of the grid hole. We found that membranous ROS more often associated with the carbon film than covered the grid holes. In general, an intact cell was likely to have regions that overlapped several contiguous holes, which provides ample opportunity to image the high-contrast specimen over the holes.
9. Copper EM grids are carbon coated on a single side. The uncoated side has a bright orange, metallic reflective appearance, while the carbon-coated side has a dull, brown appearance.
10. By placing the Petri dish in a chemical fume hood, the air flow can increase grid drying. Ensure the grids are shielded from the direct air current by the dish lid to prevent dust deposits on the clean grids.
11. The most rapid isolation of retinas can be obtained with an altered procedure. While the eye is held with forceps, a single-edge razor blade can be touched against the cornea, perpendicular to the circumference of the eye. By holding the blade angle constant and firmly pushing the blade down toward the work surface, tangent to the cornea (i.e., not using the blade to directly slice the eye), the cornea will rupture and expel the lens onto the side of the blade. Using the forceps which hold the eye, gently squeeze the tissue and firmly slide the forceps toward the cornea. This movement will force the retina out of the puncture site for collection into a 1.5 ml siliconized tube filled with 8 % OptiPrep. The rapid procedure bypasses **steps 2–7** of the standard method. In our experience, this rapid procedure provides high-quality rod outer segments and cilia suitable for tomography, but at the expense of a lower yield (typically 30–40 % less tissue) and a higher proportion of broken cells and cilia than the detailed method outlined in Subheading 3.2. While this method may be advantageous for some studies, it is not advised for retinal degeneration studies as isolation artifacts can obscure genuine structural phenotypes.

12. Once the eye is removed from the orbit, it is not necessary to remove all remnants of ocular muscle from the sclera. Attached tissue remnants provide a convenient anchor that can be grasped with forceps to aid in the dissection procedure.
13. In our experience, isolating the retina under a buffered solution allows for easier manipulation of the eye and a more careful separation of the tissues when compared with "dry" dissecting the eye.
14. As the cornea cut site is enlarged, it will be easier to grip the edges of the cornea and sclera with forceps and rotate the eye for more efficient dissection.
15. Because different variations on the Vortex-Genie shakers exist, the lowest "vortex" setting is at roughly the 10 o'clock position on the rotary dial or roughly 1/3 of the entire rotary span of movement. Higher vortexing speeds will provide larger numbers of ROS fragments and give the initial impression of being more efficient; however, ROS fragments isolated under higher speeds are less likely to separate from the retina with the cilium attached. At the preferred speed, roughly 50–60 % of ROS remain attached to the cilium, but at higher speeds this number can drop to 25 % or below.
16. If using a 1 ml syringe without a Luer lock fitting, the tip of the syringe barrel can be inserted directly into the OptiPrep solution to collect rod outer segments. Because the barrel tip diameter is larger than that of the 18 G needle, this will further reduce shearing of the tissue. If this procedure is carried out under infrared or dim light conditions, it is helpful to premeasure a 625 μl volume of 8 % OptiPrep and mark this plunger location by wrapping labeling tape around the syringe barrel. In this way, the marking tape will provide a visual and tactile cue that is easier to identify in the dark.
17. As rhodopsin is bleached by light, the rod outer segment band will change from dark red to faint orange in color and will become more difficult to visualize if an insufficient number of cells has been collected. For ROS preps where dark-adapted retinas are not used, it can still be advantageous to minimize ROS bleaching (as unbleached ROS is easier to see) by covering ROS samples in aluminum foil and by limiting direct exposure to light throughout the procedure. This additional precaution can aid in ROS band visibility.
18. The needle cannula can be moved slowly from side to side while collecting the ROS band to increase yield around the perimeter of the tube wall, but quick movements will cause mixing of the gradient and diffuse the ROS band. Ideally, each ROS band should be collected in 600 μl or less of volume, since larger collection volumes will carry more OptiPrep into the final purification step and cannot be effectively diluted with 1× Ringer's Buffer (*see* Subheading 3.5, **step 9**).

19. If too much OptiPrep is collected along with the ROS band and is not sufficiently diluted prior to pelleting, the ROS pellet will not reach the bottom of the 1.5 ml polyallomer tube and will float on a dense OptiPrep layer that forms at the bottom of the tube. If this occurs, it will be necessary to collect as much of the OptiPrep-containing supernatant, without disturbing the ROS layer, and discard. Again fill the tubes with 1× Ringer's Buffer to further dilute the remaining OptiPrep and invert the tubes to mix. Ensure the tubes are correctly balanced, and centrifuge 30 min at 26,500 × *g* at 4 °C using a TLA 100.3 rotor to correctly pellet the ROS. Remove all traces of OptiPrep and discard the supernatant.
20. The optimum concentration of ROS is such that there are ~1–2 cells per grid square to yield high-probability imaging sessions. This optimum ROS concentration can be attained through a combination of (a) manipulating the final ROS pellet resuspension volume, (b) adjusting the volume of sample applied to the grid, (c) adjusting the wait time before grid blotting, and (d) adjusting the blotting time. The desired concentration of gold fiducial markers is such that 15–20 gold markers are present in any field of view where a tilt series will be collected. Software designed to reconstruct the tomogram requires a lower limit of ten easily visible particles evenly distributed across the field of view. A smaller field of view (i.e., higher magnification) will generally require a higher gold fiducial concentration to provide the necessary parameters to avoid alignment errors.
21. If the pellet is resistant to solubilization, improved resuspension can be achieved by interspersing 2–5 min incubations on ice, which seems to aid by letting the pellet disaggregate. Mechanical trituration of the pellet with a wide-bore 20 μl micropipette tip can be helpful. If a wide-bore tip is used, extreme caution should be used to prevent "smearing" the ROS pellet and destroying a large proportion of the ROS and cilia contained in the sample.
22. If a volume larger than 20 μl is used to resuspend the ROS pellet, it will be necessary to concentrate the BSA-colloidal gold. To concentrate the fiducial marker, add 8.0 μl of BSA-gold to a microcentrifuge tube, and centrifuge 2 min at 12,000 × *g* at 4 °C in a tabletop microcentrifuge. Discard the supernatant and resuspend the BSA-gold (visible as a red pellet) in an appropriate volume before adding to the ROS sample.
23. Larger numbers of grids can be simultaneously glow discharged if desired, but grids not used within 1 h should be discarded as they readily attract debris from the environment. Practically, it is easier to glow discharge smaller batches of grids, since the process is quickly completed and can be interleaved easily with other steps under Subheading 3.6.

24. If enough time has elapsed since the ethane has been condensed, the surface will freeze over, which results in grid bending when it collides with the frozen surface (ethane gas condenses at −160 °C and solidifies at −188 °C). Frozen ethane can be thawed by bubbling more gaseous ethane against the frozen surface. As the surface thaws, the attached pipette tip can be stirred in the ethane to further break up the ice.
25. Ice thickness on each grid will vary depending on the blotting length and inconsistencies in the filter paper surface, which warps as the filter absorbs liquid from successive samples and from the humidified Vitrobot chamber. Some variation of the blotting protocol may be appropriate, but setting the Vitrobot software for a single blot with a 2 s duration is a reliable starting point for 2.5 μl of volume with ROS.
26. As the grid is lifted out of the liquid ethane, it has the likelihood of condensing atmospheric water that is visible in the cryo-electron microscope as dense, ice crystals. By keeping the grid submerged in the ethane, ice crystallization can be minimized.
27. When lifting the grid out of the liquid ethane, keep the grid as close to the liquid surface as possible. As the ethane and nitrogen evaporate, they create a gas barrier at the liquid-gas interface that excludes atmospheric moisture. By moving the grid through this gas layer, the grid can be transferred to the outer annulus and immersed in liquid nitrogen while limiting ice crystallization on the grid.
28. Take care not to damage the metal tip of the holder upon transfer to the workstation.
29. Using a small funnel fitted into the transfer holder, dewar will aid with nitrogen filling.
30. This process takes approximately 5–10 min.
31. Working through the ports of the workstation cover will limit frost formation from atmospheric water.
32. Many airlocks are designed such that the transfer holder must be tilted prior to insertion. The holder is then rotated to its upright position after the vacuum pump sequences are complete.
33. The aspects of this process are specific to the make and model of microscope used. Refer to the manufacturer's specifications before proceeding.
34. At this point, it may take from 20 to 45 min for the transfer holder temperature to equilibrate with the microscope. This thermal equilibration is essential to quality imaging since it reduces vibrations that lead to blurred images and reduced image quality.

35. This setting will vary according to the desired magnification power, brightness level, image contrast, resolution required, and specifics of the electron microscope. In TEM mode, the indicated electron beam spot-size diameter and aperture angle (Alpha) are consistent with imaging at 20,000× magnification while minimizing the electron dose that damages biological samples.
36. Magnification is chosen based upon the region of the cell to be imaged as well as the level of information desired from the data. A magnification of 12,000× is useful for imaging large regions of cells, including both the outer segment and the connecting cilium, which corresponds to the transition zone of other primary cilia. A magnification of 12,000× can provide gross structural anatomy (membranes, basal bodies, and microtubules are visible) and is useful for quickly evaluating the quality of a ROS preparation or grid freezing conditions, but it is unlikely to provide more detailed information for an in-depth research investigation. A magnification of 20,000× provides a balance between field of view size and high-resolution information. At 20,000×, the entire connecting cilium can easily be contained within the field of view. Alternatively, large regions of the inner segment (containing the rootlet) or the outer segment can be viewed. At 30,000× magnification, data collection is almost exclusively limited to the connecting cilium or the cell periphery of the outer segment or inner segment. Two problems complicate magnifications of 30,000× or greater: (a) the number of gold fiducial markers is often insufficient to accurately align the micrographs during the tomographic reconstruction steps since the markers are exclusively located outside of the cell membrane; and (b) while the magnification theoretically provides higher-resolution data, the resolution comes at the price of greatly reduced image contrast. Reduced micrograph contrast coupled with low numbers of fiducial gold greatly reduces the ability to detect biological structures away from the periphery of the cell. From our experience, a 40,000× magnification is nearly impossible to use with our experimental setup since the micrograph contrast is low enough that the automated tracking feature of SerialEM no longer functions reliably.
37. These map images can be kept active on the desktop for easy access to help track movement across grid squares once the imaging process begins. Correlating these images with the microscope specimen location window will help orient the user through the experimental process.
38. At low magnification, the ice thickness gradient can be seen as a uniform level of contrast that gradually changes from dark (low contrast) at one edge of the grid to light (high contrast) at the opposite grid edge. An initial inspection of the low-magnification

grid map will indicate regions of the grid where ice crystals may have formed on the grid. Heavy ice contamination should be avoided as it creates dense objects capable of interfering with digital image acquisition during the sample tilt process. Qualitatively, ice thickness is greatest in regions of the grid where contrast is lowest, whereas highest contrast indicates regions where ice is thin. While regions with more contrast are easier to visualize and tend to draw the user's interest for ease of data collection, our experience has been that more cellular deformation occurs in these areas. More cilia and cell membranes are ruptured in these regions (likely resulting from the blotting procedure described under Subheading 3.6) and, more importantly, outer segments and cilia are more compressed and less circular in diameter. These two structural confounds make comparisons difficult between wild-type structures and aberrant structures where deformation may be caused by genetic mutation. While lower-contrast (darker) regions are more difficult for identifying rod cells, we have found the data collected from these regions to be more rewarding since these regions consistently provided the most intact and uniformly shaped structures across multiple grids under different freezing conditions.

39. Compared with plastic-embedded biological specimens for TEM (which can sustain electron doses of 10,000 $e^-/Å^2$), cryo-specimen is more sensitive to electron dose. Therefore, the goal for imaging cryo-specimens is to maintain the cumulative electron dose at 100 $e^-/Å^2$ or less (this includes all ancillary images taken during setup and eucentricity, as well as images taken during the tilt series). Dose tolerance varies depending on the specimen, but electron damage can be detected as "bubbling" that occurs within the specimen. Rod outer segments seem fairly resilient to damage and can often be imaged at doses above 100 $e^-/Å^2$, though we avoid this practice by convention. In contrast, rod cilia are best imaged below the upper threshold since bubbling becomes clearly visible along the length of the basal body and axoneme microtubules.

40. At this point, the stage movement and brightness settings can be controlled through SerialEM. To prevent excess dose delivery to the cell, the "Focus and Trial/Tracking" images taken during the automated tracking cycles are displaced along the tilt axis and do not overlap the ROI captured in the "Record" images.

41. The gain reference is necessary for the software to correctly calculate the electron dose and distribute it across the different micrographs to be taken as the tilt angle is modified. It is useful to collect a new gain reference before each tilt series is initiated since sample parameters change across different regions of the grid.

42. At this point, it is beneficial to test the maximum tilt range under which the sample can be imaged under the "Low Dose" mode since not every sample can be imaged under the full −70° to 70° range (tilt angle walk test). The "anchor" function collects an image at a specified tilt angle that is saved by SerialEM and the image is used as a reference when the tilt series reaches that angle to enhance the tracking accuracy and image alignment.
43. The maximum electron dose for rod outer segments and rod cilia should be kept at 100 $e^{-}/Å^2$ or less. As a general starting point, doses closer to this maximum should be reserved for cells embedded in thicker ice, while lower doses are better for thinner specimen to prevent damage.
44. A finer tilt increment (1.0° or 1.5°) can be chosen, but the cumulative electron dose is delivered over a larger number of micrographs, each of lower contrast due to reduced image dose. We have not noticed a significant difference in data quality by using a finer tilt increment.
45. Image contrast for unstained, frozen-hydrated (vitrified) specimens predominantly arises from interference between scattered and unscattered electrons interacting with the specimen, a phenomenon called phase contrast. Contrast is characterized by a low signal-to-noise ratio due to the similar electrostatic potential (electron density) between the biological specimen and the surrounding vitreous ice. For this reason, image contrast is low when specimens are in focus, making cellular details and structures difficult to see. To improve phase contrast, specimens are often imaged below focus (defocused), but this contrast advantage comes with a drawback. The defocus phase contrast is influenced by the contrast transfer function (CTF), which depends on the microscope acceleration voltage and the spherical aberration of the lens. The effect of the CTF, as defocus values increase, is the loss of fine, high-frequency details within the image. This compromise between image contrast and resolution means that selecting a defocus value dramatically affects the level of detail that can be extracted from the data. For experimentalists looking to maintain the highest resolution possible, defocus values of −2 to −6 μm are often appropriate. However, if the goal is to identify larger macromolecular structures, larger defocus values may be necessary (−7 to −12 μm).
46. This process is automated through SerialEM, but it is advisable for the user to be present to observe the entire tilt processes as challenges do often arise. Low-contrast micrographs are prone to cause tracking difficulties, especially at higher tilt angles where specimen thickness increases dramatically, and can cause unwanted stage shifts that remove the cell from view.

47. Pixel size is dependent upon the specifics of the microscope, the size of the camera charge-coupled device (CCD), and the magnification. Our experimental setup, which imaged on a 4k×4k CCD at 15,000× to 30,000× magnification, routinely provided pixel sizes ranging from 1.7 to 3 nm/pixel.
48. While allowing the software to automatically choose fiducial markers can simplify many tomogram alignments, it is essential that all fiducials be verified by the user across all micrographs in the tilt series. Markers that are visible in the zero-degree tilt image, where contrast is highest, are often difficult or impossible to see at higher tilt angles. For this reason, it is preferred to begin the fine alignment procedure with a large number of fiducials (20 or more) when using the automated fiducial selection tool.
49. By limiting the reconstruction to the dimensions of the desired cellular region and the contents within the cell (thus excluding the majority of the volume in the original field of view that is extracellular to the specimen of interest), the reconstruction time can be greatly shortened by reducing the computational load of the computer as it computes a smaller three-dimensional tomogram. With some very large specimen, it is necessary to computationally bin the data during the reconstruction process to reduce the CPU computation load and prevent operating system crashes.

References

1. Wang J, Deretic D (2014) Molecular complexes that direct rhodopsin transport to primary cilia. Prog Retin Eye Res 38:1–19
2. Young RW (1967) The renewal of photoreceptor cell outer segments. J Cell Biol 33:61–72
3. Wensel TG (2012) Molecular biology of vision. In: Brady ST, Albers RW, Price D, Siegel JG (eds) Basic neurochemistry: principles of molecular, cellular, and medical neurobiology, 8th edn. Elsevier, London, pp 889–903
4. Besharse JC, Horst CJ (1990) The photoreceptor connecting cilium. A model for the transition zone. In: Bloodgood RA (ed) Ciliary and flagellar membranes. Springer, New York, pp 389–417
5. Kozminski KG, Johnson KA, Forscher P et al (1993) A motility in the eukaryotic flagellum unrelated to flagellar beating. Proc Natl Acad Sci U S A 90:5519–5523
6. Rosenbaum JL, Cole DG, Diener DR (1999) Intraflagellar transport: the eyes have it. J Cell Biol 144:385–388
7. Nair KS, Hanson SM, Mendez A et al (2005) Light-dependent redistribution of arrestin in vertebrate rods is an energy-independent process governed by protein-protein interactions. Neuron 46:555–567
8. Gilliam JC, Chang JT, Sandoval IM et al (2012) Three-dimensional architecture of the rod sensory cilium and its disruption in retinal neurodegeneration. Cell 151:1029–1041
9. Yahav T, Maimon T, Grossman E et al (2011) Cryo-electron tomography: gaining insight into cellular processes by structural approaches. Curr Opin Struct Biol 21:670–677
10. Dubochet J, Adrian M, Chang JJ et al (1988) Cryo-electron microscopy of vitrified specimens. Q Rev Biophys 21:129–228
11. Dierksen K, Typke D, Hegerl R et al (1992) Towards automatic electron tomography. Ultramicroscopy 40:71–87
12. Dierksen K, Typke D, Hegerl R, Baumeister W (1993) Towards automatic electron tomography. II. Implementation of autofocus and low-dose procedures. Ultramicroscopy 49:109–120

13. Frank J (1992) Electron tomography: three-dimensional imaging with the transmission electron microscope. Plenum, New York
14. Kremer JR, Mastronarde DN, McIntosh JR (1996) Computer visualization of three-dimensional image data using IMOD. J Struct Biol 116:71–76
15. Mastronarde DN (1997) Dual-axis tomography: an approach with alignment methods that preserve resolution. J Struct Biol 120:343–352
16. Grimm R, Singh H, Rachel R et al (1998) Electron tomography of ice-embedded prokaryotic cells. Biophys J 74:1031–1042
17. Grimm R, Typke D, Barmann M et al (1996) Determination of the inelastic mean free path in ice by examination of tilted vesicles and automated most probable loss imaging. Ultramicroscopy 63:169–179
18. Leis A, Rockel B, Andrees L et al (2009) Visualizing cells at the nanoscale. Trends Biochem Sci 34:60–70
19. Nickell S, Park PS, Baumeister W et al (2007) Three-dimensional architecture of murine rod outer segments determined by cryoelectron tomography. J Cell Biol 177:917–925
20. Nicastro D (2009) Cryo-electron microscope tomography to study axonemal organization. Methods Cell Biol 91:1–39
21. Mastronarde DN (2005) Automated electron microscope tomography using robust prediction of specimen movements. J Struct Biol 152:36–51
22. Sandberg K, Mastronarde DN, Beylkin G (2003) A fast reconstruction algorithm for electron microscope tomography. J Struct Biol 144:61–72

Chapter 19

Monitoring of Rhodopsin Trafficking and Mistrafficking in Live Photoreceptors

Kerrie H. Lodowski and Yoshikazu Imanishi

Abstract

Outer segment (OS) directed trafficking is required for accomplishing the extremely high concentration of rhodopsin and explicitly high photon sensitivity of rod photoreceptor cells. Aberrant targeting of rhodopsin often leads to blinding disorders, due to various mechanisms causing rhodopsin mislocalization. Until recently, it has been challenging to monitor the dynamics of rhodopsin biogenesis and trafficking. Here, we describe a new method to visualize rhodopsin trafficking in living and unfixed *Xenopus laevis* rod photoreceptors. By harnessing the photochemical property of a photoconvertible fluorescent protein Dendra2, it is now possible to encode temporal information into colors and resolve spatiotemporal distribution of rhodopsin-Dendra2 fusion proteins in individual rod photoreceptors.

Key words Rhodopsin, Photoreceptor, Rod, Retina, Fluorescence, Trafficking, Photoconversion, *Xenopus laevis*, Confocal microscopy

1 Introduction

Rhodopsin is mainly localized to the subciliary membranous structure, the outer segment (OS), where it activates the biochemical pathway leading to the visual sensation. Under various disease conditions which compromise rhodopsin trafficking [1–8], rhodopsin mislocalizes to non-OS membrane locations where rhodopsin may exhibit cellular toxicities [9–11]. Based on the possible mechanisms of causing toxicities, rhodopsin mutations have been classified into several categories, among which "class I" and "class II" are the major categories [12]. Class I mutations are located within the trafficking signal of rhodopsin, and mislocalization of the mutant proteins to aberrant plasma membrane regions is considered to be causative to photoreceptor cell death; however, the detailed mechanism of such cell death is under debate [9, 11]. Class II mutations are distributed throughout the primary structure of rhodopsin and considered to cause misfolding of rhodopsin. Due to the protein quality control mechanism in the ER, misfolded rhodopsin would

Beata Jastrzebska (ed.), *Rhodopsin: Methods and Protocols*, Methods in Molecular Biology, vol. 1271,
DOI 10.1007/978-1-4939-2330-4_19,

either be degraded by the ubiquitin-proteasome/lysosomal pathway [13], stimulate the unfolded protein response [14], or reach the OS where the unstable proteins may exhibit a toxic effect [15, 16]. Proper OS targeting of rhodopsin is essential to accomplish a high disk membrane concentration, which is required for an explicitly high sensitivity of rod photoreceptor cells to photons. Until recently [17], the dynamic events associated with rhodopsin trafficking have not been visualized in photoreceptor neurons in vivo. Rhodopsin localization has been studied mostly by immunohistochemical techniques which require fixation of the tissue and are not suitable for monitoring dynamic events.

While it's been challenging to monitor the specific trafficking of rhodopsin, efforts have been placed toward monitoring proteins in rod photoreceptors. Those efforts involve the combination of radiolabeling and autoradiography of fixed retina specimens. While the radiolabeling method greatly advanced our understanding of the process of disk membrane morphogenesis and renewal [18], the method is not suitable for studying the trafficking of specific proteins, including rhodopsin. The radiolabeling method takes advantage of random incorporation of radioactive amino acids to actively translated photoreceptor proteins. While the great portion of radiolabeled proteins in the OS was rhodopsin [19, 20], autoradiography is not designed to label specific proteins of interest and hence labels all the proteins that incorporate radioactive amino acids. Rhodopsin is not the only major protein in rod photoreceptors. The amount of arrestin, a soluble protein in rod cells, is comparable to that of rhodopsin [21] and would contribute to the signal observed in autoradiography. Other signaling components, such as transducin subunits, are also highly synthesized in the rod photoreceptors. Thus, random labeling is problematic in monitoring the new synthesis and trafficking of specific proteins within the inner segment. Therefore, it is desirable to develop a technique that allows monitoring newly synthesized proteins with a high signal-to-noise ratio and with labeling specificity.

We recently applied a new method, photoconversion technique, to monitor rhodopsin trafficking in photoreceptor cells [17, 22]. The method relies on a photoconvertible fluorescent protein Dendra2. Like many other fluorescent proteins, Dendra2 only requires oxygen to mature the fluorophore. Dendra2 was fused to membrane proteins of interest, including rhodopsin. In this method, labeling occurs at the genetic level and is specific to the proteins of interest. The Dendra family proteins are capable of generating a 1,000–4,500-fold photoconversion from green to red fluorescence states in response to blue or violet light [23–25]. This photoconversion is used to encode the spatiotemporal information of the fusion protein at an extremely high signal-to-background ratio. Photoconversion can occur in vivo, and the imaging can occur in unfixed and living photoreceptor neurons with minimum perturbations. By using the photoconversion technique, it is possible to distinguish between newly synthesized and

old preexisting protein and follow their distributions over time (Fig. 1a). By following the movement at the timescales of seconds to minutes, one would be able to follow the process of trafficking from the site of biogenesis toward the OS (Fig. 1a–c). At the timescales of minutes to hours, one would be able to follow the process of individual disk membrane morphogenesis (Fig. 1a, d, e). Furthermore, at the timescales of hours to days, one can understand the renewal of the OS structures (Fig. 1a, f, g).

In visualizing newly synthesized rhodopsin, one of the major obstacles is the time required for the maturation of fluorescent protein, with the maturation half-time ranging between 1 and 2 h for GFP and Dendra2 [26, 27]. Such slow maturation would be problematic, because rhodopsin, in quantities equivalent of one disk

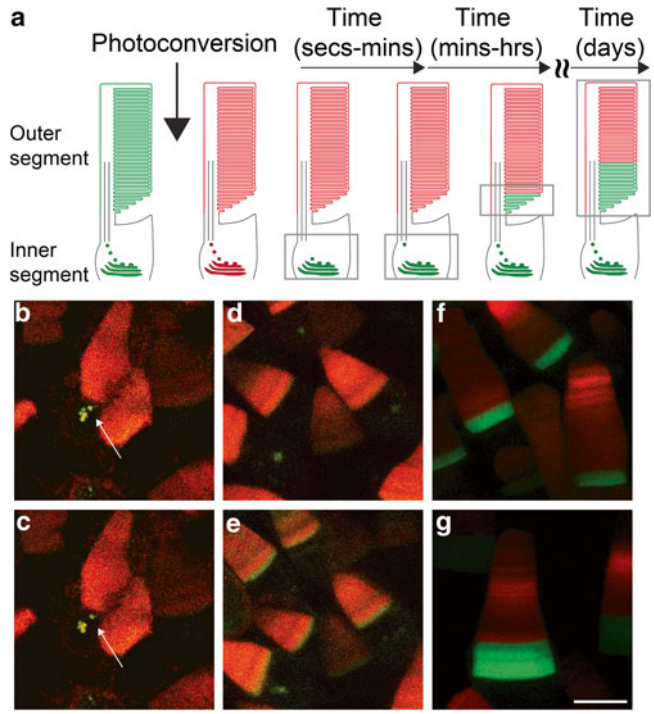

Fig. 1 Our photoconversion method, shown on three different timescales. (**a**) Schematic of a rod photoreceptor cell pre(*green*)- and post(*red*)-photoconversion. Trafficking of protein within the inner segment can be seen on a timescale of seconds to minutes (*gray boxes*). New outer segment disks are formed (*gray box*) on a timescale of minutes to hours. The outer segment is substantially renewed on a timescale of days (*gray box*). (**b**, **c**) *Xenopus* rod cells expressing rhodopsin-Dendra2. A rhodopsin-Dendra2 vesicle (*arrow*) can be seen moving toward the outer segment in (**b**) and (**c**), which are 23 s apart. (**d**, **e**) *Xenopus* rod cells expressing rhodopsin-Dendra2. Newly synthesized disks can be seen at the base of the outer segment in (**e**), which was taken 1.5 h after (**d**). (**f**) *Xenopus* rod cells expressing rhodopsin-Dendra2, 2 days (**f**) or 6 days (**g**) post-photoconversion. *Green* is non-photoconverted, new Dendra2. Red is photoconverted, old Dendra2. Images are maximum projections of optical slices (**d**–**g**) or single confocal images (**b**, **c**). Images are of live, unfixed retina. Animals were 9–10 (**b**–**e**) or 21–22 (**f**, **g**) days old at time of photoconversion. Scale bar is 10 μm

membrane, is synthesized in less than 30 min in *Xenopus* rod photoreceptor cells [28]. Therefore, one would assume that the majority of fluorescent proteins will become mature long after rhodopsin passed through the Golgi apparatus. In contrast to our anticipation, we are capable of imaging newly synthesized rhodopsin within 30 min of photoconversion, prior to observing appreciable new rhodopsin in the disk membranes [17]. These observations suggest that the maturation of fluorescent proteins is rather rapid in photoreceptor neurons. The environments surrounding photoreceptor cells are hyperoxic [29]. Accordingly, retinal neurons can be traditionally cultured under 95 % O_2 and 5 % CO_2. It is likely that such a hyperoxic culture condition helped to accelerate Dendra2 maturation, a process requiring oxygen. Thus, photoreceptor cells are a unique system that is suitable for the study of protein trafficking by fluorescent proteins under physiological conditions. The photoconversion technique, explained here, is not only limited to the studies of rhodopsin. We recently used the technique to resolve the trafficking process of peripherin/rds and the cGMP-gated channel, two important components of the OS membrane [30, 31].

2 Materials

2.1 Supplies for Photoconversion

1. Transgenic tadpoles (*see* **Note 1**). Unless otherwise noted, tadpoles are housed in a DigiTherm heating/cooling incubator (Tritech Research) maintained at 16 °C.
2. 10× Marc's Modified Ringer's (MMR) buffer: 1 M NaCl, 20 mM KCl, 20 mM $CaCl_2$, 10 mM $MgCl_2$, 50 mM 4-(2-hydroxyethyl)-1-piperazine-1-ethanesulfonic acid (HEPES); adjust the pH to 7.5 and autoclave.
3. 0.1× MMR buffer.
4. Plastic Pasteur pipettes. To transfer thick solution or tadpole heads, cut off the ends of the pipettes to allow a larger opening (~5 mm diameter).
5. Dark housing unit for tadpoles: a box with a lid (*see* **Note 2**) that can be closed completely to avoid exposing the tadpole(s) to ambient light before the photoconversion procedure.
6. Ring stand with three-finger clamp attached.
7. Cardboard box with top and bottom removed (we use a box with the dimensions of 33 × 20 × 23 cm).
8. 300 mW 405 nm laser pointer (DinoDirect.com) (*see* **Note 3**).
9. 0.026 % tricaine methanesulfonate MS-222 (Sigma-Aldrich): Make a 0.26 % (w/v) solution in water and adjust the pH to 7 with $NaHCO_3$ (the mass of $NaHCO_3$ required to adjust the pH is approximately 2× the mass of tricaine used to make the solution). Dilute to 0.026 % with water.

10. Hairloops: Glue the ends of a human hair inside the tip of a glass Pasteur pipette such that the hair outside of the tip forms a loop. The loop should be about 3 mm long.
11. 6 % methylcellulose (Sigma-Aldrich): Prepare methylcellulose solution following the previously published procedure [32] and store at room temperature.
12. 35 mm plastic dishes.
13. Timer.
14. Blue-green laser eye protection safety glasses (Orbtronic LLC).
15. Filter sheet (Rosco E-Colour #210: 0.6 Neutral Density, RE210) (PNTA), cut to 2 × 2 in. squares.
16. Aluminum foil dish: Create a dish out of foil that can hold the 35 mm dish during photoconversion (Fig. 2a). The four sides of the dish are slightly taller than the side of the 35 mm dish.

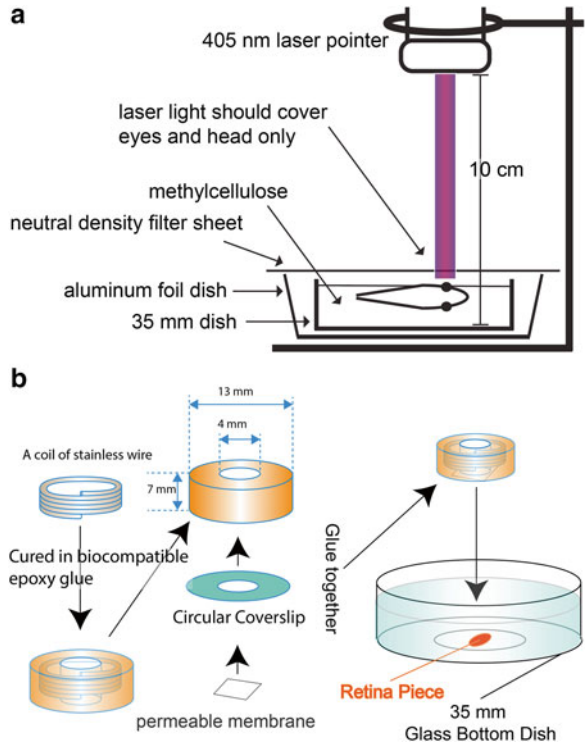

Fig. 2 (**a**) Photoconversion apparatus. The tadpole carrying the Dendra2 transgene is placed in the methylcellulose with the eye(s) to be photoconverted facing up. Clamp the laser pointer such that the distance between it and the base of the 35 mm dish is 10 cm. Place the 35 mm plastic dish containing the tadpole inside an aluminum foil dish and rest a filter sheet on top to cover the tadpole. Make sure the laser light is aimed at the eye(s) and head only. (**b**) A custom weight was made by embedding a donut-shaped coil of stainless wire in biocompatible epoxy glue, to which a circular coverslip and permeable membrane were glued. This weight is placed on retina pieces so that they can be held in place while having access to essential nutrients and gas. Biocompatible glue (USP Class VI approved) is used to avoid any leakage of toxic metal into the culture medium

17. 100 ml beakers to recover tadpoles after photoconversion.
18. Stereoscope (Leica MZ16 F Fluorescence Stereomicroscope), equipped with the GFP2 ultra filter set (10447407) and the dsRED ultra filter set (10447412).

2.2 Supplies for Retinal Excision

1. Poly-D-lysine-coated 35 mm glass bottom dishes (#1.5) (MatTek Corp.).
2. Cell-Tak (BD Biosciences).
3. Oven set to 37 °C.
4. Photoconverted transgenic tadpoles.
5. Plastic Pasteur pipettes (see above).
6. 35 mm plastic dishes (see above).
7. 0.026 % tricaine methanesulfonate MS-222 (see above).
8. Styrofoam board (approximately 900 cm^2) covered in aluminum foil.
9. Dissection tools: Straight Moria Ultra Fine Forceps, Vannas-Tübingen Spring Scissors, Vannas Spring Scissors, and Wecker Spring Scissors (Fine Science Tools).
10. A modified version of Wolf amphibian culture medium: 55 % MEM (powder, Invitrogen), 31 % Earle's sodium-free BBS, 10 % FBS, 30 mM $NaHCO_3$, and 700 mg/l D-glucose. Store at 4 °C. Add the MEM powder to pure water (purified by a Milli-Q system (Millipore)) and pass through a 0.22 μm filter into an autoclaved bottle.
11. Circular cover glass (#1) (Fisher Scientific).
12. Custom-made weight (~2 g): made from stainless wire (~1 mm diameter), USP Class VI approved biocompatible epoxy glue (EPO-TEK 730, Epoxy Technology), circular cover glass (see above), and permeable membrane (Isopore membrane filter, Millipore) (for details, *see* **Note 4**).
13. Stereoscope (see above).
14. Sealed microscope chamber (DMIRB/E ONICS-D35, Tokai Hit CO., Ltd.).
15. Gas tank (95 % O_2/5 % CO_2) and gas regulator.

2.3 Supplies for Microscope Imaging

1. Sealed microscope chamber (see above).
2. Gas tank (95 % O_2/5 % CO_2) and gas regulator.
3. A modified version of Wolf amphibian culture medium (see above).
4. Leica TCS SP2 laser scanning confocal/multiphoton microscope (Mannheim) equipped with four lasers for excitation—488 nm argon ion, 543 nm HeNe, 633 nm HeNe, and a tunable

Ti:Sapphire laser (Coherent Chameleon XR) and a HCX PL APO CS 40.0×1.25 OIL UV objective. In this system, the confocal scanning head is mounted on the Leica DM IRE2 inverted microscope. In this method, multiphoton imaging is not used.

3 Methods

3.1 Photoconversion of Dendra2 in Tadpole Eyes

Carry out all procedures at room temperature unless otherwise specified. We found that room temperature is suitable for *Xenopus* tissue dissection and culture and does not adversely affect the trafficking of rhodopsin-Dendra2:

1. Generate transgenic tadpoles expressing the rhodopsin-Dendra2 fusion protein (*see* **Note 5**) in the rod photoreceptors [17] using the previously described method [33] (*see* **Note 6**).
2. Using a fluorescence stereoscope, screen for transgenic tadpoles (stage 40–50) that are positive to rhodopsin-Dendra2 in the eyes. Place the positive tadpoles in a dark housing unit.
3. Anesthetize a positive tadpole with 0.026 % tricaine for 2–3 min.
4. Secure the 300 mW 405 nm laser pointer to the three-finger clamp so that the laser pointer is vertical with the light shining downward (Fig. 2a).
5. Transfer the tadpole to a 35 mm plastic dish containing the 6 % methylcellulose. Gently use the hair loop to position the tadpole sideways in the methylcellulose with the eye to be photoconverted facing up (Fig. 2a) (*see* **Note 7**).
6. Place the dish containing the tadpole inside the aluminum foil dish and position the tadpole such that it is underneath the laser pointer. Adjust the height of the laser pointer so that only the head of the tadpole is illuminated. The aluminum foil dish reflects the laser light back toward the tadpole's head, so that the eyes are receiving light from all directions, not just from above. In our setup, the length from light source to the base of the 35 mm dish is 10 cm.
7. Place the neutral density filter sheet on top of the dish containing the tadpole, to attenuate the intensity of 405 nm light reaching the tadpole head (*see* **Note 8**). The filter sheet is resting on the sides of the aluminum foil dish (Fig. 2a).
8. Place the cardboard box such that it is surrounding the photoconversion apparatus, allowing access to the power button on the laser pointer through the top of the box. The purpose of the cardboard box is to avoid directly gazing at the 405 nm light. Wear the blue-green laser eye protection safety glasses for the protection of your eyes.

9. Make sure the beam is aimed at the head of the tadpole. Turn on the laser pointer for 1 min. Turn it off for 15–20 s (*see* **Note 9**). Repeat this procedure 15–20 times to complete the photoconversion of Dendra2. Monitor the degree of photoconversion using the fluorescence stereoscope.
10. Check the heartbeat under the stereoscope to monitor the health status of the tadpole.
11. Using a plastic Pasteur pipette, remove the tadpole from the methylcellulose and sacrifice the tadpole for retinal excision (*see* Subheading 3.2). Otherwise, transfer the tadpole to a 100 ml beaker containing 50 ml of 0.1× MMR to allow the tadpole to recover for a future retinal excision.

3.2 Retinal Excision

1. Prior to the retinal excision, coat the 35 mm glass bottom dishes (#1.5) with Cell-Tak as follows: Pipette 3 μl of Cell-Tak on the center of the glass area of each dish, and put the dishes into a 37 °C oven to allow the Cell-Tak to dry (with the lids off) for several hours.
2. Thirty min to 1 h prior to retinal excision, equilibrate the modified version of the Wolf amphibian culture medium as follows: Add pure water (purified by a Milli-Q system) to the water reservoir of the sealed microscope chamber to maintain the humidity. Turn on the gas supply (95 % O_2/5 % CO_2) to the chamber. Pour 4 ml of Wolf media into a 35 mm plastic dish and place it in the chamber to equilibrate. Put the lid on the chamber.
3. Transfer a small amount of equilibrated Wolf media to a small plastic dish (*see* **Note 10**) and to the Cell-Tak-coated dish.
4. Using the Wecker Spring Scissors, decapitate the photoconverted tadpole on the aluminum foil-covered Styrofoam board. The soft surface of the Styrofoam allows the scissors to cut without damaging the blades. The aluminum foil does not absorb the methylcellulose and therefore allows the tadpole to stay moist during the decapitation. Use a plastic Pasteur pipette to transfer the tadpole head into the plastic dish (*see* **Note 10**) with the small amount of Wolf media. Use the stereoscope for the following dissection steps (*see* **Note 11**).
5. Cut the tadpole head in half using the Vannas-Tübingen Spring Scissors, with each half containing one eyeball.
6. Using the Vannas Spring Scissors and Moria Ultra Fine Forceps, remove the eyes from the head and remove all connective tissue from the eyes.
7. Using a plastic Pasteur pipette, transfer the eyes into the Cell-Tak-coated dish that has the equilibrated Wolf media in it.
8. Using the Vannas Spring Scissors and Moria Ultra Fine Forceps, remove the lenses from the eyes and discard, leaving only the retina and retinal pigment epithelium (RPE).

9. Cut each retina in half using the Vannas Spring Scissors (*see* **Note 12**).
10. Separate the RPE from the retinas using the Moria Ultra Fine Forceps and discard the RPE (*see* **Note 13**).
11. Orient the retinas so that the photoreceptors are facing the glass bottom of the dish (the side with the RPE removed should be touching the glass). Gently push the pieces of retina down onto the Cell-Tak to facilitate their "sticking" to the bottom of the dish.
12. Flatten the retina pieces using a circular cover glass. Place one edge of the cover glass (*see* **Note 14**) so that it's touching the inside lip of the imaging window in the center of the glass bottom dish, and let it slowly drop as it covers the pieces of retina. The cover glass will be lying flat inside the glass imaging window. Add more equilibrated Wolf media to the dish. Gently push down on the cover glass to allow the media underneath to flatten the pieces of retina. Try to keep a thin layer of media between the cover glass and retina so that the retina does not touch the cover glass and stick to it.
13. Let the cover glass sit for 1–2 min.
14. Gently remove the cover glass with Moria Ultra Fine Forceps, being careful not to disrupt the flattened retina pieces.
15. Place the custom-made weight (Fig. 2b) on the flattened retina pieces, membrane side down. Fill the center of the weight with media until all air bubbles are removed and the membrane is flush with the pieces of retina.
16. Add the remaining equilibrated Wolf media to the dish and place the dish inside the sealed microscope chamber.

3.3 Microscope Imaging

3.3.1 Visualization of Trafficking and Disk Incorporation of Newly Synthesized Rhodopsin-Dendra2

To visualize trafficking of newly synthesized green rhodopsin-Dendra2 from the site of biogenesis toward the OS (Fig. 1b, c) or to visualize individual disk membrane morphogenesis (Fig. 1d, e), excise the retina immediately after photoconversion. The following are the methods for setting the microscope parameters for the Leica SP2 confocal microscope (*see* **Note 15**):

1. Turn on the microscope system along with the computer and software associated with it. Prepare the system for confocal imaging. Turn on the 488 nm argon ion laser and set its power adjustment dial to the midpoint. Move over to the SP2 software and set the 488 nm laser power to 10 % (*see* **Note 16**), and set the dichroic mirror to TD 488/543/633. For real-time monitoring in which the same cells are repeatedly scanned, minimizing photobleaching is imperative. While the red form of Dendra2 is effectively excited by the 543 nm HeNe laser, it can be excited by the 488 nm argon ion laser as well. Thus, by simultaneously exciting the green and red forms of Dendra2 using only the 488 nm laser, we can minimize photobleaching (*see* **Note 17**).

2. Activate two photomultiplier tubes (PMTs) to simultaneously collect emission in these two separate ranges. Set the ranges of emission to 500–550 nm for green Dendra2 and 580–680 nm for red Dendra2 (*see* **Note 18**).
3. Set the pinhole size to 81 μm (1 airy unit). Increasing the size will give a brighter image but bleach the cells faster and compromise the imaging resolution.
4. Set the scan mode to bidirectional. In this mode, the laser scans left to right and right to left (as opposed to just left to right), thereby decreasing the scan time by half. Set the scan format to 512×512 with a zoom factor of 1 or 2. Zoom factors of 1 and 2 accomplish 0.73 μm/pixel and 0.37 μm/pixel, respectively.
5. Using the eyepiece of the microscope, locate the cells to image. Using continuous scanning mode on the software, locate the cells/structures of interest and bring them into focus and then stop scanning. In locating the cells, adjust the PMT voltage (also called PMT gain) so that the cells are visible.
6. Change the scan format to 1,024×1,024 pixels with a zoom factor of 4 or maintain at 512×512 pixels with an adjusted zoom factor of 8. These two settings accomplish a resolution of 0.09 μm/pixel, which is sufficient for capturing vesicle movement and/or disk morphogenesis.
7. Set the scan speed to between 800 and 1,400 Hz. For monitoring vesicle movement, faster scan speeds are suited because vesicles may move rather rapidly. For monitoring the appearance of new rhodopsin in disks, the scan speed can be slower.
8. Set the 488 nm laser power to between 10 and 25 %. Continue scanning the cells while monitoring the green and red channels simultaneously. Adjust the laser power to the lowest possible number (to limit photobleaching) while still being able to discern the green and red fluorescence brightly and clearly. To identify the oversaturated and underexposed pixels, use the Glow (O&U) color lookup table for both the green and red channels. In this lookup table, oversaturated pixels (with the maximum pixel value) are in blue and underexposed pixels (with zero pixel value) are in green. While scanning, adjust the PMT gain to be 500–650 V. Choose a value for each PMT so that there are only a small number of blue dots (saturated pixels) on the cells by continuous scanning. In addition, adjust the offset to be −0.2 to 0.2 %. Choose a value for each PMT so that the area outside the cells is about 50 % covered with green dots (underexposed pixels).
9. For monitoring disk morphogenesis, select the line averaging option and set it to scan twice. Averaging increases the signal-to-noise ratio. For monitoring vesicle movement, images are not averaged.

10. Start scanning the cells and adjust the phase so that the forward and backward scans are precisely in phase. Stop scanning after completing the phase adjustment.
11. For monitoring vesicle movement or disk morphogenesis, use the xyt or xyzt mode, respectively, to collect images at regular intervals. For monitoring vesicle movement, the time interval between scans may be adjusted as short as possible. Using the conditions listed above, it is possible to achieve a time interval of 200–300 ms. For monitoring disk morphogenesis, set an upper and lower Z to capture a 3D view of the cell. Five to ten Z slices, in 1 μm increments, are captured to monitor the cell in its entirety. The time interval between scans will be longer here to account for the collection of Z slices during each scan. Set the software to run for 30–90 min (*see* **Note 19**).

3.3.2 Visualization of the Renewal of OS Structures

To visualize the renewal of OS structures (Fig. 1f, g), excise the retina one or more days after photoconversion. The following are the methods for setting the microscope parameters for the Leica SP2 confocal microscope (*see* **Note 15**):

1. Turn on the microscope system along with the computer and software associated with it. Prepare the system for confocal imaging. Turn on the 488 nm argon ion laser and set its power adjustment dial to the midpoint. Turn on the 543 nm HeNe laser. Using two laser lines provides better separation of green and red fluorescent signals; we therefore image the green form of Dendra2 using the 488 nm argon ion laser and the red form of Dendra2 using the 543 nm HeNe laser. To minimize crosstalk, the green and red channels are collected sequentially (not simultaneously). Set the 488 nm laser power to 10 % and the 543 nm laser power to 20 % (*see* **Note 16**). Set the dichroic mirror to TD 488/543/633.
2. Set the range of emission spectra for green Dendra2 to 500–530 nm and for red Dendra2 to 570–700 nm (*see* **Note 18**).
3. Set the pinhole size to mimic what was listed in the microscope experiment above (*see* Subheading 3.3.1). Set the scan format to 512×512 with a zoom factor of 1 or 2. Use the unidirectional scan mode (as opposed to the bidirectional scan mode described in Subheading 3.3.1).
4. Using the eyepiece of the microscope, locate the cells to image. Using the continuous scanning mode on the software, locate the cells/structure of interest using one of the PMTs (either the one designated for green or for red), bring them into focus, and then immediately stop scanning. In locating the cells, adjust the PMT gain so that the cells are visible.
5. Change the scan format to 1,024×1,024 pixels with a zoom factor of 2 or maintain at 512×512 pixels with an adjusted

zoom factor of 4. These two settings accomplish a resolution of 0.18 μm/pixel, which is sufficient for visualizing the renewal of OS structures.

6. Set the scan speed to 400 Hz. Select the line averaging option and set it to scan twice.
7. Set the imaging parameters for green and red channels independently. Set the 488 laser power to 20 % (543 nm laser is not used). While scanning continuously, adjust the PMT gain and offset values of the green channel as described in Subheading 3.3.1. Save the setting for the sequential scan. Set the 543 laser power to 30 % (488 laser is not used). While scanning continuously, adjust the PMT values for the red channel. Save the setting for the sequential scan.
8. For visualizing the renewal of OS structures, conduct imaging in the xyz dimensions. Set an upper and lower Z to capture a 3D view of the cell. Five to ten Z slices, in 1 μm increments, are captured to observe the cell in its entirety.
9. Run a sequential scan of the green and red channels to achieve an overlay of the two colors in the cell. The new OS membranes will be observed in green, and old OS membranes will be observed in red. Optionally, create maximum projection images out of the Z slices.

4 Notes

1. Obtain approval for the use of *Xenopus laevis* at your research institute (e.g., IACUC in the case of institutes in the USA).
2. While any box with a sufficient size may suffice, we use a box with the dimensions of $36 \times 23 \times 11$ cm.
3. The 300 mW 405 nm laser pointer is no longer available from DinoDirect. As a substitute, a 200 mW 405 nm laser pointer can be purchased from LAZERER (Mong Kok, Hong Kong). The timing of the photoconversion or the density of the filter may have to be adjusted to accommodate the lower intensity of this laser pointer.
4. We fashioned a stainless wire (~1 mm diameter) into a donut-shaped spiral and encased it in biocompatible epoxy glue (Fig. 2b). A hole was made at the center of the weight using a diamond drill attached to a power tool. A permeable membrane was glued to one end of the weight, leaving the other end open. Detailed dimensions of this weight are as described in Fig. 2b. When the weight is placed on top of the retina, the membrane side is down. This design allowed cells access to gas and media while keeping them flat against the surface of the glass bottom dish.

5. Other rhodopsin constructs, which contain class I or class II mutations, for example, can be expressed to study the process of mistrafficking. The study using a class I mutant was published previously [17].
6. Tadpoles should be between 6 and 22 days old for best results (stage 40–50, respectively [34]). The brighter the green fluorescence in the eyes, the better the photoconversion procedure will work.
7. This procedure is for the photoconversion of one eye; however, both eyes may be photoconverted, in which case the tadpole should be laid ventral side up.
8. The neutral density filter sheet absorbs heat and decreases the intensity of the 300 mW laser pointer to about 100 mW.
9. The reason for the periodic breaks is to prevent premature aging of the laser bulb. According to the manufacturer's instructions, the laser pointer should only be on for 30 s–1 min at a time to prevent overheating.
10. We found that the lid of a 35 mm plastic dish is suitable for dissection, as the lid is shallow and allows easy access to the tissues.
11. The retina can be excised immediately after photoconversion (as outlined here) or hours/days later, depending on the design of the experiment. If the photoconverted tadpole is allowed to recover and survive for hours/days prior to retinal excision, the tadpole will need to be anesthetized with 0.26 % tricaine for 2–3 min prior to decapitation.
12. Cutting the retinas in half facilitates RPE removal and allows the retinas to lay flat during imaging.
13. Sometimes the RPE is sticky and will break or disintegrate during removal. Try to remove as much as possible while still maintaining the integrity of the retina.
14. To prevent the circular cover glass from repulsing the medium, immerse the cover glass into the Wolf media to coat it with liquid prior to this step.
15. Imaging parameters are listed as examples. They can be customized and optimized according to the individual confocal microscope system and the needs of the experiment.
16. The method for adjusting the laser power may vary among the microscope systems. In our system, the main power of the 488 nm argon laser can be adjusted by a dial. The main power of the 543 nm HeNe laser is fixed. Acousto-optic tunable filters (AOTFs) modulate the fraction (%) of the laser power delivered to the sample/objective lens. It is recommended to follow the manual of the individual microscope system and optimize the laser power as needed.

17. While some crosstalk is observed between red and green Dendra2 under this imaging condition, this technique successfully increases the contrast for newly synthesized rhodopsin-Dendra2 over old preexisting rhodopsin-Dendra2.
18. In our confocal system, there is an option to select the beam expander. The beam expander setting is to adjust the width of the laser beam before it enters the objective lens. In the confocal imaging described here, the beam expander is set to 6, which allows the overfilling of the back aperture of the lens. The beam expanders 1 and 3 are occasionally used for multiphoton microscopy, to increase the laser power at the level of the specimen.
19. While the retina can be cultured for an extended period of time (≥5 h), scanning by the laser may adversely affect the health of photoreceptor cells. Thus, it is imperative to monitor the cells' health status. For example, rhodopsin synthesis and disk morphogenesis are two good indicators of the health status. In our imaging conditions tested, cells are capable of synthesizing and carrying new rhodopsin and other OS proteins to the base of the OS [17, 22, 30, 31].

Acknowledgments

This work was supported by the US National Institutes of Health grants EY020826, EY011373, and DK007319. The authors would like to thank Richard Lee for his technical assistance with the experiments listed here.

References

1. Nir I, Papermaster DS (1986) Immunocytochemical localization of opsin in the inner segment and ciliary plasma membrane of photoreceptors in retinas of rds mutant mice. Invest Ophthalmol Vis Sci 27:836–840
2. Bowes C, van Veen T, Farber DB (1988) Opsin, G-protein and 48-kDa protein in normal and rd mouse retinas: developmental expression of mRNAs and proteins and light/dark cycling of mRNAs. Exp Eye Res 47:369–390
3. Nir I, Agarwal N, Sagie G et al (1989) Opsin distribution and synthesis in degenerating photoreceptors of rd mutant mice. Exp Eye Res 49:403–421
4. Lewis GP, Erickson PA, Anderson DH et al (1991) Opsin distribution and protein incorporation in photoreceptors after experimental retinal detachment. Exp Eye Res 53:629–640
5. Edward DP, Lim K, Sawaguchi S et al (1993) An immunohistochemical study of opsin in photoreceptor cells following light-induced retinal degeneration in the rat. Graefes Arch Clin Exp Ophthalmol 231:289–294
6. Li ZY, Kljavin IJ, Milam AH (1995) Rod photoreceptor neurite sprouting in retinitis pigmentosa. J Neurosci 15:5429–5438
7. Fariss RN, Molday RS, Fisher SK et al (1997) Evidence from normal and degenerating photoreceptors that two outer segment integral membrane proteins have separate transport pathways. J Comp Neurol 387:148–156
8. Milam AH, Li ZY, Fariss RN (1998) Histopathology of the human retina in retinitis pigmentosa. Prog Retin Eye Res 17:175–205
9. Tam BM, Xie G, Oprian DD et al (2006) Mislocalized rhodopsin does not require activation to cause retinal degeneration and neurite

outgrowth in Xenopus laevis. J Neurosci 26:203–209

10. Tam BM, Moritz OL (2007) Dark rearing rescues P23H rhodopsin-induced retinal degeneration in a transgenic Xenopus laevis model of retinitis pigmentosa: a chromophore-dependent mechanism characterized by production of N-terminally truncated mutant rhodopsin. J Neurosci 27:9043–9053
11. Alfinito PD, Townes-Anderson E (2002) Activation of mislocalized opsin kills rod cells: a novel mechanism for rod cell death in retinal disease. Proc Natl Acad Sci U S A 99:5655–5660
12. Mendes HF, van der Spuy J, Chapple JP et al (2005) Mechanisms of cell death in rhodopsin retinitis pigmentosa: implications for therapy. Trends Mol Med 11:177–185
13. Chiang WC, Messah C, Lin JH (2012) IRE1 directs proteasomal and lysosomal degradation of misfolded rhodopsin. Mol Biol Cell 23:758–770
14. Lin JH, Li H, Yasumura D et al (2007) IRE1 signaling affects cell fate during the unfolded protein response. Science 318:944–949
15. Sakami S, Kolesnikov AV, Kefalov VJ et al (2014) P23H opsin knock-in mice reveal a novel step in retinal rod disc morphogenesis. Hum Mol Genet 23:1723–1741
16. Sakami S, Maeda T, Bereta G et al (2011) Probing mechanisms of photoreceptor degeneration in a new mouse model of the common form of autosomal dominant retinitis pigmentosa due to P23H opsin mutations. J Biol Chem 286:10551–10567
17. Lodowski KH, Lee R, Ropelewski P et al (2013) Signals governing the trafficking and mistrafficking of a ciliary GPCR, rhodopsin. J Neurosci 33:13621–13638
18. Young RW (1967) The renewal of photoreceptor cell outer segments. J Cell Biol 33:61–72
19. Bargoot FG, Williams TP, Beidler LM (1969) The localization of radioactive amino acid taken up into the outer segments of frog (Rana pipiens) rods. Vision Res 9:385–391
20. Hall MO, Bok D, Bacharach AD (1968) Visual pigment renewal in the mature frog retina. Science 161:787–789
21. Strissel KJ, Sokolov M, Trieu LH et al (2006) Arrestin translocation is induced at a critical threshold of visual signaling and is superstoichiometric to bleached rhodopsin. J Neurosci 26:1146–1153
22. Tian G, Lodowski KH, Lee R et al (2014) Retrograde intraciliary trafficking of opsin during the maintenance of cone-shaped photoreceptor outer segments of Xenopus laevis. J Comp Neurol 522(16):3577–3589
23. Gurskaya NG, Verkhusha VV, Shcheglov AS et al (2006) Engineering of a monomeric green-to-red photoactivatable fluorescent protein induced by blue light. Nat Biotechnol 24:461–465
24. Chudakov DM, Lukyanov S, Lukyanov KA (2007) Using photoactivatable fluorescent protein Dendra2 to track protein movement. Biotechniques 42:553, 555, 557 passim
25. Chudakov DM, Lukyanov S, Lukyanov KA (2007) Tracking intracellular protein movements using photoswitchable fluorescent proteins PS-CFP2 and Dendra2. Nat Protoc 2:2024–2032
26. Tsien RY (1998) The green fluorescent protein. Annu Rev Biochem 67:509–544
27. Zhang L, Gurskaya NG, Merzlyak EM et al (2007) Method for real-time monitoring of protein degradation at the single cell level. Biotechniques 42:446, 448, 450
28. Besharse JC, Hollyfield JG, Rayborn ME (1977) Turnover of rod photoreceptor outer segments. II. Membrane addition and loss in relationship to light. J Cell Biol 75:507–527
29. Yu DY, Cringle SJ (2005) Retinal degeneration and local oxygen metabolism. Exp Eye Res 80:745–751
30. Tian G, Ropelewski P, Nemet I et al (2014) An unconventional secretory pathway mediates the cilia targeting of peripherin/rds. J Neurosci 34:992–1006
31. Nemet I, Tian G, Imanishi Y (2014) Submembrane assembly and renewal of rod photoreceptor cGMP-gated channel: insight into the actin-dependent process of outer segment morphogenesis. J Neurosci 34(24): 8164–8174
32. Brockerhoff SE (2006) Measuring the optokinetic response of zebrafish larvae. Nat Protoc 1:2448–2451
33. Smith SJ, Fairclough L, Latinkic BV et al (2006) Xenopus laevis transgenesis by sperm nuclear injection. Nat Protoc 1:2195–2203
34. Nieuwkoop PD, Faber J (1967) Normal table for Xenopus laevis (Daudin). North-Holland, Amsterdam, 282 pp

Chapter 20

Measurements of Rhodopsin Diffusion Within Signaling Membrane Microcompartments in Live Photoreceptors

Mehdi Najafi and Peter D. Calvert

Abstract

High-resolution multiphoton imaging of live cells has become an invaluable method to study protein dynamics in highly compartmentalized subcellular environments. Here we describe procedures that we recently developed to quantify rhodopsin mobility within and between retinal rod photoreceptor light signaling microcompartments, the disc membrane lobules, using multiphoton fluorescence relaxation after photoconversion.

Key words Multiphoton FRAP, Live cell imaging, G protein-coupled receptors, Rhodopsin diffusion, Cell signaling, Microcompartments

1 Introduction

Phototransduction in rod photoreceptors relies on serial activation of multiple copies of the G protein, transducin, by each photoactivated rhodopsin. This amplifying step in phototransduction requires lateral diffusion of both proteins within or along the surface of disc membranes located within the ciliary rod outer segment [1]. The structure of the rod outer segment discs imposes restrictions on rhodopsin diffusion. The discs are physically separated from one another, preventing rhodopsin diffusion along the length of the approximately cylindrical outer segment. Moreover, incisures, which are clefts in the disc membranes that extend radially from the disc periphery toward their centers, create no-flux boundaries that divide the disc surface into lobular microcompartments. Throughout the long history of rhodopsin diffusion studies [2–10], it has been established that rhodopsin is capable of lateral translation on the surface of the disc; however, discrepancies existed among different investigations mainly with respect to the rhodopsin diffusion coefficient and the existence of an immobile fraction of rhodopsin molecules. These discrepancies were due in large part to the inability of previous methods for visualization of

Beata Jastrzebska (ed.), *Rhodopsin: Methods and Protocols*, Methods in Molecular Biology, vol. 1271,
DOI 10.1007/978-1-4939-2330-4_20,

rhodopsin transport in disc membranes to resolve the disc ultrastructure and to directly perturb rhodopsin absorption or fluorescence states within a well-defined region smaller than an individual disc lobule.

We recently developed novel approaches to resolve the spatio-temporal dynamics of rhodopsin mobility within and between rod outer segment disc membrane lobules of live *Xenopus laevis* photoreceptors [11]. We expressed fusions of rhodopsin with EGFP (Rho-EGFP) and photoactivatable GFP [12] (Rho-PAGFP) in transgenic *Xenopus laevis* rod photoreceptors [13–15] and arranged microslices of live retinas within our custom multiphoton and confocal laser scanning microscope [16, 17] that allowed visualization of the disc membrane incisure patterns. We then employed various modalities of multiphoton fluorescent recovery after photoconversion (mFRAP), which we described previously [16], to examine the mobility of rhodopsin within the disc lobules and across the disc membranes. Multiphoton photobleaching of Rho-EGFP (mFRAPb) was used to study rhodopsin diffusion with high temporal resolution and accurately determined the membrane diffusion coefficient of rhodopsin within individual disc lobules. The high signal to noise method of multiphoton photoactivation of Rho-PAGFP (mFRAPa) [16] combined with 2D confocal scanning was used to resolve the spatial aspect of rhodopsin mobility and its equilibration between lobules of various geometries on the disc surface. A 2D mathematical membrane diffusion model that includes the no-flux boundaries imposed by disc incisures was generated to quantify the impact of disc geometry on rhodopsin mobility. Here, we review some of the important details of our experimental design and procedures.

2 Materials

2.1 Confocal and Multiphoton Microscope

The experiments described below are performed using a custom laser scanning confocal/multiphoton microscope [16, 17] (*see* **Note 1**). Our confocal/multiphoton system is equipped in the following items:

1. An argon–ion laser (AIL) and a pulsed titanium–sapphire laser (Ti:SL; Mai Tai HP) (Spectra-Physics).
2. Uniblitz shutters (Vincent Associates) to control laser outputs.
3. The argon–ion laser, which passes through a 3× Galilean collimating beam expander (Thorlabs) and neutral density filters to control power (Newport).
4. The Ti:SL excitation beam, which passes through a Pockels cell (Conoptics) for fast power modulation, and a 3× beam expander (CVI Laser).

5. The two laser beams brought into a common path by dichroic mirrors (Chroma Technology) and pass through two galvanometer scanning mirrors (Cambridge Technology) and a set of relay lenses to fill the back aperture of the objective lens (Plan Apo VC, 60×/1.2 WI, Nikon) of an inverted microscope (TE2000, Nikon).
6. A piezoelectric focus drive (PIFOC P-721.LLQ, Physik Instrumente) to provide rapid (~1 μm in <1 ms) and precise (0.5 nm resolution) movement of the objective in the *z* dimension.
7. A pair of single photon counting modules (SPCM-AQR-14; Excelitas Technologies) placed in the descanned position to detect fluorescence emission. A long-pass filter and a short-pass filter (ET500lp and ET650sp-3p, Chroma Technology) blocked scattered excitation light from the AIL and Ti:SL. A pinhole at the conjugate image plane was used for confocal scanning.
8. PC with appropriate data acquisition and control boards (National Instruments) and a custom LabVIEW program created in collaboration with Dr. Michael Coleman (Coleman Technologies) for control of scanning and data acquisition.

2.2 Materials for Generating Transgenic Xenopus and Tissue Preparation for Imaging

1. DNA constructs: DNA constructs generated to express fluorescently labeled rhodopsin in photoreceptors of transgenic *Xenopus laevis*. The constructs consist of the sequence of bovine rhodopsin fused to EGFP (Rho-EGFP) or PAGFP (Rho-PAGFP), placed downstream of the *Xenopus* opsin promoter, which ensures specific expression of the transgenes in rod photoreceptors [13–15].
2. Epifluorescence dissecting microscope for screening transgenic frogs (Nikon SMZ1500).
3. Dissection tools: straight forceps #5 (Dumont), spring scissors (Vannas, 5-mm cutting edge), Premier Edge microsurgical knives (Electron Microscopy Sciences), and curved dissecting scissors (Fine Science Tools).
4. Frog Ringer's solution: 111 mM NaCl, 2.3 mM KCl, 1 mM $CaCl_2$, 1.6 mM $MgCl_2$, 3 mM 4-(2-hydroxyethyl)-1-piperazine-1-ethanesulfonic acid (HEPES), 10 mM glucose, 1 mM $NaHCO_3$, 1 mM NaH_2PO_4.
5. 0.1× Marc's modified Ringer's (MMR) solution: 10 mM NaCl, 0.2 mM KCl, 0.1 mM $MgSO_4$, 0.2 mM $CaCl_2$, 0.5 mM HEPES, pH 7.8, 0.01 mM EDTA.
6. Imaging chambers: imaging chambers fabricated by drilling 3–4-mm diameter holes into 35-mm polystyrene petri dishes. A 22 mm × 22 mm no.1 cover glass is then adhered to the dish, covering and sealing the holes, with low melting temperature

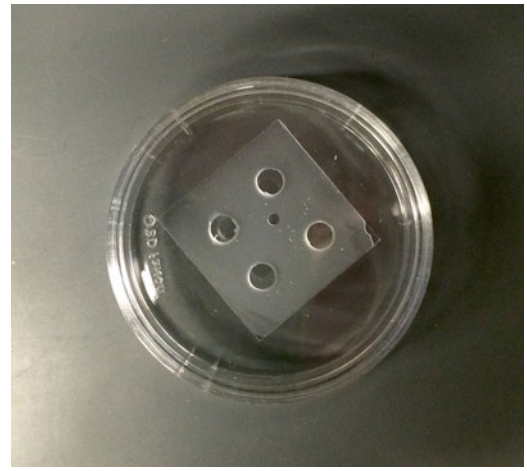

Fig. 1 Imaging chamber. A no. 1 cover glass is fixed to a 3.5-mm polystyrene petri dish into which several 3–5-mm holes have been drilled. Low melting point wax is placed on the bottom of the dish followed by the cover glass. A dedicated soldering iron, which is used solely for this purpose, is used to completely liquefy the wax. Capillary action prevents wax from covering the glass in the region of the holes

wax applied with a soldering iron held in close apposition but not touching the cover glass (Fig. 1).

7. Infrared dissecting microscope: a Zeiss Stemi 2000 dissecting microscope fitted with infrared converters (Owl, B.E. Meyers) and a 950 nm LED flashlight to illuminate the stage.

2.3 Items Needed for Image Processing and Diffusion Modeling

1. MATLAB (MathWorks) software for all post-processing of images and for diffusion models. Our scripts use elements from the image processing and parallel computing toolboxes.
2. A 64-bit personal computer with 12–64 GB of RAM and a multicore processor with the highest clock speed affordable to speed fitting diffusion model to data.
3. Optional, GeForce Graphics Processor (GPU) to speed model computation and allow running a large series of variables in parallel.

3 Methods

3.1 Transgenic Xenopus laevis Expressing Rho-EGFP and Rho-PAGFP

1. Generate transgenic *Xenopus* animals expressing Rho-EGFP or Rho-PAGFP using the restriction enzyme-mediated integration (REMI) method [13–15] (*see* **Notes 2** and **3**).
2. Divide the embryos in large petri dish plates and grow them in 0.1× MMR solution until day 7.
3. On day 7, anesthetize the embryos in 0.1× MMR containing 0.05 % tricaine (ethyl 3-aminobenzoate methanesulfonate)

and screen for fluorescence in their retinas under an epifluorescence dissecting microscope.

4. Grow positive embryos to late-stage tadpoles or adult frogs.

3.2 Xenopus Eye Dissection

All dissection procedures are done at room temperature and under infrared (IR) illumination.

1. Dark adapt a transgenic frog for ~2–10 h before dissection.
2. Anesthetize the animal in 0.05 % tricaine for 5–10 min. Confirm complete anesthesia by observing no withdrawal reflex upon pinching the hind legs.
3. Sacrifice the animal by decapitation, and enucleate and transfer the eyes onto a polypropylene sheet on the stage of a dissecting microscope equipped with IR convertors.
4. Remove the periorbital fat and connective tissues using curved scissors and straight forceps.
5. Position the globe with the cornea facing down. Cut the optic nerve as close as possible to the globe and gently push its remainder into the orbit using straight forceps.
6. Position the globe with the cornea facing up and create a small incision 1 mm below the cornea-scleral divide using spring scissors.
7. Insert the lower blade of the scissors in the incision and cut the sclera in a circular path parallel to the cornea-scleral divide.
8. Lift the iris and cornea to open the globe and transfer the retina to a 50 μl drop of Frog Ringer's solution (*see* **Note 4**).
9. Using straight forceps, gently position the retina with the photoreceptor side facing up (convex side up), cut the retina into 2–4 smaller pieces, and transfer each piece to a new drop of Frog Ringer's solution.
10. Using the dissection blade, make vertical cuts in each retina slice to create smaller retina squares of 0.5–1-mm side dimension (*see* **Note 5**).
11. Transfer retinal slices into an imaging chamber pre-filled with Frog Ringer's solution using a cut-tip 20-μl pipette. Gently position the slices using straight forceps to ensure the photoreceptor side is facing the coverslip. Place another coverslip on the top of the chamber.
12. Mount the imaging chamber on the stage of the microscope.

3.3 Multiphoton Fluorescence Recovery After Photoconversion

Crucial to the accurate estimation of the diffusivity of molecules in live cells is precise knowledge of the shape of the gradient formed by perturbing a fraction of the molecules through photobleaching or photoactivation and of the geometry of the cell compartment under investigation. The importance of precise knowledge of the perturbation field was recognized early in a seminal paper employing what

was at that time called fluorescence photobleaching recovery (FPR), where the impact of the size and shape of the bleaching field on estimation of the diffusion coefficient of rhodamine in aqueous solution was carefully examined [18]. The impact of the geometry of the compartment in estimations of the diffusion coefficient was recognized soon after in another seminal paper that examined the diffusion of rhodopsin in isolated rod outer segments [7]. However, in both of these approaches, and in virtually all subsequent approaches, the perturbation fields that generate the gradients required to estimate diffusivity are significantly larger than subcellular structures that define the geometry of the diffusion space, thus limiting the interpretation of the obtained diffusion coefficients.

We found that, owing to the size, shape, and highly organized nature of the disc membranes in *Xenopus* rod outer segments, with their highly uniform spacing and incisures that are longitudinally aligned over long distances [19, 20] and that exclude rhodopsin [21, 22], it was possible to visualize the disc ultrastructure in living rods using confocal and multiphoton microscopy (Fig. 2), providing that outer segments are oriented parallel to the MPCLSM optical path [11, 23]. Moreover, using diffraction-limited multiphoton excitation affords precise perturbation fields that are smaller than the disc lobules, thus permitting diffusion analysis within compartments of

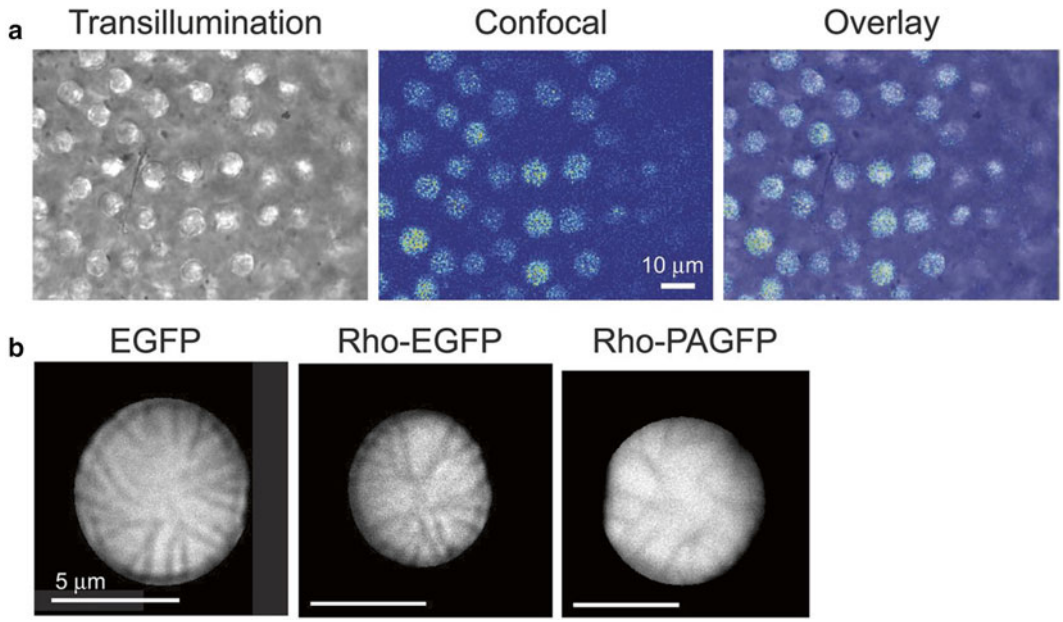

Fig. 2 Arrangement of retinal tissue in the chamber and visualization of disc incisures. (**a**) Retinal microslices are oriented with rod outer segments perpendicular to the cover glass. Transillumination of well-oriented tissue shows outer segments as bright circular structures. (**b**) Averaging of 15–20 images at a single *z*-position reveals brighter disc lobules subtended by dimmer incisures. Adapted with permission from Najafi et al. 2012, *Journal of General Physiology doi:10.1085*

known geometry [11]. Below we describe the methods we developed for mFRAP within defined rod outer segment disc lobules. We have modified the conventional term "fluorescent recovery after photobleaching" to accommodate recent technologies that allow both photoactivation and photobleaching of fluorophore for protein diffusion studies [12, 16]. The term mFRAPa therefore refers to fluorescent relaxation after multiphoton photo*a*ctivation, whereas mFRAPb refers to fluorescent recovery after multiphoton photo*b*leaching.

3.3.1 FRAPa

The FRAPa protocol described here is used to examine the 2D diffusion pattern of Rho-PAGFP across the full extent of the disc membrane. A typical FRAPa iteration consists of three main steps: (1) pre-photoactivation scans whereby a number of confocal scans across the ROS at a single *z*-position are obtained and averaged to determine the baseline fluorescence pattern of Rho-PAGFP, a step which also reveals the position of disc incisures; (2) photoactivation whereby the microscope is focused to the center of a discrete disc lobule region and a population of Rho-PAGFP molecules is photoactivated using a brief Ti:SL pulse; and (3) continuous post-photoactivation confocal scans at the same *z*-level to monitor fluorescent relaxation across the disc membrane.

1. Using IR illumination, find a retinal slice with photoreceptor tips in close apposition to the chamber bottom coverslip.
2. Take a 3D stack of the retinal slice using low-power AIL scanning to find properly aligned photoreceptors with minimal shift of their cross-section image upon *z*-scanning (*see* **Note 6**).
3. Select a photoreceptor with high level of Rho-PAGFP expression (*see* **Note 7**). Align the center of the cell with the center of the *x*–*y* imaging plane. Set the focal plane of the microscope to ~15 μm from the tip of the photoreceptor. Obtain and average multiple cross-sectional images of the photoreceptor to visualize the radial fluorescence dimming pattern that represent the incisures. A sample spacing of ~0.02 μm/pixel in each dimension is generally adequate to visualize the incisure pattern.
4. Define a region of interest (ROI) that contains the entire cross section of the photoreceptor.
5. Set the FRAPa protocol variables (*see* **Note 8**). Collect 5–10 pre-photoactivation ROI frames at 0.02 μm/pixel sampling space using confocal scanning at 488 nm, 0.02 μm *x*–*y* pixel size exceed Nyquist sampling minimum for confocal scanning >3-fold, thus avoiding aliasing. To photoactivate Rho-PAGFP, use 100–200 μs Ti:SL pulses at 820 nm for a total power measured at the objective back aperture of ~20 mW. This step is preceded and followed by a change in *z*-level to account for the *z*-offset between the lasers (*see* **Note 9**). Return to continuous confocal scanning following photoactivation to monitor fluorescent redistribution until equilibrium is reached.

3.3.2 FRAPb

The FRAPb protocol is designed to study rhodopsin diffusion with high temporal resolution. It involves multiphoton photobleaching of a population of Rho-EGFP molecules within the focal point of the Ti:SL and monitoring fluorescence recovery by continuous low-power multiphoton scanning of the photobleaching site.

1. Prepare end-on microslices of Rho-EGFP expressing *Xenopus* retinas in an imaging chamber mounted on the stage of the microscope.
2. Select and scan a properly aligned rod photoreceptor in which Rho-EGFP expression is detectable.
3. Visualize the incisures by collecting and averaging 15–20 images from a single *z*-position and select a disc lobule for FRAPb experiment.
4. Set the 3D coordinates of photobleaching by focusing the microscope to the center of the lobule. Adjust the *z*-level of the microscope to compensate for the focus shift between the lasers of different wavelengths (*see* **Note 9**).
5. Tune the multiphoton laser to 920 nm.
6. Set the pre-bleach, bleach, and post-bleach variables. We generally use 50–100-ms pre-bleach recording using low-power multiphoton excitation and 0.2–1-ms high-power multiphoton photobleaching pulses (for a total back aperture power of up to ~100 mW), followed by up to 1 s of post-bleach low-power scanning of Rho-EGFP (*see* **Notes 10** and **11**). Avoid laser powers or pulse durations that result in more than 60 % reduction from baseline fluorescence intensity in the first initial post-bleach recording (*see* **Note 12**).
7. Repeat 20–30 FRAPb iterations with ~2-min intervals between trials.

3.4 Microscope Calibration and Image Processing

Once raw data is acquired, images (FRAPa) and fluorescence levels monitored at the fixed bleach site (FRAPb) must be processed to account for instrument non-ideality. Most importantly, nonlinearities inherent to the single photon counting detectors must be corrected. Additionally, inhomogeneity in the imaging field caused by the optical train should be corrected. Finally, the 3D intensity profiles of the AIL and Ti:SL beams focused to the diffraction limit must be determined. These steps were made using a series of calibrations and stock scripts written in the MATLAB programming language:

1. Prepare a dilution series of recombinant EGFP (rEGFP) calibration standards in the nM to mM concentration range to cover the range of concentrations that might be encountered in rod photoreceptors. Standards may be expressed in bacterial expression system or purchased commercially. Dilutions should be made in pH-buffered water.

2. Scan small (~20 μl) chambers filled with the standards. Scans should be of a field size that will accommodate the region scanned in experiment. Spatial frequency should be at least twice the highest frequency used in experiment. Average 25–50 scans at a single *z*-position.
3. Average *x*–*y* scans to generate field correction templates.
4. Average fluorescence in the field scans of different rEGFP concentrations to build a calibration curve to determine the apparent concentration of Rho-EGFP in the live ROS.
5. Experimental images are then processed to yield field- and nonlinearity-corrected images of known Rho-GFP expression levels.
6. To calibrate the illumination profiles of the focused laser beams (i.e., the AIL 1p-*psf* and the Ti:SL mp-*psf*), dilute 0.1-μm diameter sub-resolution fluorescent microspheres (Fluoresbrite, Polysciences, Inc.) 10,000–100,000-fold in pH 7.5-buffered solution containing 45 % w/v sucrose, to match the refractive index of frog rod outer segments (n ~1.41) [24]. Index matching is important for accurately estimating the 1P and 2P excitation beam profiles and the shape and profile of the 2P photoconversion fields.
7. Then suspend the microspheres in low melting temperature agar in an imaging chamber with no. 1 cover glass floor (described above).
8. Scan microspheres in 3D with a spatial frequency of 0.02 μm in *x*–*y* and 0.15 μm in *z*, which satisfy the Nyquist sampling theorem in theses orthogonal directions.
9. Import images of the microspheres into an automated calibration routine written in the MATLAB programming environment. The script identifies microspheres in the 3D field via Canny edge detection, and multiple 3D images (generally 25–50) are aligned and averaged to produce the 3D profiles of the excitation beams.

3.5 Diffusion Modeling and Estimation of Diffusion Coefficients

To estimate the diffusion coefficient for molecules residing in small spaces bounded by no-flux boundaries of arbitrary shape, it is necessary to resort to numerical methods to solve the diffusion equations. We and others have published extensive descriptions of the method of lines approach that we have used to examine the diffusion of membrane and soluble proteins in live cells [16, 25–27]. For the examination of rhodopsin diffusion in outer segment discs with defined incisure patterns, we modified our previous model, implemented in MATLAB, to include a user interactive component, whereby the averaged image showing the positions of the incisure patterns is displayed and the coordinates of the photobleaching or photoactivation pulses are indicated. The user then

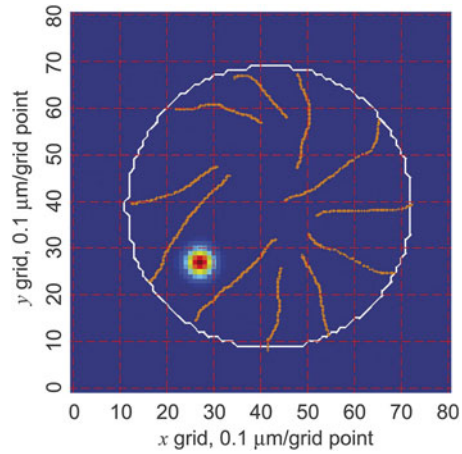

Fig. 3 A typical grid employed for solving the diffusion equations. Adapted with permission from Najafi et al. 2012, *Journal of General Physiology doi:10.1085*

interactively traces the positions of the incisures, which are transferred to the model grid as no-flux boundaries (Fig. 3). This approach allows the impact of the geometry of the diffusion space to be directly accounted for in the estimation of the diffusion coefficient. Below the implementation of this approach in mFRAPa and mFRAPb Rho-E/PAGFP experiments is outlined:

1. In the case of mFRAPb experiments where Rho-EGFP is bleached by a brief pulse from the Ti:SL laser tuned to 920 nm and the recovery is monitored at the same, fixed position by multiphoton point excitation, examine the recovery of bleach fluorescence for less than 1 s. Although this is a relatively short time compared to the time required for fluorescence relaxation across the entire disc, it is enough time for the bleach field to equilibrate across a lobule and for some Rho-EGFP from neighboring disc regions to diffuse into the bleached lobule. Thus accounting for the geometry of the specific lobule where the bleach occurred as well as that of the neighboring lobules is an important step for increasing accuracy of diffusivity estimation.
2. Use averaged "end-on" scans taken prior to the photobleach to define the grid dimension and spatial frequency.
3. Calculate the position and amplitude of the bleach or source field based on the bleach position selected in the imaging software and the calibrated laser intensity.
4. Trace then the positions of the incisures and assign as no-flux boundaries in the model grid.
5. The disc surface is assumed to have uniform distribution of Rho-EGFP, except within the incisures.

6. For FRAPb experiments subtract a sink from the grid at the blast position in the shape of the Ti:SL mp-*psf* with a depth that corresponded to the calculated fractional bleach of EGFP. For FRAPa experiments, add a source to the grid at the blast position in the shape of the Ti:SL mp-*psf* with an amplitude that corresponded to the calculated fractional photoactivation of PAGFP.
7. The sink and source fields are generated as time-dependent photoconversion events that take into account the photoconversion rates of the Ti:SL mp-*psf*. Although our model allows us to take into account diffusion during a photoconversion even as well, the diffusion of rhodopsin was slow enough as to be negligible during the 100 μs Ti:SL pulses.
8. Then allow diffusion in the model to proceed with the appropriate time step to match acquisition frequency: up to kHz for FRAPb experiments and up to 10 Hz for FRAPa experiments.
9. To account for blurring due to confocal scanning with the AIL in FRAPa experiments, the model output is convolved with a kernel representing the 1p-*psf*. Sampling in FRAPb experiments is accounted for by taking the inner product of the model output with a kernel representing the mp-*psf*.
10. Model a range of diffusion coefficients at a grain appropriate to achieve accurate estimation of diffusion coefficients from acquired data (typically 0.05–0.5 $\mu m^2/s$ at 0.01 steps). Select the best diffusion coefficient based on minimization of the squared difference between model and data.

4 Notes

1. Although custom-designed microscope systems provide a higher level of flexibility in study design, most recent commercial systems are also capable of the majority of the experiments described in this chapter.
2. A detailed and updated protocol for REMI transgenesis has been published recently [14].
3. Several other methods for *Xenopus* transgenesis have been developed and can be used [28].
4. With practice, it is possible to position the blade of the scissors between the sclera and the retina and cut the sclera without tearing the retina. This method leads to separation of the retina from the RPE once the upper part of the globe is lifted. The retina is then isolated from the cornea and the lens using the dissection blade. Otherwise, if the retina remains attached to the RPE, the lower part of the globe can be transferred into a drop of Frog Ringer's solution, and the retina is separated gently from the RPE using straight forceps.

5. The goal here is to create retinal slices suitable for end-on imaging configuration, i.e., the axis of the photoreceptor is perpendicular to the imaging plane of the microscope, as opposed to side-on imaging whereby the photoreceptor axis is parallel to the imaging plane. The size of retinal slices should be large enough so that each slice can be stably positioned with photoreceptors facing down without falling on one side but small enough for the slice to keep its natural curvature. We determined that for *Xenopus laevis* the optimum end-on retinal slice is of 0.5–1 mm side dimension. This number can be adjusted experimentally for retinas of other species.
6. At high laser intensities, confocal scanning at 488 nm results in gradual PAGFP photoactivation. The laser power should be adjusted to the level that allows visualization of the incisure pattern with minimal PAGFP photoactivation.
7. Transgenic expression under the *Xenopus* opsin promoter leads to mosaic expression in rod photoreceptors, which provides a great advantage in measuring protein mobility in multiple photoreceptors from the same retina that express Rho-E/PAGFP at broadly varying concentrations [17].
8. The FRAP protocol and the imaging parameters mentioned here are adjusted for the best outcome in our custom-designed system. They can be used as general guidelines for FRAPa experiments; however, they need to be properly adjusted to each imaging system.
9. During the FRAPa experiment, a rapid (1 μs) objective focus shift (~1 μm) in the *z* dimension is made to account for the *z*-offset between the focal positions of the two lasers caused by chromatic aberration. More accurately the *z*-step is to compensate for the difference between the point-spread-function centroid of the AIL and that of the Ti:SL, which is determined empirically by scanning sub-resolution fluorescent beads with each laser [16]. In commercial microscope systems, accommodation for the difference in focus between broadly different laser wavelengths may be adjusted during calibration procedures. In either case, great care should be taken to assess chromatic aberration because if not accounted for it can cause significant errors in quantifying lateral diffusion.
10. The proper bleach parameters depend on laser power and the optics of the microscope and are generally determined experimentally. The variables mentioned here can be used as guidelines.
11. Depending on the size of the lobule and exact dimensions of the Ti:SL mp-*psf*, 2–5 % of the rhodopsin population will be depleted immediately following every bleach trial. Higher levels of fluorescence depletion during FRAPb experiments

should raise suspicion for background bleaching. A mock, bleach pulse-free FRAPb iteration can be performed to accurately measure and account for background bleach.

12. In order to quantify protein diffusion in FRAPb experiments, it is necessary to ensure that the initial post-bleach fluorophore concentration follows a Gaussian intensity profile. The relationship between the post-bleach fluorescence profile and the reduction in fluorescence intensity (called the bleach depth) has been demonstrated [18]. To maintain a post-bleach Gaussian intensity profile, the bleach depth should be less than 60 %.
13. The methods described in this paper were developed to study dynamics of rhodopsin mobility within photoreceptor disc membrane microcompartments. We introduced live end-on imaging of photoreceptors that draws upon parallel organization of disc membranes within the outer segment as a unique approach to visualize and study membrane microcompartments in their native state. Using multiphoton photoactivation in mFRAPa approach, we were able to photoactivate a source of PAGFP-labeled rhodopsin molecules within individual lobules and examine their translational mobility across the disc membrane. We took advantage of more than a ~100-fold increase in signal/noise ratio in multiphoton photoactivation compared to photobleaching [16] which enabled us to monitor protein diffusion over longer distances and for extended periods of time. Furthermore, unlike confocal scanning, multiphoton pulses generate localized excitation in a spatially defined volume, which is critical for quantitative modeling of protein diffusion.
14. However, during mFRAPa experiments, the refocusing of the microscope to compensate for the *z*-offset between the lasers as well as 2D confocal scanning of large photoreceptor cross sections introduces a delay between the photoactivation pulse and the first confocal scan. As a result the first ~100 ms of Rho-PAGFP diffusion is not directly recorded. We overcame this limitation by employing the mFRAPb protocol, whereby photobleaching and monitoring the recovery of Rho-EGFP take place in a fixed location which is the focal point of the Ti:SL. Using this method we were able to increase our data acquisition rate to ~1 MHz and precisely measure the diffusion coefficient of rhodopsin within the disc lobules [11]. The combination of mFRAPa and mFRAPb proved to be a useful approach in studying rhodopsin diffusion with high temporal and spatial resolution.
15. The experimental and analytical approaches introduced here can be used to study other signaling networks that are regulated by interactions between functional proteins and their subcellular microenvironment. Targeted manipulations of photoconvertible fluorochromes using multiphoton imaging

allow real-time visualization of the cell ultrastructure impact on signaling proteins. Together with quantitative analyses, it has become an invaluable tool for studying fundamental biological processes in their native cellular context.

Acknowledgements

This work was supported by the National Institutes of Health grant R01EY018421 to P.D.C., a Research to Prevent Blindness, Inc. Career Development Award (P.D.C.), a grant from the Karl Kirchgessner Foundation (P.D.C.), and Lions district 20-Y1. The SUNY Upstate Department of Ophthalmology is recipient of an unrestricted grant from Research to Prevent Blindness, Inc.

References

1. Pugh EN Jr, Lamb TD (2000) Phototransduction in vertebrate rods and cones: molecular mechanisms of amplification, recovery and light adaptation. In: Stavenga DG, de Grip WJ, Pugh EN Jr (eds) Handbook of biological physics. Elsevier Science B. V., New York, pp 183–255
2. Drzymala RE, Weiner HL, Dearry CA et al (1984) A barrier to lateral diffusion of porphyropsin in Necturus rod outer segment disks. Biophys J 45:683–692
3. Govardovskii VI, Korenyak DA, Shukolyukov SA et al (2009) Lateral diffusion of rhodopsin in photoreceptor membrane: a reappraisal. Mol Vis 15:1717–1729
4. Gupta BD, Williams TP (1990) Lateral diffusion of visual pigments in toad (Bufo marinus) rods and in catfish (Ictalurus punctatus) cones. J Physiol 430:483–496
5. Liebman PA, Entine G (1974) Lateral diffusion of visual pigment in photoreceptor disk membranes. Science 185:457–459
6. Poo M, Cone RA (1973) Lateral diffusion of rhodopsin in the visual receptor membrane. J Supramol Struct 1:354
7. Poo M, Cone RA (1974) Lateral diffusion of rhodopsin in the photoreceptor membrane. Nature 247:438–441
8. Saxton MJ (1987) Lateral diffusion in an archipelago. The effect of mobile obstacles. Biophys J 52:989–997
9. Wey CL, Cone RA, Edidin MA (1981) Lateral diffusion of rhodopsin in photoreceptor cells measured by fluorescence photobleaching and recovery. Biophys J 33:225–232
10. Wang Q, Zhang X, Zhang L et al (2008) Activation-dependent hindrance of photoreceptor G protein diffusion by lipid microdomains. J Biol Chem 283:30015–30024
11. Najafi M, Haeri M, Knox BE et al (2012) Impact of signaling microcompartment geometry on GPCR dynamics in live retinal photoreceptors. J Gen Physiol 140:249–266
12. Patterson GH, Lippincott-Schwartz J (2002) A photoactivatable GFP for selective photolabeling of proteins and cells. Science 297:1873–1877
13. Knox BE, Schlueter C, Sanger BM et al (1998) Transgene expression in Xenopus rods. FEBS Lett 423:117–121
14. Haeri M, Knox BE (2012) Generation of transgenic Xenopus using restriction enzyme-mediated integration. Methods Mol Biol 884: 17–39
15. Kroll KL, Amaya E (1996) Transgenic Xenopus embryos from sperm nuclear transplantations reveal FGF signaling requirements during gastrulation. Development 122:3173–3183
16. Calvert PD, Peet JA, Bragin A et al (2007) Fluorescence relaxation in 3D from diffraction-limited sources of PAGFP or sinks of EGFP created by multiphoton photoconversion. J Microsc 225:49–71
17. Peet JA, Bragin A, Calvert PD et al (2004) Quantification of the cytoplasmic spaces of living cells with EGFP reveals arrestin-EGFP to be in disequilibrium in dark adapted rod photoreceptors. J Cell Sci 117:3049–3059
18. Axelrod D, Koppel DE, Schlessinger J et al (1976) Mobility measurement by analysis of fluorescence photobleaching recovery kinetics. Biophys J 16:1055–1069
19. Corless JM, Fetter RD, Zampighi OB et al (1987) Structural features of the terminal loop region of frog retinal rod outer segment disk

membranes: II. Organization of the terminal loop complex. J Comp Neurol 257:9–23

20. Tsukamoto Y (1987) The number, depth and elongation of disc incisures in the retinal rod of Rana catesbeiana. Exp Eye Res 45: 105–116
21. Roof DJ, Heuser JE (1982) Surfaces of rod photoreceptor disk membranes: integral membrane components. J Cell Biol 95: 487–500
22. Molday RS, Hicks D, Molday L (1987) Peripherin. A rim-specific membrane protein of rod outer segment discs. Invest Ophthalmol Vis Sci 28:50–61
23. Najafi M, Maza NA, Calvert PD (2012) Steric volume exclusion sets soluble protein concentrations in photoreceptor sensory cilia. Proc Natl Acad Sci U S A 109:203–208
24. Sidman RL (1957) The structure and concentration of solids in photoreceptor cells studied by refractometry and interference microscopy. J Biophys Biochem Cytol 3:15–30
25. Schiesser WE (1991) The numerical method of lines: integration of partial differential equations. Academic, San Diego
26. Schiesser WE, Griffiths GW (2009) A compendium of partial differential equation models: method of lines analysis with MATLAB. Cambridge University Press, New York
27. Calvert PD, Schiesser WE, Pugh EN Jr (2010) Diffusion of a soluble protein, photoactivatable GFP, through a sensory cilium. J Gen Physiol 135:173–196
28. Chesneau A, Sachs LM, Chai N et al (2008) Transgenesis procedures in Xenopus. Biol Cell 100:503–521

Part VI

Treatment Strategies of Retinal Degenerative Disease

Chapter 21

Kinetics of Rhodopsin's Chromophore Monitored in a Single Photoreceptor

Leopold Adler IV, Nicholas P. Boyer, Chunhe Chen, and Yiannis Koutalos

Abstract

Absorption of light isomerizes the retinyl chromophore of the photoreceptor pigment rhodopsin from 11-*cis* to all-*trans*, generating the photoactivated rhodopsin form. The photoisomerization of the chromophore however destroys rhodopsin, and its regeneration requires the removal of the all-*trans* and the supply of fresh 11-*cis* chromophore. The all-*trans* chromophore is removed through a series of steps beginning with its release from photoactivated rhodopsin in the form of all-*trans*-retinal, leaving behind the apoprotein opsin. All-*trans*-retinal is then reduced to all-*trans*-retinol, which is transported out of the photoreceptor. Rhodopsin is regenerated from opsin and fresh 11-*cis*-retinal arriving to the photoreceptor from the retinal pigment epithelium. Both all-*trans* and 11-*cis*-retinal can form precursors of lipofuscin, a pigment that accumulates with age in the lysosomal compartment of the retinal pigment epithelium. All-trans-retinal, all-*trans*-retinol, and lipofuscin precursors all emit significant and distinct fluorescence signals, allowing their monitoring in single photoreceptor cells with fluorescence imaging. Here we describe the procedures for measuring these fluorophores in single mouse rod photoreceptors.

Key words Photoreceptor, Rhodopsin, Vitamin A, All-*trans*-retinal, All-*trans*-retinol, *bis*-Retinoids, Lipofuscin, Fluorescence

1 Introduction

The light-sensitive properties of rhodopsin, the vertebrate rod photoreceptor pigment, originate from its 11-*cis*-retinal chromophore. The absorption of light by rhodopsin results in the isomerization of the 11-*cis*-retinal chromophore to all-*trans* forming the enzymatically active intermediate, metarhodopsin II, which commences the visual transduction process [1, 2]. Photoisomerization of the 11-*cis*-retinal chromophore to all-*trans* renders rhodopsin insensitive to light. To regain sensitivity to light, all-*trans*-retinal has to be removed and fresh 11-*cis*-retinal be supplied to regenerate rhodopsin [3, 4]. These reactions take place in the outer segment of the rod photoreceptor, where rhodopsin is densely packed. Removal of all-*trans*-retinal begins with the hydrolysis of the Schiff base that links

Beata Jastrzebska (ed.), *Rhodopsin: Methods and Protocols*, Methods in Molecular Biology, vol. 1271,
DOI 10.1007/978-1-4939-2330-4_21,

it covalently to opsin, the protein part of rhodopsin. All-*trans*-retinal is then released, leaving behind opsin, which can combine with fresh 11-*cis*-retinal to regenerate rhodopsin. The removal of all-*trans*-retinal is completed through reduction to all-trans-retinol in a reaction catalyzed by the enzyme retinol dehydrogenase RDH8 [5, 6] and using NADPH as a cofactor [7]. Subsequently, in a process facilitated by the interphotoreceptor retinoid-binding protein (IRBP), all-*trans*-retinol leaves the rod outer segment and is transferred to the adjacent cells of the retinal pigment epithelium (RPE) [8]. There, all-*trans*-retinol enters a series of reactions that culminate in the generation of 11-*cis*-retinal [3, 4, 9]. Another source of all-*trans*-retinol is the choroidal circulation, which delivers it bound on retinol-binding protein (RBP) to the basal side of the RPE cells [10]. Inside the RPE cells, all-trans-retinol is esterified by lecithin/retinol acyltransferase (LRAT) to form retinyl esters [11], which are the substrate used by the RPE65 protein to make 11-*cis*-retinol [12–14]. Retinol dehydrogenase RDH5 oxidizes 11-*cis*-retinol to 11-*cis*-retinal [15], which is then transported from the RPE cells to rod outer segments by IRBP [16].

Because of its importance for maintaining light sensitivity, rhodopsin regeneration has been and is being studied extensively at the molecular, cellular, and whole organism levels. Additional importance of the reactions involved in rhodopsin regeneration stems from the involvement of the highly reactive allylic aldehydes 11-*cis* and all-*trans*-retinal. The cytotoxic properties of all-t*rans*-retinal have been extensively documented and studied [17–19]; on the basis of its structure, the toxic effects of 11-*cis*-retinal would be expected to be similar. The cytotoxic potential of 11-*cis* and all-*trans*-retinal extends even further, as they are the source of *bis*-retinoids and lipofuscin in the retina. *bis*-Retinoids [20] constitute the major components of lipofuscin, a complex fluorescent mixture of cellular debris that accumulates with age in the lysosomal compartment of the RPE. *bis*-Retinoids, as well as lipofuscin, display broad toxicity, including photoreactivity and inhibition of lysosomal function among others [21, 22].

A prerequisite for lipofuscin and *bis*-retinoid accumulation is the generation of 11-*cis*-retinal, as animals that lack the RPE65 protein have strongly reduced levels of lipofuscin and *bis*-retinoids in the RPE [23, 24]. Another prerequisite is the phagocytosis of the outer segments by the RPE [25]. Thus, lipofuscin is thought to originate in the photoreceptor outer segments through reactions of the retinyl chromophore with components of the outer segment membranes and to end up in the RPE lysosomes through the daily phagocytosis of the outer segments [26]. 11-*cis* and all-*trans*-retinal can both form *bis*-retinoid compounds when reacting with rod outer segment membranes [27] and generate lipofuscin-like fluorescence when added to single isolated rod outer segments [23].

The intrinsic fluorescence of all-*trans*-retinal, all-*trans*-retinol, and *bis*-retinoid lipofuscin precursors can be used to determine the kinetics of their formation and removal in single photoreceptor cells with fluorescence imaging. This allows high resolution, real-time measurements of the fate of the retinyl chromophore following its release from photoactivated rhodopsin. Such studies have been carried out using photoreceptor cells from several species, such as rod and cone photoreceptors from tiger salamander (*Ambystoma tigrinum*) [28, 29], rod photoreceptors from frogs (*Rana pipiens*) [30], lizards (*Gekko gecko*) [28], and mice (*Mus musculus*—variety of wild type and genetically modified) [31, 32], and the cone-like photoreceptors from $Nrl^{-/-}$ mice [32]. Mice offer important advantages for single-cell measurements, as the results can be correlated with those from the chemical analysis of whole retinas and from whole animal experiments. In addition, the availability of genetically modified mice has allowed the detailed examination of the contribution of different enzymes to the processing of the retinyl chromophore in photoreceptors and their potential role in human disease. Measurements of all three fluorophores, all-*trans*-retinal, all-*trans*-retinol, and lipofuscin precursors, have been carried out with photoreceptors isolated from wild-type and genetically modified mice. More recently, this fluorescence has been used for the noninvasive imaging of the mouse and primate retina and RPE with two-photon microscopy [33, 34].

Figure 1 shows a diagram of the fluorescence imaging setup that is used to record the fluorescence of single isolated mouse rod photoreceptors. The procedures, general materials, and methods for obtaining single isolated photoreceptor cells and for conducting the fluorescence imaging experiments have been described in detail previously [35]. In the present chapter, the emphasis is placed on the optics used to record and distinguish the fluorescence signals from all-*trans*-retinol, all-*trans*-retinal, and lipofuscin precursors. Figure 2 shows true-color fluorescence micrographs of mouse rod photoreceptors obtained with different excitation and emission filters. With DAPI optics (excitation, broadband 365 nm; emission, >420 nm), the light blue fluorescence emission in the outer segment is due to retinoids (all-*trans*-retinal and all-t*rans*-retinol), while the darker blue emission in the inner segment and cell body is due to NADH. With FITC optics (excitation, 450–490 nm; emission, >515 nm), the orange fluorescence emission in the rod outer segment is due to lipofuscin precursors. With the large difference in emission properties, the fluorescence signals from retinoids and lipofuscin precursors can readily be distinguished and recorded separately with minimal cross-interference. The emission spectra of all-*trans*-retinal and all-*trans*-retinol however are virtually identical [5, 29], and the separation of their fluorescence signals presents a challenge. Their signals can be distinguished from the difference in their excitation spectra (*see* below, Fig. 4).

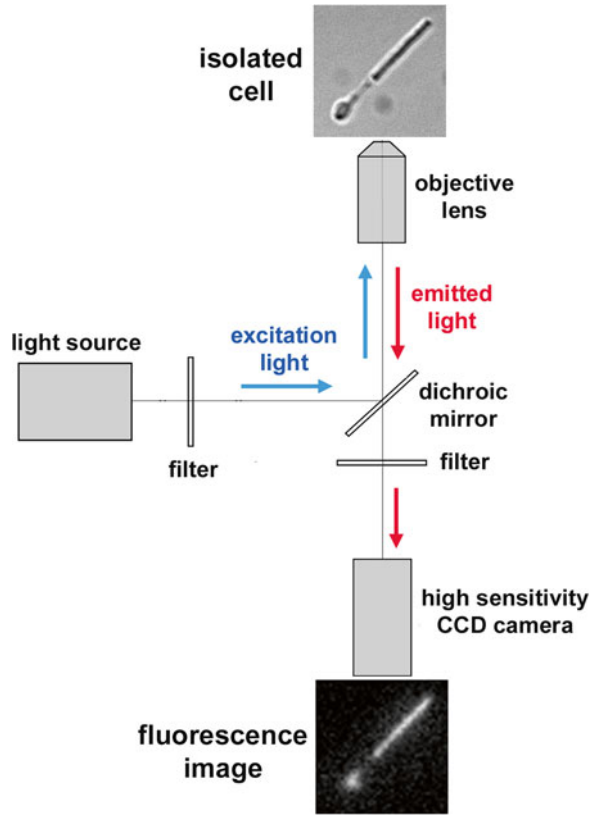

Fig. 1 Schematic diagram of the fluorescence imaging setup used to monitor rhodopsin's chromophore in single photoreceptors. Isolated mouse rod photoreceptors are placed in the experimental chamber on the microscope stage (micrograph at top). A xenon lamp provides the excitation light, from which appropriate wavelengths are selected by a filter; the filtered light is focused on a cell by the objective lens and excites its fluorophores. The emitted fluorescence is collected by the objective lens, and appropriate wavelengths are selected by a filter. A high-sensitivity CCD camera captures the fluorescence image (micrograph at *bottom*). The dichroic mirror reflects the lower excitation light wavelengths and transmits the longer emission light wavelengths. The particular fluorescence image has been obtained with the filters for imaging all-*trans*-retinol, 60 min after exposing the cell to light

Whether monitoring the kinetics of retinoids or the formation of lipofuscin precursors after exposure to light, the experiments share a general procedure. The procedure begins with the isolation of dark-adapted rod photoreceptors from a mouse retina and placing a chamber containing the cells on the stage of the microscope. Using infrared illumination, a living isolated rod photoreceptor is selected for experiment. An infrared bright-field image and fluorescence image are taken of the dark-adapted cell. The cell is then exposed to long-wavelength light to isomerize the 11-*cis* chromophore of the full complement of rhodopsin. Fluorescence images are then captured at different times after exposing the cell to light. With mouse cells, experiments are conducted at 37 °C.

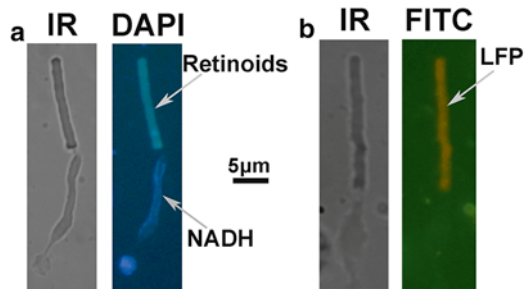

Fig. 2 True-color images of the fluorescence of isolated mouse rod photoreceptors captured with different sets of filters. (**a**) Infrared (IR) and fluorescence images of an isolated wild-type mouse rod photoreceptor. Fluorescence image captured 30 min after exposure to light using DAPI optics (excitation light, broadband 365 nm, with 60 nm FWHM; emission, >420 nm). The outer segment fluorescence is due to retinoids (all-*trans*-retinal and all-*trans*-retinol), while that of the inner segment and cell body is due to NADH. (**b**) Infrared (IR) and fluorescence images of a dark-adapted isolated *Abca4*$^{-/-}$ mouse rod photoreceptor. Fluorescence image captured using FITC optics (excitation light, 450–490 nm; emission, >515 nm). The outer segment fluorescence is due to lipofuscin precursors (LFP). Images were taken on a Zeiss Axioplan 2 microscope (Carl Zeiss, Thornwood, NY) using a 63× oil immersion objective (NA = 1.4) with a Nikon D200 (Nikon, Inc., Melville, NY) digital camera

The kinetics of all-*trans*-retinol formation have been characterized in isolated rod photoreceptors from wild-type strains, as well as from several types of genetically modified mice [31, 32]. An example from a wild-type mouse cell is shown in Fig. 3, where the rod outer segment fluorescence (excitation, broadband 360 nm; emission, >420 nm) increases with time after light exposure. In this case, the rod outer segment fluorescence increase is mostly due to the formation of all-*trans*-retinol, although there is some contribution by all-*trans*-retinal as well. It is possible to distinguish the fluorescence signals of all-*trans*-retinal and all-*trans*-retinol based on their different absorption spectra [36]. The absorption spectrum for all-*trans*-retinal peaks at ~380 nm and that for all-t*rans*-retinol at ~325 nm, with the isosbestic point at ~340 nm. Thus, the ratio of the fluorescence excited with narrowband 340 nm light to that with narrowband 380 nm light (Fex-340/Fex-380) can be used as a measure of the relative contributions of all-*trans*-retinal and all-*trans*-retinol to the total rod outer segment fluorescence [5, 37]. The reason for selecting 340 nm (instead of 325 nm) as the second excitation wavelength to go along with 380 nm (at the all-*trans*-retinal absorption peak) is due to the low transmittance of glass optics below 340 nm. Figure 4 shows an experiment that distinguishes between all-*trans*-retinal and all-*trans*-retinol using the Fex-340/Fex-380 ratio. The infrared bright-field image shows a metabolically intact cell and a metabolically compromised broken off rod outer segment (bROS). The broken off rod outer segment has been separated from the metabolic machinery of the cell and so there is no NADPH available to reduce the all-*trans*-retinal released from photoactivated rhodopsin following light excitation [37]. The slight fluorescence increase observed after light

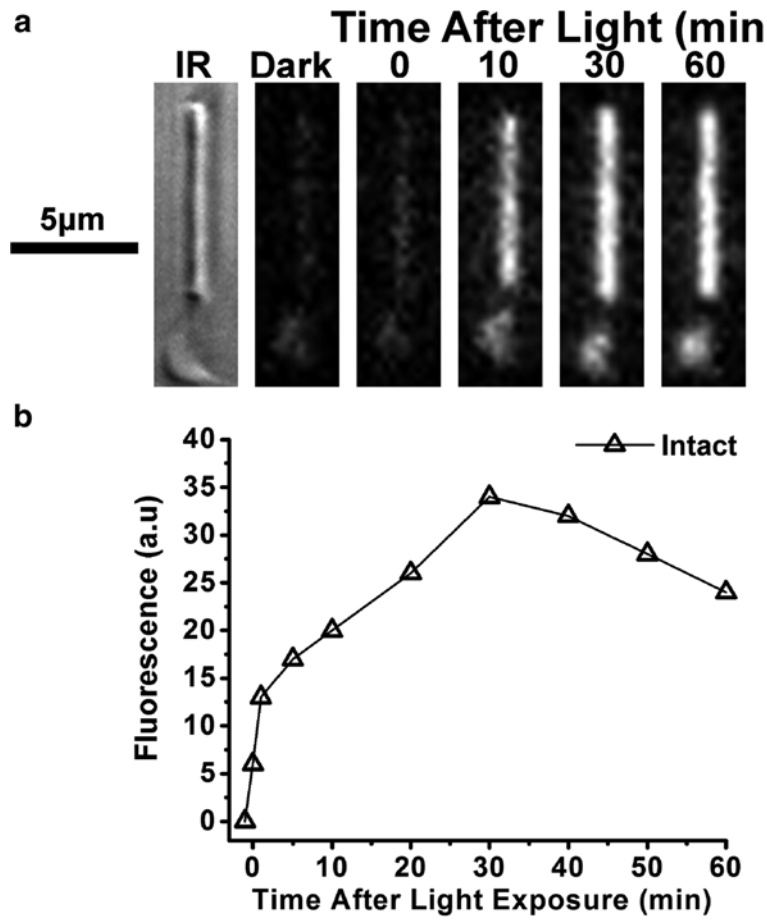

Fig. 3 Measurement of the kinetics of all-*trans*-retinol formation after light exposure in a metabolically intact wild-type mouse rod photoreceptor. Rod photoreceptor fluorescence was excited using 360 nm light, and emission was collected >420 nm. (**a**) Infrared (IR) and fluorescence images of a mouse rod photoreceptor. After the fluorescence image of the dark-adapted cell was captured, the cell was exposed to intense >530 nm light for 1 min. (**b**) Increase in rod outer segment fluorescence intensity after light exposure. Experiment at 37 °C

exposure in the bROS is therefore due to all-*trans*-retinal. On the other hand, the fluorescence increase in the outer segment of the metabolically intact cell is much larger, as in this case the released all-*trans*-retinal is converted to all-*trans*-retinol, which has a much higher fluorescence quantum yield than all-*trans*-retinal. The different origins of the increase in fluorescence for the bROS and for the metabolically intact rod are confirmed by the different Fex-340/Fex-380 ratios. Specific information about the origin of the signal is obtained by comparing the value of the Fex-340/Fex-380 ratio with the values of the ratio for all-*trans*-retinal and all-*trans*-retinol, which are measured by loading broken off rod outer segments with large concentrations of each of the retinoids [37]. For the cells in Fig. 4, the ratio is

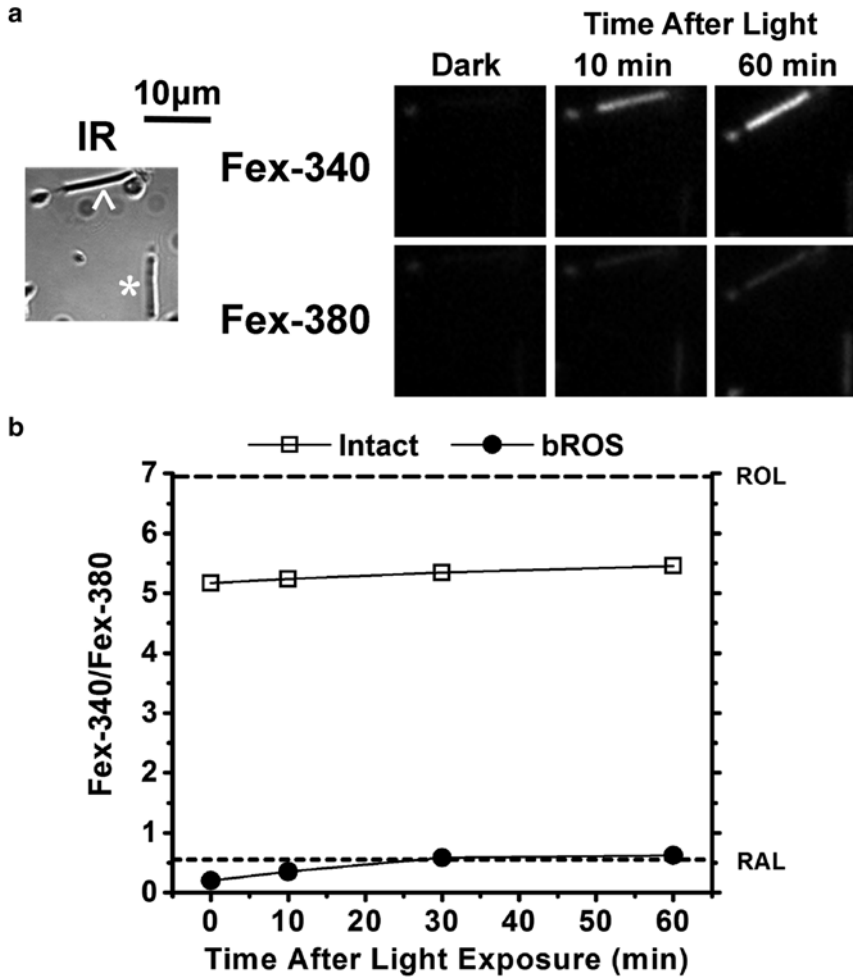

Fig. 4 Differentiation of the origins of rod outer segment fluorescence signals using 340 and 380 nm excitation light; emission collected >420 nm. (**a**) Bright-field infrared (IR) and fluorescence images of an isolated metabolically intact rod cell (*arrowhead*, ^) and a metabolically compromised broken rod outer segment, bROS (*star*, *) from a wild-type mouse. Fluorescence images of the field were captured using excitation light of 340 nm (Fex-340) and 380 nm (Fex-380) and collecting the emission >420 nm. Fluorescence images were first captured for the dark-adapted cells; the cells were then exposed to intense >530 nm light for 1 min, and fluorescence images were captured at different times following the exposure. (**b**) Fluorescence ratio Fex-340/Fex-380 for the metabolically intact (*open square*) and the bROS (*filled circle*) as a function of time after light exposure. The *dashed lines* represent the values of the Fex-340/Fex-380 ratio for all-*trans*-retinol (ROL) and all-*trans*-retinal (RAL). Experiment at 37 °C

much smaller for the bROS, and its value of ~0.5 indicates that virtually all of the chromophore released from photoactivated rhodopsin is in the form of all-*trans*-retinal. The value of the ratio is ~5.3 for the outer segment of the metabolically intact rod, close to the value of 6.95 for all-*trans*-retinol, which indicates that a large fraction of the released chromophore, ~88 %, has been converted to all-*trans*-retinol (*see* Eq. 1). The extent of conversion estimated from the Fex-340/

Fex-380 fluorescence ratio is in good agreement with the biochemical estimate of ~80 % measured from organic extracts of whole retinas at 90 min after light exposure [32] (when all of the extractable all-*trans*-retinal chromophore has been released and become available for reduction). Thus, in general, all-*trans*-retinal contributes to the rod outer segment fluorescence signal. This contribution is fairly substantial in the absence of NADPH or in the absence of retinol dehydrogenase RDH8 [5], the enzyme that catalyzes the reduction of all-*trans*-retinal to all-trans-retinol. Accordingly, it is important to always ensure that the cells are supplied with appropriate levels of metabolic substrates and to conduct experiments to establish the origin of the retinoid fluorescence signal.

Imaging of the fluorescence of lipofuscin precursors in single rod photoreceptor cells has been used to investigate the origins of lipofuscin and examine the conditions that enhance or curtail its formation [23]. Figure 5 shows an experiment monitoring the fluorescence of lipofuscin precursors after light exposure in a metabolically intact cell and a metabolically compromised bROS. There is significant fluorescence due to lipofuscin precursors present in the dark-adapted outer segments of both the metabolically intact rod and the bROS. Following light exposure, the lipofuscin precursor fluorescence increases in the metabolically compromised bROS, consistent with the formation of additional precursors from the all-*trans*-retinal that is being released but not reduced. In the case of the metabolically intact rod, the fluorescence remains relatively stable in the outer segment, consistent with the quantitative reduction of the released all-*trans*-retinal to all-*trans*-retinol.

2 Materials

2.1 Preparation of Isolated Photoreceptor Cells

For general materials required for the isolation of retina and the preparation of living isolated photoreceptors for fluorescence imaging experiments, *see* Section 2.1 in [35]. Here we describe additional required solutions:

1. Mammalian physiological solution: 130 mM NaCl, 5 mM KCl, 0.5 mM $MgCl_2$, 2 mM $CaCl_2$, 25 mM 4-(2-hydroxyethyl)-1-piperazine-1-ethanesulfonic acid hemisodium (HEPES), pH, 7.4. This solution is kept at room temperature. On the day of the experiments, glucose is added from a 1 M stock solution to a final concentration of 5 mM. Any leftover solution containing glucose is discarded at the end of the day.
2. 1 M glucose stock solution. This solution is kept frozen at –20 °C to avoid bacterial growth and is thawed just before glucose is added to the mammalian physiological solution.
3. 1 % w/v lipid-free bovine serum albumin (Sigma) BSA in mammalian physiological solution.

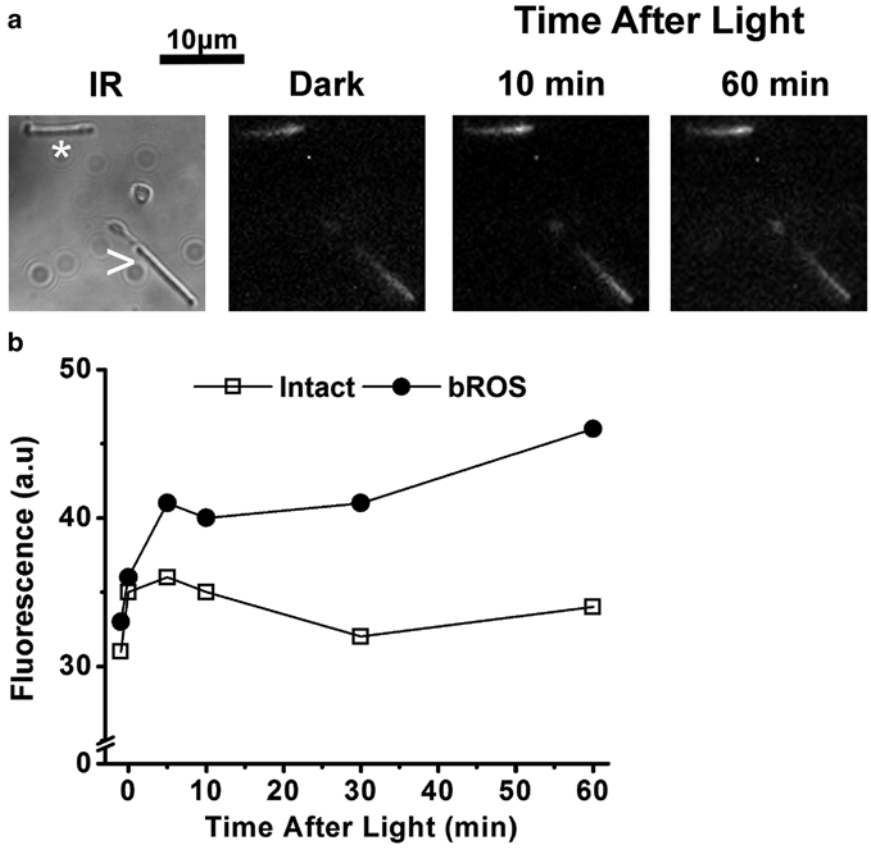

Fig. 5 Measurement of the formation of lipofuscin precursors after light exposure. (**a**) Bright-field infrared (IR) and fluorescence images (excitation, 490 nm; emission, >515 nm) of a metabolically intact rod cell (*arrowhead*, >) and a metabolically compromised bROS (*star*, *) from an *Abca4*$^{-/-}$ mouse. Fluorescence images were first captured for the dark-adapted cells; the cells were then exposed to intense >530 nm light for 1 min, and fluorescence images were captured at different times following the exposure. (**b**) Outer segment fluorescence for the metabolically intact (*open square*) and the bROS (*filled circle*) as a function of time after light exposure. Experiment at 37 °C

4. 50 mM all-*trans*-retinal (Sigma) stock solution in ethanol. Store at −80 °C (*see* **Note 1**).
5. 50 μM all-*trans*-retinal solution in 1 % BSA in mammalian physiological solution. This is prepared on the day of the experiment, by adding 0.1 % (v/v) of the 50 mM all-*trans*-retinal stock solution to the mammalian physiological solution with 1 % BSA.
6. 50 mM all-*trans*-retinol (Sigma) stock solution in ethanol. Store at −80 °C (*see* **Note 1**).
7. 50 μM all-*trans*-retinol solution in 1 % BSA in physiological solution. This is prepared on the day of the experiment, by adding 0.1 % (v/v) of the 50 mM all-*trans*-retinol stock solution to the mammalian physiological solution with 1 % BSA.

2.2 Fluorescence Imaging of Single Isolated Photoreceptor Cells

The equipment and general components necessary to conduct the fluorescence imaging experiments are listed in Section 2.2 of [35]. Here we describe the optics appropriate for the fluorescence imaging of the different forms of rhodopsin's chromophore.

2.2.1 Optics for Imaging All-trans-Retinal and All-trans-Retinol

Filter set 49025 from Chroma Technology Corporation for DAPI would be appropriate for imaging all-*trans*-retinal and all-t*rans*-retinol. Individual components are discussed below (*see* **Note 2**):

1. Excitation: a broadband UV excitation filter to select light from the region 340–380 nm, such as the AT350/50x excitation filter from the 49025 Chroma filter set. Another option would be ET360/40x-PF.
2. Dichroic mirror: the dichroic must reflect the excitation light ($\lambda < 400$ nm) and transmit the collected retinoid emission ($\lambda > 400$ nm). An appropriate component would be the T400lp beam splitter from the 49025 Chroma filter set.
3. Emission: to collect as much of the emission >400 nm as possible and ensure good separation between excitation and emission light, use a longpass filter, such as the ET425lp from the 49025 Chroma filter set.

2.2.2 Optics for Distinguishing Between All-trans-Retinal and All-trans-Retinol

1. Excitation: two narrowband (~10 nm bandwidth) filters, one centered at 340 nm (Chroma filter ET340x) and the other at 380 nm (Chroma filter ET380x) (*see* **Note 2**). These two filters will need to be mounted on a filter wheel controlled by software to allow changing the filters during the course of a measurement [35].
2. Dichroic mirror: the T400lp beam splitter from the 49025 Chroma filter set. This is the same as for the imaging of all-trans-retinal and all-*trans*-retinol.
3. Emission: the ET425lp from the 49025 Chroma filter set. The same as for the imaging of all-*trans*-retinal and all-t*rans*-retinol—the two retinoids have similar emission spectra.

2.2.3 Optics for Imaging Lipofuscin Precursors

Filter set 19002 from Chroma Technology Corporation for GFP/FITC would be appropriate for imaging lipofuscin precursors. Individual components are discussed below (*see* **Note 2**).

1. Excitation: an excitation filter to select light from the region 450–490 nm, such as the AT480/30x excitation filter from the 19002 Chroma filter set.
2. Dichroic mirror: the dichroic must reflect the excitation light ($\lambda < 500$ nm) and transmit the collected lipofuscin precursor emission ($\lambda > 500$ nm). An appropriate component would be the AT505DC beam splitter from the 19002 Chroma filter set.
3. Emission: to collect as much of the emission >500 nm as possible, a longpass filter is appropriate, such as the AT515lp from the 19002 Chroma filter set.

3 Methods

3.1 Preparation of Isolated Photoreceptor Cells

The general procedures have been described in detail previously in Section 3.1 in [35].

3.2 Fluorescence Imaging

Follow the general procedures described previously [35]. Place the isolated cells in the imaging chamber on the microscope stage. Allow ~10 min to elapse to ensure that cells have settled and are immobilized on the bottom of the imaging chamber.

3.2.1 Imaging of All-trans-Retinal, All-trans-Retinol, and Lipofuscin Precursors

1. Select the appropriate optics for the fluorescence measurements you are interested in: (a) imaging all-*trans*-retinal and all-t*rans*-retinol, (b) distinguishing between all-*trans*-retinal and all-trans-retinol, or (c) imaging lipofuscin precursors. The excitation filters for distinguishing all-*trans*-retinal and all-trans-retinol have to be mounted on a filter wheel under software control to allow changing excitation wavelength during the course of a measurement. In a fully motorized microscope, you may be able to select the optical arrangement as a whole, either from the imaging software controls or from the microscope controls. If the microscope is not fully motorized, you may have to move the holders where the dichroic and the emission filters are mounted on to their appropriate positions.
2. Under infrared illumination move the microscope stage and select a cell for the experiment (*see* **Note 3**).
3. Focus and capture an infrared image of the cell.
4. Adjust the focus under infrared illumination so that the fluorescence image(s) you are about to capture will be in focus (*see* **Note 4**). Turn off the infrared illumination and capture the fluorescence image(s) of the dark-adapted cell.
5. Expose the cell to intense long-wavelength (>530 nm) light for 1 min.
6. Capture fluorescence images of the cell at different times after exposure to light. Before capturing a fluorescence image, ensure that the cell is in focus by checking with infrared illumination (*see* **Note 5**).

3.2.2 Measuring the Fex-340/Fex-380 Ratio for All-trans-Retinal and for All-trans-Retinol

The values of the Fex-340/Fex-380 ratio for all-*trans*-retinal and all-*trans*-retinol are required for analysis of the data from the experiments designed to distinguish between the two (*see* **Note 6**).

1. Select the appropriate optics for distinguishing the fluorescence of all-*trans*-retinal and all-*trans*-retinol. If necessary, move the components where the dichroic mirror and the emission filter are mounted to the appropriate positions. The excitation filters will be mounted on a filter wheel that will be controlled by the imaging software.

2. Under infrared illumination move the microscope stage and select a broken off rod outer segment (bROS) for the experiment (*see* **Note 6**).
3. Focus and capture an infrared image of the bROS.
4. Adjust the focus under infrared illumination so that the fluorescence images you are about to capture will be in focus. Turn off the infrared illumination and capture the fluorescence images of the dark-adapted bROS with the different excitation filters.
5. Measurement of the Fex-340/Fex-380 ratio for all-t*rans*-retinal: add mammalian physiological solution containing 50 μM all-*trans*-retinal in 1 % BSA (*see* **Note 7**). Wait for 5 min and capture fluorescence images of the bROS with the different excitation filters.
6. Measurement of the Fex-340/Fex-380 ratio for all-t*rans*-retinol: add mammalian physiological solution containing 50 μM all-*trans*-retinol in 1 % BSA (*see* **Note 7**). Wait for 5 min and capture fluorescence images of the bROS with the different excitation filters.

3.3 Analysis of Fluorescence Imaging Data

3.3.1 Initial Processing of Fluorescence Images

1. Using the imaging software, for each fluorescence image define regions of interest (ROI): one should encompass the entirety of the outer segment, and the other a background, an area in the field that is clear of any debris or cells (*see* **Note 8**).
2. Using the imaging software, obtain the average fluorescence intensity for each ROI. Then, subtract the background fluorescence intensity from that of the outer segment and obtain the corrected outer segment fluorescence intensity (*see* **Note 9**).

3.3.2 Analysis for the Different Forms of Rhodopsin's Chromophore

To obtain the outer segment fluorescence due to all-*trans*-retinal and all-*trans*-retinol generated by light exposure, subtract the initial outer segment fluorescence of the dark-adapted cell (*see* **Note 10**).

Analysis for All-t*rans*-Retinal and All-*trans*-Retinol

Analysis for Distinguishing Between All-*trans*-Retinal and All-*trans*-Retinol

1. Determine the Fex-340/Fex-380 ratio for all-*trans*-retinol (*see* **Note 11**): for each excitation wavelength (340 and 380 nm), obtain the outer segment fluorescence due to the added all-*trans*-retinol by subtracting the initial outer segment fluorescence from that at 5 min after the addition (*see* **Note 12**). Calculate the ratio $\boldsymbol{R}(\boldsymbol{ROL})$ = Fex-340/Fex-380 of the fluorescence intensities Fex-340 (excited by 340 nm) and Fex-380 (excited by 380 nm).

2. Determine the Fex-340/Fex-380 ratio for all-*trans*-retinal (*see* **Note 11**): for each excitation wavelength (340 and 380 nm), obtain the outer segment fluorescence due to the added all-*trans*-retinal by subtracting the initial outer segment fluorescence from that at 5 min after the addition (*see* **Note 12**). Calculate the ratio $R(RAL)$ = Fex-340/Fex-380 of the fluorescence intensities Fex-340 (excited by 340 nm) and Fex-380 (excited by 380 nm).
3. Determine the Fex-340/Fex-380 ratio for a selected cell: for any time point after light exposure and for each excitation wavelength (340 and 380 nm), obtain the outer segment fluorescence due to the all-*trans*-retinal and all-*trans*-retinol by subtracting the initial outer segment fluorescence. Calculate the ratio FR = Fex-340/Fex-380 of the fluorescence intensities Fex-340 (excited by 340 nm) and Fex-380 (excited by 380 nm).
4. Convert the Fex-340/Fex-380 ratio to fraction of all-t*rans*-retinol: use Eq. 1 below to convert the ratio Fex-340/Fex-380 = FR to the fraction r of total retinoid (all-*trans*-retinal plus all-*trans*-retinol) present in the form of all-*trans*-retinol:

$$r = \frac{\frac{FR}{R(RAL)} - 1}{\left(\frac{FR}{R(RAL)} - 1\right) + 5.1 \times \left(1 - \frac{FR}{R(ROL)}\right)}. \quad (1)$$

Using Eq. 1, carry out the calculation for r (*see* **Note 13**). For metabolically and enzymatically intact cells, you expect values of r in the order of 80–90 % (*see* **Note 14**).

Analysis for Lipofuscin Precursors

The corrected outer segment fluorescence intensity reflects the level of lipofuscin precursors present at any time point. Lipofuscin precursors are already present in the outer segments of dark-adapted cells and are responsible for the initial outer segment fluorescence signal measured prior to light exposure. So, in general, it is not necessary to subtract the initial fluorescence intensity for any subsequent analysis.

4 Notes

1. The retinoid concentration in the stock solution might increase with time due to ethanol evaporation. The exact concentration of the all-*trans*-retinal and all-*trans*-retinol stock solutions can be checked spectrophotometrically; the volume of the retinoid-containing stock that needs to be added to achieve a final concentration of 50 μM can be adjusted accordingly.

2. Several of the optical components used in our imaging setup have been discontinued. We provide the rationale for selecting the properties of a particular that are available at the present time.
3. There are two possible selections: metabolically intact rods and metabolically compromised broken off rod outer segments (bROS) [5, 37]. bROS are easy to recognize, as they are fully separated from the rest of the cell. Metabolically intact rods can be recognized from their slender inner segments, even with slightly swollen ellipsoids. Cells with overly swollen or spherical ellipsoids are metabolically compromised. For both metabolically intact rods and bROS, the outer segment should have no morphological defect, such as breaks or blebs. Metabolically intact rods from wild-type mice should give Fex-340/Fex-380 fluorescence ratios that correspond to all-trans-retinol fractions of 80–90 % (*see* Subheading on "Analysis for Distinguishing Between All-*trans*-Retinal and All-t*rans*-Retinol" **step 4** and **Note 13**).
4. The cell will not be in focus under infrared when it is in focus for the fluorescence measurement; you need to familiarize yourself with the appropriate out-of-focus appearance of the cell under the infrared to be in focus for the fluorescence measurement [35].
5. Carry out preliminary measurements to ensure that there is no significant bleaching of the fluorophores during the course of the experiment [35]; you may need to limit the exposure time and the total number of measurements. Lipofuscin precursors are especially labile.
6. For these measurements it is necessary to use bROS to ensure that the added retinoid is not metabolically processed [5].
7. To ensure that the added retinoid-containing solution is not diluted to any significant extent, it is best that the volume of the initial solution in the chamber containing the isolated cells is kept minimal. For these measurements, the initial volume of the physiological solution in the chamber is kept to 100–200 μl, and 2–3 ml of retinoid-containing solution is added (either directly or through perfusion).
8. Background fluorescence intensity can vary modestly across the image frame, so it is best to define the background close to the outer segment of interest. In the event there is more than one cell in a frame, background can be defined separately for each cell.
9. Background fluorescence may change during the course of an experiment (it frequently does), so it is important to correct for background before any additional data processing.
10. The initial outer segment fluorescence prior to light exposure represents fluorophores other than all-*trans*-retinal and all-*trans*-retinol, so it is appropriate to subtract it.

11. The Fex-340/Fex-380 fluorescence ratios for all-*trans*-retinal and all-*trans*-retinol will depend on the light transmission properties of the particular optical components used; hence, they need to be measured for the particular setup.
12. The fluorescence signal of the endogenous all-*trans*-retinal that will be released after excitation by the light of the first fluorescence measurement (of the dark-adapted bROS) is negligible compared to the fluorescence signal from the added retinoid, and it can be ignored. It is important to use a high concentration of exogenous retinoid for these measurements (50 μM is adequate) to ensure that the fluorescence signal from the exogenously added retinoid will overwhelm the signal from the endogenous.
13. Equation 1 uses the value of 5.1 for QYR, the ratio of fluorescence quantum yields for all-*trans*-retinol and all-*trans*-retinal [5, 37], and the values of r characteristic for intact cells are calculated specifically for this QYR value. The desired absolute value of the ratio FR cannot be provided because of its dependence on the particular optical components. The ratios FR/R(RAL) and FR/R(ROL) however are independent of the optical components and can be used in place of Eq. 1. For metabolically and enzymatically intact cells, FR/R(RAL) ≈ 8.2–10.0 and FR/R(ROL) ≈ 0.65–0.80.
14. In the general case, a low value for r may be due to an enzymatic defect or due to cellular injury inflicted during isolation. Distinguishing between these possibilities can present a challenge [5]. It is therefore important to firmly establish one's capability to obtain metabolically intact rod photoreceptor cells from wild-type mice, which are enzymatically intact. When assessing metabolic integrity, ensure that the physiological solution contains 5 mM glucose, as lower substrate concentrations may result in limitations to NADPH generation [37].

References

1. Ebrey T, Koutalos Y (2001) Vertebrate photoreceptors. Prog Retin Eye Res 20:49–94
2. Fain GL, Matthews HR, Cornwall MC et al (2001) Adaptation in vertebrate photoreceptors. Physiol Rev 81:117–151
3. Lamb TD, Pugh EN Jr (2004) Dark adaptation and the retinoid cycle of vision. Prog Retin Eye Res 23:307–380
4. Kiser PD, Golczak M, Palczewski K (2014) Chemistry of the retinoid (visual) cycle. Chem Rev 114:194–232
5. Chen C, Thompson DA, Koutalos Y (2012) Reduction of all-trans-retinal in vertebrate rod photoreceptors requires the combined action of RDH8 and RDH12. J Biol Chem 287: 24662–24670
6. Maeda A, Maeda T, Imanishi Y et al (2005) Role of photoreceptor-specific retinol dehydrogenase in the retinoid cycle in vivo. J Biol Chem 280:18822–18832
7. Futterman S, Hendrickson A, Bishop PE et al (1970) Metabolism of glucose and reduction of retinaldehyde in retinal photoreceptors. J Neurochem 17:149–156
8. Okajima TI, Pepperberg DR, Ripps H et al (1989) Interphotoreceptor retinoid-binding protein: role in delivery of retinol to the pigment epithelium. Exp Eye Res 49:629–644

9. Saari JC (2000) Biochemistry of visual pigment regeneration: the Friedenwald lecture. Invest Ophthalmol Vis Sci 41:337–348
10. Kawaguchi R, Yu J, Honda J et al (2007) A membrane receptor for retinol binding protein mediates cellular uptake of vitamin A. Science 315:820–825
11. Saari JC, Bredberg DL, Farrell DF (1993) Retinol esterification in bovine retinal pigment epithelium: reversibility of lecithin:retinol acyltransferase. Biochem J 291:697–700
12. Jin M, Li S, Moghrabi WN et al (2005) Rpe65 is the retinoid isomerase in bovine retinal pigment epithelium. Cell 122:449–459
13. Moiseyev G, Chen Y, Takahashi Y et al (2005) RPE65 is the isomerohydrolase in the retinoid visual cycle. Proc Natl Acad Sci U S A 102: 12413–12418
14. Redmond TM, Poliakov E, Yu S et al (2005) Mutation of key residues of RPE65 abolishes its enzymatic role as isomerohydrolase in the visual cycle. Proc Natl Acad Sci U S A 102: 13658–13663
15. Simon A, Hellman U, Wernstedt C et al (1995) The retinal pigment epithelial-specific 11-cis retinol dehydrogenase belongs to the family of short chain alcohol dehydrogenases. J Biol Chem 270:1107–1112
16. Okajima TI, Pepperberg DR, Ripps H et al (1990) Interphotoreceptor retinoid-binding protein promotes rhodopsin regeneration in toad photoreceptors. Proc Natl Acad Sci U S A 87:6907–6911
17. Maeda T, Golczak M, Maeda A (2012) Retinal photodamage mediated by all-trans-retinal. Photochem Photobiol 88:1309–1319
18. Masutomi K, Chen C, Nakatani K et al (2012) All-trans retinal mediates light-induced oxidation in single living rod photoreceptors. Photochem Photobiol 88:1356–1361
19. Rozanowska M, Sarna T (2005) Light-induced damage to the retina: role of rhodopsin chromophore revisited. Photochem Photobiol 81:1305–1330
20. Sparrow JR, Wu Y, Kim CY et al (2010) Phospholipid meets all-trans-retinal: the making of RPE bisretinoids. J Lipid Res 51: 247–261
21. Sparrow JR, Boulton M (2005) RPE lipofuscin and its role in retinal pathobiology. Exp Eye Res 80:595–606
22. Sparrow JR, Gregory-Roberts E, Yamamoto K et al (2012) The bisretinoids of retinal pigment epithelium. Prog Retin Eye Res 31:121–135
23. Boyer NP, Higbee D, Currin MB et al (2012) Lipofuscin and N-retinylidene-N-retinylethanolamine (A2E) accumulate in retinal pigment epithelium in absence of light exposure: their origin is 11-cis-retinal. J Biol Chem 287:22276–22286
24. Katz ML, Redmond TM (2001) Effect of Rpe65 knockout on accumulation of lipofuscin fluorophores in the retinal pigment epithelium. Invest Ophthalmol Vis Sci 42:3023–3030
25. Katz ML, Drea CM, Eldred GE et al (1986) Influence of early photoreceptor degeneration on lipofuscin in the retinal pigment epithelium. Exp Eye Res 43:561–573
26. Katz ML, Robison WG Jr (2002) What is lipofuscin? Defining characteristics and differentiation from other autofluorescent lysosomal storage bodies. Arch Gerontol Geriatr 34:169–184
27. Quazi F, Molday RS (2014) ATP-binding cassette transporter ABCA4 and chemical isomerization protect photoreceptor cells from the toxic accumulation of excess 11-cis-retinal. Proc Natl Acad Sci U S A 111:5024–5029
28. Ala-Laurila P, Kolesnikov AV, Crouch RK et al (2006) Visual cycle: Dependence of retinol production and removal on photoproduct decay and cell morphology. J Gen Physiol 128: 153–169
29. Tsina E, Chen C, Koutalos Y et al (2004) Physiological and microfluorometric studies of reduction and clearance of retinal in bleached rod photoreceptors. J Gen Physiol 124: 429–443
30. Wu Q, Blakeley LR, Cornwall MC et al (2007) Interphotoreceptor retinoid-binding protein is the physiologically relevant carrier that removes retinol from rod photoreceptor outer segments. Biochemistry 46:8669–8679
31. Blakeley LR, Chen C, Chen CK et al (2011) Rod outer segment retinol formation is independent of Abca4, arrestin, rhodopsin kinase, and rhodopsin palmitylation. Invest Ophthalmol Vis Sci 52:3483–3491
32. Chen C, Blakeley LR, Koutalos Y (2009) Formation of all-trans retinol after visual pigment bleaching in mouse photoreceptors. Invest Ophthalmol Vis Sci 50:3589–3595
33. Palczewska G, Dong Z, Golczak M et al (2014) Noninvasive two-photon microscopy imaging of mouse retina and retinal pigment epithelium through the pupil of the eye. Nat Med 20:785–789
34. Palczewska G, Golczak M, Williams DR et al (2014) Endogenous fluorophores enable two-photon imaging of the primate eye. Invest Ophthalmol Vis Sci 55(7):4438–4447
35. Koutalos Y, Cornwall MC (2010) Microfluorometric measurement of the formation of all-trans-retinol in the outer segments

of single isolated vertebrate photoreceptors. Methods Mol Biol 652:129–147

36. Hubbard R, Brown PK, Bownds D (1971) Methodology of vitamin A and visual pigments. Methods Enzymol 18C:615–653

37. Adler L IV, Chen C, Koutalos Y (2014) Mitochondria contribute to NADPH generation in mouse rod photoreceptors. J Biol Chem 289:1519–1528

Chapter 22

Supplementation with Vitamin A Derivatives to Rescue Vision in Animal Models of Degenerative Retinal Diseases

Lindsay Perusek, Akiko Maeda, and Tadao Maeda

Abstract

The perception of light begins when photons reach retinal tissue located at the back of the eye and photoisomerize the visual chromophore 11-*cis*-retinal to all-*trans*-retinal within photoreceptor cells. Isomerization of 11-*cis*-retinal activates the protein rhodopsin located in photoreceptor outer segments, thereby inducing a phototransduction cascade leading to visual perception. To maintain vision, 11-*cis*-retinal is regenerated in the retinal pigmented epithelium (RPE) via the visual cycle and delivered back to the photoreceptor cells where it may again bind to rhodopsin. Distinct pathological mechanisms have been observed to contribute to inherited retinal degenerative diseases including severe delay in 11-*cis*-retinal regeneration and delayed clearance of all-*trans*-retinal, which leads to the accumulation of harmful retinoid by-products. In the last decade, our group has conducted several proof-of-concept (POC) studies with retinoid derivatives aimed at developing treatments for retinal degenerative diseases caused by an impaired visual cycle. Here, we will introduce experimental procedures, which have been developed for POC studies involving retinoid biology.

Key words 9-*cis*-Retinoid, All-*trans*-retinal, Visual cycle, Light damage, Retinoid, Retinylamine, AMD, LCA, RP

1 Introduction

Human vision is maintained by a series of biochemical and physiological reactions. Vision is initiated by the absorption of a photon via the visual pigment protein rhodopsin [1]. Rhodopsin is a member of the G-protein-coupled receptor family and consists of apoprotein bound to the visual chromophore 11-*cis*-retinal. Rhodopsin molecules are covalently bound to 11-*cis*-retinal via a Schiff base at Lys-296 which aids in the proteins' ability to dissociate from the chromophore when stimulated with light. Rhodopsin is highly concentrated in the photoreceptor disk membranes, as a homodimer, in order to trap the incoming photons with the greatest efficiency. A single photon can photo-isomerize 11-*cis*-retinal

Beata Jastrzebska (ed.), *Rhodopsin: Methods and Protocols*, Methods in Molecular Biology, vol. 1271,
DOI 10.1007/978-1-4939-2330-4_22,

to all-*trans*-retinal and induce rhodopsin activation, leading to the perception of vision.

Due to the important roles of rhodopsin in vision, dysfunction of this key protein can cause various retinal degenerative diseases (https://sph.uth.edu/retnet/disease.htm). Retinal disease can be induced by endogenous or exogenous factors such as inherited gene mutations or dysfunctions in the enzymatic reactions involved in the visual cycle. The visual cycle in the eye is responsible for regenerating 11-*cis*-retinal and for the clearance of toxic retinoid by-products, such as all-*trans*-retinal [2]. Distinct pathological mechanisms have been observed to contribute to inherited retinal degenerative diseases including the deficiency of 11-*cis*-retinal regeneration, inadequate or delayed clearance of all-*trans*-retinal from the photoreceptor cells, and the accumulation of harmful retinoid by-products within or surrounding the retinal pigmented epithelium (RPE) (Fig. 1) [3, 4].

Mutations in required visual cycle proteins such as lecithin/retinol acyl transferase (LRAT) and retinal pigment epithelium-specific 65-kDa protein (RPE65) result in severely delayed 11-*cis*-retinal regeneration and clinically manifest as early-onset severe retinal dystrophy. Early-onset severe retinal dystrophies, such as Leber congenital amaurosis (LCA) and retinitis pigmentosa (RP), are due to mutations in the essential visual cycle proteins LRAT and RPE65, respectively, and represent a total of 5 % of all such inherited disorders [5]. Late-onset macular degeneration due to a mutation in the protein retinal dehydrogenase 5 (RDH5) also occurs due to delayed 11-*cis*-retinal regeneration in the RPE and produces a significantly delayed dark adaptation and a later clinical onset of disease [6]. Accumulation of retinoid by-products other than all-*trans*-retinal has also been implied in retinal degenerative diseases [4, 7]. The excessive buildup of all-*trans*-retinal condensation products, such as pyridinium bisretinoid (A2E) and all-*trans*-retinal dimer, similarly results in an early-onset macular degeneration and is seen in Stargardt's disease patients with mutations in the gene ABCA4. Accumulation of such retinoid by-products is detected as both lipofuscin granules in the RPE and extracellular deposits (drusen) that form between the RPE and Bruch's membrane in the retinas of patients with Stargardt's disease and age-related macular degeneration (AMD).

Genetically modified mouse models of the abovementioned diseases are available and are excellent resources to understand the underlying pathology of various retinal degenerative diseases. For example, the deficiency of retinoids due to the loss of *Lrat* or the inability to regenerate visual chromophore in *Rpe65*-deficient mice shows slow progressive rod photoreceptor cell death and rapid cone photoreceptor cell death, similar to the disease progression seen in human pathologies [8–13].

The pathological accumulation of all-*trans*-retinal or its by-products can be represented using a mouse model deficient in both

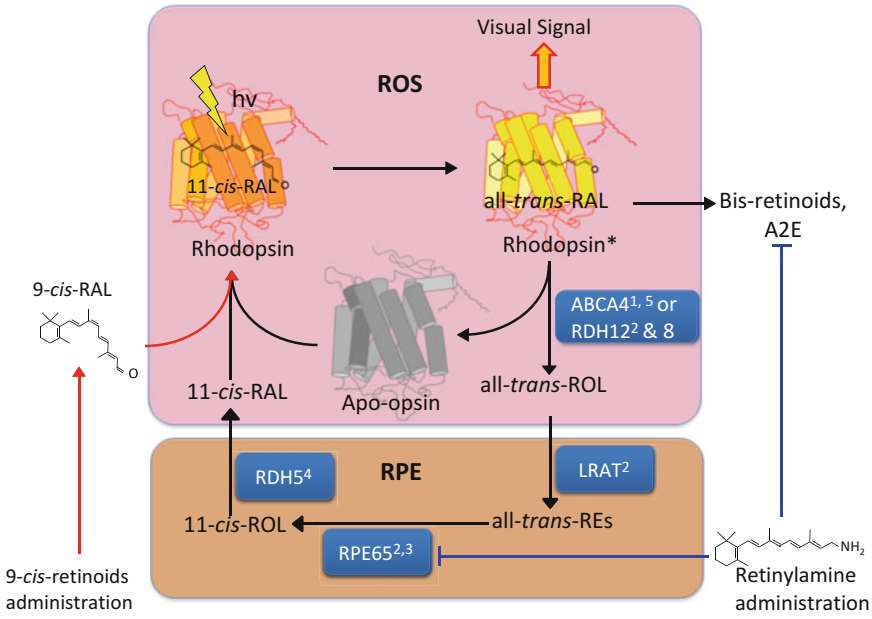

Fig. 1 Visual cycle and retinal degenerative diseases. Absorption of a photon (*hν*) by the visual pigment (rhodopsin) causes isomerization of 11-*cis*-retinal to all-*trans*-retinal, resulting in rhodopsin activation (rhodopsin*). Decay of activated rhodopsin yields apo-opsin and free all-*trans*-retinal, which is transported to the cytosol by a photoreceptor-specific ATP-binding transporter (ABCR, coded by the ABCA4 gene) and reduced to all-*trans*-retinol by all-*trans*-retinal dehydrogenases (RDH8 and RDH12). All-*trans*-retinol diffuses into the RPE where it is esterified by lecithin/retinol acyltransferase (LRAT) to all-*trans*-retinyl esters. All-*trans*-retinyl esters are isomerized to 11-*cis*-retinol in a reaction involving a 65-kDa RPE-specific protein (RPE65). To complete the retinoid cycle, 11-*cis*-retinol is then oxidized by 11-*cis*-retinal-specific RDHs (RDH5) to 11-*cis*-retinal, which then diffuses back into the photoreceptor where it combines with apo-opsin to regenerate rhodopsin. Two pharmacological inventions can be used to rescue the visual function in mouse models with impaired visual cycle. 9-*cis*-retinoids can bypass the visual cycle and regenerate apo-opsin as iso-rhodopsin. Retinylamine can prevent the accumulation of bisretinoids including A2E via two different actions. First, the free form of all-*trans*-retinal is neutralized by a Schiff base formation between all-*trans*-retinal and retinylamine. Second, retinylamine can reduce all-*trans*-retinal generation by the inhibition of RPE65 enzymatic activity. Retinal degenerative diseases caused by a defective gene related to the visual cycle are indicated as follows: (1) Stargardt's disease; (2) Leber congenital amaurosis (LCA); (3) RP, retinitis pigmentosa; (4) fundus albipunctatus; and (5) age-related macular degeneration (AMD)

Rdh8 and *Abca4* which features chronic cell death in the retina accompanied with progressive lipofuscin granule accumulation, drusen deposition, and acute and massive retinal degeneration after intensive light exposure [14, 15]. Pharmacological retinoid replacement therapy, utilizing 9-*cis*-retinal, has been developed and has provided great promise for the treatment of retinal degenerative diseases. It has been demonstrated that the administration of 9-*cis*-retinoids can bypass the visual cycle and regenerate visual pigments in the form of iso-rhodopsin in sufficient qualities to restore visual function and ameliorate the progression of retinal degeneration in the abovementioned animal models with impaired

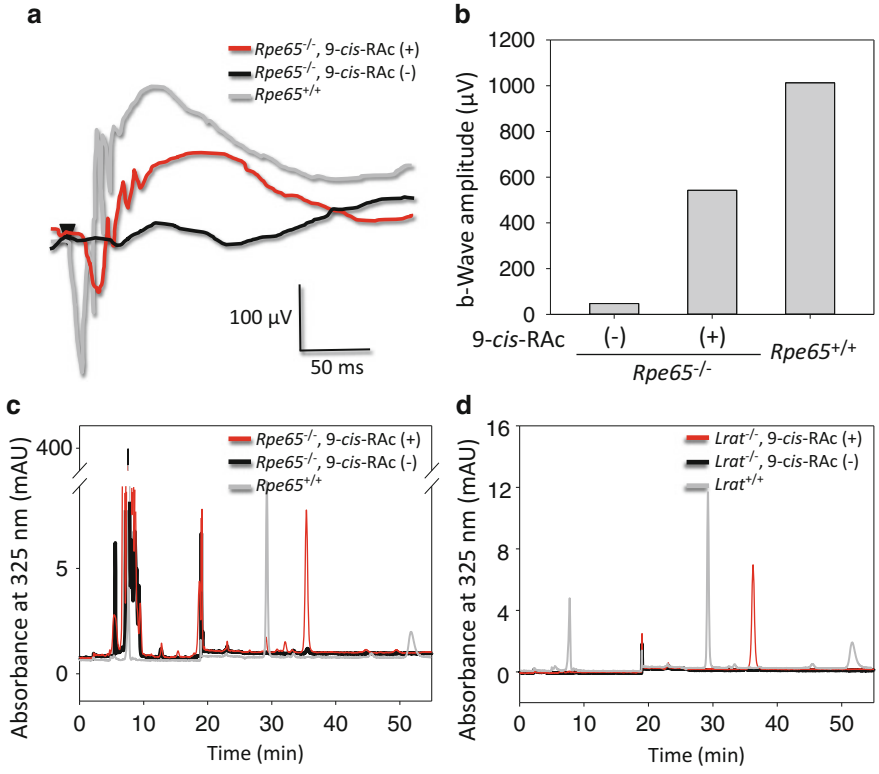

Fig. 2 Restoration of visual function in mice with impaired visual cycles. Mouse models missing the essential visual cycle proteins Rpe65 and Lrat lack the chromophore 11-*cis*-retinal and display reduced ERG responses. Supplementation with 9-*cis*-RAc at 0.25 mg/mouse of dose increases ERG responses and restores chromophore levels in Rpe65-deficient models, as well as increases chromophore regeneration in Lrat-deficient models. (**a**) ERG signals from *Rpe65*$^{-/-}$ mice display severely diminished a-wave and b-wave ERG signals (*black*) compared to *Rpe65*$^{+/+}$ (*gray*) and 9-*cis*-RAc-supplemented *Rpe65*$^{-/-}$ mice (*red*). (**b**) B-wave amplitude measured by ERG is rescued in *Rpe65*$^{-/-}$ mice after supplementation with 9-*cis*-RAc. (**c**) Regeneration of 9-*cis*-retinal chromophore in *Rpe65*$^{-/-}$ mice after supplementation with 9-*cis*-RAc. (**d**) Regeneration of 9-c*is*-retinal chromophore in *Lrat*$^{-/-}$ mice after supplementation with 9-*cis*-RAc

visual cycles (Fig. 2). In terms of clinical applications, 9-*cis*-retinoid supplements are preferred over 11-*cis*-retinal due to superior stability and ease of synthesis. Prodrugs such as 9-*cis*-retinyl esters, 9-*cis*-retinyl acetate, and 9-*cis*-retinyl succinate are used for the metabolic generation of 9-*cis*-retinal in vivo and provide visual pigment regeneration analogous to 9-*cis*-retinal. Additionally, the retinoid analog retinylamine was developed with the aim to reduce all-*trans*-retinal concentrations in the retina after light exposure and to scavenge damaging free all-*trans*-retinal by forming a Schiff base and reducing its cell toxicity in the retina.

Herein, procedures that are required to evaluate the therapeutic effects of these unique retinoid-based compounds with mouse models are described, including preparation of compounds, drug

administrative methods, pharmacokinetic analyses, and in vivo functional analyses of the retina including high-definition ophthalmic imaging systems.

2 Materials

2.1 Animals

1. *Rpe65*-deficient mice.
2. *Gnat1*-deficent mice.
3. *Lrat*-deficient mice.
4. *Rdh8*-deficient mice.
5. *Abca4*-deficient mice.

2.2 Recovery of Visual Function with 9-cis-Retinoids in Mouse Models of 11-cis-Retinal Deficiency

1. 9-*cis*-retinal (Sigma-Aldrich), 9-*cis*-retinol, 9-*cis*-retinyl acetate, and 9-*cis*-retinyl palmitate (Toronto Research Chemicals).
2. Soybean oil (United State Pharmacopeia, Spectrum Chemicals).
3. Ethanol (ACS grade).
4. Dimethyl sulfoxide (DMSO, cell culture grade).
5. UV-visible spectrophotometer (Agilent 8453 or equivalent).

2.3 Administration of Retinoids to Mouse Models

1. Gavage needle (20G straight or 23G straight, Popper & Sons, Inc.).
2. 1 ml disposable syringe.
3. Insulin syringe (28.5-G needle).

2.4 Evaluation of Retinal Health upon Retinoid Administration by Electroretinography (ERG)

1. Anesthetic solution: 6 mg/ml ketamine, 0.44 mg/ml xylazine diluted in 10 mM sodium phosphate, pH 7.2.
2. 1 % tropicamide.
3. 0.5 % phenylephrine hydrochloride saline solution (Midorin-P, Santen Pharmaceutical).
4. Electrophysiological system UTASE-3000 (LKC Technologies, Inc.).
5. Contact lens electrodes (mouse ERG electrode, 3.2 mm diameter) (LKC Technologies, Inc.).

2.5 Examination of Retinoid Distribution in the Tissues: Retinoid Extraction and Quantification

1. Hexane (HPLC grade).
2. Ethyl acetate (HPLC grade).
3. 67 mM phosphate-buffered saline (PBS): 9 mg/ml NaCl, 0.8 mg/ml Na_2HPO_4, 0.14 mg/ml $Na_2H_2PO_4$.
4. 1 M hydroxylamine, pH 7.4.
5. Liquid nitrogen.

6. Retinoid extraction buffer: 50 mM 3-(*N*-morpholino) propanesulfonic acid and 4-morpholinepropanesulfonic acid (MOPS), pH 7.4, in 50 % ethanol, containing 40 mM hydroxylamine.
7. 10 % ethyl acetate, 90 % hexane.
8. Ultrasphere-Si, 5 μm, 4.6 × 250 mm (Beckman) or Agilent-Si, 5 μm, 4.5 × 250 mm column (Agilent Technologies).
9. Synthetic standards of retinoid isomers.
10. 7-ml glass screw-top tube (Kimble Glass, Inc.).
11. Beckman J2-HS centrifuge.
12. Beckman JS13.1 swinging bucket rotor.
13. Hewlett-Packard 1100 HPLC with a photodiode array detector and Hewlett-Packard Chemstation A.03.03 software.

2.6 Prevention of Light-Induced Retinal Damage in Abca4$^{-/-}$Rdh8$^{-/-}$ Mouse with Retinylamine

1. Retinylamine (Ret-NH_2).
2. 150-W spiral lamps (Commercial Electric).
3. Optical coherence tomography (SD-OCT) (Bioptigen).
4. Scanning laser ophthalmoscope (SLO) HRAII (Heidelberg Engineering).

3 Methods

3.1 Animals

All animal procedures and experiments must be approved by the animal care committee and conformed to recommendations of both the American Veterinary Medical Association Panel on Euthanasia and the Association for Research in Vision and Ophthalmology.

All mice should be maintained on a standard diet in a 12-h light (<50 lx)/12-h dark cycle or in dim red light conditions if desired for the experiment.

Genotype all animals used for the 9-*cis*-retinoid administration experiments with sets of specific primers at the proper annealing temperatures (Fig. 3 and Table 1).

3.2 Recovery of Visual Function with 9-cis-Retinoids in Mouse Models of 11-cis-Retinal Deficiency

Animal models: *Lrat*$^{-/-}$, *Rpe65*$^{-/-}$, and *Gnat1*$^{-/-}$ mouse models and C57BL/6 wild-type mice were used in our studies. Treatments of these mice with 9-*cis*-retinoids were performed as indicated in Table 2.

3.2.1 Preparation of 9-cis-Retinyl Acetate from 9-cis-Retinal (See **Note 1**)

1. 100 mg of 9-*cis*-retinal reduced with 50 mg of sodium borohydride in 0.7 ml of ethanol at 0 °C for 30 min.
2. Then purify the product 9-*cis*-retinol by hexanes and dry under argon.

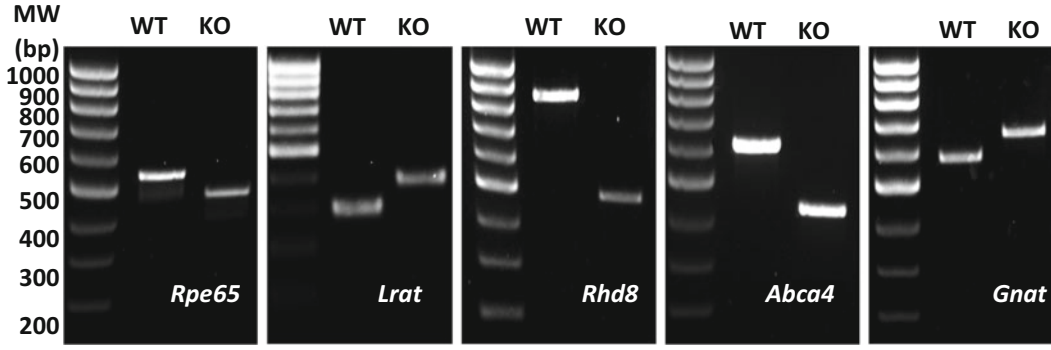

Fig. 3 Genotyping of mouse models with impaired visual cycles. PCR products observed after genotyping using primer sequences presented in Table 1 for the following genes: *Rpe65*, *Lrat*, *Rdh8*, *Abca4*, and *Gnat1*

Table 1
Genotyping for mouse models with impaired visual cycles

Genotype	Primer sequence	Annealing temperature (°C)
Rpe65	5′-CCCAATAGTCTAGTAATCACAGATG-3′ (common) 5′-GATGTGGGCCAGGGCTCTTTGAAG-3′ (WT) 5′-GGGAACTTCCTGACTAGGGGAGG-3′ (KO)	60
Lrat	5′-TCCAGTTCCAGACTCTTTCCACCCAC-3′ (common) 5′-AAGTGCTGGGCATGGTGACTTGTG-3′ (WT) 5′-TGCGAGGCCAGAGGCCACTTGTGTAGC-3′ (KO)	60
Rdh8	5′-TCCGCCTTGGAAACCTGAGCCAGAAG-3′ (KO 1) 5′-TGCGAGGCCAGAGGCCACTTGTGTAGC-3′ (KO 2) 5′-CTTCAAAGTCAGTGGTGACTGGG-3′ (WT 1) 5′-GCTATCCAGCTGCGACAATTC-3′ (WT 2)	WT: 58 KO: 65
Abca4	5′-GCCCAGTGGTCGATCTGTCTAGC-3′ (WT 1) 5′-CGGACACAAAGGCCGCTAGGACCACG-3′ (WT 2) 5′-CCACGCACACATCAGCATTTCTCC-3′ (KO 1) 5′-TGCGAGGCCAGAGGCCACTTGTGTAGC-3′ (KO 2)	65
Gnat1	5′-CACCAGCACCATGTCGTAAG-3′ (common) 5′-GTACACATGTAGATGCAGGAG-3′ (WT) 5′-CTTGGCGAATATCATGGTGG-3′ (KO)	60

3. Dissolve solid 9-*cis*-retinol and 80 mg of 4-dimethylamino pyr-idine in 0.4 ml of dichloromethane, and add 0.1 ml of acetic acid anhydride.
4. After 6 h incubation at 10 °C, quench the reaction with 0.1 ml of ethanol.
5. Remove the dichloromethane by flowing argon at 20 °C.
6. Purify 9-*cis*-retinyl acetate by hexanes and dry under argon.

Table 2
POC studies with 9-*cis*-retinoids for LCA mouse models

Mouse strains	Administration route	Compound tested	Administration regimen		Highlights	Ref.
			Dose	Age (duration) and frequency		
Rpe65$^{-/-}$	Oral gavage	9-*cis*-retinal 9-*cis*-retinol 9-*cis*-retinyl palmitate	0.5 or 2.5 mg/animal	8–12 weeks old, single dose	• ERG amplitudes: ~70 % of WT after 2.5 mg single gavage • Efficacy of 9-*cis*-retinol and esters: ~30 % of 9-*cis*-retinal	[20]
		9-*cis*-retinal	25 μg/animal	PND 7–30, every other day	• Flicker ERG: ~70 % of amplitudes of WT after 2.5 mg single-dose gavage • All-t*rans*-retinyl ester levels were decreased to 30–40 % by early age administration • Single-dose treatment lasted more than 4 months	[21]
			250 μg/animal	PND 30–90, once a week		
			200 μg/animal	PND 7, 11, and 15 at 250 μg/mouse		
			200 μg/animal	PND 30, single dose		
		9-*cis*-retinyl acetate	6.25–50 mg/kg	5 weeks old, single dose	• 50 mg/kg: ~50 % amplitudes and 2 log lower sensitivity of WT • 2 mg/kg: mild improvement of ERG responses	[22]
			1 and 4 mg/kg	5 weeks old, daily or intermittent for 8 weeks under cyclic lighting conditions	• Improvement of ERG responses was sustained in a dose-dependent manner	
			1–12.5 mg/kg	5 weeks old, 3 days administration in the dark +6 days drug holiday in cyclic lighting conditions	• ERG responses were preserved with tapering ERG amplitudes during maintenance under circulated light condition	
Rpe65$^{-/-}$, *Lrat*$^{-/-}$, *Gnat1*$^{-/-}$*Rpe65*$^{-/-}$, *Gnat1*$^{-/-}$*Lrat*$^{-/-}$	Oral gavage	9-*cis*-retinyl acetate	50 mg/kg	5 weeks old, once a week treatment for 6 months in the dark or under cyclic lighting conditions	• ERG response: ~50 % amplitudes of WT under cyclic lighting conditions • ~70 % amplitude of WT when mice were maintained in the dark	

Lrat$^{-/-}$	Oral gavage	9-*cis*-retinal 9-*cis*-retinol 9-*cis*-retinyl palpitate 9-*cis*-retinyl acetate 9-*cis*-retinyl succinate	5 mg/animal 0.3–13.2 mg/animal 1.64 mg/animal	6–12 weeks old, single dose 6–12 weeks old, single dose 5 weeks to 12 months, five times over 1 month	• Ratio of regeneration: 60–70 % opsin was regenerated by 1.6 mg of 9-*cis*-retinyl acetate single-dose gavage • More than 50 % of visual pigment remained 120 days after single oral gavage at 6.6 mg of a dose of 9-*cis*-retinyl acetate • ERG: ~50 % of WT after nine times treatments at 1.6 mg of 9-*cis*-retinyl acetate	[23]
Rpe65$^{-/-}$	Tail vein injection	9-*cis*-retinal solution	285 μg/animal	5 weeks old, single dose	• Comparable efficacy to oral gavage	[21]
Gnat1$^{-/-}$*Rpe65*$^{-/-}$, *Gnat1*$^{-/-}$*Lrat*$^{-/-}$	IP + oral gavage	9-*cis*-retinyl acetate	1 mg/kg for IP, 50 mg/kg for gavage	PND 10–19, every other day; once a week from PND 21–56	• Cone ERG amplitude: ~15 % amplitudes of *Gnat1*$^{-/-}$ • Cone population: 30–50 % remained at 8 weeks of age in drug-treated groups	[13]
Rdh5$^{-/-}$*Rdh11*$^{-/-}$	Oral gavage	9-*cis*-retinal	2.5 mg/mouse	12 months old, three consecutive daily doses	• Dark adaptation and response of 30 Hz flicker ERG were maintained	[24]
WT (C57BL/6)	Oral gavage	9-*cis*-retinyl acetate	50 mg/kg	From 4 to 14 months old, once a month	• Dysfunction of dark adaptation was ameliorated	[25]

ERG electroretinogram, *IP injection* intraperitoneal injection, *PND* postnatal day

3.2.2 Preparation of 9-cis-Retinyl Succinate from 9-cis-Retinal

1. Use 100 mg of succinic acid anhydride instead of acetic acid anhydride; otherwise, preparation processes are comparable with those of 9-*cis*-retinyl acetate as indicated in Subheading 3.2.1.

3.2.3 Preparation of 9-cis-Retinol or 9-cis-Retinyl Acetate Stock Solution

1. Prepare 9-*cis*-retinol or 9-*cis*-retinyl acetate from 9-*cis*-retinal as described in Subheading 3.2.1. Dissolve in ethanol and purge with argon under dim red light to avoid oxidation and photo-bleaching.
2. Determine the concentration of 9-*cis*-retinoid by measuring the UV-visible absorption spectrum and using extinction coefficient $\varepsilon_{323nm} = 42{,}300\ M^{-1}\ cm^{-1}$ and store at −80 °C with protection from light.
3. Prepare all-*trans*-retinol or all-*trans*-retinyl acetate stock solutions similarly as 9-*cis*-retinoids (*see* Subheading 3.2.1). All-*trans*-retinol or all-*trans*-retinyl acetate can be used in control experiments.
4. Determine the concentration of all-*trans*-retinoid by measuring the UV-visible absorption spectrum ($\varepsilon_{325nm} = 52{,}770\ M^{-1}\ cm^{-1}$) and store at −80 °C with protection from light.

3.2.4 Preparation of Retinylamine (Ret-NH_2)

Ret-NH_2 was prepared to the method described by Tong Yang et al. [16] and Marcin Golczak et al. [17].

1. React β-vinylionol and triphenylphosphonium bromide in methanol at room temperature for 48 h. During this time, the triphenylphosphonium bromide is dissolved, and the solution turns yellow.
2. Evaporate the solvent in vacuo, and dissolve the yellow residue in a minimum of acetone.
3. Add ether to crystallize β-ionylidenethyltriphenylphosphonium bromide.
4. Prepare a solution of β-ionylidenethyltriphenylphosphonium bromide in anhydrous dimethylformamide under N_2 and cool to 0 °C.
5. Add aldehyde and 1,2-butene oxide in the solution and stir for 16 h at room temperature and then for 4 h at 60 °C.
6. Add petroleum ether to the solution and pour into 20 % aqueous H_2SO_4 and evaporate in vacuo.
7. Purify yellow oil by flash chromatography (silica gel, 90:10 hexane/ether).
8. Dissolve the entire sample ethanol and add hydrazine hydrate, and then keep the mixture at room temperature under N_2 for 4 days as a white precipitate is formed gradually.
9. Filter the mixture to remove the phthalhydrazide precipitate and then dry over Na_2SO_4 and evaporate in vacuo.

10. Separate *cis*- and *trans*-isomers by purification on semi-preparative reverse-phase C18 HPLC (Microsorb C18/Rainin, particle size 5 μm, 10 × 250 mm, gradient of 60:40 to 90:10 acetonitrile/0.5 % Et_3N and 0.3 % trifluoroacetic acid in H_2O 4.7 ml/min) (*see* **Note 2**).
11. Extract purified product by hexane and wash twice with water and evaporate.

3.2.5 Formulation of Retinoid Solution for Administration to Mouse Models

Retinoids must be delivered to mice in soybean oil or DMSO vehicle (*see* **Note 3**).

1. Dissolve proper amounts of 9-*cis*-retinoids or all-*trans*-retinoids in stock solutions (6.25–50 mg/kg) in soybean oil or DMSO and store at 4 °C until use.
2. Prior to administration, measure the concentrations of the above prepared retinoid spectrophotometrically using 2 μl aliquots.
3. Prepare stock solution of synthesized Ret-NH_2 in ethanol and store at −80 °C until use.
4. Determine the concentration of Ret-NH_2 by measuring the UV-visible absorption spectrum and using extinction coefficient $\varepsilon_{325nm} = 52{,}770\ M^{-1}\ cm^{-1}$ (*see* **Note 4**).

3.3 Administration of Retinoids to Mouse Models (See Note 5)

1. Administer retinoids at specified concentrations in soybean oil to mice using a 1-ml syringe and a 20-G or 23-G gavage needle via oral administration (*see* **Notes 6** and **7**).
2. After gavage with 9-*cis*-retinoid, keep mice for 3 days in the dark.
3. Then evaluate the efficacy of 9-*cis*-retinoid administration (as described in Subheading 3.4).
4. For Ret-NH_2 administration, suspend Ret-NH_2 in 100 μl of water with less than 10 % (v/v) DMSO, and administer it by oral gavage using 20-G or 23-G feeding needle at specified doses (*see* **Note 7**).

3.4 Evaluation of Retinal Health upon Retinoid Administration by Electroretinography (ERG)

3.4.1 Preparation of the Animal

1. Prior to ERG recording, dark-adapt mice for more than 16 h. Then perform all manipulations under dim red light (*see* **Note 5**).
2. Anesthetize mice by intraperitoneal injection using 20 μl/g body weight of anesthetic solution, and maintain body temperature at proper condition (*see* **Note 8**).
3. Dilate the pupils with 1 % tropicamide and 0.5 % phenylephrine hydrochloride saline solution.
4. Place contact lens electrodes (mouse ERG electrode, 3.2 mm diameter, LKC Technologies, Inc.) on the eye, and a reference electrode and ground electrode were in the ear and on the tail, respectively.
5. Record ERG signals with the universal testing and electrophysiological system UTAS E-3000 (LKC Technologies, Inc.).

3.4.2 Single-Flash ERG Recording

1. Set up flash stimuli in the range of intensities (−3.7 to 2.8 log cd/s/m^2).
2. Adjust the white light flash duration according to intensity (from 20 μs to 1 ms).
3. Perform 3–5 recordings with >10 s intervals. For higher flash intensity, make 10-min intervals or greater. There should be no significant differences between the first and the last flash (*see* **Note 9**).
4. Examine light-adapted responses after bleaching at 1.4 log cd/m^2 for 15 min (*see* **Note 10**).
5. To measure the amplitude of a-wave and b-wave responses, follow the ISCEV standard software for full-field clinical electroretinography [18].

3.4.3 Flicker ERG

1. Set up flash stimuli in the range of intensities (−3.7 to 0.56 log cd/s/m^2).
2. Conduct ERG recording similarly as single-flash ERG as indicated in Subheading 3.4.2 (*see* **Note 11**).

3.4.4 Recovery of Dark Adaptation

1. Bleach dark-adapted mice with the background light of a ganzfeld chamber (500 cd/m^2) for 3 min.
2. After bleaching use a single-flash ERG at −0.2 cd/s/m^2 to monitor the recovery of a-wave amplitudes every 5 min for 60 min in dark conditions.
3. Calculate the recovery ratio by normalizing single-flash a-wave amplitude responses at various times, following bleaching to the dark-adapted a-wave response at the identical flash intensity of −0.2 cd/s/m^2. Then plot the recovery ratio *versus* time after bleaching using SigmaPlot or equivalent software. Evaluate the results using the one-way ANOVA (analysis of variance) test.

3.5 Examination of 9-cis-Retinoid Tissue Distribution: Retinoid Analyses (See Note 5)

Quantify retinoids in blood or plasma, in the eye and in the liver collected from the animals treated with 9-*cis*-retinoids. Note that only the first step of this protocol is slightly different for each tissue. **Steps 5–16** are applicable to all analyzed tissues:

1. Place blood or plasma samples in a glass/glass homogenizers containing 1 ml of the retinoid extraction buffer and homogenize.
2. Place two whole eyes in a glass/glass homogenizers containing 1.2 ml of the retinoid extraction buffer and homogenize.

3. Incubate homogenized samples at room temperature for 20 min (including the time spent for homogenization) and then place on ice.
4. Weigh liver samples and place in a glass/glass homogenizers containing PBS (1 ml/200 mg liver) and homogenize. To 500 μl of the liver homogenate, add 2 ml of ice-cold ethanol and then incubate for 20 min at room temperature.
5. Then add 1 ml of cold ethanol to each homogenate-rinsing pestle and transfer homogenate mixtures to 7-ml glass screw-top tubes and keep on ice.
6. Rinse the homogenizers with 3 ml of hexane, and then add it to the respective 7-ml glass screw-top tubes kept on ice.
7. Vortex samples for 1 min at high speed and then centrifuge for phase separation using Beckman J2-HS centrifuge and JS13.1 swinging bucket rotor at 1,600 × *g* for 5 min at 4 °C.
8. Collect the upper phase, leaving ~0.2 ml, and transfer to clean glass test tubes.
9. Add 3 ml of hexane to the remaining lower phase, vortex, centrifuge, and collect the upper phase again.
10. Then place the test tubes containing the collected upper phases in a heating block at 25 °C and dry down under a steam of argon.
11. Resolve dried samples in 300 μl of hexane and lightly vortex.
12. Transfer samples to clean 300-μl glass inserts of the HPLC vials using a glass pipette, and then tightly close the vials.
13. Separate retinoids by normal-phase HPLC on a silica column (Agilent-Si, 5 μm or 4.5 × 250 mm column) with 10 % ethyl acetate and 90 % hexane at a flow rate of 1.4 ml/min and with detection at 325 nm (*see* **Note 12**).
14. To quantify the retinoids identified on the chromatograms, prepare the standard curves for synthetic retinoid isomers, and then correlate integrated peak areas calculated from the chromatograms of tested samples with known amounts of synthetic standards.
15. Calculate the amount of retinoid per eye (or mg of other tissues).
16. Evaluate the significance of change (comparing treated and untreated mice) by using Microsoft Excel's one-way ANOVA (analysis of variance) and the Bonferroni-Dunn tests for multiple comparisons.

3.6 Prevention of Light-Induced Retinal Damage in Abca4$^{-/-}$Rdh8$^{-/-}$ Mouse with Retinylamine

Treat *Abca4*$^{-/-}$*Rdh8*$^{-/-}$ mice with Ret-NH_2 as indicated in Table 3.

3.6.1 Induction of Light Damage in Mouse Models of Retinal Degeneration

1. Keep mice in a 12-h light/dark cycle with ample access to food and water.
2. Before light exposure, dark-adapt mice for 24 h (*see* **Note 13**).
3. Prior to light exposure, dilate the mouse pupils with 1 % tropicamide and 0.5 % phenylephrine hydrochloride saline solution.
4. After complete pupil dilation, place mice in a well-ventilated white bucket and expose to light at an intensity of 10,000 lx using 150-W spiral lamps for 60 min.
5. Then place the animals back into a dark room and analyze the health of the retina 7 days post light exposure.

3.6.2 Evaluation of Retinal Health by Spectral-Domain Optical Coherence Tomography (SD-OCT)

1. Anesthetize mice by intraperitoneal (IP) injection with an anesthetic solution (20 μl/g body weight) containing ketamine (6 mg/ml) and xylazine (0.44 mg/ml) in 10 mM sodium phosphate, pH 7.2, and 100 mM NaCl.
2. Dilate the pupils with a mixture of 0.5 % tropicamide and 0.5 % phenylephrine hydrochloride.
3. Use SD-OCT to generate in vivo images of the retina. Images can be obtained in B-scan mode with an imaging width of 1.6 mm, in A scan/B scan at 1,200 lines, and in active A scans/B scans at 80 lines. An average of 5 B-scan images for the final OCT image (Fig. 4).

3.6.3 Measurement of Retinal Autofluorescence by Scanning Laser Ophthalmoscopy Imaging (SLO)

1. Anesthetize mice and dilate the pupils as described above.
2. Use SLO to acquire in vivo images of RPE autofluorescence in AF mode with a 55° angle lens. Adjust the sensitivity properly in order to make a cluster of bright spots on fundus recognizably well with clear margins (Fig. 4).

3.6.4 Retinoid Analysis

1. Prepare samples as described in Subheading 3.5 (**steps 1–12**). This procedure is designed for the detection and analyses of nonpolar retinoids.
2. To detect Ret-NH_2, perform a normal-phase HPLC retinoid separation on a silica column in 99.5 % ethyl acetate and 0.5 % of 7 N ammonia dissolved in methanol [19].

Table 3
POC studies Ret-NH_2 with light-damaged models

Mouse strains	Administration route	Compound tested	Administration regimen		Highlights	Ref.
			Dose age (duration) and frequency			
WT (Balb/c)	Oral gavage	Retinylamine	1 mg/mouse	6 weeks old, single dose	• Light-induced retinal damage was prevented	[26]
Abca4$^{-/-}$*Rdh8*$^{-/-}$	Oral gavage		50 mg/kg	4 weeks old, once a week for 7 months	• Retinal degeneration and A2E accumulation were prevented	[15]

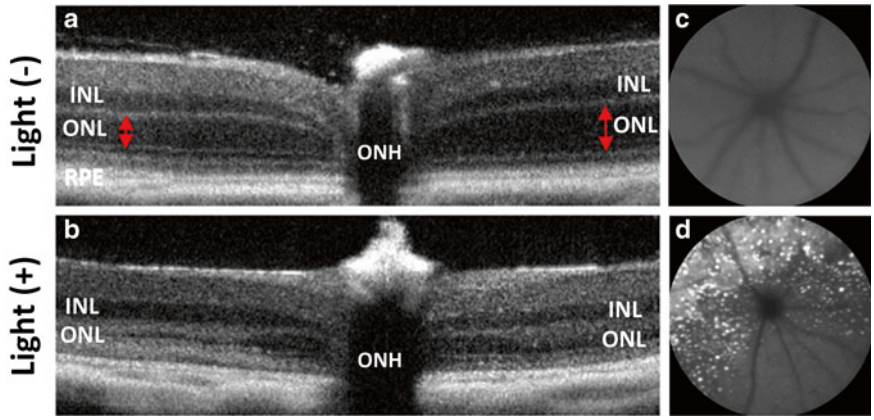

Fig. 4 In vivo ophthalmic imaging of a Stargardt's disease mouse model after light-induced retinal damage. In vivo ophthalmic imaging techniques used to measure retinal health in mouse models of retinal degeneration. (**a**) OCT imaging of the *Abca4*$^{-/-}$*Rdh8*$^{-/-}$ mouse retina prior to light-induced retinal damage. (**b**) OCT imaging of the *Abca4*$^{-/-}$*Rdh8*$^{-/-}$ mouse retina 7 days post light-induced retinal damage; of note is the loss of thickness in the ONL and increased disorganization of retinal layers. (**c**) SLO imaging of the *Abca4*$^{-/-}$*Rdh8*$^{-/-}$ retina/RPE prior to light-induced retinal damage. (**d**) SLO imaging of the *Abca4*$^{-/-}$*Rdh8*$^{-/-}$ mouse retina/RPE 7 days post light-induced retinal damage; of note are the autofluorescent spots visible in the retina/RPE. Abbreviations: *ONH* optic nerve head, *INL* inner nuclear layer, *ONL* outer nuclear layer

4 Notes

1. All-*trans*-retinyl acetate can be prepared from all-*trans*-retinol by the same method as 9-*cis*-retinyl acetate or purchased from Toronto Research Chemicals.
2. The HPLC chromatogram contains two major peaks with a 1-min separation and widths about 1 min. The faster eluting peak is identified as the *cis* isomer, and the slower peak as the corresponding *trans*-isomer.
3. Due to their hydrophobicity, retinoids must be dissolved in organic solvents. A solution of 10 % DMSO is a preferential vehicle used for retinoid administration to mice. Alternatively, to increase the efficiency of intestinal absorption, soybean oil is used as a retinoid vehicle.
4. The extinction coefficient for Ret-NH_2 was assumed to be equal to the extinction coefficient of all-*trans*-retinol and all-*trans*-retinyl esters; thus, for quantification of Ret-NH_2, use $\varepsilon_{325\text{nm}} = 52{,}770\ M^{-1}\ cm^{-1}$.
5. All manipulations must be done under dim red light transmitted through a Kodak No. 1 safelight filter (transmittance >560 nm).
6. The maximum volume of retinoid solution administered to mice is 150 μl for 5–6-week-old mice and 100 μl for 4-week-old mice.

7. The size of gavage needle should be selected with respect to the body weight of mice. 23G is recommended when mice are less than 12–16 g body weight with great care. If researchers are not confident with the levels of her/his technique, they should be in contact with veterinary staffs of animal facilities of research institutes. Alternatively, retinoids can be delivered by intraperitoneal (IP) injection of DMSO with a 28.5-G insulin syringe. The needle should be introduced perpendicularly to the lower quadrant of the abdominal cavity of mice to avoid penetrating the right liver lobe, artery, vein, and nerve in the femoral area.
8. Maintenance of body temperature and depth of anesthesia are critical for ERG recording. Dose of drugs for anesthesia must be adjusted in order to maintain proper heart rate and respiratory rate. If you are not sure about these points, please contact the veterinarian of your animal facility and obtain proper training.
9. Interval time between flash stimuli should be adjusted by phenotypes of mice or any experimental procedures which may affect the recovery of ERG responses.
10. Typically 4–8 animals are used for the recording of each point in all conditions.
11. Flicker frequency can be increased by 30 Hz to record cone dominant flicker ERG response under photopic condition.
12. The HPLC method separates and detects all-*trans*, 9-*cis*, 11-*cis*, and 13-*cis* isomers of retinal, retinol, and retinyl esters.
13. Mice should be treated with Ret-NH_2 3 h before light damage experiment. The volume of Ret-NH_2-DMSO solution should be less than 50 μl, especially when administration is performed repeatedly during a long-term study.

References

1. Palczewski K (2012) Chemistry and biology of vision. J Biol Chem 287:1612–1619
2. Kiser PD, Golczak M, Maeda A et al (2012) Key enzymes of the retinoid (visual) cycle in vertebrate retina. Biochim Biophys Acta 1821: 137–151
3. Palczewski K (2010) Retinoids for treatment of retinal diseases. Trends Pharmacol Sci 31: 284–295
4. Maeda T, Golczak M, Maeda A (2012) Retinal photodamage mediated by all-trans-retinal. Photochem Photobiol 88:1309–1319
5. den Hollander AI, Roepman R, Koenekoop RK et al (2008) Leber congenital amaurosis: genes, proteins and disease mechanisms. Prog Retin Eye Res 27:391–419
6. Miyake Y, Shiroyama N, Sugita S et al (1992) Fundus albipunctatus associated with cone dystrophy. Br J Ophthalmol 76:375–379
7. Sparrow JR (2010) Bisretinoids of RPE lipofuscin: trigger for complement activation in age-related macular degeneration. Adv Exp Med Biol 703:63–74
8. Marlhens F, Bareil C, Griffoin JM et al (1997) Mutations in RPE65 cause Leber's congenital amaurosis. Nat Genet 17:139–141
9. Redmond TM, Yu S, Lee E et al (1998) Rpe65 is necessary for production of 11-cis-vitamin A in the retinal visual cycle. Nat Genet 20: 344–351
10. Rohrer B, Lohr HR, Humphries P et al (2005) Cone opsin mislocalization in Rpe65−/− mice:

a defect that can be corrected by 11-cis retinal. Invest Ophthalmol Vis Sci 46:3876–3882

11. Batten ML, Imanishi Y, Maeda T et al (2004) Lecithin-retinol acyltransferase is essential for accumulation of all-trans-retinyl esters in the eye and in the liver. J Biol Chem 279: 10422–10432
12. Zhang T, Zhang N, Baehr W et al (2011) Cone opsin determines the time course of cone photoreceptor degeneration in Leber congenital amaurosis. Proc Natl Acad Sci U S A 108: 8879–8884
13. Maeda T, Cideciyan AV, Maeda A et al (2009) Loss of cone photoreceptors caused by chromophore depletion is partially prevented by the artificial chromophore pro-drug, 9-cis-retinyl acetate. Hum Mol Genet 18:2277–2287
14. Maeda A, Maeda T, Golczak M et al (2009) Involvement of all-trans-retinal in acute light-induced retinopathy of mice. J Biol Chem 284: 15173–15183
15. Maeda A, Maeda T, Golczak M et al (2008) Retinopathy in mice induced by disrupted all-trans-retinal clearance. J Biol Chem 283: 26684–26693
16. Yang T, Snider BB, Oprian DD (1997) Synthesis and characterization of a novel retinylamine analog inhibitor of constitutively active rhodopsin mutants found in patients with autosomal dominant retinitis pigmentosa. Proc Natl Acad Sci U S A 94:13559–13564
17. Golczak M, Kuksa V, Maeda T et al (2005) Positively charged retinoids are potent and selective inhibitors of the trans-cis isomerization in the retinoid (visual) cycle. Proc Natl Acad Sci U S A 102:8162–8167
18. Marmor MF, Fulton AB, Holder GE et al (2009) ISCEV Standard for full-field clinical electroretinography (2008 update). Doc Ophthalmol 118:69–77
19. Golczak M, Imanishi Y, Kuksa V et al (2005) Lecithin:retinol acyltransferase is responsible for amidation of retinylamine, a potent inhibitor of the retinoid cycle. J Biol Chem 280:42263–42273
20. Van Hooser JP, Aleman TS, He YG et al (2000) Rapid restoration of visual pigment and function with oral retinoid in a mouse model of childhood blindness. Proc Natl Acad Sci U S A 97:8623–8628
21. Van Hooser JP, Liang Y, Maeda T et al (2002) Recovery of visual functions in a mouse model of Leber congenital amaurosis. J Biol Chem 277:19173–19182
22. Maeda T, Maeda A, Casadesus G et al (2009) Evaluation of 9-cis-retinyl acetate therapy in Rpe65−/− mice. Invest Ophthalmol Vis Sci 50:4368–4378
23. Batten ML, Imanishi Y, Tu DC et al (2005) Pharmacological and rAAV gene therapy rescue of visual functions in a blind mouse model of Leber congenital amaurosis. PLoS Med 2:e333
24. Maeda A, Maeda T, Palczewski K (2006) Improvement in rod and cone function in mouse model of Fundus albipunctatus after pharmacologic treatment with 9-cis-retinal. Invest Ophthalmol Vis Sci 47:4540–4546
25. Maeda T, Maeda A, Leahy P et al (2009) Effects of long-term administration of 9-cis-retinyl acetate on visual function in mice. Invest Ophthalmol Vis Sci 50:322–333
26. Maeda A, Maeda T, Golczak M et al (2006) Effects of potent inhibitors of the retinoid cycle on visual function and photoreceptor protection from light damage in mice. Mol Pharmacol 70:1220–1229

Chapter 23

Sustained Delivery of Retinoids to Prevent Photoreceptor Death

Peter H. Tang and Rosalie K. Crouch

Abstract

Delivery of hydrophobic compounds to photoreceptors within the retina presents unique challenges due to the anatomy and physiology of the eye. Derivatives of vitamin A (retinoids) are essential to the function and survival of photoreceptors and in the absence of an intrinsic mechanism to metabolize these compounds (visual cycle) leads to extensive loss of photoreceptors and visual function. In this chapter, we describe a method for the sustained delivery of retinoids to young mice that lack a functioning visual cycle to promote survival of photoreceptors.

Key words Cone death, Retina, Photoreceptor, Retinoid, Sustained delivery, Visual cycle

1 Introduction

Sustained drug delivery holds numerous advantages over bolus dosing, including minimizing the risk of toxicity, increasing the duration of therapeutic efficacy, and reducing the complications associated with procedures required for bolus drug delivery. Delivering therapeutic compounds to photoreceptors of the retina presents unique challenges due to its anatomic location and the physiology of the eye. Injection of compounds directly into the vitreous chamber is a common approach to delivering therapeutics to the retina; however, this method has numerous drawbacks including infection, retinal detachment, and hemorrhage. Furthermore, its utility is further decreased when sustained therapeutic delivery is the goal, as the dynamic nature of humoral flow necessitates repeat intravitreal injections that further increases the complications already mentioned.

The visual cycle is a series of enzymatic reactions and transport systems within the retina/retinal pigment epithelium that is responsible for metabolizing nutritionally obtained vitamin A, all-trans-retinol, to 11-*cis*-retinal which is the chromophore for the photosensitive visual pigments and recycling the product of the

Beata Jastrzebska (ed.), *Rhodopsin: Methods and Protocols*, Methods in Molecular Biology, vol. 1271,
DOI 10.1007/978-1-4939-2330-4_23,

phototransduction process, all-*trans*-retinol (for reviews, *see* refs. 1, 2). Congenital diseases involving a disruption of the normal function of visual cycle proteins [3] result in the loss of intrinsic 11-*cis*-retinal production and early photoreceptor death [4, 5]. Supplementing these animals with exogenous 11-*cis*-retinal has been shown to preserve visual function and promote photoreceptor survival [6, 7]. For cases where there is complete disruption of the visual cycle and no source of chromophore, the cone photoreceptors degenerate early. So the challenge is to provide a sustained delivery of the chromophore to the young mice prior to the opening of the eyes (usually around postnatal day 6). Thus, a safe and efficacious sustained delivery system is essential.

Polymers have been successfully demonstrated through in vitro studies to provide sustained delivery of compounds to the eye [8, 9], with thermosensitive gels having the unique characteristic of allowing easy mixing of therapeutic agents within the vehicle and solidifying into a stable matrix at body temperatures for sustained release [10]. In this current chapter, we describe our previous finding that the thermosensitive polymer Matrigel™ (BD Biosciences) is capable of sustained delivery of chromophore to the retina to promote photoreceptor survival and visual function [5]. The mechanism is believed to involve the presence of growth factors including vascular endothelial growth factor (VEGF) and fibroblast growth factor (FGF) within Matrigel™ triggering a slow infiltration of blood vessels into the solidified matrix when injected into the mouse as a plug [5, 11]. The permeability of these fenestrated vessels allows for therapeutic compounds to be released from the matrix into systemic circulation and allows for sustained delivery of compounds over a period of time and with application to very young animals.

Figure 1 demonstrates the successful utilization of Matrigel for delivering retinoid and maintaining cone viability. Animals (*Rpe65*$^{-/-}$ (generous gift of T.M. Redmond) and *Wt* C57BL/6J mice (Jackson Laboratories)) were treated at P10 and analyzed at P30. The dosage of retinoid was 0.25 mg retinal/mouse. Cone opsin (M/L) increased in the animals treated with Matrigel alone or via IP injection.

2 Materials

2.1 Animals

1. All animals are reared under cyclic light (12 h light/12 h dark, with the ambient light intensity at eye level of 85 ± 18 lux) conditions until the initiation of experiments, when they are transferred to a constant dark environment. The method is applicable to any mouse model but has been used most extensively for control animals and the RPE65 knockout model [6].

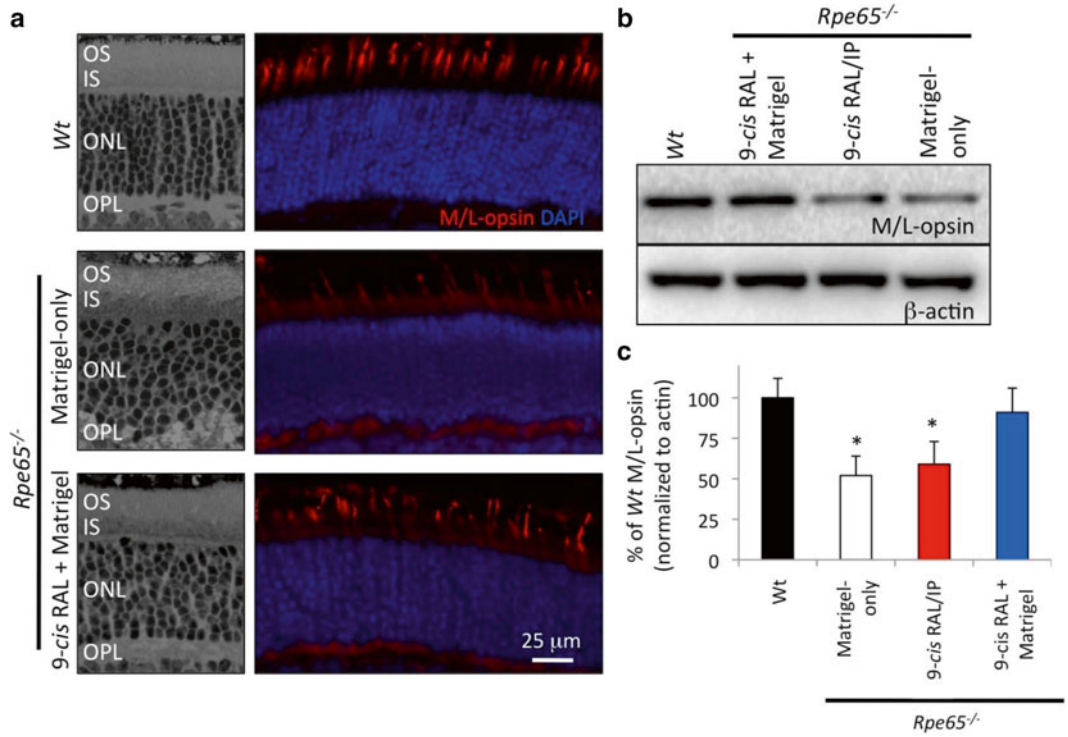

Fig. 1 Cone opsin protein (M/L) increases with Matrigel delivery of 9-*cis*-retinal in *Rpe65*$^{-/-}$ mice. Data obtained from *Rpe65*$^{-/-}$ P30 animals (generous gift of T.M. Redmond) and *Wt* C57BL/6J mice. (**a**) Cross-sectional images of the central-dorsal retina are shown for *Wt*—C (*top panel*) and *Rpe65*$^{-/-}$ mice treated with 9-*cis*-retinal using Matrigel (*bottom panel*). For control, 9-*cis*-retinal was omitted from the Matrigel preparation (Matrigel-only; *middle panel*). Paraffin-embedded retinas are sectioned and stained with hematoxylin-eosin (*left column*); cryoprotected retinas are sectioned and stained with both M/L-opsin-specific primary antibody (*red*) and DAPI (*blue*) for nuclei (*right column*). *OS* outer segment, *IS* inner segment, *ONL* outer nuclear layer, *OPL* outer plexiform layer. (**b**) Western blot images for M/L-opsin (*top*) and α-actin (*bottom*) are shown for *Wt* and *Rpe65*$^{-/-}$ Matrigel, IP, and control mice. (**c**) Densitometry band analyses are displayed as percentage of *Wt*. Matrigel alone and 9-*cis*-retinal (RAL) IP injected *Rpe65*$^{-/-}$ mice display significantly decreased M/L-opsin protein levels compared to *Wt* (*). *Black bar*, *Wt*, $n=3$; *white bar*, Matrigel alone, $n=3$; *red bar*, 9-*cis*-retinal IP, $n=3$; blue bar, Matrigel plus 9-*cis*-retinal, $n=3$. Data are presented as means ± SD and analyzed by two-sample *t*-test, accepting a significance value of $P<0.05$. Figure originally published in Tang PH, Fan J, Goletz PW, et al. (2010). Effective and sustained delivery of hydrophobic retinoids to photoreceptors. *Invest Ophthalmol Vis Sci* **51**, 5958–5964. The Association for Research in Vision and Ophthalmology is the copyright holder

2.2 Retinoids

1. 11-*cis*-Retinal is not commercially available; however, it can be synthesized according to previously published protocols and can be obtained for vision research by a request to the National Eye Institute.
2. An alternative is the functional analog 9-*cis*-retinal, which is commercially available (*see* **Note 1**).

2.3 Sustained Delivery Vehicle

1. BD Matrigel™ Basement Membrane Matrix (BD Biosciences) (*see* **Note 2**).
2. 100 % ethanol.
3. 1 ml syringe.
4. 27-gauge needle.

3 Methods

Carry out all procedures in dim red light unless otherwise specified.

3.1 Preparation of Sustained Delivery System

1. Bring the stock bottle of 11- or 9-*cis*-retinal out of −80 °C storage and keep at 4 °C on ice.
2. Divide the retinoids into aliquots of 1 mg and place into individual amber vials.
3. The maximum dosage of 11- or 9-*cis*-retinal for each mouse should not exceed 0.25 mg. To prepare these individual doses, dissolve 1 mg of retinoid into 400 μl of 100 % ethanol.
4. Extract 100 μl of the solution into individual amber vials, which are then placed under a gentle stream of nonreactive gas such as argon to facilitate evaporation of the ethanol.
5. Once ethanol has evaporated, each vial contains 0.25 mg of 11- or 9-*cis*-retinal that can be further used to prepare the sustained delivery system or be placed back into −80 °C for storage until ready to use.
6. To continue preparing the sustained delivery system, dissolve the 0.25 mg of retinoid in each vial into 20 μl of 100 % ethanol. Keep on ice.
7. Bring BD Matrigel™ from −20 °C storage and thaw on ice (*see* **Note 3**).
8. Combine the 20 μl solution from **step 6** with 180 μl of BD Matrigel™ for a total volume of 200 μl. Mix well and keep on ice to maintain the polymer in its liquid state.
9. Draw the entire 200 μl volume into a 1 ml syringe with a 27-gauge needle attached, and maintain on ice (*see* **Note 4**).

3.2 Injection of Sustained Delivery System into Animal

For the purposes of sustained delivery of retinoids to mouse eyes to preserve cone function, initiation of treatment must begin within the first week of life (ideally around postnatal day 6).

1. Place the mouse pup dorsal side facing the investigator.
2. With the nondominant hand, pinch the dorsal back skin of the mouse pup between thumb and index finger to create a small fold running parallel to the body axis.

3. With the dominant hand, insert the treatment needle into the skin fold making sure the needle stays subcutaneously placed.
4. With gentle and firm pressure, inject the entire volume of the syringe subcutaneously, forming a round nodule.
5. Slowly remove the needle and place gentle pressure for 5 s using a fingertip against the insertion site of the needle to prevent backflow as well as to help promote solidification of the Matrigel™ compound.
6. Transfer mouse pup to warming pad set at 36 °C for a few minutes prior to moving pup back to cage.
7. Analyze the effect of delivered retinoid on the retinal health with your method of choice.

4 Notes

1. Store 11-*cis*-retinal and 9-*cis*-retinal at −80 °C in light-tight container, and only handle in dim red light.
2. Store at −20 °C, and thaw at 4 °C. Avoid multiple freeze-thaws as this can degrade the polymer. We recommend separating the stock solution into 1 ml aliquots so as to minimize the freeze-thaw process.
3. Refrain from multiple freeze-thaw cycles with Matrigel™ as this can reduce its efficacy to thermo-convert between liquid and solid states. We recommend aliquoting the stock solution of Matrigel™ immediately on arrival from the manufacturer.
4. After mixing the Matrigel™-retinoid compound to be used for treatment, it may be easier to draw the solution into the body of the syringe without the needle attached. After an appropriate amount is drawn up, attach the needle and push out volume to eliminate dead space prior to treatment.

Acknowledgments

This work was supported by the National Institutes of Health Grants R01 EY04939 (R.K.C.) and CO6 RR015455 (Medical University of South Carolina); Foundation Fighting Blindness, Inc. (R.K.C.); an unrestricted grant (Department of Ophthalmology, Medical University of South Carolina) from Research to Prevent Blindness (RPB); RPB Senior Scientific Investigator Award (R.K.C.); and RPB Medical Student Research Fellowship (P.H.T.).

References

1. Tang PH, Kono M, Koutalos Y et al (2012) New insights into retinoid metabolism and cycling within the retina. Prog Retin Eye Res 32:48–63
2. Cascella M, Barfuss S, Stocker A (2013) *Cis-retinoids* and the chemistry of vision. Arch Biochem Biophys 539:187–195
3. Travis GH, Golczak M, Moise AR et al (2007) Diseases caused by defects in the visual cycle: retinoids as potential therapeutic agents. Annu Rev Pharmacol Toxicol 47:1–44
4. Znoiko SL, Rohrer B, Lu K et al (2005) Downregulation of cone-specific gene expression and degeneration of cone photoreceptors in the RPE65$^{-/-}$ mouse at early ages. Invest Ophthalmol Vis Sci 46:1473–1479
5. Tang PH, Fan J, Goletz PW et al (2010) Effective and sustained delivery of hydrophobic retinoids to photoreceptors. Invest Ophthalmol Vis Sci 51:5958–5964
6. Rohrer B, Lohr HR, Humphries P et al (2005) Cone opsin mislocalization in RPE65-/- mice: a defect that can be corrected by 11-*cis*-retinal. Invest Ophthalmol Vis Sci 46: 3876–3882
7. Fan J, Rohrer B, Frederick JM et al (2008) RPE65$^{-/-}$ and LRAT$^{-/-}$ mice: comparable models of Leber congenital amaurosis. Invest Ophthalmol Vis Sci 49:2384–2389
8. Geroski DH, Edelhauser HF (2000) Drug delivery for posterior segment eye disease. Invest Ophthalmol Vis Sci 41:961–964
9. Cruysberg LP, Nuijts RM, Gilbert JA et al (2005) Delivery of fluorescein-labeled dexamethasone and methotrexate with fibrin sealant. Curr Eye Res 30:653–660
10. Hsiue GH, Chang RW, Wang CH et al (2003) Development of *in situ* thermosensitive drug vehicles for glaucoma therapy. Biomaterials 24:2423–2430
11. Miao RQ, Agata J, Chao L et al (2002) Kallistatin is a new inhibitor of angiogenesis and tumor growth. Blood 100:3245–3252

Chapter 24

High-Throughput Screening Assays to Identify Small Molecules Preventing Photoreceptor Degeneration Caused by the Rhodopsin P23H Mutation

Yuanyuan Chen and Hong Tang

Abstract

High-throughput screening (HTS) is one of the major techniques for discovering promising molecules for drug development. Rhodopsin mutations cause the most common autosomal dominant form of retinitis pigmentosa, an inherited retinal degenerative disease that currently has no effective treatment. To find an optimal pharmacological treatment for rhodopsin-associated retinitis pigmentosa, we performed two cell-based HTSs with mammalian cells expressing the P23H rod opsin mutant and identified two sets of novel compounds for further validation and characterization. The first HTS screen identified pharmacological chaperones of P23H opsin that increased its translocation from the endoplasmic reticulum to the plasma membrane. The second HTS screen selected small molecules that enhanced the clearance of the mutant opsin while vision could be sustained by the healthy gene allele expressing wild-type rhodopsin. Here we describe the methodology of these two HTS assays in detail.

Key words P23H rhodopsin, Retinitis pigmentosa, High-throughput screen, Drug discovery

1 Introduction

High-throughput screening (HTS) has been employed for drug discovery since the 1990s and associated technologies have evolved to the third generation [1–3]. Until 2008, among the 58 FDA approved drugs with their starting compounds documented, 19 drugs were developed from hit compounds identified in HTS [3]. Compared to other drug discovery methods such as structure-based or ligand-based virtual screening [4] and fragment-based drug design [5], HTS requires little knowledge of the target structure or the availability of an active model compound [6]. Resulting from a state-of-the-art automated facility, optimized drug-like compound libraries, and multiple quality control algorithms, hit compounds from about 50 % of HTS projects have led to the successful development of drugs in pharmaceutical pipelines [3].

Beata Jastrzebska (ed.), *Rhodopsin: Methods and Protocols*, Methods in Molecular Biology, vol. 1271,
DOI 10.1007/978-1-4939-2330-4_24,

Retinitis pigmentosa (PR) is a retinal degenerative disease with a heterogeneous genetic background. Mutations of the gene encoding rhodopsin, the visual pigment of rod photoreceptor cells, are found in about 25 % of individuals with autosomal dominant retinitis pigmentosa (adRP) [7, 8]. The P23H rhodopsin mutation causes the most common form of adRP, accounting for 12 % of cases in the United States [7]. To date, there is no effective treatment for this disease, although multiple experimental efforts have been reported [9–17]. Currently, active compounds which showed protective effects in P23H rhodopsin-associated adRP models are limited to two categories: (1) the native chromophore and its analogs with high light sensitivity, low stability, and relatively high toxicity [18–21] and (2) natural antioxidant substances which require high dosages for efficacy and are not suitable for human treatment [12–14].

Two models have been proposed for the molecular basis of P23H opsin-triggered photoreceptor cell death: (1) the overwhelmed unfolded protein response (UPR) model. Here the Pro to His mutation at codon 23 disrupts the local hydrophobic cluster in the rod opsin protein, leading to its immature glycosylation, misfolding, and resulting activation of the UPR in the endoplasmic reticulum (ER). Consistent expression of the misfolded P23H opsin could overwhelm the UPR system and result in apoptosis of photoreceptor cells, the first step in the progression of RP [21–26]. (2) The disrupted rod outer segment (ROS) model. In the P23H knock-in mouse model wherein most of the P23H opsin is degraded, a residual amount of the mutant rhodopsin pigment could be transported to the ROS where it disrupts disc organization and causes photoreceptor death [27–29].

Based on these two models, we designed two different HTS discovery strategies as follows: (1) identify small-molecule chaperones that stabilize the proper folding of P23H opsin and increase its translocation from ER to the plasma membrane (equivalent to ROS in rod photoreceptor cells) thereby reducing the UPR and (2) find small-molecule compounds that clear the mutant opsin, leaving only normal opsin derived from the healthy gene copy to maintain retinal structure and vision.

For the HTS of active compounds that increase the translocation of P23H opsin from the ER to plasma membrane, we generated a stable cell line (PathHunter U2OS mRHO(P23H)-PK total GPCR translocation cells) which expressed two active recombinant fusion proteins (Fig. 1a): (1) mRHO(P23H)-PK, the mouse P23H opsin fused with a small subunit of β-galactosidase (β-Gal), and (2) PLC-EA, a membrane-associated peptide (the PH domain of phospholipase C-δ, PLC) fused with a large subunit of β-Gal. Without treatment, misfolded mRHO(P23H)-PK accumulates in the ER, whereas PLC-EA associates with the plasma membrane. Hence, the separation of the two subunits of β-Gal into different

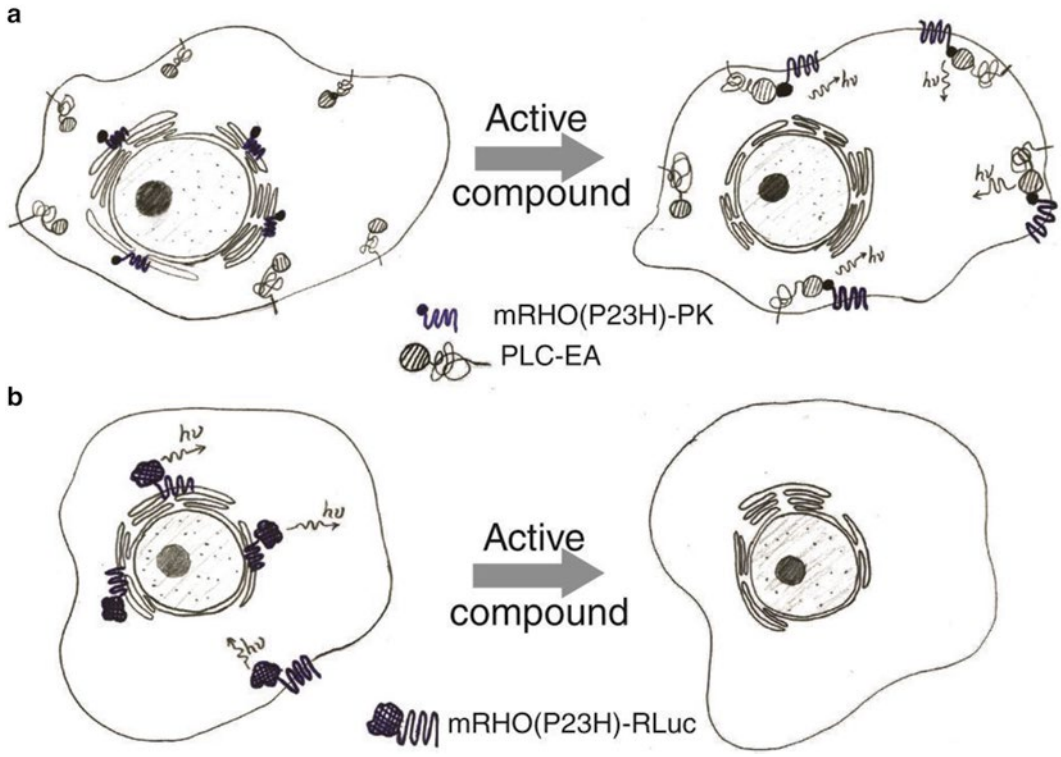

Fig. 1 Diagrams of the β-Gal complement assay for the P23H opsin translocation HTS (**a**) and the RLuc assay for the P23H opsin clearance HTS (**b**)

cell compartments results in little β-Gal activity when substrate is added. But upon the treatment with an active compound, mRHO(P23H)-PK is transported from ER to the plasma membrane, leading to reconstitution of intact β-Gal. The restored activity of β-Gal can be measured by luminescence after the addition of substrate.

For the HTS of active compounds that promote the P23H opsin clearance, we generated another stable cell line (Hek293 mRHO(P23H)-RLuc total GPCR quantification cells) using *Renilla* luciferase (RLuc) as a reporter for the mutant opsin (Fig. 1b). Here the P23H opsin is fused with RLuc expressed in human embryonic kidney 293 (Hek293) cells. The amount of the P23H-RLuc protein is correlated with the RLuc activity, which can be read by the luminescence recorded by a microplate reader.

Both HTS assays have been optimized with respect to cell seeding number, substrate conditions, and dimethyl sulfoxide (DMSO) tolerance to ensure that they are reliable and reproducible as indicated by the quality control parameters Z' (i.e., $Z' > 0.5$) and signal-to-background (S/B) ratio (i.e., S/B ratio > 3) [30] (*see* Subheading 3.1.4 for more detailed description).

Here the two HTSs are described in three tiers: primary HTS, hit confirmation screen, and dose-response screen. Initially, each compound from a Diversity Set of compound library is tested at a single concentration. Then identified "hit" compounds with the desired effect are retested at the same concentration in triplicate. Finally, each confirmed hit compound is tested at 10 concentrations in triplicate. EC_{50} values for the final hit compounds are obtained from their dose-response curves fitted by the Hill function.

2 Materials

2.1 Cells

1. PathHunter U2OS mRHO(P23H)-PK total GPCR translocation cells for the P23H opsin translocation screen. U2OS cells expressing mRHO(P23H)-PK (the 40 amino acid PK subunit of β-Gal fused on the C-terminus of the P23H mouse opsin mutant) and PLC-EA (the EA subunit of β-Gal fused on the C-terminus of PLC peptide) recombinant proteins were generated by a collaboration between Dr. Nevin A. Lambert (Georgia Regents University, GA) and DiscoveRx, CA. A total of 4×10^8 cells were collected at passage 7 and frozen in liquid nitrogen.
2. Hek293 mRHO(P23H)-RLuc total GPCR quantification cells for the P23H opsin clearance screen. The cDNA of RLuc (RLuc8, a spectrally shifted mutant of luciferase from *Renilla reniformis*, was fused on the C-terminus of the P23H mouse opsin (mRHO(P23H)-RLuc)) constructed in the pcDNA3.1/Zeo vector provided by Dr. Nevine A. Lambert (Georgia Regents University, GA). The DNA vector was transfected into Hek293 cells with polyethylenimine (*see* **Note 1**) to generate cells continuously expressing the P23H opsin-RLuc recombinant protein (*see* **Note 2**).

2.2 Tissue Culture

1. Heat-inactivated fetal bovine serum (FBS, HI): Thaw a 500 ml bottle of FBS (HyClone) at room temperature and heat-inactivate by incubation at 65 °C for 1 h. Then aliquot into 50 ml conical tubes and store at −20 °C. Thaw at 37 °C before use.
2. Cell growth medium: Dulbecco's modified Eagle medium (DMEM), 12 % FBS, 5 μg/ml Plasmocin. To a 500 ml bottle of DMEM high glucose medium (HyClone), add 60 ml of thawed FBS, HI, and 100 μl of 25 μg/ml Plasmocin (InvivoGen) in a tissue culture hood. Store medium at 4 °C and warm to 37 °C before use.
3. Cell plate medium: DMEM, 10 % FBS, 1 unit/ml penicillin, 1 μg/ml streptomycin and 2.92 μg/ml L-glutamine. To a 500 ml bottle of DMEM high glucose medium add, 50 ml of thawed FBS, HI, and 5 ml of 100× penicillin-streptomycin-glutamine

(HyClone) in a tissue culture hood. Store medium at 4 °C and warm to 37 °C before use.

4. 0.05 % trypsin solution (HyClone).
5. Sterile 1× phosphate buffered saline 10 mM Na2HPO4, 1.8 mM KH2PO4, pH 7.4, 137 mM NaCl and 2.7 mM KCl, pH 7.4.
6. Growth-enhanced treated 150 mm tissue culture plates (TPP).
7. 70 μm cell strainer (BD Falcon).
8. 15 ml and 50 ml conical tubes (BD Falcon).
9. 200 ml conical bottom centrifuge bottles with adaptors (Thermo Scientific).
10. Hemocytometer (Fisher Scientific).

2.3 HTS

1. β-Gal Assay Substrate Buffer (for P23H opsin translocation screen): 4 % of Gal Screen Substrate and 96 % Gal Screen Buffer A. To prepare 12 ml of β-Gal Assay Substrate Buffer for one 384-well plate (25 μl/well), add 0.48 ml Gal Screen Substrate and 11.52 ml Gal Screen Buffer A from the Gal Screen System (Applied Biosystems) to a 15 ml tube and vortex to mix (*see* **Note 3**).
2. RLuc Assay Substrate Buffer (50 μM ViviRen) (for P23H opsin clearance screen): Dissolve 3.7 mg of ViviRen (Promega) in 100 μl of DMSO to prepare 60 mM ViviRen stock solution. Add 33.3 μl of ViviRen stock solution to 40 ml of PBS in a 50 ml conical tube to prepare 40 ml 50 μM RLuc Assay Substrate Buffer.
3. 2 % n-dodecyl β-D-maltoside (DDM) in PBS.
4. Positive Control Solution for the P23H opsin translocation screen: 25 μM 9-*cis*-retinal in cell growth medium. In a dark room with dim red light, dissolve 1 mg 9-*cis*-retinal powder (Sigma) in 178 μl of DMSO to prepare a 20 mM stock solution. For a 25 μM 9-*cis*-retinal working solution, dilute 6.25 μl of 9-*cis*-retinal stock solution into 5 ml of growth medium, and vortex to mix. Wrap the tube with aluminum foil to protect from light.
5. Positive Control Solution for P23H opsin clearance screen: 1 mM Evans Blue solution. To prepare Evans Blue 25 mM stock solution, dissolve 24 mg Evans Blue powder (Sigma) in 1 ml of ddH_2O. For 1 mM working solution, dilute 200 μl of 25 mM Evans Blue stock solution into 4.8 ml of cell growth medium.
6. Neutral control for both the β-Gal and RLuc assays: cell Plate medium (*see* **Note 4**).
7. Assay plate: A 384-well, white-walled, clear flat bottomed, sterile plate with lid (BD Falcon) or a 384-well, white-walled, clear flat bottomed, sterile plate with lid (Greiner Bio-One).
8. Compound plate: A 384-well, polypropylene, flat bottomed plate (BD Falcon).

2.4 Instruments

1. Perkin Elmer plate::explorer™ uHTS system: This consists of an HW workstation (plate storage and incubation), an LW workstation (liquid handling), and an RW workstation (signal detection). It includes the following components: two Multidrop dispensers (dispenser A and B), a CyBi-Well dispenser, a microplate washer, a Rotanta 46 microplate centrifuge, a plate Lift storage device, a tissue culture incubator I189 (37 °C in 5 % CO_2 with 95 % humidity), a storage incubator I30, turn tables, a bar-code reader, conveyor belt, and a Perkin Elmer Plate::Vision™ Detector.
2. Stand-alone Perkin Elmer EnVision™: A plate reader for luminescence signal detection.

2.5 Compound Library

1. The 25,000 Diversity Set of University of Cincinnati Compound Collections (used for the P23H opsin translocation screen).
2. The 10,000 Diversity Set of University of Cincinnati Compound Collection (used for P23H opsin clearance screen) (*see* **Note 5**).

3 Methods

3.1 The P23H Opsin Translocation HTS

The 25,000 Diversity Set including 83 compound plates is separated into 2 cycles of HTS. Each cycle of HTS tests 42 or 41 compound plates that are further broken down into two sets of 21 or 20 plates for an automated experiment.

3.1.1 Preparation for HTS

1. Design and test-run the workflow of an automated experiment with used plates. Figure 2 shows the plate map of a P23H opsin translocation assay. Defined by the compound plate design, each assay plate has a maximum of 4 columns for controls (Columns 21–24).
2. Calibrate the pin tools (50 nl pin tool for primary HTS and hit confirmation screens and a 200 nl pin tool for the dose-response screen). Calculate the actual dispensing volume of each pin tool and the corresponding final concentration of the tested compounds for each screen (*see* **Note 6**).
3. Before starting each experiment, sterilize the dispenser tubes by priming with 70 % ethanol. Rinse the dispenser tubes again with sterile PBS buffer or cell plate medium to wash out residual ethanol.

3.1.2 Cell Preparation (See **Note 7**)

The following procedures are performed in a tissue culture hood under sterile conditions:

Day 1 Revival of frozen cells

1. Prewarm cell growth medium in a 37 °C water bath.
2. Place 25 cryo-vials with frozen PathHunter U2OS mRHO(P23H)-PK total GPCR translocation cells (*see* **Note 8**)

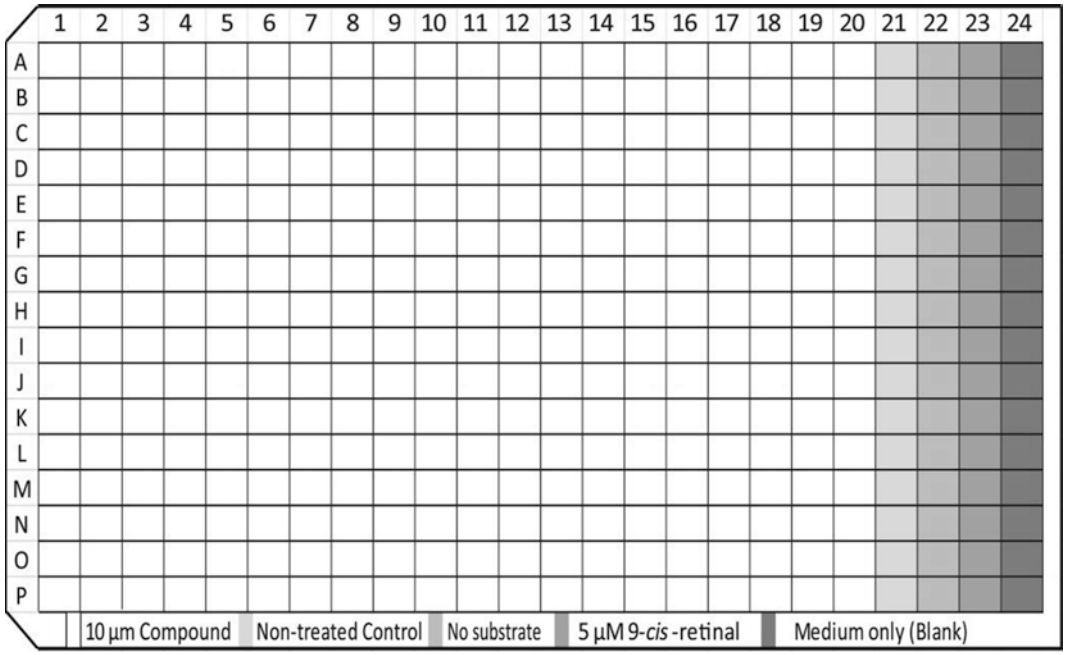

Fig. 2 Plate map of the HTS for the correction of P23H opsin localization

in a 37 °C water bath until only small ice crystals remain and the cell pellet is almost completely thawed (30 s to 1 min).

3. Transfer every five vials of thawed cells to a 50 ml conical tube containing 25 ml of prewarmed cell growth medium. Centrifuge at 300 × *g* for 4 min to pellet cells. Remove medium.
4. Resuspend cell pellet with 12.5 ml prewarmed cell growth medium (add 0.5 ml cell growth medium to cells from each cryo-vial). Combine cell suspensions into one conical tube and mix well.
5. Add 1 ml of cell suspension and 29 ml of prewarmed cell growth medium to each 150 mm cell culture plate. Gently rotate the plate to mix well. Incubate at 37 °C in 5 % CO_2 with 95 % humidity for 24 h.

Day 2 Cell growth medium replacement

6. Gently remove medium from the 150 mm cell culture plate and replace with 30 ml of prewarmed cell growth medium. Incubate plates at 37 °C in 5 % CO_2 with 95 % humidity until cells reach more than 90 % confluence on *Day 5* (*see* **Note 9**).

Day 5 Preparation of cell suspensions for HTS plate seeding

7. Confirm the full confluence of cells under a light microscope. Prewarm the cell plate medium in a 37 °C water bath.
8. Remove growth medium and wash each plate with 20 ml of PBS. Remove PBS, and add 2 ml of trypsin (0.05 %) to each plate.

Incubate at 37 °C for 5–8 min until cells are detached. Add 8 ml of cell plate medium to each plate, mix well, and filter through a 70 μm cell strainer to capture cell clusters. Collect the flow-through in a 200 ml conical bottomed centrifuge bottle.

9. Count cells with a hemocytometer and dilute them to 25×10^4 cells/ml in cell plate medium to prepare a cell suspension for HTS plate seeding. The total volume of cell suspension should be more than 190 ml, sufficient for distribution in 21 × 384-well plates at 20 μl/well (21 × 400 × 20 μl = 168,000 μl = 168 ml) leaving 22 ml as the dead volume of dispenser (*see* **Notes 10** and **11**).
10. Revive and prepare the cells for the 2nd cycle of HTS experiment (e.g., revive cells on *Day 5* if the 2nd cycle of HTS starts on *Day 9*).

3.1.3 Primary HTS Screen

Day 5 Cell seeding

1. Place 21 (or 20 for the last experiment set of the 2nd HTS cycle) assay plates in the stackers of Plate::Life storage.
2. Prime and fill the tubes of dispenser A with cell plate medium and confirm that liquid flows through each of the 8 tubes of the dispenser without air bubbles in the tubes.
3. Similarly, prime and fill the tubes of dispenser B with cell suspension prepared in Subheading 3.1.2 for plate seeding.

Perform **steps 4–8** by automation (*see* **Note 12**):

4. Add 25 μl of cell plate medium to Column 24 of each assay plate with dispenser A.
5. Add 20 μl of the cell suspension (prepared in Subheading 3.1.2) to Columns 1–23 of each assay plate with dispenser B.
6. Centrifuge the assay plates at 300 × *g* for 30 s to bring down cells to the bottom of each well.
7. Place assay plates in incubator I189.
8. Incubate assay plates at 37 °C in 5 % CO_2 with 95 % humidity overnight.
9. Repeat **steps 1–8** to seed cells in another set of 21 assay plates (or 20 plates for the last experiment of the 2nd HTS cycle).

Day 6 Compound treatment

10. Thaw 42 (or 41 for the 2nd HTS cycle) compound plates from the 25,000 Diversity Set (stored at −20 °C) at room temperature (*see* **Note 13**). Centrifuge each plate at 450 × *g* for 30 s to bring down liquid to the bottom of each well.
11. Remove the sealing foil of 21 compound plates. Record the plate IDs with a handheld bar-code scanner and input the

compound plate ID into a spreadsheet to be paired with the assay plates (*see* **Note 14**).

12. Place 21 (or 20 for the last experiment of the 2nd HTS cycle) compound plates in the stackers of Plate::Lift storage.

Perform **steps 13–17** by automation:

13. Add 5 μl of cell plate medium to Columns 1–22 of assay plates with dispenser A, to achieve a final volume of 25 μl in each well.
14. In dim light, transfer compounds from compound plates to assay plates with the 50 nl pin tool (11.26 μM of each compound should be added according to the pin tool calibration).
15. Add 5 μl 9-*cis*-retinal working solution (positive control) to Column 23 of assay plates with dispenser B. Shake the assay plates for 3 s to mix the compounds with medium.
16. Place the assay plates in incubator I189.
17. Place the compound plates back in the stackers of Plate::Lift storage.
18. Incubate assay plates at 37 °C in 5 % CO_2 with 95 % humidity overnight.
19. Seal the tested compound plates with sealing foil and re-store them at −20 °C.
20. Repeat **steps 11–19** to finish the treatment of another set of 21 assay plates (or 20 if for the last experiment of the 2nd HTS cycle) (*see* **Note 15**).

Day 7 luminescence reading

Perform **steps 21** and **22** by automation:

21. Add 25 μl β-Gal Assay Substrate Buffer to each well of assay plates under dim light.
22. Incubate the assay plates at 25 °C in incubator I30 for 60 min.
23. Take out the assay plates sequentially and read their luminescence with the Perkin Elmer EnVision detector (100 ms integration time).
24. Repeat **steps 21–23** to obtain luminescence readings for the 2nd set of 21 (or 20 for the 2nd HTS cycle) assay plates. In total, 42 out of the 83 compound plates from the 25,000 Diversity Set of compounds should be screened in the 1st HTS cycle.

Repeat Subheadings 3.1.2 and 3.1.3 to perform primary HTS for the other 41 compound plates of the 250,000 Diversity Set.

3.1.4 Data Analysis for Primary HTS Screen

1. Analyze the HTS screen data with Genedata Screener Assay Analyzer Software (10.0.2 Standard). Normalize the measured luminescence intensity to the controls for each assay plate. The normalized activity score (%) for compounds facilitating proper localization of P23H rhodopsin is calculated as shown in Table 1 (*see* **Note 16**).

Table 1
Calculation of normalized activity scores for the P23H opsin translocation HTS

Control	Measurement	Activity score (%)
Untreated control	Minimum amount of P23H opsin on the plasma membrane	0
Positive control (5 μM 9-*cis*-retinal)	Maximum amount of P23H opsin on the plasma membrane	100
$\text{Activity score of compound} = \frac{\text{Luminescence}_{\text{compound}} - \text{Luminescence}_{\text{untreated}}}{\text{Luminescence}_{9\text{-}cis\text{-retinal}} - \text{Luminescence}_{\text{untreated}}} \times 100\%$		

2. Calculate the HTS quality control parameters for each assay plate:

$$Z' = 1 - \frac{3 \times \left(\text{STD}_{\text{positive control}} + \text{STD}_{\text{untreated control}}\right)}{\left(\text{Mean}_{\text{positive contorl}} - \text{Mean}_{\text{untreated control}}\right)} \quad \textbf{(a)}$$

where STD represents the standard deviation of luminescence intensities and mean represents the average luminescence intensities:

$$\text{S} / \text{B ratio} = \frac{\text{Mean}_{\text{positive control}}}{\text{Mean}_{\text{untreated control}}}. \quad \textbf{(b)}$$

3. Export the results of normalized compound activity and quality control parameters from the Genedata Screener. Sort the data by activity score from high to low in Excel. Define "hits" as those with activity scores (%) equal or higher than 15. Import the data for hits (including their compound ID and activity score from the Genedata Screener) into Accelrys Pipeline Pilot software to incorporate the chemical structure, simplified molecular-input line-entry (SMILE) specification, and predicted physiochemical properties of hit compounds into the data set.

*3.1.5 Dose-Response Screen (See **Note 17**)*

Prepare compound plates for dose-response screen.

1. Based on the IDs of hit compounds, pull out the stock vials of these compounds in the UC Compound Collection. Transfer 40 μl of each hit (10 mM in DMSO) from the stock vial to a well in Column 1 or 11 of a 384-well Falcon polypropylene plate.
2. Add 20 μl of DMSO to Columns 2–10 and 12–20 and perform a twofold dilution of each compound. Use a multichannel pipette to transfer 20 μl of each compound from Column

1 to Column 2. Mix well by pipetting up and down 3 times. Then transfer 20 µl from Column 2 to Column 3, and so on, until each well of Column 10 is filled with 40 µl of diluted compound. Remove and discard 20 µl of liquid in each well of Column 10.

3. Repeat **step 2** to make a twofold dilution series for compounds in Columns 11.
   In summary, a dose-response compound plate is prepared by serial twofold dilution of each compound to achieve a total of ten concentrations.

Repeat steps in Subheadings 3.1.1–3.1.3 to perform the dose-response screen with freshly prepared compound plates. Instead of a 50 nl pin tool, use a 200 nl pin tool for compound transfer here to obtain higher concentrations for the dose-response curve. Each compound plate is tested in triplicate with three assay plates.

3.1.6 Data Analysis for Dose-Response Screen

1. Analyze the dose-response screen data with Genedata Screener Assay Analyzer Software (10.0.2 Standard). Normalize measured luminescence intensities to the controls for each assay plate as described in Table 1. Calculate Z' and the S/B ratio of each assay plate for quality control.
2. Generate a dose-response curve of each tested compound using Genedata Screener Condoseo Software (10.0.2 Standard). Use Smart Fit Model to fit the dose-response curves. Set S_{inf} and S_0 to +100 and 0, respectively (for definition of S_{inf} and S_0 *see* **Note 18**). Define AC_{50} value as the concentration of compound (µM) that causes an activity score of 50 (*see* **Note 19**).
3. Define the final hits as compounds with $AC_{50} \leq 100$ µM. Use Accelrys Pipeline Pilot software to incorporate their chemical structures and related properties (*see* **Note 20**).

3.2 The P23H Opsin Clearance HTS

The 10,000 Diversity Set includes 32 × 384-well compound plates which are separated into two cycles of HTS. Each cycle of HTS tests 16 compound plates.

3.2.1 Preparation for HTS

Follow procedures described in Subheading 3.1.1.

3.2.2 Cell Preparation

Day 1 Revival of frozen cells

1. Revive 3 vials of Hek293 mRHO(P23H)-RLuc total GPCR quantification cells (*see* **Note 21**) in 7 × 150 mm plates by procedures described in Subheading 3.1.2 *Day 1.*

Day 2 Replacement of cell growth medium

2. Follow procedures described in Subheading 3.1.2 *Day 2.*

Day 4 Preparation of cell suspensions for HTS plate seeding

3. Harvest confluent cells following procedures described in Subheading 3.1.2 *Day 5*. Count cells and dilute them to 25×10^4 cells/ml, so that the cell seeding number is 8,000 cells/well (32 μl/well). Prepare a total of 250 ml cell suspension in two sterile conical bottomed bottles (*see* **Note 22**).
4. Three days before the 2nd cycle of the primary HTS for P23H opsin clearance, revive 3 vials of P23H-RLuc Hek293 cells in 7×150 mm plates as described in **steps 1–3** (e.g., revive cells on *Day 4* if cells are to be seeded on *Day 7*).

3.2.3 Primary HTS Screen

Day 4 Cell seeding

1. Place 16 assay plates in the stackers of Plate::Lift storage.
2. Prime and fill the tubes of dispenser A with cell plate medium.
3. Prime and fill the tubes of dispenser B with the cell suspension prepared in Subheading 3.2.2.

   Perform **steps 4–9** by automation.
4. Add 8 μl of cell plate medium to Columns 1–22 of each assay plate with dispenser A.
5. Add 40 μl of cell plate medium to Column 24 of each assay plate with dispenser A.
6. Add 32 μl of cell suspension to Columns 1–23 with dispenser B.
7. Centrifuge the plate at $300 \times g$ for 30 s to bring down cells to the bottom of the plate.
8. Place assay plates in incubator I189.
9. Incubate plates at 37 °C in 5 % CO_2 with 95 % humidity for 24 h.

Day 5 Compound treatment

10. Thaw 16 compound plates from the 10,000 Diversity Set (stored at −20 °C) at room temperature. Centrifuge each plate at $450 \times g$ for 30 s to bring down liquid to the bottom of each well.
11. Tear off the sealing foil of 16 compound plates. Record the plate ID using a handheld bar-code scanner and input the compound plate ID into a spreadsheet to be paired with the assay plates.
12. Place 16 compound plates in the stackers of Plate::Lift storage.
13. Prime and fill the tubes of dispenser A with Evans Blue working solution and confirm that no air bubbles are visible in the dispensing tubes.

Perform **steps 14–19** by automation:

14. Transfer compounds from compound plates to assay plates with the 50 nl pin tool (final concentration of each compound should be 9.93 μM according to pin tool calibration).
15. Add 8 μl Evans Blue working solution to Column 23 with dispenser A.
16. Shake for 3 s to mix the compound with the medium.
17. Replace the compound plates in the stackers of Plate::Lift storage.
18. Replace the assay plates in incubator I189.
19. Incubate the assay plates at 37 °C in 5 % CO_2 with 95 % humidity for 24 h.
20. Bring out the compounds plates from stackers of Plate::Lift storage and cover them with sealing foil.
21. Re-store the 16 compound plates at −20 °C.

Day 6 Luminescence measurement

22. Prime and fill the tubes of dispenser A with 2 % DDM in PBS and confirm there are no air bubbles in any of the dispensing tubes (*see* **Note 23**).
23. Prime and fill the tubes of dispenser B with RLuc Assay Substrate Buffer (*see* **Note 24**).

Perform **steps 24–29** by automation:

24. Add 5 μl of 2 % DDM in PBS to Columns 1–24 of assay plates with dispenser A.
25. Shake each assay plate for 5 s to mix well.
26. Incubate assay plates at 25 °C in the I30 incubator for 5 min.
27. Add 5 μl of RLuc Assay Substrate Buffer (final concentration, 5 μM) to Columns 1–24 with dispenser B.
28. Shake each assay plate for 5 s to mix well.
29. Incubate assay plates at room temperature in the stackers of Plate::Lift storage for 60 min.
30. Take out the assay plates sequentially and read luminescence with the Perkin Elmer EnVision detector (100 ms integration time).

Repeat Subheadings 3.2.2 and 3.2.3 to perform primary HTS to test the remaining 16 compound plates in the 10,000 Diversity Set (*see* **Note 25**).

3.2.4 Data Analysis for Primary HTS

1. Analyze the HTS screen data with Genedata Screener Assay Analyzer Software (10.0.2 Standard). Normalize the luminescence intensity to the controls for each assay plate. Calculate the normalized activity score for each compound according to Table 2.

Table 2
Calculation of normalized activity scores for the P23H opsin clearance HTS

Control	Measurement	Activity score (%)
Untreated control	Unaffected amount of P23H opsin reporter signal	0
Evans Blue (200 μM)	Minimum amount of P23H opsin reporter signal	−100
$\text{Activity score of compound} = \frac{\text{Luminescence}_{\text{compound}} - \text{Luminescence}_{\text{untreated}}}{\text{Luminescence}_{\text{untreated}} - \text{Luminescence}_{\text{Evans Blue}}} \times 100\%$		

2. Calculate quality control parameters Z' and S/B values as described in Subheading 3.1.4.
3. Incorporate compound IDs, activity scores, chemical structures, and SMILEs into a list. Sort the data by activity score from low to high. Export the data as an Excel file. Hit compounds are defined as those with activity scores ≤ −50.

3.2.5 Hit Confirmation Screen

1. Generate compound plate maps on an Excel sheet. Based on the IDs of hit compounds, pull out the corresponding stock vials of hit compounds in the UC Compound Collection.
2. Transfer 20 μl of each hit compound (10 mM) into a well of a 384-well compound plate.

Repeat Subheadings 3.2.2 and 3.2.3 to perform the P23H clearance assay with freshly prepared compound plates. Each compound plate is tested in triplicate with 3 assay plates.

3.2.6 Data Analysis for Hit Confirmation Screen

1. Calculate the normalized activity score of each compound, Z' and S/B values as described in Subheading 3.1.4.
2. Calculate the average and standard deviation of the three activity scores for each compound.
3. Sort the data set by average activity scores from low to high. Select compounds with average activity scores ≤ −50 as confirmed hits.

3.2.7 Dose-Response Screen

1. Generate compound plate maps for dose-response screen. "Cherry-pick" confirmed hit compounds from hit compound plates used in Subheading 3.2.5 and transfer 18 μl of each compound into a well in Column 1 or 11 of blank compound plates. Add 18 μl of DMSO to Columns 1–20 and perform serial twofold dilutions of each compound as described in Subheading 3.1.5, **step 2**.

Repeat Subheading 3.2.2 and 3.2.3 to perform the P23H clearance assay with freshly prepared compound plates. Test each compound plate in triplicate with 3 assay plates.

3.2.8 Data Analysis for Dose-Response Screen

1. Analyze data and generate a dose-response curve for each tested compound as described in Subheading 3.1.6. Set S_{inf} and S_0 to −100 and 0, respectively.
2. Define the EC_{50} value as the concentration of the compound (μM) that causes an activity score of −50. Define the final hits as compounds with $EC_{50} \leq 20$ μM.
3. Use Accelrys Pipeline Pilot software to incorporate their chemical structures, SMILEs, and predicted chemical properties in an Excel file (*see* **Note 26**).

4 Notes

1. Protocol of DNA transfection with polyethylenimine (PEI).
   (a) Prepare a 150 mM NaCl solution. Filter the solution through a 0.45 μm filter in a tissue culture hood to sterilize it. Store at 4 °C.
   (b) Prepare a 1 mg/ml PEI solution. Add 33.75 mg PEI (Sigma-Aldrich) into 100 ml ddH_2O in a 250 ml glass beaker, and stir vigorously after the addition of 0.5 ml of 12.1 M HCl until all powder is dissolved. Adjust pH to 7 by careful titration with 10 M NaOH. Filter the solution through a 0.45 μm filter in a tissue culture hood and collect 10 ml aliquots in 15 ml conical tubes. Store at −20 °C.
   (c) Seed 0.5×10^6 Hek293 cells in a 6-well plate containing 2 ml of DMEM/10 % FBS medium 1 day before transfection and incubate plate at 37 °C in 5 % CO_2 with 95 % humidity in an incubator, so that the cells reach >90 % confluence.
   (d) Bring all reagents to room temperature prior to transfection.
   (e) Add 1 μg DNA to 100 μl of 150 mM NaCl solution in a sterile 1.5 ml tube and then add 8 μl of PEI solution to 92 μl of 150 mM NaCl solution in another sterile 1.5 ml tube (8 μl of PEI is added per 1 μg DNA; if the amount of DNA is increased, increase also PEI). Vortex both tubes briefly.
   (f) Add the 100 μl diluted PEI to the 100 μl DNA solution and gently mix by using a finger to tip the bottom of the tube. Let the mixture sit at room temperature for 15–30 min.
   (g) Add the 200 μl mixture of PEI and DNA to cells in a well of a 6-well plate drop by drop. Shake the plate gently. Incubate the plate at 37 °C in 5 % CO_2 with 95 % humidity.

2. Protocol for the generation of a stable cell line expressing the P23H opsin-RLuc recombinant protein.
   (a) After 2 days of transfection, subculture the cells from a 6-well plate in a 100 mm plate with DMEM + 10 % FBS + 500 μg/ml Zeocin (Life Technologies) for a week and incubate at 37 °C in 5 % CO_2 with 95 % humidity.
   (b) Count cells with a hemocytometer and seed 1,000 cells in a 100 mm plate in 15 ml of DMEM + 10 % FBS + 500 μg/ml Zeocin and incubate at 37 °C in 5 % CO_2 with 95 % humidity.
   (c) Positive cell clones should appear after 3–7 days. Pick up 10–20 clones with trypsin-immersed filter paper pieces (3 mm in diameter). Place each clone of cells in a well of a 24-well plate containing 1 ml DMEM + 10 % FBS + 500 μg/ml Zeocin solution and incubate 37 °C in 5 % CO_2 with 95 % humidity.
   (d) Select 10 clones after they reach 90 % confluence and subculture each clone in a well of a 6-well plate and a well of 96-well plate (20,000 cells/well). Cultures in the 6-well plate are for collection of a large amount of cells, whereas cultures in the 96-well plate are for positive clone confirmation. Incubate both plates at 37 °C in 5 % CO_2 with 95 % humidity overnight.
   (e) Test each clone for its RLuc activity by adding coelenterazine h (5 μM) (NanoLight Technology) and read luminescence intensity after 5 s with an integration time of 0.2 s. Retain only the RLuc positive clones (luminescence reading > 10^6 RLU) in the 6-well plate and subculture each clone in a 100 mm plate.
   (f) When each RLuc positive clone reaches confluence in a 100 mm plate, detach and resuspend cells of each clone in 10 ml DMEM in a 15 ml conical tube. Transfer 1 ml of cells from each clone into a 1.5 ml tube and pellet both the 1 ml and 9 ml fractions of cells with a 300 × *g* centrifugation. Remove medium from both tubes. Suspend the pellet from the 9 ml fraction in 0.9 ml DMEM + 10 % FBS + 10 % DMSO in a cryo-tube for storage. Freeze cells slowly in a Styrofoam box at –80 °C overnight. Then transfer the cryotubes to a liquid nitrogen tank for long-term storage.
   (g) Wash the cell pellet of each clone from the 1 ml fraction with PBS and resuspend in 50 μl PBS. Confirm the expression of P23H-RLuc by immunoblots using the cell lysates in 50 μl PBS. Use mouse monoclonal B6-30 antibody recognizing the N-terminus of rod opsin for immunoblotting. Select the positive clone with highest expression level of P23H-RLuc for large scale culture and assay optimization for the P23H opsin clearance HTS.

3. Each well requires 25 μl of substrate buffer. For an HTS assay of 25,000 compounds (83 plates), we need 25 μl × 384 × 83 = 796,800 μl = 796.8 ml of substrate buffer plus ~10 % dead volume (876.48 ml in total) in a 1 L glass bottle. Thus, we will add 876.48 ml × 4 % = 35.06 ml of Gal Screen Substrate and 841.42 ml of Gal Screen Buffer A to the solution in the 1 L glass bottle.
4. DMSO tolerance at concentrations ranging from 0.1 % to 1 % has been tested. The DMSO vehicle does not affect the assay performance within the test range.
5. The 25,000 and 10,000 Diversity Sets of the University of Cincinnati Compound Collection are representative subsets of its total number of ~340,000 compounds. Different Diversity Sets contain different compound collections, while each Diversity Set was designed to uniformly fill up the "drug-like" space.
6. Protocol of pin tool calibration.
   Liquid volumes and properties in an assay plate affect the volume of compounds transferred by a pin tool from a compound plate to an assay plate. Therefore, the pin tool needs to be calibrated under the same conditions used for the HTS experiments. For pin tool calibration prepare 10 mM Tamara stock solution dissolved in DMSO and use following plates: a 384-well, polypropylene, flat bottomed plate (BD Falcon) to represent a compound plate and a 384-well, polystyrene, black walled, ultra-clear bottomed plate (Greiner Bio-One) to represent an assay plate.
   (a) Prepare 10 ml of 50 μM TAMRA in DMSO by adding 50 μl of 10 mM TAMRA stock solution to 9.95 ml of DMSO in a 15 ml conical tube.
   (b) Add 15 μl of 50 μM TAMRA to a well of a 96-well plate containing 285 μl cell plate medium and prepare a twofold dilution series: Add 150 μl of cell plate medium to Wells A2–A10 of the same plate. Mix the solution in Well A1 and transfer 150 μl to Well A2 and mix well. Transfer 150 μl of solution in Well A2 to Well A3 and repeat this transfer-and-mix step from well to well, until Well A10 has 300 μl of diluted TAMRA. Discard 150 μl of solution from Well A10.
   (c) Add 25 μl of each dilution of TAMRA and cell plate medium in triplicate to a 384-well Greiner polystyrene plate (11 columns in total). Read fluorescence intensity at 530 nm/580 nm excitation/emission with a PerkinElmer Plate::Vision detector (1 % light intensity and a 200 ms integration time). Generate a standard curve. A linear correlation of fluorescence intensity vs. TAMRA concentration should be obtained.

(d) Dispense 20 μl of 50 μM TAMRA solution into all wells of a 384-well Falcon polypropylene plate to represent a compound plate.

(e) Dispense 25 μl of cell plate medium into all wells of a 384-well Greiner polystyrene plate to represent an assay plate.

(f) Transfer compounds from the compound plate to assay plate using a 50 nl or 200 nl pin tool.

(g) Centrifuge assay plates at $450 \times g$ for 30 s to bring liquid down to the bottom of the assay plate. Read fluorescence of the assay plate at 530/580 nm with a PerkinElmer Plate::Vision detector.

(h) Calculate the average concentration of TAMRA (xnM) in the assay plate by using the standard curve generated in **step** (**d**). Calculate the average pin tool transfer volume by the function: $y\text{nl} = 25\ \mu\text{l} \times (x)\ \text{nM}/50\ \mu\text{M}$. The average pin tool transfer volume is the calibrated pin tool volume and will be used to calculate the final concentration of a test compound. The final concentration of a test compound is $z\mu\text{M} = (y \times 10^{-3}\ \mu\text{l} \times 10 \times 10^{3}\ \mu\text{M})/(a\ \mu\text{l}) = 10y/a\ \mu\text{M}$, where "$a$ μl" is the total volume of liquid in each well of assay plate after compound treatment.

7. The β-Gal assay has been tested with cells seeded directly from thawed cryo-vials and also with cells revived and grown on 150 mm cell culture plates for one passage. The β-Gal assay data showed much less variation when the cells revived and grown for one passage were used.

8. For HTS screen of 25,000 Diversity Set (26,120 compounds in total), a total of 83 plates should be screened since each plate contains 320 compounds. The entire screen is divided into 2 cycles with each cycle further separated into two sets of automated experiments (21 or 20 plates per automated experiment). Each experiment needs 25 vials of cryo-frozen cells (4×10^6 cells/vial) that were revived and grown in 13 of 150 mm plates to reach confluence.

9. The timing for revived cells to reach confluence needs to be tested on-site before the HTS to ensure that enough cells are obtained at a scheduled time.

10. To prevent cells from dying or settling down, an autoclaved stir bar can be placed into the cell suspension bottle which is bathed in water at 37 °C in a glass beaker. Stabilize the water temperature with a heated plate and magnetic stirring.

11. The cell seeding number needs to be optimized during assay development. Cell numbers were tested from 1,000 to 10,000 cells/well under four conditions. Results showed that

5,000 cells/well provided the highest assay quality as suggested by Z' and S/B ratio values.

12. Each assay plate contains a lid. Thus, in the HTS program, assay plate lids are removed and replaced before and after each dispensing step.
13. Each 384-well compound plate has 320 compounds (10 mM in DMSO) in Column 1–20 (Fig. 2). A compound plate map contains information about compound IDs, compound position in the plate, and the plate bar code.
14. It is important to ensure that the bar code of a compound plate and the bar code of its corresponding assay plate match and are recorded correctly.
15. Do not open the door of incubator I189 after the end of Day 6, because the positive control 9-*cis*-retinal regenerates P23H isorhodopsin which is light-sensitive. Any leakage of light after treatment with 9-*cis*-retinal and before substrate addition will compromise assay quality.
16. If an obvious plate pattern is observed, e.g., very high or very low activity scores show up in several adjacent rows and/or columns of an assay plate, record the plate bar codes of the assay plate and the corresponding compound plate. Retest the compound plate at the end of the primary HTS.
17. A hit confirmation screen (single dose of each compound tested in triplicate) normally is performed after a single-point HTS to reduce the number of hits to be tested in the dose-response screen. However, the primary HTS of P23H translocation yielded only 16 hit compounds. Due to this low hit number, a dose-response screen was performed directly after the primary HTS screen.
18. S_{inf} is defined as infinite activity, namely, the fitted activity score at infinite test compound concentration, whereas S_0 is defined as zero activity, i.e., the fitted activity score at zero concentration. The Smart Fit Model automatically changes parameters of the Hill equation to optimize the fitting curve.
19. Due to cytotoxicity, atypical dose-response curves can be observed (Fig. 3) such as an increase followed by a decrease of activity score upon increasing dosage of a compound. Decreased activity scores due to cytotoxicity must be masked before curve fitting, as they will affect the dose-response curve.
20. The final hit compounds identified from HTS must be further validated by orthogonal screens and other assays to confirm their activity in correcting the P23H opsin localization. A neighboring search for selected hit compounds and activity tests of these similar compounds will enhance understanding

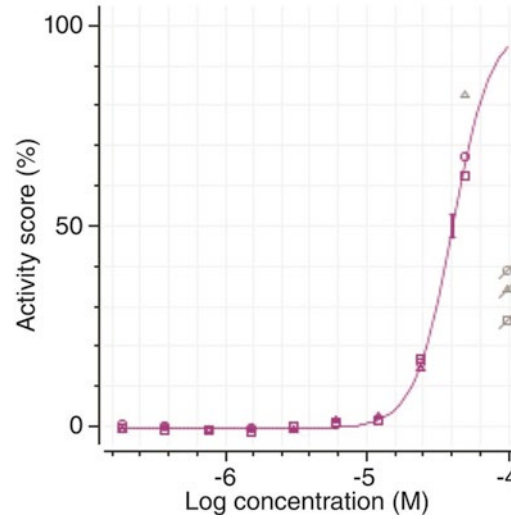

Fig. 3 Dose-response curve of a hit compound fitted by the Hill equation. Data points with reduced activity affected by cytotoxicity are masked (*gray*) and not included for curve fitting

of the structure-activity relationship (SAR) of the pharmacophore that is critical for lead optimization.

21. Each cryo-vial contains confluent cells harvested from a 150 mm plate.
22. For one cycle of primary HTS with 16 × 384-well assay plates, a total of 16 × 400 × 32 μl = 204,800 μl of cell suspension is expected to be dispensed. About 30 ml of dead volume will be needed for the dispenser. Therefore, a total of 250 ml of cell suspension should be prepared for seeding 16 assay plates.
23. Air bubbles are readily generated in DDM solutions. Thus, the 10 % DDM stock should be prepared at least a day before use, so that bubbles will have disappeared before the working solution is prepared. It also is important to make certain that there are no air bubbles in the dispenser tubes. Therefore, if air bubbles are observed, prime the dispenser with more DDM solution until they are washed out of the tubes.
24. Add 5 μl RLuc Assay Substrate Buffer working solution to each well. For 16 × 384-well plates (5 μl RLuc Assay Substrate Buffer per well) 16 × 400 × 5 μl = 32,000 μl = 32 ml plus about 6 ml dead volume, i.e., a total of 38 ml ViviRen working solution needs to be prepared.
25. Cells for the 2nd cycle of primary HTS should be revived on *Day 4*, so that cells are confluent on the 150 mm plates and ready for cell seeding immediately after the completion of the 1st primary HTS on *Day 7*.

26. RLuc is used as a reporter for P23H opsin clearance HTS. Compounds interfering with RLuc activity would be identified as hits as well [31]. Follow-up with a counter screen testing RLuc activity and a hit validation assay (such as immunoblotting) should be carried out to remove false positives.

References

1. Persidis A (1998) High-throughput screening. Advances in robotics and miniturization continue to accelerate drug lead identification. Nat Biotechnol 16:488–489
2. Carnero A (2006) High throughput screening in drug discovery. Clin Transl Oncol 8:482–490
3. Macarron R, Banks MN, Bojanic D et al (2011) Impact of high-throughput screening in biomedical research. Nat Rev Drug Discov 10: 188–195
4. Zoete V, Grosdidier A, Michielin O (2009) Docking, virtual high throughput screening and in silico fragment-based drug design. J Cell Mol Med 13:238–248
5. Caliandro R, Belviso DB, Aresta BM et al (2013) Protein crystallography and fragment-based drug design. Future Med Chem 5:1121–1140
6. Hoelder S, Clarke PA, Workman P (2012) Discovery of small molecule cancer drugs: successes, challenges and opportunities. Mol Oncol 6:155–176
7. Daiger SP, Bowne SJ, Sullivan LS (2007) Perspective on genes and mutations causing retinitis pigmentosa. Arch Ophthalmol 125: 151–158
8. Hartong DT, Berson EL, Dryja TP (2006) Retinitis pigmentosa. Lancet 368:1795–1809
9. Gorbatyuk MS, Gorbatyuk OS, LaVail MM et al (2012) Functional rescue of P23H rhodopsin photoreceptors by gene delivery. Adv Exp Med Biol 723:191–197
10. Gorbatyuk MS, Knox T, LaVail MM et al (2010) Restoration of visual function in P23H rhodopsin transgenic rats by gene delivery of BiP/Grp78. Proc Natl Acad Sci U S A 107: 5961–5966
11. Aguila M, Bevilacqua D, McCulley C et al (2014) Hsp90 inhibition protects against inherited retinal degeneration. Hum Mol Genet 23:2164–2175
12. Fernandez-Sanchez L, Lax P, Esquiva G et al (2012) Safranal, a saffron constituent, attenuates retinal degeneration in P23H rats. PLoS One 7:e43074
13. Vasireddy V, Chavali VR, Joseph VT et al (2011) Rescue of photoreceptor degeneration by curcumin in transgenic rats with P23H rhodopsin mutation. PLoS One 6:e21193
14. Fernandez-Sanchez L, Lax P, Pinilla I et al (2011) Tauroursodeoxycholic acid prevents retinal degeneration in transgenic P23H rats. Invest Ophthalmol Vis Sci 52:4998–5008
15. Rossmiller B, Mao H, Lewin AS (2012) Gene therapy in animal models of autosomal dominant retinitis pigmentosa. Mol Vis 18: 2479–2496
16. Wert KJ, Davis RJ, Sancho-Pelluz J et al (2013) Gene therapy provides long-term visual function in a pre-clinical model of retinitis pigmentosa. Hum Mol Genet 22:558–567
17. Petrs-Silva H, Linden R (2014) Advances in gene therapy technologies to treat retinitis pigmentosa. Clin Ophthalmol 8:127–136
18. Kaushal S (2006) Effect of rapamycin on the fate of P23H opsin associated with retinitis pigmentosa (an American Ophthalmological Society thesis). Trans Am Ophthalmol Soc 104:517–529
19. Noorwez SM, Malhotra R, McDowell JH et al (2004) Retinoids assist the cellular folding of the autosomal dominant retinitis pigmentosa opsin mutant P23H. J Biol Chem 279:16278–16284
20. Noorwez SM, Kuksa V, Imanishi Y et al (2003) Pharmacological chaperone-mediated in vivo folding and stabilization of the P23H-opsin mutant associated with autosomal dominant retinitis pigmentosa. J Biol Chem 278: 14442–14450
21. Chen Y, Jastrzebska B, Cao P et al (2014) Inherent instability of the retinitis pigmentosa P23H mutant opsin. J Biol Chem 289:9288–9303
22. Sung CH, Schneider BG, Agarwal N et al (1991) Functional heterogeneity of mutant rhodopsins responsible for autosomal dominant retinitis pigmentosa. Proc Natl Acad Sci U S A 88:8840–8844
23. Kaushal S, Khorana HG (1994) Structure and function in rhodopsin. 7. Point mutations associated with autosomal dominant retinitis pigmentosa. Biochemistry 33:6121–6128
24. Lin JH, Li H, Yasumura D et al (2007) IRE1 signaling affects cell fate during the unfolded protein response. Science 318:944–949
25. Mendes HF, van der Spuy J, Chapple JP et al (2005) Mechanisms of cell death in rhodopsin

retinitis pigmentosa: implications for therapy. Trends Mol Med 11:177–185

26. Saliba RS, Munro PM, Luthert PJ et al (2002) The cellular fate of mutant rhodopsin: quality control, degradation and aggresome formation. J Cell Sci 115:2907–2918
27. Sakami S, Kolesnikov AV, Kefalov VJ et al (2014) P23H opsin knock-in mice reveal a novel step in retinal rod disc morphogenesis. Hum Mol Genet 23:1723–1741
28. Sakami S, Maeda T, Bereta G et al (2011) Probing mechanisms of photoreceptor degeneration in a new mouse model of the common form of autosomal dominant retinitis pigmentosa due to P23H opsin mutations. J Biol Chem 286:10551–10567
29. Haeri M, Knox BE (2012) Rhodopsin mutant P23H destabilizes rod photoreceptor disk membranes. PLoS One 7:e30101
30. Zhang JH, Chung TD, Oldenburg KR (1999) A simple statistical parameter for use in evaluation and validation of high throughput screening assays. J Biomol Screen 4: 67–73
31. Auld DS, Southall NT, Jadhav A et al (2008) Characterization of chemical libraries for luciferase inhibitory activity. J Med Chem 51: 2372–2386

Chapter 25

Gene Therapy to Rescue Retinal Degeneration Caused by Mutations in Rhodopsin

Brian P. Rossmiller, Renee C. Ryals, and Alfred S. Lewin

Abstract

Retinal gene therapy has proven safe and at least partially successful in clinical trials and in numerous animal models. Gene therapy requires characterization of the progression of the disease and understanding of its genetic cause. Testing gene therapies usually requires an animal model that recapitulates the key features of the human disease, though photoreceptors and cells of the retinal pigment epithelium produced from patient-derived stem cells may provide an alternative test system for retinal gene therapy. Gene therapy also requires a delivery system that introduces the therapeutic gene to the correct cell type and does not cause unintended damage to the tissue. Current systems being tested in the eye are nanoparticles, pseudotyped lentiviruses, and adeno-associated virus (AAV) of various serotypes. Here, we describe the techniques of AAV vector design as well as the in vivo and ex vivo tests necessary for assessing the efficacy of retinal gene therapy to treat retinal degeneration caused by mutations in the rhodopsin gene.

Key words Rhodopsin, Subretinal injection, Intravitreal injection, Autosomal dominant retinitis pigmentosa, Mouse model, Adeno-associated virus, Inverted terminal repeat, Outer nuclear layer, Electroretinography, Optical coherence tomography

1 Introduction

Mutations in rhodopsin are rarely tolerated and often lead to rod photoreceptor apoptosis causing the disease retinitis pigmentosa (RP) [1, 2]. The death of the rod photoreceptors ultimately leads to the death of the cone photoreceptors causing near or total blindness [3]. Mutations in rhodopsin account for approximately 30 % of the cases of autosomal dominant retinitis pigmentosa (adRP) or approximately 10 % of the total population burden of RP [4]. In the USA, this could mean between 6,000 and 10,000 affected individuals. Fortunately, the human rhodopsin gene (*RHO*) and mouse rhodopsin gene (*Rho*) are highly conserved, suggesting that therapies validated in mouse models will have high translatability to humans (*see* **Note 1**) [5]. For these reasons, rhodopsin mutations are actively studied as a key candidate for gene therapy.

Beata Jastrzebska (ed.), *Rhodopsin: Methods and Protocols*, Methods in Molecular Biology, vol. 1271,
DOI 10.1007/978-1-4939-2330-4_25,

The eye is an excellent candidate for the evaluation of gene therapies because of the accessibility of the organ, the suppressed immune system of the uninjured eye, and the numerous quantitative and qualitative vision measurements available. Ocular gene therapy using AAV has already proven partially effective in clinical trials treating Leber congenital amaurosis type 2 (LCA2) patients [6–9]. In this case, a virus expressing a normal *RPE65* gene was delivered to patients by subretinal injection [8]. While light sensitivity was increased and patients reported improved vision, photoreceptors continued to degenerate even in the treated area of the retina, suggesting incomplete protection. AAV is well suited for ocular gene therapy due to its low immunogenicity and its many characterized serotypes which successfully transduce the retina [10]. AAV has a limited carrying capacity, however. Since recombinant genomes over 4.7 kb are not efficiently packaged in the viral capsid, several groups are attempting recombination strategies to overcome this limitation using simultaneous infection with two viruses [11–14].

Gene therapy for *RHO* mutations presents a more difficult problem than gene therapy for a recessive disease like LCA2. Because the mutations are most often dominant, it may be necessary to suppress the expression of the mutant *RHO* in addition to supplementing a wild-type *RHO*. This is a two-stage process: RNA inhibitors such as ribozymes or small interfering RNAs and transcriptional inhibitors containing zinc finger DNA-binding domains have been used to suppress endogenous *Rho* in rodent models [15–18]. This approach has been reviewed elsewhere [5]. Despite its limited genome size, recombinant AAV has sufficient capacity to carry a tissue-specific promoter, *RHO*, and microRNAs, shRNAs, or ribozymes if suppression plus supplementation of RHO is desired [16]. In addition, if therapeutic constructs can remain smaller than 2.5 kb, the use of self-complementary AAV can greatly enhance the rate of gene expression [19].

Subretinal injections are usually employed in order to achieve efficient transduction of photoreceptors. However, capsid modifications of AAV have permitted transduction of up to 25 % of photoreceptors in mice following intravitreal injections [20].

Here, we will discuss the methods necessary to design an AAV vector for the delivery of *RHO* plus and minus RNA inhibitors and necessary in vivo and ex vivo measurements to assess visual preservation. Basic procedures for electroretinography, optical coherence tomography, and optokinetic measurements have been well described in earlier papers, but our methods are summarized below [21–24].

2 Materials

2.1 Constructs

1. Target plasmid: Luciferase assay – psiCHECK™2.1 plasmid (Promega) expressing two luciferase genes, *Renilla* and firefly, with a 100 base pair region of *RHO* under the SV40 early enhancer/promoter. Western blot – plasmid expressing RHO under a ubiquitous promoter such as cytomegalovirus immediate early promoter (CMV) or the CMV/chicken β-actin hybrid promoter (CBA).
2. Knockdown plasmid: pSilencer expressing RNA knockdown method of interest, shRNA or ribozyme genes (Life Technologies), and pTR-UF11 expressing miRNA.
3. Control plasmid: expressing GFP and miRNA, shRNA, or ribozyme. GFP and RNA knockdown genes are expressed from separate promoters.

2.2 Screening Constructs

1. Lipofectamine 2000 kit.
2. HEK293 cells.
3. 24 well non-pyrogenic, polystyrene tissue culture plate (Costar).
4. Dual-Luciferase Reporter Assay System kit (Bio-Rad).
5. Luminometer.
6. DC protein assay (Bio-Rad).
7. iBlot Gel Transfer System (Life Technologies).
8. Odyssey Infrared Imaging System blocking buffer (LI-COR).
9. 1× phosphate buffered saline (PBS), 0.1 % Tween 20.
10. Anti-RHO primary antibody: (Abcam antibody ab5417) 1D4 for RHO C-terminus; B6-30 for N-terminus.
11. Anti-Rabbit IRDye secondary antibody (LI-COR).
12. Odyssey Infrared Imaging System (LI-COR).

2.3 Animal Preparation

1. 1 % atropine sulfate ophthalmic solution (Akorn).
2. 1 % proparacaine.
3. 10 % phenylephrine hydrochloride ophthalmic solution (Akorn).
4. 100 mg/ml TranquiVed xylazine (Vedco).
5. 100 mg/ml ketamine (Ketved).
6. 2 mg/ml yohimbine (Yobine Injection) (LLOYD).
7. 0.9 % sterile sodium chloride injection (saline) (Baxter, US).
8. Neomycin/polymyxin B/dexamethasone ophthalmic ointment (Akorn).
9. Lo-Dose™ 1/2cc U-100 Insulin Syringe 28½G.
10. Slide warmer (Fisher Scientific).

2.4 Subretinal Injection

1. Dissecting microscope.
2. Nikon NI-150 Fiber Optic Episcopic Illuminator (Nikon Instruments).
3. Micron 4 Microsyringe pump and controller (World Precision Instruments).
4. RPE injection kit (World Precision Instruments).
5. 10-μl NanoFil syringe (World Precision Instruments).
6. Gonak 2.5 % Hypromellose Solution (Akorn).
7. 30½-gauge disposable needles.
8. 33-gauge blunt needle.
9. 5-μl Hamilton syringe.
10. 10 % AK-FLUOR sodium fluorescein.

2.5 Ocular Coherence Tomography

1. SD-OCT Ophthalmic Imaging System (Bioptigen).
2. Systane Ultra Lubricant Eye Drops.

2.6 Electroretinography

1. UTAS visual diagnostic system with BigShot Ganzfeld (LKC Technologies).
2. Gonak 2.5 % Sterile Hypromellose Ophthalmic Demulcent Solution (Akorn).

2.7 Fundus Imagery

1. Micron III retinal Imaging Microscope (Phoenix Research Labs).
2. Gonak 2.5 % Sterile Hypromellose Ophthalmic Demulcent Solution (Akorn).

2.8 OptoMotry

1. OptoMotry system (CerebralMechanics).
2. OptoMotry VR 1.7.7 software.

2.9 Light Damage

1. Dual Gooseneck Fiber Optic Illuminator (AmScope.com).
2. Traceable light meter (Fisher Scientific).

2.10 Assessment of Gene Replacement

1. Razor blade.
2. RNA*Later*, RNA Stabilization Reagent (Qiagen).
3. RNAeasy Mini kit for total RNA purification (Qiagen).
4. iScript cDNA synthesis kit (Bio-Rad).
5. SsoFast EvaGreen Supermix, real-time PCR mix (Bio-Rad).
6. CFX96™ Real-Time system with C1000™ Thermal Cycler (Bio-Rad).

3 Methods

3.1 Adeno-Associated Vector Design

Vector design relies on an understanding of the disease progression and the genetic causation of the retinal degeneration in the chosen animal model.

1. A typical AAV construct consists of a therapeutic gene cassette flanked by viral inverted terminal repeats (ITRs) [25, 26] (*see* **Note 2**).
2. A rod photoreceptor specific promoter such as the proximal mouse or human opsin promoter is cloned upstream of the therapeutic cassette to suppress gene expression to the rod photoreceptors [27]. Depending on the method of degeneration, either a wild-type or a resistant *RHO* with a segment of the 5′ and 3′ untranslated region will be used as the therapeutic cassette. The resistant *RHO* is used for RNA replacement by containing changes in the *RHO* nucleotide sequence but not amino acid sequence to prevent knockdown of the injected *RHO*.
3. The resistant *RHO* is accompanied by either an miRNA in the 3′ UTR, an shRNA, or ribozyme under an additional promoter after the *RHO* SV40 poly-A sequence site (Fig. 1) (*see* **Note 3**).

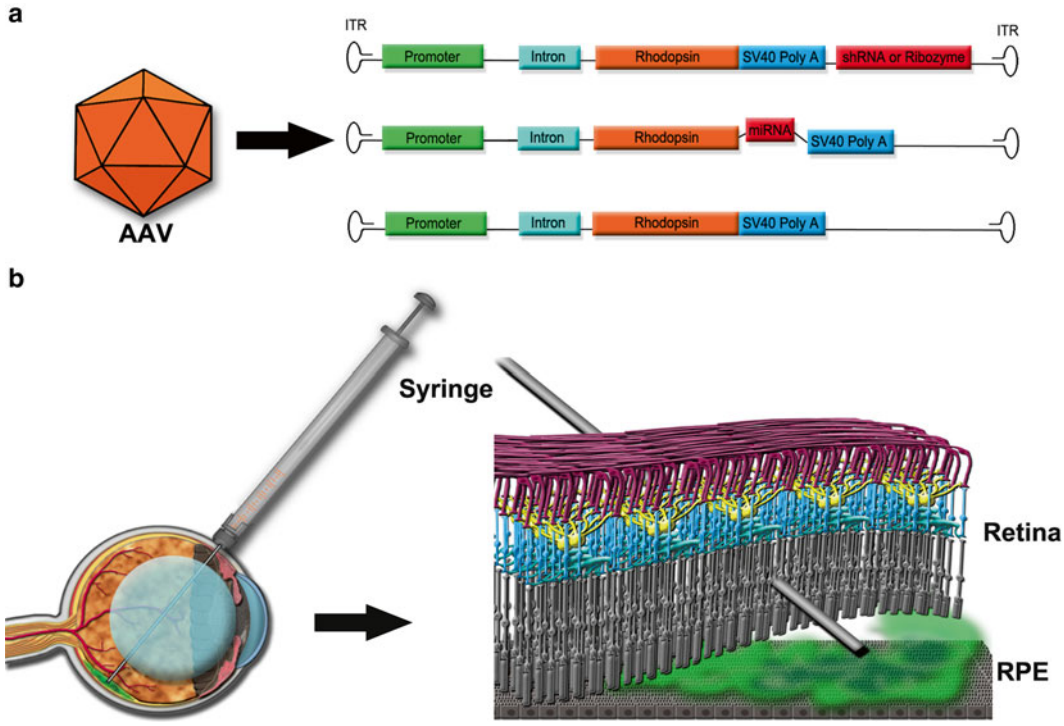

Fig. 1 Vector design and injection. (**a**) Typical AAV construct consisting of a promoter, intronic region, the gene of interest, and, optionally, a knockdown method. (**b**) Proper syringe location is at 45° angle to the cornea and inserted trans-scleral to deposit the virus subretinally

3.2 Screening Constructs

To assess the efficacy of the constructs created, it is necessary to quantify the knockdown of wild-type *RHO* and *Rho* as well as the resistance of the sequence-modified *RHO*. For this purpose, we transiently transfect either HeLa or HEK293 cells (*see* **Note 4**). Then we perform quantification assays, luciferase assay, Western blot, or RT-PCR (*see* **Note 5**).

3.2.1 Transfection

Three plasmids are necessary: (1) target plasmid, either encoding RHO or a reporter luciferase gene with linked target region (*see* **Note 6**); (2) plasmid encoding the knockdown instrument: miRNA, shRNA, or ribozyme; and (3) control plasmid expressing only GFP and miRNA, shRNA, or ribozyme. The plasmid containing the RNA knockdown instrument (miRNA, shRNA, or ribozyme) is transfected in increasing molar ratios to the target plasmid, from 2:1 to 6:1. Each ratio is run in replicates of six for both time points: 24 and 48 h. To control for differences in transfection, the control plasmid, expressing GFP, is used to ensure that all wells receive the same amount of plasmid DNA. In addition, the control plasmid is used to normalize the knockdown data in the final analysis (*see* **Note 7**).

1. Seed a 24-well plate with HEK293 cells (5×10^4 cells/well).
2. Begin transfection when the cells are 95 % confluent.
3. Mix the DNA to give 2 μg total DNA per well at the following ratios of target plasmid to knockdown agent (1:2, 4, 6). Fill the remaining DNA with a control plasmid, and set up a control ratio of target to control knockdown agent at (1:6). Perform all ratios with six replicates.
4. Transfection is performed utilizing Lipofectamine 2000 according to the manufacturer's instructions.
5. Collect the cells at 24 and 48 h time points by vigorously pipetting the media against the cells and transferring the detached cells into a 1.5-ml tube.
6. Pellet the cells and remove the media. Store cells at −20 °C. These cells contain the item to be measured, luciferase, protein, or mRNA.

3.2.2 Quantification Assays

Luciferase Assay

1. The psiCHECK™2.1 dual luciferase plasmid is used for the target plasmid. The psiCHECK™2.1 plasmid is engineered to contain a 100 bp section of *RHO* including the region targeted by the knockdown agent and is ligated between the *Renilla* stop codon and the poly-A site (*see* **Note 6**).
2. Use Dual-Luciferase Receptor Assay System kit to perform luciferase assay.
3. Prepare psiCHECK™2.1 transfected cell samples by resuspending the pelleted cells in 100-μl passive lysis buffer.

4. Place 20 μl of each cell lysate into an opaque 96-well plate, and then add 100 μl of buffer LAR II.
5. Read the luminosity for firefly luciferase, as no target is added to the firefly luciferase. The measured luminosity will serve as a control luciferase expression and loading control (*see* **Note 8**).
6. Add 100 μl of Stop & Glo to each well, and read *Renilla* luciferase activity. *Renilla* contains the *RHO* target region and will be reduced in expression by the knockdown agent (*see* **Note 9**). The ratio of *Renilla* to firefly luciferase normalized to control transfection will give the percent expression of luciferase.

Western Blot Assay

1. To quantify the expression of introduced *RHO* using Western blot assay, first determine the total protein concentration in lysed cell extract using Bio-Rad DC™ Protein Assay according to manufacturer's instructions.
2. Run 10 μg of protein on a 12 % acrylamide SDS-PAGE gel.
3. Perform protein transfer to PVDF membrane using the iBlot Gel Transfer System.
4. Once protein transfer is finished, wash the membrane in 5 ml methanol for 5 min, and then move it into a 10-ml Odyssey Infrared Imaging System blocking buffer for 1 h.
5. Add mouse monoclonal antibody (1D4 for RHO C-terminus; B6-30 for N-terminus) at a dilution of 1:800 directly to the blocking buffer, and incubate for 2 h at room temperature before removing the buffer and applying 3 times 5 min washes with PBS, 0.1 % Tween 20 solution.
6. Add the secondary anti-Rabbit IRDye antibody, and incubate for 1 h before again applying 3 times 5 min washes with PBS, 0.1 % Tween 20 solution.
7. The Western blot is then imaged and analyzed using the LI-COR Odyssey Infrared Imaging System.

Selected vectors are used for AAV production. Methods of AAV production and purification can be found in [28, 29].

3.3 Animal Preparation

Prior to performing subretinal injections, optical coherence tomography, electroretinography, or fundus photography, mouse eyes must be properly dilated. The necessary steps to prepare animals for injections or vision tests and procedures necessary to ensure animal recovery are listed below.

1. Begin dilation by administering one drop of 1 % atropine to both eyes of all mice. In 10 min, add one drop of 10 % phenylephrine hydrochloride ophthalmic solution to each eye of all mice. Repeat 10 % phenylephrine hydrochloride ophthalmic solution drops 3 times every 5 min.

2. Anesthetize each mouse with ketamine (72 mg/kg)/xylazine (4 mg/kg) intraperitoneally (*see* **Notes 10** and **11**).
3. Apply topical anesthetic to the cornea for procedures such as electoretinography or ocular injection.
4. Place one drop of neomycin/polymyxin B/dexamethasone ophthalmic ointment on each eye.
5. Once the procedures are finished, administer yohimbine (0.2 mg/kg) and 0.9 % saline (25 μl/g).
6. Place the mice on a 37 °C heating pad until the mouse has recovered as evidenced by full return of mobility.

3.4 Subretinal Injection

AAV transduction of rod photoreceptors relies on a successful subretinal injection. Placement of the AAV between the photoreceptors and retinal pigmented epithelium greatly increases viral uptake and gene expression in the photoreceptors. However, retinal detachment occurs which increases the risk of retinal damage (Fig. 1).

1. Load a 33-gauge blunt needle 5-μl Hamilton syringe with 1 μl of vector suspension (10^9 viral particles) with 0.5 % fluorescein.
2. Apply one drop 2.5 % hypromellose solution to the dilated eye to maintain ocular lubrication and clarify visualization of the eye (*see* **Note 12**).
3. Using forceps, place on either side of the eye, and apply gentle outward pressure to better open the eye and cause the eye to move slightly out.
4. Under a dissecting microscope, use a 30½-gauge disposable needle to puncture a hole in the sclera of the dilated eye. The needle is withdrawn once the full bevel end of the needle has entered, as placing the needle too far can damage the lens or the retina (*see* **Note 13**).
5. The 5-μl Hamilton syringe is guided through the hole parallel to the table on which the mouse is resting. Once in, the syringe is moved to 45 °C to the plane of the table to better target the anterior retina.
6. Once the needle makes contact with the opposing retinal surface, the virus may be delivered via manual pushing of the plunger by an assistant or by automated injection (*see* **Note 14**).
7. For manual injections, have an assistant gently push down on the syringe plunger for approximately 30 s to expel the virus while resisting any movements in the Hamilton syringe. Hold the plunger for 5 s after all viruses have been expelled before gently releasing (*see* **Note 15**).

Alternatively, an automated injector pump and controller may be used at this step (**steps 8–11**).

8. Prime the NanoFil™ syringe by first assembling the syringe according to manufacturer's instructions and then loading the syringe with 5 μl of saline. Attach the RPE injection kit to the syringe, and discharge the saline and attach the syringe to the Micron 4™ Microsyringe pump and controller.
9. Turn on the Micron 4™ Microsyringe pump, and set up the injection parameters for the output number corresponding to the output port the syringe is connected to. Select "W" in the first field for withdrawal to load the syringe. The withdrawal rate is set to 407 nl/s. Set the volume to 1,000 nl and the device type to "L."
10. Place the syringe tip in the virus and press the "RUN STOP" button. Once loaded, change the syringe settings to "I" for inject, rate 34 nl/s.
11. Follow **steps 2–5**. Once the needle makes contact with the posterior retina, press the foot pedal to start the injection.

3.5 Ocular Coherence Tomography

Ocular coherence tomography (OCT) uses constructive and deconstructive interference of a near infrared laser to obtain a live image of retina morphology without causing harm to the retina. Information gathered from the image can be used to measure changes to the outer segment layer over time (Fig. 2). Primary scans of each mouse also serve as a means to remove mice from the study that have damaged or detached retinas due to the subretinal injection (*see* **Notes 16** and **17**).

1. Switch on the power supply and computer.
2. For first time use, select the "Study" tab and "Add Study." Input the study name and click "Create Treatment Arm" to specify individual treatments that will be tested before selecting "Save Changes."
3. Select the "Patient/Exams" tab, and then "Setup Examiners & Physicians" icon to input the name of the individuals conducting the exam and the principle investigator.
4. Click the "Add Patient" icon to add mice to the study or select an individual mouse from the list that has already been added.
5. Once the mouse has been input into the database and selected, click on the "Add Exam" followed by "Begin Exam" icon. This will automatically load the "Imaging" tab.
6. Select the create custom scan icon and create two high-resolution scans for aiming and two lower-resolution scans for averaging, one each for OD (right eye) and OS (left eye). The scan parameters are as follows:
7. Click on the "Aiming" icon to ensure proper retina positioning and focus. This is achieved with the aid of one B-scan along each the X- and Y-axis. The mouse positioning is adjusted

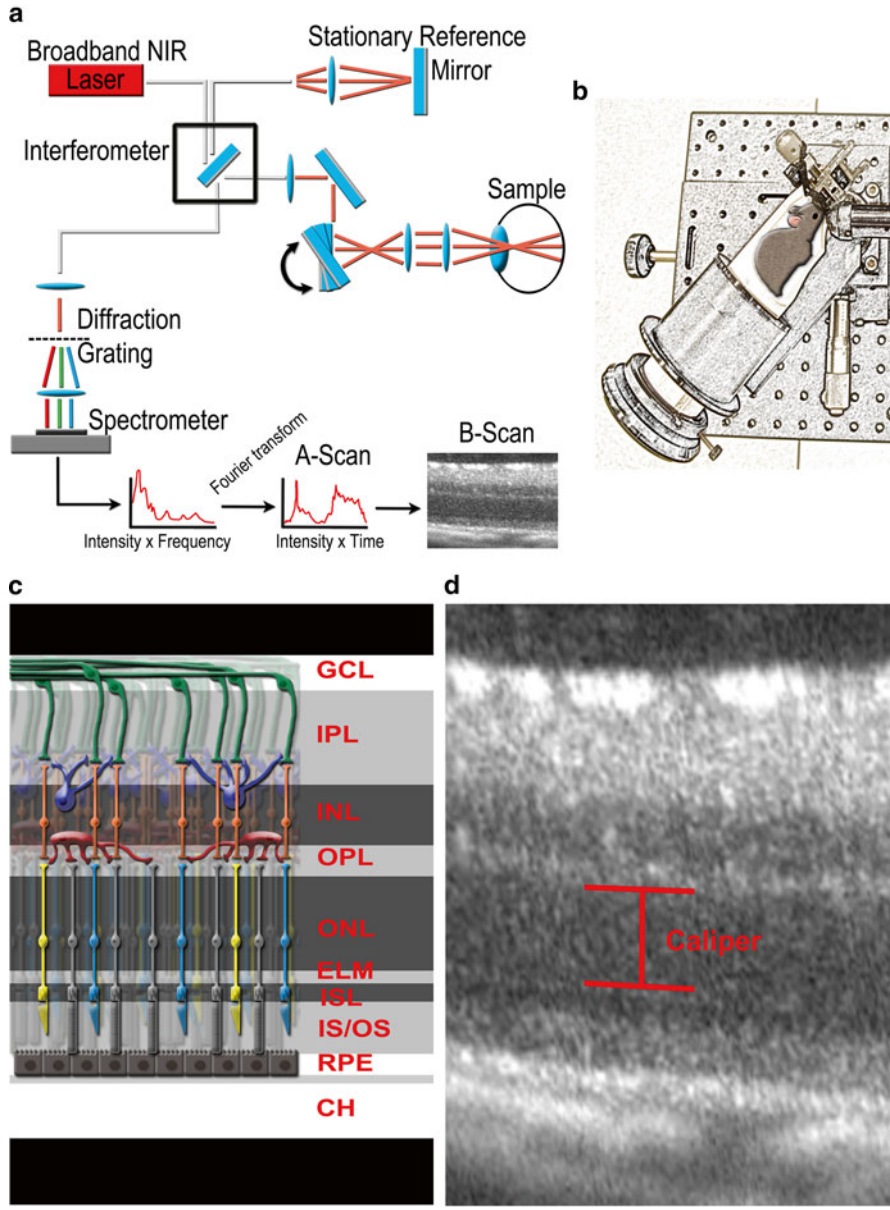

Fig. 2 Optical coherence tomography. (**a**) Illustrated overview of the operational principle of spectral domain OCT. OCT builds an image of changes in refractive indexes and the depths of these changes in a sample using constructive and deconstructive interference of a broadband near infrared laser centered at 840 nm. The resulting intensity by frequency data is then converted using a Fourier transformation and graphed as intensity by time. Each point of data is called an A-scan. A linear cross section of the eye is built by compiling several A-scans to form a B-scan. (**b**) Proper placement of the mouse. Central animal tube rotated to 45° and base at 120° from laser. (**c**) Representation of the cell layers represented in an OCT B-scan. (**d**) The outer nuclear layer is measured using calipers to follow changes in thickness over time

until the focus centered the retina on the *X*-axis, and each of the axis B-scans is horizontal.

8. After aiming, click "Stop Aiming" and perform "Free Run" to position the optic nerve at coordinates (0, 0) using the fundus view. This is accomplished through using the different axis control knobs on the mouse platform.
9. Stop the high-resolution scan and "Abort scan." The high-resolution scan is used for aiming and can be deleted to avoid excess data storage.
10. Click "Free Run" to start the lower-resolution averaging scan and immediately click "Stop Free Run" and "Save scan."
11. Repeat **steps 7–10** for the left eye.
12. After all mice have been scanned, load OCT data for each mouse, and average the data in the "Imaging" tab.
13. Using the caliper tool, take measurements from four points around the optic nerve (0, 0) at (2, 0), (0, –2), (–2, 0), and (0, 2). Average all control versus experimental measurements (*see* **Note 18**).
14. Take several representative images of the retina with caliper and save as Bitmap files.

3.6 Electroretinography

Electroretinography (ERG) measures the electrical response generated by the retina in response to flashes of light. The resulting waves of hyper- and hypo-polarization of the retina provide information of rod, cone, and bipolar cell function (Fig. 3).

1. Place the animals to be measured in the dark for 2–16 h prior to the ERG.
2. Turn on the MGIT-100 power supply, computer, and UTAS system.
3. Unplug the UBA-4204 Patient Amplifier and Interface from the charger and power on.
4. When the operating system starts, the EMWIN software will automatically load.
5. For first time use, it will be necessary to create a database into which the waveforms and a protocol will be stored.
6. To create a database, click on "Utilities," "Create New Database," and "Standard Database." Finally, enter the desired name and click "OK."
7. For protocol creation, begin by selecting "Protocols" and "Create New Protocol." Click "Add a Step" and add two steps for three total steps. For light-sensitive models of retinal degeneration, the light intensities are as follows, –40, –30 dB, –20 dB, and –10 dB, while non-light-sensitive models will be tested using –30 dB, –20 dB, –10 dB, and 0 dB flashes (s*ee* **Note 19**). The complete list of settings is presented in Table 1.

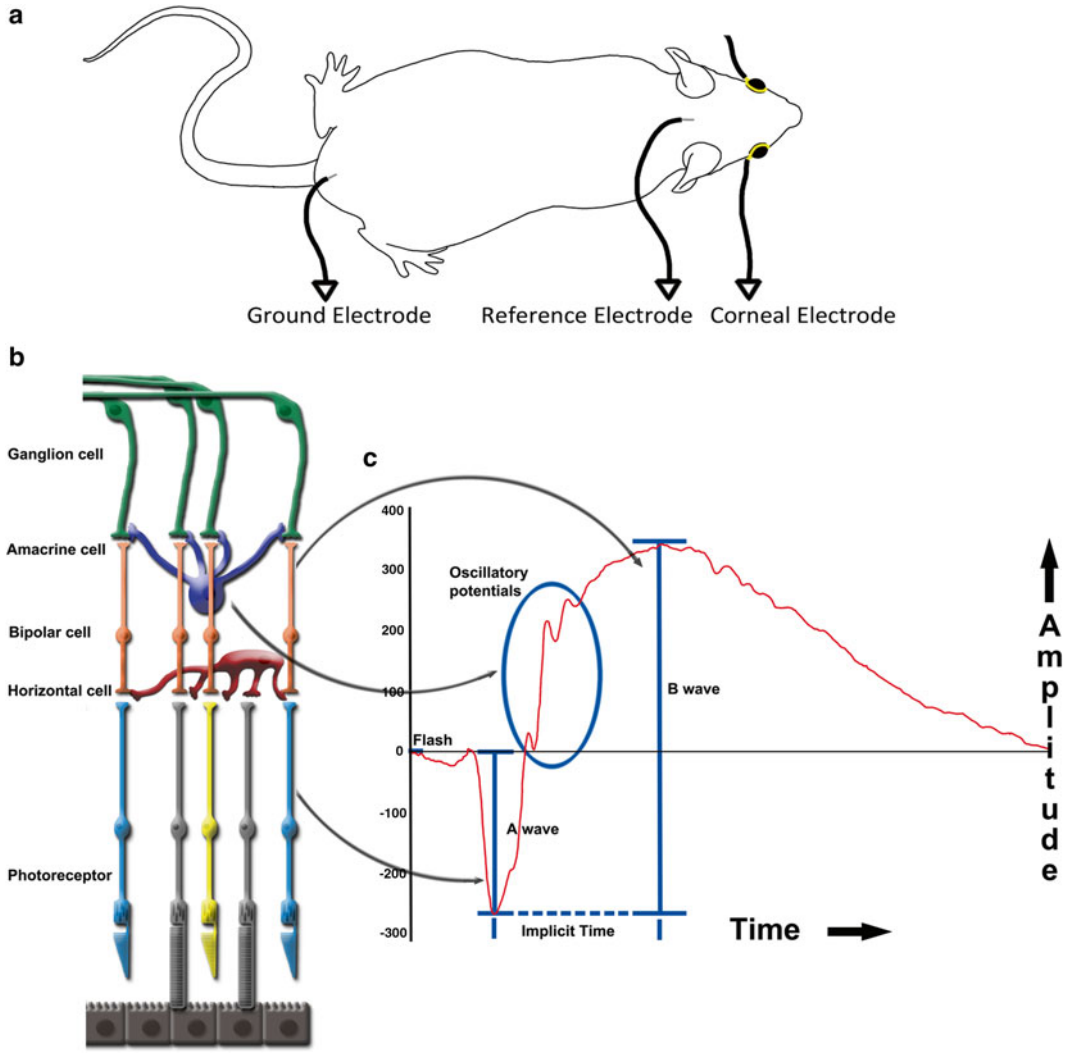

Fig. 3 Electroretinography. (**a**) Proper electrode placement with electrode centered and surrounding the cornea. (**b**) Different cell types each contribute different components of the recorded ERG. (**c**) Measured from the recorded ERG are the a-wave, b-wave, and the implicit time. The amplitude of the a-wave is measured from the baseline to the maximum negative deflection, while the amplityude of the b-wave is measured from the a-wave maximum to the peak of the b-wave in the positive direction.

8. If all previous setup has been done, select "Utilities," click on the existing database from the provided list, and select "OK."
9. Anesthetize 1–3 mice 5 min before performing the ERG according to the animal preparation section.
10. While the first mouse is anesthetized, select "Tests" from the main menu, "User-Defined Protocol," and the created protocol.
11. The mouse number must now be entered including mouse ID, treatment, and any additional information before selecting "Continue."

Table 1
Electroretinography protocol design

Tab		Scan intensity	
		Low	**High**
Averaging	Number of signals to average	5	5
	Time between stimulus (seconds)	5	60
	Sweeps before update	5	5
Sunburst flash	Test type	Single flash	Single flash
	Intensity	–40, –30, –20, –10 dB	0 dB
	Custom color	0.329, 0.329	0.329, 0.329

12. Click "Continue on Channel Information" window to bring up the exam window.
13. Place the anesthetized mouse on the mouse platform, and apply one drop 2.5 % hypromellose ophthalmic solution to each eye. Then place the reference electrode in the mouse tail or posterior, recording electrode on the head and contact electrodes on the appropriate eye (*see* **Note 20**) (Fig. 3).
14. Slide the plate into the Ganzfeld dome.
15. Select the "Baseline icon" on the parameters toolbar. The two lines are recording from each eye and should be near flat. If large oscillations are observed, check and reposition electrodes as needed until the baseline is corrected (*see* **Note 21**).
16. Select "Record," save icon on parameters toolbar, "Store All Waves" and "Next Step."
17. Repeat **step 16** until all three steps are completed before clicking main menu icon on the parameters toolbar.
18. The mouse can now be removed and treated according to Subheading 3.4, and the protocol can be repeated for any subsequent mice.
19. Once completed, analysis of the raw data can be conducted using the supplied software or by first clicking "Reports" and "Export Waves" and selecting all desired waveforms before naming and saving the file. All waveforms will now be in the Exported waves folder as a .CSV file and can be analyzed with spreadsheet software to find the a-wave and b-wave amplitudes (Fig. 3).
20. To complete ERG, shut down the computer and UTAS system first. Turn off the UBA-4204 Patient Amplifier and plug back into the charger. Leave on the MGIT-100 power supply to charge the UBA-4204 Patient Amplifier. Clean the acrylic contact lens electrodes with a mixture of 1:1 liquid detergent and sterile water, and then rinse with sterile water.

3.7 Fundoscopy

Fundoscopy assesses gross changes in retinal structure due to degeneration including pigmentary deposits, yellowing of the retina, and changes in blood vessel structure. It also provides qualitative measures of viral transduction via GFP expression.

1. Power on the computer, light box, and the light.
2. Set the microscope to utilize white light by turning both filters to setting 1.
3. Open the program "Micron III imaging."
4. For first time use, set up the program by selecting "Steam pix settings" icon and select "Works space" to change location to autosave data. Under "Recording," select "Auto-create a sequence file in RAM" and click "OK."
5. Prepare the mice and anesthetize one mouse at a time according to Subheading 3.3.
6. Once anesthetized, place the mouse on the positioning plate, and administer one drop of 2.5 % hypromellose ophthalmic solution (*see* **Note 22**).
7. Slowly bring the microscope to the eye. Adjust focus while bringing the microscope closer to the mouse eye, and reposition the mouse as needed to position the optic nerve in the center of the image.
8. Click the "Snap" icon and then the "TIFF" icon to save the image as a .tiff file.
9. For qualitative measurement of viral transduction using fluorescent proteins, the light settings may now be changed. Additionally, fluorescein may be administered to observe retinal vasculature.

3.8 OptoMotry

1. Turn on computer and camera. Start the OptoMotry VR 1.7.7 software.
2. To calibrate the system, press the button with a cross on top of a circle. Once that icon appears on the screen, place the mouse cursor on the black dot of the pedestal. Move the mouse cursor from the black dot to the black circle on the pedestal. Make sure the red circle meets the black circle. Once these two circles are aligned, hit the button with a cross on top of a circle so the icon disappears.
3. To conclude the calibration process, press the button that looks like a star (five lines coming together at one point). This icon is referred to as the OptoMotry cursor. Move this cursor to different positions on the screen. While the cursor is located at different positions, look at the widths of the black and white bars that appear on the computer screens within the OptoMotry system. The bars should get thinner if the cursor is in close

proximity and wider if the cursor is further away. For example, if the cursor is placed on the right side of the screen, the white and black bars that appear on the right OptoMotry screen should be thin, whereas the bands on the left OptoMotry screen should be wide. If the band sizes don't change as the cursor is moved, restart the machine.

4. To test spatial frequency, click the stimulus tab then the gratings tab. Set spatial frequency to 0.042c/d, contrast to 100 %, and the drift speed to 12 d/s. Then press the testing tab and the psychophysics tab. Under psychophysical methods, chose simple staircase; under directions, chose randomized/separate; and under threshold, chose frequency (*see* **Notes 23** and **24**).
5. To test contrast sensitivity, press the stimulus tab then the gratings tab. Set the spatial frequency to 0.128c/d (or a value the mouse model being tested responds to), contrast to 100 %, and the drift speed to 12 d/s. Press the testing tab and the psychophysics tab. Under psychophysical methods, chose simple staircase; under directions, chose randomized/separate; and under threshold, chose contrast.
6. Press the compass button. The compass will indicate which direction the bars are moving on the OptoMotry screens. Customize the compass by pressing the camera tab then the overlays tab. Change compass size, cursor size, tick spacing, and tick size to a helpful setting.
7. Place the first mouse on the pedestal within the OptoMotry system. If the mouse jumps off the pedestal, pick it up and put it back on the pedestal (*see* **Note 25**).
8. Place the OptoMotry cursor (the compass will move too) in between the mouse's ears. It is best to line up the cursor with the nose of the mouse.
9. Once the cursor is in alignment with the mouse's head, release the computer mouse so the gratings appear, and determine if the mouse tracks. Tracking is defined as a small and steady head movement in the direction of the gratings. The mouse is tracking if the mouse's nose and ears move in the same direction of the compass. If the compass is moving clockwise, left eye function is being analyzed. If the compass is moving in a counterclockwise direction, the right eye function is being analyzed.
10. If the mouse tracks, press the Yes button. If mouse does not track, press the No button.
11. The next step in the simple staircase test will populate after pressing yes or no. Keep testing the mouse's tracking until you cannot press yes or no, and the done button is highlighted.
12. The results will populate in the results tab. A CW (right) value and a CCW (left) value will be given. CW (right) means

clockwise; the gratings were moving to the right so left eye function was measured. CCW (left) means counterclockwise; the gratings were moving to the left so right eye function was measured.

13. When the test of one animal is finished, take it out and place the next animal on the pedestal. Press the Reset button to start the test over for the next animal.
14. Save results, close software, and shut down machine.

3.9 Methods in Light Damage

Some mouse models, such as those containing *Rho* I307N, suffer rapid retinal degeneration in response to intense light. The following methods describe how to use a light damage model to assess the effectiveness of a gene therapy.

1. Prior to light damage, perform a pre-injury damage assessment of retinal function and structure with both an ERG and OCT using the above methods.
2. Follow the methods described in Subheading 3.3 to ensure the eyes are properly dilated and the mouse is properly anesthetized.
3. Using the Traceable light meter, dial the light intensity knob on the AmScope.com Dual Gooseneck Fiber Optic Illuminator until light intensity reaches 10,000 cd·sr/m^2 (*see* **Note 26**).
4. Place the mouse between the two fiber optic illuminators so each eye is perpendicular to the light source and equidistant.
5. Subject the eye to 3 min light exposure.
6. Following light exposure, treat the recovering mouse as described in Subheading 3.3.
7. One week post-light damage, assess retinal structure and function by ERG and OCT. The precise preservation of retinal function can now be calculated as a percent post- to pre-light damage.

3.10 Assessment of Gene Replacement

Real-time PCR is employed to assess changes in gene expression for validation and quantification of gene replacement. First, primers capable of distinguishing viral-mediated *RHO* expression from native *Rho* expression are designed. At postnatal day 15, 8 mice receive a subretinal injection of the experimental treatment according to Subheading 3.4. At the first month postinjection, retinas are collected. RNA extraction is performed using the Qiagen RNAeasy Mini kit and the cDNA created by using the Bio-Rad cDNA synthesis kit. Finally, once the cDNA is created, the SsoFast EvaGreen® Supermix is used in setting up the samples for RT-PCR. After running a standard RT-PCR reaction, analyzing the results can be done using the software with the RT-PCR thermocycler (*see* **Notes 27** and **28**).

1. For removal of the mouse retina, first euthanize the mouse using CO_2 followed by cervical dislocation.

2. Cut horizontal along the border between the limbus and sclera using a razor blade.
3. Apply gentle pressure with forceps and pull and move the forceps toward the limbus.
4. The lens will come out along with a white or pinkish material which is the retina. Immediately place the retina in 30 μl of RNA*Later*, and store in −20 °C for immediate use or −80 °C for long-term storage.

4 Notes

1. Mouse rhodopsin is abbreviated *Rho* for the gene and Rho for the protein, whereas human rhodopsin gene is *RHO* and the protein is RHO.
2. Maintaining the ITRs is essential for high-yield vector packaging. To maintain the ITRs, grow the cells at 30 °C and for no more than 16 h. Following each cloning step, the ITRs should be checked using digestion with an appropriate restriction enzyme (usually Xma1 for AAV 2 ITRs). There is increased difficulty maintaining the ITRs during the construction of a self-complementary AAV; therefore, it may be necessary to grow the cells for as short as 10–12 h.
3. Check all knockdown methods using a BLAST search on NCBI to ensure low homology with other rod photoreceptor genes. Additional genes, such as cone opsins, may need to be checked if using a nonspecific cell promoter. In addition, search engines are available for siRNA design, and these frequently identify siRNAs with "seed matches" in the 3′ end of unintended target genes. Avoiding such siRNAs can avoid off-target effects caused by the miRNA pathways. Even after checking the sequence, all knockdown agents should be tested in the model organism to ensure that there are no serious off-target effects.
4. The cell passage number can affect knockdown results. Therefore, all knockdown experiments should be performed in cells at a similar passage number. In addition, all samples of any knockdown method should be run at the same time to avoid variation in transduction efficiency.
5. To analyze knockdown using RT-PCR assessment of changes in mRNA of RHO knockdown, *see* Subheading 3.10.
6. The knockdown target regions should be placed in the center of the 100 bp region inserted into the dual luciferase plasmid. This will provide sufficient RNA structural context to properly assess knockdown in the full length mRNA. Do not exceed more than a 300 bp segment as this greatly reduces the luciferase expression.

7. Twenty-four hours after transfection, the efficiency of transfection can be determined using the 1:6 target plasmid to control GFP as the marker for successfully transfected cells by comparing that to the total number of cells in the well.
8. Measuring of the firefly luciferase should start 90 s after adding LAR II to allow for peak luminance.
9. Add LAR II and Stop & Glo buffers to only six samples at a time to prevent signal loss before samples are read.
10. An anesthetized mouse will typically afford 40–60 min toward a procedure before recovering from the anesthesia.
11. If a boost of anesthesia is required, use only ketamine and not the ketamine/xylazine mixture.
12. In light-sensitive mouse models, dilation may be avoided, and injections should be performed in lights containing red light filters. The increased difficulty of these injections invariably leads to more retinal detachments reducing the efficiency of the injections and requiring additional mice.
13. After each mouse, discard the 30½-gauge needle.
14. The fluorescein can be visualized under the microscope and serves as an aid in determining viral location. If there is an initial bright green diffuse cloud seen through the cornea, the injection has gone into the vitreous. A proper subretinal injection will show a pale green glow along the inferior portion of the eye.
15. Stopping and starting of the manual injection should be very slow as to avoid either damage to the retina or a vacuum that could remove viral particles.
16. Given the angles used in scanning the eye, it is advisable to restrain the mouse with an elastic band across the mouse abdomen and around the bioptogen animal tube.
17. Begin imaging of the retina soon after the mouse is anesthetized, and complete all scans in approximately 10 min. After this time, the cornea will begin to cloud and obscure imaging.
18. Averaging the image is optional but provides for a much clearer image.
19. Using the Fisher Scientific™ Traceable® light meter, the −30, −20, −10, and 0 dB instrument settings correspond to a light intensity of 1, 6, 55, and 322 cd·sr/m^2, respectively.
20. The anesthesia and long scan times make the mice more susceptible to hypothermia. It is, therefore, recommended to use a heating pad (37 °C) on the mouse platform during the ERG.
21. Ensure the recording amplifier is utilizing direct current during the ERG as the alternating current can influence the ERG recordings.

22. Begin imaging of the retina soon after the mouse is anesthetized, and complete all scans in approximately 10 min. After this time, the cornea will begin to cloud and obscure imaging.
23. OptoMotry is useful primarily for assessing photopic vision.
24. Due to the bright screens used for OptoMotry, non-light-dependent degeneration *RHO* mouse models should be used. If light-dependent models are needed, assess just before euthanasia.
25. Mice do not require any preparation prior to OptoMotry testing. Make sure mouse eyes have not been dilated in the past 7 days.
26. It may be necessary to test several light intensities prior to injection of the treatment as successive breeding and background strain used may influence light damage susceptibility.
27. Primers designed to target the 3′ UTR can easily distinguish the endogenous mouse *Rho* and the human transgene *RHO*. There are also sufficient nucleotide differences to separate human *RHO* from mouse *Rho*.
28. If possible, design all primers to anneal at the same temperature. This will allow all reactions to be run at the same time.

References

1. Athanasiou D, Aguila M, Bevilacqua D et al (2013) The cell stress machinery and retinal degeneration. FEBS Lett 587:2008–2017
2. Mendes HF, van der Spuy J, Chapple JP et al (2005) Mechanisms of cell death in rhodopsin retinitis pigmentosa: implications for therapy. Trends Mol Med 11:177–185
3. Komeima K, Rogers BS, Lu L et al (2006) Antioxidants reduce cone cell death in a model of retinitis pigmentosa. Proc Natl Acad Sci U S A 103:11300–11305
4. Bowne SJ, Sullivan LS, Koboldt DC et al (2011) Identification of disease-causing mutations in autosomal dominant retinitis pigmentosa (adRP) using next-generation DNA sequencing. Invest Ophthalmol Vis Sci 52:494–503
5. Rossmiller B, Mao H, Lewin AS (2012) Gene therapy in animal models of autosomal dominant retinitis pigmentosa. Mol Vis 18: 2479–2496
6. Cideciyan AV, Hauswirth WW, Aleman TS et al (2009) Human RPE65 gene therapy for Leber congenital amaurosis: persistence of early visual improvements and safety at 1 year. Hum Gene Ther 20:999–1004
7. Cideciyan AV, Hauswirth WW, Aleman TS et al (2009) Vision 1 year after gene therapy for Leber's congenital amaurosis. N Engl J Med 361:725–727
8. Hauswirth WW, Aleman TS, Kaushal S et al (2008) Treatment of leber congenital amaurosis due to RPE65 mutations by ocular subretinal injection of adeno-associated virus gene vector: short-term results of a phase I trial. Hum Gene Ther 19:979–990
9. Al-Saikhan FI (2013) The gene therapy revolution in ophthalmology. Saudi J Ophthalmol 27:107–111
10. Alexander JJ, Hauswirth WW (2008) Adeno-associated viral vectors and the retina. Adv Exp Med Biol 613:121–128
11. Trapani I, Colella P, Sommella A et al (2014) Effective delivery of large genes to the retina by dual AAV vectors. EMBO Mol Med 6:194–211
12. Ghosh A, Yue Y, Duan D (2011) Efficient transgene reconstitution with hybrid dual AAV vectors carrying the minimized bridging sequences. Hum Gene Ther 22:77–83
13. Ghosh A, Yue Y, Lai Y et al (2008) A hybrid vector system expands adeno-associated viral vector packaging capacity in a transgene-independent manner. Mol Ther 16:124–130
14. Ghosh A, Yue Y, Duan D (2006) Viral serotype and the transgene sequence influence overlapping

adeno-associated viral (AAV) vector-mediated gene transfer in skeletal muscle. J Gene Med 8: 298–305

15. Greenwald DL, Cashman SM, Kumar-Singh R (2013) Mutation-independent rescue of a novel mouse model of Retinitis Pigmentosa. Gene Ther 20:425–434
16. Mao H, Gorbatyuk MS, Rossmiller B et al (2012) Long-term rescue of retinal structure and function by rhodopsin RNA replacement with a single adeno-associated viral vector in P23H RHO transgenic mice. Hum Gene Ther 23:356–366
17. Millington-Ward S, Chadderton N, O'Reilly M et al (2011) Suppression and replacement gene therapy for autosomal dominant disease in a murine model of dominant retinitis pigmentosa. Mol Ther 19:642–649
18. Mussolino C, Sanges D, Marrocco E et al (2011) Zinc-finger-based transcriptional repression of rhodopsin in a model of dominant retinitis pigmentosa. EMBO Mol Med 3:118–128
19. McCarty DM (2008) Self-complementary AAV vectors; advances and applications. Mol Ther 16:1648–1656
20. Kay CN, Ryals RC, Aslanidi GV et al (2013) Targeting photoreceptors via intravitreal delivery using novel, capsid-mutated AAV vectors. PLoS One 8:e62097
21. Goto Y, Peachey NS, Ripps H et al (1995) Functional abnormalities in transgenic mice expressing a mutant rhodopsin gene. Invest Ophthalmol Vis Sci 36:62–71
22. Pennesi ME, Michaels KV, Magee SS et al (2012) Long-term characterization of retinal degeneration in rd1 and rd10 mice using spectral domain optical coherence tomography. Invest Ophthalmol Vis Sci 53:4644–4656
23. Umino Y, Solessio E, Barlow RB (2008) Speed, spatial, and temporal tuning of rod and cone vision in mouse. J Neurosci 28:189–198
24. Prusky GT, Alam NM, Beekman S et al (2004) Rapid quantification of adult and developing mouse spatial vision using a virtual optomotor system. Invest Ophthalmol Vis Sci 45:4611–4616
25. Mueller C, Flotte TR (2008) Clinical gene therapy using recombinant adeno-associated virus vectors. Gene Ther 15:858–863
26. Grieger JC, Samulski RJ (2012) Adeno-associated virus vectorology, manufacturing, and clinical applications. Methods Enzymol 507:229–254
27. Flannery JG, Zolotukhin S, Vaquero MI et al (1997) Efficient photoreceptor-targeted gene expression in vivo by recombinant adeno-associated virus. Proc Natl Acad Sci U S A 94: 6916–6921
28. Wang L, Blouin V, Brument N et al (2011) Production and purification of recombinant adeno-associated vectors. Methods Mol Biol 807:361–404
29. Zolotukhin S, Potter M, Zolotukhin I et al (2002) Production and purification of serotype 1, 2, and 5 recombinant adeno-associated viral vectors. Methods 28:158–167

INDEX

A

AAV. *See* Adeno-associated virus (AAV)
Acetylation 102
Adeno-associated virus (AAV) 392, 395, 397, 398, 407
AFM. *See* Atomic force microscopy (AFM)
Age-related macular degeneration (AMD) 346, 347
All-*trans*-retinal (ATR) 10, 39, 63, 235–238, 244, 245, 327–329, 331–341, 346–348
All-*trans*-retinol 328–341, 347, 354, 360, 364
Arrestin (Arr) 4, 10, 14, 77–93, 235–249, 252, 258, 294
Atomic force microscopy (AFM) 173, 175–177, 180–182, 189–201, 222
ATR. *See* All-*trans*-retinal (ATR)

B

Bacteriorhodopsin 5, 63, 197
Bicelle 67–75, 77–93, 236
Bioreactor 40, 42, 48, 52, 161–164, 170
Bis-retinoids 328, 329

C

Camera charge coupled device (CCD) 291, 330
Chromophore 3–5, 7–9, 11–14, 30, 35, 39, 56, 61, 63, 115, 142, 174, 199, 249, 255, 258, 327–341, 345, 346, 348, 363, 364, 370
Chromophore hydrolysis 11
9-*cis*-retinal 8, 10, 41, 46, 52, 347–350, 352–354, 365–367, 373, 377, 378, 387
11-*cis*-retinal 3, 4, 8, 9, 39, 43, 47, 49, 50, 52, 53, 82, 135, 138–140, 146, 150, 153, 161, 164, 165, 174, 175, 196, 199, 236, 237, 249, 327, 328, 345–355, 363–365, 367
Concanavalin A (Con A) 21, 22, 68–71, 74, 222
Concanavalin A affinity chromatography 21, 22, 70
Cone 4, 14, 67, 252, 329, 346, 353, 361, 364–366, 391, 401, 407
Confocal microscopy 301, 303, 305
Conformational change 11, 13, 14, 78, 79, 97, 108, 113–121, 123–131, 159, 236, 243, 244, 261
Connecting cilium 27, 267, 268, 281, 288
Crosslinking 222, 229–230
Cryo-electron tomography (Cryo-ET) 268, 269, 271
Crystal imaging 59–60
Crystallization 3, 5, 26, 31, 37, 39–53, 55, 61, 63, 75, 80, 276, 287
Crystals 22, 39, 51, 53, 55–63, 80, 98, 103, 105, 108, 109, 153, 197, 222, 268, 287, 289, 375

D

1D4 antibody affinity chromatography 22, 40, 52
Dark-adapted bovine retinas 21–38, 129
DDM. *See n*-dodecyl-β-D-maltopyranoside (DDM)
Degenerative retinal diseases 345–361
Dendra2 ..... 294–297, 299–303, 306
Detergent 3, 21, 22, 24, 25, 30–33, 35–38, 0, 51, 67–71, 74, 78, 80–83, 87, 98, 102, 106, 107, 114, 116, 126, 127, 131, 134, 135, 137–141, 152, 153, 164, 165, 168, 170, 192, 224, 228, 230, 232, 236, 403
Deuterated 11-*cis*-retinal 135, 139, 140
Deuterium oxide (D_2O) 84, 85, 89–91, 113–117, 119, 121, 123, 125, 127–131
Dialysis 24, 31–33, 35, 36, 115, 134, 135, 141, 142, 223, 227, 232
Diffusion coefficient 151, 152, 207, 211, 213, 309, 310, 314, 317–319, 321
Disk membranes 4, 77, 78, 82, 90, 92, 134, 136–141, 152, 153, 155, 189–201, 222, 236, 267, 294–296, 301, 345
Disulfide bridge 6–7
D_2O. *See* Deuterium oxide (D_2O)
n-Dodecyl-β-D-maltopyranoside (DDM) 24, 25, 32, 33, 35, 68, 74, 81, 83, 87, 98, 99, 115, 116, 125–127, 131, 152, 161, 164, 165, 170, 223, 224, 227, 230, 245, 246, 373, 381, 388
Dose response 102–106, 108, 372, 378–379, 382–383, 387, 388

E

Electroretinography (ERG) 348, 349, 352, 353, 355–356, 361, 392, 394, 397, 401–403, 406, 408
ERG. *See* Electroretinography (ERG)
Escherichia coli 40, 43, 238
Extinction coefficient 30, 50, 70, 86, 101, 115, 226, 237, 238, 242, 246, 354, 355, 360

F

Fluorescence relaxation after photoconversion (FRAP) 315, 320
Fluorescence spectroscopy 205–218, 236, 242–244

Beata Jastrzebska (ed.), *Rhodopsin: Methods and Protocols*, Methods in Molecular Biology, vol. 1271,
DOI 10.1007/978-1-4939-2330-4, © Springer Science+Business Media New York 2015

Fluorophore.....56, 106, 206, 208, 211, 216, 218, 236, 238, 242, 294, 315, 321, 329, 330, 340

G

Gene therapy.....391–409
Glycosylation.....6–9, 40, 370
G protein-coupled receptor (GPCR).....3–14, 21, 40, 67, 77, 80–82, 98, 104, 133, 159, 174, 175, 190, 209, 216, 221, 222, 253, 345, 370–372, 374, 379
GRK1. *See* Rhodopsin kinase (GRK1)
GTP_gS exchange assay.....72, 73

H

HEK293S GnTI-cells.....40, 43–46, 48, 52
Heterotrimeric G protein.....71–73, 75, 104, 221
High performance liquid chromatography (HPLC).....24, 42, 50, 102, 107, 115–117, 119, 126, 236, 349, 350, 355, 357, 358, 360, 361
High-throughput screening (HTS).....369–389
Histidine hydrogen-deuterium exchange mass spectrometry (His-HDX-MS).....123, 125
HPLC. *See* High performance liquid chromatography (HPLC)
HTS. *See* High-throughput screening (HTS)
Hydrogen-deuterium (H/DX or HDX) exchange.....113–121, 123–125, 127, 128, 130, 131
Hydrometer.....23, 34
Hydroxyapatite column chromatography.....140–141
Hydroxyl radical heteronuclear multiple-quantum correlated (HMQC) spectroscopy.....91, 93

I

Image processing.....191, 195, 200, 201, 312, 316–317
Imaging.....55–63, 176, 180, 189–201, 206, 215, 216, 218, 231, 268, 275–277, 279, 281, 286–289, 294, 296, 298–299, 301–306, 311–313, 315–318, 320, 321, 329, 330, 334, 336–340, 349, 358, 360, 393, 394, 397, 399, 401, 404, 408, 409
Interphotoreceptor retinoid binding protein (IRBP).....328
Intramolecular interactions.....152
Intraperitoneal (IP) injection.....353, 355, 358, 361, 364
Intravitreal injection.....363, 392
Isotope labeling.....161

L

Lauryl-maltose-neopentyl-glycol (LMNG).....25, 32, 33, 68, 224, 230, 232
LCA. *See* Leber congenital amaurosis (LCA)
LC/MS. *See* Liquid chromatography coupled with mass spectrometry (LC/MS)
LC-MS/MS.....126–128, 130, 131
Leber congenital amaurosis (LCA).....10, 252, 346, 347, 352
Light damage.....358, 359, 361, 394, 406, 409
Lipids.....22, 31, 37, 43, 51, 67–69, 71, 74, 78, 80–83, 85–87, 134, 135, 140–142, 145, 147–149, 154–156, 170, 173, 174, 183, 189, 190, 194, 197–199, 201, 205, 267, 273
Lipofuscin.....328–331, 334–337, 339, 340, 346, 347
Liquid chromatography coupled with mass spectrometry (LC/MS).....97, 100–107
LMNG. *See* Lauryl-maltose-neopentyl-glycol (LMNG)
LTQ-Orbitrap.....100, 126
Luciferase assay.....393, 396–397
Luminescence.....371, 374, 377–379, 381, 382, 384

M

MassMatrix.....102, 117
Mass spectrometry.....10, 97, 113–121, 123, 126, 129, 131
MatLab scripts.....152, 212, 254, 257, 259
Membrane protein.....22, 30, 31, 37, 40, 67, 75, 77, 80, 106, 107, 113, 114, 161, 167, 173, 175, 180, 182, 189, 190, 196, 197, 207, 221, 232, 294
Meta I. *See* Metarhodopsin I (Meta I)
Meta II. *See* Metarhodopsin II (Meta II)
Metarhodopsin I (Meta I).....4, 11, 72, 135, 141, 145–149, 154, 155, 236, 239, 246, 248
Metarhodopsin II (Meta II).....4, 11, 13, 39, 47, 49, 50, 69, 71–74, 97, 100, 135, 141, 143, 146–149, 151, 154, 155, 169, 235, 236, 239–244, 246–248, 327
Methyl-TROSY spectra.....91
MicroRNA (miRNA).....392, 393, 395, 396, 407
miRNA. *See* MicroRNA (miRNA)
Mislocalization.....293
Multiphoton microscopy.....298, 306, 310–311, 314

N

NADPH. *See* Nicotinamide adenine dinucleotide phosphate (NADPH)
NanoScope Control software.....191, 195, 200
Near UV circular dichroism (CD) spectroscopy.....82, 83, 87
Nicotinamide adenine dinucleotide phosphate (NADPH).....328, 331, 334, 341
NMR. *See* Nuclear magnetic resonance (NMR)
Non-linear optical (NLO) imaging.....55–57
Nuclear magnetic resonance (NMR).....11, 14, 67, 85, 89–92, 133–157, 159–162, 165–170

O

Oligomer.....14, 210, 211, 221, 222
Opsin.....4, 5, 10–14, 21, 30, 31, 33, 40, 49–51, 53, 62, 63, 82, 97–98, 120, 125–130, 134, 139, 140, 166, 175, 199, 200, 213, 215, 216, 222, 235, 244, 245, 248, 255, 311, 320, 328, 347, 353, 364, 365, 370–384, 387, 395

P

Palmitoylation 6–8, 174
PEI. *See* Polyethylenimin (PEI)
P23H opsin 370–384, 387
Phosphorylation 6, 10, 77, 82, 102, 237, 240, 249, 251, 255, 258
Photoactivation 8, 10, 11, 13, 34, 35, 56, 60, 63, 98, 159–170, 238, 310, 313, 315, 317, 319–321
Photoconversion 294–301, 303–305, 310, 313–317, 319
Photoisomerization 327
Phototransduction 251, 254, 255, 260–262, 267, 309, 364
PIE-FCCS. *See* Pulsed-interleaved excitation fluorescence cross-correlation spectroscopy (PIE-FCCS)
pK_a 123–125, 129, 130
Polyethylenimin (PEI) 41, 45, 51, 372, 383
Post-translational modification 5–8, 174, 267
Prodrugs 348
Protein dynamics 133–157, 310, 321
Protein proteolytic digest 102, 107
Protein unfolding 174, 177, 181
ProtMapMS 103
Pulsed-interleaved excitation fluorescence cross-correlation spectroscopy (PIE-FCCS) 205–218, 222

R

Radiolytic protein footprinting 97
RDH. *See* Retinol dehydrogenase (RDH)
Regeneration 8–10, 30, 135, 138–140, 164–165, 224, 230, 238, 328, 346, 348, 353
Renewal of outer segments (OS) 295, 303–304
Retina 3–5, 21–38, 77, 174, 175, 190, 237, 269, 271, 273–274, 284, 285, 294, 295, 297, 300, 301, 303–306, 313, 319, 328, 330, 334, 347–349, 358, 360, 363–365, 392, 398, 399, 401, 404, 406–409
Retinal 2, 21, 39, 63, 82, 134, 165, 174, 236, 252, 269, 296, 313, 328, 345–361, 363, 370, 391–409
Retinal pigment epithelium (RPE) 3, 36, 300, 301, 305, 319, 328, 329, 346, 347, 358, 360, 363, 394, 399
Retinitis pigmentosa (RP) 8, 12, 346, 347, 370, 391
Retinol dehydrogenase (RDH) 328, 334, 347
Retinylamine 347, 348, 350, 354, 358–360
Rhodopsin
  concentration 24, 37, 75, 86, 87, 115, 153, 226, 227, 238
  diffusion 309–322
  dimer 194, 199–201, 205–218, 222
Rhodopsin-arrestin binding 77–93
Rhodopsin kinase (GRK1) 4, 14, 77, 78, 82, 235, 237
Rhodopsin mutants 48–50, 177, 178, 180, 181
Rhodopsin purification 21–38, 140–141
Rhodopsin-transducin complex 221–232
Rhodopsin transient complexes 251–262
Rod 10, 21, 28, 39, 67, 78, 98, 235, 253, 255, 258, 259, 267–291, 294–296, 299, 310, 311, 316, 320, 327, 329–335, 341, 346, 370, 384, 391, 395, 398, 401, 407
Rod outer segments (ROS) 4, 5, 21, 23–24, 27–37, 40, 68–70, 77, 83, 86, 87, 100, 114, 115, 125–127, 129, 131, 134, 136–138, 140, 174–178, 180, 181, 190, 191, 193, 194, 198–201, 222–227, 231, 232, 236, 237, 240–242, 244, 248, 269–271, 274–281, 283–290, 314, 315, 317, 328, 332, 340, 370
Rod photoreceptor cilium 267–291
ROS. *See* Rod outer segments (ROS)
ROS purification 30–33, 129

S

Scanning laser ophthalmoscope (SLO) 350, 358, 360
Schiff base 4, 8, 9, 13, 47, 49, 138, 236, 238, 244–246, 327, 345, 347, 348
SDS-PAGE 22, 49, 50, 225–227, 229, 231, 232, 242, 397
Second harmonic generation (SHG) 55, 56, 61, 63
shRNA 392, 393, 395, 396
Signaling microcompartments 309–322
Single-molecule force spectroscopy (SMFS) 173–184
Size exclusion chromatography 21, 24–25, 30–33, 40, 49, 223, 224, 228, 230, 232
SLO. *See* Scanning laser ophthalmoscope (SLO)
SMFS. *See* Single-molecule force spectroscopy (SMFS)
Solid-State Deuterium NMR Spectroscopy 133–157
Solid-state magic angle spinning (MAS) NMR spectroscopy 159, 161, 165
Solubilization 35, 37, 68, 69, 98, 100, 153, 170, 223, 226, 232, 286
Spectral-domain optical coherence tomography (SD-OCT) 350, 358, 392, 394, 397, 400
Stargardt's disease 346, 347, 360
Structural dynamics 97–109
Structural waters 97–109
Subretinal injection 392, 394, 397–399, 406, 408
Sustained drug delivery 363
Systems biology 251–262

T

Toxicity 328, 348, 363, 370
TPEF. *See* Two-photon excited fluorescence (TPEF)
TPM. *See* Two-photon microscopy (TPM)
Trafficking 268, 293–306
Transducin 4, 11, 14, 75, 77–79, 82, 135, 174, 221–232, 235, 237, 251, 268, 294, 309
Transducin-derived high-affinity GαCT2 peptide 135, 147, 154
Transfection 162, 213, 215, 383, 384, 396, 397, 408
Transmembrane (TM) domain 98, 104, 105, 108, 109
Transmembrane helix 6
Transmission electron microscopy 222, 224, 230, 279

Two-photon excited fluorescence (TPEF) 55–57, 60–63
Two-photon microscopy (TPM) 55–63

U

Urea-washed ROS membranes 68, 69
UV-visible spectrophotometer 40, 41, 43, 52, 349

V

Visual cycle 10, 346–348, 351, 363, 364
Visual pigment 4, 8, 14, 251, 345, 347, 348, 353, 363, 370
Vitamin A 252, 345–361, 363
Vitrification 276–277

W

Water molecules 11, 12, 14, 98, 105, 109

X

Xcalibur 118, 126, 128
Xenopus laevis 304, 310–313, 320
X-ray crystallography 11, 14, 67, 79, 113, 134, 149

Z

Zinc extraction 24, 30–31, 35, 37